

2011

EXPERIMENTAL INVESTIGATION OF HEAT
TRANSFER AND PRESSURE DROP
CHARACTERISTICS OF WATER AND
GLYCOL-WATER MIXTURE IN MULTI-
PORT SERPENTINE MICROCHANNEL
SLAB HEAT EXCHANGERS

Md Mesbah-ul Khan
University of Windsor

Follow this and additional works at: <http://scholar.uwindsor.ca/etd>

Recommended Citation

Khan, Md Mesbah-ul, "EXPERIMENTAL INVESTIGATION OF HEAT TRANSFER AND PRESSURE DROP CHARACTERISTICS OF WATER AND GLYCOL-WATER MIXTURE IN MULTI-PORT SERPENTINE MICROCHANNEL SLAB HEAT EXCHANGERS" (2011). *Electronic Theses and Dissertations*. Paper 462.

This online database contains the full-text of PhD dissertations and Masters' theses of University of Windsor students from 1954 forward. These documents are made available for personal study and research purposes only, in accordance with the Canadian Copyright Act and the Creative Commons license—CC BY-NC-ND (Attribution, Non-Commercial, No Derivative Works). Under this license, works must always be attributed to the copyright holder (original author), cannot be used for any commercial purposes, and may not be altered. Any other use would require the permission of the copyright holder. Students may inquire about withdrawing their dissertation and/or thesis from this database. For additional inquiries, please contact the repository administrator via email (scholarship@uwindsor.ca) or by telephone at 519-253-3000ext. 3208.

EXPERIMENTAL INVESTIGATION OF HEAT TRANSFER AND PRESSURE DROP
CHARACTERISTICS OF WATER AND GLYCOL-WATER MIXTURE IN MULTI-PORT
SERPENTINE MICROCHANNEL SLAB HEAT EXCHANGERS

by
Md. Mesbah-ul Ghani Khan

A Dissertation
Submitted to the Faculty of Graduate Studies
through the Department of Mechanical, Automotive and Materials Engineering
in Partial Fulfillment of the Requirements for
the Degree of Doctor of Philosophy at the
University of Windsor

Windsor, Ontario, Canada

2011

@ 2011 Mesbah G. Khan

EXPERIMENTAL INVESTIGATION OF HEAT TRANSFER AND PRESSURE
DROP CHARACTERISTICS OF WATER AND GLYCOL-WATER MIXTURE IN
MULTI-PORT SERPENTINE MICROCHANNEL HEAT EXCHANGERS

by
Md. Mesbah-ul Ghani Khan

APPROVED BY:

M. Schumack, External Examiner
University of Detroit Mercy

S. Das
Department of Civil & Environmental Engineering

G. Rankin
Department of Mechanical, Automotive & Materials Engineering

N. Zamani
Department of Mechanical, Automotive & Materials Engineering

A. Fartaj
Department of Mechanical, Automotive & Materials Engineering

X. Chen, Chair of Defense
Department of Electrical & Computer Engineering

20 May 2011

AUTHOR'S DECLARATION OF ORIGINALITY

I hereby certify that I am the sole author of this thesis and that no part of this thesis has been published or submitted for publication.

I certify that, to the best of my knowledge, my thesis does not infringe upon anyone's copyright nor violate any proprietary rights and that any ideas, techniques, quotations, or any other material from the work of other people included in my thesis, published or otherwise, are fully acknowledged in accordance with the standard referencing practices. Furthermore, to the extent that I have included copyrighted material that surpasses the bounds of fair dealing within the meaning of the Canada Copyright Act, I certify that I have obtained a written permission from the copyright owner(s) to include such material(s) in my thesis and will included copies of such copyright clearances to my appendix.

I declare that this is a true copy of my thesis, including any final revisions, as approved by my thesis committee and the Graduate Studies office, and that this thesis has not been submitted for a higher degree to any other University or Institution.

ABSTRACT

Microchannels have several advantages over traditional large tubes. Heat transfer using microchannels recently have attracted significant research and industrial design interests. Open literatures leave with question on the applicability of classical macro-scale theory in microchannels. Better understanding of heat transfer in various microchannel geometries and building experimental database are continuously urged. The purpose of this study is to contribute the findings and data to this emerging area through carefully designed and well controlled experimental works.

The commercially important glycol-water mixture heat transfer fluid and multi-port slab serpentine heat exchangers are encountered in heating and cooling areas, e.g. in automotive, aircraft, and HVAC industries. For a given heat duty, the large diameter tubes experience turbulent flow whereas the narrow channels face laminar flow and often developing flow. Study of low Reynolds number developing glycol-water mixture laminar flow in serpentine microchannel heat exchanger with parallel multi-port slab is not available in the open literature. Current research therefore experimentally investigates glycol-water mixture and water in simultaneously developing laminar flows. Three multi-port microchannel heat exchangers; straight and serpentine slabs, are used for each fluid.

Friction factors of glycol-water mixture and water flows in straight slabs are higher than conventional fully developed laminar flow. If a comprehensive pressure

balance is introduced, the results are well compared with conventional Poiseuille theory. Similar results are found in serpentine slab. The pressure drop for the straight core is the highest, manifolds are the intermediate, and serpentine is the least; which are beneficial for heat exchangers.

The heat transfer results in serpentine slab for glycol-water mixture and water are higher and could not be compared with conventional fully developed and developing flow correlations. New heat transfer correlations are therefore developed in current study. The experimental data are compared with improved scheme of modified Wilson Plot Technique and numerical simulation having the same geometries and operating conditions. Very good agreements in results were found in all cases. The presence of adiabatic serpentine bend in multi-port flat slab heat exchanger enhances more heat transfer with less pressure drop penalty as compared to the initial entrance condition caused by the inlet manifold.

Dedicated

First, to the Almighty ALLAH

Who kept me alive and without HIS supports and guidance

My PhD program would not have moved forward to the end.

Second, to my beloved

wife **Sharmin Shahriar Akhter,**

son **Samin Arman Khan,**

and

daughter **Maleeha Nawar Khan**

who sacrificed a lot for my dream to come true

ACKNOWLEDGEMENTS

First and foremost, the author is all along thankful to the Almighty for sustaining and pulling him through this research work and all his life.

The author expresses deep appreciation to his advisor Dr. Amir Fartaj for sincere and tireless guidance, supports, and astute suggestions throughout the research work. Without his expert supervision, appreciation, and continuous inspiration, author's successful completion of this research would not have been possible with the same strength, caliber and zest as carried out and presented in this dissertation.

The author would like to thank his advisory committee members, Dr. G. Rankin, Dr. N. Zamani, and Dr. S. Das for their expensive suggestions and comments. The author deeply acknowledges the generous dedication of their time through invaluable inputs and directions at various stages of the research as well as in reviewing the dissertation write-up.

Appreciation and intense acknowledgement go to Mr. Andy Jenner for friendly providing the technical supports and services in fabricating, installing, and troubleshooting of various equipment and components during and after the construction phase of the developed experimental test facility. The author also acknowledges the cordial services by Mr. Pat Seguin for technical and electronic supports associated with the experimental facility.

Thanks must also go to Ms. Rose Gignac for providing friendly secretarial supports throughout the author's research at the Department of Mechanical, Automotive, and Materials Engineering. The secretarial supports for graduate and teaching assistantships provided by Ms. Barb Denomey are also acknowledged.

Financial supports provided by the Natural Sciences and Engineering Research Council of Canada (NSERC) in the forms of research and equipment grant for setting up the experimental facility and for conducting the research are highly acknowledged.

NSERC Canada Graduate Scholarship (CGS) awarded to the author in carrying out the research is gratefully acknowledged. The author is also thankful for being awarded the Ontario Graduate Scholarship (OGS), Ontario Graduate Scholarship for Science and Technology (OGSST), Canada Research Scholarship, University of Windsor Tuition Scholarship, and University of Windsor President Excellence Scholarship. The financial supports in the form of Graduate and Teaching Assistantships provided by the department of Mechanical, Automotive, and Materials Engineering at University of Windsor are sincerely acknowledged.

It is indeed to be thankful to Mustafizur Rahman for being a great friend who, in addition to author's family members, was one of the continuous sources of inspiration for completing this program.

Including Mosa, Moinuddin, Ataul Bari, Jahir, Bappee, and Faisal, there are many colleagues and friends to mention to whom the author is thankful for various supports, cooperation and wonderful companies.

At last, the author would like to thank and express his sincere appreciation to his wife Sharmin, son Samin, and daughter Maleeha for their continued patience, understanding, and inspiration throughout the duration of this research and until the printing of the dissertation. Thank you all for your sacrifices by allowing me to pursue my PhD dream to come true.

TABLE OF CONTENTS

AUTHOR’S DECLARATION OF ORIGINALITY	iv
ABSTRACT	v
DEDICATION	vii
ACKNOWLEDGEMENTS	viii
NOMENCLATURE	xxiii
LIST OF PEER-REVIEWED PUBLICATIONS FROM CURRENT RESEARCH	xxiv
CHAPTERS:	
CHAPTER-1 INTRODUCTION	1
1.1 Motivation	14
1.2 Objectives and method of approach	16
CHAPTER-2 BACKGROUND THEORY AND CORRELATIONS	19
2.1 Dimensionless parameters in heat transfer and fluid flow	20
2.2 Available equations or correlations for traditional pipe flow	35
2.2.1 Fluid flow equations and correlations	37
2.2.2 Heat transfer equations and correlations	47
2.3 Conclusions on the availability of correlations	64
CHAPTER-3 LITERATURE SURVEY AND SCOPE OF CURRENT STUDY	65
3.1 Fluid flow and heat transfer characteristics in microchannels and MCHX	67
3.1.1 Flow friction (f) and Poiseuille number (Po) for single phase flow in microchannels	67
3.1.2 Critical Reynolds number (Re_{cr}) for single phase flow in microchannels	74
3.1.3 Heat transfer characteristics – the Nusselt number (Nu) for single phase flow in microchannels	77

3.1.4	Fluid flow and heat transfer characteristics in MCHX	85
3.1.5	Summary of literature review on fluid flow and heat transfer in microchannels and MCHXs	86
3.2	Scope of current research	91
3.3	Basis of test specimen designs and working fluid selection for current study	92
3.3.1	Channel size – hydraulic diameter range	94
3.3.2	Channel cross section – circular or non-circular	95
3.3.3	Flow passage – multi-port slab or single bare tubes	97
3.3.4	Multi-port slab shape – flat tube or round tube	99
3.3.5	Multi-port slab patterns – straight and serpentine	102
3.3.6	Multi-port slab material – metallic or non-metallic	103
3.3.7	Working fluids	105
3.4	Choice of operating flow regimes in current study	107
3.5	Conclusions and recommendations	109
CHAPTER-4	DEVELOPMENT & COMMISSIONING OF EXPERIMENTAL FACILITY AND DESIGN OF TEST PROCEDURES	112
4.1	Design and fabrication of microchannel test specimens	117
4.2	Design and fabrication of wind tunnel test chamber	125
4.3	Air handling system – the closed-loop thermal wind tunnel	127
4.3.1	Air velocity modeling in wind tunnel test section using Log-Tchebycheff point distribution method	130
4.3.2	Thermal grids for air temperature measurements in wind tunnel test section	133
4.4	Liquid handling system	136

4.5	Instrumentation and calibration	143
4.5.1	Calibration of liquid flow meters (DFM & IFM)	148
4.5.2	Calibration of liquid side pressure transducers (PTD)	152
4.5.3	Calibration of RTD and Thermocouple probes	153
4.5.4	Installation and calibration of Pitot Static probe	160
4.5.5	Calibration of airside differential pressure transducer (PTDD) & test section inlet wind tunnel air velocity	167
4.6	Data acquisition (DAQ) scheme	169
4.7	Commissioning and trouble shooting of the developed test facility and the experimental preparations and procedures	171
4.8	Heat balance (HB) on the developed test rig using MCHX #1	177
CHAPTER-5	DATA REDUCTION, EMPLOYMENT OF WILSON PLOT TECHNIQUE AND UNCERTAINTY ANALYSES	185
5.1	Evaluations of thermophysical properties of working fluids	188
5.2	Consolidated mean data sets of measured parameters	189
5.2.1	Liquid side measured parameters	191
5.2.2	Air side measured parameters	195
5.2.3	Test specimen side surface temperature measurement	198
5.3	Heat transfer rates and heat balance of the working fluids	200
5.4	Heat transfer performance parameters	203
5.4.1	Overall heat transfer coefficient (U)	203
5.4.2	Thermal resistances (R_{th})	206
5.4.3	Airside overall surface or fin efficiency (η_o)	208
5.4.4	Effectiveness and NTU	209

5.5	Employment of Wilson Plot technique to isolate the individual thermal resistances	211
5.6	Uncertainty analysis and error estimation	222
5.7	Calculations and data analyses tools	224
CHAPTER-6	PRESSURE DROP AND FLOW FRICTION OF WATER AND 50% ETHYLENE GLYCOL-WATER MIXTURE FLOWS IN MULTI-PORT STRAIGHT MICROCHANNEL SLABS	225
6.1	Treatment and separation of pressure losses in the test slab	227
6.2	Experimental procedures for water and glycol-water flows	243
6.3	Data reduction for water and glycol-water mixture flows	245
6.4	Results and discussions on water flow	248
6.4.1	Pressure drop in the test slab core, Δp_{mc}	249
6.4.2	Flow friction in the test slab channel, f_{ch}	253
6.4.3	Effect of Re on Po in the test slab channel	256
6.4.4	Conclusions on water flow in the test slab	259
6.5	Results and discussions on glycol-water mixture flow	261
6.5.1	Pressure drop in the test slab core, Δp_{mc}	262
6.5.2	Flow friction in the test slab channel, f_{ch}	267
6.5.3	Effect of Re on Po in the test slab channel	269
6.5.4	Conclusions on glycol-water flow in the test slab	271
CHAPTER-7	HEAT TRANSFER AND PRESSURE DROP CHARACTERISTICS OF WATER FLOW IN 2-PASS MULTI-PORT SERPENTINE MICROCHANNEL SLAB HEAT EXCHANGER	273
7.1	Methods of experiments and measurements	275

7.2	Treatment and separation of pressure losses in the test slab	279
7.3	Results and discussions on water flow	282
7.3.1	Total, core and segment-wise pressure drops	284
7.3.2	Heat transfer characteristics	289
7.4	Conclusions on water flow	297
CHAPTER-8	HEAT TRANSFER AND PRESSURE DROP CHARACTERISTICS OF ETHYLENE GLYCOL-WATER MIXTURE FLOW IN 2-PASS MULTI-PORT SERPENTINE MICROCHANNEL SLAB	300
8.1	Methods of experiments and measurements	302
8.2	Treatment and separation of pressure losses in the test slab	303
8.3	Results and discussions on glycol-water mixture flow	304
8.3.1	Total, core and segment-wise pressure drops	308
8.3.2	Heat balance between glycol-water mixture and air	311
8.3.3	Heat transfer rate and temperature variations	313
8.3.4	The NTU and Effectiveness of the test specimen	316
8.3.5	Overall thermal resistance ($R_{ov} = 1/UA$)	318
8.3.6	Nusselt number characteristics	319
8.4	Conclusions on glycol-water mixture flow	327
REFERENCES		331
APPENDIX-A	TABLE A1: TABULAR REPRESENTATION OF KEY OBSERVATIONS IN PREVIOUS LITERATURE SURVEY	358
APPENDIX-B	DETAILS OF THE DEVELOPED TEST FACILITY, TEST SPECIMENS, TEST CHAMBERS, INSTRUMENTS ETC.	373

B1. Details of the developed experimental test facility	374
B2. Details of the designed and fabricated MCHX test specimens	385
B3. Details of the designed & fabricated test chambers for MCHX	399
B4. Details of the designed and constructed water flow mixing and supply network for wind tunnel internal heat exchanger	407
B5. Details of flow meter (DFM) calibration certificate and curve	410
B6. Details of liquid side pressure transducer (PTD) calibration	419
B7. Details of airside differential pressure transducers (PTDD) and wind tunnel air velocity calibrations	427
B8. Temperature distribution and profiles at wind tunnel thermal grids and on test specimen surface	435
APPENDIX-C FLOW CHART AND TABLE FOR SOLVING THE NON- LINEAR REGRESSION EQUATIONS OF WILSON PLOT TECHNIQUE TO FIND HEAT TRANSFER COEFFICIENT	444
Figure C1: Developed flow chart for iteratively solving the equations of Wilson Plot Technique using non-linear regression analysis	445
Table C1: Developed data table for iteratively solving the equations of Wilson Plot Technique using non-linear regression analysis	446
APPENDIX-D TABLES OF EXPERIMENTALLY OBTAINED DATA FOR WATER AND 50%-50% ETHYLENE GLYCOL-WATER MIXTURE FLOWS IN MCHX TEST SPECIMENS	447
Table D1: Data for Water flow in multi-port straight microchannel slab (MCHX-1)	448

Table D2: Data for 50% Ethylene glycol-water mixture flow in multi-port straight microchannel slab (MCHX-2)	452
Table D3: Heat transfer and pressure drop data for Water flow in multi-port serpentine microchannel slab (MCHX-4)	454
Table D4: Heat transfer and pressure drop data for 50% Ethylene glycol-water mixture flow in multi-port serpentine microchannel slab (MCHX-4)	455
APPENDIX-E UNCERTAINTY ANALYSIS	457
E1 Addressing the uncertainty issues	458
E1.1 Uncertainty in independent (primary) parameters	460
E1.2 Uncertainty in dependent (secondary) parameters	462
E1.3 Uncertainty in thermophysical property evaluations	463
E2 Uncertainties in instruments, DAQ system, and sensors	464
E2.1 Digital caliper and geometric measurements	464
E2.2 Data Acquisition (DAQ) System	466
E2.3 Temperature sensors – RTDs and Thermocouples	473
E2.4 Pressure transducers (PTDs) – Liquid side	476
E2.5 Mass flow rate measurements – Liquid side	478
E2.6 Velocity and mass flow measurements – Air side	483
E3 Uncertainty in basic dependent parameters	486
E3.1 Bulk flow temperatures – Liquid and Air	486
E3.2 Inlet-exit temperature differentials – Liquid and Air	487
E3.3 Microchannel cross-sectional area – Single channel	488
E3.4 Heat transfer surface area – Liquid side	489

E3.5	Surface temperature – Test specimen wall	489
E3.6	Log-mean temperature difference (LMTD) – Overall	489
E3.7	Mass velocity or mass flux – Liquid side	490
E3.8	Reynolds number – Liquid side	491
E4	Uncertainty in fluid flow parameters – Liquid side	491
E4.1	Pressure drops – Total measured & core theoretical	491
E4.2	Friction factor – Liquid side	492
E4.3	Poiseuille number – Liquid side	493
E5	Uncertainty in heat transfer results	493
E5.1	Heat transfer rates – Liquid and Air sides	493
E5.2	Heat transfer coefficient – Liquid side	494
E5.3	Nusselt number – Liquid side	495
E5.4	Thermal resistances – Overall and Liquid side	495
E5.5	Test specimen Effectiveness	496
E5.6	Test specimen NTU	498
APPENDIX-F LIST OF CONTRIBUTIONS		499
VITA AUCTORIS		504

NOMENCLATURE

\dot{m}	Mass flow rate of working fluid [kg/s]
\dot{V}	Volume flow rate of working fluid [m^3/s]
2-D	Two dimensional
3-D	Three dimensional
A	Area [m^2]; Variable in Equation (2.19)
A_c	Cross-sectional area ($\pi D^2/4$) of a channel or tube [m^2]
A_{ff}	Free flow area (at airside) of the finned-tube MCHEX [m^2]
A_{fr}	Frontal area of the finned-tube MCHEX [m^2]
Al	Aluminum and Precision error component in uncertainty analysis
A_s	Channel or tube surface area ($\pi DL = PL$) [m^2]
AVDEV	Average deviation
B	Variable in Equation (2.19)
Br	Brinkman number $\left(\frac{\mu V^2}{k \Delta T} \right)$
C	Constant in Poiseuille number Equation (2.10)
C^*	Ratio of experimental to theoretical Poiseuille numbers
CAD	Computer aided design
c_p	Specific heat of working fluid at a given temperature [$\text{J}/\text{kg} \cdot ^\circ\text{C}$]
Cu	Copper
D	Diameter [m]
DFM	Digital flow meter
D_h	Hydraulic diameter of a port in the multi-port microchannel slab [m]
D_i	Inside diameter of a port in the multi-port microchannel slab [m]

D_o	Outside diameter of a single microchannel port or MPE tube slab [m]
f	Friction factor
F	LMTD correction factor
f_d	Darcy friction factor ($4f_f$)
f_f	Fanning friction factor ($f_d/4$)
g	Gravitational acceleration [m/s^2]
G	Mass velocity or mass flux [$kg/m^2 \cdot s$]
Gr	Grashof number $\frac{g\beta(T_b - T_s)D^3}{\nu^2}$
h	Heat transfer coefficient [$W/m^2 \cdot ^\circ C$]
H	Test slab thickness i.e. height in Y-direction [mm]
h_L	Head loss [m]
HVAC/R	Heating, ventilation, air-condition, and refrigeration
HX	Heat exchanger
ID	Inner diameter
k	Thermal conductivity [$W/m \cdot ^\circ C$]
Kn	Knudsen number ($Kn = \lambda / D_h$)
L	Flow length; test slab length [m]
L_{hy}	Hydrodynamic entrance length [m]
LMTD	Log-mean temperature difference
L_{th}	Thermal entrance length [m]
m	Mass of the fluid [kg]
MC	Microchannel
MCHS	Microchannel heat sink

MCHX	Microchannel heat exchanger
MEMS	Micro-Electro-Mechanical Systems
MFD	Micro-Flow Devices or Micro-Fluidic Devices
MPE	Multi-port extruded
MSE	Mean square error
NTU	Number of transfer unit
Nu	Nusselt number (hD/k)
P	Perimeter or circumference of tube or channel port [m]
Pe	Peclet number ($VD/\alpha = Re.Pr$)
Po	Poiseuille number (fRe)
Pr	Prandtl number $\left(\frac{\mu c_p}{k}\right)$
PTD	Pressure transducer (for liquid side)
PTDD	Differential pressure transducer (for airside)
q	Heat transfer rate [W]
R	Universal gas constant [J/kg.K]
Re	Reynolds number ($\rho VD/\mu$)
RTD	Resistance temperature detector (for liquid side)
Si	Silicon
SS	Stainless steel
STDEV	Standard deviation
T	Temperature [$^{\circ}C$]
t	Thickness
T_b	Bulk flow temperature of working fluid $(T_i + T_o) / 2$ [$^{\circ}C$]

$T_{f,a}$	Film temperature of flowing air $(T_{b,a} + T_{s,o}) / 2$ [$^{\circ}\text{C}$]
T_s	Surface temperature of flow channel [$^{\circ}\text{C}$]
U	Overall heat transfer coefficient; Uncertainty variable
V	Heat exchanger volume or heat transfer volume in channel [m^3]
V	Mean velocity of flowing fluid [m/s]
W	Test slab width in Z-direction i.e. airflow direction [mm]
WC	Water column (measuring instruments' capacity)
x^+	Dimensionless axial distance in Equation (2.16b)
y	Coefficient in Equation (2.12)
Z	Characteristic length [m]

Greek letters

δ	Boundary layer thickness [m]
β	Coefficient of thermal expansion [K^{-1}]
ρ	Density of working fluid [kg/m^3]
θ	Dimensionless temperature
μ	Dynamic viscosity of working fluid [kg/m.s or N.s/m^2]
ν	Kinematic viscosity or Momentum diffusivity of working fluid [m^2/s]
λ	Molecular mean free path [μm]
σ	Smaller-to-larger area ratio at point where flow area changes
ε	Surface roughness height [m]
Δp	Pressure difference or Pressure Drop [Pa]
ΔT	Mean temperature difference between two locations [$^{\circ}\text{C}$]
τ_w	Wall shear stress [Pa]

Subscripts

a	Air
b	Bulk
bucket	Bucket-weigh-stop watch method
ch	Channel
cr	Critical
d	Darcy
dev	Developing
DFM	Digital flow meter
em	Exit manifold
emt	Exit manifold tube
emt-c	Exit manifold tube contraction
f	Fanning; fin
F	Fitting
g	Glycol-water mixture
H	H-boundary condition (constant surface heat flux)
hy	Hydrodynamic
i	Inlet or entrance; inner side
im	Inlet manifold
imt	Inlet manifold tube
imt-e	Inlet manifold tube expansion
L	Loss
lam	Laminar

liq	Liquid
LMTD	Log-mean temperature difference
m	Mean & Exponent in Equation (2.12)
mc	Microchannel
mc-c	Microchannel port contraction
mc-e	Microchannel port expansion
n	Exponent in Equation (2.12)
o	Outlet or exit; outer side
p	Port & Exponent in Equation (2.12)
s	Surface
serp	Serpentine
serp-bend	Serpentine bend
T	T-boundary condition (constant surface temperature)
th	Thermal
total	Measured total in experiment
turb	Turbulent
v	Velocity
w	Water; channel wall

LIST OF PEER-REVIEWED PUBLICATIONS FROM CURRENT RESEARCH

1. Flow and heat transfer characteristics of water and ethylene glycol-water in a multi-port serpentine meso-channel heat exchanger. *International Journal of Thermal Sciences* 2011; DOI: 10.1016/j.ijthermalsci.2011.03.004.
2. The numerical study of fluid flow and heat transfer in a multi-port serpentine meso-channel heat exchanger. *Applied Thermal Engineering* 2011; DOI:10.1016/j.applthermaleng.2011.01.035.
3. A review on microchannel heat exchangers and potential applications. *International Journal of Energy Research* 2010; DOI:10.1002/er.1720.
4. Heat transfer experiments of ethylene glycol-water mixture in multi-port serpentine meso-channel heat exchanger slab (FEDSM-ICNMM2010-31131). In: *Proceedings of the 3rd Joint US-European Fluids Engineering Summer Meeting (FEDSM) and 8th International Conference on Nanochannels, Microchannels, and Minichannels (ICNMM)*, August 1-5, 2010, Montreal, Quebec, Canada 2010.
5. Experimental comparative study on heat transfer performances of circular, elliptical, and microchannel heat exchangers. In: *Proceedings of the Canadian Society for Mechanical Engineering Forum, CSME FORUM 2010*; Victoria, British Columbia, Canada, June 7-9, 2010.
6. Experiments of ethylene glycol-water mixture in multi-port circular straight microchannel slab. In: *Proceedings of the Society of Automotive Engineers (SAE) World Congress 2010* (Paper #2010-01-0326), Detroit, MI, USA, April 13-15.
7. Heat transfer correlation of a glycol-water mixture in a finned serpentine meso-channel slab. *Experimental Thermal and Fluid Science* 2010 (ETFS-D-10-00280), (Under review).

CHAPTER – 1

INTRODUCTION

1.0 INTRODUCTION

Energy use is a vital part of everyday life, and thus its production and appropriate consumption are the keys to sustainable economic growth. Environmental concerns with respect to thermal, air, and water pollution, as well as the disposal of waste have resulted in the proliferation of energy conservation and recovery measures, and the implementation of clean new and renewable energy sources. Heat exchangers are a central component of many of the above processes. The importance and diverse application of heat exchangers have witnessed significant gains over the decades across multiple industry sectors including power generation, transportation, HVAC/R, electronics, and manufacturing. The dominant use of heat exchangers, however, is encountered in the energy and thermo-hydrodynamic areas.

Heat exchangers provide for the flow of thermal energy and allow the heat transfer between two fluids at different temperatures separated by a flow passage wall. Entropy is generated by the transfer of heat across a finite temperature difference and by irreversible friction flow by the flow friction dissipated losses [1]. Because the minimization of entropy generation generally leads to the conservation of energy, there is a focus on both enhanced heat transfer as well as improved flow performance. A forced convection mechanism accounts for heat transfer in almost all heat exchangers. It is governed by the total thermal resistance of the participating fluids, the heat transfer surface, and the tube walls. The thermal resistance is determined by the boundary layer

thickness that develops on the heat transfer surface. Generally, performance improvements are achieved by augmenting the heat transfer coefficient between the fluid and the wall surface, which in turn increases the thermodynamic efficiency and reduces the operating cost.

In broad terms, the enhancement of heat transfer is associated with thermal design modifications that minimize entropy generation and improve the heat transfer coefficient. The dependence of numerous industry sectors on heat exchangers has driven the development of techniques to reduce the thermal resistance and to enhance the convective heat transfer in order to improve efficiency and reduce cost.

Numerous studies [1-6] have proposed various methods to enhance heat transfer performance, minimize pressure drops, and reduce the unit sizes of conventional heat exchangers already available. In the laminar flow regime, the maximum heat transfer enhancement limit associated with many of the proposed augmentation techniques is of the same order of magnitude, and it is independent of the wall boundary condition [1]. Applications where size is limited have led to the development of compact heat exchangers with a variety of tube shapes and sizes in various orientations; they offer high heat transfer surface density of about $700 \text{ m}^2/\text{m}^3$ [6-7].

Traditional air-to-liquid crossflow heat exchangers consist of conventional tubes of varying shapes and sizes; the airside generally accounts for about 80% of the total thermal resistance. Some authors have reported the airside thermal resistance up to 96%

[8-9]; such values indicate the importance of selecting the proper airside heat transfer correlation for the relevant heat exchanger design and application. Traditional heat exchangers generally use the flow passage sizes of 6 mm and larger with various geometries, orientations, and enhanced surfaces. However, the research into efficiency gains based on heat transfer augmentation, size shrinking, and thermal resistance diminution techniques has almost reached its limits with respect to the sizes and shapes of flow passages that are commercially available today.

Growing energy demands, space limitations for device packaging, energy and materials savings, ease of unit handling, etc., have focused the demand for miniaturized, light weight heat exchangers that can provide high heat transfer. The heat transfer intensification in thermo-fluid applications, which refers to the practices of obtaining increased heat transfer out of decreased sized heat exchangers has become a progressively demanding and growing research area [10]. The viability of small flow conduits has now come to the forefront because it is intuitive that smaller channel sizes increase heat transfer and reduce the unit size.

Current advancements in micro-machining and micro-miniaturization techniques have made possible the fabrication of small flow passages or 'microchannels'. Microchannels are broadly characterized by small flow passages of 1 mm in diameter or less, which allows for heat transfer surface densities to be $10000 \text{ m}^2/\text{m}^3$ or more [7, 10-11]; this value contrasts with compact heat exchangers having a density of $700 \text{ m}^2/\text{m}^3$. Note that the heat exchanger density in current study is $4000 \text{ m}^2/\text{m}^3$, which is about 6

times higher than the traditional compact heat exchanger. Due to the higher heat transfer, lower weight, and their space, energy, and materials savings potentials over their traditional tube and enhanced surface heat exchanger counterparts, microchannels can meet all the above mentioned challenges.

Microchannel thus represents an emerging technology in heat transfer enhancement research [12]. In the field of advanced energy systems, micro and nanotechnology have widespread potential such as to: improve energy storage, enhance renewable energy sources, achieve energy savings through advanced materials, and reduce combustion pollutants through nanoporous filters etc.; as well as in fuel cell catalysts and in hydrogen storage [13]. Advancement has also been made in generating electricity using novel nano-electromechanical systems and microfluidic devices such as the nano-engine, microchannel battery, micro-heat engine etc. [14]. Because of small diameters, microchannel arrays can increase the effective area for reactants and hence increase the power density of a fuel cell for the same flow rates [15-16].

To improve the efficiency and effectiveness of such narrow channel devices, superior understanding of the thermodynamic behaviors in microchannel flows is necessary [17]. As primary candidates for future heat exchanger components, microchannels and the technology have attracted extensive research attentions.

The heat transfer process in microchannels depends on the heat transfer surface area A_s , which varies linearly with the channel diameter D or hydraulic diameter D_h . The

channel flow rate, on the other hand, depends on the cross sectional area A_c of the channel, which varies linearly with D^2 . Hence the heat transfer surface area to volume ratio, A_s/V varies as $1/D$. As D decreases, the A_s/V increases. In the laminar flow regime for a microchannel, the local heat transfer coefficient, h , varies inversely with the channel diameter i.e. $h \propto 1/D$. Therefore as the channel diameter decreases the heat transfer coefficient increases as can be seen in Figure 1.1. As a result, the decreased channel diameter improves both the compactness of the unit as well as the heat transfer rate.

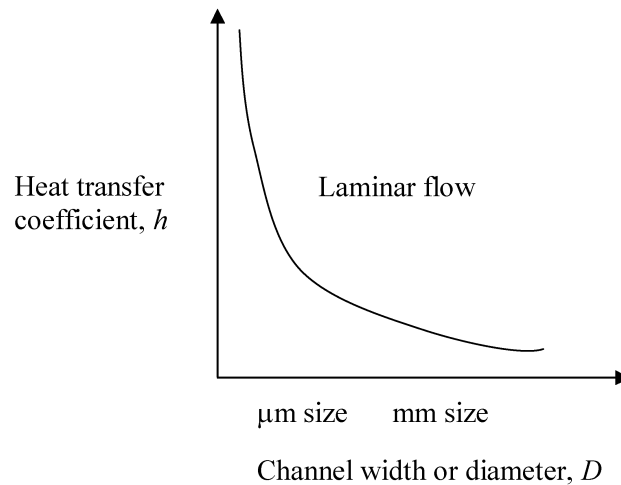


Figure 1.1. Effect of channel size D on heat transfer coefficient h in laminar flow

Efforts to explore smaller sized channels have resulted in a steady shift from larger diameter tubing (10 to 20 mm) to smaller diameter channels (1 mm to 0.01 mm). The term ‘microchannel’ has become an accepted classifier for heat transfer and fluid flow processes at smaller scale [18]. Some authors have attempted to classify small flow passages of typical thermal heat exchanger technology at microscale geometry with

respect to some key biological and engineering systems [19-20]. Any flow channel diameter or hydraulic diameter of 1 mm or below is broadly classified in the heat transfer and fluid flow literature as “microchannel”, “microtube” or “micro-device” [10, 21-28]. Figures 1.2 (a) and (b) illustrate two sample flow passages for different uses.

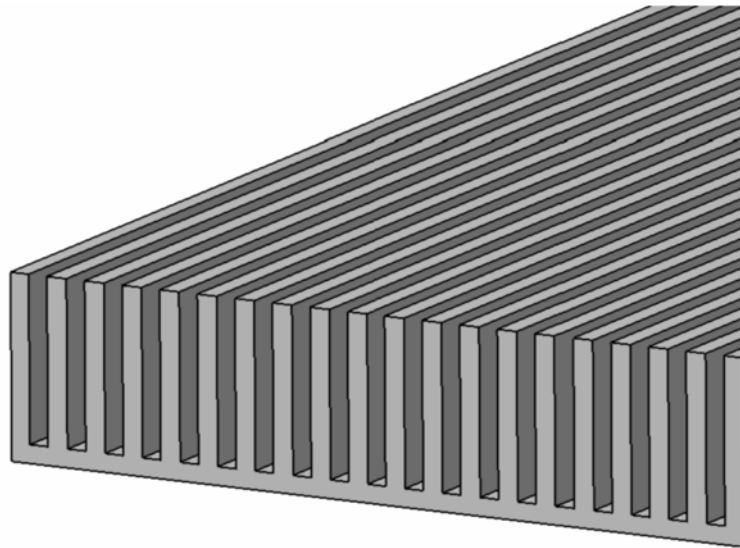


Figure 1.2a. Non-circular microchannel flow passages seen in heat sinks in electronics cooling.

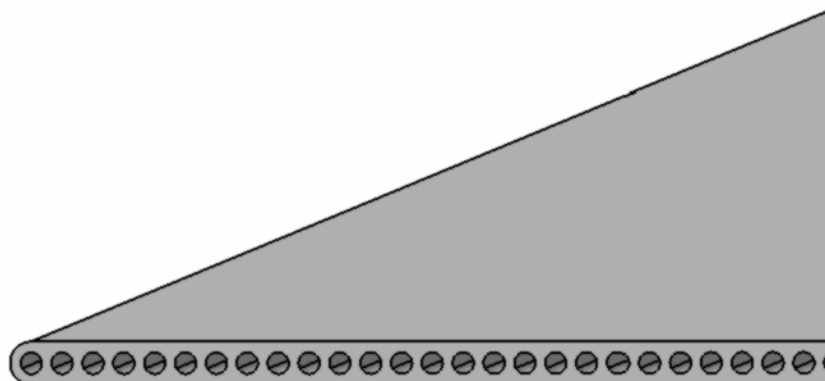


Figure 1.2b. Microchannel slab with circular ports used as core in thermal heat exchangers.

Some narrative features of a crossflow air-to-water microchannel heat exchanger (MCHX) relative to a conventional sized heat exchanger are: increased heat transfer rate, minimized air supply fan or blower capacity, reduced water supply pump power for a given flow rate, lower weight, and reduced unit size [12, 22, 29-31]. The flatness of a multi-port microchannel slab, which is the focus of current long-term research, can reduce the airside flow resistance, and result in increased airflow or reduced fan or blower power, or both.

For a given heat duty, the high heat transfer property of microchannels results in shorter channel lengths. Undesired axial heat conduction is also minimized because the channel length and fluid residence time are shortened as well as the entire bulk fluid stays in close contact with the microchannel walls. The fluid flow in multi-port MCHX slab is parallel and usually well distributed over a large number of small passages. This distribution reduces the flow velocity in each individual channel. Therefore the shorter parallel channel lengths and minimal axial heat conduction, combined with the well distributed flow, result in a low channel side pressure drop and hence reduce the requirements of liquid side pump capacity.

In the early stages of the development of microchannel heat sinks (MCHS), fin arrays both with and without variable tip clearance were analyzed for fully developed laminar flow [32]. It was confirmed that a capped, finned heat sink exhibits significant improvement in thermal performance over designs that are open at the fin tips. By

conducting experiments on the heat transfer characteristics of water flow in MCHS fabricated in a silicon wafer, it was demonstrated that the cooling of electronic components can be accomplished by the use of forced convective flow of fluid through microchannels [33-34]. With the surface temperature maintained at less than 130°C, the dissipated heat flux was observed to be on the order of $1.3 \times 10^7 \text{ W/m}^2$. The study confirmed the potential of microchannel technology in the field of electronics cooling and other heat transfer applications.

The concepts of electronics cooling have been further developed using MCHX [35]. A comprehensive review of published works on MCHS for electronics cooling is available, including critical findings and the effectiveness of such devices [36]. Research in this area focuses on solving the problems of electronics cooling using microchannels and MCHS. The heat generated by the circuitry is removed either by a liquid coolant flow through the channels or by airflow over the heated face of the object and thereby the heat transfer rates are investigated. For some investigation the channel surface was heated electrically and cold air was blown. In either case, the airflow is located as close as possible to the heat source. In some typical thermal-hydraulic applications, such as the single phase gas-to-liquid orientation, the heat exchangers generally use a metallic multi-port-in-flat-slab geometry.

The process of parallel, counter, or crossflow heat transfer in heat exchangers occurs between two fluids that are in motion, such as in the air-to-liquid crossflow heat exchanger in automotive applications. The magnitude of heat duty of heat exchangers

used in thermal and energy applications is typically higher than the heat duty of heat sinks used in electronics cooling. In many cases the geometric configurations, fluid flow orientations, and heat exchange processes of MCHX and MCHS are also different. Direct comparison of MCHX for thermal applications with MCHS used in electronics cooling research may not be relevant [22]. There is limited research in the open literature that focuses on heat transfer and fluid flow on MCHX for such thermal applications. Moreover, research data on MCHX is rarely cited in the open literature.

Compared to MCHS for electronics cooling applications, the research and development of microchannels and MCHX for thermal and other engineering applications is relatively recent. The investigation and application of microchannels can be found primarily in laboratory, micro-electro-mechanical systems (MEMS), micro-fluidic devices (MFD) settings. Applications for automotive heat exchangers exist as proprietary or in-house packages only. The mass production and application of microchannels as MCHX core elements are not very common in the commercial marketplace yet. Microchannels have yet to penetrate current heating and cooling applications, possibly due to: the lack of availability of adequate and well established data and design correlations in the open literature; insufficient understanding of heat transfer and fluid flow behaviors in microchannels; or the lack of systematic thermo-hydrodynamic characteristics and mechanical procedures for MCHX design methods.

The review of the literature reveals an open question: *do the classical fluid flow and heat transfer theories, correlations, and design methodology equally hold valid for*

microchannel flow and geometry? In recent studies it is however still not clear whether the correlations developed for classical macro-size tubes (>6 mm) are directly applicable for use in further down-sized flow passage such as in mini or microchannels (<3 mm). Existing arguments can be made to both sides of the question. Many authors thus emphasize the needs for more research in this area to develop data to help consolidate the arguments. In light of this view, research needs to be devoted to building the fluid flow and heat transfer correlations for microchannels, and thereby establish appropriate design parameters for the MCHX. From there, this information must be widely disseminated to foster growth and in today's various heating and cooling application needs.

The current paper surveys the open literature on the status and potential of microchannels and MCHX, identifies research needs, and scopes the potential of current research, as presented in the next sections. "Open literature" here implies access to the information.

Current research objectives focus on the experimental investigation of liquid flow friction factor in multi-port straight microchannel slab; and liquid heat transfer in multi-port serpentine microchannel slab and prototype MCHX in the air-to-liquid crossflow orientation. It aims at developing and validating the design correlations for microchannels and MCHX and addressing the discrepancies seen in previous studies [23, 37-38]. An example of such discrepancies in published results can be visualized in Figure 1.3 [37].

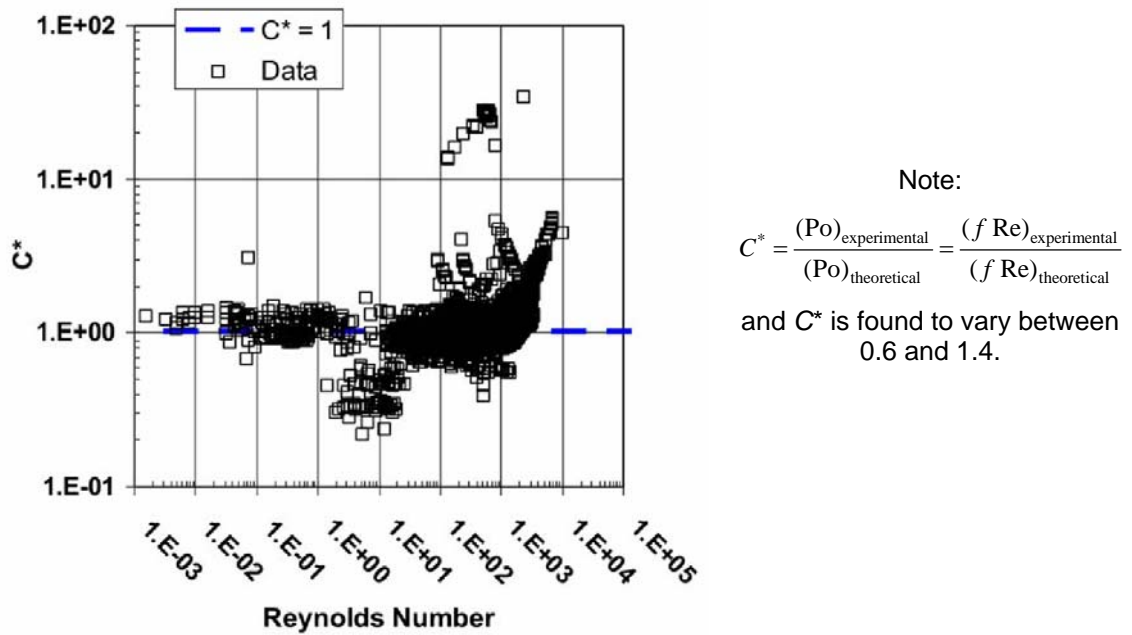


Figure 1.3. Variation of Poiseuille number, Po ratio (C^*) with Reynolds number (Re); where C^* , as defined above, is the ratio of the published experimental results for microchannel flow to the theoretical values for traditional pipe
 (Source: Steinke and Kandlikar 2006 [37], with permission)

The execution of a rigorous test procedure with high quality equipment and instruments may lead to a relatively more accurate data set with results that may be inline with a subset of the published results, possibly leading to the establishment of a consensus on microchannel quantitative results within the research community. This research will assess, quantify, and qualify the thermo-hydraulic performance and potential of MCHX for thermal applications.

The review of open literature included such issues as the critical Reynolds number for microchannel flow, and the applicability of classical heat transfer and fluid flow correlations in microchannels. In an attempt to explore some of these issues, a dynamic single phase crossflow experimental test facility is developed and microchannel test specimens with various flow passage geometries are fabricated in support of the current research. The test facility incorporates modern high accuracy instrumentation and automated data acquisition features into a highly flexible and versatile test bench. It provides heat transfer and fluid flow research capability for different microchannel geometries and shapes, across a number of fluids, in laminar to turbulent flow regimes, for a wide range of pressure and temperature.

Each fabricated microchannel test specimen can be used to investigate the fundamentals of heat transfer and pressure drop. Data on the mentioned test specimens are used to compare friction factor versus Reynolds number (f -Re) and to develop Nusselt number versus Reynolds number (Nu-Re) relationships. The main focus of current research was the heat transfer characteristics of internal working fluid flowing inside MCHX test slabs. Nevertheless, the other associated performance parameters like the heat exchanger effectiveness, NTU, and overall and individual thermal resistances etc. for the MCHX test specimens have also been studied and analyzed as additional works.

The information on the designed test specimens, test chamber, test facility, and instrumentation is presented in relevant chapters. The integrity of the developed experimental setup is examined through liquid-to-air crossflow heat balance experiments.

1.1 Motivation

Microchannel technology and the use of microchannels in heat transfer and fluid flow applications are heading to replace the use of traditional tubes [12, 19-20, 39-41]. Microchannels represent the next generation heat exchangers because a MCHX made of microchannel cores in general can offer some advantages over the traditional and compact heat exchangers, which are summarized below.

- Improved heat transfer performance per unit volume (about 10 times or more) – giving a cost-effective and high efficiency heat exchanger [12, 42-44].
- Reduced air-side pressure drop – requiring less fan or blower power, hence cutting the initial costs for fan and cutting the energy consumption thus saving the cost and environment [42-43].
- Highly compact, reduced coil size, and very lightweight heat exchanger - Larger heat transfer surface area per unit volume, which is $10,000 \text{ m}^2/\text{m}^3$ or more, i.e. about 15 times higher than the traditional heat exchangers or more [12, 30, 42-44].

- Substantial refrigerant charge reduction, less risk of pollutant emission due to leakage, and hence less complexity in refrigerant handling [44, 45-49].
- For a given heat duty, lower tube-side fluid flow rate and hence the pressure drop – lowering the pump power leading to less initial costs for pumping and less energy consumption thus saving the cost and the environment [30-31, 43].
- Increased reliability as a result of better corrosion resistance with improved materials and enhanced structural robustness [12, 30, 42-44].
- Future research needs for huge experimental data on heat transfer and fluid flow correlations and design parameters for complete heat exchanger [43].

The motivation of using flat tube multi-port microchannel slabs as the test specimens in current study is that the flat tubes present better heat transfer and pressure drop performances for both internal and external working fluids over other comparable geometries. These advantages are quantitatively and qualitatively described below in section 3.0 in literature survey. Also aluminum flat tubes provide better device compactness and light-weightiness, which are an important concern for many heating and cooling industries; particularly in the automotive and aviation heat transfer applications.

1.2 Objectives and method of approach

- Comprehensive literature review on previous works in microchannel heat transfer and fluid flow in order to realize the potential applications of MCHX, identify current investigation and design necessity, and future research needs.
- Acquire understandings on microchannel geometries, flow regimes, and heat transfer correlations required to investigate, analyze and design the MCHX.
- Summarize the information of literature on needs for design and experimental investigation of microchannels and MCHXs for thermal applications.
- Sum up the investigation and correlations requirements and the best methods for analyzing and designing the air-to-liquid crossflow MCHX.
- Design, construct, and develop a fluid flow and heat transfer experimental test facility with modern instrumentation and data acquisition (DAQ) system.
- Design straight and serpentine multi-port microchannel slab and prototype MCHX test specimens and wind tunnel test chamber for their experiments.
- Experimentally investigate the pressure drop and friction factor characteristics of 50% ethylene glycol-water mixture and water flow in straight microchannel slab and examine the results with traditional pipe flow characteristics.

- Experimentally investigate the heat transfer characteristics of ethylene glycol-water mixture in serpentine microchannel slab and prototype MCHX in laminar developing flow and compare the results with traditional pipe flow.
- From experimental data - determine Nu using measured surface temperatures around the serpentine bend of the test specimens, obtain $Nu = f(Re, Pr)$ correlation by employing Wilson plot technique, and compare the results.
- Generate thermo-hydrodynamic experimental database for water and glycol-water mixture flow in multi-port serpentine microchannel slab and MCHX, which is a continuous need in the research community in this promising area.

To successfully accomplishing the above objectives of current research, a flow chart was developed on step-by-step action plan, which was followed to reach the goal. The chart is presented in Figure 1.4 below.

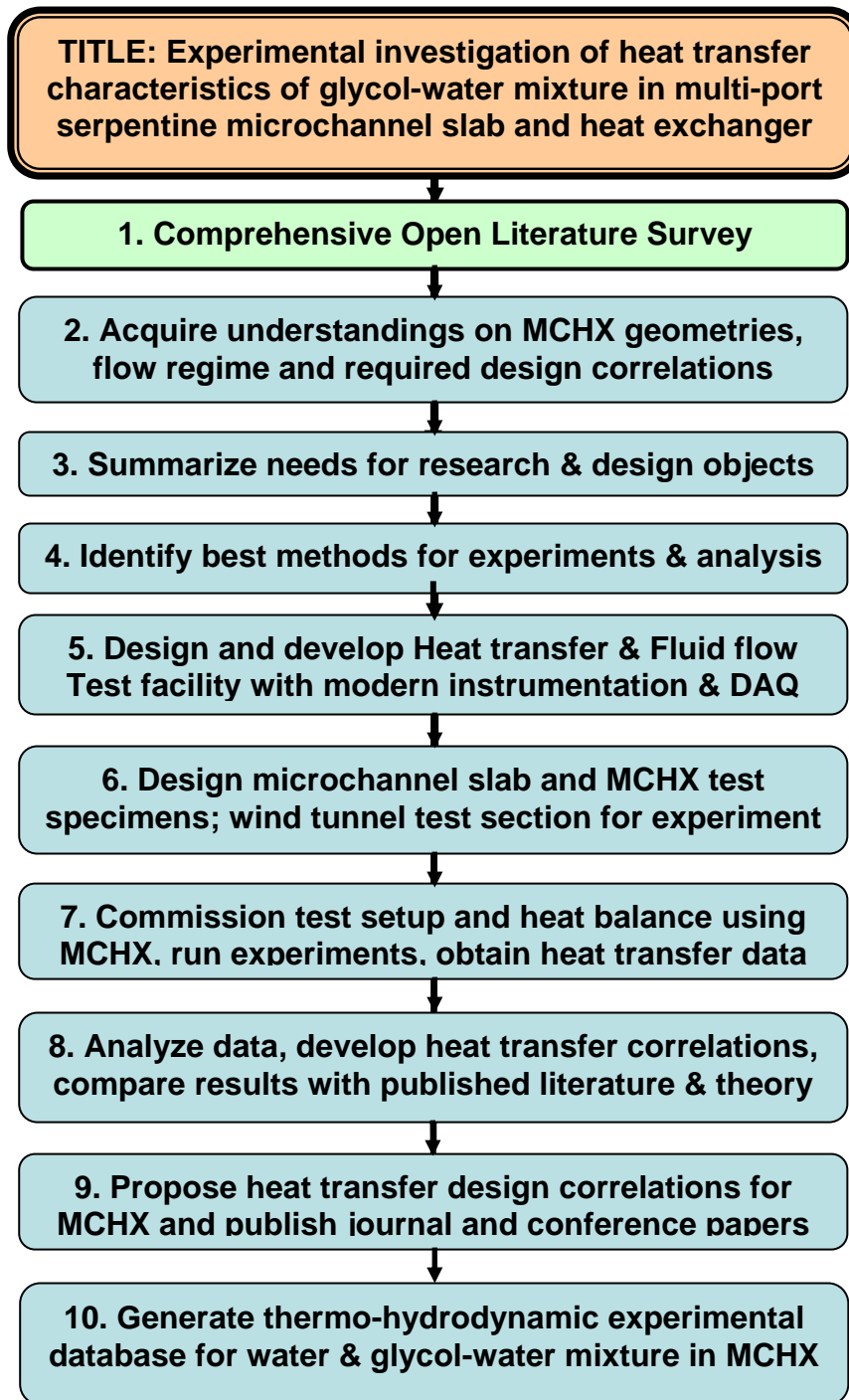


Figure 1.4. Flow chart of method of approach in reaching current research goal

CHAPTER – 2

BACKGROUND THEORY AND CORRELATIONS

2.0 BACKGROUND THEORY AND CORRELATIONS

Fundamentally the heat transfer and fluid flow mechanisms in microchannels are similar to that of the conventional pipe flow except for the different ways, in some cases, of experimenting, analyzing, error estimating, and treating the contributing parameters as well as consolidating the correlations as appropriate for narrow channel flow. Traditionally the heat transfer and fluid flow phenomena and parametric relationships are functionally represented by various non-dimensional parameters each of which has certain physical and thermo-hydrodynamic significance as described below. If not stated otherwise, all fluid properties are evaluated at bulk temperature for all equations below.

2.1 Dimensionless parameters in heat transfer and fluid flow

In forced convection heat transfer to and from any object or surface, the non-dimensional heat transfer coefficient is usually expressed by the Nusselt number (Nu). The Nu depends on at least two other important dimensionless parameters namely the Reynolds number (Re) and the Prandtl number (Pr), which are described at the firsthand. The flow velocity, fluid type, and the channel diameter together determine the Re. And the Re is used to describe the nature and regime of the flow. The Pr on the other hand explains the growth of thermal boundary layer thickness on the heat transfer surface. The thermal boundary layer is a barrier to the heat transfer.

There are a few other important dimensionless parameters associated to heat transfer and fluid flow. The Grashof number (Gr), which identifies and quantifies the existence of natural convection in forced convection heat transfer. The Knudsen number (Kn) used to quantify the rarefaction effect, which is a measure of the departure from the classical continuum assumption. The Brinkman Number (Br) measures the relative importance of viscous heating. Relative roughness (ε/D) that describes how smooth a pipe surface is relative to its diameter. The friction factor (f) attributed to the surface roughness of the flowing channels is related to the pressure drop along the flow length. The Poiseuille number (Po) relates the f and Re depending on flow channel geometry. These dimensionless numbers are further defined below.

2.1.1 Reynolds Number (Re):

It is named after the founder the British engineer and physicist “Osbourne Reynolds”. The Re is defined as the ratio of the inertial force to the viscous force within the flowing fluid. As defined below, it is used in momentum, and heat and mass transfer areas to account for the dynamic similarity, fluid flow velocity, and to characterize the nature of the flow.

$$\text{Re} = \frac{\text{Inertia Force}}{\text{Viscous Force}} = \frac{\text{Mass} \times \text{Acceleration}}{\text{Shear Stress} \times \text{Area}} = \frac{\rho AV^2}{\mu \frac{V}{Z} A} = \frac{\rho VZ}{\mu} = \frac{VZ}{\nu} \quad (2.1)$$

where Z is the characteristic length and traditionally defined by $Z = D_h = 4A / P$, for circular and non-circular cross sections. The pressure drop of fully developed laminar single-phase flow in smooth channels of arbitrary cross-sections has been numerically modeled [50]. The model was compared and found to be within 8% of the published results for a variety of cross-sections. The authors used and proposed a new characteristic length, as $Z = \sqrt{A}$, to define the Reynolds number and concluded that this characteristic length scale is superior to the conventional hydraulic diameter D_h [50]. For water and glycol-water mixture flows in current study, Z was replaced with the diameter of a single channel D of the multi-port microchannel slab.

For external working fluid flowing over the test slab surface, which is airflow in current study, the characteristic length Z and the product ρV are replaced respectively with airside hydraulic diameter $D_{h,a}$ and the airside streamwise mass velocity G across the heat exchanger as defined by Kays and London [51]. Typically the viscous stresses within a fluid tend to stabilize and organize the flow, whereas excessive fluid inertia tends to disrupt the organized flow leading to a chaotic turbulent behavior. Therefore the Re governs the flow regime in forced convection and determines the flow whether it is viscous dominated or inertia dominated.

2.1.2 Prandtl Number (Pr):

A German scientist “Ludwig Prandtl” pioneered the concept of thermal boundary layer in 1904 and developed a dimensionless parameter, which was named after him as “Pr”. It is defined as the ratio of the momentum diffusivity to the thermal diffusivity and is generally described in the following form.

$$\text{Pr} = \frac{\text{Momentum Diffusivity}}{\text{Thermal Diffusivity}} = \frac{\nu}{\alpha} = \frac{\mu/\rho}{k/\rho c_p} = \frac{\mu c_p}{k} \quad (2.2)$$

Generally in heat transfer and particularly in free and forced convection analyses, the convection heat transfer rate anywhere along the surface of a body is directly related to the temperature gradient at that location. The fluid flow velocity has a strong influence on the temperature profile, and hence the development of the velocity boundary layer relative to the thermal boundary layer has strong effect on the convection heat transfer.

In laminar flow regime, the relative thickness of the velocity and the thermal boundary layers are best described by the Pr as follows.

$$\text{Pr} = \left(\frac{\delta_v}{\delta_{th}} \right)^{1/n} \quad (2.2a)$$

where the exponent n is taken to be $1/3$ and the velocity boundary layer thickness, δ_v , is obtained in terms of the local Re and corresponding to the local distance from the leading edge [52]. In laminar flow Pr provides a measure of the relative effectiveness of momentum and energy transport by diffusion in the velocity and thermal boundary layers. The velocity boundary layer gets thinner as the free stream velocity gets higher. Compared to the momentum, the heat diffusion is quicker in fluids with $Pr \ll 1$, and slower in fluids with $Pr \gg 1$ [53].

Consequently as compared to the velocity boundary layer, the thermal boundary layer is thicker for fluids with $Pr \ll 1$ and thinner for fluids with $Pr \gg 1$. On the other hand in turbulent flow the boundary layer development is influenced strongly by the random fluctuations in the fluid and not by the molecular diffusion, and hence, the relative boundary layer growth does not necessarily depend on the value of Pr. In such cases both thicknesses are similar, i.e. $\delta_v \approx \delta_{th}$, and therefore the turbulent Pr is defined in the form of the ratio of energy of fluctuating components.

2.1.3 Grashof Number (Gr):

It is defined as the ratio of the buoyancy force to the viscous force acting on the flowing fluid. Like the Re dictates the flow regime in forced convection, the Gr governs the flow regime in natural convection. The Gr, as defined below, determines whether the forced convection or the natural convection is dominant in a flow system.

$$\text{Gr} = \frac{\text{Buoyancy Forces}}{\text{Viscous Forces}} = \frac{g(\Delta\rho)(\text{Volume})}{\rho v^2} = \frac{g\beta\Delta T(\text{Volume})}{v^2} = \frac{g\beta\Delta TZ^3}{v^2} \quad (2.3)$$

where, $\beta = \frac{1}{T_f + 273.15} [K^{-1}]$, $\Delta T = \Delta T = |T_i - T_s| [^\circ\text{C}]$, and $Z = \text{characteristic length}$.

2.1.4 Knudsen Number (Kn):

It is named after its founder the Danish scientist and researcher “Knudsen”. As the size of a flow channel gets smaller and smaller it approaches the mean free path between two molecules, which is particularly true for a gaseous flow. The traditional continuum assumption in flow analysis may not hold valid in such smaller channel flows. The Kn is a measure of the departure from the continuum assumption.

As Kn gets larger, the departure from the continuum becomes significant and as a result a simple wall velocity correction can no longer handle the complex wall and intermolecular interactions within the flow field. In such cases, e.g. for gas flow in very narrow channel, the heat transfer and fluid flow problems are treated and solved by using statistical mechanics or molecular dynamics simulations. The Kn is also used to further classify the fluid flow based on its degree of departure from the continuum assumption [19-20]. The **Kn** is defined as the ratio of the fluid molecular mean free path (λ) to the flow channel size D_h .

$$\text{Kn} = \frac{\lambda}{D_h}, \quad \text{where } \lambda = \frac{\mu\sqrt{\pi}}{\rho\sqrt{2RT}} \times 10^6 \quad [\mu\text{m}] \quad (2.4)$$

where, R , T , ρ , and μ are the universal gas constant [J/kg.K], absolute temperature [K], density [kg/m³], and dynamic viscosity [kg/m.s] respectively.

2.1.5 Brinkman Number (Br):

The Br measures the relative importance of viscous heating (i.e. the work done against viscous shear) to the conduction of flowing fluid along the channel. It is defined as the ratio of heat generated by viscous dissipation to the heat transferred by conduction. Over any cross-section of heat transfer interest, it is expressed as follows.

$$\text{Br} = \frac{\mu V^2}{k\Delta T} \quad (2.5)$$

where, V , ΔT , k , and μ are the mean fluid flow velocity, wall flow temperature difference, thermal conductivity of the channel material, and dynamic viscosity respectively.

The Br is usually ignored for low-speed and low-viscosity flows through conventional sized channels of short lengths. It can become most important for long pipe

flow. The length-to-diameter ratio can be very large in flow through narrow tubes and microchannels that can be compared to flows through conventional-sized long pipelines. Thus the Br may become important for heat transfer analyses in narrow channels [54].

2.1.6 Relative roughness (ε/D)

The roughness height (ε) in pipe flow problem refers to the surface finish of a pipe. The relative roughness (ε/D) describes how smooth or rough a pipe surface relative to its diameter. The magnitude of this parameter varies from zero (perfectly smooth) to 0.05 (considerably rough) [59]. The pressure drop in conventional pipe is independent of the relative roughness in laminar flow regime and for very high Re, but is dependent in turbulent flow regime for moderate Re. The conventional turbulent correlations for rough pipe flow relating friction factor with the relative roughness and Re are available. They are however rare for laminar rough or smooth pipe flows.

For a given surface finish, the narrow diameter pipe has more relative roughness than a large diameter pipe. As described in literature review, some authors indicated that the pressure drop and friction factor could be dependent on the relative roughness in microchannels even in laminar flow. No correlation however is found for microchannel flow that relates the relative roughness with friction factor and Re. Current study uses 1 mm diameter channel cut with laser beam, which is reasonably considered as smooth channel where the effect of relative roughness can be ignored without much error.

2.1.7 Friction factor (f)

The friction factor is a non-dimensional shear stress attributed to the surface roughness and often related to the pressure head loss. The friction factor is never zero even for a hydrodynamically smooth pipe ($\varepsilon = 0$) since there is always some microscopic surface roughness acting as no-slip boundary condition that requires a fluid to stick to any solid surface it flows over. In traditional pipe flow the f is commonly termed as the Darcy friction factor (f_d). From dimensional analysis it is non-dimensionally given as follows.

$$f_d = \Delta p \frac{D/L}{\rho V^2 / 2} = \Delta p \frac{D}{L} \frac{2}{\rho V^2} \quad (2.6)$$

where, Δp is the frictional pressure loss over the flow length L and D , ρ , and V are the channel diameter, fluid density, and mean flow velocity respectively. By rearranging Equation (2.6) the frictional pressure drop Δp can be represented in terms of friction factor as follows.

$$\Delta p = f_d \frac{L}{D} \frac{\rho V^2}{2}. \quad (2.7)$$

In heat transfer literature another form of friction factor representation is often observed is the Fanning friction factor (f_f). It generally represents primarily the frictional

component of the Δp and is used when a given heat transfer surface has roughly the same frictional Δp per unit length along the direction of the flow [3]. The Fanning friction factor and the Darcy friction factor are basically the same thing. There is no fundamental difference in the physical interpretation.

For a horizontal pipe flow, the pressure gradient of the flow is related to the wall shear stress as follows.

$$\frac{dp}{dx} = \frac{4\tau_w}{D} = \frac{\Delta p}{L} \quad (2.8)$$

The dimensionless wall shear stress and friction factor can be obtained from above as,

$$f_d = 4 \left(\frac{\tau_w}{\frac{1}{2}\rho V^2} \right) = 4f_f \quad (2.9)$$

From the above equation, it is seen that the Darcy and Fanning friction factors are related to each other by a factor of 4 as expressed below.

$$f_d = 4f_f \quad (2.9a)$$

The friction factors and their relationships expressed above depend on a variety of situations such as the flow regimes (laminar or turbulent), flow conditions (fully

developed or developing flow), flow channel cross-sectional geometry, the channel surface conditions (smooth or rough wall) etc. The f can be determined from above equations if the parameters and the specific flow and channel conditions are known. In order to determine the f in a variety of practical situations, a number of studies have been carried out and various correlations are proposed by various researchers. Some key correlations are described in the next section.

2.1.8 Poiseuille number (Po)

In the study of fluid flow resistance in tubes in laminar flow, Jean Louis Poiseuille devised a dimensionless group “Poiseuille number”, which was named after him. It is a constant and depends on the flow channel geometry and given by the product of the f and Re to represent the fully developed laminar flow friction data as expressed below.

$$Po = f Re = C, \text{ where } C \text{ is a constant that depends on channel geometry} \quad (2.10)$$

2.1.9 Nusselt Number (Nu) – the dimensionless heat transfer coefficient

The most familiar and convenient method of representing the heat transfer is through a non-dimensional group called the Nusselt Number (Nu), which was named after a German notable heat transfer luminary Ernst Kraft Wilhelm Nusselt. It is often

called the dimensionless form of the heat transfer coefficient (h) and is defined as the ratio of the convection to the conduction heat transfer rates. In other words, it is described as the ratio of the fluid layer resistance to the convective resistance as represented below.

$$\text{Nu} = \frac{\text{Fluid layer resistance}}{\text{Convective resistance}} = \frac{Z/k}{1/h} = \frac{hZ}{k} \quad (2.11)$$

where k and h are the thermal conductivity and convection heat transfer coefficient of the participating fluids. The term $Z = D_h = 4A / P$ is the characteristic length that depends on the shape and orientation of the heat transfer surface. In current study for water and glycol-water mixture flow inside microchannel, the Z is replaced with the diameter of a single channel D of the multi-port slab. On the other hand for airflow over the slab or MCHX surface, the Z is replaced with airside hydraulic diameter $D_{h,a}$ as and defined by Kays and London [51].

The Nu can be readily calculated from Equation (2.11) if the h is known. A variety of heat exchanger geometries, channel shapes, orientations and heat transfer surfaces are used in practical applications where the h may not be known a priori. In such cases the h is estimated either by experimental investigation or from two fluid heat balance using heat rate equations or from any other available heat transfer correlations.

The well known fact is that the heat transfer either for a single tube, channels in multi-port, or for a tube bank in heat exchanger is influenced by the flow velocity, fluid thermophysical properties, heat flux intensity, heat flux direction, wall temperature

conditions, arrangement of the flow channels etc. Thus most of the available heat transfer correlations exist in the form of dimensionless heat transfer coefficient, i.e. the Nu with its dependency on other controlling parameters like the Re, Pr, fluid properties, tube arrangement etc. The dimensionless relation can therefore be generalized as follows [55].

$$\text{Nu} = f \left(\text{Re}, \text{Pr}, \frac{\mu}{\mu_s}, \frac{k}{k_s}, \frac{c_p}{c_{p,s}}, \frac{\rho}{\rho_s}, \frac{S_c}{Z}, \frac{Z}{L}, \dots \right) \quad (2.12)$$

The geometric factor Z/L accounts for the effects on local Nu. Current study used the fixed geometry and orientation of the test samples on both fluid sides for a given experimental run and estimates the overall mean Nu that includes all the local effects. The effects of variations of tube orientations S_c/Z (airside) and length to diameter ratio Z/L (liquid side) on Nu are absent in current study and therefore are excluded.

The forced convection heat transfer is usually simplified through the dimensional analysis. After the simplification the overall Nu is seen to depend on the fluid flow velocity and the thermal boundary layer thickness. The velocity is represented by the Re and the thermal boundary layer by the Pr. The effects of the variations of thermophysical properties of viscous fluids in the thermal boundary layer are often accounted for by the

ratios of $\frac{\mu}{\mu_s}, \frac{k}{k_s}, \frac{c_p}{c_{p,s}}, \frac{\rho}{\rho_s}$.

For flow of fluids with temperature-dependent properties, the associated property ratio terms are often added in the heat transfer correlations for external and internal flows. In less viscous external fluid flow over a surface, such as the air, the property variation effect is accounted for by the addition of the Pr ratio $\left(\frac{Pr_b}{Pr_s}\right)$. For moderately viscous fluid flow inside channel like water it is mainly the viscosity that varies with the temperature across the boundary layer. This variation is then taken in to account by the inclusion of viscosity ratio $\left(\frac{\mu_b}{\mu_s}\right)$. Therefore by taking the major influencing factors into consideration, the heat transfer experimental data can be generalized in the following functional relationships [56].

$$Nu = y Re^m Pr^n \left(\frac{Pr_b}{Pr_s}\right)^p, \text{ for external flow over a surface} \quad (2.12a)$$

and

$$Nu = y Re^m Pr^n \left(\frac{\mu_b}{\mu_s}\right)^p, \text{ for internal flow (liquid flow in current study)} \quad (2.12b)$$

where y is the coefficient and m , n , and p are the exponents determined by experimental analyses and curve fitting. The exponent n is taken as $n = 1/3$ depending on the nature of the temperature profile in thermal boundary layer determined by the Pr. However, for a variety of flow conditions, from an comprehensive study on various fluids in different tubes in cross flow, the exponent n is proposed as 0.37 for $Pr < 10$ and 0.36 for $Pr > 10$.

The introduced property ratios, $\left(\frac{Pr_b}{Pr_s}\right)$ for external flow over a surface and $\left(\frac{\mu_b}{\mu_s}\right)$ for internal flow inside channel also account for the effect of direction of heat flow (i.e. the heating or cooling of the fluid). These two parameters can be dropped from any heat transfer correlations in flow conditions when these variations are absent or very little. Present study used hot water and hot glycol-water mixture as the working fluids. These hot fluids were cooled down by the constant flow of cold air. The properties of these fluids do not significantly change with a little variation in temperature such as $\pm 1^\circ\text{C}$. Although glycol property may slightly vary but the test condition was maintained such that, without much error, the property could be considered as independent of temperature variation. Therefore these variations can also be excluded and the above equations could further be simplified in a generalized form as expressed below.

$$Nu = y Re^m Pr^n \quad (2.12c)$$

This equation takes the form of Dittus-Boelter [57] generalized correlation for traditional liquid pipe flow in turbulent regime. Their proposed relationship was reviewed, verified and explained by Winterton [58] and for liquid flow the exponent n was recommended to be 0.4 for heating the liquid and 0.3 for cooling the liquid. The above generalized equation is traditionally used in determining heat transfer correlations for both laminar and turbulent flow regimes. Depending on flow conditions and regimes

the values of m and n exponents are different. Current study presents the results in the above form for laminar developing flow in multi-port serpentine bend microchannel slab.

2.2 Available equations or correlations for traditional pipe flow

Over time, a number of researchers have proposed a variety of fluid flow and heat transfer correlations for conventional pipe flow for various fluids in different geometry, cross-section, and orientations of flow channels and heat exchangers. Some of the key and commonly used and referred correlations are briefly described below. The detail information however can be available in most heat exchanger [3, 6, 11, 51], heat transfer [52-53], fluid mechanics [59] and hydraulics [60] books as well as in some key review, edition and comprehensive research works in this area [61-63].

The fluid flow in any duct or channel experiences different regimes dictated by the magnitude of the flow velocity. The Reynolds number (Re) usually determines three regimes of flow in conventional channel namely the *laminar*, *laminar-to-turbulent transition* and *turbulent* flows. A classification of flow regimes, are given in Table 2.1 below. A generalized schematic of laminar duct flow is shown in Figure 2.1 below for the purpose of pictorial illustrations of fluid flow and heat transfer parameters that appear in the correlations provided in this section.

Table 2.1. Classification of flow regimes for traditional pipe flow [5, 53]

Flow regimes	Range of Reynolds number (Re)
Laminar	$Re < 2300$
Laminar-to-turbulent transition	$2300 \leq Re \leq 4000$
Turbulent	$Re > 4000$

Re = 2300 is considered as the critical Re at which flow transition occurs

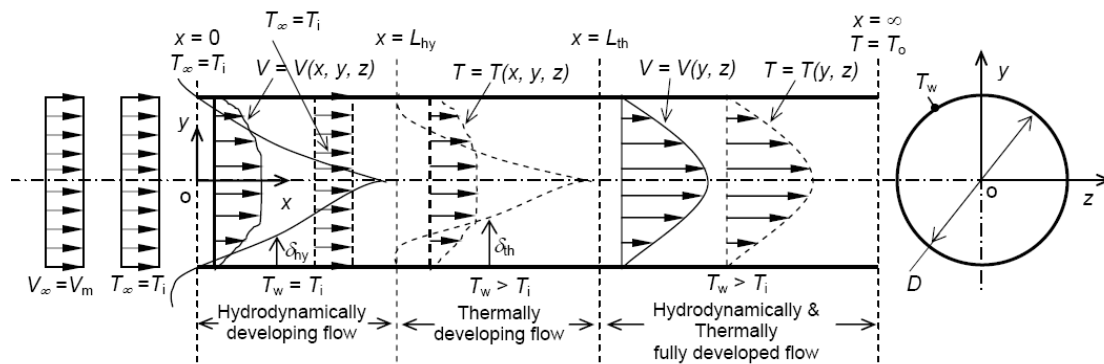


Figure 2.1. Hydrodynamically developing followed by thermally developing flows in a laminar ducts flow at constant wall temperature ($T_w = \text{constant}$) boundary condition.

Although the main focus of current study is laminar flow in general and developing laminar flow in particular, for the completeness of the sequence of understanding the correlations and functional parameters e.g. the flow rate (\dot{V} or \dot{m}), pressure drop (Δp), Reynolds number (Re), pressure head loss (h_L), friction factor (f), Poiseuille number (Po), hydrodynamic and thermal entrance lengths (L_{hy} and L_{th}), Nusselt number (Nu) etc. for all flow regimes are briefly summarized in the next sub sections.

2.2.1 Fluid flow equations and correlations

LAMINAR FLOW IN CIRCULAR PIPES

The laminar flow is characterized by the smooth parallel streamlines (i.e. the lines tangent to the velocity field) with no rotation and the highly ordered motion of fluid particles (i.e. particle velocities are free from random fluctuations at every point in the flow field). The type of flow for steady incompressible laminar flow through a straight circular duct of constant cross-section is commonly called the *Hagen-Poiseuille flow* or simply the *Poiseuille flow*. The well known *Navier-Stokes* equations and the solution for steady incompressible laminar flow are tagged to the experimental works independently done by Hagen and Poiseuille.

Flow rate (\dot{V}) and pressure drop (Δp) in laminar pipe flow

In fully developed (i.e. the velocity profile is same at any cross-section of the pipe) laminar horizontal pipe flow, Poiseuille's law relates the volume flow rate (\dot{V}) and the pressure drop (Δp) as given below.

$$\dot{V} = \frac{\Delta p \pi D^4}{128 \mu L} \quad \Rightarrow \quad \Delta p = \frac{128 \dot{V} \mu L}{\pi D^4} = \frac{128 \dot{m} \nu L}{\pi D^4} = \frac{32 \mu L V}{D^2} \quad (2.13)$$

where L is the pipe length in fully developed section and μ is the viscosity of the fluid.

In heat exchanger device the frictional pressure drop dominates the core pressure drop. The core pressure drop usually refers to the pressure drop in the straight flow path. The overall pressure drop is dependent on the geometric parameters and some times on the type of fluids [5]. In heat exchanger pressure drop analysis for fully developed laminar flow Shah and Sekulic [5] presented another form of equation that relates the Δp with the mass flow rate (\dot{m}), and Poiseuille number (Po) as follows.

$$\Delta p = \frac{1}{D^3} \left[\frac{1}{2} \frac{\mu (2L)^2}{\rho A_s} \dot{m} (f_d \text{Re}) \right] = \frac{1}{D^3} \left[\frac{1}{2} \frac{\mu (2L)^2}{\rho A_s} \dot{m} \text{Po} \right] \quad (2.14)$$

where A_s is the heat transfer surface area of the core.

The pressure head loss (Δp) in fully developed laminar pipe flow with a variety of pipe cross sections and surface roughness can also be derived from Darcy-Weisbach head loss equation for h_L in terms of Darcy friction factor and dynamic pressure [5, 53, 59].

$$\text{Darcy-Weisbach Equation for Head Loss: } h_L = f \frac{L V^2}{D 2g} \Rightarrow \Delta p = f \frac{L \rho V^2}{D 2} \quad (2.15)$$

Friction factor (f) and Poiseuille number (Po) in laminar pipe flow

Fully developed laminar f and Po are defined above in Equations (2.6) through (2.10). Various researchers proposed different correlations for f as a function of Re depending on particular flow situation, which can be theoretically and experimentally derived as described in many available sources [5, 18, 61-63]. The Po for fully developed laminar flow in conventional circular pipe is dependent on channel cross-section and usually independent of Re and has a constant value of 64 (if used Darcy f_d) and 16 (if used Fanning f_f). The common representation of the f as a function of Re for traditional circular pipe is as follows.

$$\text{Using Darcy friction factor, } f = \frac{64}{\text{Re}} \Rightarrow \text{Po} = f \text{ Re} = C = 64 \text{ (Laminar flow)} \quad (2.15)$$

Either for fully developed or developing laminar flow in microchannel well established f -Re correlation is not found in the open literature. Some researchers reported that the Po in microchannel is dependent on Re even in laminar flow and showed different values than the conventional tubes. This information can be found next in the literature review in Section 3.

Hydrodynamic entrance region in laminar pipe flow

As shown in Figure 2.1 when the fluid from free stream velocity enters a pipe, the fluid particles in contact with the wall comes to a complete stop because of wall friction and also causes the adjacent fluid particle to slow down. To conserve the mass flow rate through the pipe this velocity reduction must be compensated by the increase in midsection velocity and thus a velocity boundary layer is developed along the pipe. The thickness of this layer increases in the flow direction until it reaches the pipe centre and fills the entire pipe. The length of this region from inlet to a location where the boundary layer merges at the centerline of the pipe is called the hydrodynamic entrance length (L_{hy}). Beyond this point the flow is hydrodynamically fully developed where the *velocity profile* is *parabolic* in laminar pipe flow and somewhat *flatter* in turbulent flow.

The pressure drop (Δp) is always higher in entrance region because of the higher friction factor (f) attributed to the highest wall shear stress at the zero boundary layer thickness [53]. The f gradually decreases along the pipe up to the point where the flow is fully developed. The length from the pipe entrance to the point where the f reaches within $\pm 2\%$ of the fully developed value is often taken as the entrance length. Alternately it is the length along a pipe flow that is required to achieve a maximum pipe cross-section velocity as 99% of the fully developed flow when the entering fluid velocity is uniform [5]. The analytically derived entrance length is given by Equation (2.16a) [5, 18, 53, 61,

64] and the dimensionless axial distance (x^+) for the hydrodynamically developing flow region is given by Equation (2.16b) [5, 61] as follows.

$$L_{\text{hy, lam}} \approx 0.056 \text{Re} D \quad \text{for flow of } \text{Re} \leq 2100 \quad (2.16a)$$

In addition there is another loss that contributes to the pressure drop (Δp) is the effect of the entrance geometry of the flow passage. In estimating the Δp or f in a pipe, a flow developing pressure loss given by Equation (2.17) is often considered [5, 18].

$$\Delta p_{\text{dev}} = K_{\infty} \frac{\rho V^2}{2}. \quad (2.17)$$

where the K_{∞} is the loss coefficient at pipe entrance also known as the Hagenbach's factor [18] or the incremental pressure drop number [5, 62] that accounts for the pressure loss due to the entrance flow friction, developing region effects, and the change of momentum rate.

For circular tube, it is estimated that the fully developed region begins at $K_{\infty} = 1.28$ [65]. The same value is analytically obtained and presented by Shah and Sekulic for fully developed circular duct flow [5]. However, Shah and Sekulic mentioned that this value may not truly represent the flow in microchannel geometry. The K_{∞} values for relatively small diameter pipes are not yet available. In this absence, as given by

Equation (2.17a), a Reynolds number dependent K_{∞} relationship for circular conventional pipe is sometimes used, which was proposed by Chen [66] and recommended by Olsson and Sunden [67].

$$K_{\infty} = 1.20 + \frac{38}{\text{Re}} . \quad (2.17a)$$

LAMINAR-TO-TURBULENT TRANSITION FLOW IN CIRCULAR PIPES

The flow regime between the laminar and turbulent is termed as the *transition* flow where the laminar boundary layer tends to become locally unstable with a little flow disturbances. As the Re increases and exceeds the critical value of 2300 the orderly pattern of fluid particles transform to a disordered turbulent pattern.

Bhatti and Shah [63, 68] proposed a Darcy friction factor correlation for transitional flow in conventional smooth pipes as given below.

$$f_d = 0.0216 + 9.2 * 10^{-8} \text{Re}^{3/2} \quad \text{for} \quad 2100 \leq \text{Re} \leq 4000 . \quad (2.18)$$

Another correlation for Darcy friction factor for conventional smooth pipe was empirically proposed by Churchill [69], which interestingly spans all over the laminar, transition, and turbulent flow regimes and Re ranges. The correlation is given below.

$$f = 8 \left[\left(\frac{8}{\text{Re}} \right)^{12} + \frac{1}{(A+B)^{3/2}} \right]^{1/12}, \text{ for } A = 2.457 \left[\ln \left(\frac{7}{\text{Re}} \right)^{0.9} \right]^{16} \text{ and } B = \left[\frac{37530}{\text{Re}} \right]^{16}. \quad (2.19)$$

TURBULENT FLOW IN CIRCULAR PIPES

A flow is considered *turbulent* when the fluid particles do not travel in orderly manner. The turbulence is difficult to define and quantify in simple terms as it depends on several factors such as the irregular fluctuations of velocity, presence of eddies, large scale mixing etc. Unlike laminar flow, turbulent boundary layer has multi-layer character. It is very complex flow process much of which still remains to be understood [59]. Most of the correlations developed for turbulent flow are based on experimental studies and empirical correlations because of the difficulty in dealing with the complex process theoretically. The available and commonly encountered correlations are listed below.

Friction factor (f) in turbulent pipe flow

Blasius correlation: As expressed by Equation (2.20), this is considered the most widely used friction factor versus Reynolds number relationship in traditional smooth pipe for relatively low Reynolds number turbulent flow [5, 11, 64, 68].

$$f_d = \frac{0.316}{\text{Re}^{0.25}} \quad \text{or} \quad f_f = \frac{0.0791}{\text{Re}^{0.25}} \quad \text{for } 4 \times 10^3 \leq \text{Re} \leq 10^5. \quad (2.20)$$

Karman-Nikuradse correlation: The approximated and simplified form of their original correlations for turbulent flow in conventional smooth circular pipes is given by Equation (2.21) [11]. This correlation is also cited by other authors but as the McAdams correlation [5, 68].

$$f_d = \frac{0.184}{\text{Re}^{0.2}} \quad \text{or} \quad f_f = \frac{0.046}{\text{Re}^{0.2}} \quad \text{for} \quad 3 \times 10^4 \leq \text{Re} \leq 10^6 \quad . \quad (2.21)$$

Petukov correlation [53, 70]: Presented by Equation (2.22), it is said to be Petukov's 1st correlation for friction factor in fully developed turbulent flow in traditional smooth circular pipes.

$$f_d = [0.790 * \ln(\text{Re}) - 1.64]^{-2} \quad \text{for} \quad 3 \times 10^3 \leq \text{Re} \leq 5 \times 10^6 \quad . \quad (2.22)$$

Bhatti and Shah correlation [5, 68]: As defined by Equation (2.23), their correlation for turbulent flow in smooth conventional circular and non-circular pipes that covers a wide range of Reynolds number starting near the transition regime.

$$f_d = 0.00512 + 0.4572 \text{Re}^{-0.311} \quad \text{for} \quad 4 \times 10^3 \leq \text{Re} \leq 10^7 \quad . \quad (2.23)$$

Colebrook formula: The moody chart, found in most fluid mechanics textbook, presents the friction factor as a function of Re and relative roughness. The Colebrook turbulent friction factor formula, as expressed by Equation (2.24), is said to be valid for the entire non-laminar range of the Moody chart [59].

$$\frac{1}{\sqrt{f_d}} = -2.0 \log \left(\frac{\varepsilon/D}{3.7} + \frac{2.51}{\text{Re} \sqrt{f_d}} \right). \quad (2.24)$$

Pressure drop (Δp) in turbulent pipe flow

The theoretical Δp relationship for fully developed turbulent flow in horizontal traditional pipe is presented for the Re range of $3 \times 10^4 \leq \text{Re} \leq 10^6$ [5]. As given by Equation (2.25), this expression shows the dependency of Δp on friction factor, flow rate, fluid property, and surface geometry.

$$\Delta p = \frac{1}{D^3} \left[\frac{1}{2} \frac{\mu}{\rho} \frac{(2L)^2}{A_s} \dot{m} (f_d \text{Re}) \right] = \frac{1}{D^3} \left[\frac{0.368}{2} \frac{\mu^{0.2}}{\rho} \frac{(2L)^{2.8}}{A_s^{1.8}} \dot{m}^{1.8} \right] \quad (2.25)$$

The Darcy friction factor f_d in Equation (2.25) is taken from Karman-Nikuradse correlation from Equation (2.21). There may be different relations for Equation (2.25) depending on the turbulent range and the use of f from any of the above correlations.

Hydrodynamic entrance region in turbulent pipe flow

The basics of hydrodynamic entrance region are described above in laminar flow sub-section. As opposed to laminar flow, the hydrodynamic entrance lengths in turbulent flow are known to be almost independent of Reynolds number. The turbulent flow friction factors in entrance region are also higher than the fully developed flow. The entrance length is much shorter in turbulent flow than the laminar flow, which is generally less than 10 times the diameter of the pipe. This is because the other sources of losses in the entrance region dominate the pressure drop in turbulent flow as compared to viscous shear effect. Thus the pressure drop evaluation in turbulent flow usually ignores the contribution from turbulent developing flow region. Most commonly, the entrance length in turbulent flow for any Reynolds number is considered to be as follows.

$$L_{hy, turb} \approx 10D \quad (2.26a)$$

For developing turbulent flow in a circular pipe, from the analysis of apparent friction factor and Reynolds number product it was observed that this product is dependent on dimensionless hydrodynamic entrance length and the Reynolds number [68]. A different entrance length correlation was proposed, as given below, showing the dependency of entrance length on Reynolds number for $Re > 10000$ [5, 68].

$$L_{hy, turb} \approx 1.359 Re^{1/4} D \quad \text{for turbulent flow } Re > 10^4 \quad (2.26b)$$

2.2.2 Heat transfer equations and correlations

LAMINAR FLOW HEAT TRANSFER IN CIRCULAR PIPES

Since the flow physics of laminar flow is briefly described above in sub-section 2.2.1, only the associated equations and available correlations are summarized in short in this section. In fully developed laminar flow the forced convection Nusselt number Nu is a constant, which is independent of Reynolds number Re and Prandtl number Pr but is dependent on the conditions of the thermal boundary layer [5]. Figure 2.1 above illustrates the hydrodynamic and thermal boundary layers. There are several thermal boundary conditions adopted in heat transfer problems such as the constant and uniform wall temperature (*T boundary conditions*) and the constant wall heat flux (*H boundary conditions*); and rest are their supplementary sub-category combining these two.

The dynamic crossflow situation in current study practically might not follow strictly either of the T or H boundary conditions but could be a mixture of the two. However, the experimental operating conditions in current study (i.e. keeping both fluids inlet temperatures at a constant value) and there is no constant heat input to the test slab, ideally a T boundary condition is considered. Therefore to analyze the experimental data and compile the correlations, major focus is given on the T boundary conditions; and the correlations for T boundary conditions are mainly summarized below.

Heat transfer in fully developed laminar flow in smooth circular pipe

In circular flow passage, for hydrodynamically fully developed laminar flow corresponding to the thermally fully developed temperature distribution profile, the mean Nu achieves constant values, which, for T and H boundary conditions, are presented in several sources [11, 53, 62].

$$\left. \begin{array}{l} \text{Nu}_T = 3.657 \\ \text{Nu}_H = 4.364 \end{array} \right\} \begin{array}{l} \text{for } \text{Pe}_b D/L < 10^2 \\ \text{for } \text{Pe}_b D/L < 10 \end{array}, \text{ with the Peclet number, } \text{Pe} = \text{Re} \cdot \text{Pr} \quad (2.27)$$

where Nu is independent of Re, Pr, and the surface roughness ε .

The effect of fluid axial conduction for fully developed flow with T boundary condition is negligible since the dimensionless temperature becomes a function of the radial coordinate alone, as seen in Figure 2.1 and Equation (2.29). This is especially the case for higher Pe when $\text{Pe} = \text{Re} \cdot \text{Pr} = \text{VD}/\alpha > 10$. For the lower Pe, the axial conduction may exist. This effect is taken into account via Michelsen and Villadsen [71] recommended different, as presented below.

$$\text{Nu}_T = \begin{cases} 4.180654 - 0.183460\text{Pe}_b & \text{for } \text{Pe}_b = \text{Re}_b \text{Pr}_b < 1.5 \\ 3.656794 + 4.487/\text{Pe}_b & \text{for } \text{Pe}_b = \text{Re}_b \text{Pr}_b > 5 \end{cases} \quad (2.28)$$

Developing laminar flow in smooth circular pipe

The heat transfer in developing laminar flow is greatly influenced by the thermal entrance length (L_{th}). It is also dependent on the flow situations whether the flow is simultaneously developing or any of the hydrodynamic or thermal boundary layers developed earlier and the other one is still developing determined by the entrance lengths dictated by Pr. A generalized schematic is provided by Figure 2.2 for a simultaneously developing laminar flow in traditional smooth pipe with T boundary condition (i.e. the wall temperature is constant), which can be closely compared to the case of current study.

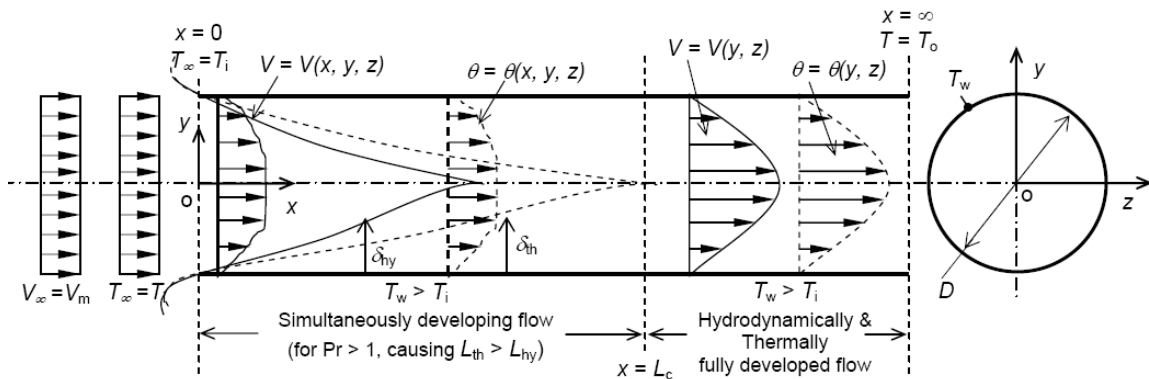


Figure 2.2. Simultaneously developing laminar flow in a traditional circular pipe at constant wall temperature ($T_w = \text{constant}$) boundary condition.

Temperature profile in thermally fully developed laminar flow

The local temperature T of a flowing fluid is a function of both the radial and axial co-ordinates, the bulk mean temperature T_b is the function of the axial coordinate, and the dimensionless temperature θ_m defined by Equation (2.29) is the function of the radial coordinate alone [5]. The general temperature profile in the thermally developed region may vary in the axial flow direction; however the dimensionless temperature profile θ_m remains unchanged. This dimensionless profile is termed as hydrodynamically and thermally developed or simply fully developed temperature profile for $\theta_m \geq 0.99$.

$$\text{Dimensionless temperature, } \theta_m = \frac{T_w - T}{T_w - T_b}, \text{ where w and b refer to wall and bulk.} \quad (2.29)$$

Thermal entrance length

The thermal entrance length L_{th} is defined as the axial distance required for the dimensionless temperature profile θ_m to achieve fully developed state or a value of 0.99 or for the local Nu value to achieve a value 1.05 times of the fully developed Nu value. To the extent at which the thermal effects diffuse normally from the pipe wall towards the centre of the pipe until the flow is developed is referred to as the thermal boundary layer thickness, δ_{th} .

As seen in Figure 2.2, in a simultaneously developing flow the viscous and thermal effects diffuse simultaneously from the pipe wall starting at $x = 0$ and the rates of diffusions depend on the Pr. For a fluid flow with $Pr > 1$, the boundary layer thicknesses at any given point are $\delta_v > \delta_t$ that means that the velocity boundary layer grows faster and the thermal entrance length becomes longer than the hydrodynamic entrance length i.e. $x = L_c = L_{th} > L_{hy}$. Opposite scenario is observed when $Pr < 1$.

For $Pr = 1$, the viscous and the thermal effects diffuse at the same rate. In internal flow this equality is not a sufficient condition to say that the boundary layer thicknesses are equal i.e. $\delta_v = \delta_t$ or the entrance lengths are equal i.e. $L_{th} = L_{hy}$, although it is the case for external flow. This is because the applicable differential equations for energy and momentum do not become analogous to each other in internal flow as they do in external flow. As seen in Figure 2.2, the region $0 \leq x \leq L_c$ is usually called the *combined entrance region*. The magnitude of the Pr determines whether the thermal or the hydrodynamic entrance length is dominating the flow. The thermal entrance length in developing laminar flow is generally expressed in the following form [61, 64, 68].

$$L_{th, \text{lam}} \approx 0.056 Re_b Pr_b D \approx 0.056 Pe_b D \quad (2.30a)$$

Dimensionless entrance length: The dimensionless entrance length for hydrodynamically developed but thermally developing flow is given as follows [5, 61-62, 68].

$$x^* \approx \frac{x/D}{Re_b Pr_b} \approx \frac{x/D}{Pe_b} \approx \frac{x^+}{Pr_b} \quad (2.30b)$$

The dimensionless thermal entrance lengths at H and T boundary conditions with $Pr = 0$, $Pr = 1$ and $P \gg 1$ for two different flow situations are presented below [5, 62].

Hydrodynamically developed and thermally developing flow:

$$L_{th-H, lam}^* \approx \begin{cases} 0.0430 & \text{for } Pr \gg 1 \\ 0.500 & \text{for } Pr = 1 \\ 0.0335 & \text{for } Pr \gg 1 \end{cases} \quad (2.30c)$$

Simultaneously developing flow:

$$L_{th-H, lam}^* \approx \begin{cases} 0.042 & \text{for } Pr = 0 \\ 0.053 & \text{for } Pr = 0.7, \text{ e.g. Air} \\ 0.043 & \text{for } Pr = \infty \end{cases} \quad (2.30d)$$

$$L_{th-T, lam}^* \approx \begin{cases} 0.028 & \text{for } Pr = 0 \\ 0.037 & \text{for } Pr = 0.7, \text{ e.g. Air} \\ 0.033 & \text{for } Pr = \infty \end{cases}$$

Heat transfer correlations

Hydrodynamically developed and thermally developing laminar flow in smooth traditional pipe:

The solution of *Nusselt-Graetz* problem for heat transfer to an incompressible fluid flow through circular duct with constant fluid property was numerically solved at T and H boundary conditions [11, 61-62], which are given in Equation (2.31) below.

$$\text{Nu}_T = 1.61 \left(\frac{\text{Re}_b \text{Pr}_b D}{L} \right)^{1/3}; \quad \text{where} \quad \left(\frac{\text{Re}_b \text{Pr}_b D}{L} \right) = \left(\frac{\text{Pe}_b D}{L} \right) > 10^3 \quad (2.31a)$$

And

$$\text{Nu}_H = 1.953 \left(\frac{\text{Re}_b \text{Pr}_b D}{L} \right)^{1/3}; \quad \text{where} \quad \left(\frac{\text{Re}_b \text{Pr}_b D}{L} \right) = \left(\frac{\text{Pe}_b D}{L} \right) > 10^2 \quad (2.31b)$$

Gnielinski [72] proposed a correlation for circular smooth duct in laminar developing flow with T boundary condition as given below. The axial conduction effects must be considered when $\text{Pe}D/L < 0.1$ and in such case Equation (2.28) should be used.

$$\text{Nu}_T = \left[3.66^3 + 1.61^3 \left(\frac{\text{Re}_b \text{Pr}_b D}{L} \right) \right]^{1/3}; \quad \text{for } 0.1 < \left(\frac{\text{Re}_b \text{Pr}_b D}{L} \right) = \left(\frac{\text{Pe}_b D}{L} \right) < 10^4 \quad (2.32)$$

Sieder and Tate [73] proposed one heat transfer correlation for developing laminar flow in circular duct with T boundary condition to take into account for the entrance region effect as well as the effect of thermo-physical property variation with temperature. The correlation is given below by Equation 2.33.

$$\text{Nu}_T = 1.86 \underbrace{\left(\frac{\text{Re}_b \text{Pr}_b D}{L} \right)^{1/3} \left(\frac{\mu_b}{\mu_w} \right)^{0.14}}_A \begin{cases} \text{for } 0.48 < \text{Pr}_b < 16,700 \\ \text{and } 0.0044 < \left(\frac{\mu_b}{\mu_w} \right) < 9.75, \mu_w @ T_{\text{wall}} \end{cases} \quad (2.33)$$

Whitaker [74] further recommended that the *Sieder and Tate* [73] correlation should be used only for a value of $A \geq 2$ in Equation 2.32. This is because the fully developed flow status will be established from developing flow for $A < 2$ and then the fully developed Nu has to be approximated using Equation (2.27) from above.

Simultaneously developing laminar flow in smooth traditional pipe with entrance effect:

When the heat transfer starts as soon as the fluid enters a flow passage (as the case in current study), the velocity and temperature profiles start developing simultaneously as

mentioned above in the entrance length section. These complex problems are mostly solved by numerical methods [61-62].

Hausen (1959) developed an empirical correlation for laminar flow in the thermal entrance region of a circular duct with constant fluid properties and constant wall temperature [11], which is given below.

$$\text{Nu}_T = \left[3.66 + \frac{0.19 \left(\text{Re}_b \text{Pr}_b \frac{D}{L} \right)^{0.8}}{1 + 0.117 \left(\text{Re}_b \text{Pr}_b \frac{D}{L} \right)^{0.467}} \right]; \text{ for } 0.1 < \left(\frac{\text{Re}_b \text{Pr}_b D}{L} \right) < 10^4 \quad (2.34)$$

Edwards et al. [75] expressed one correlation for laminar flow in the thermal entrance region of a circular duct with constant fluid properties and constant wall temperature, which is presented below. *It is based on the assumption that the flow is already hydrodynamically developed before entering the heat transfer section.* However approximation is made that it could be used for simultaneously developing flow as well.

$$\text{Nu}_T = \left[3.66 + \frac{0.065 \left(\frac{D}{L} \right) \text{Re}_b \text{Pr}_b}{1 + 0.04 \left[\left(\frac{D}{L} \right) \text{Re}_b \text{Pr}_b \right]^{2/3}} \right]. \quad (2.35)$$

Pohlhausen (1921) represented the Nu values by one asymptotic equation for simultaneously developing laminar flow over a flat plate in the case of short duct length with a T boundary condition [11] as given below.

$$\text{Nu}_T = 0.664 \left(\frac{\text{Re}_b \text{Pr}_b D}{L} \right)^{1/2} \text{Pr}_b^{-1/6}; \quad \text{for} \left(\frac{\text{Re}_b \text{Pr}_b D}{L} \right) > 10^3 \text{ and } 0.5 < \text{Pr}_b < 500 \quad (2.36)$$

For most engineering applications with short circular pipe (i.e. $D/L > 0.1$), whichever of the Gnielinski, Hausen, and Pohlhausen correlations given above in Equations (2.32), (2.34), and (2.36) gives the highest Nu can be used [11].

LAMINAR-TO-TURBULENT TRANSITIONAL FLOW IN CIRCULAR PIPES

The initiation of transition flow is influenced by the entrance configurations of the flow channel (e.g. smooth, abrupt, sharp etc.), which dictate the lower limits of the critical Reynolds number (Re_{cr}). For a sharp square inlet configuration the Re_{cr} is about 10 to 15% lower than that of the rounded inlet conditions [5]. The availability of heat transfer correlations in smooth circular pipes is limited because of the complexity of the flow process in this regime. One correlation for transitional flow in non-circular duct is developed [5, 68]. Tam and Ghajar developed the Nu correlations in transitional flow for

various inlet conditions are proposed [5, 53], which are not similar to the configurations of current study test specimen.

Taborek proposed the heat transfer correlation for transitional flow in circular smooth duct [5], which is given below.

$$Nu = \phi Nu_{lam} + (1 - \phi) Nu_{turb}; \text{ where } \phi = 1.33 - \frac{Re}{6000}; \text{ applicable for } 2000 < Re < 8000 \quad (2.37)$$

where Nu_{lam} is the value of Nu for fully developed laminar flow taken from Equation (2.27) above. The Nu_{turb} is the value of Nu in fully developed turbulent flow, which can be estimated from any of the reasonable turbulent flow correlations discussed and given by Equations (2.39), (2.40) and (2.43) below depending on the range of Re .

TURBULENT FLOW HEAT TRANSFER IN CIRCULAR PIPES

Like the laminar flow, the turbulent flow can also be divided into four types namely the fully developed, hydrodynamically developing, thermally developing, and simultaneously developing flows. The divisions are similar to laminar flow illustration as shown in Figure 2.1 and 2.2. The developing turbulent flow starts right after laminar-to-turbulent transition flow. The hydrodynamic and thermal entrance lengths are much shorter in turbulent flow and the boundary layer thickness is multi-layer in character. The

value of Re in fully developed turbulent flow depends on the pipe cross-section, surface roughness, inlet geometry etc.

Thermal entrance length in turbulent pipe flow

The thermal entrance length in turbulent flow, for both gas and liquid, is almost independent of both the Re and the boundary condition. In circular smooth pipe flow, the dimensionless entrance length L_{th}/D varies approximately between 8 and 15 for air and less than 3 for liquid. In non-circular flow passage this length could be higher, from 30 to 40, because of the presence of corners that creates the laminar flow [5]. The following generalized relation is often used in most practical cases [5, 53, 61, 64, 68].

$$L_{th, turb} \approx 10D \quad (2.38)$$

Heat transfer correlations in turbulent pipe flow

In fully developed turbulent forced convection for $Pr > 0.7$ the effect of thermal boundary conditions on Nu is almost negligible [5], which is particularly the case in current study since the used working fluids water and glycol-water mixture both have $Pr > 0.7$. Therefore the correlations for transitional flow given above and the correlations for fully developed turbulent flow summarized below can both be used for either H or T boundary conditions [5-11]. However, for fluids with $Pr < 0.7$, the thermal boundary

conditions and hence the Nu are dependent on both Re and Pr. The Nu values in fully developed laminar flow on the other hand is independent of Re and Pr but dependent on thermal boundary conditions. In turbulent flow, most of the thermal resistances gather near the wall and within the viscous sub-layer causing temperature and velocity profiles relatively flat over major portion of the pipe cross-section. Therefore except for the non-rounded inlet configuration the influence of channel shape on the heat transfer in turbulent flow is less significant as compared to the laminar flow.

In turbulent forced convection through traditional ducts, numerous studies have proposed a number of analytical solutions and empirical correlations, which are available in many sources, such as [5-11, 68]. Since the developing laminar flow in circular smooth microchannel slab is the main focus of current study, only the best recommended heat transfer correlations for turbulent flow are compiled here for circular smooth ducts and the preference is given on liquid correlations unless otherwise mentioned.

Petukov-Popov [76] 1st correlation for heat transfer for fully developed turbulent flow in smooth circular duct.

The proposed heat transfer correlation for fully developed turbulent flow in smooth circular ducts for liquids and gases with $Pr > 0.5$ [76] is given by Equation (2.39a). According to some authors, it is the very accurate correlation that correlates most of the experimental data well within $\pm 5\%$ [5-68].

$$\text{Nu} = \frac{\left(\frac{f}{8}\right) \text{Re}_b \text{Pr}_b}{C + 12.7 \sqrt{\left(\frac{f}{8}\right)} \left(\text{Pr}_b^{\frac{2}{3}} - 1\right)}; \text{ for } 4000 < \text{Re}_b < 5 \times 10^6 \text{ and } 0.5 < \text{Pr}_b < 10^6 \quad (2.39a)$$

where $C = 1.07 + \frac{900}{\text{Re}_b} - \frac{0.63}{1 + 10 \text{Pr}_b}$ and f can be estimated from any of the above Equations

(2.20) through (2.23) or preferably from Equation (2.22), i.e. Petukov's 1st correlation.

Petukov-Popov [70] 2nd correlation for heat transfer for fully developed turbulent flow in smooth circular duct.

It was proposed for the heat transfer for fully developed turbulent flow in smooth circular ducts for liquids and gases with $\text{Pr} > 0.5$ [70]. It is a simplified version of the 1st correlation having little less accuracy as given by Equation (2.39b) below.

$$\text{Nu} = \frac{\left(\frac{f}{8}\right) \text{Re}_b \text{Pr}_b}{1.07 + 12.7 \sqrt{\left(\frac{f}{8}\right)} \left(\text{Pr}_b^{\frac{2}{3}} - 1\right)}; \text{ for } 4000 < \text{Re}_b < 5 \times 10^6 \text{ and } 0.5 < \text{Pr}_b < 10^6 \quad (2.39b)$$

Gnielinski [77] heat transfer correlation for transitional and fully developed turbulent flow in smooth circular duct.

Gnielinski [77] modified the Petukov-Popov 2nd correlation (Equation 2.39b) to extend its applicability in the lower Re regime starting from $\text{Re} = 2300$ and arrived in a

form which is given by Equation (2.40a) below. This correlation is said to be one of the most widely used Nu-Re correlations. Shah and Sekulic [5] and Bhatti and Shah [68] mentioned that it is in best accord with Petukov-Popov 2nd correlation within -2% and +7% accuracy and they had taken this correlation as the basis of comparison for all other correlations in this series. They however pointed out that this correlation does not translate data very good in the transition regime.

$$\text{Nu} = \frac{\left(\frac{f}{8}\right)(\text{Re}_b - 1000)\text{Pr}_b}{1 + 12.7\sqrt{\left(\frac{f}{8}\right)}\left(\text{Pr}_b^{\frac{2}{3}} - 1\right)}, \text{ for } 2300 < \text{Re}_b < 5 \times 10^6; \text{ and } 0.5 < \text{Pr}_b < 2000 \quad (2.40a)$$

Gnielinski [77] provided a further simplified version of the above correlation for easy use in the higher Re without major error that is given in Equation (2.40b).

$$\text{Nu} = 0.012\left(\text{Re}_b^{0.87} - 280\right)\text{Pr}_b^{0.4}, \text{ for } 3000 < \text{Re}_b < 10^6 \text{ and } 1.5 < \text{Pr}_b < 500 \quad (2.40b)$$

Churchill [78] heat transfer correlation for fully developed flow in smooth circular duct that spans over all the laminar, transitional, and turbulent regimes.

Churchill [78] provided one comprehensive Nu-Re correlation for fully developed flow in smooth circular ducts that spans over all the laminar, transition and turbulent flow

regimes [78]. Bhatti and Shah [68] compared this correlation with the widely used Gnielinski [77] correlation and concluded that it has good accuracy with Gnielinski [77] correlation in laminar and transitional regimes but relatively less accuracy, i.e. -12% to +17%, for higher Re above $Re = 104$ [68]. The correlation for the range of $10 < Re_b < 10^6$ and $0 < Pr_b < 10^6$ is presented below.

$$Nu^{10} = (Nu_{lam})^{10} + \left\{ \frac{\exp\left[\frac{(2200 - Re_b)}{365}\right]}{(Nu_{lam})^2} + \frac{1}{(Nu_{turb})^2} \right\}^{-5} \quad (2.41)$$

Where the Nu_{lam} is the fully developed value of Nu in laminar flow in smooth circular duct as determined by Equation (2.27) above, i.e. $Nu_{lam, T} = 3.657$ (T-boundary condition) and $Nu_{lam, H} = 4.364$ (H-boundary condition). The Nu_{turb} is the fully developed Nu value for turbulent flow, which is determined from Equation (2.41a) given below.

$$Nu_{turb} = Nu_o + \frac{0.079 \sqrt{\left(\frac{f}{8}\right)} Re_b Pr_b}{\left(1 + Pr_b^{4/5}\right)^{5/6}}; \text{ here, } Nu_o = \begin{cases} 4.8 & \text{for T-Boundary condition} \\ 6.3 & \text{for H-Boundary condition} \end{cases} \quad (2.41a)$$

Dittus-Boelter [57] heat transfer correlation for fully developed turbulent flow in smooth circular duct.

Dittus-Boelter [57] proposed heat transfer correlation for both heating and cooling of liquids and gases in fully developed turbulent flow in smooth circular duct as given by Equation (2.42) below. This correlation is in the form of theoretically simplified Equation (2.12c) as described in section 2.1.8. Winterton [58] further detailed and explained this correlation as described in section 2.1.8 above. According to Bhatti and Shah [68], this correlation estimate 17 to 33% higher Nu for air and -26% (lower) to +7% (higher) Nu for water as compared to the widely used Gnielinski [77] correlation. They concluded that this correlation can be used for approximate calculation of Nu but not for accurate estimation [68].

$$\text{Nu} = \begin{cases} 0.024 \text{Re}_b^{0.8} \text{Pr}_b^{0.4} & \text{(heating of liquid)} \\ 0.026 \text{Re}_b^{0.8} \text{Pr}_b^{0.3} & \text{(cooling of liquid)} \end{cases} \quad \text{for } 2500 < \text{Re}_b < 1.24 \times 10^5 \text{ \& } 0.7 < \text{Pr}_b < 120. \quad (2.42)$$

Shah and Sekulic [5] simplified the Petukov-Popov 1st correlation (Equation 2.39a) by taking a fixed value of Pr exponent as ‘0.4’ as recommended by [64, 77] and leaving the Re exponent values open as ‘n’, where the ‘n’ is dependent on both the Re and Pr. The value of ‘n’ can be extracted from their presented graph [5].

$$\text{Nu} = 0.024 \text{Re}_b^n \text{Pr}_b^{0.4}; \quad \text{for } 2500 < \text{Re}_b < 1.24 \times 10^5 \text{ and } 0.7 < \text{Pr}_b < 120. \quad (2.43)$$

2.3 Conclusions on the availability of correlations

As seen from above, the detailed correlations for fluid flow and heat transfer in traditional pipe flow are well established and widely available. Unfortunately, except for a few proposed (as can be noticed in literature review in next section) and still unconsolidated, no well established correlation for microchannel flow is available yet that can be utilized in designing a microchannel heat exchanger.

This unavailability of correlations does not necessarily indicate the complete validity of traditional correlations in microchannel flow nor does it conclude that the correlations in microchannel flow are different. This area needs more and more research and experimental data for the scientific community to conclude on either of the above statements; and we will observe this continuous call in the literature survey in next section.

CHAPTER – 3

LITERATURE SURVEY AND SCOPE OF CURRENT STUDY

3.0 LITERATURE SURVEY AND SCOPE OF CURRENT STUDY

Along the avenue of exploring the smaller sized channels for better heat transfer performance, there has been a steady shift from larger diameter tubing (10 to 20 mm) to smaller diameter channels (1 mm to 0.01 mm). The term ‘microchannel’ has become an accepted classifier for heat transfer and fluid flow processes at smaller scale [18]. A few authors have proposed some classification of small flow passages for typical thermal heat exchanger technology at microscale geometry with respect to some key biological and engineering systems, where 1 mm diameter size is termed as meso-channel [19-20]. However, generally yet a flow channel diameter or hydraulic diameter of 1 mm or below is broadly classified in the heat transfer and fluid flow literature as “microchannel”, “microtube” or “micro-device” [10, 21-28].

It has been observed after the works of Tuckerman and Pease [33], Tuckerman [34], Mundinger et al. [35], and a review article by Goodling [36] in the area of electronics cooling using microchannels that more interest has been paid to diversify the applications of microchannels in other areas of heating and cooling applications. There are studies found in the open literature that extend research on both single phase and two phase fluid flow and heat transfer in microchannels. Based on the objectives of current research in this area, the major review focus was given on the experimental works on fluid flow and heat transfer of single phase liquids. Some relevant facts were also

extracted from numerical study and works on gas and two phase flows in microchannels, MCHXs, or MCHS.

As a part of current research, a number of papers on narrow channel heat transfer and fluid flow appearing between 1928 and 2009 have been critically reviewed to develop a statistical history on some key information including the types of channel cross sections, channel materials, and working fluids used in previous studies. Among the reviewed papers, a review summary of 123 such works [24-27, 33, 37-39, 41, 79-192] is chronologically presented in Table A in the Appendix-A. Throughout this dissertation, wherever it mentions any percentage share of previous investigations, current study refers to these summarized 123 papers. This percentage chart gives a glimpse but critical key information on the past works that helps identify and justify further research needs.

3.1 Fluid flow and heat transfer characteristics in microchannels and MCHXs

3.1.1 Flow friction (f) and Poiseuille number (Po) for single phase flow in microchannels

The friction factor (f), as mentioned in section 2.1.6 above, is a gage of surface roughness that influences the pressure drop (Δp) and heat transfer. The Poiseuille number (Po) described in section 2.1.7 in Equation 2.10 is a measure in fluid flow to represent the fully developed laminar flow friction data for traditional pipe flow. For fully developed

laminar flow in conventional pipe, the Po is usually independent of Re and has a constant value of $Po = fRe = 64$ for circular pipe using Darcy friction factor.

The friction coefficient or Fanning friction factor (f_f) in heat transfer literature and the Darcy friction factor (f_d) in fluid mechanics are commonly used with their relationship as $f_d = 4f_f$. The conventional conduit flow correlations for f and Po in the laminar range and f in the post laminar regimes are well established, which are usually offered as a function of Re depending on flow situation and duct cross section. They can be readily theoretically and experimentally derived [61, 63, 68].

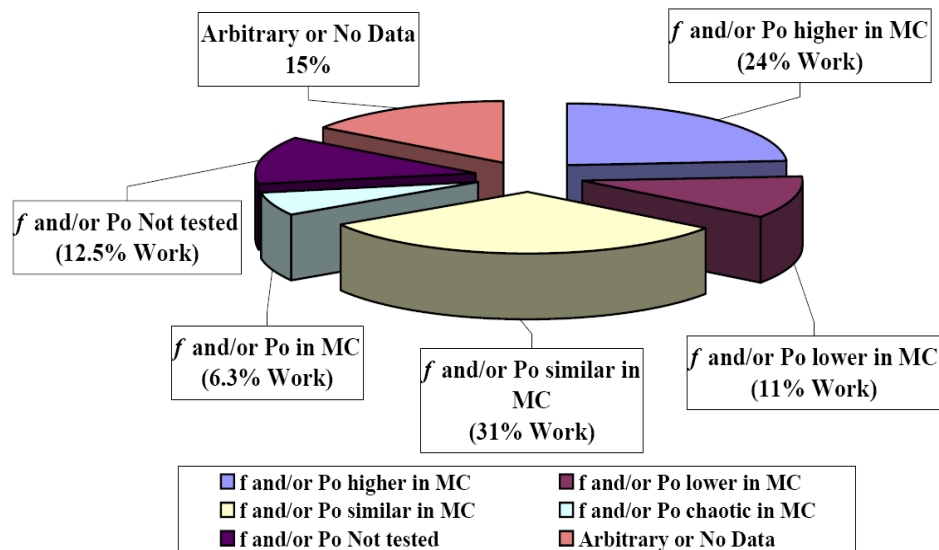


Figure 3.1. Statistics on f and/or Po observations in microchannels in reviewed past works

It is generally said that the f in microchannel is higher than the conventional pipes. Among the reviewed and summarized key works [24-27, 33, 37-39, 41, 79-192], the f or Po in microchannel was observed both higher, lower, similar, and anarchic (i.e. simultaneously lower, higher, similar or inconclusive) as compared to the classical values. For some of the works this information could not be extracted. The statistics is portrayed in Figure 3.1. The lower values of f and/or Po were observed particularly for gas flow where f decreased with the Knudsen number (Kn) and increased with the Mach numbers (Ma) for $Ma > 0.3$, which according to some authors might have been caused by the gas compressibility or rarefaction effects [88, 97, 100, 105, 107, 116-117, 132, 136].

In conventional pipe flow, it is well known that the f is influenced by the relative roughness of the pipe walls in turbulent flow regimes. For microchannel flow however, some works reported that the f depends on the wall relative roughness even in laminar flow [81, 110, 123, 133-134, 137-139, 161, 163, 168, 171]. While several authors reported that the Po in laminar microchannel flow is similar to the classical value, a large group however observed the Po to depend on the Re in laminar flow and showed different values than the values for conventional smooth pipe [87, 96, 103, 113, 134, 139, 151, 171, 174].

Friction factor (f) in laminar flow in microchannel

A few f -Re correlations proposed for fully developed laminar flow in straight smooth non-circular narrow channels, mostly in rectangular cross-section, can be found such as one by Hartnett and Kostic (1989) as cited by Kim et al. [166]. The correlation is given by Equation (3.1) below.

$$Po = f Re = 24 \left(\begin{array}{l} 1 - 1.3553AR + 1.9467AR^2 - 1.7012AR^3 \\ + 0.9564AR^4 - 0.2537AR^5 \end{array} \right), \text{ for } Re < 2100, \quad (3.1)$$

where Re is based on hydraulic diameter and AR is the height-to-width known aspect ratio of the flow channel.

The proposed correlation for fully developed laminar flow in circular microchannel is rare. A correlation for fully developed laminar flow in straight smooth circular micro-tube available in the open literature was proposed by Yu et al. [110] as given in Equation (3.2) below. The authors experimentally investigated the characteristics of nitrogen gas and water flows through silica made micro-tubes in the Reynolds number range of $220 \leq Re \leq 19500$. They observed lower Darcy f in micro-tubes, which are lower than the established value of 64 for conventional circular pipe. The lower values were from 0.77 to 0.81 times of the conventional value. Although the reported critical Re was 2000, the transition however observed from $Re = 1700$ to 6000.

$$f = \frac{50.13}{\text{Re}}, \text{ for } \text{Re} < 2000 \text{ (Fully developed laminar flow in micro-tube)}. \quad (3.2)$$

Pressure drop (Δp) in laminar flow in microchannel

The pressure drop (Δp) in fully developed laminar flow in traditional pipe is a direct function of the Darcy friction factor (f_d), which is given by Equation (2.7) in section 2.1.6 above. The Poiseuille law in fully developed laminar flow in traditional pipe relates the pressure drop (Δp) to the volume flow rate (\dot{V}) as presented by Equation (2.13) in section 2.2.1 above. For developing laminar flow in traditional pipe, in addition to the effect of entrance region, another effect often contributes to the pressure drop is the active apparent friction factor attributed to the flow developing effect, which could be more prominent in narrow flow passage.

To account for this effect, a flow developing pressure loss as given in Equation 2.17 in section 2.2.1 often considered when estimating the pressure drop or friction factor in a pipe flow [5, 18]. For K_∞ in Equation 2.17, Shah and Sekulic [5], from an analytical solution, presented a constant value of $K_\infty = 1.28$ for fully developed circular duct flow. However, they mentioned that this value may not truly represent the flow in microchannel geometry. In the absence of an established correlation for this K_∞ for microchannel geometry, Olsson and Sunden [67] recommended that the Re dependent

K_{∞} relationship for circular conventional pipe flow proposed by Chen [66] can be employed for microchannel flow. Some authors also supported the use of this relationship for narrow channels [18]. Thus, as applicable, this correlation is used in estimating pressure drop or friction factor in current work.

Friction factor (f) in turbulent flow in microchannel

There are a number of established f -Re correlations available for turbulent flow in traditional pipe as described in section 2.2.1 above. However, such any correlation for turbulent flow in microchannel is not readily available. Kim et al. [166] proposed that, for turbulent flow in both circular and non-circular microchannels, the well known Blasius correlation [5, 11, 64, 68] established for conventional smooth pipes, given in section 2.2.1 in Equation 2.20, could be employed in microchannel flow to represent the f data without much error.

Some modifications to the Blasius Equation 2.20 was also proposed by Phillips [193] by defining it through the apparent Fanning friction factor ($f_{f,app}$) as a function of Re as expressed by Equation (3.3), which is said to cover both the developed and developing turbulent flow regimes in conventional pipe flow. Kandlikar et al. [18] has suggested that this modified Blasius Equation (3.3) can also be attempted for microchannel flow.

$$f_{f,app} = A Re^B = \left(0.0929 + \frac{1.01612}{x/D} \right) Re^{\left(-0.268 - \frac{0.3293}{x/D} \right)}; \text{ (Turbulent pipe flow)}. \quad (3.3)$$

Yu et al. [110], in their investigation of nitrogen gas and water flows through silica made micro-tubes, proposed the f -Re correlation in the Reynolds number range of $220 \leq Re \leq 19500$. They observed some lower Darcy f in micro-tubes, which are 0.7 to 0.9 times of that of the values estimated from traditional Blasius equation. They observed the transition-to-turbulent regime over the Reynolds number range of $1700 \leq Re \leq 6000$. Their proposed correlation is cited below by Equation (3.4).

$$f = \frac{0.302}{Re^{0.25}}, \text{ for } 6000 < Re < 20000 \text{ (Developed turbulent flow in micro-tube)}. \quad (3.4)$$

Webb and Zhang [125] studied the turbulent flow and heat transfer natures of liquid R134a in 9-channel multi-port circular and rectangular microchannels in the Reynolds number range of $5000 \leq Re \leq 25000$. Their friction data compared well with traditional pipe flow correlations such as Blasius correlation [5, 11, 64, 68] given by Equation (2.20); and Petukov correlation [53, 70] given by Equation (2.22). The authors proposed an f -Re correlation for turbulent flow in circular and rectangular microchannels in form, which is defined by Equation (3.5) below.

$$f = 0.0605 \text{Re}^{-0.22}, \text{ for } 5000 < \text{Re} < 25000 \text{ (Turbulent flow in microchannel)}. \quad (3.5)$$

Comments on friction factor (f) for flow in microchannel

From the above review it is seen that the f values for microchannel flow are about 0.5 to 5 times of that of the f values for traditional pipe flow. This trend of data scatter and discrepancies in microchannel flow are also compiled and reported by some authors [37]. Examples of these deviations in published result are displayed by Figure 1.3.

It is also seen that the differences in the reported results spread among a broad range of diameters or hydraulic diameters as surveyed for single phase flows in microchannels in current study. Important fact is that the study or the proposed correlation for developing flow in either straight or in serpentine bend circular microchannel is not available in the open literature.

3.1.2 Critical Reynolds number (Re_{cr}) for single phase flow in microchannels

The critical Reynolds number (Re_{cr}) for fully developed laminar classical internal circular pipe flow is well established to be $\text{Re}_{\text{cr}} \approx 2300$. Traditionally for $\text{Re} > 2300$ in internal pipe flow the onset of laminar to turbulent flow transition begins. The findings

from one study to the other in the past work [24-27, 33, 37-39, 41, 79-192] give information that the Re_{cr} in microchannels to occur at some values which are higher, lower or similar compared to classical value of 2300.

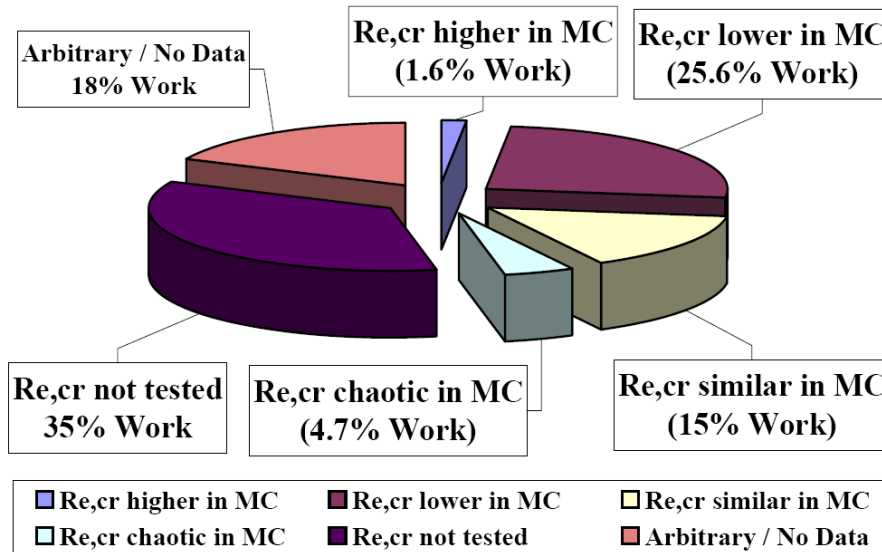


Figure 3.2. Statistics on observations of Re_{cr} natures in microchannels in reviewed past works

Information on Re_{cr} could not be extracted from some work for either not studied or not reported. The observations on Re_{cr} in microchannel flow are illustrated in percentile form in Figure 3.2 above. Early transition from laminar to turbulent i.e. $Re_{cr} < 2300$ in microchannels are reported by many researchers. According to some authors, early transition occurs when the hydraulic diameter of the channel decreases [28, 88, 103, 114, 138, 145, 174]. A delayed transition in other words relatively higher Re_{cr} in microchannel i.e. $Re_{cr} \geq 2500$ was also reported by some authors [110, 163, 181].

Some works pointed that the Re_{cr} in microchannel flow depends on the channel wall roughness and occurs in a different way as compared to the conventional pipe [39, 81, 101, 104, 106, 108, 114, 121, 130, 133-134, 148, 163]. Several works indicated that the transition from laminar to turbulent flow in microchannels begins at a Re value similar to the conventional value of 2300 [27-28, 38, 95, 132, 136, 142, 149, 152-153, 155, 158-159, 165, 182-183, 186]. While many these works, with acceptable data deviations, reported that the Re_{cr} in microchannel flow are similar to the conventional value, much lower Re_{cr} in microchannel flow i.e. $Re_{cr} < 1100$ were however observed by many other researchers [39, 81, 99, 101, 103, 114, 148, 174, 184, 191].

Some authors reported that the flow in microchannels can be considered in transition for $2300 < Re < 3000$ for circular microchannels and $2100 < Re < 2700$ for rectangular microchannels [166]. The fully developed turbulent flows are established in microchannels when $Re > 4000$ [166]. They also suggested that the transition flows in microchannels can not be analyzed using the classical correlations before any modifications are introduced [166]. The details of such modifications however are not explained in their article.

3.1.3 Heat transfer characteristics – the Nusselt number (Nu) for single phase flow in microchannels

The Nusselt number (Nu), as described and expressed by Equations 2.11 and 2.12 in section 2.1.8 above, is a non-dimensional group usually used to represent the dimensionless heat transfer coefficient of a heat exchanging device. An accepted notion is that the Nu generally is higher in microchannels. The review of the past work [24-27, 33, 37-39, 41, 79-192] sees that the Nu observations follow similar trends to that of f , Po , and Re_{cr} trends described in above section. This means that the observed Nu in past works has also different values.

A number of authors reported the Nu in microchannels is higher while others found lower than conventional tube. A few researcher observed chaotic and different trends of Nu in microchannels as compared to the conventional pipe flow situation (i.e. simultaneously higher, lower, similar or inconclusive) [93, 108-109, 111, 113-114, 128, 133, 146, 152-153, 157, 162, 179, 191]. It is well intuited that the Nu increases with the increase of Re. The Nu decreases when Re increases were also observed by some authors [93, 101, 121, 153]. The Nusselt number (Nu) for fully developed laminar flow in traditional pipe is generally independent of Re and Pr but is dependent on the thermal boundary conditions [5,11]. Some authors observed the Nu dependency on Re and Pr in laminar microchannel flow. In laminar microchannel flow, several authors reported that

the Nu increases with the increase of Re and the exponent of Re ranged from 0.3 to 1.96 [82, 88, 95, 112, 115, 125, 148, 171].

Many works stated that the Nu in microchannels can be predicted, without much error, by employing the classical correlations developed for conventional pipe flow. Figure 3.3 above depicts a glimpse of this statistics.

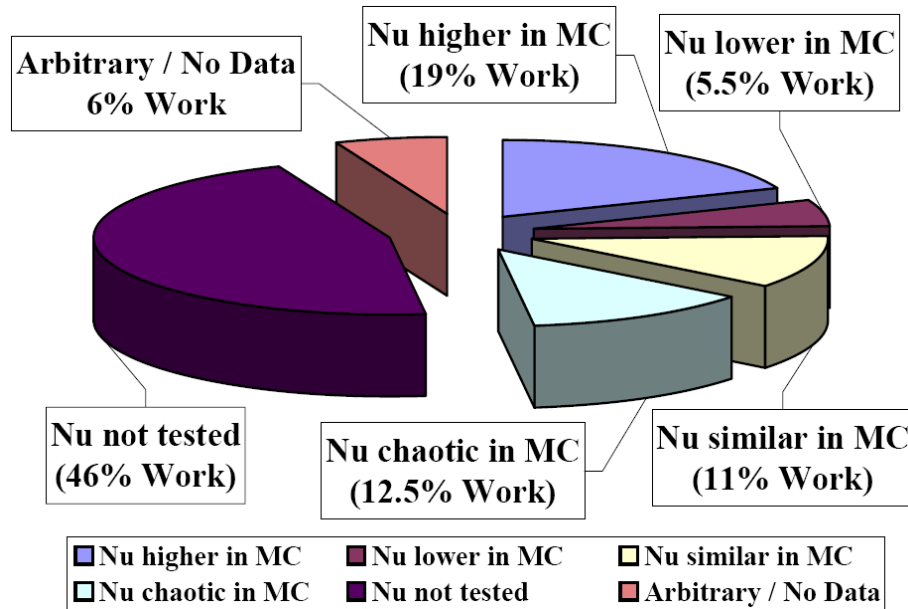


Figure 3.3. Statistics on observations of Nu nature in microchannels in reviewed past works

Heat transfer characteristics (Nu) in laminar flow in microchannel

Some authors have proposed the heat transfer correlations for fully developed laminar flow in straight smooth narrow channels, mostly on rectangular and few on circular cross-sections, as discussed below.

As cited by Kim et al. [166], Hartnett and Kostic (1989) proposed one heat transfer correlation for fully developed laminar flow in smooth straight narrow rectangular duct with H boundary condition (i.e. the constant wall heat flux), which is presented by Equation (3.6) below.

$$\text{Nu}_H = 8.2354 \left(\begin{array}{l} 1 - 2.0421AR + 3.0853AR^2 - 2.4765AR^3 \\ + 1.0578AR^4 - 0.1861AR^5 \end{array} \right), \text{ for } \text{Re} < 2100, \quad (3.6)$$

where Re is based on hydraulic diameter and AR is the height-to-width known aspect ratio of the flow channel. For the fully developed laminar flow in smooth straight rectangular duct with any other arbitrary boundary conditions, i.e. the wall heat flux or wall temperature boundary conditions, the Nu may stay somewhere between 3 and 6.5 unless the aspect ratio AR approaches zero or infinity (which are the situation of being vertical or horizontal flat plates).

Proposed heat transfer correlation for fully developed laminar flow in circular microchannel is limited in the open literature. In developing flow the Nu exhibits higher value than the developed flow. The heat transfer correlation for developing laminar flow in straight circular microchannels in general and channels with serpentine bend in particular is not available in the open literature. Some heat transfer correlations for fully developed laminar flow in narrow channels are proposed in the open literature, which are described below.

Choi et al. [88] conducted experiments on nitrogen gas in laminar and turbulent flow regimes using silica made straight circular rough micro tubes in the range of $30 \leq Re \leq 20000$. The relative roughness of the tubes was between 0.0023 and 0.08. The laminar flow Nu was found higher than that predicted using conventional correlations. Their proposed correlation however predicts lower Nu values than that predicted by Hausen correlation [11] given by Equation (2.33) for traditional laminar flow. The authors reported that the Nu depends on both the Re and the Pr even in laminar flow regime. As given by Equation (3.7) below, their correlation is in the similar form of the simplified Nu-Re-Pr relationship described in section 2.1.8 (Equation 2.12c).

$$Nu = 9.72 \times 10^{-4} Re^{1.17} Pr^{1/3}; \text{ for } Re < 2000 \text{ (Laminar flow in micro-tube)} \quad (3.7)$$

Heat transfer characteristics (Nu) in turbulent flow in microchannel

In turbulent flow, most of the thermal resistances gather near the wall and within the viscous sub-layer, which causes the temperature and velocity profiles to become relatively flat over major part of the pipe cross-section [5]. Therefore except for the non-rounded inlet configuration, the influence of channel cross-sectional geometry on the heat transfer in turbulent flow is less significant as compared to the laminar flow. A few authors proposed the heat transfer correlations for fully developed turbulent flow in straight smooth narrow channels, as discussed below.

Wang and Peng [101] proposed a heat transfer correlation for turbulent flow in straight narrow rectangular duct as given by Equation (3.8) below.

$$\text{Nu} = 0.00805 \text{Re}^{0.8} \text{Pr}^{1/3}; \text{ for } \text{Re} > 1500 \text{ (Turbulent flow, rectangular duct)} \quad (3.8)$$

Jiang et al. [148] proposed another correlation for developed turbulent flow in smooth straight narrow rectangular duct as given by Equation (3.9) below.

$$\text{Nu} = a \left(\frac{\text{Re} \cdot \text{Pr} \cdot D_h}{\underbrace{L}_X} \right)^b, \quad (3.9)$$

where the coefficient a and the exponent b depend on the parameter X in parenthesis, i.e. for $X < 0.05$, $a = 0.52$, $b = -0.62$ and for $X > 0.05$, $a = 2.02$, $b = -0.31$.

Webb and Zhang [125] studied the turbulent flow and heat transfer natures of liquid R134a in 9-channel multi-port circular and rectangular microchannels in the Reynolds number range of $5000 \leq Re \leq 25000$. Their single-phase heat transfer data showed acceptable agreements with the traditional pipe flow correlation provided by Petukov [70, 76] as given by Equation (2.38) above. The authors proposed a Nu-Re correlation valid for turbulent flow both in circular and rectangular microchannels as given by Equation (3.10) below. Their correlation is similar to the simplified Nu-Re-Pr relationship described in section 2.1.8 in Equation 2.12c and presented in the form of Dittus-Boelter turbulent correlation [57-58] as given in Equation (2.41) above.

$$Nu = 0.0172 Re^{0.84} Pr^{1/3}; \text{ for } 5000 < Re < 25000 \text{ (Turbulent flow in microchannel)} \quad (3.10)$$

Choi et al. [88] conducted experiments on nitrogen gas in laminar and turbulent flow regimes using silica made straight circular rough micro tubes in the range of $30 \leq Re \leq 20000$. The Nu is significantly higher in turbulent regime, i.e. from 7 to 16 times of that predicted by conventional turbulent correlations such as the Colburn analogy. They proposed a Nu-Re-Pr correlation for turbulent flows in micro-tubes, which is given by Equation (3.11) below. Their correlation is presented in similar form of the simplified Nu-Re-Pr relationship as described above in section 2.1.8 (Equation 2.12c).

$$\text{Nu} = 3.82 \times 10^{-6} \text{Re}^{1.96} \text{Pr}^{1/3}; \text{ for } 2500 < \text{Re} < 20000 \text{ (Turbulent flow in micro-tube)} \quad (3.11)$$

For turbulent flow in microchannel, some authors suggest that the employment of the Gnielinski correlation [77] given by Equation (2.39) or the Dittus–Boelter correlation [57] given by Equation (2.41) could estimate the Nu in microchannels without serious error [24, 27, 125, 159, 183]. According to several other authors, some corrections are necessary for these traditional correlations to be suitably employed in in turbulent flow in microchannels [24, 27, 93, 101, 110, 112, 125].

One such modification to the Gnielinski [77] correlation, for both circular and non-circular cross-section, was proposed by Adams et al. [122] and verified by Adams et al. [127] to employ it in microchannels. The modified version can be expressed by Equation (3.12) below, where the adopted factor F depends on the Re and the channel diameter D or the hydraulic diameter D_h .

$$\text{Nu} = \text{Nu}_{\text{Gn}}(1 + F) \quad (3.12)$$

where, $F = 7.6 \times 10^{-5} \text{Re} \left[1 - \left(\frac{D}{D_0} \right)^2 \right]$ and $D_0 = 1.167$ mm. The Nu_{Gn} is the Gnielinski's [77]

heat transfer correlation for fully developed turbulent flow in conventional smooth pipe as given by Equation (2.39) above, which is invoked and presented below.

$$\text{Nu}_{\text{Gn}} = \frac{\left(\frac{f}{8}\right)(\text{Re}-1000)\text{Pr}}{1+12.7\sqrt{\left(\frac{f}{8}\right)}\left(\text{Pr}^{\frac{2}{3}}-1\right)} \quad \text{for } 2300 < \text{Re} < 5 \times 10^6 \text{ and } 0.5 < \text{Pr} < 2000. \quad (2.39a)$$

where the friction factor f is the Darcy friction factor, which is determined using Petukov's turbulent friction correlation given by Equation (2.22) as repeated below. All the fluid properties for Equations (2.22) and (2.39a) are evaluated at bulk temperature.

$$f_d = [0.790 * \ln(\text{Re}) - 1.64]^{-2} \quad \text{for } 3 \times 10^3 \leq \text{Re} \leq 5 \times 10^6 \quad (2.22)$$

Comments on heat transfer characteristics (Nu) for flows in microchannel

The surveyed literature for single phase flow and heat transfer in microchannels spanned the channel size range of $0.001 \leq D_h \leq 4.1$ mm. Within this size range, it is observed that there appear noticeable disparities in heat transfer results i.e. the Nu values in microchannels are found about 0.21 to 16 times of that of the conventional value. When a flow is not fully developed, the Nu can be locally significantly higher than the value of Nu in developed flow. In such conditions the Nu can be estimated experimentally or from any appropriate correlation (if available). While few correlations for developing laminar flow for traditional pipe are available as seen in section 2.2.2, the correlation for developing laminar flow in circular microchannel is not available yet.

Therefore the important statistics summarized from the above review is that the study or any proposed correlation for liquid flow in developing laminar regime in either straight or in serpentine bend circular microchannel is not available in the open literature. No study is found in the open literature that focuses glycol-water mixture flow in narrow channel in developing laminar flow regime, which is the main focus in current research.

3.1.4 Fluid flow and heat transfer characteristics in MCHX

Compared to the research on MCHS for electronics cooling the works on single phase gas-to-liquid fluid flow and heat transfer on MCHX for thermal and energy applications are limited in the open literature. Some researcher reported the aspects of fabrication process of MCHX such as one on crossflow micro heat exchanger [157] and the other on extruded channel structures [194]. In other study, better performance was observed in un-finned micro bare tube heat exchanger as compared to the conventional gas-liquid heat exchangers [195-196]. Some authors studied the effects of fin spacing in condensation using finned MCHX. They found a reduced airside pressure drop and about 30 to 40% increased overall heat transfer coefficient and up to 70% increased heat duty compared to traditional coil for a given face area [197].

The effectiveness and pressure drop in micro crossflow heat exchanger have been studied to develop a model that predicts the thermal and fluidic characteristics to be used

in the design [187]. Some authors studied the single phase pressure drop measurements in microchannels and MCHX using liquid, vapor, and nitrogen flows [186, 198]. Their studied configuration and shape somewhat comparable to the crossflow air-to-liquid MCHX. Works on glycol-water mixture flows in narrow channels are rare in the open literature. A work investigated rectangular minichannels with hydraulic diameter of $D_h = 2.6$ mm and larger [177, 200]. The authors found both the f and Nu to vary with Re in the trend of turbulent f and Nu even for $Re < 1000$. The study in prototype air-to-liquid single phase MCHX comparable to automotive and other thermal heat exchangers is still limited in the open literature and the systematic design data are also rare.

3.1.5 Summary of literature review on fluid flow and heat transfer in microchannels and MCHXs

The fluid flow and heat transfer behaviors in microchannels in laminar, turbulent, and especially in the transition flow regimes are reported to be similar to or different from the conventional sized tubes. Not only in flow regimes, have the results reported in previous works also deviated from one investigation to the other. Many reasons for these deviations, in general, are mentioned that include the effects of channel surface roughness, entrance region, channel curvature, and more importantly the measurement uncertainty. Effects of any one or all of these factors might have contributed to these deviations.

Several authors showed that the transitional flows in microchannels are influenced by the fluid temperature, velocity, and channel sizes [81-82, 88, 90, 92, 101, 109, 113, 166]. High relative wall roughness in microchannels increases the convective heat transfer but they also contribute to the high pressure drop [140-141, 149, 171]. The existence of channel roughness affects the flow velocity profile and hence the Re in transitional flow regime [27].

The variation of viscosity with temperature in microchannels also affects the heat transfer [94, 106, 109, 120, 130, 143, 146, 164, 173]. To take the effect of viscosity variations into account the inclusion of the Brinkman number (Br) in the heat transfer correlation are also proposed [143, 190]. Some researcher reported that, to some extent, the friction factor (f) depends on the channel materials and also on the types of the test fluids evidencing the importance of electro-osmotic phenomena or electric double layer (EDL) effect at microscales [39, 87, 90, 135, 143, 155].

The measurement uncertainty affects the accuracy of investigation prominently; especially those are propagated from the channel dimension measurement [18, 23, 37, 162, 181, 199]. Many authors confirmed that the fluid flow and heat transfer phenomena for the single phase flow in microchannels can be predicted by employing the classical correlations within some acceptable accuracy limits. A large number of works on the other hand reported different and opposite observations. A critical review of experimental works on single phase convective heat transfer in microchannels summarized that many

of the experimental results for microchannels largely deviate from the classical correlations and interestingly these deviations increase as the channel flow rates and hence the Re increases [23]. For a flow passage, a lower size limit of 1.2 mm was stated by some authors above which these deviations might not occur [122, 127].

These divisive observations in microchannel flows still continue to exist even in the recent studies. For example, one study in the year 2007 did not find any unexplained physical phenomena for rectangular channel's hydraulic diameter falling in these channels size [183]. A later study in the same year 2007 found the Po to agree with the standard laminar flow predictions only up to $Re < 1500$ instead of up to $Re_{cr} = 2300$ [184]. They observed the Re_{cr} to occur in the range from $Re = 1500$ to 1700 for the straight microchannels and from $Re = 100$ to 200 for the serpentine microchannels [184]. The authors pointed that the unaccountability of increased pressure drop in the entrance region and the undependable accounting process of inlet and outlet losses may be the reasons for the discrepancy in published results. Other authors mentioned that the liquid flow friction and heat transfer in microchannel can be adequately described by the classical conventional correlations in the hydraulic diameter range of and $0.001 \leq D_h \leq 1$ mm [28, 189].

Park and Punch (2008) investigated the friction factor f and the heat transfer Nu of water flow in rectangular microchannels in the size and Re ranges of $0.1 \leq D_h \leq 0.3$ mm and $69 < Re < 800$ respectively [190]. While the classical fully developed laminar flow theory could predict their experimental f data, the Nu data however deviated from the

classical fully developed laminar theory. By incorporating the Brinkman number (Br), they proposed a correlation to predict the heat transfer in microchannels applicable within their experimental range and condition.

Jiang et al. [191] studied the fluid flow and heat transfer of water in rectangular microchannel with $D_h \approx 0.5$ mm and found that the f decreases as the Re increases and the f values are 20 to 30% smaller than the value for classical duct flow. They observed $Re_{cr} \approx 1100$, which is also smaller than the conventional value of $Re_{cr} = 2300$. Their Nu data showed chaotic nature, which is constant and lower than classical value in the laminar regime but greatly exceeds the conventional value for transition and turbulent flow regimes. They suggested the necessity for further research in this area by stating that the fluid flow and heat transfer nature in microchannel is complex and less understood.

Mokrani et al. [27] reported the fluid flow and heat transfer characteristics of water flow in rectangular microchannel in the size range of $0.1 \leq D_h \leq 1$ mm. They remarked that the classical correlations for smooth tubes should remain valid in microchannel flow and the Re_{cr} should be similar to the conventional value of 2300. In the same year Naphon and Khonseur [192] examined the airflow in rectangular MCHS in the Reynolds number range of $200 < Re < 1000$ focusing electronics cooling and concluded that the f and heat transfer in microchannels still need to be validated.

These varied observations, differing results, and opposing opinions regarding the fluid flow and heat transfer characteristics in small size flow passages still continue even

in recent studies. Jokar et al. [200] investigated the single-phase laminar flow ($Re < 1000$) and heat transfer of glycol-water mixture in rectangular meso-channel compact heat exchangers for air-conditioning applications. They observed the fluid flow and heat transfer behaviors in their meso-channels having $d_h = 2.6$ mm to 4.1 mm, which were very different from that of the conventional laminar theory. Both the f and Nu were higher than the conventional values. None of the well-established traditional macro-scale heat transfer and pressure drop correlations through the circular or non-circular channels could directly predict their experimental data. Therefore, according to their conclusion it is still unclear whether the traditional correlations are directly applicable for use in small size flow passages with hydraulic diameters of $d_h < 3$ mm [200].

Noticeable is that compared to the deviation and difference in earlier results, the divergence in recent investigations are less, which is inline with the observation as reported in a critical review [23]. This may probably be attributed to the availability of modern microchannel fabrication techniques; sophisticated experimental instrumentation, automated data collection, and computer based data processing facilities etc. From the review, it is observable that the differences in results and observations and divisive comments still appear in the recent studies. The validity of conventional fluid flow and heat transfer theories to be applicable in microchannel flows is still disputed and there exists information and data sets that support both sides of the arguments.

Thus, further research is needed in this promising area is truly understandable to reconcile the issues. Many of the investigations used non-circular and non-metallic

standalone microchannels as the basic shapes. More research using different applied microchannel geometries and shapes such as the multi-port straight and serpentine test slabs (for thermal heat exchangers applications) and various working fluids are necessary in developing experimental database to help establish design guideline for MCHX.

3.2 Scope of current research

The scope of further research is the experimental investigation of fluid flow and heat transfer characteristics of glycol-water mixture flow inside flat tube multi-port serpentine microchannel slab heat exchanger in air-to-liquid crossflow orientation. In order to carryout the proposed research, the required heat transfer and fluid flow experimental facility in a closed-loop thermal wind tunnel environment has been designed and developed. In addition to the principal heat transfer study of internal working fluid, the investigation of pressure drops and friction factors of water and glycol-water mixture flows in multi-port straight microchannel slab have also been carried out.

The geometries of the flat tube multi-port microchannel test specimens chosen in current study are one 1-pass straight slab, one 2-pass slabs with serpentine bend, and one prototype heat exchanger having 15-pass slabs with serpentine bends (for heat transfer investigation). As portrayed in the experimental infrastructure in next section, the multi-port slab test specimens and the prototype microchannel heat exchanger (MCHX) are made of the same material with identical dimensions and geometric configurations.

The outcome of the investigation will help consolidate the fundamental fluid flow and heat transfer data, validate them with conventional correlation, to be useful as a systematic design guideline. Current research, in the developed versatile experimental test facility with high accuracy instrumentation, expects to obtain reasonably accurate measurement data that can be analyzed and compared with the available similar works. The investigation will be carried out in a variety of Re regimes with particular focus on developing laminar flow to obtain heat transfer correlation in this regime, which is not available in the open literature yet.

3.3 Basis of test specimen designs and working fluid selection for current study

Figure 3.4 below represents the test slab cores that have been used in current study. The selection criteria of channel size and cross-section; the flow passage geometry, shapes, patterns, and materials of test slabs; and working fluids are described below.

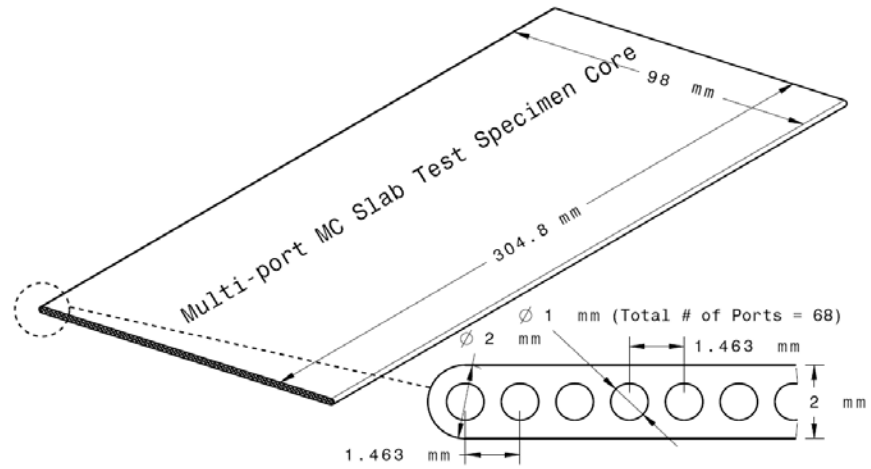


Figure 3.4a. Channel cross section and shape used in current research (Straight slab)

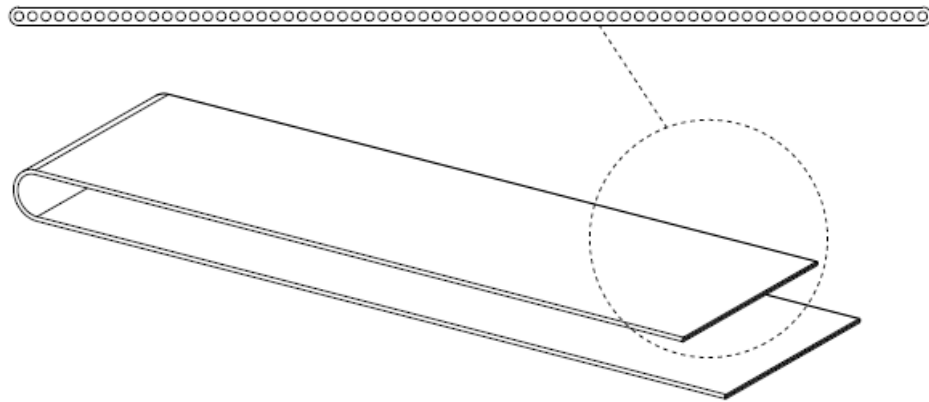


Figure 3.4b. Channel cross section and shape used in current research (Serpentine slab)

3.3.1 Channel size – hydraulic diameter range

All the works reviewed in this article [24-27, 33, 37-39, 41, 79-192, 200] spanned in the size range of $0.001 \leq D_h < 4$ mm. In general, a channel diameter or hydraulic diameter of 1 mm and less is broadly termed as microchannel in small scale fluid flow and heat transfer [10, 21-28].

The work of Adams et al. [122] on capillary tubes with $D_h = 0.76$ and 1.08 mm was further verified in a later study by Adams et al. [127] using non-circular microchannel with $D_h = 1.13$ mm. Adams et al. [122, 127] suggested that the $D_h = 1.2$ mm could be a reasonable lower size limit of a flow channel for the conventional fluid flow and heat transfer correlations to hold valid. On the other hand Jokar et al. [200] verified that the traditional correlations are not directly applicable for rectangular channels having hydraulic diameters of $D_h = 2.6$ mm to 4.1 mm. Since Adams et al. [127] suggested a lower size limit of 1.2 mm, the channel size of 1 mm was chosen in current study as a generalized dimension limit of microchannel, which is also less than the size range of conventional compact heat exchangers (3 mm) and also less than the size range studied by Jokar et al. [200]. The selected size is well within the size limits of most of the reviewed works. As a result the outcomes of current heat transfer investigations could well be compared with the available works and the applicability of classical correlations in this size range could be verified.

3.3.2 Channel cross section – circular or non-circular

The reviewed papers [24-27, 33, 37-39, 41, 79-192] used a number of flow channel cross sections such as rectangular, circular, trapezoidal, triangular, square, and few others. Figure 3.5 gives a quick quantitative view of the types of channel cross sections used in past works. No information on the channel cross section could be extracted from few of the works. As seen in Figure 3.5, the majority of the works used the rectangular cross section. The specific reason of using a particular type of channel cross section is not available in most of the papers.

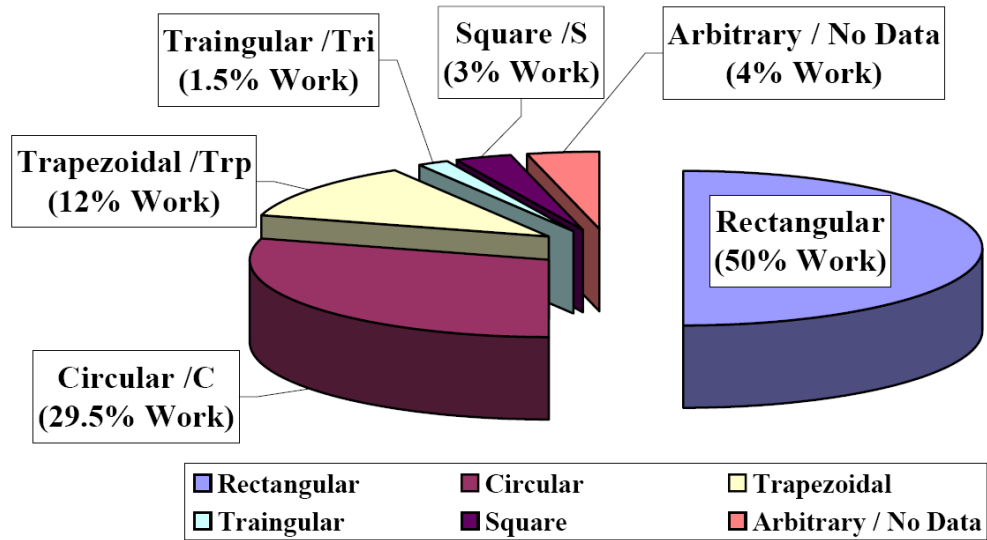


Figure 3.5. Statistics of cross sections used in microchannels in the reviewed past works

The circular channels offer overall best thermo-hydrodynamic performance for a MCHX among various other shapes [21]. The work on circular ports is less in the open literature. This may be because of the easier fabrication process of non-circular ports than

the round ones. A square or rectangular port can be easily made by slot cutting on a plate and then covering the top with a flat lid. In most of the earlier studies, the ports were made with chemical etching. Etching leaves higher channel surface roughness and non-uniform channel dimensions as compared to the ports made with laser beam or multi-port extruded (MPE) tubing.

Present study thus chooses the multi-port microchannel slabs with circular cross sections as the basic flow passages. The test slabs are MPE tubing which have smoother channel surface and more uniform channel diameter than the ports made with etching process. The test specimens have 1 mm port diameter with surface roughness height of about 0.05% of the channel diameter making a relative roughness, $e/D = 0.0005$; and the maximum uncertainty in channel diameter is about $\pm 1.5\%$ [202].

Kandlikar et al. [149] investigated the effect of channel roughness on pressure drop and heat transfer in 1.067 and 0.62 mm diameter circular tubes in the Re range from 500 to 3000. The tubes were treated with acid solutions to create three different relative roughness (ϵ/D) values for each tube. They observed more increase in Nu and Δp in 0.62 mm tube than in 1.067 mm tube. Negligible variations of Nu and Δp with Re in 1.067 mm tube due to varying ϵ/D from 0.00178 to 0.00225 were observed. But significant variations were noticed in 0.62 mm tube for ϵ/D from 0.00161 to 0.00355. They recommended that the larger diameter tubes above 1.067 mm with $\epsilon/D = 0.003$ may be treated as smooth tube but for the small size tubes below 0.62 mm diameter is treated as rough tubes since the Nu and Δp depend on ϵ/D for tube size of < 0.62 mm. The transition to turbulence also gets affected by the change in ϵ/D above 0.003. In current

study the relative roughness value is $\varepsilon/D = 0.0005$ [202] and 1 mm diameter channel is within the size range between 0.62 and 1.067 mm. Therefore the channels in this study are considered smooth and the effects of ε/D on Nu and Δp are ignored.

3.3.3 Flow passage – multi-port slab or single bare tubes

A multi-port slab, i.e. a slab with multiple channels, is an applied geometry usually used as core elements in many practical heat exchangers. A single tube is a basic geometry used in laboratory and in other applications different from the interests of thermal heat exchangers. A slab with multiple ports has several advantages over any single or isolated bare tubes of the same numbers and diameter as the ports of the slab.

As an example, Figure 3.6 (not to scale) displays a multi-port slab with N number of channels each has a diameter of D , which are separated by very thin metallic walls making the liquid flow unmixed. Figure 3.6 also shows the equal N number of isolated bare tubes of diameter D , which are separated by low conductive but thermally highly resistive air media. The outside total heat transfer surface areas of the slab and the bare tubes are the same or similar. The thermal conductivity of a solid, such as Aluminum in current test slab, is always higher than air, water, and glycol-water mixture.

In force convective liquid cooling in a liquid-to-air heat exchanger, the high conductive metallic walls collectively pick and transfer most of the bulk liquid's heat from the centers of the channels to the slab surface where the quick heat transfer takes place with the flowing air. For the isolated bare tubes the flowing air is the only heat

transfer media for the tubes and between the separating gaps of the individual tubes. Since the air has very high thermal resistance compared to bulk liquid and solid walls, for a given operating condition the heat transfer is slower and weaker than the slab.

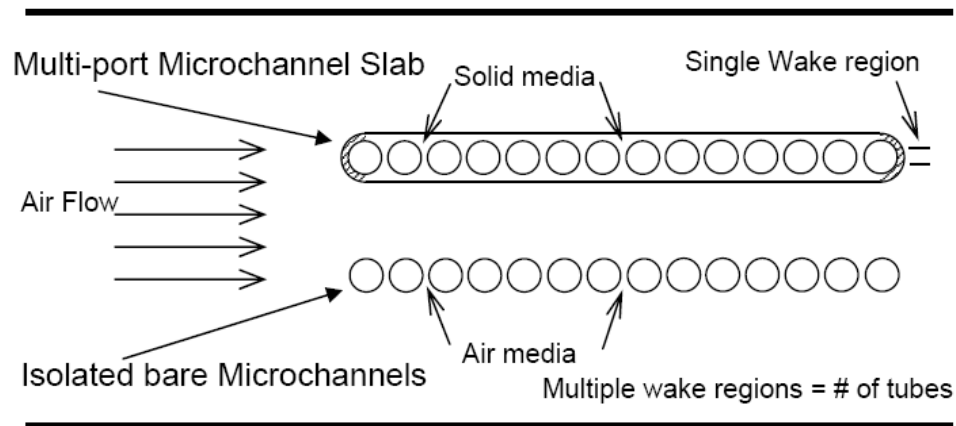


Figure 3.6. Comparison of a multi-port flat slab with same number and diameter of bare tubes.

Because of the flatness and the presence of solid walls in the slab, the temperature distribution is more uniform than the isolated bare tubes. Wake region usually reduces the heat transfer on the downstream tube and airside fin region. For the bare tubes, multiple wake regions i.e. one on the downstream of each tube form and as a result the heat transfer greatly reduces. As seen in Figure 3.6, the slab has only a single wake region at the downstream of the slab. Most of the flowing air comes in close contact with the slab surface due to the flat profile in the slab. This and the single wake region together help higher heat transfer to occur in the slab than in bare tubes. The flatness of the slab also helps reduce the airside pressure drop significantly and hence lowers the pumping cost as compared to the tubes. Due to these inherent features, slabs are obviously preferred over single or isolated bare tubes for typical thermal heat exchanger applications.

As seen in literature review above, most of the earlier works on narrow-size tubes recommended and emphasized the research on MCHX. Very little works on MCHX are found in the open literature that used slabs having multiple ports and majority of them used rectangular and square shapes of the ports. The work on slabs with circular ports is limited in the open literature. As discussed in section 3.3.2 above, the circular cross-section offers best thermal and hydraulic performance over other non-circular cross-sections [21]. Therefore, flat slabs with multi-port circular microchannels, as shown in Figure 3.4, were chosen in current research.

3.3.4 Multi-port slab shape – flat tube or round tube

In an air-to-liquid crossflow heat exchanger, for the airside the flat-tube configuration or the multi-port slab offers some demanding advantages over the round tubes, which have been described by many authors such as by Webb and Kim [2]. As discussed above, the wake region downstream of flat-tube does not reduce heat transfer as much as it does in round-tube. Flat-tube offers less airside pressure drop and occupy less space than the round tube. The flat-tube has also better fin efficiency and its study has expanded from the applications in automotive heat exchangers to the applications in heating, ventilation, air-conditioning and Refrigeration (HVAC&R) [203].

In an effort to explore the efficient microtube profiles for outdoor evaporator applications, Ozdemir [204] numerically studied both the liquid side and airside

performances of the straight microchannel (SMC) tube and the round microchannel (RMC) tube. The SMC tube has rectangular and the RMC tube has trapezoidal multi-ports. All the ports both for SMC and RMC tubes have the same hydraulic diameter. In fact if the SMC tube is bent to form a circular pattern, it takes the form of the RMC tube with its rectangular multi-ports taking the trapezoidal shapes.

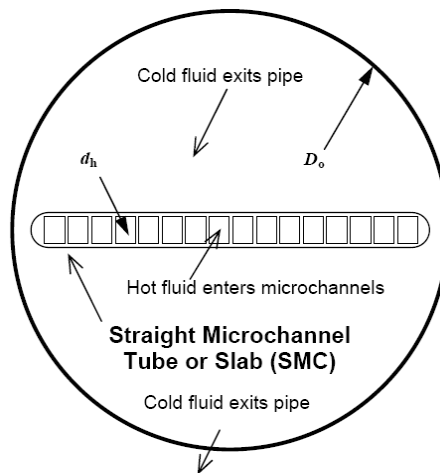


Figure 3.7a. Multi-port straight microchannel (SMC) tube inside large pipe

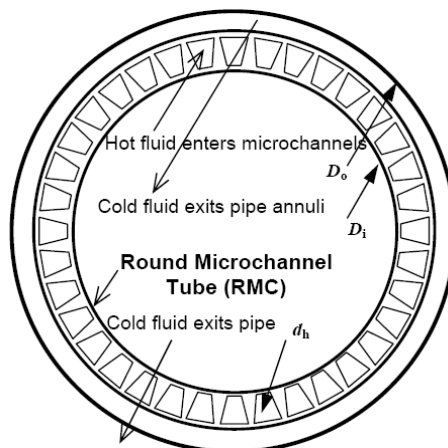


Figure 3.7b. Multi-port round microchannel (RMC) tube inside large pipe

Figures 3.7a and 3.7b (drawn not to scale) depict the SMC and RMC tubes. As seen in the Figures, the SMC and RMC tubes were placed inside large round pipes to form tube-in-pipe counter flow heat exchangers shell where the shell will act as water jacket. The large pipe shell for SMC has the similar diameter as the pipe shell of RMC tube shell. Hot fluid entered the multi-ports in SMC and in RMC tubes in one direction and the cold fluid as coolant entered the large pipe (water jacket) from opposite direction in counter flow orientation.

Ozdemir [204] reported the comparative performances of the SMC and RMC tubes as follows.

- SMC showed 24% higher liquid-side Nu than RMC
- 40% increased (cooling effect) airside heat transfer in SMC than RMC
- 2.6 times higher liquid-side pressure drop in RMC than SMC
- In SMC less liquid-side mass flow rate ($Re = 15$) gives high Nusselt number ($Nu = 15.3$) and in RMC relatively high mass flow rate ($Re = 32$) gives still low but comparable Nusselt number ($Nu = 13.1$)
- SMC provides higher compactness factor, CF, than RMC, i.e. $CF_{SMC} = 90$ over $CF_{RMC} = 39$; where the CF was defined by Equation 3.13 below;

$$CF = \frac{A_{coil}}{\dot{m}_{coil}} \left[\frac{m^2}{kg/s} \right], \text{ where } A_{coil} = \text{Perimeter} * \text{Length} * \text{No. of Channels} \quad (3.13)$$

- For an outdoor evaporator of 4 tons of refrigeration capacity, the RMC will take as much as 6 times more space than the SMC; space-wise one RMC will fit 3 SMCs.

3.3.5 Multi-port slab patterns – straight and serpentine

Curved or serpentine circular flow passages with or without fins are common in most practical heat exchangers in thermal and energy applications. Intuitively, the channel curvature can increase both the heat transfer and flow friction. Any application specific tradeoff between the heat transfer and the fluid flow can be adjusted if the heat transfer and pressure drop data on such channels are widely available.

Most of the previous studies [24-27, 33, 37-39, 41, 79-192] used fundamental configuration in their investigations such as the straight and standalone single stream flow passage. Some authors conducted studies in straight and multiple rectangular channels or grooves [22, 29-30, 33, 37, 92, 109, 111, 125, 128, 159-160, 177, 179, 191, 200]. Only a few works presented the observations on curved or serpentine channels [180, 184, 189]. Two other authors reported that the channel curvature can enhance the heat transfer significantly at the expense of increased flow resistance and the mean Nusselt number (Nu) alters radically when the flow changes from stable steady to temporal oscillating in curved zone [189].

Studies on microchannel slabs having multiple circular channels are also limited in the open literature. One evaluation was made for the effects of size and shape of the channels on the performance of MCHX [21]. The results indicate that for the same heat exchanger volume, increased number of channels give augmented effectiveness but also raise the pressure drop. Work that deals with finned microchannels to account for the relative contributions of the fins to the increased heat transfer, are rare in the open literature. Therefore the straight and serpentine circular multi-port slabs (Figures 3.4a and 3.4b above) with and without external fins at airside were designed and fabricated as the test specimens to conduct current research.

3.3.6 Multi-port slab material – metallic or non-metallic

In reviewed open literature [24-27, 33, 37-39, 41, 79-192], it is summarized that the flow channels used in the investigations were fabricated using various materials such as Silicon (Si), Stainless Steel, Copper (Cu), Aluminum (Al), Glass, and other Metals as shown in Figure 3.8 below. No data on the channel materials could be extracted for about 17% of the total works reviewed in this study.

The reasons for using particular type of materials in most studies are however not well explained. It is assumed that the fabrication facility and access to availability may be the reason to use certain type of materials. From the view point of electronics cooling

devices, conceivably due to the compatibility of micromachining and micro fabrication techniques in the semiconductor producing processes in electronics industries, Silicon possibly was the most used materials for microchannels [157].

Different materials have different thermal conductivities (k) and surface finishes or roughness (ε). The k dictates the heat transfer and the ε influences the frictional pressure drop. With the same ε , surface finish can vary from one material to the other and hence the friction factor (f). The f depends on the material of the channel walls (metals, semiconductors etc.) and also on the type of test fluids. These phenomena were reported by several authors [39, 87, 90, 135, 143, 155, 171].

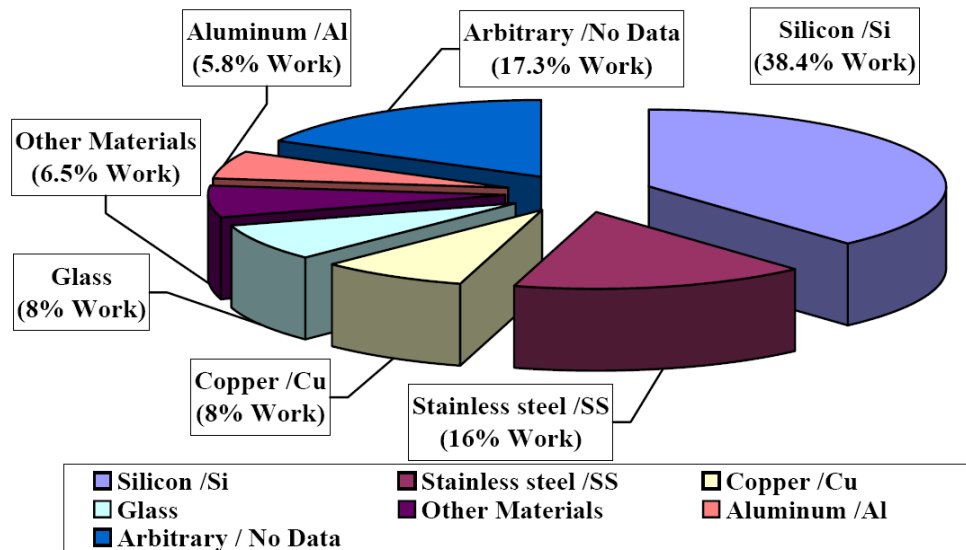


Figure 3.8. Statistics of materials used in microchannels in the reviewed past works

No statements, however, clearly found in the literature on the particular type of channel material that has either high or low ε . The f depends on the relative roughness of the channel walls in laminar regime were reported by some authors [81, 110, 123, 133-134, 137-139, 144, 148-149, 161, 163, 168, 171]. Aluminum made metallic flow passages have been very common to use as heat exchanger components in automotive, thermal, energy, HVAC and other industries. The k of Al is higher than stainless steel but relatively lower than Cu. For light weight feature while holding comparable structural strength of stainless steel and greater pressure limit than Cu, Al alloy is chosen to fabricate the test specimen for further study, which also has smooth surface finish.

3.3.7 Working fluids

In the review [24-27, 33, 37-39, 41, 79-192], it is noticed that various kinds of working fluids were used in internal channel flow. As portrayed by Figure 3.9, water is seen the most used fluid and air and other gases are next to water. Other fluids include nitrogen (gas and liquid), common refrigerants, alcohols, and silicon oils. Some works reported that the f to some extent depends on the types of test fluids evidencing the importance of electro-osmotic phenomena or electric double layer (EDL) effect at microscales [39, 87, 90, 135, 143, 155, 171]. Statement on any particular fluid type for EDL however, not clearly found in the reviewed literature.

It appears that the water, as the fundamental working fluid, used in majority of the previous research in basic geometries. The study with applied geometry and orientation such as the MCHX at cross flow of air for typical thermal applications is limited in the open literature. Only a few studies are available that deals with the single phase air-to-liquid cross flow orientation using microchannel slabs or MCHXs having non-circular shape of multi-port [22, 177, 200]. Viscosity, which varies from one fluid to other, plays an important role in fluid flow and heat transfer processes [94, 106, 120, 130, 143, 146, 164, 173]. The development and validation of necessary correlations for different fluids in microchannels need fluid based diverse investigations. Different fluids have different industrial interests. In this research, the distilled deionized (DDI) water as the fundamental and the 50% ethylene glycol-water mixture as the applied working fluids were chosen to conduct the experiments.

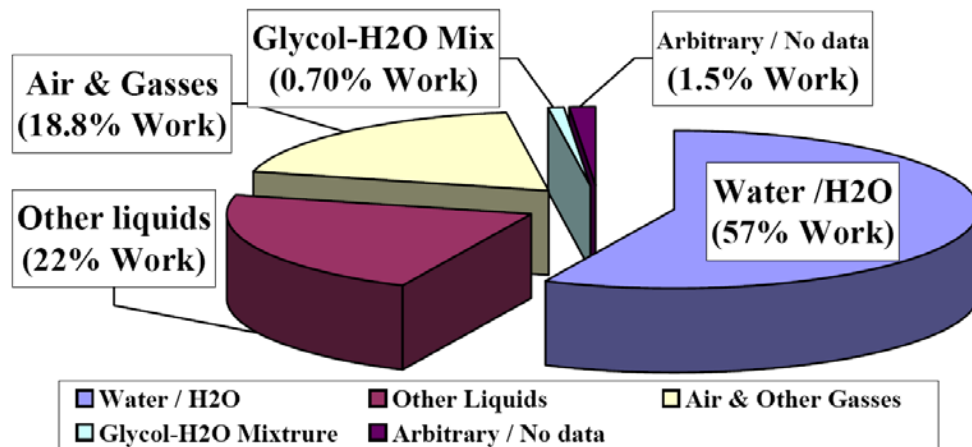


Figure 3.9. Statistics of working fluids used in microchannels in the reviewed past works

3.4 Choice of operating flow regimes in current study

The works on small diameter channel flows, as mentioned in the above literature survey summary [24-27, 33, 37-39, 41, 79-192], spanned all over the laminar, transitional, and turbulent flow regimes as seen from the scale of Re range $0.0008 \leq Re \leq 40000$ in Table-A1. Interestingly two works one very earlier and the other relatively the recent, extended the investigations to the high flow regimes, which are outside of the general flow regimes tested by most of the other researchers as reviewed in current study. Among these works one was by Gambill and Bunby [80] in the range $9000 \leq Re \leq 270000$ and the other by Qi et al. [26] in the range $10000 \leq Re \leq 90000$. However the overall observation in the literature survey is that the laminar flow in narrow channels is less studied and the differences in reported results is more in laminar flow than in turbulent flow. This suggests the necessity of further research in single-phase laminar flow regime.

Single-phase heat transfer and fluid flow have many practical interests for example in automotive and fuel cell heat exchangers among other applications. Heat transfer fluids in such heat exchangers usually have relatively higher viscosities and hence the flow regime is laminar. It is known that the better heat transfer is associated with a turbulent flow regime or a change of phase such as condensation or evaporation. The operation of the process and the system maintenance of the two-phase heat transfer is always more complex than the single-phase. A single-phase narrow tube system can be a

competitor of two-phase flow heat exchange device and thereby can simplify the overall necessity and complexity of a two-phase device [4]. Even in laminar flow through small diameter tube achieving a high heat transfer coefficient is possible if an appropriately optimized heat exchanger design can be applied. The laminar flow offers a better heat transfer and pressure drop ratio than a turbulent flow [203].

The flat tubes have some advantages over the round tubes such as less airside pressure drop, good fin efficiency, better fluid to surface contact and hence the heat transfer, and less wake region. Because of these features the flat tube air-to-liquid heat exchangers have been dominantly used in automotive and similar other applications. If the multi-port flat-tubes are used in such a heat exchanger, the multi-port is usually used at the liquid side and fins on the flat surface are assigned for the airside since air has high thermal resistance. For these applications such as the radiator, condenser, intercooler, air-conditioner etc., the compactness is very important. Better energy efficiency in these kinds of heat exchangers can be achieved in laminar flow if the smaller cross-sectional geometries of the flow passages are adopted [205].

The Reynolds number usually does not exceed 10000 in most practical automotive heat exchanger applications [6]. The typical flow regime for various automotive heat exchangers falls within the range of $1 \leq Re \leq 10000$ [206]. The design parameters for many automotive heat exchangers usually prescribe the low Reynolds number flow, which may be classified as laminar flow regime for $Re \leq 2000$ [207]. As discussed in the literature survey, not much investigation is found in the open literature

that deals with heat transfer in multi-port narrow channels in the laminar flow regime. Even no study is found in developing laminar flow. And no correlation is available for glycol-water mixture flow in narrow channels in developing laminar flow regime. In order to select a suitable flow cross-section and to predict the heat transfer performance in such flow passage for the design of a microchannel heat exchanger, further study is very important. It is of great necessity for engineers and scientists to understand how to predict narrow channel side liquid flow heat transfer performance.

Therefore, in view of the automotive and similar other typical thermal heat exchanger applications, the hot water and ethylene glycol-water mixture flows in multi-port MCHX slabs in developing laminar flow regimes ($Re \leq 2300$) were chosen in current study. The cold air as the external fluid was chosen to flow over the test slab surface at a given inlet temperature. The liquid flow Reynolds number inside the MCHX slab was varied between 200 and 2000 and the airflow was maintained constant in the range between 50 and 70 km/h.

3.5 Conclusions and recommendations

Ever increasing energy demands, and concerns for space, energy and materials savings highlight the necessity for miniaturized light weight heat exchangers that can provide high heat transfer. Microchannels have superior features in this respect compared to other conventional counterparts. As such, they have significant potential for use as heat

exchanger components in typical thermal and energy applications. Relative to the microchannel heat sinks in the electronics cooling industry, there is only limited research and development on microchannel heat exchangers for large scale thermal and energy applications.

The sort of widely available fluid flow and heat transfer correlations and design procedures for traditional heat exchanger tubes are not yet well established for microchannels. Indeed, the arguments are mixed on the validity and the applicability of classical macroscale theories in microchannel flows. Many authors thus emphasize the need for more research to develop experimental databanks to help reconcile the arguments and supplement the data in the research community.

The current study surveys the literature to date on the status and potential of microchannels for thermal and energy applications. It identifies further research needs and the scopes of such research. While deviations and differences in results were reported in earlier studies, the variations and discrepancies are less in recent investigations. Divergence of findings and divisive comments, however, continue to appear in the recent investigations. This difference calls for additional research and experimental works to consolidate the data and close the disparity gap. Moreover, with a few exceptions, most of the reviewed works used a basic, stand alone microchannel geometry and fundamental working fluids. Practical heat exchangers in typical thermal applications tend to use core elements with complex geometric configurations. Therefore, extended investigations

using various applied channel shapes, configurations, manifold geometries, and a variety of working fluids are required to represent the real life heat exchangers.

The present work provides information on the test specimens and experimental infrastructure that have been designed and developed to undertake the type of research indicated by the presented literature review. In particular, a versatile single phase air-to-liquid crossflow dynamic test rig was developed that is capable of offering fluid flow and heat transfer research facility, for various working fluids (liquids and gases), with a variety of microchannel geometries, as well as prototype microchannel heat exchangers, for use under wide operating conditions. The execution of a rigorous test procedure with the introduced high quality equipment and accurate instruments may lead to a relatively more accurate data set with results that may be inline with a subset of the published results, possibly leading to the establishment of a consensus on microchannel quantitative results within the research community in this area.

The findings of this literature review, identification of further research, and the scope and proposals for current study were documented and sent for journal publication. Current objectives are recognized as the necessity for further research and are published in peer-reviewed journal [201].

CHAPTER – 4

DEVELOPMENT & COMMISSIONING OF EXPERIMENTAL FACILITY AND DESIGN OF TEST PROCEDURES

4.0 DEVELOPMENT & COMMISSIONING OF EXPERIMENTAL FACILITY AND DESIGN OF TEST PROCEDURES

A significant part and challenge of current research were to design and fabricate the microchannel test specimens and to design, develop and commission of a heat transfer and fluid flow test facility from the scratch for conducting the proposed experimental investigation. With some pros and cons, finally these challenges were met successfully, which are described below. It is worth mentioning that the requirements for developing an experimental test facility and selecting the types of test specimens in current study were recognized by the scholars in this area and the details of the developed test facility and proposed research were accepted and documented through journal publication [201].

In the literature review, the differences in reported results from one work to other, large scatter in experimental data, and the deviations from classical theory may have been originated from the measurement uncertainty being one of the major sources of errors and discrepancies [23, 199]. The measurement uncertainty includes but not limited to the capability of the test facility, experimental method, instrumentation, data collection and the data processing system. All the key parameters the i.e. f , Δp , and Nu are driven by the flow rate, temperature and pressure of the working fluids. Literature survey reveals many works that used manual flow measurements such as the timed catch-weigh method [27, 87, 155, 180] and several others used graduated rotameter [4, 29, 122, 127, 149, 177, 182, 187, 191, 196, 208]. Some works used mechanical pressure gages to measure Δp in

microchannel [29, 87], which usually has less accuracy and also poses human error. Most of the works used type T or K thermocouples in measuring the fluid temperature through microchannel instead of highly accurate other possible means, such as the Resistance Temperature Detector (RTD) [4, 27, 29, 33, 99, 149, 182, 177, 183, 191, 199, 208].

Minimizing the flow fluctuations and ensuring better accuracy in flow, pressure, and temperature measurements to obtain reasonably accurate data could significantly reduce the measurement error and hence the deviations in reported results. The reliable experimental data depend on the high accuracy measuring instruments such as the digital flow meters, pressure and temperature sensors, and automated data acquisition systems including the proper choice of components of experimental facility such as the liquid pump, flow control and monitoring devices etc.

A large group in the surveyed works used test rig where major focus was given on the internal fluid flow and/or heat transfer through a single standalone microchannel or multi-port MCHS, where the heat transfer role of the external fluid flow was realized by electrical heating i.e. constant heat flux [4, 27, 33, 127, 149, 183, 208]. Many works used open-loop experimental setup where the liquid flow was pressure driven or syringe pushed and exited to the atmosphere [39, 87, 149, 180, 182, 184, 196]. These types of experimental setup and methods may not be relevant for current heat exchanger in focus [22]. A few studies used liquid-to-liquid crossflow experiments but their cubical heat exchanger configurations and orientations do not represent the crossflow automotive or other similar thermal heat exchanger applications [157, 187]. Comparable operating

conditions for crossflow automotive or similar other typical thermal heat exchanger applications, as the capacity factor of a test facility is also limited in the literature.

A crossflow heat transfer and fluid flow test facility, where the liquid flows internally through the MCHX flow passages and the air flows externally across the MCHX, is rare in the open literature. Papers that describe and provide comprehensive information on the test facility are also limited in the open literature. A single phase liquid flow test facility was developed by earlier authors focusing the internal flow [208], which provided relatively more information over others. Other review works on liquid flow experimental procedure in microchannels also give some useful information [199]. This promising area however is in short supply of established guidelines for setting up an experimental facility and lacks the standard or recommended procedures for investigating the fluid flow and heat transfer in microchannels and MCHX.

In current study, on the basis of statistics gathered from the literature survey and necessity of further research, as described above in section 3.3, first the test specimens were designed and fabricated. Depending on the necessity of current research, a dynamic well instrumented single phase crossflow experimental infrastructure has been developed to investigate the fluid flow and heat transfer in microchannel and MCHX test specimens. A great deal of attention was paid to the key components, high accuracy measuring instruments, and automated data monitoring and acquisition systems. The concept design, 3-D modeling and 2-D drafting of the test facility and its components were done by the candidate using CATIA V5 R16 CAD package. While a schematic and picture of the

developed test facility are given in Figure 4.1 below, other details and photographs of the test facility and components are provided in Figures B1 through B5 in Appendix B1.

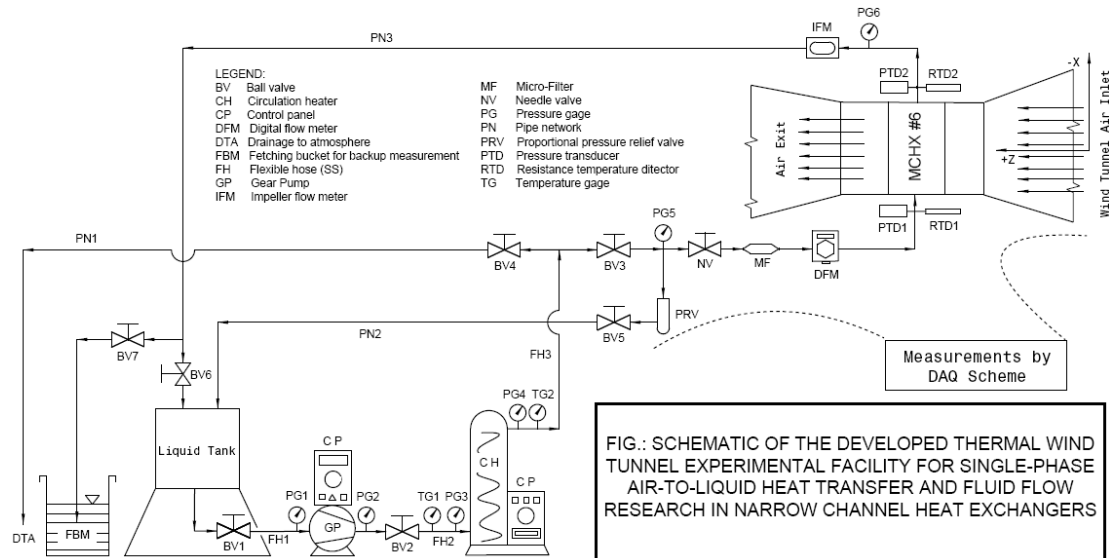


Figure 4.1a. Schematic of the developed thermo-fluid experimental facility in current research.

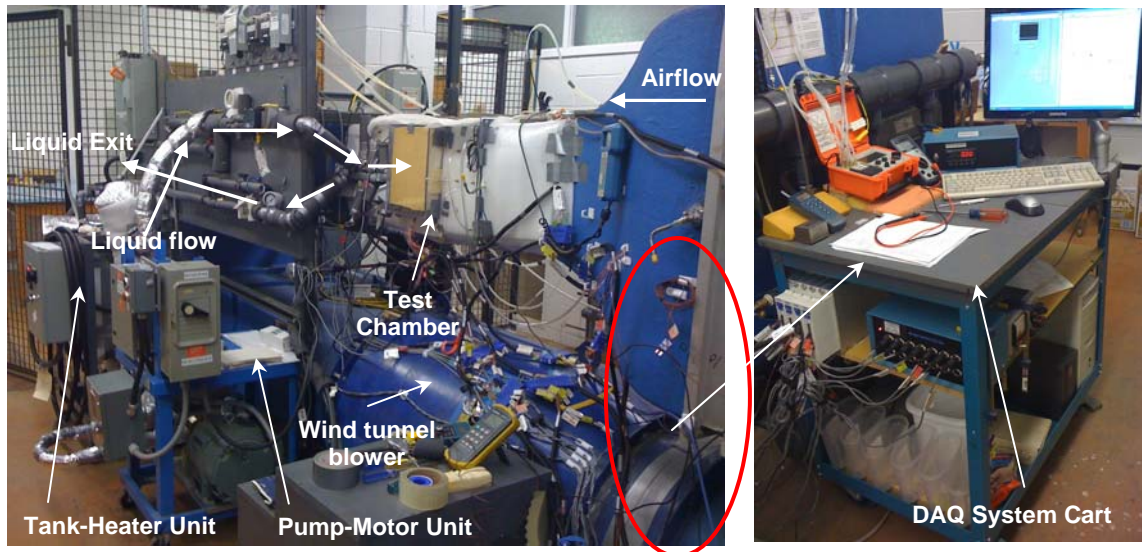


Figure 4.1b. Photograph of the developed thermo-fluid experimental facility in current research.

The test rig contains a closed loop thermal wind tunnel for producing airflow and a liquid handling system. The flexibility of the liquid handling system and the incorporated instrumental capability make the test bench versatile that provides fluid flow and heat transfer research facilities for different microchannel geometry in a broad laminar to turbulent flow regime and in wide pressure and temperature ranges. The setup is designed in a way, if the pump-tank unit is replaced by a pressurized gas reservoir, it can also handle various gas flow through microchannel. As required the test setup is capable of being operated in closed-loop or open-loop by just maneuvering two valves.

Starting with the details of the test specimens, this section introduces with the liquid handling system, supporting components, air handling systems, instruments required to deliver and handle metered working fluids, data acquisition scheme, experimental procedure, commissioning of test rig, and system's heat balance. This section also provides information on experimental comparative comparisons of two traditional and one prototype microchannel heat exchangers, which were performed in the test rig as a preparedness step for next subsequent experiments.

4.1 Design and fabrication of microchannel test specimens

The concept design of the test specimens were made right after the first phase of literature review. Since commercial laser fabrication of microchannel was not readily

available, majority of the works in reviewed literature used the standalone custom built test samples made in house mostly by etching method using chemical solutions. This etching process leaves microchannel surface with countable roughness. Channels cut with laser beams virtually leave no surface roughness. Therefore in current study, the process of searching sophisticated fabrication technology using laser beam and the associated manufacturer started in late 2005. At the time only two such manufacturers could be found (to the best of candidate's knowledge) who are USA based and used to commercially fabricate the narrow flow channels. They are Hydro Aluminum and Modine Manufacturing Company.

Communications were developed with both of the manufacturers for possible fabrication of microchannel test specimens. They make bulk production and supply. Since few different test samples for current research need different manufacturing settings and adjustments, getting the test specimens fabricated by the vendor was very difficult. However, design communications with Hydro Aluminum through 2005 to 2007 made all the test specimens fabrication possible. Therefore, in addition to candidate's proposed research goal, every effort was given in developing the test facility and in designing the test samples in a way so that the laboratory can extend and conduct its further research in a long-term basis.

With this view, five independent microchannel slab test specimens and a prototype MCHX were designed by the candidate, which were supplied by Hydro Aluminum in mid 2007. The flow passages of all the 1 mm multi-port extruded (MPE)

test slabs were fabricated using laser beam technology. At the manufacturing facility, each of the test slabs was hydro tested to check the pressure endurance capability and to see if there is any blockage in any of the 68 independent channels. The MPE test slabs are capable of withstanding a moderate to high working pressure of 15 MPa and no blockage was found [202]. The ends of the slabs were set thru the inlet and exit manifolds where the brazing technology was applied to join the surfaces only on the outside. This method of joining needs no internal weld. Thus there is no presence of residues or scraps that could otherwise cause the blockage to the manifolds. The cross-sectional view and dimensions of a single straight slab and a serpentine slab are shown in Figures 3.4b and 3.4c in section 3.3.2 above. The inlet and exit connection configurations of a basic slab is illustrated in a not-to-scale Figure 4.2 below, where not all the 68 channels are shown.

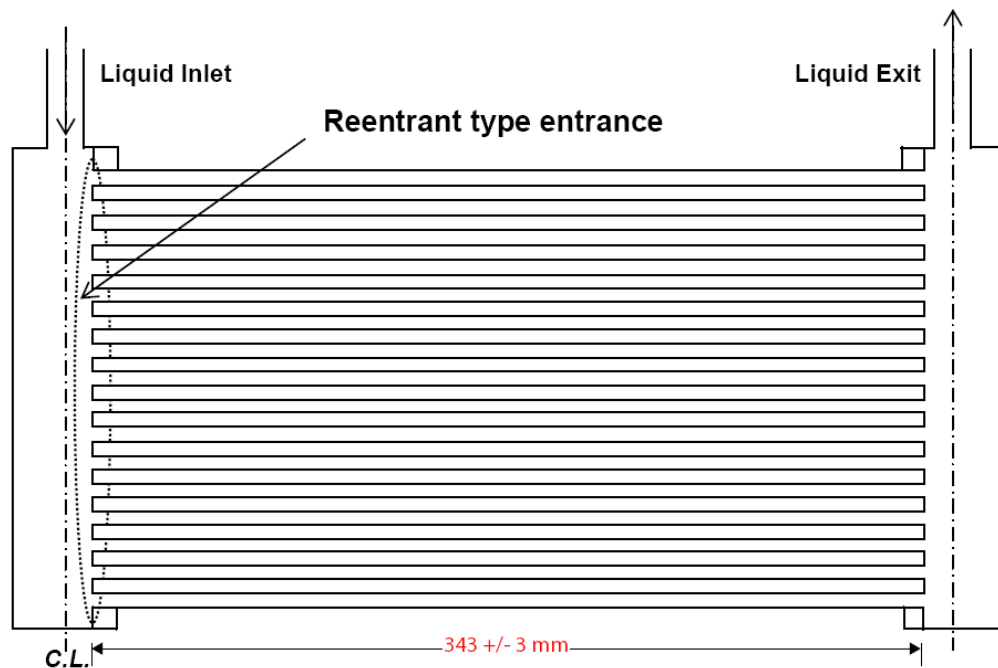


Figure 4.2. Inlet and exit connections and configurations of multi-port MCHX test slab.

These highly engineered and high precision MPE test slabs were fabricated using Aluminum alloys; Al 3102 for the microchannel slabs and Al 6005 for the manifolds [202]. Each of the test specimens has the identical dimensions. The uncertainty in diameter measurement of these new and smooth flow passages was reported to be no more than maximum $\pm 1.5\%$, i.e. $U_D = \pm 1.5\%$ [202]. The average surface roughness height of the ports is about 0.05% of the channel diameter making a relative roughness of $\epsilon/D = 0.0005$ [202]. Each of the ports in the multi-port microchannel slabs are equally spaced over a 100 mm width as shown in Figure 3.4 above and in Figure 4.3 below.

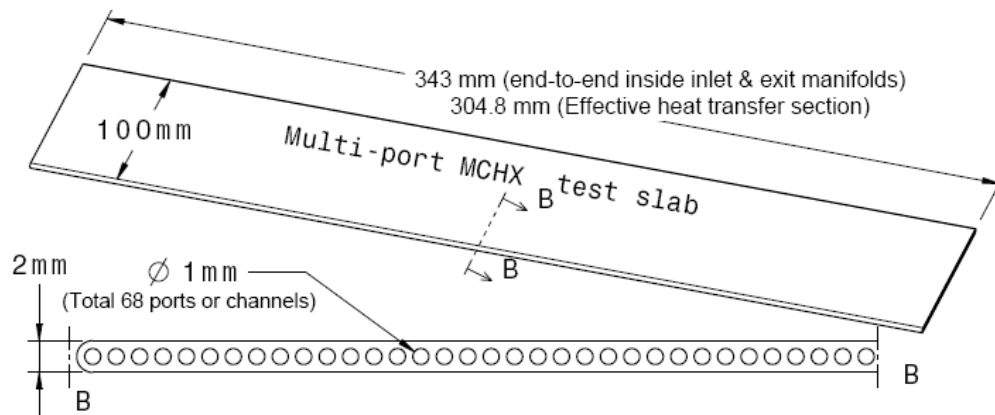


Figure 4.3. Cross-sectional view and dimensions of a single 1-pass MCHX test slab.

Kandlikar et al. [149] investigated the effect of channel roughness on pressure drop and heat transfer in 1.067 and 0.62 mm diameter circular tubes in the Re range from 500 to 3000. The tubes were treated with acid solutions to create three different relative roughness (ϵ/D) values for each tube. They observed more increase in Nu and Δp in 0.62 mm tube than in 1.067 mm tube. Negligible variations of Nu and Δp with Re in

1.067 mm tube due to varying ϵ/D from 0.00178 to 0.00225 were observed. But significant variations were noticed in 0.62 mm tube for ϵ/D from 0.00161 to 0.00355. They recommended that the larger diameter tubes above 1.067 mm with $\epsilon/D = 0.003$ may be treated as smooth tube but for the small size tubes below 0.62 mm diameter is treated as rough tubes since the Nu and Δp depend on ϵ/D for tube size of < 0.62 mm. The transition to turbulence also gets affected by the change in ϵ/D above 0.003. In current study the relative roughness value is $\epsilon/D = 0.0005$ [202] and 1 mm diameter channel is within the size range between 0.62 and 1.067 mm. Therefore the channels in this study are considered smooth and the effects of ϵ/D on Nu and Δp are ignored.

For identification purposes, each of the designed six test specimens was named by microchannel heat exchanger (MCHX) as follows.

1. MCHX #1: Un-finned 1-pass straight test slab (Figure 4.4a)
2. MCHX #2: Finned 1-pass straight test slab (Figure 4.4b)
3. MCHX #3: Un-finned 2-pass serpentine test slab (Figure 4.4c)
4. MCHX #4: Finned 2-pass serpentine test slab (Figure 4.4d)
5. MCHX #5: Un-finned 3-pass (3-circuit) straight distributor test slabs; 3 open exits at one ends and other ends connected to manifold (Figure 4.4e)
6. MCHX #6: Finned 3-circuit 15-pass (5 passes per circuit) serpentine prototype microchannel heat exchanger (Figure 4.4f)

The design concepts were based on typical thermal heat exchanger applications. Figures 4.4a through 4.4f portray all of the designed and fabricated test specimens and Table 4.1 provides the geometric data and specifications of each of the test samples. The inlet and exit manifold tubes were compressed fitted with the liquid handling flow loop as discussed next.

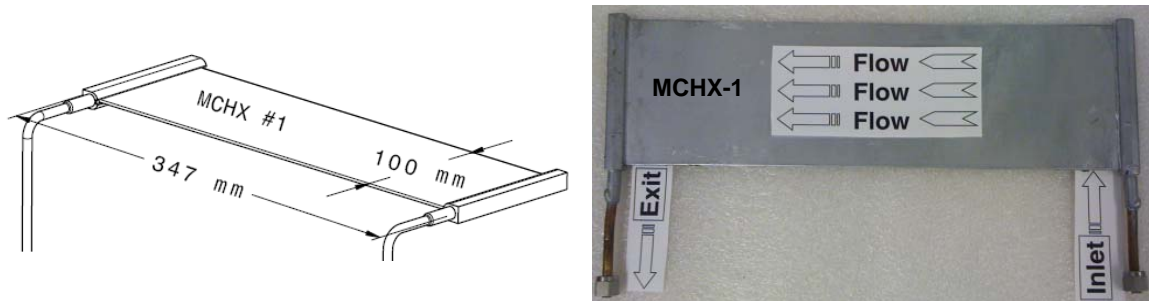


Figure 4.4a. MCHX #1: Un-finned 1-pass straight microchannel test slab.

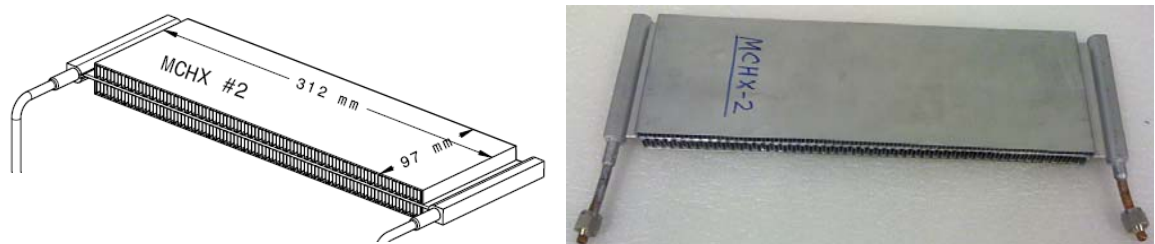


Figure 4.4b. MCHX #2: Finned 1-pass straight microchannel test slab.

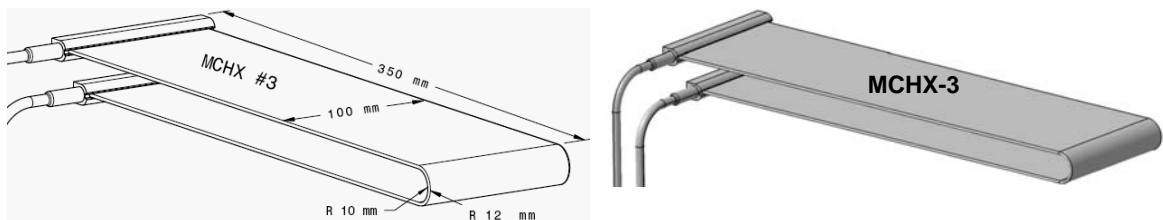


Figure 4.4c. MCHX #3: Un-finned 2-pass serpentine microchannel test slab.

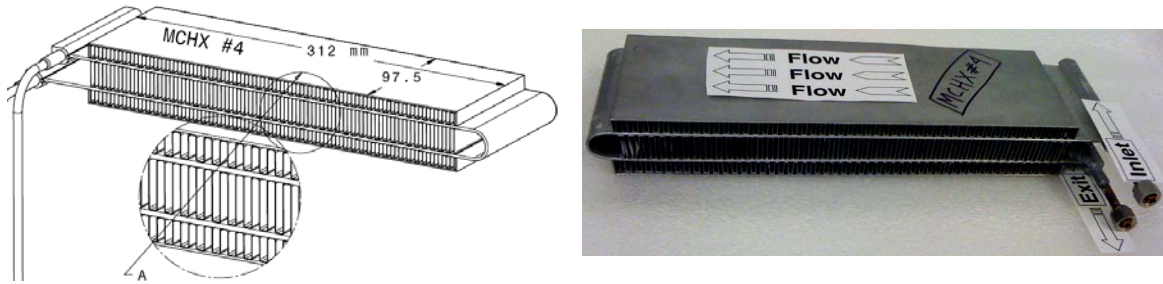


Figure 4.4d. MCHX #4: Finned 2-pass serpentine microchannel test slab.

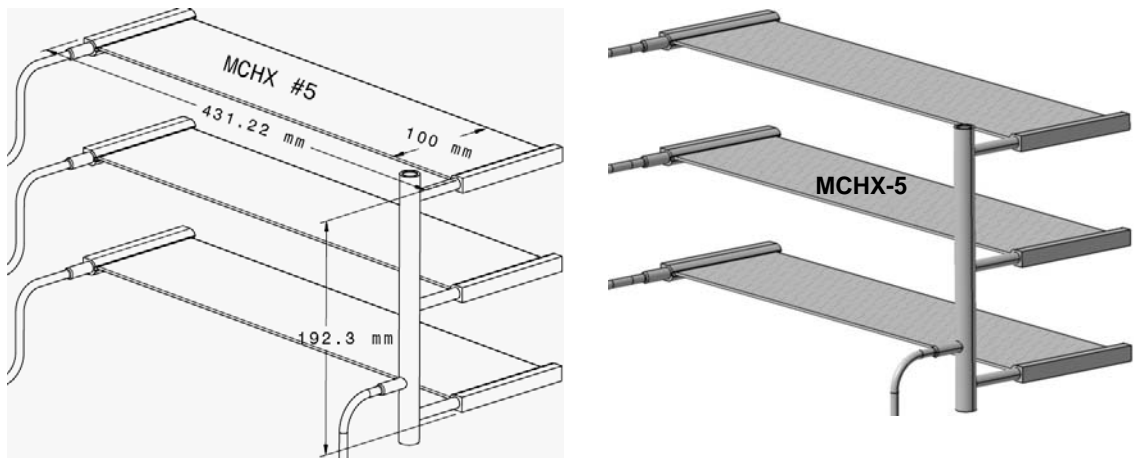


Figure 4.4e. MCHX #5: Un-finned 3-pass (3-circuit) straight microchannel distributor test slabs with 3 open exits at one ends and other ends are connected to a manifold.

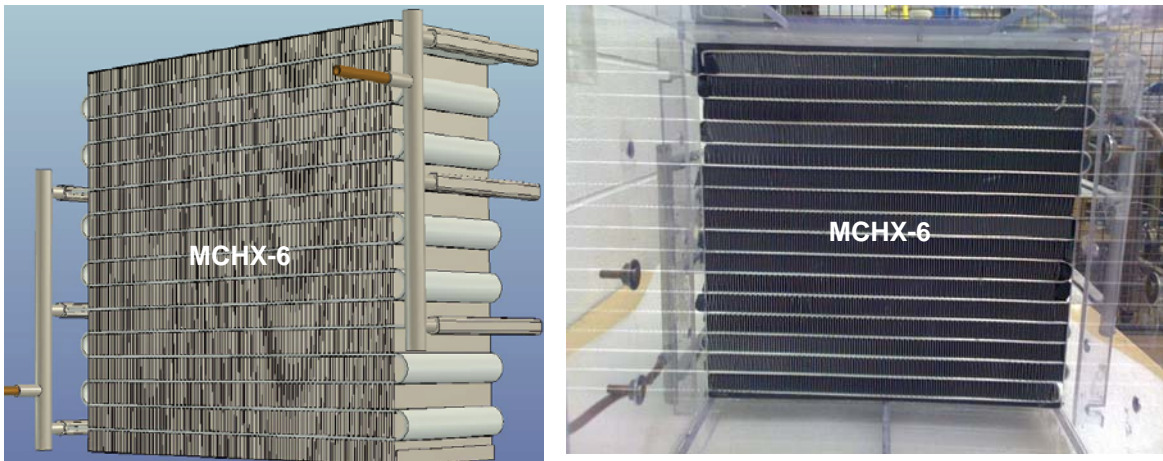


Figure 4.4f. MCHX #6: Finned 3-circuit 15-pass (5 passes per circuit) serpentine prototype microchannel heat exchanger.

Table 4.1. Geometric data and specifications of the MCHX test specimens (units are in mm)

PARAMETERS	MCHX #1	MCHX #2	MCHX #3	MCHX #4	MCHX #5	MCHX #6
Illustrating Figure #	4.4a	4.4b	4.4c	4.4d	4.4e	4.4f
# of channels / ports in a slab	68	68	68	68	68	68
Port or channel diameter, D	1	1	1	1	1	1
Port-to-port distance, S	1.463	1.463	1.463	1.463	1.463	1.463
Slab web thickness, W_T	0.463	0.463	0.463	0.463	0.463	0.463
Slab length (X -axis, liquid), L	304	304	304	304	304	304
Slab width (Z -axis, airflow), W	100	100	100	100	100	100
Slab thickness (Y - axis), H	2	2	2	2	2	2
Serpentine curve ID, d_{sp}	-	-	20	20	-	20
# of Flow circuits	1	1	1	1	3	3
# of Flow passes	1	1	2	2	3	15
Fin type	-	Wavy	-	Wavy	-	Wavy
Fin density per 25.4 mm	-	8	-	8	-	12
Fin height, H_f	-	20	-	20 – top 10 – bot	-	16
Fin thickness, t_f	-	0.10	-	0.10	-	0.10
Inlet-exit Header tube:						
Inner diameter, d_i	4.76	4.76	4.76	4.76	4.76	4.76
Outer diameter, d_o	6.35	6.35	6.35	6.35	6.35	6.35

In current study, the MCHX #1, MCHX #2, MCHX #3, and MCHX #6 were investigated. As mentioned before, the developed laboratory will use rest of the test specimens to conduct further research. The test specimen MCHX #5 is specifically

designed to observe and investigate the distribution nature of liquid or gas flow through each of the independent channels in the test slabs. Other details of the modeling and photographs of the test specimens are given in Figures B6 through B11 in Appendix B2.

4.2 Design and fabrication of wind tunnel test chamber

Rendered by Figure 4.5 below, a unique wind tunnel test chamber made with 6.5 mm thick Plexiglas is designed by the candidate and locally fabricated by technical support centre at university of Windsor. It has slotted slider mechanism that can fit all the above five test specimens i.e. MCHX #1 to MCHX #5. For the prototype MCHX #6, a separate test chamber was built. The inside dimensions of the test section are 304.8 mm x 304.8 mm in the X - Y plane and 609.6 mm long in the $+Z$ direction i.e. in the direction of airflow. The thick walled test chamber forms a sealed cubicle that helps the heat transfer domain not participate in any heat transfer activity with the outside environment. Yet, some extra insulation was provided properly as a double protection. Therefore only the portion of the MCHX test specimen is of interest remains exposed inside the test chamber for the heat transfer to take place between the liquid and the air.

For measuring the airflow velocity at the inlet of the test canal, a P012A-CF 12 inch Pitot static probe (shown in Figure 4.16a) along with a thermocouple probe is installed at the center of the X - Y cross sectional plane. The static and total pressure ports of the Pitot static tube are tapped and paralleled to connect to a high accuracy digital duct

calibrator, an airside differential pressure transducer (PTDD), and to the data acquisition (DAQ) scheme. The duct calibrator, PTDD, and DAQ are shown in Figures 4.17, 4.19 and 4.20. The digital duct calibrator with computerized data logging and processing features is used to calibrate the wind tunnel, which is also used to monitor the experimental condition and record backup data. As seen the circular holes in Figure 4.5 on the test chamber and solid circular pairs (P1-P1', P2-P2', and P3-P3') in Figure 4.7a on the front view of the test section, several pressure taps on two vertical side walls of the test chamber were drilled to measure the airflow pressure drop across the MCHX at various vertical locations in the Y -direction.

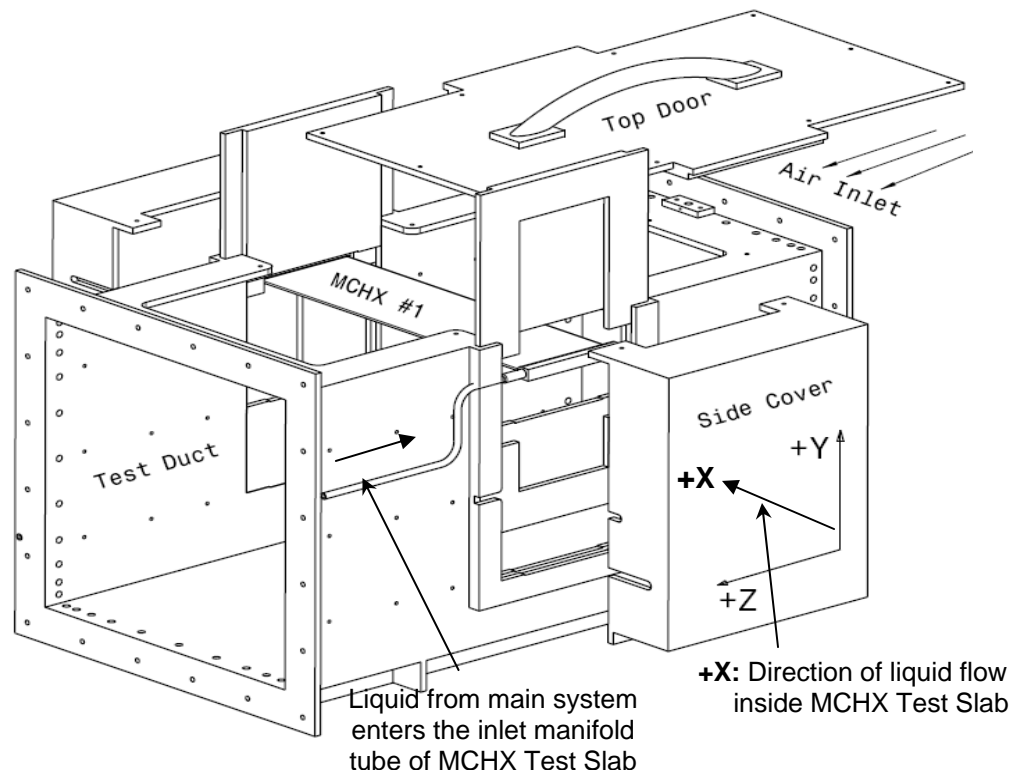


Figure 4.5. Designed and fabricated test chamber in current research.

As seen in Figure 4.5 above, several small holes are also drilled along the circumference of the test chamber at the inlet ($A-A'$) and exit ($B-B'$) to measure the airflow velocity and temperature to make their flow profiles. Additionally two other holes are drilled at the top of the chamber to measure the humidity of the flowing air using the duct calibrator's digital humidity sensor. The large door of the test chamber located at the top assists easy replacement of the test specimens from one experiment to the other. The detail modeling, 2D layouts and photographs of the test chambers are presented in Figures B3 to B3.6 in Appendix B3.

4.3 Air handling system – the closed-loop thermal wind tunnel

The source of cold and hot air supply in present study is a closed loop thermal environmental wind tunnel whose detailed descriptions can be found in [209-210]. The key segment including the view of the test chamber in $Y-Z$ plane is shown in Figure 4.5 above. The wind tunnel has a test section with square cross-section in the middle of the circulating loop, which is 305 mm x 305 mm x 610 mm (i.e. 1 ft x 1 ft x 2 ft). With a contraction ratio of 6.25 the wind tunnel is capable of producing the air velocities up to 30 m/s with no blockage and up to 17 m/s at full blockage i.e. in the presence of the prototype MCHX #6 in current study. The pressurized hot or cold water supply, as required, is tapped from the building district facility between 275 and 345 kPa (i.e. 40 and 50 psi) and mixed in a mixing network to prepare for wind tunnel internal heat

exchanger. As displayed by Figure 4.6, the water flow mixing network is designed by the candidate and locally fabricated by the technical support centre at university of Windsor. The detail models and photographs are given by Figures B4 to B4.2 in Appendix B4.

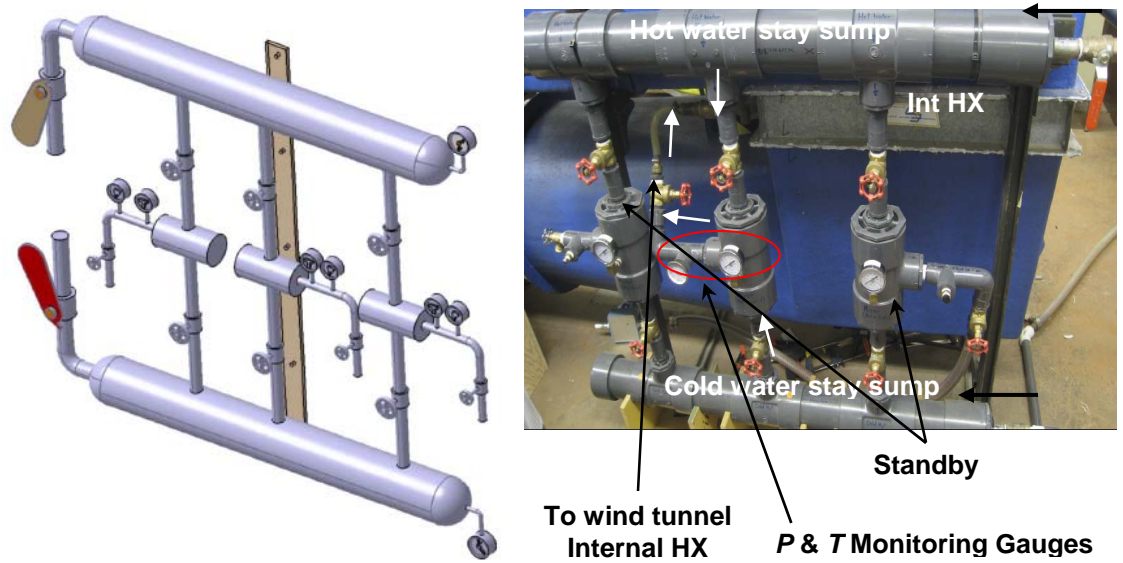


Figure 4.6. Designed and fabricated water flow mixing network used in current test setup.

The mixing chamber can mix and make up the hot and cold water anywhere between 5 and 45°C. This prepared water is fed into the open-loop internal heat exchanger of the wind tunnel. The wind tunnel internal heat exchanger makes up the hot or cold air, as required in the experiment, through the heat transferred by the drawn water to the circulating loop air inside wind tunnel.

Earlier experiments had been conducted in this wind tunnel at different blockage ratios to model the inlet air velocity profile [209-210]. At different air velocities, it was

observed that the free stream airflow in the +Z direction exhibited nearly flat velocity profiles throughout the entire X-Y cross sectional plane, which is the inlet A-A' section in Figure 4.7a below. The centerline air velocity measurement at the inlet (A-A') could account for the entire inlet cross section with a multiplying factor of 0.90. Further in current research several Pitot traverse surveys in the test chamber have been made using *Log-Tchebycheff* point distribution method [211]. This is one of the accurate methods recommended by the ASHRAE to measure and model the air velocity or the mass flow rate in a duct. This method, as used in current study, is described next.

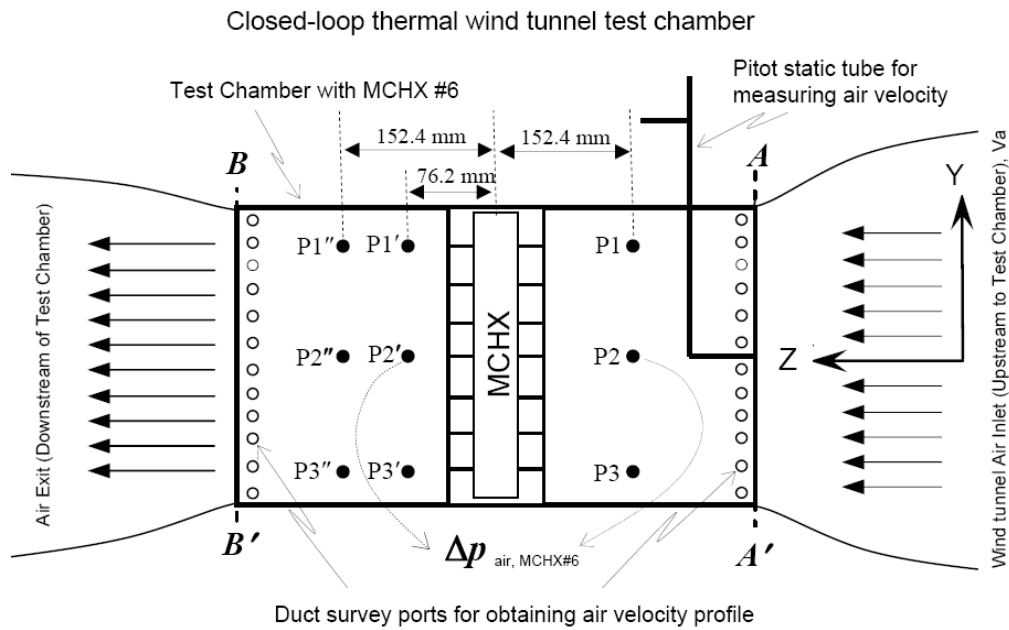


Figure 4.7a. Schematic of the measurement locations in the test chamber.

4.3.1 Air velocity modeling in wind tunnel test section using Log-Tchebycheff point distribution method

Pitot traverse survey is usually necessary to perform when the mean velocity or mass flow rate throughout an entire cross-sectional plane of a duct is required. The traverse survey involves measurements at various positions or points across the duct. Selection of suitable points has to be made prior to conducting a traverse survey. Either of the methods of *Centroids of Equal Areas* or *Log-Tchebycheff point distribution* may be used. The simple average of the selected individual point velocities however provide reasonably accurate results if *Log-Tchebycheff* points distribution is used [211]. Because of location of traversing points, this method accounts for the effect of wall friction and the reduction of velocity at near wall of the ducts and thereby provides the highest accuracy in measurement [211].

In current study the *Log-Tchebycheff* point distribution method was therefore used to model the air velocity at the entrance plane upstream to the test specimen inlet sitting in the test section. Since the duct size in current study was relatively smaller (H or $W < 750$ mm), measurement at the recommended 5-point distribution (i.e. $5 \times 5 = 49$) [211-212] was used as shown in Figure 4.7b below. The time-weighted average reading at each point was taken in the calculation in order to account for any fluctuating velocity at the traverse plane.

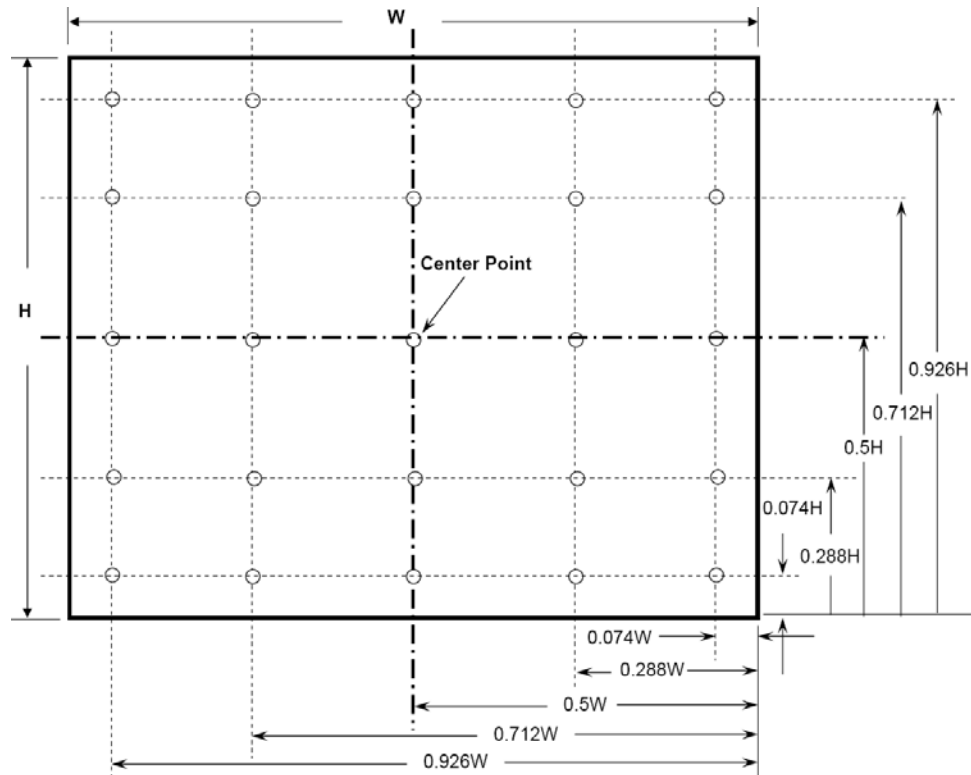


Figure 4.7b. Log-Tchebycheff 5-point distribution locations for air velocity measurement

The time weighted average velocity measurement at each of the 25 points was taken as follows.

$$\bar{V}_{a,i} = \frac{1}{k} \sum_{j=1}^k V_j; \quad \text{where } j = 3 \text{ to } 5, \quad (4.1)$$

The mean velocity across the traverse plane, i.e. the upstream of the test section, was then consolidated using Equation (4.2) below.

$$\bar{V}_a = \frac{1}{n} \sum_{i=1}^n V_{a,i}; \quad \text{where } i = 1 \text{ to } 25, \quad (4.2)$$

This gives the mean mass flow rate by the following continuity relations,

$$\bar{m}_a = (\rho_a \dot{V}_a) = A_{\text{duct}} \frac{1}{n} \sum_{i=1}^n (\rho_{a,i} V_{a,i}); \quad \text{where } i = 1 \text{ to } 25, \quad (4.3)$$

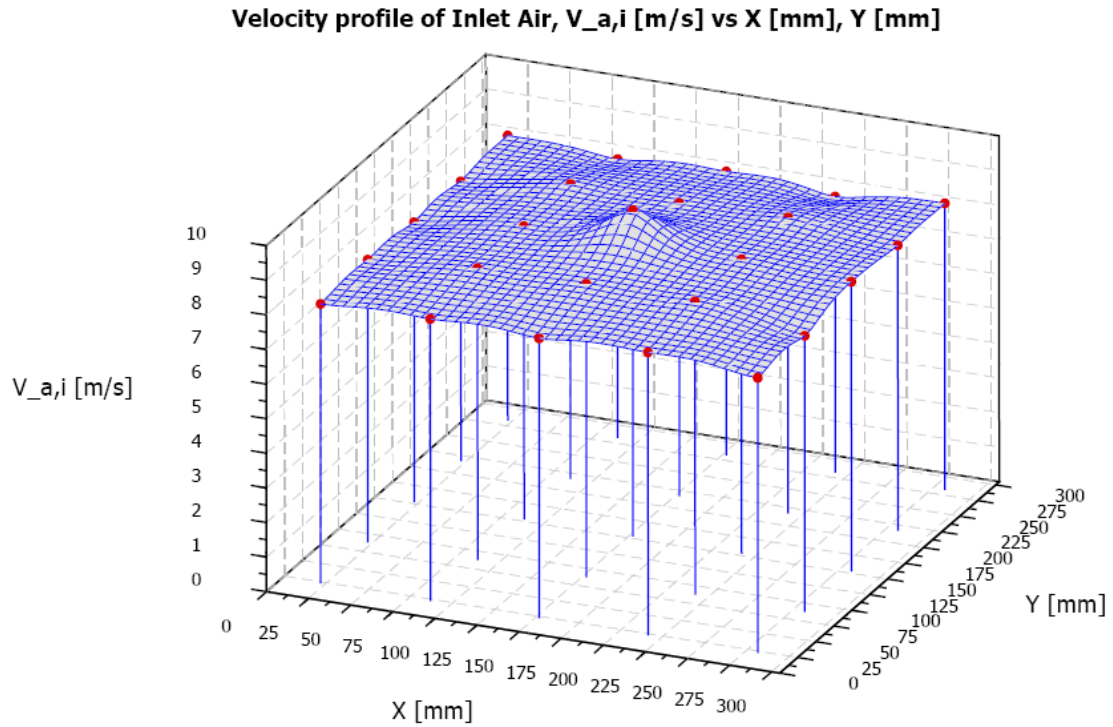


Figure 4.7c. Air velocity profile at the inlet plane using *Log-Tchebycheff* 5-point distribution

Figure 4.7c above shows the air velocity profile at nominal velocity of 8.5 m/s at the inlet cross-sectional plane of the wind tunnel test section (A-A' in Figure 4.7a), which was measured using *Log-Tchebycheff* 5-point distribution method. The velocity contour plots of this survey are provided in Figure B7.5 in Appendix B7. The mean values of the traverse surveys were compared with the values measured by single point measurement at

the center of the traverse plane. In this measurement, the standard and the average deviations were 0.31 m/s and 0.22 m/s respectively. The survey results suggest that the single-point centerline velocity measurement could fairly represent the mean velocity across the entire plane with the use of a consolidated multiplication factor of 0.87.

Therefore, for the air velocity all the experimental measurements were performed at the inlet centre location of the test section (see Figure 4.7b above and balloon 5 in Figure 4.8a below) and the new multiplication factor (0.87) was taken into account in velocity translation. A hot wire anemometer (shown in Figure 4.18) was also installed at the inlet section of the test chamber for monitoring and also for backup measurements of the centerline air velocity. The measurement data from hot-wire anemometer also agreed with the measurements data using Pitot static tube and the duct calibrator.

4.3.2 Thermal grids for air temperature measurements in wind tunnel test section

Two thermal measurement grids were designed and installed, one at the inlet and the other at the exit of the test section in order to precisely measure the airflow temperatures across the MCHX. As seen in Figure 4.7 above, the cross-sections *A-A'* and *B-B'* are the inlet and exit locations of the test chamber. The thermal grids are expanded and illustrated in Figure 4.8. As seen in Figure 4.8a above and 4.8b below, the inlet thermal grid has equally spaced $3 \times 3 = 9$ grid points (from T100 to T108) and the exit grid has equally spaced $5 \times 5 = 25$ grid points (from T109 to T131 and T200 to T201).

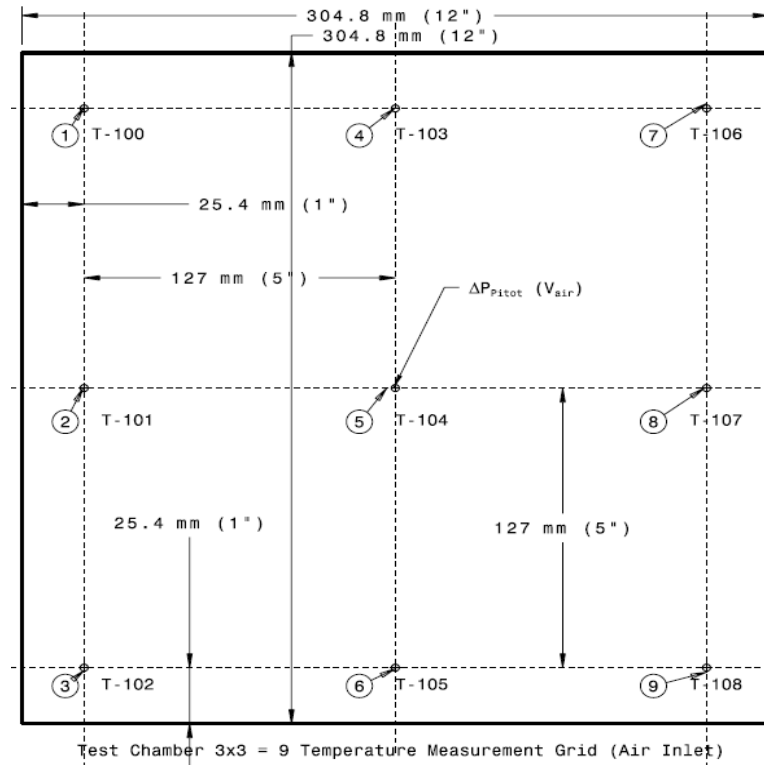


Figure 4.8a1. Schematic of the thermal grid points at the test section inlet in the wind tunnel.

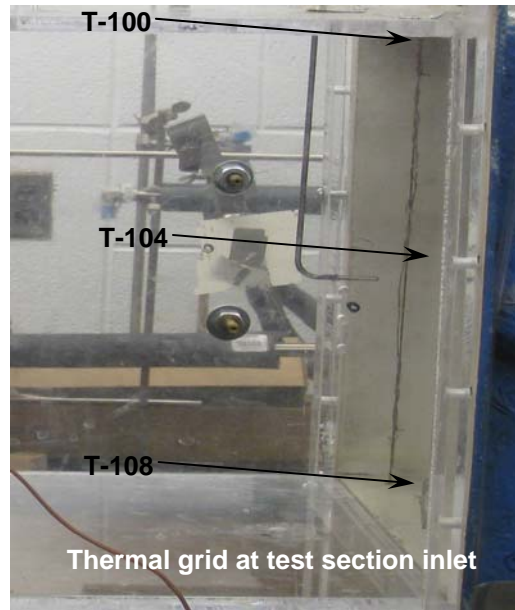


Figure 4.8a2. Photograph of the thermal grid points at the test section inlet in the wind tunnel.

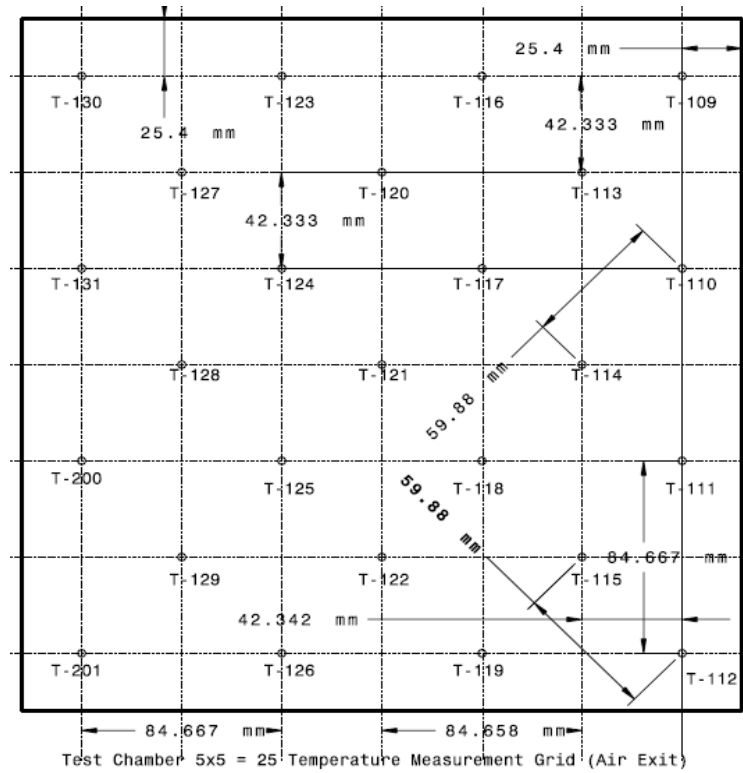


Figure 4.8b1. Schematic of the thermal grid points at the test section exit in the wind tunnel.

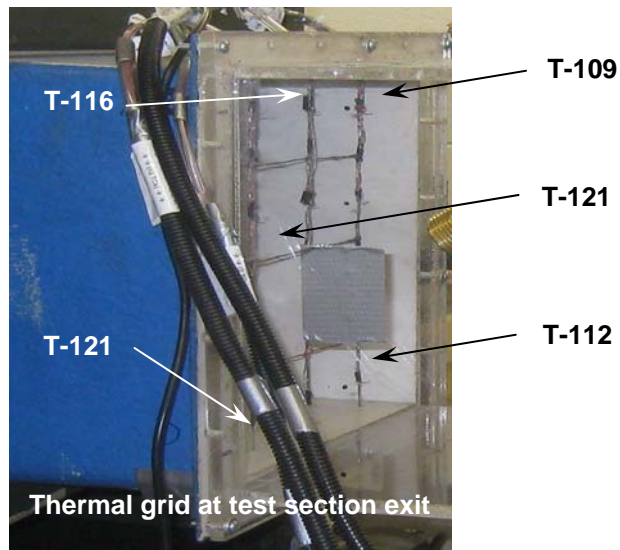


Figure 4.8b2. Photograph of the thermal grid points at the test section exit in the wind tunnel.

The well calibrated type-T thermocouple probes were installed at each grid points, which were then hooked up with a data acquisition (DAQ) for automated measurements. As defined by Equations 4.4 and 4.5 below, the mean inlet and exit airflow temperatures, $T_{a,i}$ and $T_{a,o}$, were sampled from the time-averaged data of several experimental runs and then used in the calculation and analysis.

$$T_{a,i} = \frac{1}{n} \sum_{n=1}^n (T100 + \dots + T108); \text{ for } n = 1 \text{ to } 9, \text{ (Mean air inlet temperature)} \quad (4.4)$$

and

$$T_{a,o} = \frac{1}{n} \sum_{n=1}^n (T109 + \dots + T201); \text{ for } n = 1 \text{ to } 25, \text{ (Mean air exit temperature)}. \quad (4.5)$$

4.4 Liquid handling system

The liquid handling system in current study is shown in developed experimental facility in Figure 4.1 above. The liquid pump draws liquid from the source tank and impels to the microchannel slab test specimen via heating unit. The hot liquid transfers heat to the cold air flowing over the test slab and then returns back to the source tank or exits to the atmosphere.

The system contains the liquid tank, pump motor unit, circulation heater (CH), piping network (PN), flow management accessories, flow monitoring devices, and flow measurement instruments. The flow management accessories include ball valves (BV), bypass arrangement, pressure relief valve (PRV), needle valve (NV), micro-filter (MF), flow drainage facet etc. The flow monitoring and measurement instruments consist of pressure gauges (PG), temperature gages (TG), digital flow meter (DFM), impeller flow meter (IFM), pressure transducers (PTD), and Resistance Temperature Detector (RTD). The 3D, 2D and pictorial illustrations of the above components of the liquid handling system are provided in details in Appendix B1 via Figures B1 through B5.

A centrifugal pump is undesirable because the flow rate is dependent on the change in upstream pressure [197]. Many authors used gear pumps (GP) in their investigations since they deliver a constant volume of liquid at a fairly steady flow rate regardless of the change in upstream system pressure [149, 208]. Garimella and Singhal [28] discussed the single-phase flow, heat transfer and pumping requirements for MCHS, which can be useful in selecting proper pump over required flow rate. As shown in Figure 4.9, a variable speed gear pump was therefore selected for the developed test facility.

The pump is operated by a frequency driven 5.6 kW electrical motor. The pump can handle water, glycol, and other moderately viscous oils and operate up to a maximum

working pressure of about 1 MPa. To provide additional precision to the flow stability, a needle valve NV is also installed in the flow loop in addition to the gear pump.

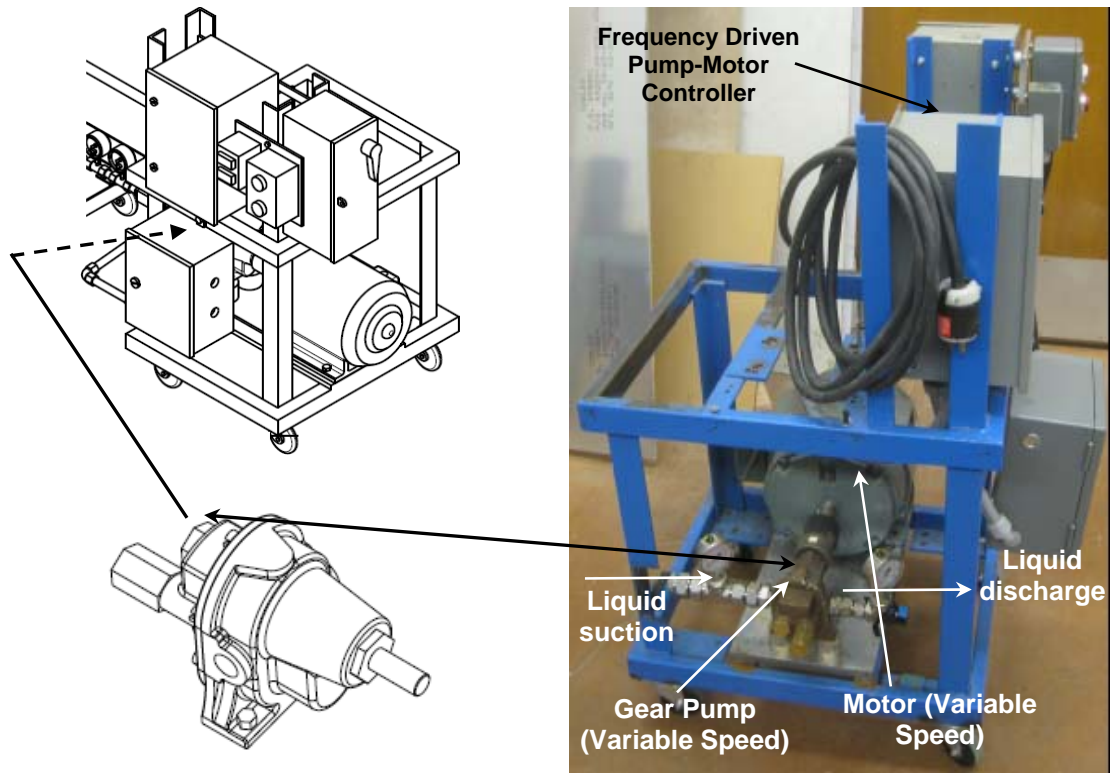


Figure 4.9. Schematic of the liquid flow gear pump-motor unit used in current test setup.

As shown in Figure 4.10 below, the liquid heating element in the system is an inline 6 kW circulation heating coil (CH) that serves as a constant heating source for the flowing liquid. The heater unit can handle water, glycol, and other liquid oils as well as various gases with a working pressure up to 6.8 MPa and temperature of 150°C. The heater is assembled in the liquid tank cart-unit. The heater is integrated with a

programmed control panel that allows setting, controlling, and maintaining a certain heating temperature. After commissioning the test facility, the shell of the heating unit was locally changed because of finding some debris from original source.

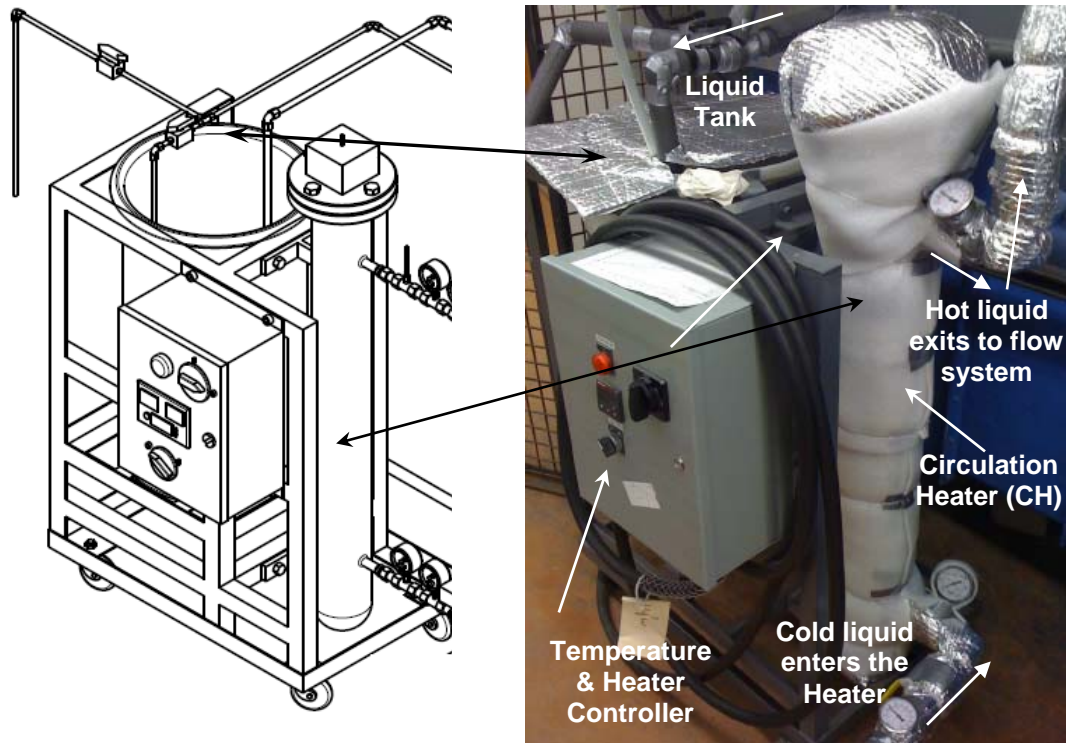


Figure 4.10. Schematic of the liquid tank and circulation heating coil used in current test setup.

An inline micro filter (MF) is installed before the digital flow meter DFM. The digital flow meter DFM, as shown in Figure 4.11(a) below, was installed after the MF to measure the volume flow rate through the microchannel slab. Three FV4000 series DFM for different flow ranges are used depending on the experimental conditions. This DFM has several special features: handles water, glycol, and other oils as working fluids; simultaneously measures and displays \dot{V} , T , and p of the flowing fluid; and sends voltage

signals of all these parameters to the DAQ system for automated data acquisition. Because of this instant and simultaneous measurements of all three parameters, by evaluating the density (ρ) the \dot{V} can be instantly converted into mass flow rate (\dot{m}). One Impeller Flow Meter (IMF), shown in Figure 4.11(b), was also installed at the exit of the flow loop to take the backup measurement for verification as well as for the event if DFM seizes to function during any experimental runs.

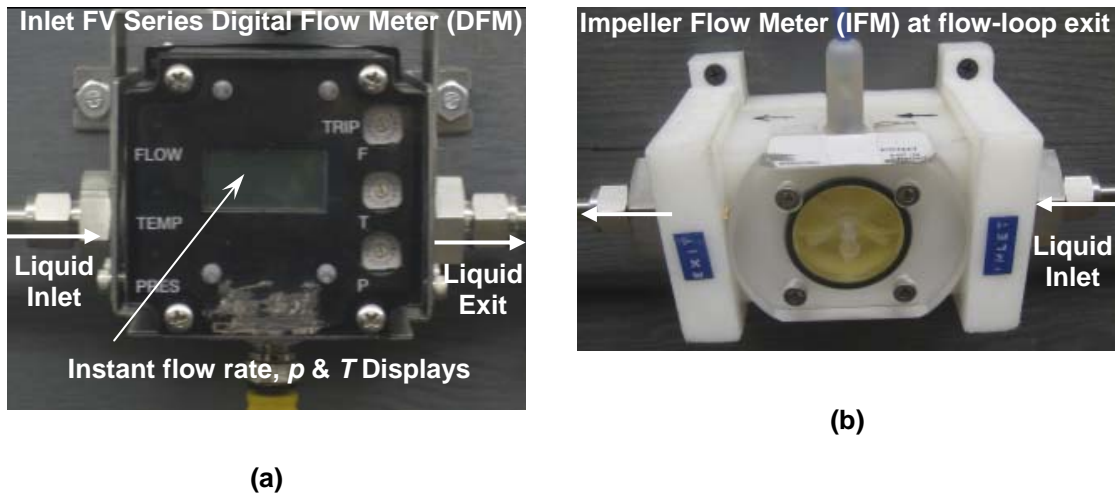


Figure 4.11. (a) Digital flow meter, DFM and (b) Impeller flow meter, IMF used in current setup.

Two sets of pressure transducers (PTD) and temperature sensors (RTD) are installed; one set (PTD1 and RTD1) at the inlet and the other set (PTD2 and RTD2) at the exit of the microchannel test slab. Before and after the PTD1 and PTD2, two mechanical pressure gauges (PG) were installed to visually monitor the experimental operating conditions and to check the status of the digital pressure measurements. A sample PTD and a mechanical pressure gauge are shown in Figure 4.12 below.

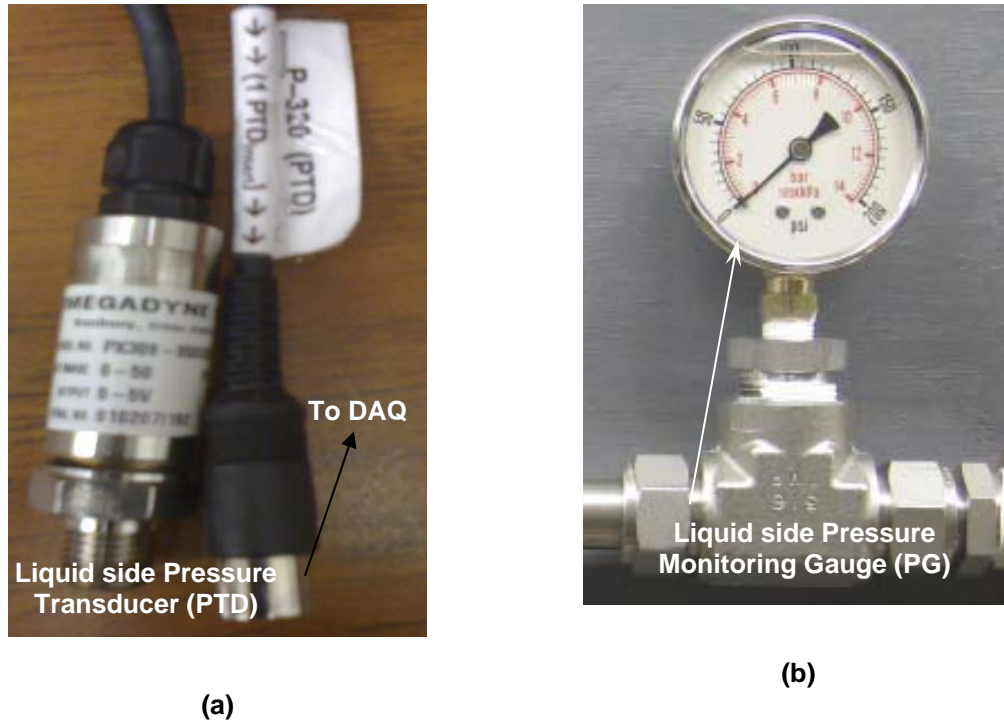


Figure 4.12. (a) Pressure transducer (PTD) and (b) pressure gauge (PG) used in current setup.

Different flow rate gives different system pressure p and hence different Δp . With respect to accuracy, a single broad ranged PTD unit is a poor choice to measure flow pressure in a wide span. In order to measure the p accurately in both low and moderate ranges, several PTDs with various slim measurement band widths will be used. They offer different narrow measurement ranges covering pressure capacity from 0 to 680 kPa. As described below, the ultra precision Resistance Temperature Detector (RTD) sensors with a high 1/10 DIN accuracies ($\pm 0.012^\circ\text{C}$) were used in current study to measure the liquid side inlet and exit temperatures. All the PTDs and RTDs were connected with the DAQ panel for data recording and processing.

The most common resistance value of a Pt100 RTD is 100 ohms at 0°C. The temperature coefficient (α) is used in dealing with RTD, which is the average slope between 0°C and 100°C. According to DIN 43760 standard, a Pt100 RTD has a value of $\alpha = 0.00385$ ohm/ohms/°C that for a 100 ohm wire corresponds to +0.385 ohms/°C at 0°C. Both the slope and the lead impedance of the wire can contribute a significant error to temperature measurement. To minimize these errors, bridge connection is usually used where the bridge output voltage is considered an indirect measure of the RTD resistance. A bridge needs four connection wires, one external source, and three resistors with zero temperature coefficients. The 3-wire Wheatstone bridge connection creates some non-linear relationship between the change of resistance and the output voltage of the bridge. A 4-wire connection eliminates this problem and provides better measurement accuracy.

The Resistance Temperature Detector (RTD) is a more linear and accurate device than any thermocouple and a 4-wire bridge connection measurement has also the best measurement accuracy over either of 2 or 3 wire RTD connections (National Instruments DAQ User Manual). Therefore, the ultra precision RTD sensors (Pt100) with a high 1/10 DIN accuracies ($\pm 0.012^\circ\text{C}$) in 4-wire bridge connections were used in measuring the liquid side inlet and exit temperatures.

4.5 Instrumentation and calibration

The measuring instruments in developed experimental facility are carefully selected giving major attention on their accuracy and ability for DAQ connectivity. The better accuracy and performance are achieved if an instrument is used in medium scale span of measuring capacity. In order to ensure this choice, several sets of instruments and sensors of different measurement ranges are laid on the test facility. As required, the narrow range higher accuracy instruments were hooked up with the DAQ for data monitoring and collection.

The specifications of the instruments are provided in Table 4.2. The accuracy information of the instruments as provided in Table 4.2 based on manufacturer's supplied data, accompanying documentation, and on instruments' label of specification. The accuracy of each instrument, probe, and sensor as provided in Table 4.2 represents the overall instrument error estimated from the root sum square (RSS) of all known errors as given by Equation 4.6. These may include any or all of the known errors e.g. the resolution, absolute error, sensitivity, linearity, repeatability, hysteresis, effects of scale range (FSO), stability, zero offset, various drifts, reproducibility, precision etc.

$$e_1 = \sqrt{e_1^2 + e_2^2 + \dots + e_N^2} , \quad (4.6)$$

where e is the known error(s) 1, 2, 3,N and the e_1 is the overall instrument error some times used as consolidated accuracy term by manufacturer and denoted by $\pm\%$ or by absolute value. Table 4.3 describes the information and specifications of the precision calibrators those were used to calibrate the instruments in current research.

Table 4.2. Specifications of the components, equipment, measuring instruments and DAQ system used in current test facility

Code	Descriptions of instruments	Qty	Model / Type	Capacity /Range	Accuracy	Manufacturers / Suppliers	Figures
MF	Micro-filter 40 μm	1	F-Series Inline	> 4000 kPa	-	Swagelok	4.21
-	Fittings, valves, hoses & pipes	-	Various	> 4000 kPa	-	Swagelok	-
DFM	Digital flow meter FV4000:	1	04004SN06-xxx	0.2 ~ 2.2 LPM	\dot{v} : $\pm 0.5\%$ FS; T :	Proteus Ind.	4.11a
	Flow rate: 0.2 ~ 60 LPM;	1	04004SN1-xxx	0.4 ~ 5.3 LPM	$\pm 1.1\%$ FS;		
	$0 \leq T \leq 100^\circ\text{C}$; $0 \leq p \leq 680$ kPa	1	04012SN16-xxx	4.5 ~ 60 LPM	p : $\pm 1.1\%$ FS		
IFM	Impeller flow meters	1	FPR-301	0.3 ~ 19 LPM	$\pm 1\%$ FS	Omega	4.11b
		1	FPR-303	0.8 ~ 75 LPM	$\pm 1\%$ FS		
PTD	Pressure transducers (gage)	1	PX419-001G5V	0 ~ 6.8 kPa	$\pm 0.08\%$ BSL	Omega	4.12a
		2	PX309-005G5V	0 ~ 345 kPa	$\pm 0.25\%$ FS		
		2	PX219-015G5V	0 ~ 689 kPa	$\pm 0.25\%$ FS		
RTD	Ultra precise RTDs (Pt100)	4	PM1/10-1/4-xxx	-100 ~ 400 $^\circ\text{C}$	$\pm 0.012^\circ\text{C}$	Omega	-
TC	Thermocouple probe (TTT-30)	82	Type-T	-200 ~ 350 $^\circ\text{C}$	$\pm 0.8^\circ\text{C}$	Omega	-

Code	Descriptions of instruments	Qty	Model / Type	Capacity /Range	Accuracy	Manufacturers / Suppliers	Figures
HWA	Hotwire anemometer (VelociCalc)	1	8345A	0 ~ 30 m/s -18 ~ 93°C	±3% of rdg ±0.3°C	TSI	4.18
PTDD	Pressure transducer differential	1	PX653-0.5D5V	0 ~ 125 Pa	±0.25% FS	Omega	4.19
	Selectable: 0 ~31, ~62, ~125	1	PX277-01D5V	0 ~ 249 Pa	±1% FS		
	#Selectable: 0 ~156, ~310, ~622, and ~1250 Pa	1	PX653-03D5V	0 ~ 748 Pa	±0.25% FS		
		1	PX653-05D5V	0 ~ 1.25 MPa	±0.25% FS		
		1	PX277-05D5V#	0 ~ 1.25 MPa	±1% FS		
DAQ	Data Acquisition System (with chassis and all the accessories)	1	16-bit 6052E	-10 to+10VDC	±(29 μ V+0.035% of rdg)	National Instruments	4.1b, 4.20, B4
-	Digital p -abs manometer	1	HHP-2025	0 ~ 204 kPa	±0.1%rdg+0.2kPa	Omega	-
-	Digital p -diff. manometer	1	HHP-90	0 ~ 13 kPa	±0.2% of rdg+26Pa	Omega	-
-	Digital relative humidity meter	1	HH-311	0 ~ 100% RH -200~ 1370°C	±2.5% RH ±0.7°C	Omega	-
DTM	Digital T -meter (thermometer)	1	HH506R	-200~ 1370°C	±(0.3°C+0.05% rdg)	Omega	-

Table 4.4 (Cont'd...)

Table 4.3. Specifications of the precession calibrators used to calibrate the instruments in current study

Descriptions of calibrator units	Qty	Model	Capacity / Range	RSS Accuracy	Manufacturers / Suppliers	Illustrating Figures
Dry block calibrator (resolution $\pm 0.01^\circ\text{C}$, stability in 5 min $\pm 0.05^\circ\text{C}$):	1	CL-770A	-45°C (below ambient) to +140°C	$\pm 0.03^\circ\text{C}$	Omega	4.15
Dual TC & RTD calibrator:	1	CL-543	-25 – +80°C	$\pm 0.1^\circ\text{C}$	Omega	4.15
Pitot Static tube probe (PSTP)	2	P012A-CF	Up to 426°C	Coefficient = 1	FlowKinetics	4.16
Flow calibrator (Air or gases):	1-set	FKT-3DP1A			FlowKinetics	4.17
1) Absolute pressure transducer		Selectable	1) 15 ~ 115 kPa	1) $\pm 0.5\%$ FS*	LLC	
2) Differential pressure transducer-1		range: Pa, in WC, psi	2) ± 100 Pa	2) $\pm 0.22\%$ FS		
3) Differential pressure transducer-2			3) ± 248.8 Pa	3) $\pm 0.22\%$ FS		
4) Differential pressure transducer-3			4) ± 1.25 kPa	4) $\pm 0.22\%$ FS		
5) Temperature sensor (TC reader)			5) -200 ~ 177°C	5) $\pm 0.5^\circ\text{C}$ FS		
6) Relative humidity (RH) sensor			6) 0 ~ 100% RH	6) $\pm 2\%$ FS		

4.5.1 Calibration of liquid flow meters (DFM & IFM)

The digital flow meters (DFM) shown in Figure 4.11(a) above were supplied with the calibration data and response curves for water and 50%-50% ethylene glycol-water mixture. The DFMs are capable of handling a variety of liquids with low to moderate viscosities, therefore the calibration data and the curves were provided with respect to liquid viscosity versus DFM output voltage followed by other data. Table 4.4 shows the data and Figure 13 presents the calibration curves. The detail calibration certificates, data and response curves for the DFMs are provided in Figures B5.1 to B5.3 in Appendix B5.

Table 4.4. DFM Flow meter's calibration data: LPM vs. VDC vs. kinematic viscosity (ν)

DFM: 04012SN16-TPD **S/N** 00143490

Flow rate	Output VDC at different kinematic viscosities, ν [cSt]					
	$\nu = 0.31$	$\nu = 0.68$	$\nu = 1.00$	$\nu = 2.00$	$\nu = 4.00$	$\nu = 7.00$
60.57	5.31	5.21	5.07	4.84	4.79	4.75
53.00	4.64	4.55	4.43	4.23	4.19	4.15
45.42	3.96	3.89	3.79	3.62	3.58	3.55
37.85	3.29	3.22	3.15	3.01	2.98	2.96
30.28	2.61	2.56	2.51	2.40	2.38	2.36
22.71	1.94	1.90	1.88	1.79	1.78	1.76
15.14	1.26	1.23	1.24	1.18	1.18	1.16
7.57	0.58	0.57	0.60	0.58	0.58	0.57
3.79	0.29	0.29	0.28	0.26	0.26	0.26

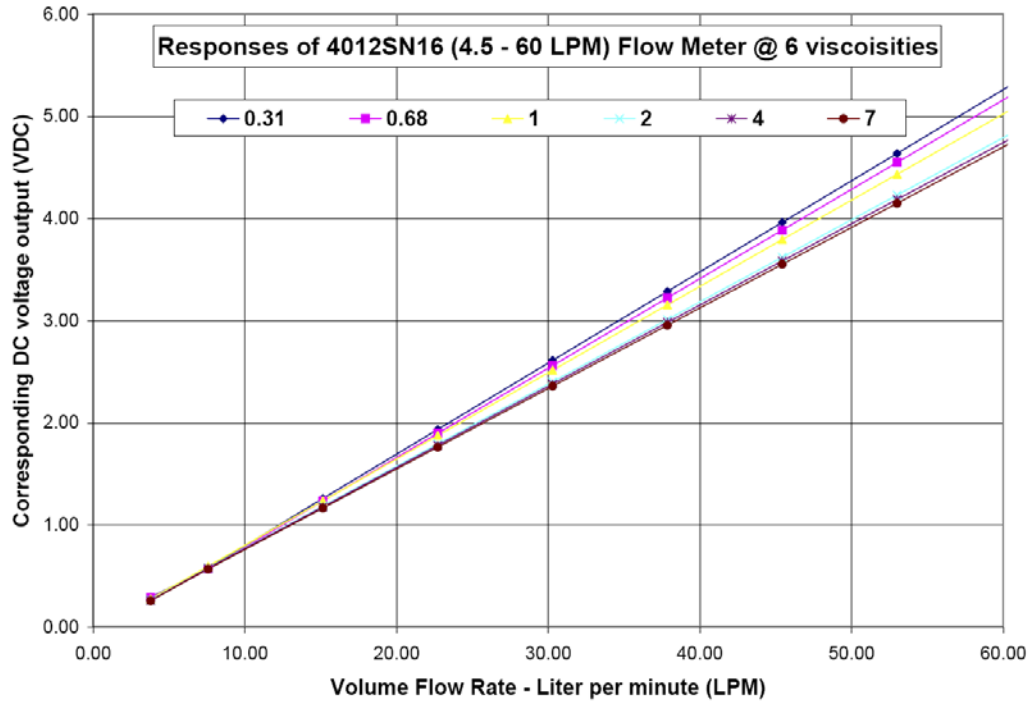


Figure 4.13a. DFM, Flow meter calibration data - LPM vs. VDC vs. kinematic viscosity (ν).

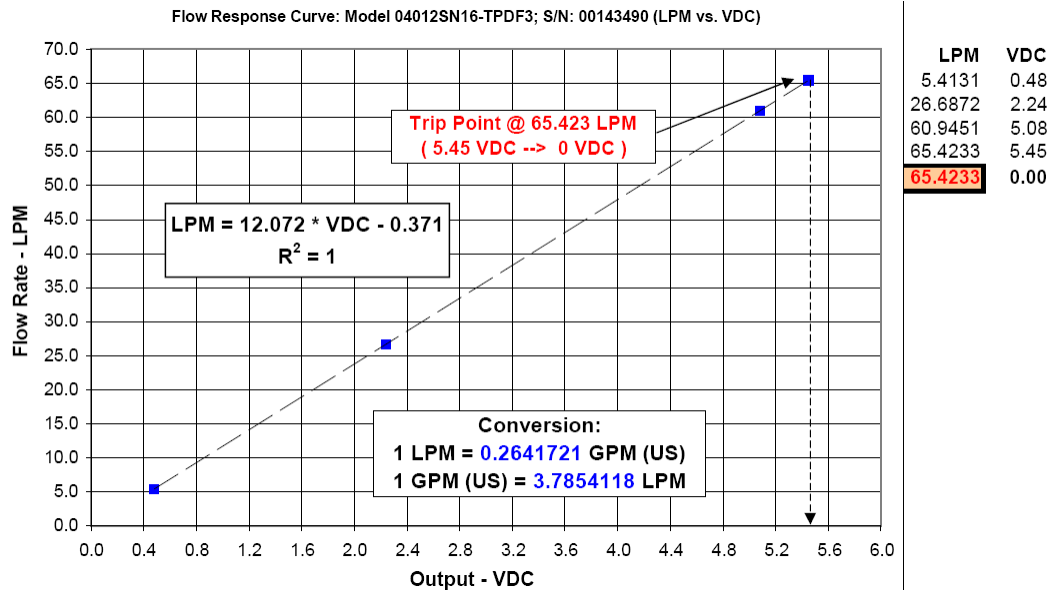


Figure 4.13b. DFM, Flow meter response & calibration curve - LPM vs. VDC (Water).

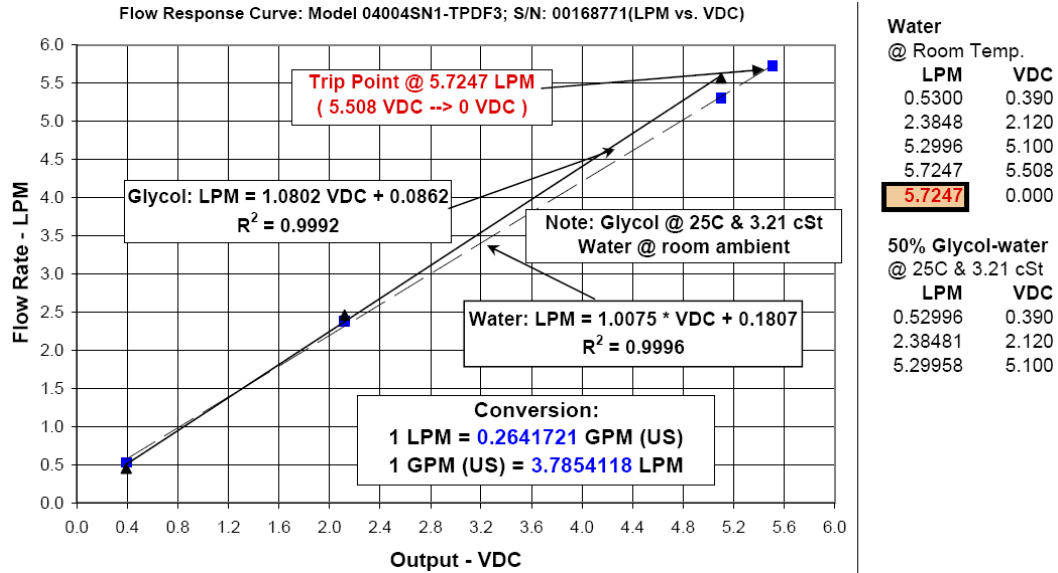


Figure 4.13c. DFM, Flow meter response & calibration curve - LPM vs. VDC (Glycol & Water).

The impeller flow meter (IFM) is installed at the exit of the liquid loop downstream of the test specimen. Shown in Figure 4.11(b) above, the meter gives pulse, i.e. numeric counts for each rotation of its impeller, which was calibrated for water flow at 39°C using the readings of the DFM and backed up by bucket-weigh-stop watch measurements. Table 4.5 shows the data and Figure 14 presents the calibration curves.

Table 4.5. Flow meter’s calibration data: LPM vs. VDC vs. kinematic viscosity (ν)

Step	Display Count	VDC	LPM	Kg/Sec
1	38.48	1.902	5.00	0.1023
2	54.37	2.973	7.50	0.1400
3	72.17	4.190	10.00	0.1814
4	89.65	5.460	12.50	0.2215
5	110.38	6.747	15.00	0.2655
6	124.61	7.850	17.50	0.3006
7	147.79	9.437	20.82	0.3556

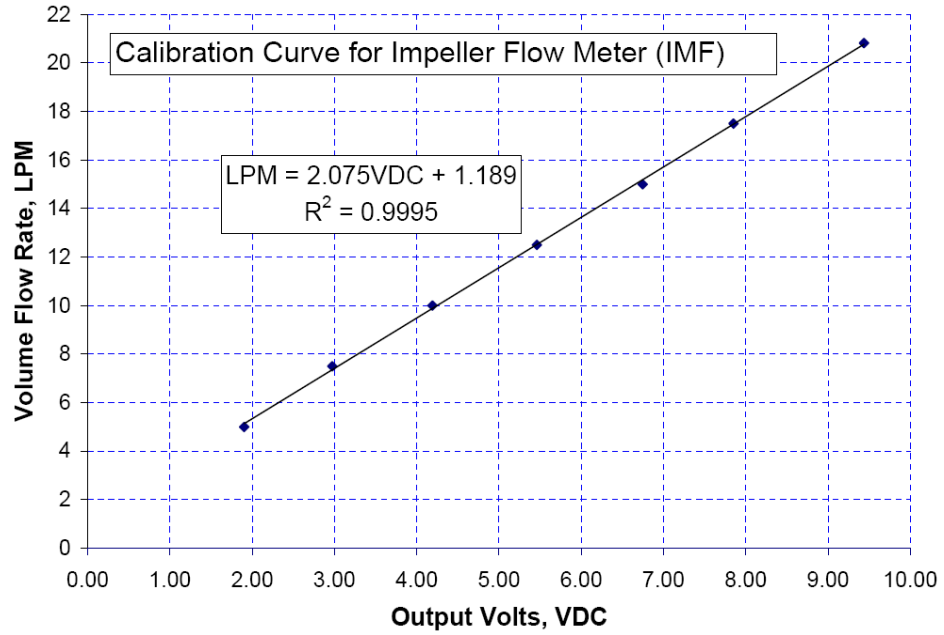


Figure 4.14a. IFM, Calibration curve - LPM vs. VDC (for water).

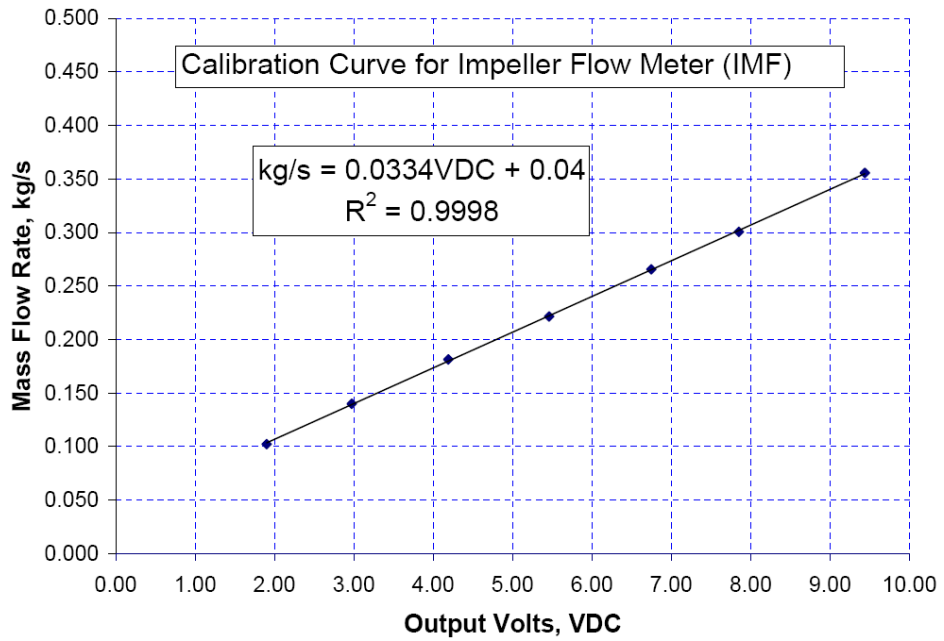


Figure 4.14b. IFM, Calibration curve – kg/s vs. VDC (for water, manual measurements).

During all experiments, for almost all the data sets the manual flow measurements were also taken as backup and to verify the automated recorded data. Excellent consistency was achieved and followed for all the data sets, which can be seen from Figure 4.14b. Experiments were repeated for data sets those are not consistent or have little large variations among these three systems of flow measurements. The details of bucket and stop watch methods as used in current study are briefly described in uncertainty analysis section in Appendix E.

4.5.2 Calibration of liquid side pressure transducers (PTD)

The liquid pressure transducers PTDs were supplied with calibration data by the manufacturer (Omegadyne Inc). The calibrations were performed by NIST traceable instrumentation and standards. The pressures in psi are fairly linear with the DC voltage output of the transducers. The functionality and responses of the liquid side PTDs were tested in the system by running the liquid loop at some given pressure. The PTDs were then compared with the readings of the installed PGs and the outputs of pressure sensors of the DFM. The supplied calibration data were found in excellent agreement with DFM and PGs. As mentioned before, different sets of liquid side PTDs were used depending on the flow and narrow pressure ranges to allow maximum accuracy in measurements. The PTD calibration equations are presented in Table 4.6 by Equation 4.7 and the calibration curves and data reports are provided in Appendix B6 via Figures B6.1 to B6.7.

Table 4.6. Calibration equations of liquid side pressure transducers (PTDs) – VDC vs. psi

PTD name and range	Serial number	Calibration Equation	Eqn. #
P1A: 5 psig, 0 – 5 VDC	0717071034	$p = 0.9998 * \text{VDC} - 0.0002$ [psig]	(4.7a)
P2B: 5 psig, 0 – 5 VDC	0717071039	$p = 1.0001 * \text{VDC} - 0.0005$ [psig]	(4.7b)
P1B: 15 psig, 0 – 5 VDC	58721	$p = 3.0071 * \text{VDC} - 0.0213$ [psig]	(4.7c)
P2C: 15 psig, 0 – 5 VDC	55391	$p = 3.0076 * \text{VDC} - 0.0426$ [psig]	(4.7d)
P1C: 100 psig, 0 – 5 VDC	60044	$p = 20.015 * \text{VDC} - 0.0712$ [psig]	(4.7e)

4.5.3 Calibration of RTD and Thermocouple probes

The resistance temperature detectors RTDs and the thermocouples both were directly connected to the measurement channels of the DAQ scheme. They were configured and calibrated online with the DAQ as such that they display and record data directly in °C without the need for further application of offline offsets or adjustments. The RTD and thermocouple sensors were online calibrated generally at 5°C intervals directly in DAQ LabVIEW using a highly stable CL-770A precision dry block and highly accurate one handheld RTD-Thermocouple calibrators shown in Figure 4.15 below. The calibration curve for the calibrator is given in Figure 4.15c. A sample online calibration data for thermocouple probes and the mean square error are presented in Table 4.7 below.

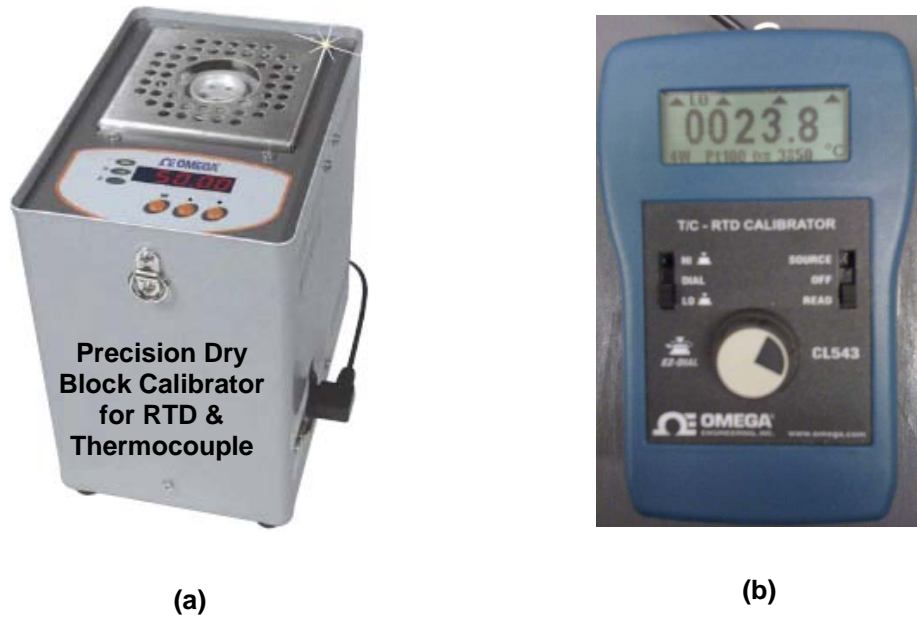


Figure 4.15. (a) Precision thermocouple and RTD calibrator (Dry block) and (b) Highly accurate handheld digital dual thermocouple-RTD calibrator used in current study.

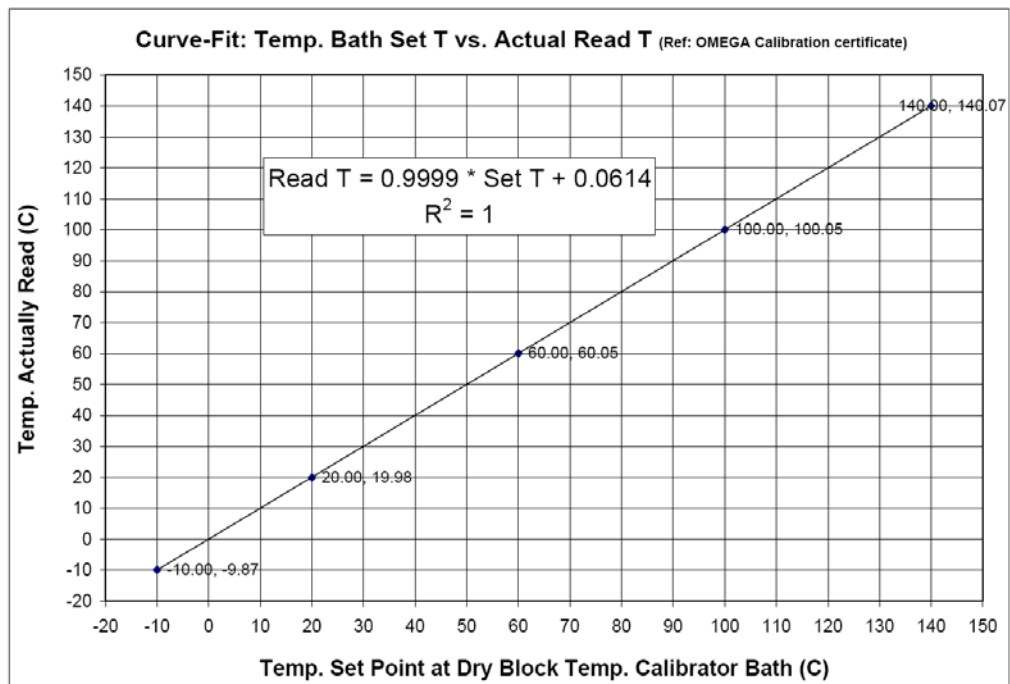


Figure 4.15c. Calibration curve for precision dry block calibrator bath.

Table 4.7. Sample calibration data in °C for T-104 probe located at the centre of air inlet

Reference temperature (X)	Un-calibrated T-104 reading (Y)	Difference in reading (Y – X)	Squared Error (Y – X) ²	Calibrated reading of T-104 (Y1)	Difference in reading (Y1 – X)
0	-0.093	- 0.093	0.0086	0	0
22.110	22.221	0.111	0.0123	22.110	0
25.075	25.254	0.179	0.0320	25.075	0
26.663	26.841	0.178	0.0317	26.663	0
30.011	30.079	0.068	0.0046	30.011	0
45.015	45.171	0.156	0.0243	45.015	0
50.000	50.217	0.217	0.0471	50.000	0
Mean Squared Error shown by DAQ:			0.0150	-	-

The mean square error (MSE) often statistically given as follows,

$$MSE = \frac{1}{N} \sum (Y - X)^2, \text{ from where } MSE = 0.014959 = 0.0149. \quad (4.8)$$

After adopting the calibrations all the thermocouple probes were carefully and firmly installed at the wind tunnel inlet and exit thermal grids and on the surface of the test specimens. The same wind tunnel thermal grids (Figures 4.8a and 4.8b) were used for all the experiments. However, since each test specimen is unique, the surface temperature locations were different for each test specimen. The thermocouple locations for the airside inlet and exit to the test chamber are shown via wind tunnel thermal grids in Figures 4.8a and 4.8b above and details in Figure B5 in Appendix B1 below.

The post-calibrated recordings of the thermocouple probes were verified during *Log-Tchebycheff* point distribution Pitot traverse survey on wind tunnel duct. These included the thermal grids at wind tunnel inlet and exit and at the surface of MCHX #1. Figures 4.15d and 4.15e below portray the temperature profiles at wind tunnel thermal grids. The temperature contours are plotted in Figures B8.1 and 8.2 in Appendix B8. As seen from Figure 4.15d and 4.15e, all the thermocouples read fairly similar readings with reasonably flat profiles at both inlet and exit cross-sectional planes of the wind tunnel.

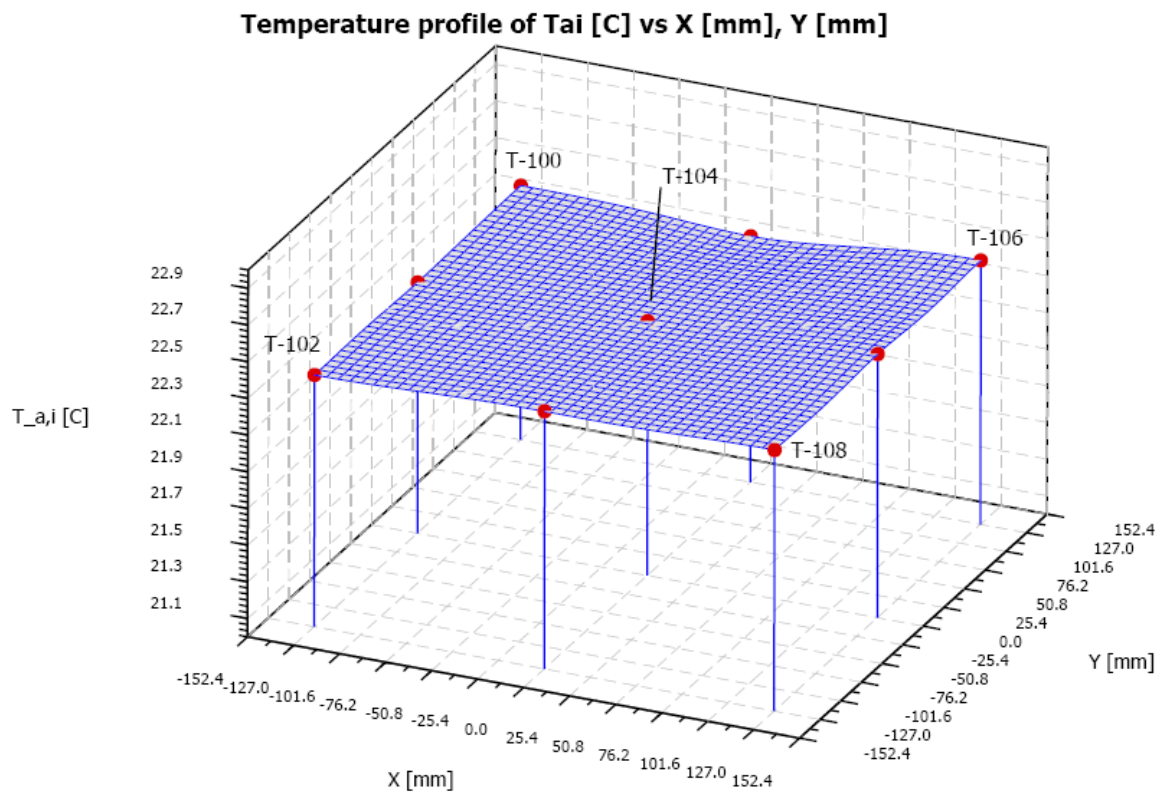


Figure 4.15d. Airside temperature profile at inlet thermal grid at A-A' (Figures 4.7a & 4.8a).

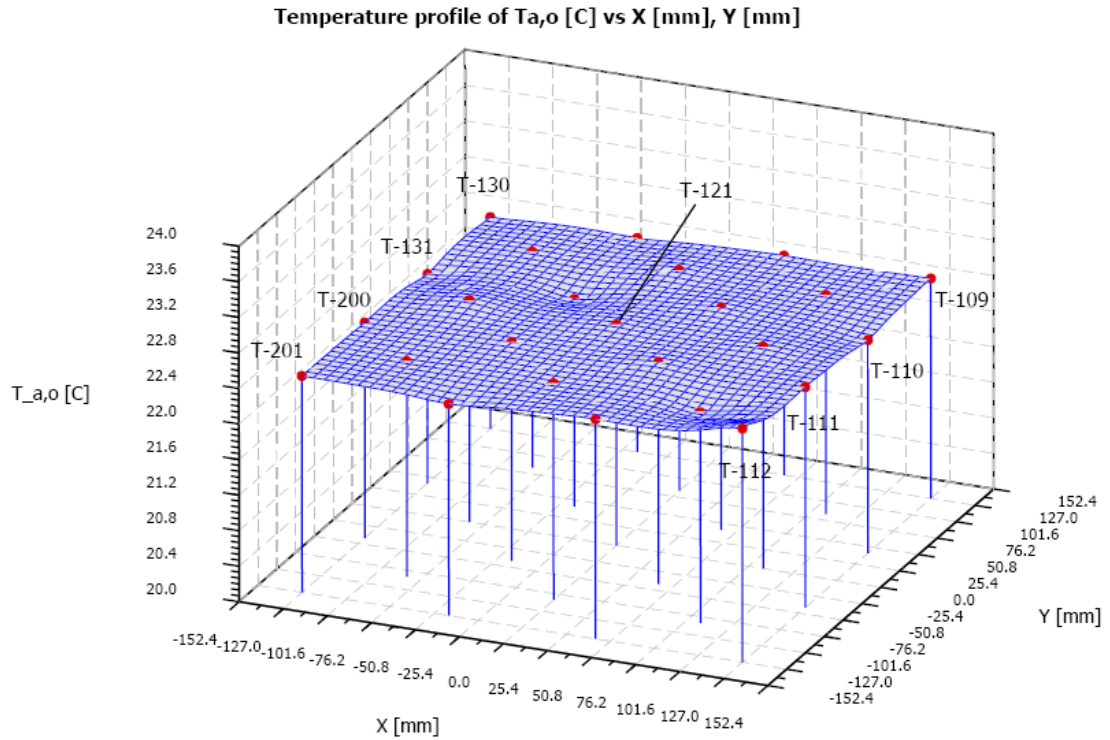


Figure 4.15e. Airside temperature profile at exit thermal grid at B-B' (Figures 4.7a & 4.8b).

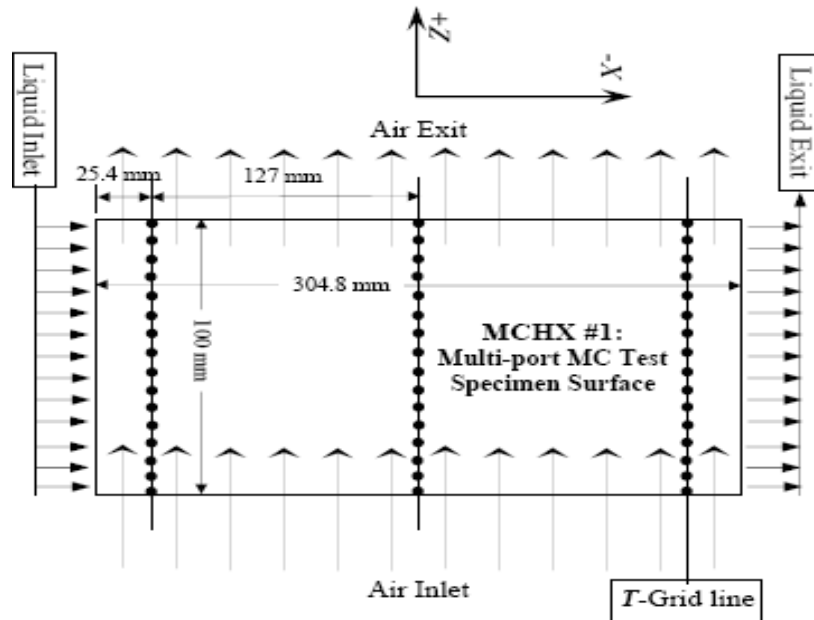


Figure 4.15f Schematic of test specimen surface thermocouple locations – MCHX #1.

The thermocouple locations for the test specimen MCHX #1 are displayed in Figure 4.15f and details in Figure B8.3a in Appendix B8. Figure 4.15g shows the surface temperature profile for the same mean data set as used in Figures 4.15d and 4.15e above. The surface temperature contours are plotted in Figures B8.3b and 8.3c in Appendix B8.

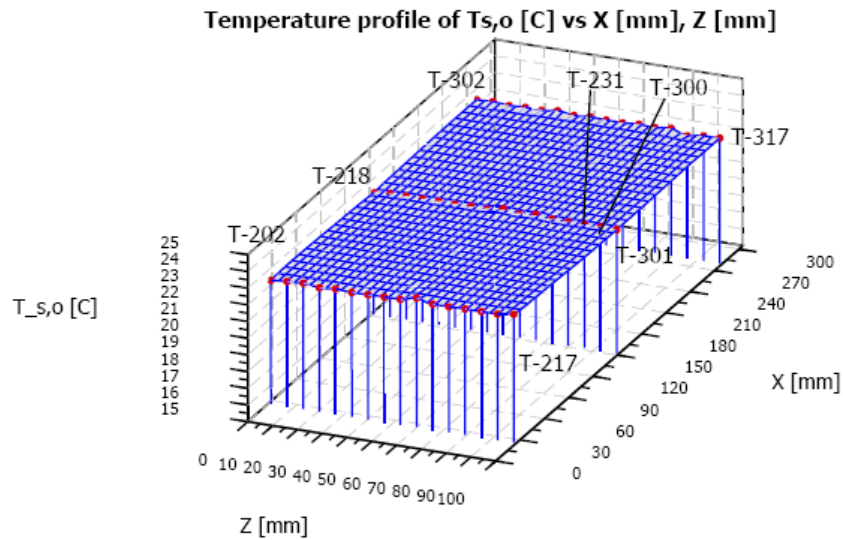


Figure 4.15g. Test slab surface temperature profile at surface thermal grid (Figure 4.15f).

The liquid side inlet and exit temperatures were measured using two insertion RTDs (RTD1 and RTD2). The locations are shown in Figure 4.1a above and details in Figure B5 in Appendix B1 and in Figure B3.6b in Appendix B3. According to Table 4.7 and Equation 4.8, the pre-calibrated readings of these RTDs are plotted against calibrator reference temperature in Figure 4.15h. After adopting the calibrations, their readings were also verified for the same mean data set as wind tunnel duct survey. It is noted that there was only air flow but no liquid flow. The data are plotted in Figure 4.15i below.

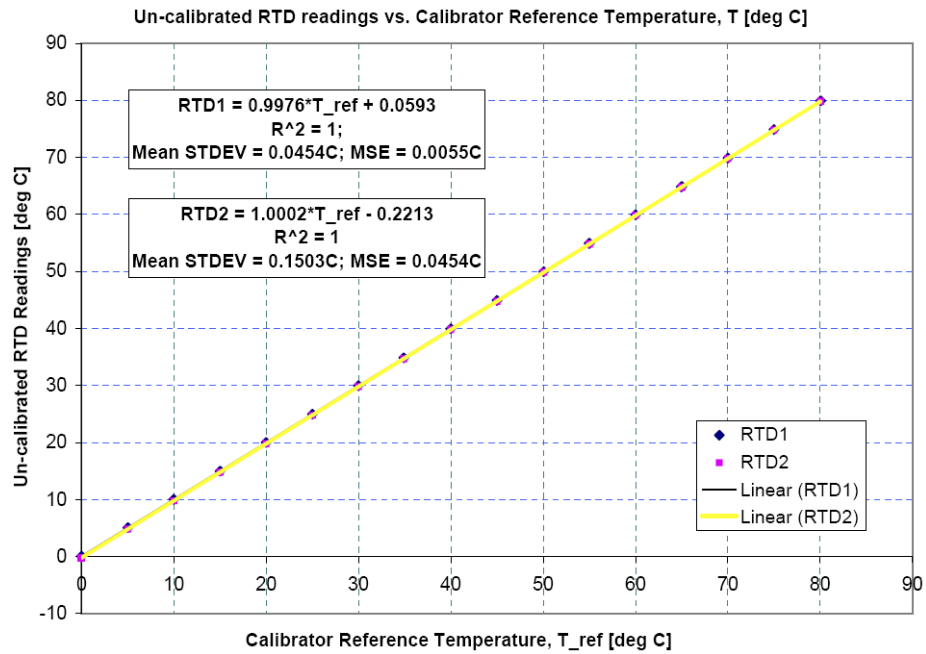


Figure 4.15h. Pre-calibrated RTD readings vs. Calibrator reference Temperature [C].

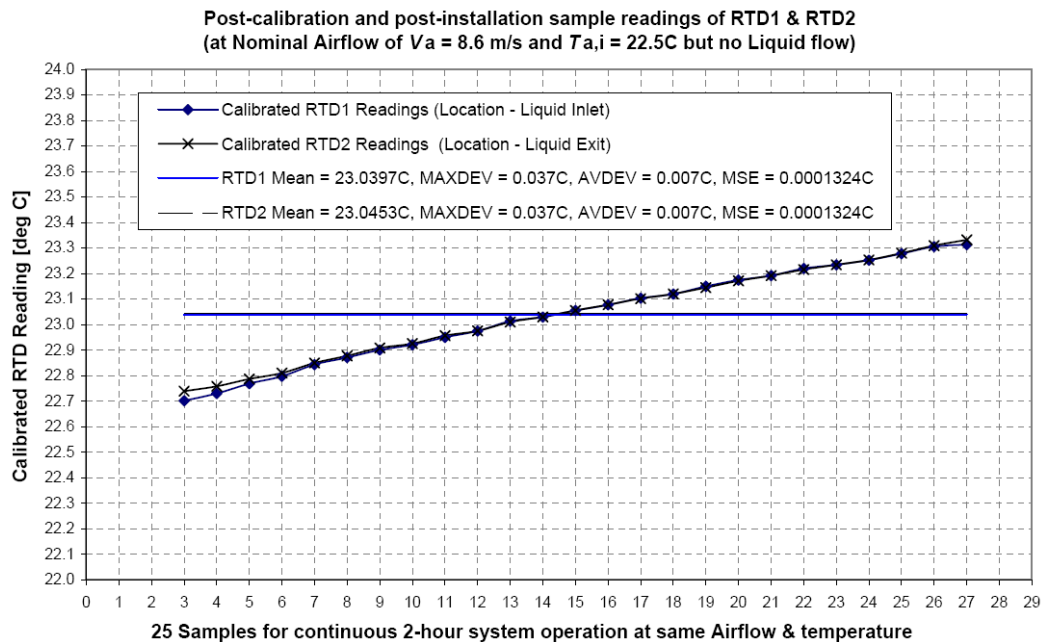


Figure 4.15i. Post-calibrated RTD1 & RTD2 readings for 2 hours (25 samples for nominal Airflow over test specimen at $V_a = 8.5$ m/s and $T_{a,i} = 22.5^\circ\text{C}$ but no Liquid flow inside test specimen).

Overall for all the 82 thermocouples the average and standard deviations were 0.082°C and 0.103°C respectively. The plots of calibrated RTD1 and RTD2 readings show the maximum and average deviations of 0.037°C and 0.007°C and a mean square error (MSE) of 0.00013°C . These slight variations could be the combined effect of the probe uncertainty as well as the positional (spatial) variation of real temperature within the envelope. However, the fatnesses of the temperature graphs indicate the goodness of the calibration as well as the proper functionality of the probes that allowed acquiring better accuracy in experimental data in current study.

4.5.4 Installation and calibration of Pitot Static probe

Shown by Figures 4.16 below and B7.1 in Appendix B7, two Pitot Static Tube probes of model P012A-CF and temperature limit of 426°C were supplied by FlowKinetics LLC. The probes were made such that they have correction coefficient of 1 for the tip-to-static holes correction factor. One was installed at the center of the test section inlet cross-section 1 diameter upstream of the test specimen. The other was kept reserved and some times used in parallel with the first one to model the air velocity at the test section inlet.

The Pitot static probe was carefully installed to make the probe head as parallel to the flow direction as possible (i.e. $\lll 15$ degrees), which was periodically checked

during and after each experimental run. The probes have suitable insertion lengths (12'' \approx 304 mm) to cover the wall-to-wall locations inside the test section as required. The stem diameters of the probes (1/8'' \approx 3 mm) were selected such that the hydraulic diameter of the test section duct was sufficiently larger (i.e. $\gg \gg$ 30 times) than their stem diameters [213].

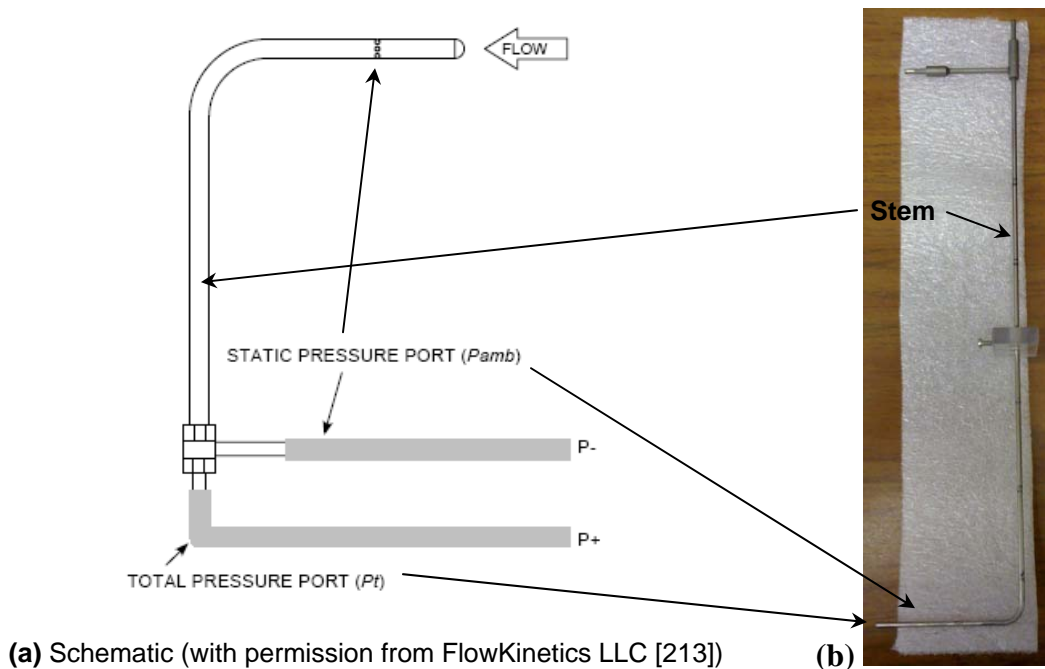


Figure 4.16. (a) Schematic and (b) Photograph of Pitot Static Probe used in current study.

The Pitot static probe was connected in parallel with the FlowKinetics FKT series precision duct calibrator manometer and a differential pressure transducer (PTDD). The output of the PTDD was connected to the data acquisition system (DAQ). The precision duct calibrator manometer is shown in Figure 4.17 below. The pictorial illustrations of the PTDD and the DAQ are given next in Figures 4.19 and 4.20.

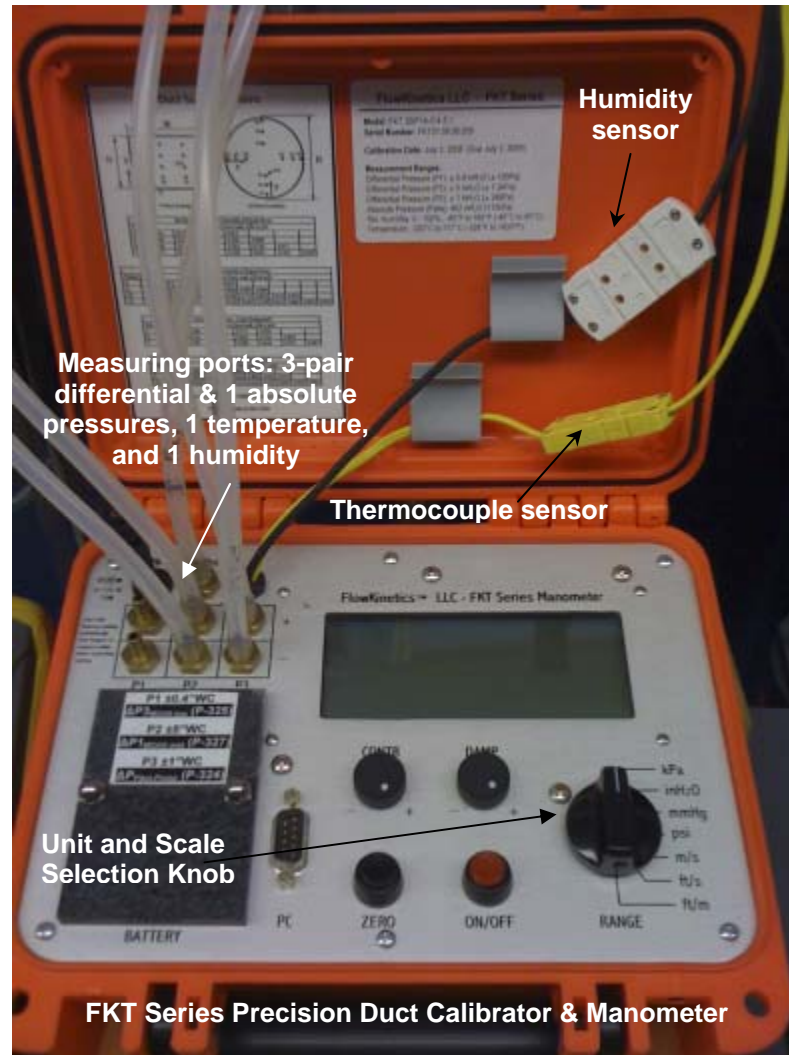


Figure 4.17. Precision duct calibrator manometer used in current study.

The FKT series calibrator manometer shown in Figure 4.17 has built-in thermophysical properties of air and other ideal gases that can be selected during operation. It can measure the absolute air pressure, temperature, density, humidity, three differential pressures through 3-pair of pressure ports, and the velocity in various units such as kPa, psi, m/s, ft/s, inch of water column, and inch of mercury column. To use all

$$V_{a,i} = K \sqrt{\frac{2\Delta p}{\rho_{a,i}}} = K \sqrt{\frac{2\Delta p}{\left[\frac{p_{\text{abs}} + (1 - K^2)\Delta p}{R(T + 273.15)} \right]}}, \quad (4.9)$$

where the gas constant is $R = 287.026 \text{ J/kg.K}$ and the flow coefficient of Pitot static probe $K = 1$ in current study. The p_{abs} and T are the absolute pressure and temperature inside the test chamber at the velocity measuring location. The Δp is the differential pressure reading from the Pitot static probe.

In current study the p_{abs} and T were measured by FKT unit. Since the p_{abs} and T sensors were fed into the FKT calibrator manometer, the unit could measure the air velocity directly in m/s by evaluating the air density and by using Equation 4.9. For comparison and calibration purpose, the DAQ recorded VDC corresponding to Pitot probe's each differential pressure was first converted into pressure unit using the calibration curve of the PTDD. Then the pressure unit was converted into velocity unit using Equation 4.9. The DAQ measured velocity was compared with the FKT measured velocity as shown in Figure 4.16d. The standard deviation in this velocity measurement by DAQ was 0.095 m/s and the mean square error calculated by Equation 4.10 was 0.01. The curves were fairly linear to each other with an R -squared value of 0.9997 indicating both readings to be in excellent agreement.

$$\text{The mean square error, } MSE = \frac{1}{N} \sum (Y - X)^2 = 0.00947. \quad (4.10)$$

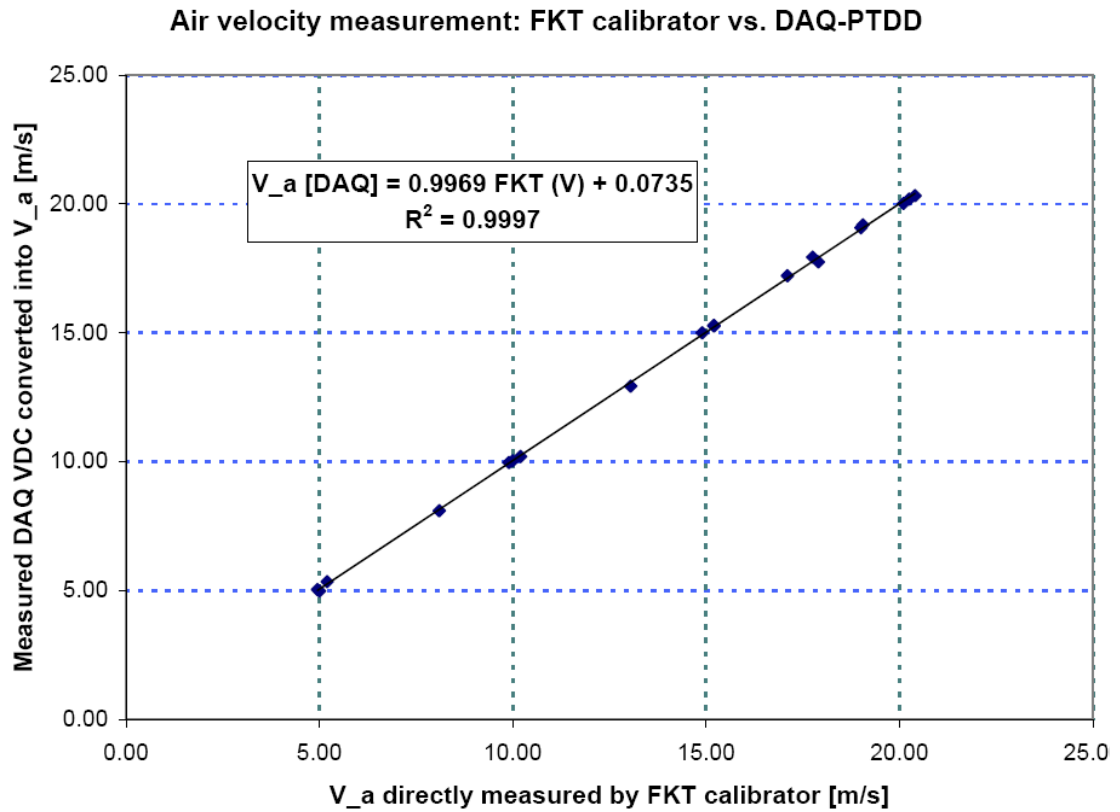


Figure 4.16d. Calibration of wind tunnel air velocity – DAQ VDC converted into velocity (m/s) vs. Velocity (m/s) directly measured by FKT.

First the installed Pitot static probe was calibrated using the FKT series precision duct calibrator manometer and then it was connected with the DAQ scheme via a differential pressure transducer (PTDD). The calibration was done for 23 different wind tunnel speeds at different temperature and in different days. All the data were then compiled to develop a consolidated velocity versus VDC relationship. The calibration curve-fit and plot are given by Equation 4.11 and Figure 4.16e below. The measured velocity data from where the calibration curve is produced are provided in Table B7.1 in

Appendix B7. During each experiment, the FKT was always kept connected in parallel with Pitot static probe for backup measurements and verification of DAQ measured data.

Calibration equation: $V_{a,i} = 6.387 * (\text{VDC})^{0.504}$ [m/s]; with an $R^2 = 0.9997$. (4.11)

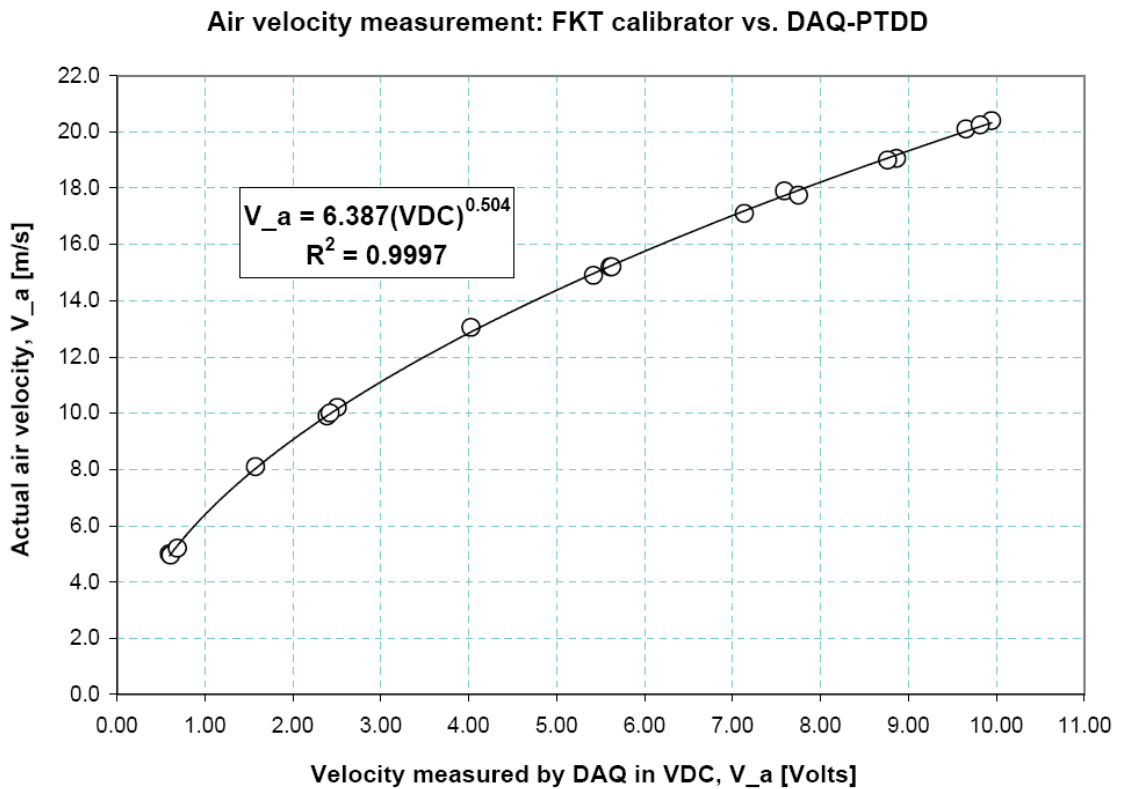


Figure 4.16e. Calibration of wind tunnel air velocity – DAQ [volt] vs. FKT velocity [m/s].

After calibration, all the PTDDs are tested and verified by running the system at a variety of air velocities and their outputs are recorded and verified. The Pitot system readings were further verified using one independently installed hotwire anemometer

probe (HWA), which is shown in Figure 4.18 below. The adopted calibrations for all the PTDDs found consistent with the calibration data supplied by the manufacturer.

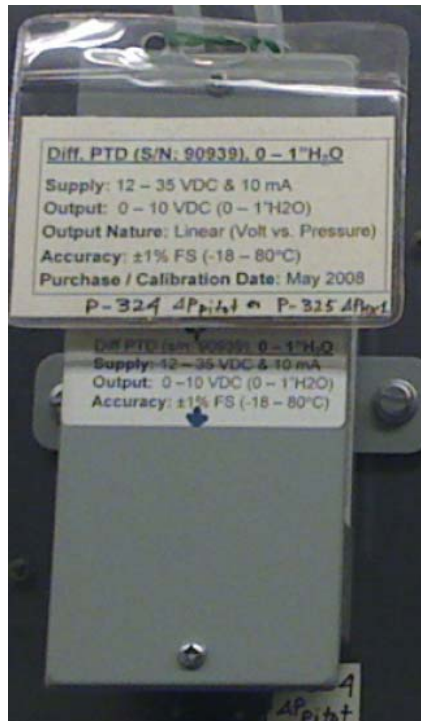


Figure 4.18. Handheld digital hot-wire anemometer (HWA) – backup air velocity measurement.

4.5.5 Calibration of airside differential pressure transducer (PTDD) & test section inlet wind tunnel air velocity

The airside differential pressure transducers PTDDs were also supplied with calibration data by the manufacturer. The calibrations were performed by NIST traceable instrumentation and standards. The functionality and responses of the PTDDs were tested in the system by running the wind tunnel at some given velocity. The output voltage of PTDD received at the DAQ end was then compared with the readings of the FKT calibrator and hotwire anemometer (HWA). Consistent and excellent agreements were

observed in all the readings. Depending on the wind tunnel speed, blockage ratio and the ranges of the operating pressures, two of the PTDDs were alternately used with Pitot static tube probe for air velocity measurements. The PTDDs are shown in Figure 4.19. Further details on calibration are provided in Figures B7.2 to B7.4 in Appendix B7.



(a)



(b)

Figure 4.19. Differential pressure transducers (PTDD) used in current study; **(a)** 0 – 1” WC, and **(b)** 3” WC [NOTE: WC = Water column].

4.6 Data acquisition (DAQ) scheme

The investigations of fluid flow and heat transfer in a dynamic test facility, like the one developed in current study, may involve several operating parameters at many measurement locations to deal with. The total capability of the data acquisition system (DAQ) is 128-channel (4 x 32), which are gradually developed in different phases based on the necessity of current research (Figure 4.20). One 32-channel terminal block is used to feed the excitation current to the RTDs and the rest three 32-channel blocks are used for receiving experimental data. The DAQ system thrice malfunctioned and went down, which took considerable amount of time to troubleshoot, fix and replace components.

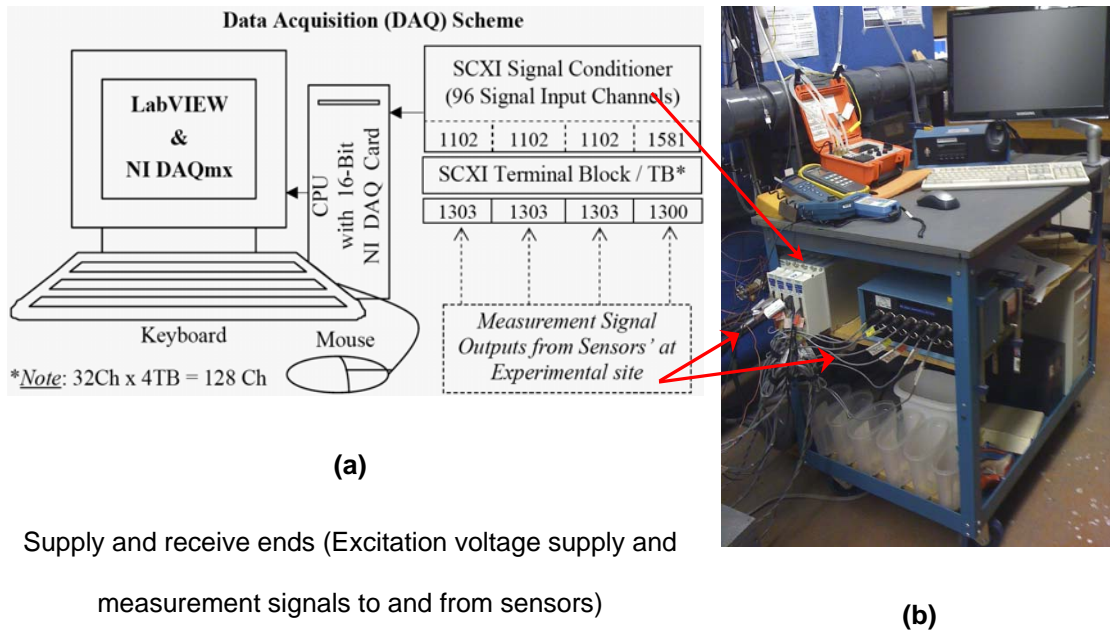


Figure 4.20. The data acquisition (DAQ) scheme used in present study. **(a)** General load flow schematic, and **(b)** On-site physical installation

All the accessories such as the card, modules, components, and computers were selected and purchased by the candidate. Except for the computer, all the components of the DAQ were purchased from National Instruments. The instruments electromechanical probe wiring, connectivity, and configurations were also done by the candidate.

The 128-channel DAQ system has multiplex mode reception. This means that it receives data simultaneously for all the channels through single cable connectivity with the DAQ card installed in the PC. The system has a 16-bit high resolution type NI-PCI-6052E DAQ card. The multiplex mode allows the system to receive and process measurement signals simultaneously from many locations. The faster data sampling rate offers better accuracy in measurements. The scheme is capable of sampling the data at a rate of 100 kHz. More details on DAQ components, assembly and installations are provided in Figures B4 (s, t, u, and w) in Appendix B1.

The DAQ unit could receive and process the voltage, current and frequency as the measurement signals. To maintain homogeneity in installations and measurements, all the measuring instruments and sensors, except for the thermocouples and RTDs, were selected and purchased in such a way that they require voltage for excitation and return only voltage outputs as measurement signals. The common range of excitation voltage is 5 – 32 V DC and the signal outputs are within regular range of 0 – 5 V DC. The 16-bit DAQ card translates into $\pm 28.6 \mu\text{V}$ measurement accuracy for the measuring signals range of 0 – 5 V DC. The major components of the scheme are the chassis, modules,

signal conditioner, terminal block, and the signal cable. No matter how small but each of these components has individual error parameters that contribute to the measurement uncertainty. Details of these errors are discussed and treated in combined in the uncertainty analysis section below.

All the measuring instruments and sensors were connected to the DAQ system. Only exception is that the humidity sensors for the test section are two isolated handheld digital devices that manually monitor the experimental conditions separately. As a result, current configurations and sensors incorporations have made the DAQ scheme capable of monitoring, reading, and recording data for 96 individual experimental parameters from 96 different measurement locations via 96 channels. The parameters are monitored and the data was recorded for processing using National Instruments' software LabVIEW 8.0.

4.7 Commissioning and troubleshooting of developed test facility and experimental preparations and procedures

Once developed, the test facility was successfully commissioned and all the problem areas such as the leakages, operation of valves, heater functionality, pressure loads, drainage, insulation, temperature loads, maximum and minimum liquid and air flow capability, and the micro-filter sieve performance etc. were checked and troubleshot. In a broad range of hot and cold water and air flows the response of the test developed test facility and the performance of all the components, instruments, and sensors are

scrutinized and documented [201]. This information was applied to set and select the proper range of components and instruments pertinent to the certain operating conditions during experiments in current study.

In trial operation of the test facility, on third day increased pump pressure with decreased flow rate were observed even the distilled water was used. Any blockage or increase of flow constrictions somewhere in the flow loop may cause this pressure rise. Intuitively, as a first attempt the micro-filter (MF) was dismantled from the loop for checking. The 45 micron filter element, i.e. the inside sieve of the MF, was found severely blocked with debris and un-dissolved iron oxide as seen in Figure 4.21 below.

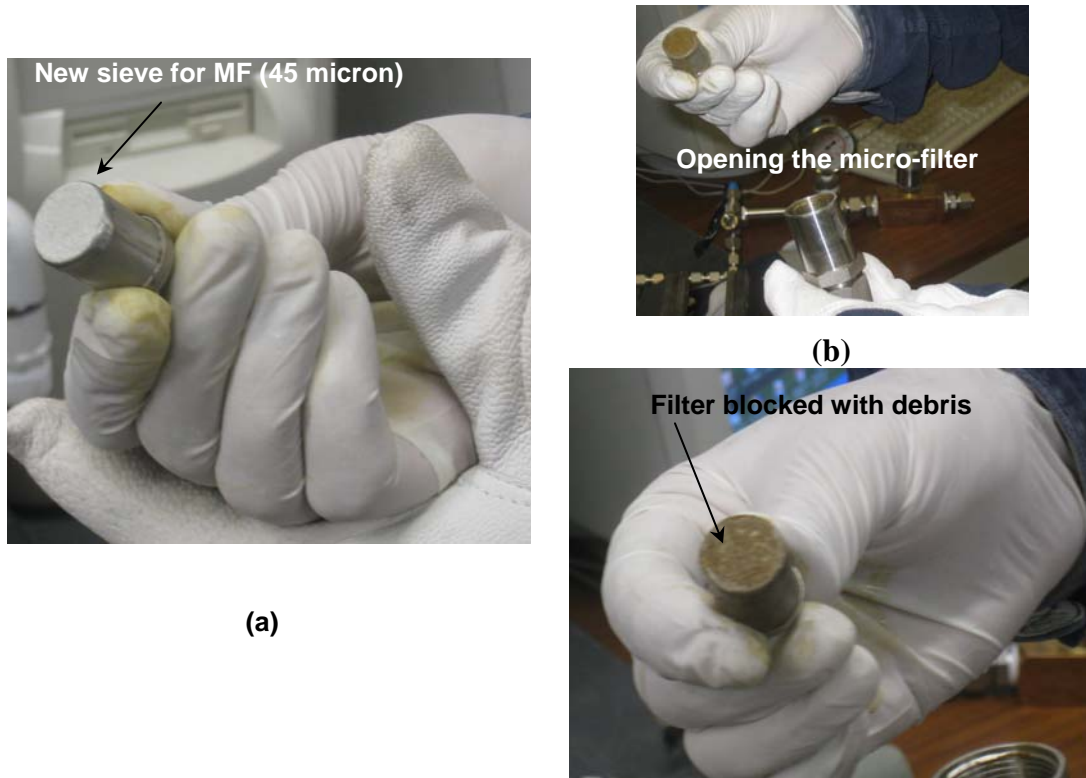


Figure 4.21. Inline micro-filter (MF): **(a)** New sieve and **(b)** Blocked sieve with debris.



(c)



(d)



Figure 4.21. Inline micro-filter (MF): (c) Cleaning of filter housing and (d) Filter re-installation.

Considering such unforeseen situation, several filter elements were stocked from Swagelok Ontario. The MF housing was properly cleaned in beaker, as seen in Figure 4.21c. The dirty sieve was not re-used; rather a new filter element from stock was re-installed, as seen in Figure 4.21d. After installation of MF in the flow loop, the liquid system was further operated but it appeared that the problem is not solved. It was spotted that the circulation heater was the source debris since the inside wall of the shell was rusty from origin (i.e. vendor). A new shell was replaced locally with the help of the technologist of this University.

Owing to the contribution of the gear pump itself and additionally the needle valve, the liquid flow rates could quickly stabilize, in about 20 minutes for higher flow rates and in about 30 minutes for lower flow rates. The inline circulation heater unit performed well to give a fairly stable inlet measurement temperature, which within $\pm 1^\circ\text{C}$ for the range of $60\text{-}75^\circ\text{C}$ and within $\pm 0.5^\circ\text{C}$ for the range of $40\text{-}60^\circ\text{C}$. The thermal wind tunnel took about 20 minutes to stabilize the velocity and temperature of the airflow at the test section inlet.

Before beginning any data collection, on an average 25 minutes were needed to allow to monitor the running system and to ensure that the overall system stabilization and hence the steady state is achieved. For a given setting of any operating condition, the steady state was considered achieved when the fluctuations in flow rates and temperature of the working fluids were no more than 3% at any location in the system.

As mentioned above, the working fluids used in current research were the 50% ethylene glycol water solution and distilled deionized water, which have different Reynolds number for the same flow rates and hence their operating conditions were different. Therefore test matrices were produced for a number of operating conditions for each set of experiment, which are presented in respective chapters in the next for each test specimen investigated. These matrices covered mainly the laminar flow regime in the test specimens with a few exceptions for friction factor study for water flow in MCHX #1 (chapter 6, section 6.1) where some turbulent flow regime was possible to achieve.

The principal focus of current study was the liquid flow inside microchannels. Therefore for a given inlet temperature the liquid side flow velocities were varied and the airside flow rate and temperature were kept constant for each set of experiment. The variation of liquid flow velocities was achieved by changing the speed of the variable speed gear pump; in addition a further precision to the flow velocity was provided by operating the needle valve. The temperature of the liquid flow was regulated with the aid of electronic control panel integrated with the heater-tank unit (Figures 4.10, B4k, B4x). The airflow temperature at the inlet of the test section was kept fixed by maneuvering the cold water flow through the internal heat exchanger of the wind tunnel via flow mixing network (Figures 4.6 and B4).

The inlet and exit temperatures of liquid and air flows; inlet and exit pressures of liquid flow; liquid flow rates; airflow velocity at the inlet of the test chamber; and the surface temperature of the multi-port test slabs were the major parameters to be experimentally determined in current study. All these parameters were measured and recorded using the DAQ scheme. Corresponding to each separate setting of flow rate and temperature, several fluid flow and heat transfer data sets were collected to observe the effects of Re on f (for the test samples of MCHX #1 and MCHX #2) and the effects of Re on pressure drop and Nu (for the test specimens of MCHX #4 and MCHX #6).

The DAQ scheme is capable of sampling the data at a rate of 100 kHz. The faster data sampling rate offers better accuracy in measurements. Initially the DAQ channels were sampled at various rates along with the information of signal amplitudes and frequencies to optimize a reasonable faster rate for the current system. Out of 128 channels in the DAQ system, 32 channels were used for RTD excitation. The rest 96 channels were used to read the data individually and simultaneously in multiplex mode from 96 different measurement locations in the flow system. For this reason, to stay away from any possible data jam or data inaccuracy or the system interruptions, a better sampling rate could be set at 1 kHz. Thousands of samples for each measurement parameter were collected and their mean and standard deviations were documented.

A single data set in current study is defined as the steady state time averaged mean data set (*TAMDS*) of around 3000 to 6000 samples for each of the 96 parameters via 96 independent channels in the DAQ system for a given operating set point. This measurement and sampling method can be represented by Equation (4.12) below.

$$TAMDS = \frac{1}{n} \sum_{n=1}^n \left(\frac{1}{k} \sum_{j=1}^k TAMDS_j \right), \quad \text{where } n = 3 \sim 5 \text{ repetitions,} \quad (4.12)$$

where the variable k is the sample counter ranging from 1 to 6000 samples and n is the total number of repetitions. This gives an independent total number of sample population $N = n*k$. This multi populated mean data set obtained by following Equation (4.12) not

only assists in reaching superior measurement reliability, but it also facilitates the better statistical evaluation of the data and improved error estimation in uncertainty analysis.

The main focus of current study is laminar flow. Therefore the operating flow regimes were mainly laminar and developing laminar flow. For pressure drop and heat balance tests in MCHX #1, the flow regime was extended to turbulent flow. The details of necessity for flow regime selection in current study are described in section 3.4 above.

4.8 Heat balance (HB) on the developed test rig using MCHX #1

The appropriate balance between the heat released by one fluid and heat transported away by the other fluid is important in heat transfer study in a two-fluid heat exchanger. The heat released by the external fluid, which in majority of the studies the applied wall heat flux boundary condition, was considered as equivalent to the heat taken away by the internally flowing fluid such as [22, 94, 108, 171, 173]. This consideration may be relevant for the situation of constant wall heat flux condition (H -condition) but not for the condition of constant wall temperature (T -condition). For an air-to-liquid heat exchanger the temperature difference drives the heat transfer mechanism and therefore the T -condition often more closely describes the conditions at the wall better than the H -condition [214-215]. Other works regarded the heat rate as simply the average of the heat delivery rate by hot fluid and capture rate by cold fluid without any heat balance between two working fluids, such as [152].

In the heat transfer study of a two-fluid typical thermal heat exchanger the proper heat balance between two fluids is necessary for a dynamic test configuration where both fluids are in motion, which is the case of current study. In order to examine the integrity of the developed test facility, initial heat balance experiments were conducted on MCHX #1 (shown in Figures 4.4a, B2.1c, B3) in air-to-water crossflow orientation. The heat transfer mode in this heat balance experiments was water cooling i.e. $T_{w,i} > T_s > T_{a,i}$, where the subscripts a, i, s and w refer to air, inlet, surface and water respectively. The distilled deionized hot water, collected from the Chemistry laboratory at university of Windsor, was passed through the microchannel test specimens and the cold air in the wind tunnel was blown over the test slab.

The temperature and velocity of wind tunnel cold airflow, which are inlet to the test chamber, were kept constant at $21.85 \pm 0.05^\circ\text{C}$ and 8.05 ± 0.15 m/s respectively. For this preset air velocity and temperature, the water flow rates through the test slab were varied for a given temperature. The temperature of hot water flow at the test specimen inlet was maintained constant at $76 \pm 0.8^\circ\text{C}$ while the flow rates were varied in the Reynolds number range of $1170 < Re < 3780$. Upon reaching the steady state condition, the flow rate and for each flow rate the inlet and exit temperatures differentials of both water and air flows were measured. Unless otherwise stated, all the thermophysical properties were evaluated for both water and air at their respective bulk temperatures.

The steady state heat transfer between the hot water and the cold air via test slab wall was essentially due to the forced convection mechanism, which can be estimated from the respective fluid side heat rate Equations 4.13a and 4.13b as follows.

$$q_w = \dot{m}_w c_{p,w} (T_{w,i} - T_{w,o}) = \dot{m}_w c_{p,w} \Delta T_w; \quad (\text{Waterside heat transfer rate}) \quad (4.13a)$$

and

$$q_a = \dot{m}_a c_{p,a} (T_{a,o} - T_{a,i}) = \dot{m}_a c_{p,a} \Delta T_a; \quad (\text{Airside heat transfer rate}) \quad (4.13b)$$

where q , \dot{m} , c_p and T are the heat transfer rate, mass flow rate, specific heat and temperature respectively. As usual the subscripts 'w' stands for water, 'a' for air, 'i' for inlet and 'o' for outlet or exit. The above heat rate should ideally be the same for both the internal and external fluids to give $q_w \approx q_a$. However in practice this is never the case. Several factors include but not limited to the system response, experimental error, heat gain or loss due to improper insulation etc. are responsible for these differences, which practically give $q_w \neq q_a$.

The percentile difference of the heat released by water q_w and the heat gained by air q_a is defined as the heat balance (HB) in current study. The heat balance between the water and the air flows with respect to waterside heat rate q_w can be expressed by Equation 4.14a as follows.

$$HB_w = \frac{q_w - q_a}{q_w} * 100; \quad (\text{Heat balance with respect to waterside heat rate}). \quad (4.14a)$$

For an air cooled heat exchanger the ASME PTC 30-1991 [216] recommended a heat balance method, which has to be performed with respect to the effective or mean heat transfer rate in the form as given by Equation 4.14b below.

$$HB_{avg} = \frac{q_w - q_a}{q_{avg}} * 100 \quad (\text{Heat balance with respect to effective heat rate}), \quad (4.14b)$$

where the q_{avg} is defined as the arithmetic average of waterside and airside heat transfer rates as given in Equation (4.14c) below.

$$q_{avg} = \frac{(q_w + q_a)}{2}; \quad (\text{Effective or mean heat transfer rate}). \quad (4.14c)$$

According to the ASME PTC, if the result obtained from Equation (4.14b) exceeds beyond $\pm 15\%$, an inspection of the test setup, equipment and instruments should be made to determine the causes for the differences or the heat transfer tests need to be repeated. If the result agrees within $\pm 15\%$, then any of the heat loads such as the q_w , q_{avg} or q_a can be used to interpret the experimental heat transfer data. Since the liquid flow temperatures in current study were measured using ultra precision RTDs with better

accuracy ($\pm 0.012^\circ\text{C}$), the waterside heat transfer rate was more reliably used in heat transfer calculations.

The heat balance results here are presented as function of waterside Reynolds number. The Reynolds number, in general, is defined by Equation (2.1) above, which is adapted to the flow situations in MCHX #1 via Equation 4.15 below. Assuming an equal and uniform flow distribution of water from the manifold through N channels in the multi-port test slab, the Reynolds number of water flow through a single channel is determined from the following expression.

$$\text{Re}_w = \left(\frac{\rho V Z}{\mu} \right)_w = \frac{4\dot{m}_w}{N\pi\mu D_{\text{ch}}}, \text{ (Waterside Reynolds number in a single channel).} \quad (4.15)$$

where μ and \dot{m}_w are the dynamic viscosity and total mass flow rate of water through the main liquid handling system and D_{ch} is the diameter of a single channel or port in the test specimen MCHX #1. The number of ports or channels N in current study is 68 for all the test specimens.

The water side heat rate q_w is plotted against water side Reynolds number Re_w in Figure 4.22. As expected, the q_w increased with the increase of Re_w . Few scatters in data might have resulted from the fluctuations of flow or temperature or both during the experiments. As shown by the solid line in Figure 4.22, as expected a power law curve fit with a positive exponent correlated q vs. Re data well with an R-squared value of 0.96.

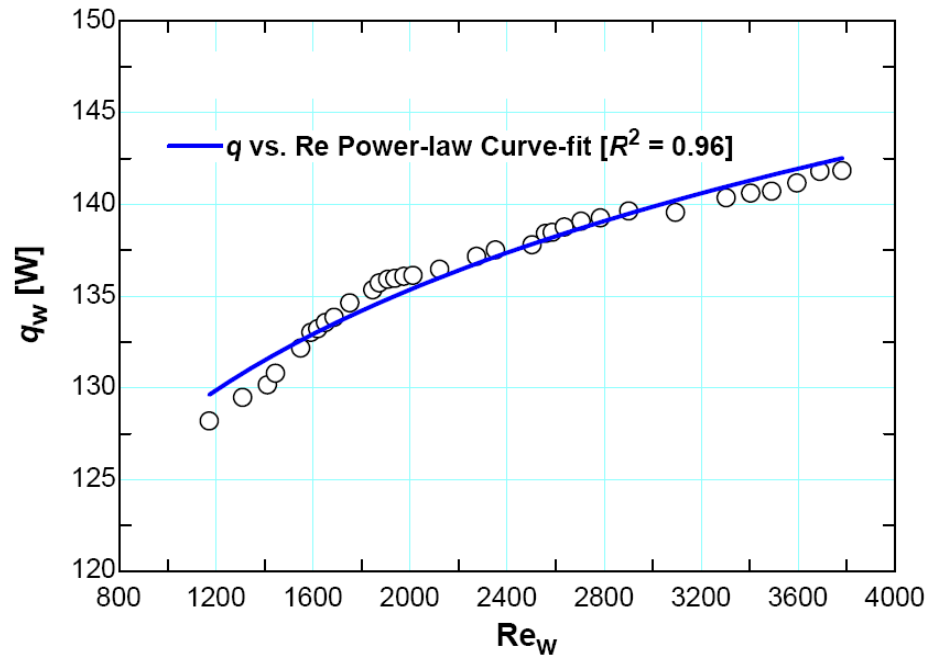


Figure 4.22. Variations of waterside heat rate (q_w) with waterside Reynolds number (Re_w).

The variations of non-dimensional water flow temperatures are also plotted against waterside Reynolds number in Figure 4.23. The dimensionless temperature was defined as the ratio of the difference in inlet and exit temperatures to the inlet temperature of water flow as given in Equation 4.12 [201]. The dimensionless temperature decreased with the increase of water mass flow rate and hence with the increase of Re. This data also followed a power law relationship but with a negative exponent as expected.

$$\text{Non-dimensional temperature of water flow} = \frac{T_{w,i} - T_{w,o}}{T_{w,i}} = \frac{\Delta T_w}{T_{w,i}}. \quad (4.12)$$

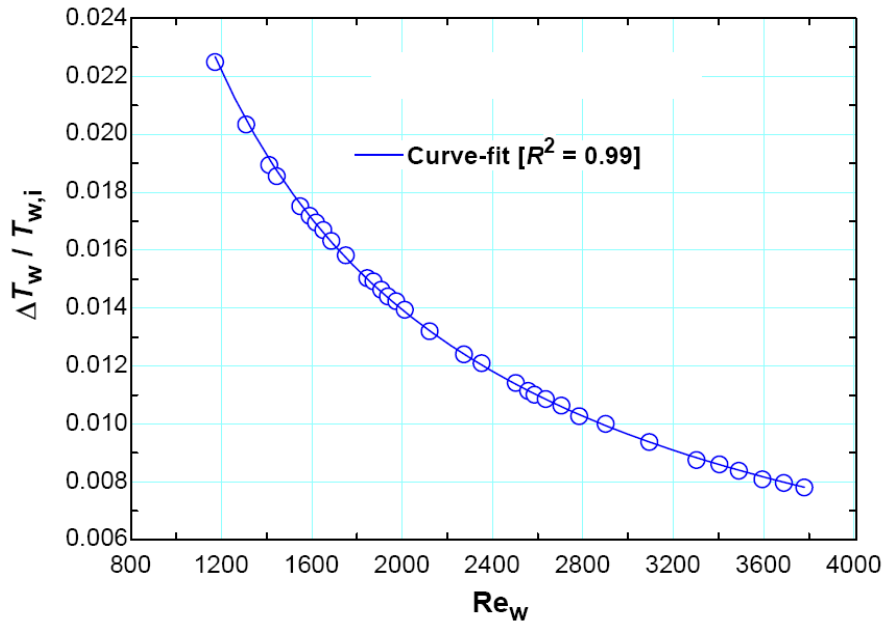


Figure 4.23. Variations of waterside non-dimensional temperature with waterside Re_w .

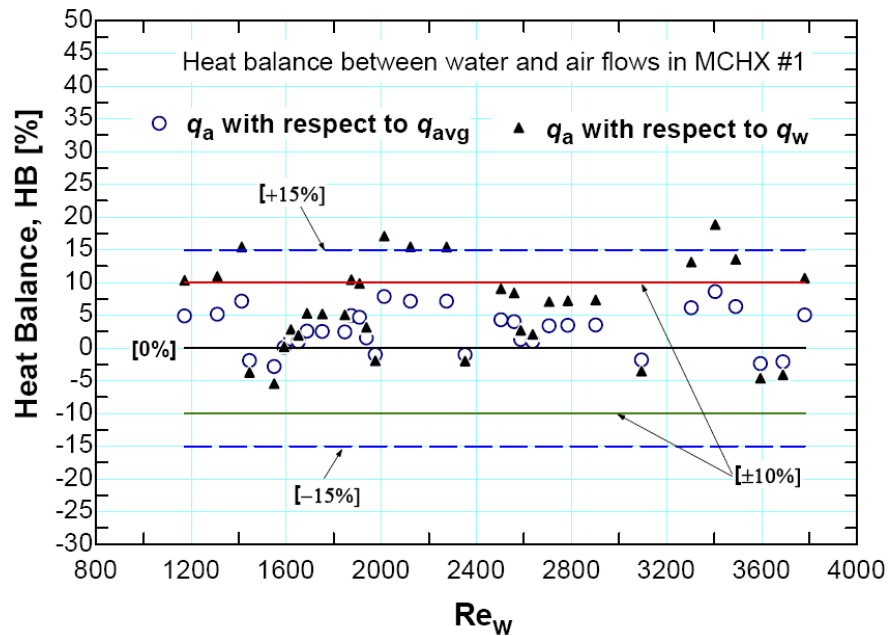


Figure 4.24. Variations of heat balance (HB) with respect to waterside Reynolds number Re_w .

Thus the heat balance between water and air with respect to waterside heat rate q_w and the effective heat balance between water and air with respect to the average heat rate q_{avg} were estimated from Equations 4.14a and 4.14b respectively. Both the heat balance results are plotted in Figure 4.24 above against water side Reynolds number.

As seen in Figure 4.24 above, the variation of q_a is found from -5% to +15% with respect to q_w and from -3% to +7% with respect to q_{avg} respectively. The mean effective heat balance in conducted experiments with respect to q_{avg} is $\pm 7\%$, which is well within the acceptable limit of $\pm 15\%$ as recommended by the ASME PTC 30-1991 [216].

The above result represents a very good heat balance performance of the developed test facility and hence its better integrity. Nevertheless, further insulation was provided and extra attention was paid to minimize any possible error that could occur in all other subsequent experiments. For better measurement and analyses, the data that falls within $\pm 5\%$ of the heat balance with respect to q_{avg} or q_w could be the reasonable choice to interpret the experimental data. Therefore this thought was applied in all heat transfer experiments in current research.

CHAPTER – 5

DATA REDUCTION, EMPLOYMENT OF WILSON PLOT TECHNIQUE, AND UNCERTAINTY ANALYSES

5.0 DATA REDUCTION, EMPLOYMENT OF WILSON PLOT TECHNIQUE, AND UNCERTAINTY ANALYSES

As mentioned before two internal working fluids, i.e. the 50%-50% ethylene glycol-water solution and distilled deionized water and one external working fluid i.e. the air were used in current study. In this dissertation the subscripts g, w, a, and s represent the glycol-water mixture, water, air, and surface of the test specimen respectively. For clarity and for general representation the subscript 'liq' for liquid is used in this chapter in place of either 'g' or 'w'. This is applicable to situations where a certain relationship or equation equally hold valid for both the liquids. In this dissertation, the 50%-50% ethylene glycol-water solution sometimes named as glycol-water or just glycol for clarity.

Assumptions were made that the used fluids are incompressible Newtonian fluids and their properties are independent of pressure but the functions of temperature only. The liquids were assumed to be uniformly distributed through all the channels in the test slab. This is a reasonable assumption because the distributing and collecting manifolds were about 10 times larger than the diameter of a single channel of the test slab.

In the experiments the measurements and data were taken for the fundamental and independent parameters. These parameters were as follows.

Liquid side (Internal working fluid):

1. Mass flow rate (\dot{m}_{liq} ;)
2. Inlet or entrance temperature ($T_{liq,i}$)
3. Exit or outlet temperature ($T_{liq,o}$)
4. Inlet or entrance pressure ($p_{liq,i}$) and
5. Exit or outlet pressure ($p_{liq,o}$)

Air side (External working fluid):

1. Flow velocity (V_a), through differential of total to static pressures
2. Inlet or entrance temperatures ($T_{a,i}$)
3. Exit or outlet temperatures ($T_{a,o}$)
4. Absolute pressure at the inlet or entrance ($p_{a,abs}$) and
5. Differential pressure across test specimens ($p_{liq,o}$)

Test specimen structure (heat transfer wall):

1. Outer surface temperature ($T_{s,o}$)

Depending on which test specimen was tested (as described in next chapters), all the above parameters were measured for a number of liquid side flow rate settings to gather a plenty of data sets for better evaluation. The data from these measurements was then deduced to obtain the other dependent fluid flow and heat transfer parameters as

outlined in this section below. On purpose the data reduction processes for some of the parameters already are described before, which are repeated in this section but no detail descriptions are provided.

5.1 Evaluations of thermophysical properties of working fluids

Unless otherwise stated, usually the thermophysical properties of the working fluids in current study were evaluated at bulk flow temperature between the inlet and exit of the flow path. Considering a linear variation of temperature between the inlet and exit of both fluids, the bulk temperatures were deduced as follows.

$$\text{Liquid side bulk flow temperature, } T_{b,\text{liq}} = \frac{(\overline{T}_{\text{liq},i} + \overline{T}_{\text{liq},o})}{2} \quad (5.1a)$$

and

$$\text{Air side bulk flow temperature, } T_{b,a} = \frac{(\overline{T}_{a,i} + \overline{T}_{a,o})}{2} \quad (5.1b)$$

where the $\overline{T}_{\text{liq},i}$, $\overline{T}_{\text{liq},o}$, $\overline{T}_{a,i}$ and $\overline{T}_{a,o}$ are the consolidated mean inlet and exit temperatures of the flowing liquid and air. The processes of the consolidated mean values of these parameters are described in sections 5.2.1 through 5.2.3 below.

Unless otherwise stated, all the thermophysical properties of all the working fluids were evaluated at their respective bulk temperature defined by Equation 5.1 above. The properties of 50% ethylene glycol-water mixture for each data point were derived from the ASHRAE Handbook of Fundamentals 2005 [212]. The properties for water and air were evaluated from the built-in database of EES (Engineering Equation Solver) using the bulk temperature and bulk flow pressure [218].

5.2 Consolidated mean data sets of measured parameters

The independent parameters were measured at various locations and for a number of repeated times. The mean data sets were produced from the time averaged collection of data samples, which are described above in section 4.7 via Equation (4.4). However, some of the parameters need to be described further that are used in data reduction to obtain other dependent secondary parameters.

As mentioned before, in addition to the low thermally conductive thick Plexiglas wall, the test domain was properly insulated so that virtually it did not take part in any heat transfer activity with the outside environment but the test section only. As sample examples, the pictorial comparative illustrations of the un-insulated and insulated test sections are provided in Figure 5.1 below.

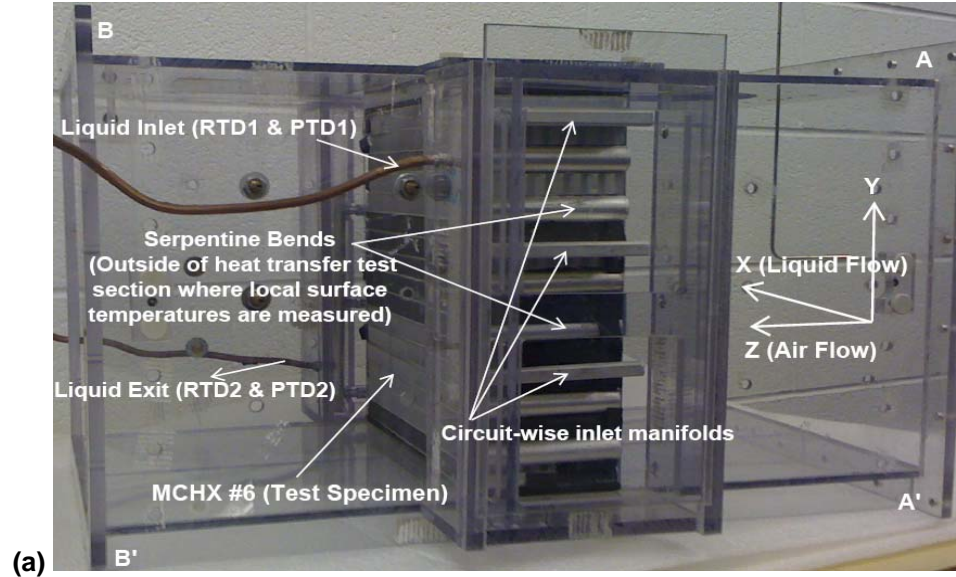


Figure 5.1. (a) Display of un-insulated test specimen inside the test section.

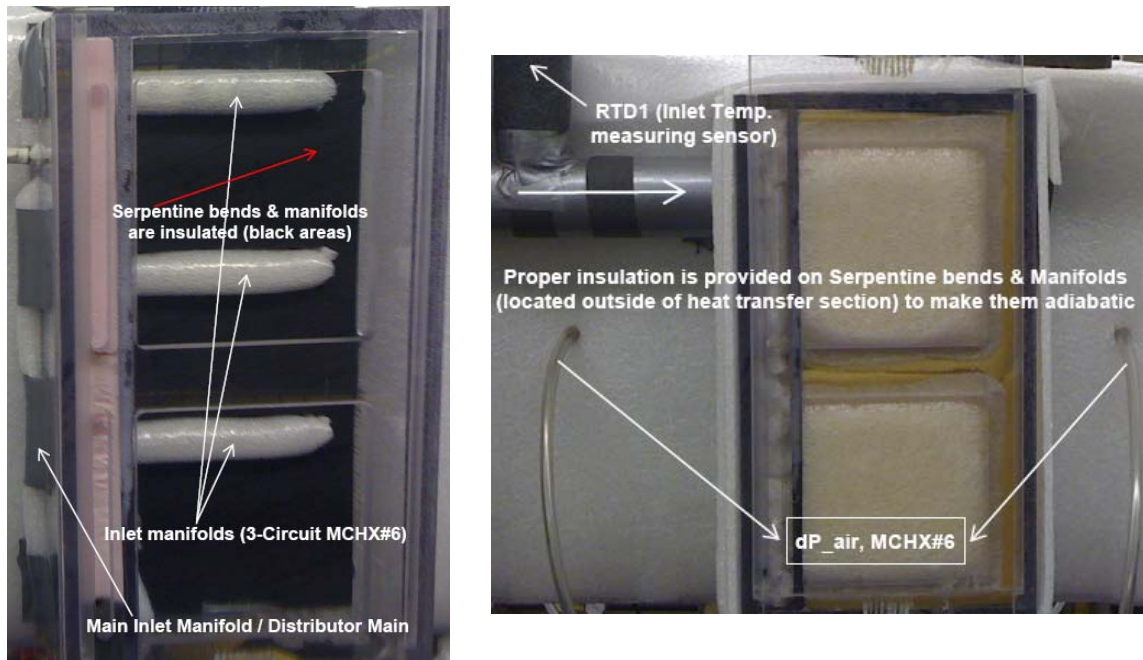


Figure 5.1. (b) Display of insulated test specimen inside the test section.

It is worth mentioning that all the measuring sensors were within the insulated domain and the outside environment did not affect or very minimally affected their functionality and performance. The serpentine bend portions of the test specimens were also within the insulated domain but outside of the heat transfer section. As a result the bend portion served as a non-heat transfer section in other words as adiabatic section. The local outside surface temperatures of the test specimen were measured around this serpentine bends and at manifold entrance and exit for each of the flow circuits.

5.2.1 Liquid side measured parameters

Liquid side temperature measurements

The inlet and exit temperatures of the liquid flow were measured using two calibrated insertion-type ultra precision RTD with accuracy of $\pm 0.012^\circ\text{C}$, the RTD1 at the inlet and the RTD2 at the exit, as shown in Figures 4.1a, 5.1, and B1-B5. By following Equation 4.4 in section 4.3.2, the consolidated mean of the inlet and exit temperatures of the liquid flow, $\overline{T_{\text{liq},i}}$ and $\overline{T_{\text{liq},o}}$ were determined as follows.

$$\overline{T_{\text{liq},i}} \text{ or } \overline{T_{\text{liq},o}} = \frac{1}{n} \sum_{n=1}^n \left(\frac{1}{k} \sum_{j=1}^k (T_{\text{liq},i} \text{ or } T_{\text{liq},o})_j \right), \text{ where } n = 3 \sim 5 \text{ repetitions,} \quad (5.2)$$

where k is the time averaged mean of 3000 to 6000 samples at steady state condition. Since each of the experiments was conducted to cool the hot liquid, the inlet temperature was always higher. The temperature differentials of liquid flow were deduced as follows.

$$\text{Liquid side temperature differential, } \Delta T_{\text{liq}} = \left(\overline{T_{\text{liq},i}} - \overline{T_{\text{liq},o}} \right) \quad (5.3)$$

Liquid side pressure measurements

The inlet and exit pressures of the liquid flow through MCHX test slab were measured using two pressure transducers (PTD); the PTD1 at the inlet and the PTD2 at the exit, as can be seen in Figures 4.1a and 5.1 above. Within various capacities of the collected sensors (0 – 100 psig or 0 – 690 kPa) a minimum of three sets of PTDs were alternately used depending on the flow rate. The narrow pressure range of each PTD at each flow rate was selected and maintained for better measurement accuracy. The accuracies of the PTDs are tabulated in Table 4.2 in section 4.5.

All the PTDs give 0 – 5 DC voltages as measurement outputs to the DAQ system, which were compared with manufacturer's supplied calibration data and curves. The voltage signals were almost linear with the corresponding psi pressure units. By following Equation 4.4 in section 4.3.2, the consolidated mean of the inlet and exit pressures of the liquid flow, $\overline{p_{\text{liq},i}}$ and $\overline{p_{\text{liq},o}}$, were first recorded in voltage unit in DAQ. The voltage units were then converted into psi units according to the obtained psi vs.

VDC calibration equations as listed in Table 4.6 by Equations 4.7. Finally the pressure values in psi units were converted into Pa (Pascal) unit to use in further analyses.

The pressure differential between the inlet and exit (uncorrected raw pressure drop) and the bulk flowing pressures were deduced as follows.

$$\text{Liquid side pressure differential (i.e. pressure drop), } \Delta p_{\text{liq}} = \left(\overline{p_{\text{liq,i}}} - \overline{p_{\text{liq,o}}} \right) \quad (5.4)$$

and

$$\text{Liquid side bulk flow pressure, } p_{\text{b,liq}} = \frac{\left(\overline{p_{\text{liq,i}}} + \overline{p_{\text{liq,o}}} \right)}{2} \quad (5.5)$$

Liquid side mass flow rate measurements

As described in section 4.4 and shown in Figure 4.11a, the main system flow meter was installed at the upstream of the test section inlet as shown by DFM in Figure 4.1a. This digital flow meter gives a measurement output voltages from 0 – 5 VDC to the DAQ. The calibration data and curves for both glycol-water mixture and water for a variety of viscosity values were supplied by the manufacturer. The calibration data were supplied by the vendor, which was done by using NIST procedure and instrumentation. Nevertheless, before the experiments the calibrations were compared with measured mass flow rate using bucket-stop watch-weigh method and found reasonably comparable. During each experiment, randomly direct mass flow rate

measurements were taken as back up to DFM data. These data were later verified and found quite consistent.

The voltage signals for the flow meter were linear with little off-set with corresponding liter per minute (LPM) or gallon per minute (GPM) units. By following Equation 4.4 in section 4.3.2, the consolidated mean liquid volume flow rate $\overline{\dot{V}}_{\text{liq}}$ was first determined in voltage unit. The voltage units were then converted into LPM and in kg/s ($\overline{\dot{m}}_{\text{liq}}$) units according to the supplied and produced calibration curves. The total liquid mass flow rate through the system was determined as follows.

$$\text{Total liquid mass flow rate through the system, } \overline{\dot{m}}_{\text{liq,DFM}} = \frac{\overline{\rho}_{\text{liq}} \overline{\dot{V}}_{\text{liq,DFM}}}{60000} \quad (5.6a)$$

where $\overline{\dot{V}}_{\text{liq,DFM}}$, $\overline{\rho}_{\text{liq}}$ and $\overline{\dot{m}}_{\text{liq,DFM}}$ are in LPM, kg/m^3 , and kg/s units. The total mass flow rates that were measured during experiment using bucket-stop watch-weigh method could be expressed as follows.

$$\text{Total liquid mass flow rate through the system, } \overline{\dot{m}}_{\text{liq,bucket}} = \frac{\overline{\Delta m}}{\overline{\Delta t}} \quad (5.6b)$$

5.2.2 Air side measured parameters

Air side temperature measurements

The inlet and exit temperatures of the air flow were measured using two thermal grids attached with the wind tunnel at the test section inlet ($A-A'$) and exit ($B-B'$) as shown in Figures 4.7a and 4.8 in section 4.3 above and in Figure B5 in Appendix B below. By following Equation 4.4 in section 4.3.2, the consolidated mean of the inlet and exit temperatures of the air flow $\overline{T_{a,i}}$ and $\overline{T_{a,o}}$ were determined as follows.

Air inlet:

$$\overline{T_{100}} \dots \overline{T_{108}} = \frac{1}{k} \sum_{k=1}^k \left(\frac{1}{j} \sum_{i=1}^j (\text{any of } T_{100} \dots T_{108})_i \right), \text{ where } k = 3 \sim 5 \text{ repetitions,} \quad (5.7a)$$

From there the mean temperature of air for the entire inlet cross-section was deduced as,

$$\overline{T_{a,i}} = \frac{1}{n} \sum (\overline{T_{100}} + \dots + \overline{T_{108}}), \text{ where } n = 9 \text{ thermocouples.} \quad (5.7b)$$

Air exit:

$$\overline{T_{109}} \dots \overline{T_{201}} = \frac{1}{k} \sum_{k=1}^k \left(\frac{1}{j} \sum_{i=1}^j (\text{any of } T_{109} \dots T_{201})_i \right), \text{ where } k = 3 \sim 5 \text{ repetitions,} \quad (5.8a)$$

From there the mean temperature of air for the entire exit cross-section was deduced as,

$$\overline{T_{a,o}} = \frac{1}{n} \sum (\overline{T_{109}} + \dots + \overline{T_{201}}), \quad \text{where } n = 25 \text{ thermocouples,} \quad (5.8b)$$

For the Equations 5.7 and 5.8 above, the j is the time averaged means of 3000 to 6000 samples at steady state condition.

Since each of the experiments was conducted to cool the hot liquid flow inside MCHX by the flow of cold air, the exit temperature of air flow was always higher. The temperature differentials of air flow were deduced as follows.

$$\text{Air side temperature differential, } \Delta T_a = (\overline{T_{a,o}} - \overline{T_{a,i}}) \quad (5.9)$$

Air side velocity measurements

As mentioned in section 4.3, the air velocity was measured at the centre of the test section inlet at A-A' (Figure 4.7a). The combination of Pitot static probe (Figure 4.16) and differential pressure transducer (PTDD) (Figure 4.19) with DAQ as well as separately by using the FKT duct calibrator (Figure 4.17). The PTDD gives measurement outputs from 0 – 5 VDC to the DAQ. The calibration data and curves for all the PTDDs, based on NIST instrumentation and procedures, were supplied by the manufacturer.

Nevertheless, as mentioned above, prior to the experimental runs the calibrations were compared with directly measured air velocity using the duct calibrator and a handheld hot-wire anemometer and found good agreements. During each experiment, as backup the velocity was also measured directly using FKT calibrator and hot-wire anemometer.

The voltage signals for the air velocity were fairly linear with the differential pressure unit of the PTDD in inch of water column. However the DAQ voltage was not linear with the velocity directly measured by the FKT calibrator in m/s since the differential pressure is a function of velocity squared and density. Therefore the DAQ voltage was converted into velocity unit in m/s according to obtained and produced calibration as defined by Equation 4.11 repeated below.

$$\text{Calibration equation: } V_{a,i} = 6.387 * (\text{VDC})^{0.504} \text{ [m/s]; with an } R^2 = 0.9997. \quad (4.11)$$

By following Equation 4.4 in section 4.3.2, the consolidated mean air flow velocity $\overline{V}_{a,i}$ was first determined in voltage unit and then converted into m/s according to Equation 4.11. Since this measurement was taken at the center location of the inlet plane, to account for the entire cross-sectional plane the converted value was further corrected with the multiplication factor of 0.87. This multiplication factor was obtained through Pitot traverse survey on test section inlet cross-sectional plane using *Log-Tchebycheff* point distribution method [211], which is described in section 4.3.1 above.

Air side pressure measurements

For evaluating thermophysical properties of air using EES built-in library, the pressure and temperature both were required. The absolute pressure of airflow in the test section was measured using FKT duct calibrator's absolute pressure sensor as described in section 4.5.4 in Figures 4.16c and 4.17. The humidity of airflow at test section inlet and exit were also monitored to observe the operating conditions. The airflow pressure drops across MCHX test specimens were measured at the middle of the test section at the pressure port pair of P2-P2'' (Figure 4.7a). The voltage signal transformation process of the PTDD used here are similar to the PTDD used with Pitot static tube probe. Since the current study dealt with internal working fluid the flow rate of the external fluid, i.e. the air, was kept constant that gave a single data point for pressure drop.

5.2.3 Test specimen side surface temperature measurements

The outside surface temperatures of the MCHX test specimens were measured for heat transfer tests. Calibrated Type-T thermocouple probes were used and the tip of each thermocouple was gently but firmly fixed on the surface of the test specimen using Omega supplied highly conductive special surface adhesive for thermocouple probe attachment. Because of using this material, there was no surface left around each thermocouple that could cause a barrier to heat transfer. Total 48 thermocouples were

used to measure the surface temperature with their identifying names from T202 ... T231 and T300... T317. For each of the test specimens the surface temperature locations were different and every time a test specimen was removed and changed from the test section, all the thermocouple probes were removed, checked, and re-calibrated for further installation. Any damaged thermocouple was replaced with a calibrated new one.

By following Equation 4.4 in section 4.3.2, the consolidated mean surface temperature $\overline{T_s}$ was determined as follows.

$$\overline{T_{202 \dots T_{317}}} = \frac{1}{k} \sum_{k=1}^k \left(\frac{1}{j} \sum_{i=1}^j (\text{any of } T_{202} \dots T_{317})_i \right), \text{ where } k = 3 \sim 5 \text{ repetitions,} \quad (5.10a)$$

and

$$\overline{T_{s,o}} = \frac{1}{n} \sum (\overline{T_{202}} + \dots + \overline{T_{317}}), \text{ where } n = 48 \text{ thermocouples,} \quad (5.10b)$$

By running the system the surface temperatures were measured for MCHX #1 just to observe the nature of variation and profile of surface temperatures. The measurement locations are displayed in Figure 5.2 and other details are provided in Appendix –B8. Different scenarios were analyzed such as hot and cold liquid flow with no air flow, hot and cold air flow with no liquid flow, hot liquid and cold air flow, cold liquid and hot air flow, and no liquid or air flow at room temperature. The surface temperature profile with

no liquid or air flow was very flat and each of the thermocouples read and measured almost the same temperature within a maximum variation of $\pm 0.05^\circ\text{C}$. All other profiles have different but consistent nature, which are shown in Figure B17 in Appendix – B8.

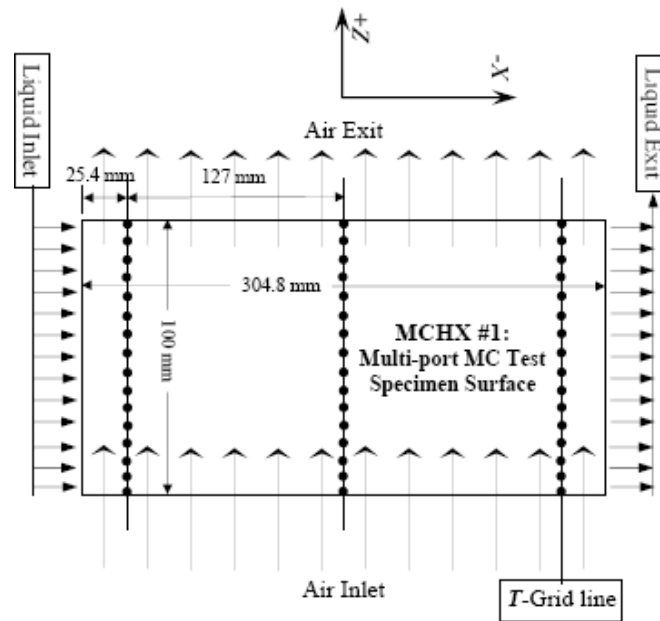


Figure 5.2 Schematic of test specimen surface thermocouple locations – MCHX #1.

The locations of thermocouples for other test specimens are described in their respective chapter, i.e. chapters 7 and 8 and in Appendix – B8.

5.3 Heat transfer rates and heat balance of the working fluids

The respective fluid side forced convection heat transfer rates are described in section 4.8 above and defined by Equations 4.13a and 4.13b. In this section the heat rate equation for liquid flow is generalized and rewritten as follows.

Liquid side heat transfer rate through heat rate equation,

$$q_{\text{liq}} = \dot{m}_{\text{liq}} c_{p,\text{liq}} (T_{\text{liq},i} - T_{\text{liq},o}) = \dot{m}_{\text{liq}} c_{p,\text{liq}} \Delta T_{\text{liq}} = C_{\text{liq}} \Delta T_{\text{liq}}; \quad (5.11)$$

where q , \dot{m} , c_p and T are the heat transfer rate, mass flow rate, specific heat and temperature of liquid respectively.

The heat transfer rates can also be determined from Newton's law of cooling if other parameters are known, such as the heat transfer coefficients of each side of the fluid or their respective thermal resistances and the surface temperature of the flow passage.

Liquid side heat transfer rate determined from Newton's law of cooling,

$$q_{\text{liq}} = h_{\text{liq}} A_{\text{liq}} (T_{b,\text{liq}} - T_s), \quad (5.12a)$$

and

Airside heat transfer rate determined from Newton's law of cooling,

$$q_a = h_a A_a (T_{b,a} - T_{f,a}), \quad (5.12b)$$

where h and A are the respective fluid side heat transfer coefficients and the heat transfer surface areas. The $T_{f,a}$ is the film temperature at airside, which is defined as the average temperature of wall surface and the approach airflow as given below.

$$T_{f,a} = \frac{(T_{a,i} + T_{s,o})}{2}, \quad (5.12c)$$

The heat balance on MCHX #1 is described in details in section 4.8 in light of ASME PTC [216], which was followed to perform the heat balances on other test specimens investigated in current study. The heat balance is given by Equation 5.13.

Heat balance with respect to liquid side heat transfer rate,

$$HB_{liq} = \left(\frac{q_{liq} - q_a}{q_{liq}} \right) * 100 \quad (5.13a)$$

and

Heat balance with respect to effective or mean heat transfer rate,

$$HB_{eff} = \left(\frac{q_{liq} - q_a}{q_{eff}} \right) * 100, \quad (5.13b)$$

where the q_a is defined by Equation 4.13b and the effective or mean heat transfer rate q_{eff} is defined as the arithmetic average of liquid side and airside heat transfer rates as expressed by Equation 5.13c below.

$$q_{\text{eff}} = \frac{(q_{\text{liq}} + q_a)}{2} \quad (5.13c)$$

5.4 Heat transfer performance parameters

The heat transfer performance of any heat exchange device is associated to some key parameters such as the overall heat transfer coefficient, thermal resistance, number of transfer units (NTU), effectiveness, fin efficiency, individual fluid side heat transfer coefficients, etc., which are described and deduced in this section.

5.4.1 Overall heat transfer coefficient (U)

Traditionally for a two-fluid crossflow heat exchanger the overall heat transfer coefficient in forced convection is determined in light of Newton's law of cooling as given by Equation 5.14, provided the mean heat transfer rate and the inlet and exit temperatures of the working fluids are known, which is the case in current study.

$$q_{\text{eff}} = (UA)(\Delta T_{\text{LMTD}})(F) \quad (5.14)$$

where the q_{eff} , A , ΔT_{LMTD} , and F are respectively the effective or mean heat transfer rate, heat transfer surface area, log-mean temperature difference, and log-mean temperature difference correction factor for crossflow orientation.

Because of using ultra precise RTD for liquid side temperature measurements, for more reliably the liquid side heat transfer rate q_{liq} was used in current study as the overall heat transfer rate in place of q_{eff} . The heat transfer surface area A can be either internal fluid side or the external fluid side depending on how the equation is presented or which area is readily available without any complexity. In present study the internal surface area could be easily calculated rather than external although both the areas were calculated.

The log-mean temperature difference (LMTD) used in Equation 5.14 was defined by Equation 5.15 as follows [219]:

$$\Delta T_{\text{LMTD}} = \frac{\Delta T_1 - \Delta T_2}{\ln\left(\frac{\Delta T_1}{\Delta T_2}\right)}, \quad \text{where} \begin{cases} \Delta T_1 = T_{\text{hot, in}} - T_{\text{cold, out}} = T_{\text{liq, i}} - T_{\text{a, o}} \\ \Delta T_2 = T_{\text{hot, out}} - T_{\text{cold, in}} = T_{\text{liq, o}} - T_{\text{a, i}} \end{cases} \quad (5.15)$$

The crossflow correction factor F is defined as the ratio of the true mean temperature difference to the log-mean temperature difference, i.e. $F = \Delta T_{\text{m}}/\Delta T_{\text{LMTD}}$. While the ΔT_{LMTD} is the same for all flow arrangements except for the parallel flow, the ΔT_{m} values are different for various flow configurations. This dimensionless F is a function of the effectiveness of temperature loadings P , capacity ratio R , and the flow arrangement. The definitions of P and R are widely available in many textbooks on heat

transfer. The F is unity for a true counter flow arrangement and for all other arrangements it is determined from some empirical relationship or graphical charts [5, 11].

Most of the reference books on heat transfer and heat exchangers present the values of F by equations or charts only for some common flow-pass configurations [5, 11, 52-53]. Current study used some unique flow-pass configurations for which the F value is not readily available in any available sources. Haglund Stignor [203] and Haglund Stignoret et al. [214] mentioned that the heat exchangers with eight or more flow-passes behave like a counter flow heat exchanger where F can be set to unity. In light of this recommendation and by consulting the Bowman et al. [219] work, the crossflow correction factor F for current study could be set to unity. The F however was determined for the respective P and R temperature loadings and found to vary between 0.994 and 0.998, which are close to unity.

The product of the overall heat transfer coefficient U and the heat transfer surface area A was calculated using Equation 5.16 as follows.

$$UA = \frac{q_{\text{eff}}}{F \Delta T_{\text{LMTD}}} \approx \frac{q_{\text{liq}}}{F \Delta T_{\text{LMTD}}}. \quad (5.16)$$

From Equation 5.16 the U can be easily determined based on the heat transfer surface area on a particular side of the heat exchanger if it is known.

5.4.2 Thermal resistances (R_{th})

Thermal resistance in heat transfer is the barrier that resists the heat transfer, which is deduced by following the electrical analogy. In forced convection heat transfer, the Equation 5.14 above can be expressed in the following form.

$$q_{\text{eff}} \approx q_{\text{liq}} = \frac{F \Delta T_{\text{LMTD}}}{1/UA} = \frac{F \Delta T_{\text{LMTD}}}{R_{\text{ov}}} \quad (5.17)$$

where $R_{\text{ov}} = 1/(UA)$ is defined as the overall thermal resistance from the bulk liquid flow inside MCHX through the free stream air flow in the test chamber. This overall resistance includes all the individual resistances in the heat flow path, which for current study are defined by Equation 5.18 below.

$$R_{\text{ov}} = \sum R_{\text{th}} = R_{\text{th,liq}} + R_{\text{th,wall}} + R_{\text{th,a}} = \frac{1}{UA} \approx \frac{F \Delta T_{\text{LMTD}}}{q_{\text{liq}}} \quad (5.18)$$

where $R_{\text{th,liq}}$, $R_{\text{th,wall}}$, and $R_{\text{th,a}}$ are the individual thermal resistances at liquid side, for test specimen wall, and at air side respectively.

The liquid side and airside thermal resistances are deduced from Equations (5.12a) and (5.12b) as follows.

$$R_{th,liq} = \frac{1}{h_{liq}A_{liq}} = \frac{(T_{b,liq} - T_s)}{q_{liq}} = \frac{\Delta T_{b,s}}{q_{liq}}, \quad (5.19)$$

and

$$R_{th,a} = \frac{1}{h_a A_a} = \frac{T_{b,a} - T_{f,a}}{q_a}, \quad (5.20)$$

In current study, except for the MCHX1 the other test specimens have identical fins at airside but no internal fins at liquid side. Therefore to account for this fin effect, the Equation 5.18 was re-written by introducing the airside overall surface or fin efficiency as follows.

$$R_{ov} = \frac{1}{UA} = R_{th,liq} + R_{th,wall} + R_{th,a} = \frac{1}{h_{liq}A_{liq}} + R_{th,wall} + \frac{1}{\eta_o h_a A_a}. \quad (5.21)$$

There are some straight methods available in the heat transfer textbooks to deduce the $R_{th,wall}$ for single circular or non-circular walls. The flow passage configuration in current study is such that these available equations cannot be directly applied, although choosing the circular tube (cylindrical) relation can be a reasonable approximation. The thickness of the test specimen wall is very small and the thermal conductivity of the wall material is relatively high. Therefore for simplicity in the subsequent analyses the wall

thermal resistance in Equation 5.21 could be ignored and set to $R_{th,wall} \approx 0$ without much error, which can be seen in next in section 5.5 and in chapters 6 and 7 below.

5.4.3 Airside overall surface or fin efficiency (η_o)

There have been several studies on heat exchanger fin geometry [51]. To characterize an array of fins at airside, the overall surface efficiency or the temperature effectiveness or the overall airside fin efficiency η_o was first expressed as follows [5].

$$\eta_o = 1 - \frac{A_{fin}}{A_{tot}}(1 - \eta_{fin}), . \quad (5.22)$$

The details of the airside fin geometry for current test specimens are given in not-to-scale Figure 5.3 below. Although current test specimens have very low wavy fins in the direction of airflow, the flat fin geometry is drawn in Figure 5.3 for simplicity. The fin efficiency η_{fin} in Equation 5.22 for both flat and wavy fins is described by Shah and Sekulic [5]. For uniform fin cross-section, as is the case in current test specimens, the fin efficiency η_{fin} can be calculated for both flat and low wavy fin geometries using Equation 5.23 below [5]. Therefore Equation 5.22 was adopted in current study to deduce the fin efficiencies η_{fin} for the test samples. The fin efficiencies in current study varied between 0.90 and 0.92 for η_{fin} and between 0.92 and 0.93 for η_o .

$$\eta_{\text{fin}} = \frac{\tanh(ML)}{ML}, \quad \text{where} \quad \begin{cases} M \approx \sqrt{\frac{2h_a}{k_{\text{fin}}t_f}} \\ L = \frac{H_f}{2} - t_f \end{cases} \quad (5.23)$$

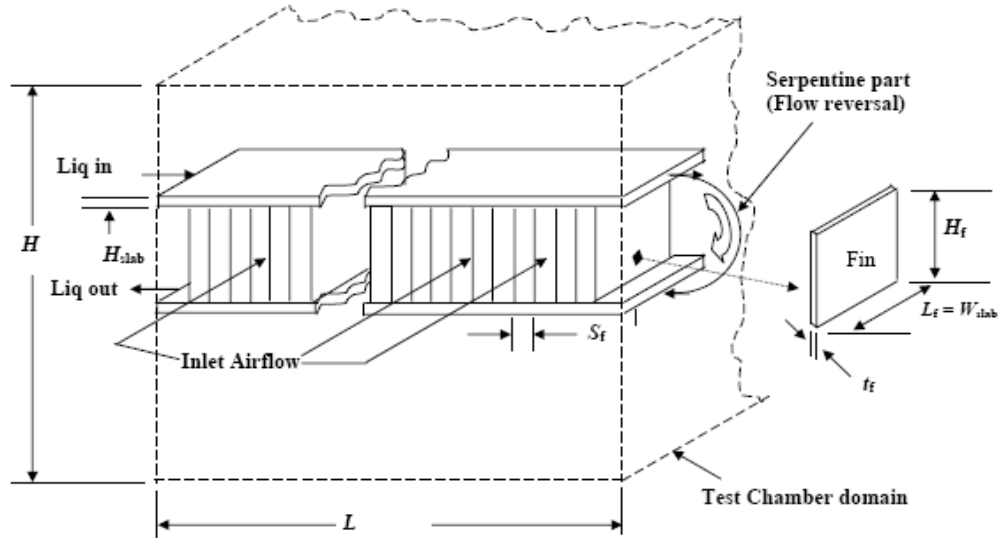


Figure 5.3 Airside fin geometry for test specimens MCHX #4 & MCHX #6 in current study.

5.4.4 Effectiveness and NTU

The heat exchanger effectiveness of the test specimens were realized from the following relation.

$$\text{Effectiveness, } \varepsilon = \frac{q_{\text{liq}}}{q_{\text{max}}}, \quad (5.24)$$

where the q_{liq} was determined from Equation 5.11a and q_{max} was defined as follows.

$$q_{\text{max}} = C_{\text{min}} (T_{\text{liq},i} - T_{\text{a},i}) = C_{\text{min}} \Delta T_i, \quad (5.25)$$

The C in Equation 5.25 is the heat capacity ratio, which is the product of mass flow rate and the specific heat of respective fluid and the C_{min} is defined below.

$$C_{\text{min}} = \min \begin{cases} C_{\text{liq}} = \dot{m}_{\text{liq}} c_{p,\text{liq}} \\ C_{\text{a}} = \dot{m}_{\text{a}} c_{p,\text{a}} \end{cases} \quad (5.26)$$

The number of transfer unit (NTU) is usually proportional to the heat transfer surface area A . Traditionally the larger the NTU the larger the heat exchanger. However, in a MCHX the value of NTU may indicate how large is the heat transfer surface area as compared to the total size or in other words how small a MCHX can be for a given heat load. The NTU were determined from the following relationship.

$$NTU = \frac{UA}{C_{\text{min}}} = \frac{1}{R_{\text{ov}} C_{\text{min}}}; \quad (\because R_{\text{ov}} = \frac{1}{UA} \text{ see Equation 5.18 and 5.21}). \quad (5.27)$$

5.5 Employment of Wilson Plot technique to isolate the individual thermal resistances

The information on surface temperature T_s is necessary to calculate the individual fluid side heat transfer coefficient from the measured heat rate. Measuring T_s for a finned surface, like the one used in this study, is very difficult. In this event the Wilson Plot Technique plays a great role to isolate the individual fluid side thermal resistances without the information of surface temperature T_s . This method was originally devised by Wilson in 1915 for separating the individual thermal resistances from a two-fluid single-phase flow heat exchanger without the information of surface temperature [220]. By assuming a tube side Re exponent of 0.82, the two unknowns i.e. the shell side resistance and the tube side Re coefficient were determined from a regression analysis.

Over the decades, few modifications and improvements have been proposed by different authors to apply this method on a variety of heat exchangers situations in the presence of more than two unknowns. In other words, in the situations when the Re coefficients and exponents are unknown for both the fluids. For determining three unknowns rather than only two, Briggs and Young (1969) proposed a modification to the original Wilson plot technique through two-step successive linear regression analyses of a non-linear equation, which is so called the “modified Wilson Plot Technique” [221].

In the literature survey it is seen that the study using Wilson Plot Technique is limited although it is a useful tool in deducing heat transfer coefficient in the absence

surface temperature information. Some available works on the review, applicability comparisons, and modifications of this technique are consulted [222-223]. Briggs and Young proposed some modification to the original technique to widen its applicability [221]. Khartabil and Christensen [222] compared their experimental data using the Briggs and Young modified version of the technique and noticed some convergence problem. In this event Khartabil and Christensen [224] proposed and presented an improved non-linear regression scheme, which according to them guarantees the convergence if a solution exists. To the best of candidate's knowledge from literature review, the Khartabil and Christensen work [224] is so far the latest improvement on Wilson Plot technique in finding the heat transfer coefficient. Therefore this improved scheme was adopted in employing the Wilson Plot technique in current study.

Application of the Wilson plot technique is not very straight-forward job for any general experimental situations. In order to employ the Wilson Plot Technique, some minimum restrictions in conducting the experiments apply as follows [222-223].

1. All the data sets must be taken within a single flow regime,
2. The flow rates of the fluid of interest must be varied and the flow rate of the other fluid must be kept constant for the entire data taking process, and
3. The bulk temperature of the constant flow fluid should be kept constant to allow the thermal resistances of that fluid and wall to remain unchanged.

In current study the liquid side was the main focus and therefore the experiments were accordingly carried out by maintaining the airside conditions fairly constant. Attempts were made to measure the T_s on the surface of the MCHX #4 and MCHX #6 immediate before and after the test section and around the serpentine bends using 48 thermocouples placed on un-finned exposed surfaces (chapters 6 and 7 and Figure B17 in Appendix – B8). As mentioned before and as shown in Figure 5.1 above, these un-finned exposed surfaces were well insulated and located outside of the effective heat transfer zone in the test section. The effective heat transfer zone is marked in Figures B9a and B11a in Appendix – B2. Although difficult, the T_s measurements were performed to compare the results obtained from the Wilson Plot Technique with that of the results calculated using Equation 5.12. As explained before, constant wall temperature boundary condition (T -condition) was assumed to be closer to the current experimental situations.

The liquid side and the airside thermal resistances, $R_{th,liq} = \frac{1}{h_{liq}A_{liq}}$ and $R_{th,a} = \frac{1}{\eta_o h_a A_a}$, in Equation 5.21 and hence the individual fluid side heat transfer coefficients, h_{liq} and h_a , were separated using modified Wilson Plot Technique as described next. The measured mean T_s for each data set was used to separately calculate the liquid side and the airside heat transfer coefficients, h_{liq} and h_a , using Newton's law of cooling defined in Equation 5.12 in the following forms.

$$h_{\text{liq}} = \frac{q_{\text{liq}}}{A_{\text{liq}}(T_{\text{liq}} - T_s)}, \quad (5.28)$$

and

$$h_a = \frac{q_{\text{liq}}}{\eta_o A_{a,\text{tot}}(T_s - T_a)}, \quad (5.29)$$

The estimation of liquid side Nusselt number Nu_{liq} from the deduced heat transfer rate q_{liq} and measured surface temperature T_s was based on Equation 2.11 as follows.

$$\text{Nu}_{\text{liq}} = \frac{h_{\text{liq}} D_{\text{ch}}}{k_{\text{liq}}} = \frac{h_{\text{liq}} D_{\text{port}}}{k_{\text{liq}}} = \frac{h_{\text{liq}} D}{k_{\text{liq}}}, \quad (5.30)$$

The operating conditions for current heat transfer experiments were in the developing laminar flow regime. In a developing laminar pipe flow the Nusselt number generally depends on Reynolds number and Prandtl number. Therefore, by following the simplified form given in Equation 2.12c, the liquid side Nusselt number was defined as follows to employ the Wilson Plot Technique in current experimental data.

$$\text{Nu}_{\text{liq}} = C_1 \text{Re}_{\text{liq}}^a \text{Pr}_{\text{liq}}^{1/3}, \quad (5.31)$$

By combining the above Equations 5.30 and 5.31, the liquid side heat transfer coefficient was given in the following form.

$$h_{\text{liq}} = \left(\text{Nu} \frac{k}{D_{\text{ch}}} \right)_{\text{liq}} = C_1 \text{Re}_{\text{liq}}^a \text{Pr}_{\text{liq}}^{1/3} \frac{k_{\text{liq}}}{D_{\text{ch}}}, \quad (5.32)$$

Khartabil & Christensen Improved Modified Wilson Plot Technique [224]:

By rearrangement of Equations 5.21 and 5.32, the overall thermal resistance in the heat flow path, $R_{\text{ov}} = 1/UA$ could be given by the following expression.

$$\begin{aligned} R_{\text{ov}} &= \frac{1}{UA} = \frac{1}{h_{\text{liq}} A_{\text{liq}}} + R_{\text{th,wall}} + \frac{1}{\eta_o h_a A_a}, \quad \text{or} \\ \frac{1}{UA} &= \frac{1}{C_1 \text{Re}_{\text{liq}}^a \left(\underbrace{\text{Pr}_{\text{liq}}^{1/3} \frac{k_{\text{liq}}}{D_{\text{ch}}} A_{\text{liq}}}_W \right)} + \underbrace{\left(R_{\text{th,wall}} (\approx 0) + \frac{1}{\eta_o h_a A_a} \right)}_{C_2} \quad \text{or} \\ \frac{1}{UA} &= \frac{1}{C_1 \text{Re}_{\text{liq}}^a W} + C_2 \end{aligned} \quad (5.33)$$

where W is constant since all the values within the parenthesis are known for a given operating point. The C_2 is also constant since the experiments were conducted by keeping the airside flow and temperature constants.

If the restrictions mentioned above are properly followed in employing Wilson plot technique, the constant airflow will essentially lead to the un-altered thermal resistances at both airside and at test specimen wall for all varied flow rates at liquid side. For simplicity, since the test specimen wall is very thin and relatively highly conductive, the term $R_{th,wall}$ can be dropped from Equations 5.21 and 5.33 without countable error.

Now the Equation 5.33 is re-written in a linear form as given below, which is the main equation that needs to be solved by regression analysis in Wilson Plot Technique.

$$Y = mX + C; \quad \text{where} \quad \left\{ \begin{array}{l} \text{Variable, } Y = R_{ov} = \frac{1}{UA} \\ \text{Slope, } m = \frac{1}{C_1} \\ \text{Variable, } X = \frac{1}{Re_{liq}^a W} \\ \text{Constant, } C = C_2 \end{array} \right. \quad (5.34)$$

Application of least-square method to Equation 5.34 requires the minimization of the following quantity if not zero.

$$S = \sum_{i=1}^N (Y_i - mX_i - C)^2 \quad (5.35)$$

Normal equations can be produced from Equation 5.35 by taking partial derivatives and by solving the normal equations one can form the set of equations for the slope m and constant C in terms of the two other variables X and Y as follows.

$$m = \frac{N \sum_{i=1}^N X_i Y_i - \sum_{i=1}^N X_i \sum_{i=1}^N Y_i}{N \sum_{i=1}^N X_i^2 - \left(\sum_{i=1}^N X_i \right)^2}, \quad (5.36)$$

and

$$C = \frac{\sum_{i=1}^N X_i^2 \sum_{i=1}^N Y_i - \sum_{i=1}^N X_i \sum_{i=1}^N X_i Y_i}{N \sum_{i=1}^N X_i^2 - \left(\sum_{i=1}^N X_i \right)^2}, \quad (5.37)$$

Taking partial derivatives with respect to Re exponent a in Equation 5.35, the minimization quantity requires that the function $f(a)$ to be zero or at least the minimum.

$$f(a) = \left[\sum_{i=1}^N X_i Y_i \ln((\text{Re}_{\text{liq}})_i) \right] - \left[m \sum_{i=1}^N X_i^2 \ln((\text{Re}_{\text{liq}})_i) + C \sum_{i=1}^N X_i \ln((\text{Re}_{\text{liq}})_i) \right], \quad (5.38)$$

For the solution of the above equations, a parametric table is always helpful as given in Table 5.1 below. Because of the presence of the unknowns in the equations, to produce results from Wilson Plot Technique, some computer iteration steps need to be performed as per following steps. Manual iteration of such problem is nearly impossible.

Table 5.1. Parametric table for variables that are used to employ Wilson plot technique

Tests	Re_{liq}	W	$X = \frac{1}{Re^a W}$	$Y = R_{ov} = \frac{1}{UA}$	$m = \frac{1}{C_1}$	C	$\ln(Re_{liq})$	$f(a)$
1	Measure experimentally	Deduce from known and measured parameters	Deduce by assuming an initial value of “ a ” with small increment	Deduce from experimental data	For N data points, find from iteration using Eqn. (5.36)	For N data points, find from iteration using Eqn. (5.37)	Deduce from experimental data	Deduce from Eqn. (5.38) and Check for zero or the minimum
2	Measure	Deduce	Deduce	Deduce			Deduce	
3	Measure	Deduce	Deduce	Deduce			Deduce	
4	Measure	Deduce	Deduce	Deduce			Deduce	
5	Measure	Deduce	Deduce	Deduce			Deduce	
NOTE: Do it for several values of ‘ a ’. If $f(a)$ in Eqn. (5.38) is not the minimum, repeat the process.								

Computer scheme for iteration:

- [1] Start with a low guess value of Re exponent “ a ” and find X values for all the data points and find the m and C using Equations (5.36) and (5.37).
- [2] Check the function $f(a)$ in Equation (5.38) for the requirement $f(a) \approx 0$, which could rarely be achieved. However, preferably a convergence criterion can be set as follows.

$$\left| \frac{f(a + \delta_{n-1}) - f(a + \delta_n)}{f(a + \delta_{n-1})} \right| \leq 10^{-6}, \tag{5.39}$$

- [3] When the process in **step-2** is stopped or **converged**, write an output file for the new values of a , m , and C for further processing in another sub-routine.
- [4] If the process in **step-2** is **not converged**, keep continuing the loop within **step-1** and **step-2** until a solution is obtained.

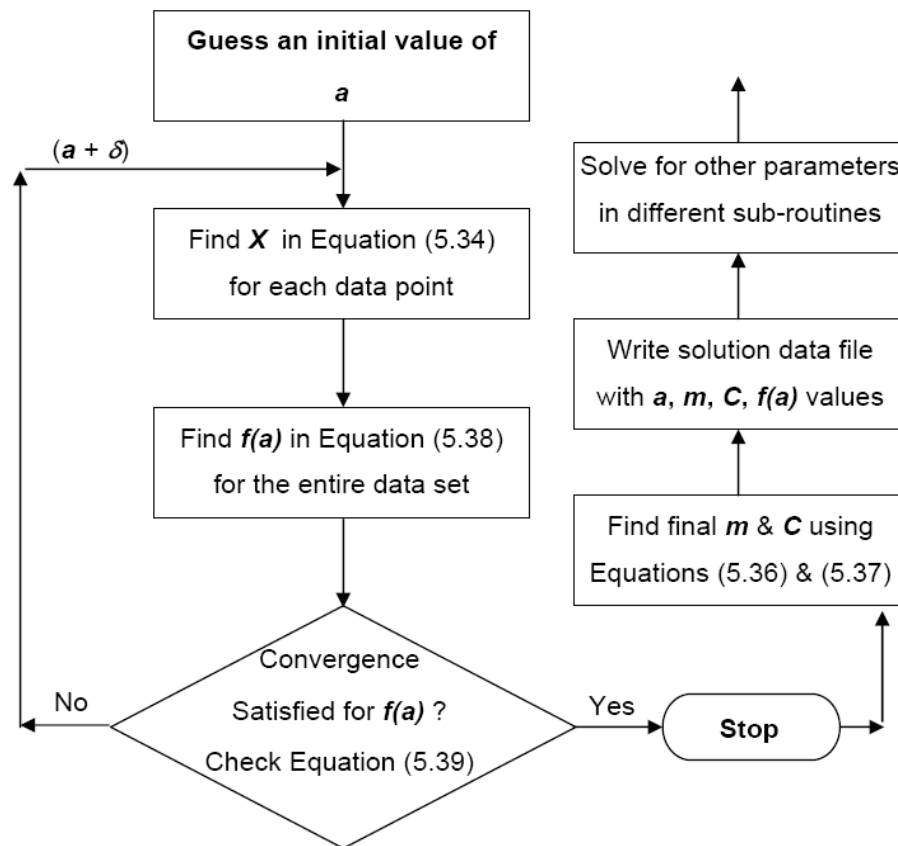


Figure 5.3. Solution and iteration flow chart for Wilson Plot Technique described above.

To perform the iteration process and to solve for the unknowns in experimental data using the Wilson Plot technique, the detail computer solution algorithm was written in and solved by MATLAB.

Upon finding the appropriate exponent “ a ” for the Re and the value of C_1 , the Nusselt number correlation in Equation (5.31) were consolidated in different sub-routine in EES and in Excel spreadsheet. The values of the individual and overall thermal resistances were determined by using Equations (5.33) and (5.34), which also give the way to deduce the heat transfer coefficient of the liquid side as well as airside.

Briggs & Young Modified Wilson Plot Technique [221]:

They made two-step successive linear regression analyses of a non-linear equation (5.40) to solve for the Re exponent and slope of the Wilson Plot curve as follows.

$$(hA)_{liq} = \left(Nu \frac{kA}{D_{ch}} \right)_{liq} = \left(C_0 Re^p Pr^n \frac{kA}{D_{ch}} \right)_{liq} \Rightarrow \left(\frac{1}{hA} \right)_{liq} = \underbrace{\left(\frac{1}{C_0 Pr^n \frac{kA}{D_{ch}}} \right)}_Z \frac{1}{Re^p} = \left(Z \frac{1}{Re^p} \right)_{liq} \quad (5.40)$$

From Equation (5.33) the 1st linear equation was derived to solve as follows.

$$R_{ov} = \underbrace{Z}_{m_1} \underbrace{\left(\frac{1}{Re_{liq}^p} \right)}_{X_1} + \underbrace{\left(\frac{1}{\eta_o h_a A_a} \right)}_{C_1} \Rightarrow Y_1 = m_1 X_1 + C_1 \quad (5.41)$$

The 2nd linear equation was produced from Equation (5.41) and solved as follows.

$$R_{ov} - C_1 = Z \frac{1}{Re_{liq}^p} \Rightarrow \frac{1}{R_{ov} - C_1} = \frac{1}{Z} Re_{liq}^p$$

$$\underbrace{\ln\left(\frac{1}{R_{ov} - C_1}\right)}_{Y_2} = \underbrace{\ln\left(\frac{1}{Z}\right)}_{C_2} + \underbrace{p}_{m_2} \underbrace{\ln(Re_{liq})}_{X_2} \Rightarrow Y_2 = m_2 X_2 + C_2 \quad (5.42)$$

The solution procedure (Y_1 is calculated beforehand from experimental data).

- (1) Guess a small value of Re exponent “p” in Eqn. (3) and calculate “ X_1 ”
- (2) Iteratively solve Eqn. (3) to find m_1 & C_1 using entire data set
- (3) Calculate X_2 & Y_2 using m_1 & C_1 found in step ‘2’
- (4) Iteratively solve Eqn. (4) to find m_2 & C_2 using the same data set
- (5) Continue steps 1 to 4 if $(m_2 - p_{guess}) \neq 0$ or $|m_2 - p_{guess}| / p_{guess} \geq 0.0001$
- (6) Stop if $(m_2 - p_{guess}) \approx 0$ or set criteria $|m_2 - p_{guess}| / p_{guess} \leq 0.0001$
- (7) Write final values of m_2 (i.e. p_{final}), m_1 , C_2 , C_1 for further analysis in other sub-routine
- (8) Determine h_{liq} , Nu_{liq} , and $R_{th,liq}$ and the Nu-Re correlation

According to Khartabil & Christensen [224], there are some data sets that may not be converged using Briggs & Young [221] two successive linear regression analyses of a non-linear equation. Therefore they improved the solution using non-linear regression.

5.6 Uncertainty analysis and error estimation

The accuracy information of the instruments and sensors is based on manufacturer's data and the accompanying documentation, which were listed in Table 4.2. The accuracies in Table 4.2 are the overall instrument error that were accounted from the root sum square (RSS) of all known sources of errors such as the resolution, linearity, repeatability, sensitivity, hysteresis, scale effect (FSO), zero offset, precision, various drifts, reproducibility etc. according to the Equation given below.

$$I_{\text{RSS}} = \sqrt{I_1^2 + I_2^2 + \dots + I_N^2} \quad (5.43)$$

where I is the instruments' known error(s) from various sources e.g. 1, 2,N and the I_{RSS} is the overall instrument error.

The experimental uncertainty analysis was carried out in light of the ASME Journal of Heat Transfer Editorial (1993) and ASME Journal of Fluids Engineering Editorial (1991) [225-226]. Other available resources were also consulted [227-230]. Errors from the on the measured primary parameters propagate into the secondary variables depending on their relationships. If A is a secondary parameter, which depends on other primary measured parameters like A_1, A_2, A_3, \dots then the errors from measured primary parameters propagate into the secondary parameter A according to the

relationship between A and A_1, A_2, A_3, \dots . The absolute uncertainty U of A was then calculated using root sum square (RSS) method as given by Equation (5.44).

$$U_A = \sqrt{\left(\frac{\partial A}{\partial A_1} U_{A_1}\right)^2 + \left(\frac{\partial A}{\partial A_2} U_{A_2}\right)^2 + \dots} \quad (5.44)$$

The partial derivatives $\frac{\partial A}{\partial A_1}, \frac{\partial A}{\partial A_2}, \frac{\partial A}{\partial A_3}, \dots$ of the secondary or dependent parameters are derived from their relationship with the primary or independent parameters.

The individual uncertainties of the independent parameters $U_{A_1}, U_{A_2}, U_{A_3}, \dots$ are estimated from the bias and precision errors of both the experiments and the instruments (I_{RSS} from Equation 5.43). The relative uncertainty is generally obtained dividing the absolute uncertainty by the mean value as shown in Equation (5.45) below.

$$\frac{U_A}{A} = \sqrt{\frac{\left(\frac{\partial A}{\partial A_1} U_{A_1}\right)^2 + \left(\frac{\partial A}{\partial A_2} U_{A_2}\right)^2 + \dots}{[f(A_1, A_2, \dots)]^2}} \quad (5.45)$$

The detailed uncertainty analyses procedure and a sample calculation for some selected key parameters are provided in Appendix – E.

5.7 Calculations and data analyses tools

The time averaged raw data from experimental runs were recorded and stored in DAQ system where they were one step filtered and processed using NI LABVIEW software. The data were then summarized to obtain time averaged mean data sets (TAMDS) and parametric data tables were developed using Microsoft Excel spread sheet. In engineering equation solver (EES), based on the relationships and equations defined in data reduction section, different equation codes and calculation procedures were written for data analysis, calculations, and data plotting. Most of the TAMDS were analyzed using EES and few were directly analyzed using Microsoft Excel spreadsheet.

CHAPTER – 6

PRESSURE DROP AND FLOW FRICTION OF WATER AND 50% ETHYLENE GLYCOL-WATER MIXTURE FLOWS IN MULTI-PORT STRAIGHT MICROCHANNEL SLABS

6.0 PRESSURE DROP AND FLOW FRICTION OF WATER AND 50% ETHYLENE GLYCOL-WATER MIXTURE FLOWS IN MULTI-PORT STRAIGHT MICROCHANNEL SLABS

As seen in earlier review works discussed above in section 3.1 (Figures 1.3, 3.1, and 3.2), there have been a lot of controversy and differences in reported results on pressure drop and hence the friction factor as well as on the early or delay occurrence of critical Re in narrow channel flow. The deviations are more in laminar flow than in turbulent flow. Moreover, study of pressure drop in developing laminar flow in narrow channel is limited. To the best of candidate's knowledge, the work on developing laminar flow in microchannels using 50% ethylene glycol-water mixture as the working fluid is not available in the open literature. This commercially important heat transfer fluid has a lot of use and significance in industries like automotive, heating-cooling, HVAC, and similar other thermal applications.

The understanding of flow frictional characteristics in narrow channels and building experimental database are important. This is required to verify the validity of macroscale theories in microchannel flow as well as to optimize the design and application tradeoffs between the pressure drop expense and the heat transfer duty.

Therefore the pressure drop and friction behavior of water and 50%-50% ethylene glycol-water mixture flow in 1-pass multi-port straight microchannel test slabs have been

experimentally investigated. Current research results on glycol-water mixture flow in the test slab have been peer-reviewed and documented [231]. The experimental results for both water and glycol-water mixture flows in two test slabs are presented in this chapter.

The test specimen MCHX-1 was used for water flow and MCHX-2 for 50% glycol-water mixture flow. The internal configurations and geometries for liquid flow for the test specimens MCHX-1 and MCHX-2 are the same. The schematics and geometrical specifications of these two test specimens are provided in Figures 4.3, 4.4a, and 4.4b and in Table 4.1 in section 4.1 above.

6.1 Treatment and separation of pressure losses in the test slab

The internal configurations of two employed test specimens are the same. The temperature and pressure sensors and the measurement locations for both the test specimens during both fluid operations were the same. Therefore the treatments and considerations of pressure losses in their cores and the separation of the losses from that of the measured total pressure drop are also similar and common for both fluids, which are described below via Figure 6.1 and Equations 6.1 through 6.16.

The test specimens employed in current study can be viewed as typical thermal heat exchanger cores. While the pressure drop estimation for large diameter pipe is somewhat straight forward, it is however very involved and tedious in heat exchanger core made with narrow flow channels. As summarized in the literature review, improper

considerations or underestimation of various losses may lead to very differing result. In this study attempts have therefore been made to account for all possible area of various losses in the flow route. From the total measured pressure drop Δp_{total} the isolation of core loss, i.e. the pressure drop of a port in the test slab (5) Δp_{mc} , are performed according to Equation 6.1 [5, 18, 175, 198]. The subscripts associated with Figure 6.1 and Equation 6.1 for nine pressure drop segments (1) to (9) are defined in the nomenclature.

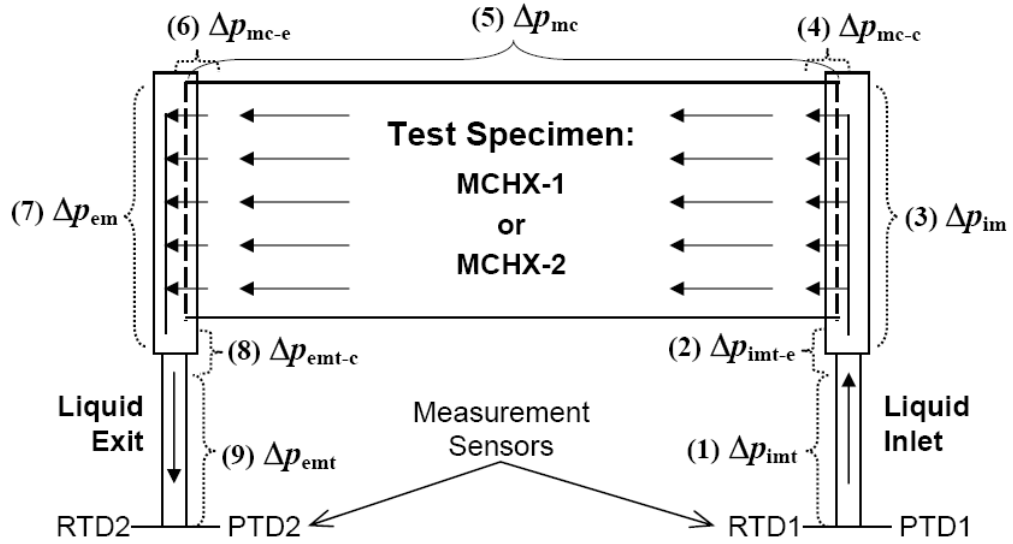


Figure 6.1. Segment-wise pressure losses from inlet to exit flow route of MCHX-1 or MCHX-2.

$$\begin{aligned} \Delta p_{total} &= p_i - p_o \\ &= \underbrace{\Delta p_{imt}}_{(1)} + \underbrace{\Delta p_{imt-e}}_{(2)} + \underbrace{\Delta p_{im}}_{(3)} + \underbrace{\Delta p_{mc-c}}_{(4)} + \underbrace{\Delta p_{mc}}_{(5)} + \underbrace{\Delta p_{mc-e}}_{(6)} + \underbrace{\Delta p_{em}}_{(7)} + \underbrace{\Delta p_{empt-c}}_{(8)} + \underbrace{\Delta p_{empt}}_{(9)} \end{aligned} \quad (6.1)$$

It is noted here that the temperature at which the fluid properties are evaluated in Equation 6.1 were considered at the inlet for (1) to (4), at the bulk for (5) Δp_{mc} and at the

exit for (6) to (9). The bulk flow pressure, as given by Equation 5.5, was taken to evaluate the fluid properties for all losses since the variation of fluid properties were mainly temperature dependent and very weakly on pressure.

During all the experiments the total mass flow rates through the system were measured according to the expressions given by Equations 5.6a and 5.6b. The total mass flow rate is the quantity that flows through (1) to (3) and through (7) to (9) in Figure 6.1 and Equation 6.1. The flow passages in these segments have hydraulic diameters larger than 4.7 mm; therefore the traditional friction factor correlations were employed to deduce the pressure drops in these segments. By considering new and smooth circular pipes, depending on Reynolds number (Re) values, the flow friction factors (f) in all the manifold tubes and manifolds are estimated from $f = 64/Re$ for laminar flow and from Blasius relation given in Equation 2.20 for turbulent flow.

Each of the 1-pass multi-port test specimens has 68 internal channels or ports. The hydraulic diameter of the inlet manifold was approximately 10 times larger than the diameter of a channel in the test slab. Assumption was made that the liquid is incompressible and the total liquid mass flow rate is equally distributed through all the channels. The assumption was reasonable as described next in chapter 7. Therefore the mass flow rates in a single channel in the test slab \dot{m}_{ch} were calculated as follows.

$$\dot{m}_{ch} = \frac{\dot{m}_{liq,DFM}}{68} = \frac{\rho_{liq} \dot{V}_{liq,DFM}}{4.08 * 10^6}, \quad (6.2a)$$

or

$$\dot{m}_{ch} = \frac{\overline{\dot{m}_{liq,bucket}}}{68} = \frac{\overline{\Delta m}}{68 * \Delta t}, \quad (6.2b)$$

where $\dot{V}_{liq,DFM}$ is the total liquid volume flow rate through the system measured in LPM at the inlet flow meter (DFM) and Δm is the weight of fetched liquid over a time of Δt .

The mass velocity or the mass flux (G) is often used in heat exchanger engineering in order to eliminate or minimize the effect of variation of fluid density on the result if the Δp is presented against G rather than either \dot{m} or Re. Also, different heat exchanger frontal areas can be taken into comparable account if the Δp is plotted with respect to G rather than \dot{m} [5]. The mass velocity (G) is defined in terms of flow velocity, mass flow rate and flow cross-sectional area, in generalized form as follows.

$$G = \rho V = \frac{\dot{m}}{A_c}, \quad \text{where } A_c \text{ is the flow cross-sectional area.} \quad (6.3)$$

The definitions and treatment of pressure losses in each of the nine segments, from (1) to (9) in Figure 6.1 and in Equation 6.1, are presented below.

(1) The losses in the inlet manifold tube, Δp_{imt}

The working fluid flows into the heat exchanger core through the pipe or tube connected to the flow dividing inlet manifold. The major and minor pressure losses associated with this tube are the factors for flow or wall friction (f) over the straight flow length and geometric or fitting loss (K_F), as estimated from following derived expression.

$$\begin{aligned}\Delta p_{\text{imt}} &= \left[\frac{\rho_i V_{\text{liq}}^2}{2} \left(f \frac{L}{d} + \Sigma K_F \right) \right]_{\text{imt}}, \quad \text{in terms of velocity head} \\ &= \frac{8 \dot{m}_{\text{liq}}^2}{\pi^2 \rho_i d_{\text{imt}}^4} \left[f \frac{L}{d} + \Sigma K_F \right]_{\text{imt}}, \quad \text{in terms of mass flow rate, and} \quad (6.4) \\ &= \frac{G_{\text{liq}}^2}{2 \rho_i} \left[f \frac{L}{d} + \Sigma K_F \right]_{\text{imt}}, \quad \text{in terms of mass velocity.}\end{aligned}$$

where \dot{m}_{liq} is the total mass flow rate through the system; and L , d , V_{liq} and K_F are length, internal diameter, liquid velocity and fitting loss factor in the inlet manifold tube.

(2) Pressure drop or rise due to area increase at the inlet manifold tube exit, $\Delta p_{\text{imt-e}}$

The fluid experiences sudden expansion at the exit of the inlet manifold tube, i.e. at the entrance of the manifold. This is attributed to the changes in flow cross-sectional area from smaller diameter inlet manifold tube to the larger diameter inlet manifold. The

pressure drop due to expansion can be presented in terms of velocity head, mass flow rate, and mass velocity with an expansion coefficient of K_e as given in Equation 6.5a.

$$\Delta p_{\text{imt-e}} = \left[K_e \frac{\rho V_{\text{liq}}^2}{2} \right]_{\text{imt-e}} = \frac{8 \dot{m}_{\text{liq}}^2}{\pi^2 \rho d_{\text{imt}}^4} [K_e]_{\text{imt-e}} = \frac{G_{\text{liq}}^2}{2\rho} [K_e]_{\text{imt-e}} \quad (6.5a)$$

By applying the momentum and Bernoulli equations across the expansion section the *Borda-Carnot equation* can be derived as follows [5] to give the value of K_e [18, 59].

$$K_e = (1 - \sigma)^2 = \left[1 - \frac{A_{\text{smaller}}}{A_{\text{larger}}} \right]^2, \quad (6.5b)$$

The σ in Equation 6.5b is the smaller-to-larger area ratio at the cross-sectional plane where the flow area changes. The Equation 6.5b is valid for $\text{Re} = \infty$ and the obtained value of K_e is usually used for sudden expansion in a single pipe. The K_e in Equation 6.5a is usually obtained from Equation 6.5b, which is not a function of Re . The values can also be derived from other graphical charts representing the K_e from one extreme for sharp-edged exit where $\sigma \approx 0$ (flow area changes from very small to very large area) with $K_e = 1$ to the other extreme where $\sigma = 1$ (no area change) with $K_e = 0$ [59]. The fluid property, i.e. the density in Equation 6.5a has to be evaluated at the bulk temperature and pressure. The pressure drop calculation based on Equations 6.5a and 6.5b is a liberal estimate for general pipe flow.

A heat exchanger and its pumping device should not be oversized or undersized for a given flow and heat duty. For the interest of such design, the pressure drop calculation needs to be performed in more conservative and involved manners so that all possible effects are taken into consideration. At sudden expansion, the fluid experiences two phenomena. One is the pressure gain due to the deceleration caused by area increase and the other is the pressure loss associated with the irreversible free expansion and momentum rate changes following a sudden expansion. These two effects are lumped together to account for the total rise or drop of pressure at the expansion, which is presented in the following form as given in Equation 6.6 [5].

$$\begin{aligned}
 \Delta p_{\text{imt-e}} &= \underbrace{\frac{G_{\text{liq}}^2}{2\rho_i} [K_e]}_{\Delta p_{\text{loss}}} - \underbrace{\frac{G_{\text{liq}}^2}{2\rho_i} [1 - \sigma^2]}_{\Delta p_{\text{gain}}} \\
 &= \frac{G_{\text{liq}}^2}{2\rho_i} [K_e - 1 + \sigma^2]_{\text{imt-e}}, \quad \text{in terms of mass velocity} \\
 &= \frac{8\dot{m}_{\text{liq}}^2}{\pi^2 \rho_i d_{\text{imt}}^4} [K_e - 1 + \sigma^2]_{\text{imt-e}}, \quad \text{in terms of mass flow rate, and} \\
 &= \frac{\rho_i V_{\text{liq}}^2}{2} [K_e - 1 + \sigma^2]_{\text{imt-e}}, \quad \text{in terms of velocity head.}
 \end{aligned} \tag{6.6}$$

where the loss coefficient K_e is a function of the area ratio σ , Re , and flow cross-sectional geometry. For use in Equation 6.6, Kays and London [51] presented the values for K_e with respect to σ , Re , and flow passage geometry in graphical form, which can also be obtained from few other sources [5, 11, 18].

(3) The losses in the inlet manifold, Δp_{im}

Before entering the MCHX ports, the working fluid inside the flow dividing inlet manifold experiences major and minor losses. The major loss is attributed to the flow or wall friction (f) over the straight flow length. The minor loss is due to the geometric configuration of the manifold, which is taken into account via a manifold loss coefficient (K_{mf}). This loss is estimated from the expression given in Equation 6.7 below.

$$\begin{aligned}\Delta p_{im} &= \left[\frac{\rho_l V_{liq}^2}{2} \left(f \frac{L}{d_h} + K_{mf} \right) \right]_{im}, & \text{in terms of velocity head} \\ &= \frac{8\dot{m}_{liq}^2}{\pi^2 \rho_l (d_h^4)_{im}} \left[f \frac{L}{d_h} + K_{mf} \right]_{im}, & \text{in terms of mass flow rate and} \\ &= \frac{G_{liq}^2}{2\rho_l} \left[f \frac{L}{d_h} + K_{mf} \right]_{im}, & \text{in terms of mass velocity.}\end{aligned} \quad (6.7)$$

where \dot{m}_{liq} is the total mass flow rate through the system; and L , d_h , V_{liq} and K_{mf} are the straight flow length, hydraulic diameter, liquid velocity and manifold loss coefficient of the inlet manifold. The end of the MCHX test slab are slightly extended inside the manifold as can be seen in Figure 4.2, which makes the geometric configuration of current manifold quite unique.

(4) Losses at the inlet of the MCHX slab port, Δp_{mc-c}

The fluid experiences sudden contraction at the entrance of the MCHX port as it flows from the large diameter inlet manifold to the small diameter microchannel port. The entrance geometry of the multi-port MCHX test slab can be viewed in Figure 4.2. The pressure drop due to contraction can be expressed in terms of velocity head, mass flow rate, and mass velocity with a contraction coefficient of K_c as follows.

$$\begin{aligned}\Delta p_{mc-c} &= \left[K_c \frac{\rho V_{ch}^2}{2} \right]_{mc-c}, && \text{in terms of velocity head} \\ &= \frac{8\dot{m}_{ch}^2}{\pi^2 \rho D_{ch}^4} [K_c]_{mc-c}, && \text{in terms of mass flow rate} \\ &= \frac{G_{ch}^2}{2\rho} [K_c]_{mc-c}, && \text{in terms of mass velocity.}\end{aligned}\tag{6.8a}$$

To obtain the value of K_c the experimentally derived ratio of *vena contracta* area to the pipe area is necessary. As quoted by Shah and Sekulic [5], the Crane Co. in 1976 presented a technical paper on K_c vs. σ relationship for a single pipe as follows.

$$K_c = 0.5(1 - \sigma) = 0.5 \left[1 - \frac{A_{\text{smaller}}}{A_{\text{larger}}} \right],\tag{6.8b}$$

The Equation 6.8b is valid for $Re = \infty$ and the obtained value of K_c is usually used for sudden contraction in a single pipe. The K_c in Equation 6.8a is usually obtained from Equation 6.8b, which is not a function of Re . The values can also be derived from other graphical charts representing the K_c from one extreme for the sharp-edged entrance where $\sigma \approx 0$ (flow area changes from very large to very small) with $K_c = 0.5$ to the other extreme where $\sigma = 1$ (no area change) with $K_c = 0$ [59]. The fluid property, i.e. the density in Equation 6.8a has to be evaluated at the bulk temperature and pressure. The calculation of contraction pressure drop based on Equations 6.8a and 6.8b is a liberal estimate for general pipe flow problem.

As mentioned before, for the interest of compact or narrow heat exchanger design, the pressure drop calculation needs more rigorous considerations to account for all the possible effects. At sudden contraction, the fluid flow encounters two phenomena. One is the pressure loss due to area change and the other is associated with the irreversible free expansion that follows the sudden contraction. The flow separation and secondary flows are created at the region of *vena contracta* and cause the pressure loss [5]. The change in momentum rate due to any non-uniformity in flow also produces pressure loss. The resulting pressure is caused by the change in momentum rate at the downstream of the *vena contracta*. All these effects are taken into account through a combined expansion, which is presented by Equation 6.9 below.

$$\begin{aligned}
 \Delta p_{\text{mc-c}} &= \underbrace{\frac{G_{\text{ch}}^2}{2\rho_i} [1 - \sigma^2]}_{\Delta p_{\text{loss, due to change in flow area}}} + \underbrace{\frac{G_{\text{ch}}^2}{2\rho_i} [K_c]}_{\Delta p_{\text{loss, due to change in momentum rate after the vena contracta}} \\
 &= \frac{G_{\text{ch}}^2}{2\rho_i} [K_c + 1 - \sigma^2]_{\text{mc-c}}, \quad \text{in terms of mass velocity} \\
 &= \frac{8\dot{m}_{\text{ch}}^2}{\pi^2 \rho_i D_{\text{ch}}^4} [K_c + 1 - \sigma^2]_{\text{mc-c}}, \quad \text{in terms of mass flow rate and} \\
 &= \frac{\rho_i V_{\text{ch}}^2}{2} [K_c + 1 - \sigma^2]_{\text{mc-c}}, \quad \text{in terms of velocity head.}
 \end{aligned} \tag{6.9}$$

where the contraction loss coefficient K_c is a function of the area ratio σ , Re , and flow cross-sectional geometry. The K_c includes the effects of expansion and the rate of change in momentum immediate downstream of the *vena contracta*. For use in Equation 6.9, Kays and London [51] presented the values for K_c with respect to σ , Re , and flow passage geometry in graphical form, which can also be obtained from few other sources [5, 11, 18].

(5) The pressure losses in the multi-port MCHX test slab channel, Δp_{mc}

The core pressure drop Δp_{mc} in a single channel in the MCHX test slab consists of the pressure required to accelerate the fluid through the channel (Δp_a), pressure loss due to the wall or flow friction (f) along the straight flow length of the channel (Δp_f), and the pressure fault or pressure defect resulting from the flow development effect at the

entrance region of the channel ($\Delta p_{mc,dev} = \Delta p_{\infty}$). The core pressure drop Δp_{mc} associated with current test condition can be expressed by Equation 6.10 below [5, 18].

$$\Delta p_{mc} = [\Delta p_a + \Delta p_f + \Delta p_{\infty}]_{mc} = \frac{G_{ch}^2}{2\rho_i} \left[\underbrace{2 \left(\frac{\rho_i}{\rho_o} - 1 \right)}_{\Delta p_a} + \underbrace{\frac{\rho_i}{2} \left(\frac{1}{\rho_i} + \frac{1}{\rho_o} \right) \left(f_{ch} \frac{L}{D_{ch}} \right)}_{\Delta p_f} + \underbrace{K_{\infty}}_{\Delta p_{\infty}} \right]_{mc}, \quad (6.10)$$

where ρ_i and ρ_o are the fluid densities evaluated at the inlet and exit temperatures respectively.

The contribution of the acceleration loss Δp_a in current experiment is very small as compared to other loss components. For simplicity, this part can thus be dropped from Equation 6.10. The flow developing pressure loss term Δp_{∞} can also be discarded from Equation 6.10 if the flow is already fully developed before entering the MCHX ports. The status of the flow in current study is discussed in sections 6.1 and 6.2 for respective working fluids. The above Equation 6.10 could therefore be simplified as follows.

$$\begin{aligned} \Delta p_{mc} &= \frac{G_{ch}^2}{2\rho_i} \left[\frac{\rho_i}{2} \left(\frac{1}{\rho_i} + \frac{1}{\rho_o} \right) \left(f_{ch} \frac{L}{D_{ch}} \right) + K_{\infty} \right]_{mc} && \text{in terms of mass velocity,} \\ &= \frac{8\dot{m}_{ch}^2}{\pi^2 \rho_i D_{ch}^4} \left[\frac{\rho_i}{2} \left(\frac{1}{\rho_i} + \frac{1}{\rho_o} \right) \left(f_{ch} \frac{L}{D_{ch}} \right) + K_{\infty} \right]_{mc} && \text{in terms of mass flow rate, and} \quad (6.11) \\ &= \frac{\rho_i V_{ch}^2}{2} \left[\frac{\rho_i}{2} \left(\frac{1}{\rho_i} + \frac{1}{\rho_o} \right) \left(f_{ch} \frac{L}{D_{ch}} \right) + K_{\infty} \right]_{mc} && \text{in terms of velocity head.} \end{aligned}$$

The flow development loss coefficient K_∞ for narrow channel flows is not available. Therefore in this absence as suggested by some researchers [18, 67], the value could be estimated from Chen [66] proposed K_∞ vs. Re relationship for large size tube as given in Equation 2.17a above.

(6) Losses at the exit of the MCHX slab port, Δp_{mc-e}

The fluid flow experiences sudden expansion again at the exit of the MCHX slab port during entering the exit manifold i.e. the flow combining manifold. This is attributed to the changes in flow cross-sectional area from smaller channel diameter of MCHX slab to the larger diameter exit manifold. The pressure drop calculation processes and the physical flow phenomenon for this expansion segment are the same as (2) Δp_{imt-e} and Equations 6.5 and 6.6 above. Only exceptions are that the parameters need to be employed for this segment, which are shown through Equations 6.12 and 6.13 below.

$$\Delta p_{mc-e} = \left[K_e \frac{\rho V_{ch}^2}{2} \right]_{mc-e} = \frac{8\dot{m}_{ch}^2}{\pi^2 \rho D_{ch}^4} [K_e]_{mc-e} = \frac{G_{ch}^2}{2\rho} [K_e]_{mc-e}, \quad (6.12)$$

where the K_e is deduced from Equation 6.5b by applying the area ratio σ for this segment. The fluid property, i.e. the density in Equation 6.12 has to be evaluated at the bulk

temperature and pressure. Again the pressure drop calculation based on Equations 6.12 and 6.5b is a liberal estimate for the interest of general pipe flow problem.

Detail considerations for the interest of heat exchanger are presented through Equation 6.13 below [5].

$$\begin{aligned}\Delta p_{\text{mc-e}} &= \frac{G_{\text{liq}}^2}{2\rho_o} [K_e - 1 + \sigma^2]_{\text{mc-e}}, && \text{in terms of mass velocity} \\ &= \frac{8\dot{m}_{\text{ch}}^2}{\pi^2 \rho_o D_{\text{ch}}^4} [K_e - 1 + \sigma^2]_{\text{mc-e}}, && \text{in terms of mass flow rate, and} \\ &= \frac{\rho_o V_{\text{ch}}^2}{2} [K_e - 1 + \sigma^2]_{\text{mc-e}}, && \text{in terms of velocity head.}\end{aligned}\quad (6.13)$$

where the Re and σ dependent expansion loss coefficient K_e can be obtained from the original graphical presentation by Kays and London [51] or from the other available sources [5, 11, 18].

(7) The losses in the exit manifold, Δp_{em}

The exit end of the MCHX test slab are slightly extended inside the exit manifold as can be seen in Figure 4.2. This makes the geometric configuration of current manifold quite unique, as mentioned before. The pressure loss calculation in the exit manifold is same as the inlet manifold described above for (3) Δp_{em} . Therefore this loss can be

estimated using the same Equation 6.7 above with fluid property, i.e. the density evaluated at exit temperature.

(8) Pressure drop due to area decrease at the exit manifold tube entrance, $\Delta p_{\text{emt-c}}$

The fluid flow experiences sudden contraction again at the end of the exit manifold during entering the exit manifold tube. This is attributed to the changes in flow cross-sectional area from larger manifold diameter to the smaller diameter exit manifold tube. The pressure drop calculation processes and the physical flow phenomenon for this contraction segment are the same as (4) $\Delta p_{\text{mc-c}}$. Only exceptions are that the parameters need to be employed for this segment, which are shown in Equations 6.14 and 6.15.

$$\begin{aligned}\Delta p_{\text{emt-c}} &= \left[K_c \frac{\rho V_{\text{liq}}^2}{2} \right]_{\text{emt-c}}, & \text{in terms of velocity head} \\ &= \frac{8\dot{m}_{\text{liq}}^2}{\pi^2 \rho d_{\text{emt}}^4} [K_c]_{\text{emt-c}}, & \text{in terms of mass flow rate, and,} \\ &= \frac{G_{\text{liq}}^2}{2\rho} [K_c]_{\text{emt-c}}, & \text{in terms of mass velocity.}\end{aligned}\tag{6.14}$$

where the K_c is deduced from Equation 6.8b by applying the area ratio σ for this segment. The fluid property, i.e. the density in Equation 6.14 has to be evaluated at the bulk temperature and pressure. Again the pressure drop calculation based on Equations 6.14 and 6.8b is a liberal estimate for the interest of general pipe flow problem.

For the interest of typical heat exchanger design, the detail considerations for contraction losses at this segment are presented via Equation 6.15 below [5].

$$\begin{aligned}
 \Delta p_{\text{emt-c}} &= \frac{G_{\text{liq}}^2}{2\rho_0} [K_c + 1 - \sigma^2]_{\text{emt-c}}, && \text{in terms of mass velocity} \\
 &= \frac{8\dot{m}_{\text{liq}}^2}{\pi^2 \rho_0 d_{\text{emt}}^4} [K_c + 1 - \sigma^2]_{\text{emt-c}}, && \text{in terms of mass flow rate, and} \\
 &= \frac{\rho_0 V_{\text{liq}}^2}{2} [K_c + 1 - \sigma^2]_{\text{emt-c}}, && \text{in terms of velocity head.}
 \end{aligned} \tag{6.15}$$

where the Re and σ dependent contraction loss coefficient K_c can be obtained from the original graphical presentation by Kays and London [51] or from the other available sources [5, 11, 18].

(9) The losses in the exit manifold tube, Δp_{emt}

The working fluid flows out of the heat exchanger core through the exit manifold pipe or tube connected to the flow combining exit manifold. The major and minor losses associated with this tube are the same as the inlet manifold tube (1) Δp_{imt} . Only exceptions are that the parameters such as L , d , and K_F have to be employed for this segment of the tube and the fluid property, i.e. the density be evaluated at the exit

temperature. Therefore Equation 6.4 is modified to take these changes into account, which is presented by the Equation 6.16 below.

$$\begin{aligned}\Delta p_{\text{emt}} &= \left[\frac{\rho_o V_{\text{liq}}^2}{2} \left(f \frac{L}{d} + \Sigma K_F \right) \right]_{\text{emt}}, \quad \text{in terms of velocity head} \\ &= \frac{8 \dot{m}_{\text{liq}}^2}{\pi^2 \rho_o d_{\text{emt}}^4} \left[f \frac{L}{d} + \Sigma K_F \right]_{\text{emt}}, \quad \text{in terms of mass flow rate, and} \\ &= \frac{G_{\text{liq}}^2}{2 \rho_o} \left[f \frac{L}{d} + \Sigma K_F \right]_{\text{emt}}, \quad \text{in terms of mass velocity.}\end{aligned} \quad (6.16)$$

Now, by plugging the Equations 6.4 through 6.16 into Equation 6.1, the pressure drop in a straight channel in the multi-port MCHX test slabs could be isolated from the experimentally measured total pressure drop.

6.2 Experimental procedures for water and glycol-water flows

The descriptions of the experimental setup and the test specimen are provided in chapter 4 via Figures 4.1 through 4.4a and 4.4b. With the help of a gear pump (Figure 4.9) the liquid from the supply tank was passed through the test specimens. The inline circulation heater (Figure 4.10) was used to prepare the hot liquid as required. To obtain a number of pressure drop data of the fluids in multi-port test slab, the flow rate was varied by operating the gear pump and by adjusting the needle valve NV

(Figure 4.1a). The flow rate was measured both using calibrated FV4000 series digital flow meters (shown in Figure 4.11) and manually by fetch-weigh method with a digital balance. The differences in measurements between the flow meters and the manual method were observed well within $\pm 1\%$ for water flow and $\pm 2.5\%$ for 50% ethylene glycol-water mixture flow.

At each flow rate step, sufficient time was allowed to achieve a fairly steady state condition before starting any data collection. The steady-state was assumed to reach when the fluctuations in liquid flow rate and mean inlet flow temperature were no more than 3% at any location in the flow system. The inlet temperatures of the liquids were kept constant at certain value for all flow rates to achieve various Reynolds numbers, Re in the test slab channel in the range from laminar to turbulent regime.

The liquid flow temperatures and pressures were measured at the inlet and exit of the test slab using two pairs of temperature and pressure sensors, RTD1 & PTD1 and RTD2 & PTD2 as shown in Figures 4.1a and 6.1. The PTD is shown in Figure 4.12a. The descriptions of the measuring sensors, functionality and their locations are given in section 4.4 and their capacity and accuracy data in Table 4.2. The instrumentation and calibration information of the measuring instruments are provided in section 4.5 and in Table 4.3. After adopting the calibrations, both RTD readings were checked by running the test rig at some given temperatures from 22.7 to 23.3°C and they were found to read and measure within a maximum difference of $\pm 0.037^\circ\text{C}$.

The fundamental key parameters i.e. the flow rate, inlet and exit temperatures and inlet and exit pressures data of the flowing fluids were measured and collected using a DAQ system. The information on DAQ system is provided in section 4.6 and in Figure 4.20. According to Equations 4.12 and 5.2, the time averaged mean data sets (TAMDS) for each of the key parameters were then acquired for analysis.

6.3 Data reduction for water and glycol-water mixture flows

As required, the thermophysical properties of water were evaluated at their inlet and exit temperatures as well as at their respective bulk flow temperatures and pressures; according to section 5.1, Equation 5.1a and section 5.2.1 Equation 5.5. The properties for water were evaluated from built-in library of EES [218] and for 50% ethylene glycol-water mixture the properties were extracted from ASHRAE Handbook of Fundamentals 2005 [212]. The deduction of the Re and fully developed Darcy friction factor (f) in a channel in the test slab are discussed below.

Using Equation 2.1 the liquid side Reynolds number in a single channel in the test slab, Re_{ch} , was calculated from Equation 4.15. The Re_{liq} for undivided flow in the segments (1) through (3) and (7) through (9) in Figure 6.1 was deduced as follows.

$$\begin{aligned} \text{Re}_{\text{liq}} &= \frac{4\dot{m}_{\text{liq}}}{\pi\mu d}, \quad \text{in terms of mass flow rate and} \\ &= \frac{G_{\text{liq}}d}{\mu}, \quad \text{in terms of mass velocity,} \end{aligned} \quad (6.17)$$

where \dot{m}_{liq} and G_{liq} are the total mass flow rate and total mass velocity through the system and d is the diameter of the respective segment. The \dot{m}_{liq} and G_{liq} were calculated from experimental data using Equations 5.6 and 6.3 respectively.

In order to obtain the friction factor (f) in a channel in the test slabs, the Equation 6.11 was rearranged as expressed by Equation 6.18 below. For current test situation, Equation 6.18 compares and represents the Darcy friction factor (f) for fully developed traditional pipe flow as given in Equation 2.6 above.

$$\begin{aligned} f_{\text{ch}} &= \frac{\rho_o}{\rho_b} \left(\frac{D}{L} \right)_{\text{ch}} \left[\frac{2\rho_i \Delta p_{\text{mc}}}{G_{\text{ch}}^2} - K_{\infty} \right], \quad \text{in terms of mass velocity,} \\ &= \frac{\rho_o}{\rho_b} \left(\frac{D}{L} \right)_{\text{ch}} \left[\frac{2\rho_i A_c^2 \Delta p_{\text{mc}}}{\dot{m}_{\text{ch}}^2} - K_{\infty} \right], \quad \text{in terms of mass flow rate, and} \\ &= \frac{\rho_o}{\rho_b} \left(\frac{D}{L} \right)_{\text{ch}} \left[\frac{2\Delta p_{\text{mc}}}{\rho_i V_{\text{ch}}^2} - K_{\infty} \right], \quad \text{in terms of velocity head.} \end{aligned} \quad (6.18)$$

where ρ_b is the fluid density at bulk temperature and A_c is the flow cross-sectional area of a channel in the test slab. In Equation 6.18, the Δp_{mc} was deducted from Equation 6.1 and the Hagenbach's factor, K_{∞} , was estimated from Equation 2.17a.

Another parameter that was compared with current experimental pressure drops data for both fluids is the theoretical pressure drops for traditional fully developed laminar pipe flow, which is the Poiseuille pressure drop and flow rate relationship given in Equation 2.13. In current test condition, these Equations were rearranged as follows.

$$\Delta p_{\text{theory, Po}} = \frac{128\mu\dot{m}_{\text{ch}}L_{\text{ch}}}{\rho\pi D_{\text{ch}}^4} = \frac{32\mu G_{\text{ch}}L_{\text{ch}}}{\rho D_{\text{ch}}^2}, \quad (\text{Poiseuille relation from Eqn. 2.13}), \quad (6.19)$$

where ρ is the fluid density at bulk temperature; and A_c and A_s are the internal flow cross-sectional area and heat transfer surface area of a channel in the test slab.

The loss coefficients ΣK_F in Equations 6.4 and 6.16 for fittings and tube bends were obtained from available sources [59-60]. As mentioned before, the inner geometry for both inlet and exit manifolds and their connectivity with the straight part of the test slab port are unique in current study whose loss coefficient is not readily available. In the absence of a loss coefficient K_{mf} in Equation 6.7, a value was chosen by consulting the work of Yin et al. [198] on pressure drop in microchannel heat exchanger.

There is no correlation available on hydrodynamic entrance lengths for microchannel flows. Therefore the hydrodynamic entrance lengths in current study were calculated using traditional hydrodynamic entrance length correlations for laminar and turbulent flows as described in section 2.2.1 through Equations 2.16 and 2.25.

6.4 Results and discussions on water flow

The DDI water flows inside the test specimen were investigated from laminar-to-turbulent regimes in the range $480 \leq Re \leq 3800$. The detail uncertainty analysis of all the parameters associated with current study was carried out according to the procedures described in Chapter 5 in Section 5.6. The estimated mean uncertainties of some key parameters are presented in Table 6.1 below.

Table 6.1. Mean experimental uncertainty in the study of water flow

Parameters	Mean uncertainty
Measured pressure drop, $\Delta p_{\text{total, w}}$ [Pa]	± 4.00 %
Measured total mass flow rate, \dot{m}_w , [kg/s]	± 1.5 %
Reynolds number in a channel in test slab, Re_{ch}	± 5.3 %
Friction factor in a channel in test slab, f_{ch}	± 10 %
Poiseuille number in a channel in test slab, $Po_{\text{ch}} = (fRe)_{\text{ch}}$	± 11 %

In order to determine whether the flow is fully developed or developing, the hydrodynamic entrance length in the test slab channel was calculated for each flow rate using Equations 2.16 and 2.25. The straight part of the test slab is 343 mm long. For the lowest flow rate at $Re = 480$, the hydrodynamic entrance length was found to be 27 mm occupying about 8% of the slab length. The flow then stayed fully developed for the rest 316 mm along the flow path until exiting from the test slab. At the flow rate in the

laminar regime boundary at $Re = 2300$, the flow was developing up to 129 mm along the flow path. For the highest flow rate at $Re = 3800$, the entrance length was 10 mm since the flow was in the turbulent regime.

It is now evident that none of the flows was hydrodynamically fully developed before entering the test channels. This is because the flow had to take a 90-degree turn in the inlet manifold to enter to the channels as can be seen in Figures 4.2 and 6.1. All the flows however exited from the channels to the exit manifold with fully developed status. Therefore K_{∞} in Equation 6.11 was considered and was obtained from Equation 2.17a.

6.4.1 Pressure drop in the test slab core, Δp_{mc}

As mentioned before, the channel side pressure drops were separated using Equations 6.11 through 6.16. The Re_{ch} was achieved between 482 and 2013 for relatively colder water flow at $23 \pm 1^{\circ}C$, which gave the pressure loss per unit length of the flow channel $\Delta p_{mc}/L_{mc}$ ranging from 30 to 146 kPa/m. For the water flow at $75.5 \pm 1^{\circ}C$, the Re_{ch} attained the values from 1310 to 3780 with relatively lower pressure gradients i.e. from 16 to 100 kPa/m. This is expected because the pressure drop in the channel is dictated by the viscosity of the flowing water, which for the same flow rate was lower for the hot water than the cold water. This lower viscosity accounts for a higher Re even at lower or same flow rate than cold water.

The measured Δp_{total} and calculated Δp_{mc} are plotted against Re_{ch} and G_{ch} in Figures 6.2a and 6.2b respectively with sample uncertainty error bars. For comparison the theoretical pressure drops calculated from Equations 6.19 are also plotted in these figures. As expected, the Δp in general increased with the increase of Re and G .

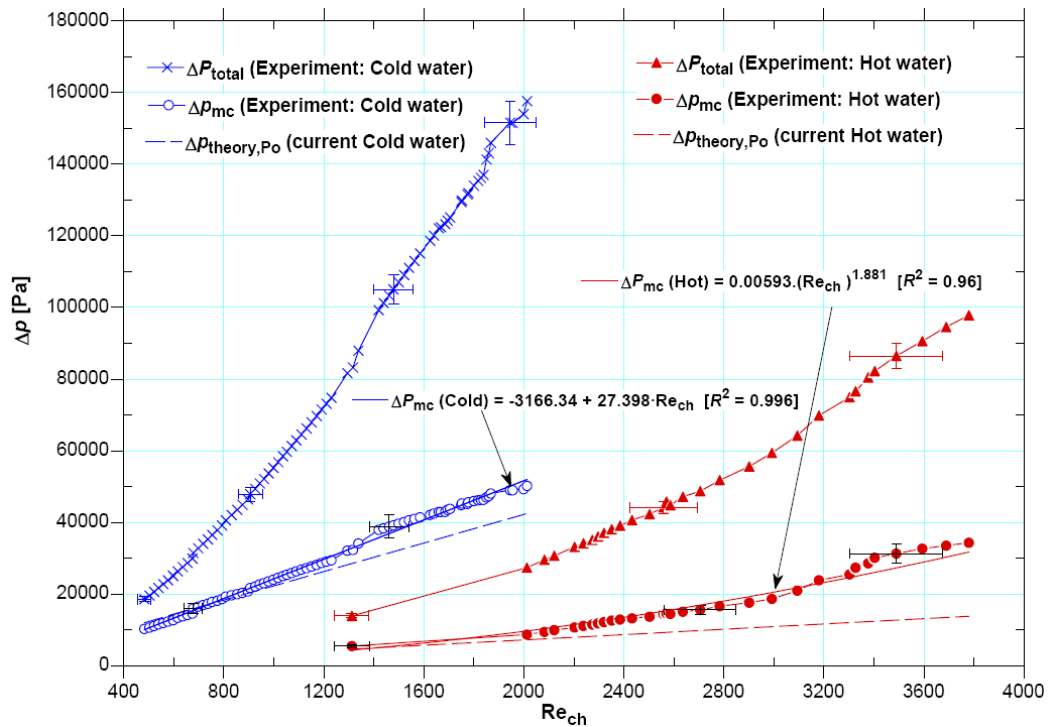


Figure 6.2a. Variation of Δp with respect to Re_{ch} for Water flow in MCHX-1.

The measured total pressure drops varied non-linearly with Re because of the presence of other losses. As seen in Figure 6.2a, there are some scatters in both for cold and hot flow data, which could be due to some flow and temperature fluctuations during experiments. The fluid property in the channel segment was evaluated at bulk mean temperature assuming a linear temperature variation between inlet and exit, which to

some extent might have supplemented to this variation. The horizontal variation along Re axis in Figure 6.2a is however due to the fluid property variation between cold and hot water that depended on operating conditions. Plotting of Δp against G helped collapsing the data scatter and reducing the horizontal variation significantly as seen in Figure 6.2b.

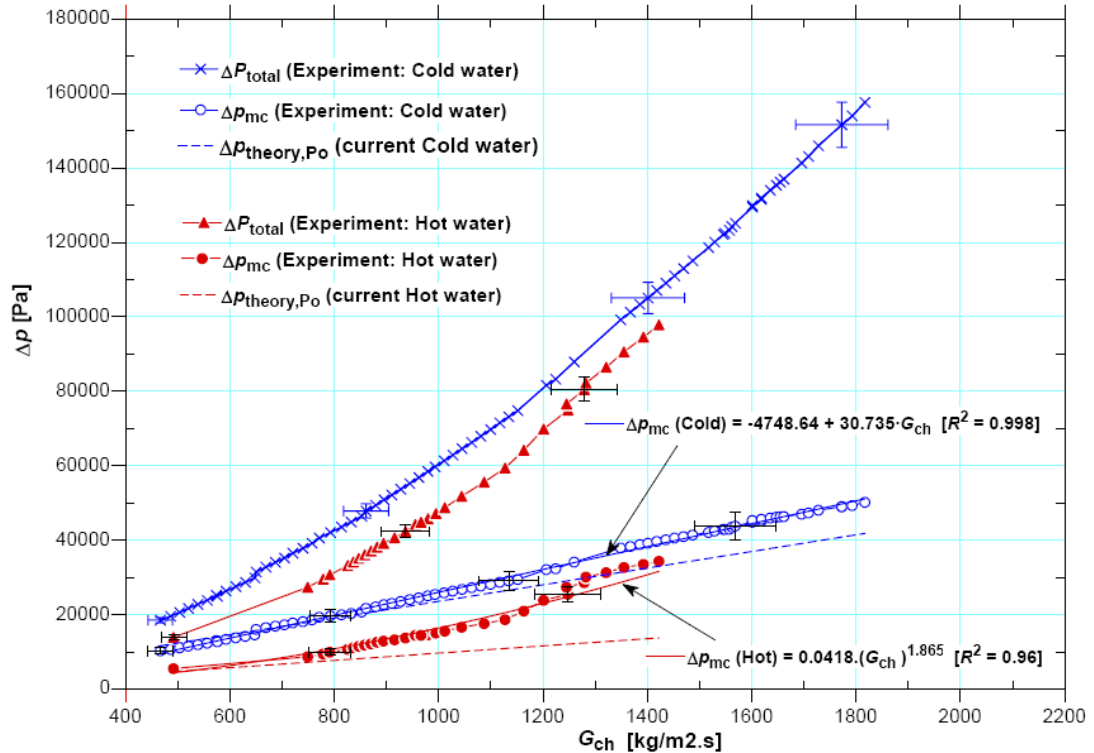


Figure 6.2b. Variation of Δp with respect to G_{ch} for Water flow in MCHX-1.

As can be seen in Figure 6.2, the theoretical fully developed laminar Δp deduced from Poiseuille flow law (Equations 6.19) covered experimental data well. Expectedly the theoretical Δp for cold and hot water flows exhibited linear increment with the increase of both Re and G for the entire Re range tested. The experimental Δp_{mc} however increased linearly with Re only in the range $482 \leq Re \leq 2013$, for cold water and

$1310 \leq Re \leq 2012$ for hot water. The linear curve-fits within these ranges captured current experimental data well, which can be seen from the R^2 values of 0.996 and 0.998 in Figures 6.2a and 6.2b respectively. It is noted here that the linear curve-fits correlated current data better than power-law curve fits. At lower Re the experimental and theoretical Δp curves are in-line and fell well within the experimental uncertainty. This is because the flow gets fully developed faster at lower Re than at higher Re within the laminar flow regime.

As compared to the theoretical Δp line for the cold water flow, there are two little jumps rather than gradual shifts in experimental Δp_{mc} data at around $Re \approx 700$ and $Re \approx 1400$. The reasons could be the change of pressure sensors from lower to higher capacity range during the measurement at these moments. Although the experimental Δp varied fairly linearly with Re , it however started deviating from the theoretical Δp line at $Re \approx 1200$. It can be reiterated that the theoretical curves are based on the fully developed flow for the entire flow length of current test slab. The flows were not fully developed and there was hydrodynamic entrance length at each flow rate. Therefore the deviations of experimental Δp from theoretical Δp line for $Re > 1200$ is sensible.

The variation of experimental Δp_{mc} with Re is non-linear for higher Re range, which visibly diverged from the theoretical Δp curve at about $Re \approx 2100$ as seen in Figure 6.2a for hot water flow. Past this point the curve difference (experimental to theoretical) no longer falls within the experimental uncertainty nor within any data scatter as seen by the red solid circular data points in Figure 6.2a. Rather than the linear curve-

fit, the power-law curve-fit with an R^2 value of 0.96 correlated the experimental Δp_{mc} data well within the experimental uncertainty.

Mala and Li [39] and Xiong and Chung [184] studied the water flow in microchannels and found significant deviation of their Δp from the theoretical value even in laminar flow regime. Mala and Li [39] observed the deviations at $Re \approx 300-900$ and as the reasons they pointed on the early transition and the surface roughness effect even in the laminar regime. Xiong and Chung [184] on the other hand observed this deviation at about $Re \approx 1500$. They pointed to the improper accounting or not accounting for the additional pressure losses as the reasons rather than the early transition. Although present data showed very little qualitative similarity with their findings, the difference of current data with the theory is not noticeable as their result. The reasons could be the use of little higher diameter in current study than they used; and accounting for all possible losses in the pressure loss calculation method than their process. The divergence of Δp - Re slope from theoretical line at $Re \approx 2100$ may be an indication of laminar-to-turbulent flow transition in current study, which is the general case for traditional pipe flow.

6.4.2 Flow friction in the test slab channel, f_{ch}

Current experimental Darcy friction factor f_{ch} and the theoretical Darcy flow friction for fully developed laminar circular pipe flow ($f = 64/Re$) are estimated from Equations 6.18 and 2.15. They are portrayed with respect to Re_{ch} in a log-log plot in

Figure 6.3. As expected, the f linearly decreased with the increase of Re , which continued up to about $Re \approx 2100$ showing a strong dependence on Re . The theoretical f line and present data both are nearly parallel and overlapping in the range $480 \leq Re \leq 2100$.

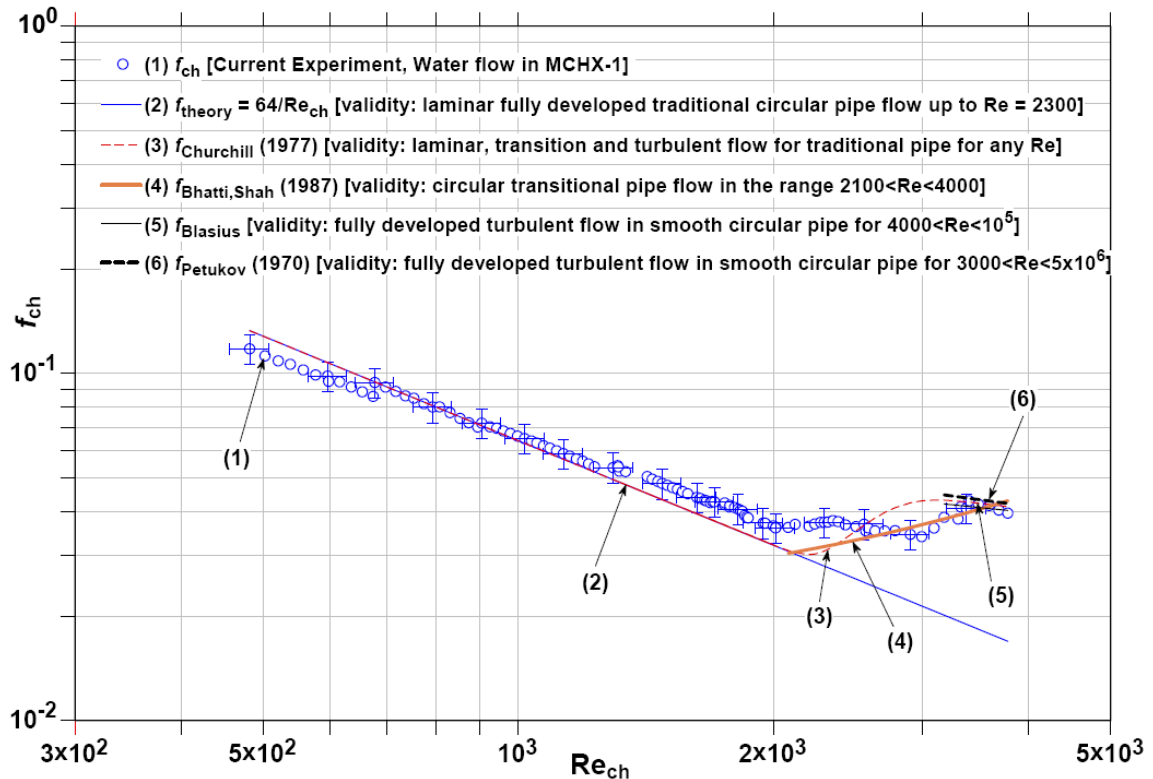


Figure 6.3. Variation of channel side flow friction f_{ch} with respect to Re_{ch} for Water flow in MCHX-1.

As seen in Figure 6.3, there are two vertical shifts in data, one at around $Re \approx 700$ and the other at $Re \approx 1400$. As mentioned before, these shifts are at the locations where the measuring pressure sensors were changed from lower to higher range as the flow rates were increased. The pressure for entire Re range as tested in current study could be measured using a single set of broad range pressure transducer, which could lead to a higher measurement uncertainty. To avoid inaccuracy in data, several sensors were used.

It appears that the current experimental f data in the range $480 \leq Re \leq 2100$ could be predicted by the classical laminar flow theory. Again, the departure of f - Re curve from the theoretical line for $Re > 2100$ is an indication of flow transition from laminar to turbulent regime. Although $Re \approx 2100$ is a little lower than the conventional value of $Re_{cr} \approx 2300$, it is however still within the neighborhood of experimental uncertainty. Therefore current study concludes that the occurrence of flow transition and hence the critical Re for water flow in 1 mm channel is similar to traditional laminar flow theory.

The experimental f data deviated from the classical laminar flow f curve for $Re > 2100$ and showed independency or minimal dependency on Re , which continued for rest of the Re range tested. The well known Blasius and Petukov expressions [5, 11, 53, 68] for Darcy f vs. Re correlations for traditional turbulent flow in smooth circular duct (Equations 2.20 and 2.22) are compared with current data in Figure 6.3 in the range $3180 \leq Re \leq 3780$. As seen in Figure 6.3, the above traditional turbulent correlations compared current f data well. The experimental data and the turbulent theoretical predictions have good agreements and they fall within the experimental uncertainty as can be seen from the error bars. Current f - Re relationship in the turbulent regime suggests that the classical turbulent correlations established for smooth circular tube can predict the f - Re data well for the channel size tested in current study.

Correlations for transitional flow are limited in the open literature because of its complex patterns. The transition flow regime in current study fell in the range of

$2100 < Re < 3100$. Two available correlations, one proposed by Bhatti and Shah [63, 68] given in Equation 2.18 and the other by Churchill [69] given in Equation 2.19 were compared with current data in Figure 6.3. It is worth mentioning that a single correlation proposed by Churchill [69] is valid for all laminar, transitional, and turbulent flow regimes for any value of Re . The Bhatti and Shah [63, 68] correlation is only valid for transition regime within the Re values of $2100 < Re < 4000$. As seen in Figure 6.3, the Churchill correlation predicted current data very well for laminar and turbulent flows. In transitional flow none of these two correlations captured current f data very well. However taking the experimental uncertainty into account, the correlation by Bhatti and Shah [63, 68] could compare majority of the experimental data in this range.

6.4.3 Effect of Re on Po in the test slab channel

The channel side Poiseuille number ($Po = fRe$) for current experimental data is calculated by multiplying Equations 6.17 and 6.18. The theoretical Poiseuille number for fully developed traditional laminar circular pipe flow ($Po = fRe = 64$) is estimated from Equation 2.10. Both the experimental and theoretical Po are plotted against Re in Figure 6.4. The experimental Po data exhibited the independency on Re in the range $480 \leq Re \leq 2100$, which is expected since the Po is supposedly to be geometry dependent in laminar flow regime but not on the Re . In this range, the data points run almost parallel and overlapped with the theoretical Po line. Within the experimental uncertainty, all the data could be represented by the theoretical Po curve for $Re \leq 2100$ as seen from the error

bars. The mean experimental fRe in the range $480 \leq Re \leq 2100$ is found to be 67, which is only about 5% higher than the theoretical value of 64. This higher value however belongs to the experimental uncertainty band.

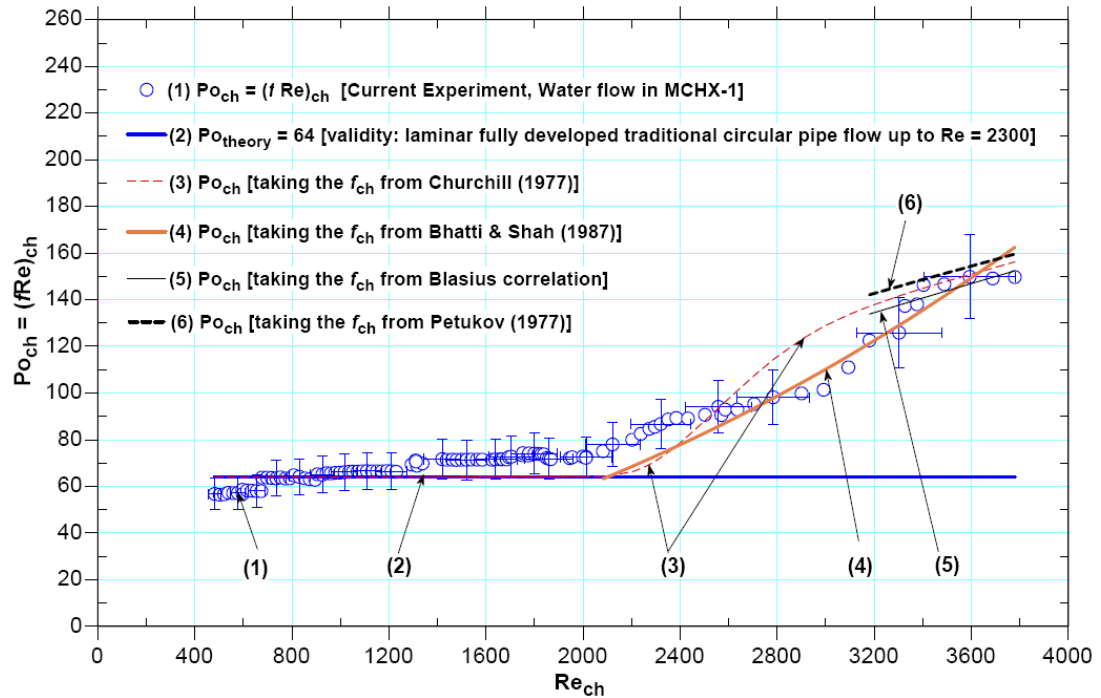


Figure 6.4. Variation of channel side Po_{ch} with respect to Re_{ch} for Water flow in MCHX-1.

As seen in Figure 6.4, the experimental Po remained almost the same in a horizontal line for $Re \leq 2100$ and then started deviating from the theoretical laminar Po curve. The experimental Po curve then continued to increase with Re for the rest of the Re range investigated. This phenomenon demonstrates the fRe dependency on Re for $Re > 2100$, which can be explained by the onset of laminar to turbulent flow.

Current Po data in the turbulent range are compared with theoretical Po by extracting the f from the Blasius and Petukov correlations from Equations 2.20 and 2.22. Within the range of $3180 \leq Re \leq 3780$, all the theoretical fRe increment with Re compared current data well. Little scatters in data as seen in Figure 6.4 can be bound by the experimental error bars. The theoretical Po calculated using Blasius relationship confined the experimental data better than other theoretical curves. This is reasonable since Blasius correlation is recommended for low Re turbulent flow, which is the case in current study. The pattern of $f-Re$ variation in current data confirms that the classical turbulent correlations developed for traditional smooth circular duct can predict the water flow in multi-port microchannel slab.

In the transitional regime of current data i.e. in $2100 < Re < 3100$, the Bhatti and Shah [63, 68] and Churchill [69] correlations, which are explained above, are also compared in Figure 6.4. As seen in Figure 6.3, the Churchill correlation predicted current data very well for laminar and turbulent flows. In transitional flow none of the correlations predicted current f data very well. Considering the experimental error bar, the correlation by Bhatti and Shah [63, 68] could compare majority of the experimental data in this range. Both the correlations however are comparable with current Po data in the transitional regime.

6.4.4 Conclusions on water flow in the test slab

Open literatures leave with varied opinions on fluid flow nature and the applicability of traditional theory in microchannel flows. Better understanding of frictional characteristics in various microchannel geometries and building the experimental database are therefore important to optimize the design and application tradeoffs between the pressure drop expense and the heat transfer duty. In this view, to obtain and analyze the pressure drop and friction data, experiments are conducted in multi-port straight microchannel slab on water flows in the range $480 \leq Re \leq 3800$.

Water flow inside multi-port microchannel is investigated from laminar-to-turbulent regimes in the range of $480 \leq Re \leq 3800$. For the range of $480 \leq Re \leq 2100$, the experimental Δp linearly increased with the increase of Re and agreed with the theoretical Δp , which is estimated from Poiseuille flow-pressure relationship. The Δp however non-linearly increased with the increase of Re for $Re > 2100$ evidencing the flow transition. The macroscale laminar and turbulent correlations could predict current experimental water flow friction data well within $480 \leq Re \leq 2100$ and $3100 \leq Re \leq 3780$ respectively. The Blasius classical turbulent correlation envisaged current water flow f data very well in the range $3100 \leq Re \leq 3800$. The Bhatti and Shah [63, 68] and Churchill [69] correlations could compare current data also in the transitional regime i.e. in $2100 < Re < 3100$, although the comparison is not as good as the laminar and turbulent

flow regimes. Based on experimental uncertainty consideration, no evidence of early transition for water flow in current test specimen is reported here.

Current study therefore confirms the validity of classical flow theory in multi-port straight microchannel slab for the channel size and Re range investigated. The experimental pressure drop data for multi-port MCHX-1 test slab are tabulated in Table D1 in Appendix D. The present finding will be helpful to the research community in this area and the obtained experimental data will be useful in the design of heat exchanger using multi-port microchannel slab.

6.5 Results and discussions on glycol-water mixture flow

The 50% ethylene glycol-water mixture flows in MCHX-2 were investigated in developing laminar flow regime in the Reynolds number range of $346 \leq Re \leq 1637$. A maximum Re of 1637 was achieved for glycol-water flow at $64 \pm 1^\circ\text{C}$ in this test specimen with the current test set up. The detail uncertainty analysis associated with current study was performed according to the procedures described in Chapter 5 in Section 5.6. The estimated mean uncertainties of some key parameters are presented in Table 6.2 below.

Table 6.2. Mean experimental uncertainty in the study of glycol-water mixture flow

Parameters	Mean uncertainty
Measured pressure drop, $\Delta p_{\text{total, g}}$ [Pa]	$\pm 4.5 \%$
Measured total mass flow rate, \dot{m}_g , [kg/s]	$\pm 1.75 \%$
Pressure drop in a channel in the test slab, $\Delta p_{\text{mc, g}}$ [Pa]	$\pm 6.3 \%$
Reynolds number in a channel in the test slab, Re_{ch}	$\pm 5.8 \%$
Friction factor in a channel in the test slab, f_{ch}	$\pm 11 \%$
Poiseuille number in a channel in test slab, $Po_{\text{ch}} = (fRe)_{\text{ch}}$	$\pm 13 \%$

Same procedure as water flow was followed to determine the fully developed or developing status of the flow. The hydrodynamic entrance length was calculated for each

flow rate using Equations 2.16 and 2.25. The straight part of the test slab is 343 mm long. At the lowest flow rate i.e. at $Re = 346$, the hydrodynamic entrance length was found to be 20 mm, which occupied about 6% of the total slab length. The flow then gained fully developed status for the rest of the 323 mm length along the flow path and exited at the exit manifold. For the highest flow rate i.e. at $Re = 1637$, the flow was still developing along the entrance region of the test slab, with a hydrodynamic entrance length of 92 mm.

It was observed that none of the flows was hydrodynamically fully developed before approaching the test slab channels. This is because of 90-degree flow turn in the inlet manifold as discussed above in water flow section. The flow developing loss coefficient K_{∞} obtained from Equation 2.17a was therefore considered in Equation 6.11. All the flows however exited from the channels with fully developed status.

6.5.1 Pressure drop in the test slab core, Δp_{mc}

As mentioned before, the channel side measured pressure drops were corrected using Equations 6.1 through 6.16. Within the investigated range of $346 \leq Re \leq 1637$, the pressure drop for hot glycol-water mixture flow per unit channel length $\Delta p_{mc}/L_{mc}$ varied from 17 to 138 kPa/m. The measured Δp_{total} and corrected Δp_{mc} are plotted against Re_{ch} and G_{ch} in Figures 6.5a and 6.5b respectively with uncertainty error bars. For comparison the theoretical pressure drops calculated from Equations 6.19 are also plotted in these figures. As expected, the Δp in general increased with the increase of both Re and G .

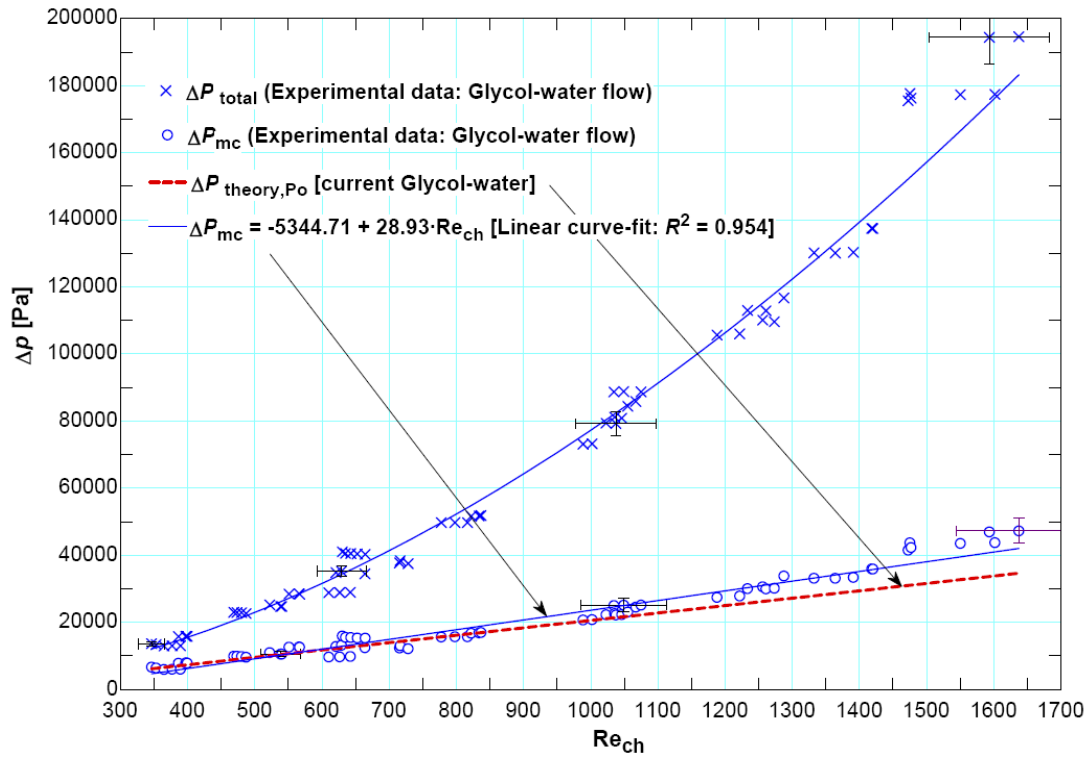


Figure 6.5a. Variation of Δp with respect to Re_{ch} for Glycol-water mixture flow in MCHX-2.

For all the data points in the investigated Re range, the measured total pressure drops varied non-linearly with Re , which probably because of the presence of other losses in it. There are some data scatters seen in the figure, which could be due to some flow and temperature fluctuations during the experiments. Although the experiments were conducted in a well insulated sealed test section without any heat transfer, still some 0.3 to 1.2% temperature rise in experimental periods was observed at the channel exit compared to the inlet. The fluid property in the channel segment was evaluated at bulk mean temperature assuming a linear temperature variation from the inlet to the exit. The

linear temperature variation may not be the case always, which to some extent could have supplemented to this data scatter via fluid viscosity variation. Credited to the property, the hotter fluid bids less pressure drop than a colder one for the same Re or \dot{m} . Owing to the sensitivity of viscosity, a little instability or rise in glycol-water mixture temperature can cause both the Δp and the Re to vary even for the same \dot{m} and hence can result in data scatter. As seen in Figure 6.5b, the plotting of Δp with respect to G has helped collapsing the scatters and reducing the horizontal variation significantly.

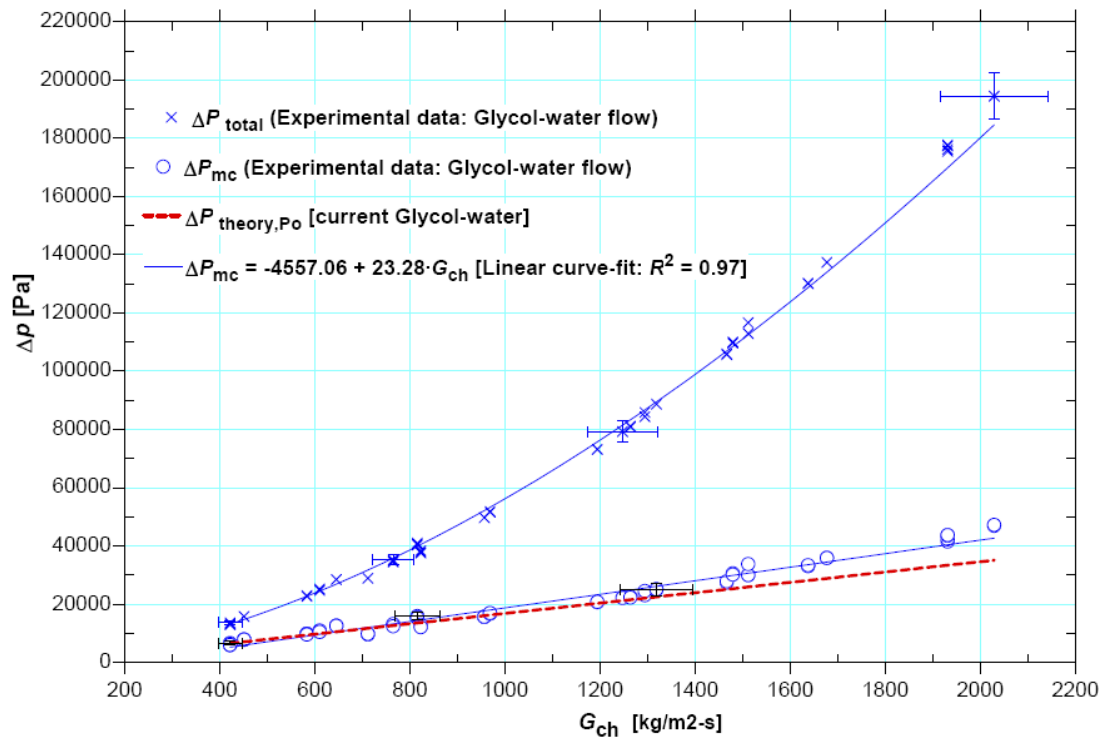


Figure 6.5b. Variation of total and channel side Δp with respect to mass velocity G_{ch} for Glycol-water mixture flow in MCHX-2.

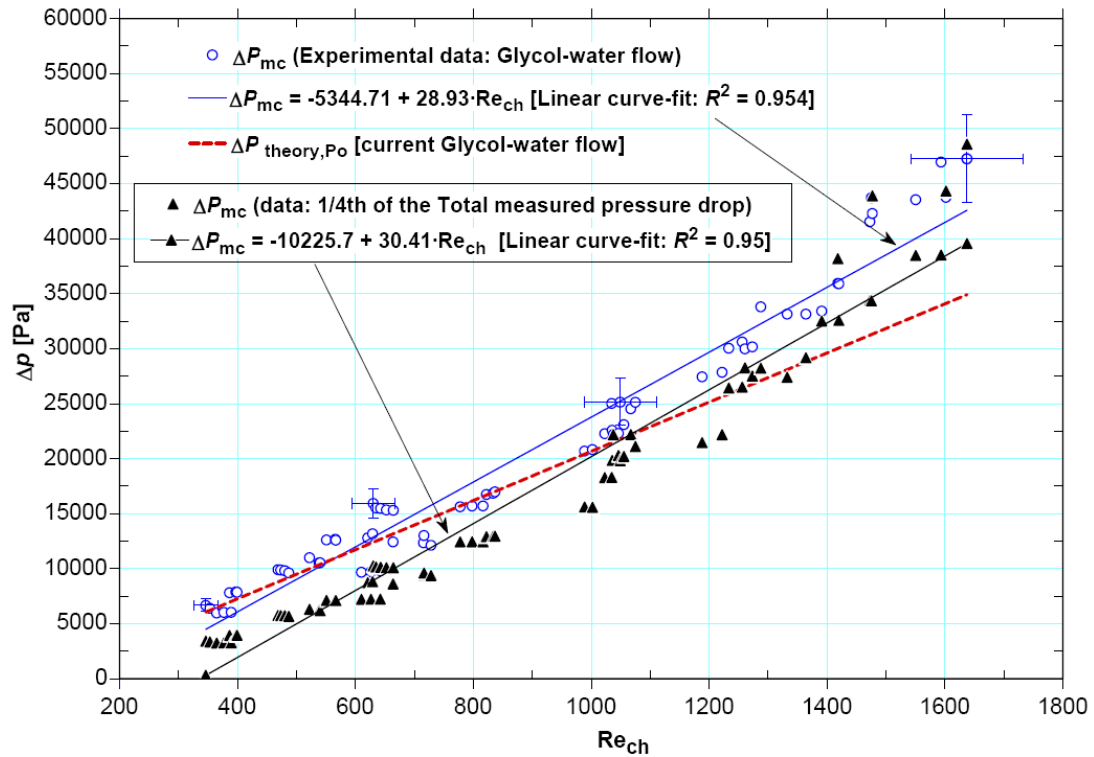


Figure 6.5c. Variation of channel side (core) Δp with respect to Re_{ch} for Glycol-water mixture flow in MCHX-2.

For better visibility, only the channel side experimental and theoretical pressure drops are presented against Re in Figure 6.5c. As can be seen in Figures 6.5a, 6.5b, and 6.5c the theoretical fully developed laminar Δp deduced from Poiseuille flow law (Equations 6.19) compared experimental data well. Expectedly both the theoretical and experimental Δp showed linear increment with the increase of both Re and G for the entire Re range tested. The experimental Δp_{mc} data was better correlated by a linear curve-fit than other fits with the R^2 values of 0.95 and 0.97 in Figures 6.5a and 6.5b respectively. Around relatively lower Re range the experimental and theoretical Δp

curves are fairly in-line and fell well within the experimental uncertainty as seen from the error bars. This is because of the reason that the flow develops faster at lower Re than at higher Re in the laminar flow regime.

Although the experimental Δp varied fairly linearly with Re, it however slightly is deviated from the theoretical Δp line at around $Re \approx 800$. It is worth noting here that the theoretical curve is based on the fully developed flow for the entire flow length of current test slab. As mentioned before, the experimental flows were not fully developed and there were some hydrodynamic entrance length at each flow rate. Therefore this slight deviation of experimental Δp from the theoretical Δp line at $Re \approx 800$ is reasonable. The variation of experimental Δp data with Re is somewhat non-linear for higher Re range, which visibly started departing from the theoretical Δp line at about $Re \approx 1300$ as seen in Figure 6.5. Beyond this point the curve difference (experimental to theoretical) no longer falls within the experimental uncertainty or within any data scatter.

As mentioned in water flow section above, Mala and Li [39] observed the deviations at $Re \approx 300-900$ for their water flow in microchannels. They defined the reasons to be due to early transition and the surface roughness effect even in the laminar regime [39]. Xiong and Chung [184] on the other hand observed similar deviation at about $Re \approx 1500$. According to them this deviation is not because of early transition, rather it is due not to properly account for the additional pressure losses at the entrance region. Current investigation did not span over the entire laminar Re range. Therefore the conclusion on the divergence of the Δp -Re slope from the theoretical line at about

$Re \approx 1300$ is not proper to make. It may be an indication of laminar-to-turbulent flow transition in current glycol-water mixture study in narrow channel or may still be within the experimental error and variations.

Attempts were also made to examine whether the channel side core pressure drop has any direct relationship such as any arithmetic multiple with the total measured pressure drop. Various multiplication factors are verified and one-fourth of the total measured pressure drop seems like compare the channel side pressure drop closer, which is plotted and curve-fitted in Figure 6.5c. It is seen that the $0.25\Delta p_{total}$ data underestimated the channel side pressure drop, which on average is about 27% lower than the experimental Δp_{mc} calculated from Equation 6.1. Nevertheless, the pressure drop relationship for current test specimen proposed by Equation 6.20 below will provide a rough estimate that can be a guideline prior to conducting similar pressure drop experiments.

$$\Delta p_{mc} \approx 0.25\Delta p_{total} \text{ (approximately 28\% lower estimate than actual) .} \quad (6.20)$$

6.5.2 Flow friction in the test slab channel, f_{ch}

The experimental and theoretical Darcy friction factors are estimated from Equations 6.18 and 2.15 and are plotted with respect to Re_{ch} in a log-log plot in

Figure 6.6. As expected, the f linearly decreased with the increase of Re . This decrease of f continued up to $Re \approx 1300$ showing a strong dependence on Re . Within the experimental uncertainty, with some rises and falls, present data fairly overlap the traditional theoretical f line up to the range of $346 \leq Re \leq 1300$. This suggests that current experimental f data could be predicted by the classical laminar flow theory for $Re < 1300$.

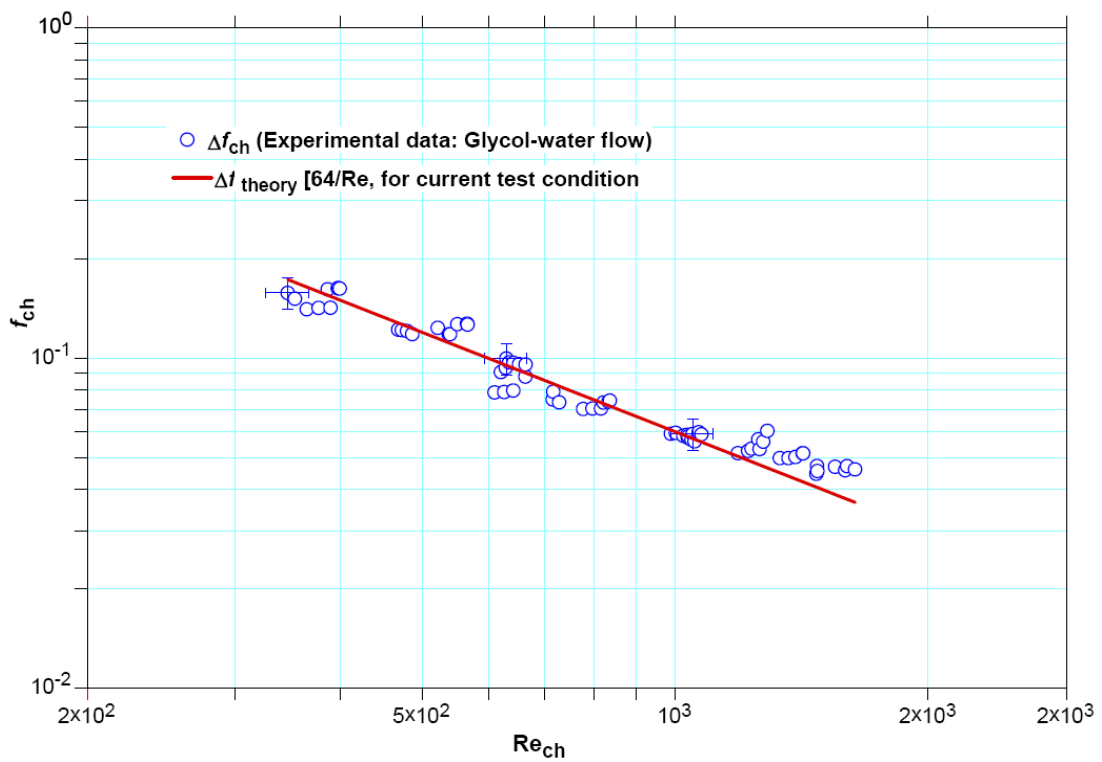


Figure 6.6. Variation of channel side flow friction f_{ch} with respect to Re_{ch} for Glycol-water mixture flow in MCHX-2.

As seen in Figure 6.6, current f data started deviating from the theoretical line for $Re > 1300$ and none of the data shows any falls to become overlapping with the

theoretical line. This departure could be a message of flow transition from laminar to turbulent regime anytime for $Re > 1300$. It could also be any other different phenomena other than the experimental uncertainty. Further study on glycol-water flow in current test specimen in the range of $1300 \leq Re \leq 2300$ will help concluding on this deviation.

6.5.3 Effect of Re on Po in the test slab channel

Calculated from Equations 6.17, 6.18 and 2.10, the experimental and theoretical Poiseuille numbers ($Po = fRe$) are plotted against Re in Figure 6.7. As mentioned before, the Po in traditional fully developed laminar pipe flow is usually dependent on flow passage geometry but independent of Re. Expectedly the experimental Po data in Figure 6.7 exhibited the independency on Re in the range $346 \leq Re \leq 1300$. In this range the data points ran almost parallel and overlapped with the theoretical Po curve. Therefore all the data in this range are covered by the theoretical Po line. There are some variations in data, which are well bound by the experimental error bars. The mean experimental fRe is found to be 67 for the entire investigated range of $346 \leq Re \leq 1637$, which is 4.7% higher than the theoretical value of 64. The average experimental fRe in the range $346 \leq Re \leq 1637$ is found to be 64.5, which is similar to the theoretical value of 64. This suggests that the experimental data within $346 \leq Re \leq 1300$ should be predicted by classical laminar flow theory.

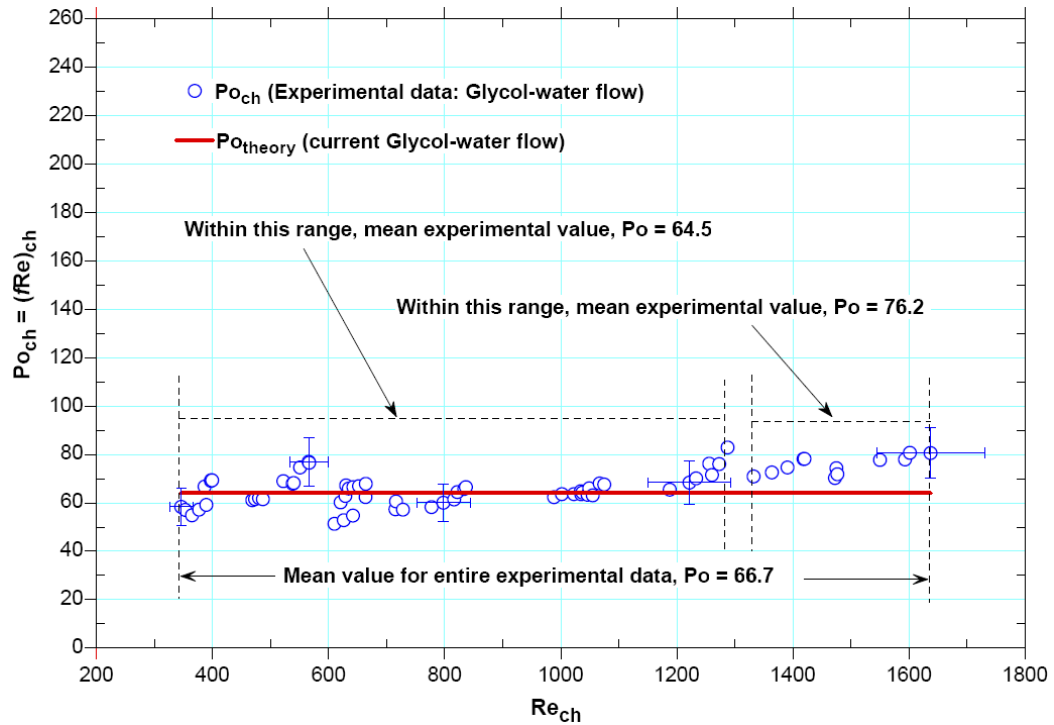


Figure 6.7. Variation of channel side Poiseuille number Po_{ch} with respect to Re_{ch} for Glycol-water mixture flow in MCHX-2.

As seen in Figure 6.7, the experimental Po leaves sign of departing from the theoretical Po line for $Re \approx 1300$. The Po curve then continued to increase with Re for the rest of the Re range investigated i.e. showing some dependency of Po on Re . The mean experimental fRe in the range $1300 < Re \leq 1637$ is calculated to be 76.2, which is about 20% higher than the theoretical value of 64. The deviation tendency of current data at $Re > 1300$ could be a hint to flow transition anytime sooner or due to some other reasons, which further study in the range of $1300 \leq Re \leq 2300$ can help to answer.

6.5.4 Conclusions on glycol-water flow in the test slab

Microchannel flow passages have attracted significant research attention in fluid flow and heat transfer areas because of their enhanced characteristics as compared to larger sized tubes. As mentioned before, open literatures on small diameter tube flows reported differing opinions on the applicability of macro-scale correlations in narrow channel flows. Better understanding of frictional characteristics in narrow geometries and building the experimental database are therefore important to optimize the design and application tradeoffs between the pressure drop expense and the heat transfer duty.

The ethylene glycol-water mixture is a commercially very important fluid encountered in many heating and cooling applications. Research data on ethylene glycol-water mixture flows in multi-port test slab in general and in developing laminar flow in particular are not available in the open literature. Therefore, experiments were conducted on 50% ethylene glycol-water mixture flows in multi-port straight microchannel slab in developing laminar flow in the range $346 \leq Re \leq 1637$ in order to obtain and analyze the pressure drop and friction data.

Expectedly the pressure drop increased with the increase of Re . The Δp fairly linearly varied with Re in the range $346 \leq Re \leq 1300$ and agreed with the theoretical Δp , which is estimated from Poiseuille flow-pressure relationship. In this range the traditional macro-scale correlation could predict present Δp , f and Po data well. The glycol-water

mixture flow did not show any sign of early transition in the range $346 \leq Re \leq 1300$. However, it left with signs of departure from the theoretical line for $Re > 1300$. This deviation tendency could be an indication of flow transition or could be a result of little larger experimental error beyond $Re = 1300$. Any conclusion on this phenomenon cannot be drawn without further flow investigation in the higher range of Re that spans through laminar and transition regimes.

Present results confirm that the traditional macro-scale flow theory should be applicable for glycol-water flow in 1 mm multi-port straight microchannel in the range of $346 \leq Re \leq 1300$. The experimental pressure drop data for multi-port MCHX-2 test slab are tabulated in Table D2 in Appendix D. Present finding, which has been documented through peer reviewed publication [231], will be beneficial to the research community in this area. The obtained experimental data will be useful in the design of heat exchanger using multi-port microchannel slab for glycol-water mixture as the working fluid.

CHAPTER – 7

HEAT TRANSFER AND PRESSURE DROP CHARACTERISTICS OF WATER FLOW IN 2-PASS MULTI-PORT SERPENTINE MICROCHANNEL SLAB HEAT EXCHANGER

7.0 HEAT TRANSFER AND PRESSURE DROP CHARACTERISTICS OF ETHYLENE GLYCOL-WATER MIXTURE FLOW IN 2-PASS MULTI-PORT SERPENTINE MICROCHANNEL SLAB HEAT EXCHANGER

The principal focus of current research is the investigation of heat transfer and pressure drop characteristics of glycol-water mixture flow in multi-port slab serpentine microchannel heat exchanger, which is described in Chapter-8. An experimental facility was developed in current study that needed to be commissioned and tested. Since the glycol-water mixture fluid is expensive and hazardous in handling, the functionality check of the test setup and the preparatory experiments were conducted using water. The preparatory experiments were conducted with water for acquiring better understanding on the test setup for next experiments on glycol-water mixture as well as for comparing the data with glycol-water mixture results.

Water being the fundamental heat transfer fluid is used in a number of practical heat exchangers. Heat exchangers with multi-port configurations have many applications. Literature review revealed that research on multi-port parallel narrow channels having serpentine bend is rare. While works on large diameter developing laminar pipe flow are available, such studies in narrow channels with serpentine bend are scarce. Study of water flow in simultaneously developing laminar regime in applied core geometry is limited in the open literature. Therefore the experiments have been conducted on water flow in multi-port parallel microchannel test slab (MCHX-4) in 2-pass flow configurations with

U-type serpentine bend to serve two purposes. The experimental descriptions and the pressure drop and heat transfer results of the water flow are presented in this chapter.

7.1 Methods of experiments and measurements

The details of the experimental facility instrumentation and calibration, and the test procedures in general are provided in Chapter 4. The schematics of the test facility are given in Figures 4.1, B1, and B5. The design details and specifications of MCHX-4 test specimen are provided in Figures 4.3, 4.4d and B2.4 and in Table 4.1 and 4.2. Figures 4.5 and 7.1 show the position of the test specimen and the directions fluid flow.

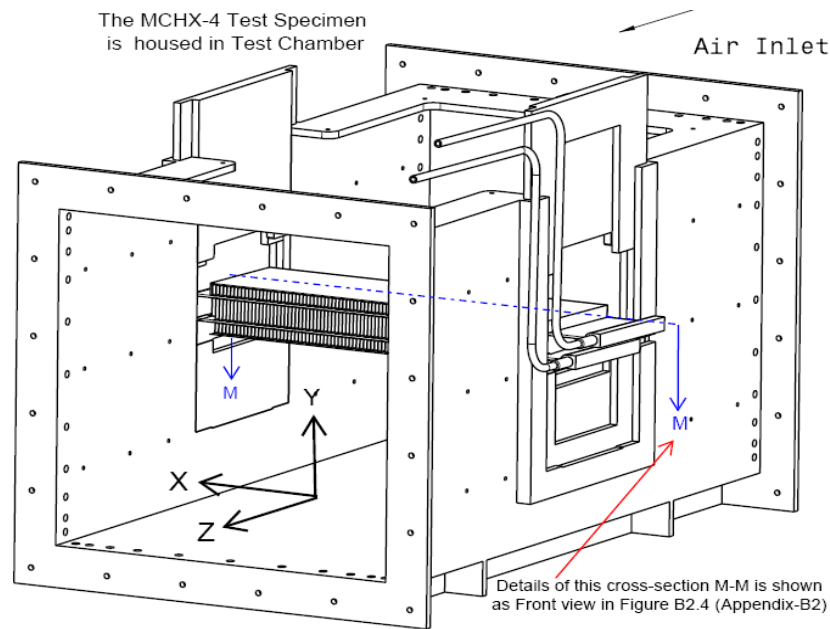


Figure 7.1a. Schematic of test chamber with MCHX-4 test specimen

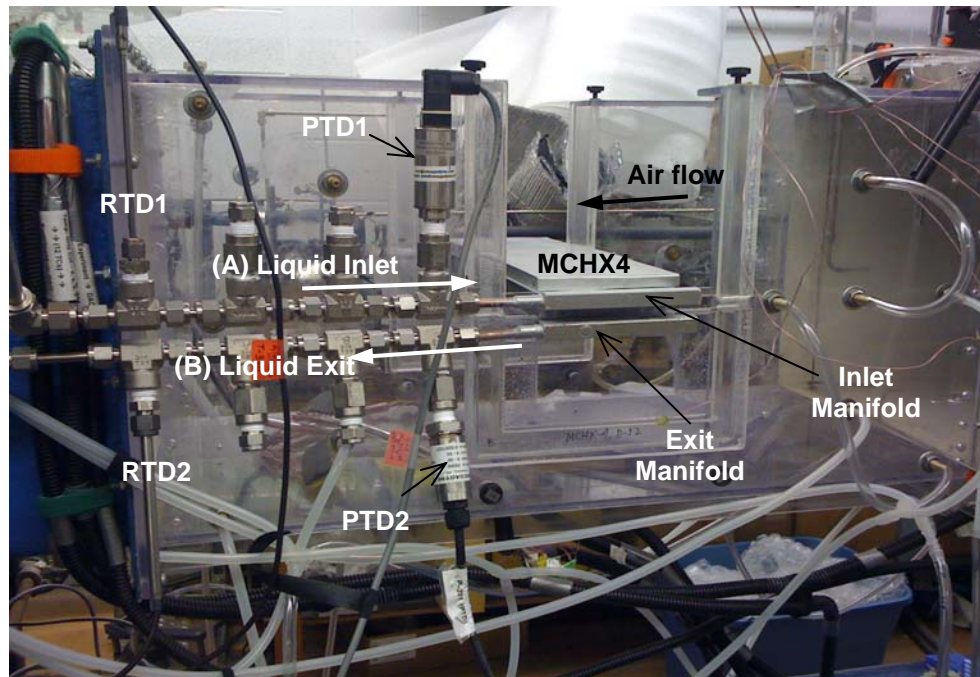


Figure 7.1b. Test specimen MCHX-4 housed in test chamber (Photo before insulation is made)

As seen in Figures 7.2, 4.4d, B2.4, and B8.4a, the 2-pass MCHX-4 test specimen has two slabs (top & bottom) forming U-shape via a continuous serpentine. The 366 mm straight length of the top slab runs from inside the inlet manifold through the entrance of the serpentine bend. The 343 mm straight length of the bottom slab starts at the exit of the serpentine bend and runs up to the inside of the exit manifold. These are the straight part of the hydrodynamic flow lengths of top and bottom slabs. The serpentine U-bend (semi-circular) has a mean diameter of 22 mm, which gives a circumferential flow length of about 34.5 mm. The effective heat transfer length for each of the top and bottom slabs is 304.8 mm, which remains inside the test chamber. Whether the flow is developed or

developing before entering the straight parts of the channels was estimated from the magnitude of hydrodynamic entrance lengths by using Equations 2.16 and 2.25.

As shown in Figure 7.1, the hot liquid (here water) flow entered the inlet at 'A' and took a 90-degree flow turn to the left at the inlet manifold. From exit manifold the stream distributed through all the 68 channels and flowed towards positive X-direction. After the first pass, the liquid flow reversed by taking U-turn around the serpentine bend and again flowed back through the channels in negative X-direction in 2nd pass. At the exit manifold the liquid streams combined together and exited at 'B'. The wind tunnel cold air on the other hand flowed inside the test chamber across the test specimen along positive Z-direction. The heat transfer took place between the liquid and the air within the effective heat transfer section in the test chamber (see Figure B2.4a).

The parameters that were necessary to measure in these experiments are the flow rate and inlet and exit temperatures of liquid flow; velocity and inlet and exit temperatures of air flow; and the surface temperature of the test specimen. As seen in Figure 7.1b, the RTD1 and RTD2 were used to measure the inlet and exit temperatures of the flowing liquid. The inlet and exit flow pressures of the liquid were measured with PTD1 and PTD2. The flow rate of the liquid was measured using an electronic digital flow meter (section 4, Figure 4.11) installed upstream of RTD1 location. The inlet and exit temperatures of air flow were measured using the inlet and exit thermal measurement grids, which are described in section 4.3.2 and Figure 4.8. As described in section 4.5.4 in Figures 4.16 through 4.19 and B7.1, a Pitot static probe in combination with airside

differential pressure transducer (PTDD) and FKT series duct calibrator manometer was used to measure the air velocity inside the test chamber.

The surface temperatures of the MCHX-4 test slab were measured using 48 calibrated thermocouples. They were affixed at 4 major and 2 minor positions along the liquid flow (X-direction). For each of the major positions at liquid side, 8 to 10 thermocouples were placed along the air flow (Z-direction) as shown in Figure B8.4. Due to the presence of the airside fins, all the thermocouples were placed on the un-finned exposed surface of the test slab, which are just outside of the test chamber. The test chamber and the surroundings were well insulated in such a way that these thermocouples were virtually measuring within the adiabatic (no heat transfer) zone. The major positions mentioned here are the locations immediate before and after the effective heat transfer section including the adiabatic serpentine zone.

All the measurements were taken at steady state condition, which for current study, is explained in section 4.7. The data were monitored and recorded into a DAQ system. The descriptions of the DAQ are provided in section 4.6 via Figures 4.20 and B4 and the data sampling methods are discussed in section 4.7. According to Equation 4.12, the time averaged mean data set was acquired for each of the parameter and stored for post processing and analyses.

7.2 Treatment and separation of pressure losses in the test slab

As seen in the literature review, improper considerations and under or over estimation of various pressure losses and ignoring some minor losses in narrow channels heat exchangers may lead to very differing results. A comprehensive pressure balance is necessary in such heat exchanger. The test specimen used in current study is viewed as typical thermal heat exchanger. The pressure drop separation in this type of heat exchanger is therefore not straight forward as it is for the large diameter pipe. Many minor losses are neglected in large size pipe flow because of their fewer magnitudes as compared to the other loss areas. These minor losses are however important to consider when dealing with pressure drop in heat exchangers having narrow channels flow.

The locations of the temperature and pressure sensors, segment-wise pressure drops route for current test specimen and the procedure for pressure balancing are described below via Figure 7.2. A comprehensive pressure balance model is formulated for the test specimens MCHX-1 and MCHX-2, which is described in section 6.1 via Figure 6.1 and Equations 6.2 through 6.16 above. The same model and Equations are applied to isolate the pressure drop in MCHX-4 except for the addition of serpentine bend loss and another straight multi-port slab at the bottom. The pressure balance model for MCHX-4 is given by Equation 7.1 and described below.

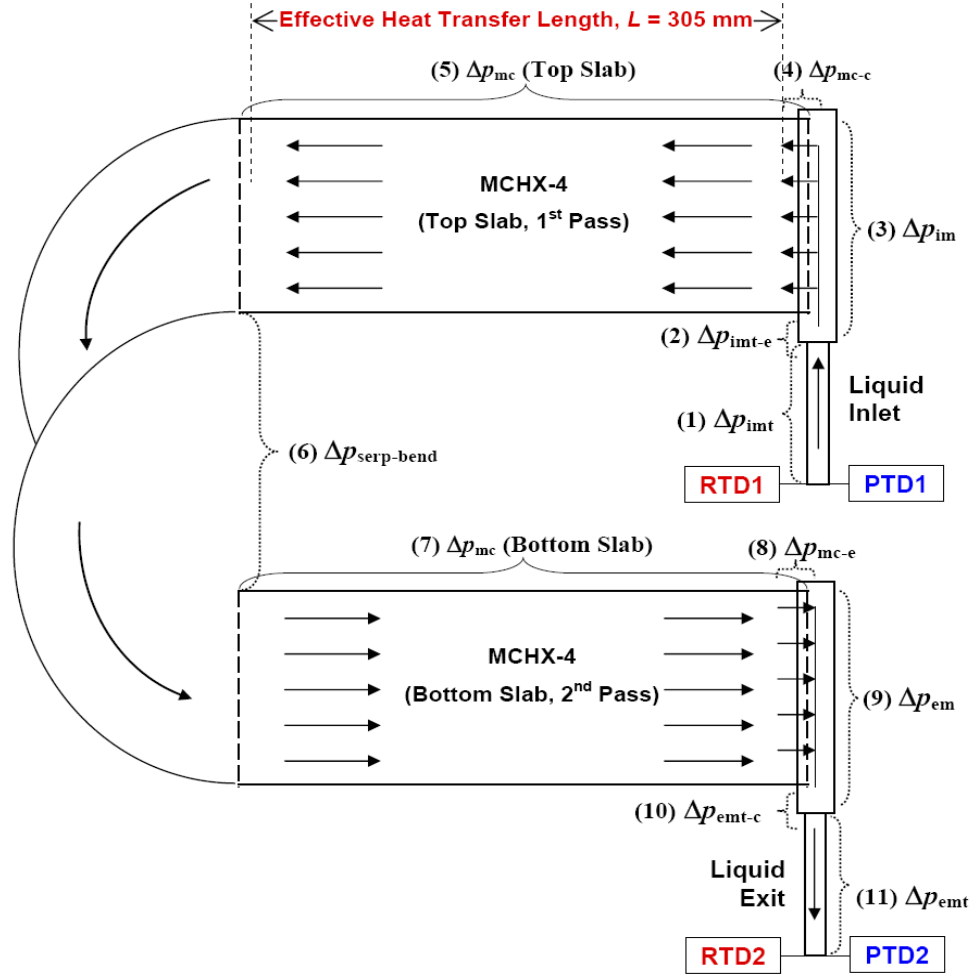


Figure 7.2. Segment-wise pressure losses from inlet to exit flow route of MCHX-4.

$$\begin{aligned}
 \Delta p_{\text{total}} &= p_i - p_o \\
 &= \underbrace{\Delta p_{\text{imt}}}_{(1)} + \underbrace{\Delta p_{\text{imt-e}}}_{(2)} + \underbrace{\Delta p_{\text{im}}}_{(3)} + \underbrace{\Delta p_{\text{mc-c, top}}}_{(4)} + \underbrace{\Delta p_{\text{mc-top}}}_{(5)} + \underbrace{\Delta p_{\text{serp-bend}}}_{(6)} + \\
 &\quad \underbrace{\Delta p_{\text{mc-bottom}}}_{(7)} + \underbrace{\Delta p_{\text{mc-e, bottom}}}_{(8)} + \underbrace{\Delta p_{\text{em}}}_{(9)} + \underbrace{\Delta p_{\text{emt-c}}}_{(10)} + \underbrace{\Delta p_{\text{emt}}}_{(11)}
 \end{aligned} \tag{7.1}$$

Some K-loss factors for turbulent flow U-bends are available [5] and some are available for U-bends connected with fittings such as via flanges, threads etc. [59]. The

serpentine U-bend in current test specimen is not connected to any fittings (it is continuous with the multi-port slabs) and the flow in current study is not turbulent either. The method of pressure drop consideration for the U-type serpentine bend in laminar developing flow, as is the case in present study, is not widely available. Therefore the pressure drop for serpentine U-bend was estimated from a relationship presented in a comprehensive source by Idelchick [60]. The smooth bend of circular cross-section is a function of Re, bend radius-to-channel diameter ratio, and the angle of the flow, which for current situation is given by Equation 7.2 below.

$$K_{\text{serp-bend}} = \frac{\Delta p_{\text{serp-bend}}}{\rho V^2 / 2} = 0.0175 \lambda \delta \frac{R_{\text{sp}}}{D_{\text{ch}}}, \quad (7.2)$$

where δ is the turn angle and $\lambda = f\left(\text{Re}, \frac{R_{\text{sp}}}{D_{\text{ch}}}\right)$. The above relationship is valid for

$\frac{R_{\text{sp}}}{D_{\text{ch}}} \geq 3$ and $\frac{L}{D_{\text{ch}}} \geq 10$, which are the cases in current study since the MCHX-4 has

these ratios as $\frac{R_{\text{sp}}}{D_{\text{ch}}} = 11$ and $\frac{L}{D_{\text{ch}}} = 343$ respectively.

The factor λ has different functional relationships depending on Re and D/R ratio. Since current test conditions, both for water and glycol-water mixture flows, fall within

the range of $50 < \text{Re} \sqrt{\frac{D_{\text{ch}}}{2R_{\text{sp}}}} < 600$, the factor λ could be defined by Equation 7.3.

$$\lambda = \frac{20}{\text{Re}^{0.65}} \left(\frac{D_{\text{ch}}}{2R_{\text{sp}}} \right)^{0.175} \quad (7.3)$$

The K-loss factor for serpentine U-bend in current experiments takes the following form.

$$K_{\text{serp-bend}} = 71.125 \left(\frac{R_{\text{sp}}}{D_{\text{ch}}} \right)^{0.825} \text{Re}^{-0.65} \quad (7.4)$$

7.3 Results and discussions on water flow

In the experiments the inlet temperature of hot water was maintained at $76 \pm 0.3^\circ\text{C}$ and the flow rate was varied five steps in the Reynolds number range from 850 to 2250. The temperature and velocity of cold wind tunnel airflow at the inlet to the test chamber was kept constant at $14.0 \pm 0.1^\circ\text{C}$ and 4.5 ± 0.1 m/s for all five water flow rate steps. At each flow rate the TAMDS of about 5000 to 6000 steady state samples were recorded for analysis for which the mean uncertainties of some key parameters are listed in Table 7.1. The analyses were carried out according to the procedures described in Section 5.6.

Table 7.1. Mean experimental uncertainty in the study of water flow

Parameters	Mean uncertainty
Measured pressure drop, $\Delta p_{\text{total, w}}$ [Pa]	± 5.7 %
Measured total mass flow rate, \dot{m}_w , [kg/s]	± 1.65 %
Reynolds number in a channel in test slab, Re_{ch}	± 5.7 %
Heat transfer rate, q_w [W]	± 4.8 %

Dehghandokht, Mesbah and co-workers (2011) numerically simulated current test specimen with same geometry and same experimental operating conditions [232]. They compared the numerical results with current experimental data set. The numerical model compared current data very good and the experimental findings were reflected well.

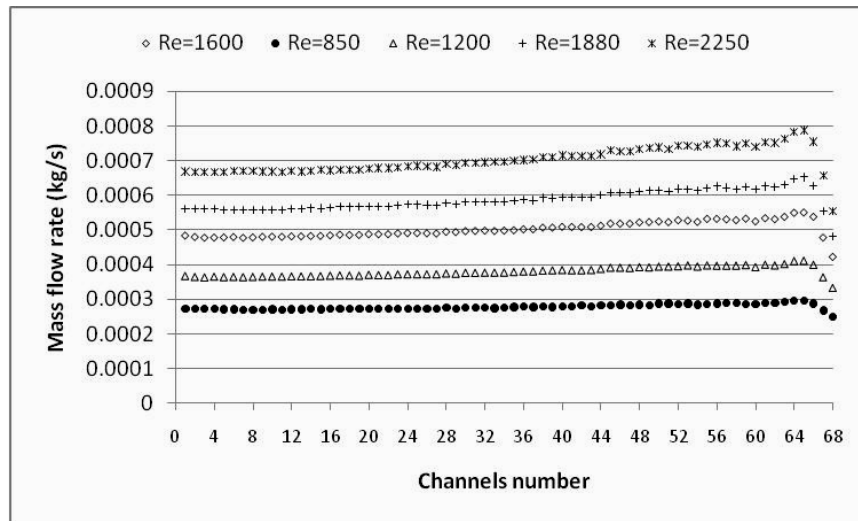


Figure 7.3. Flow distribution of water through all the channels in MCHX-4 test slab.

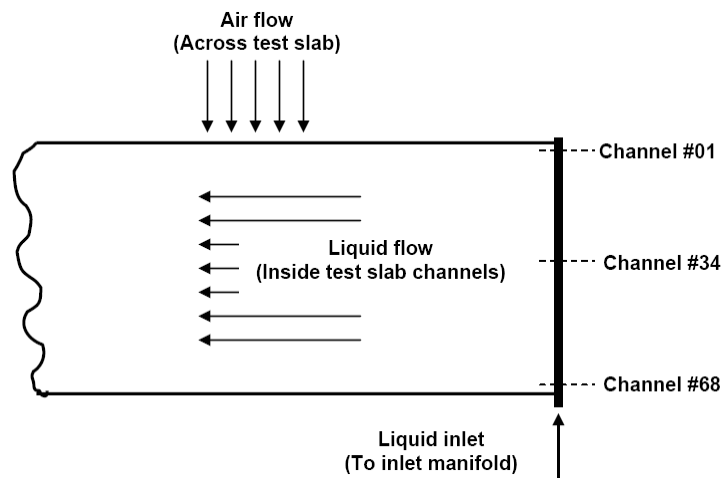


Figure 7.4. Channel number designation along flow directions.

The system liquid mass flow rate was well distributed through all the channels in the test slab from the inlet manifold as can be seen in from Figure 7.3 [232]. This justifies the assumption of equal and uniform flow distributions in all the channels. The flow directions and the channel number designations for Figure 7.3 is illustrated in Figure 7.4.

The maximum and minimum hydrodynamic entrance lengths were found to be 48 mm and 125 mm at $Re_{ch} = 850$ and 2200 respectively; occupying 13% to 33% of the test slab length. This indicated that no flow step was fully developed before approaching the channels. The maximum and minimum hydrodynamic entrance lengths are shorter than the straight flow length of the top slab, which signifies that all the flow steps exited from the top slab and entered the serpentine bend with fully developed status. Due to the flow reversal, the flow may gain developing status again at the exit of the serpentine bend i.e. at the entrance of the straight part of the bottom slab, which will be discussed next.

7.3.1 Total, core and segment-wise pressure drops

The pressure drops in the core of MCHX-4 i.e. in the straight parts of top and bottom slabs were isolated from the measured total pressure drop as per Figure 7.2 and Equations 6.1 to 6.16 and 7.1 to 7.4. In order to compare the experimental data, the pressure drop in the core of current test slab was isolated according to Kasagi et al.[233] one-third approximation and Jokar et al. [200] estimation. Jokar et al. [200] deducted the

manifold pressure losses from the total measured pressure drop to extract the core loss. The theoretical Δp for fully developed conventional laminar pipe flow for current test conditions was deduced from Equation 6.19. The measured total pressure drop Δp_{total} is plotted with respect to Re_{ch} in Figure 7.5. All the experimental, approximated, and theoretical core pressure drops, the separated segment-wise pressure drops for the inlet and exit manifolds and for the serpentine bend are also plotted.

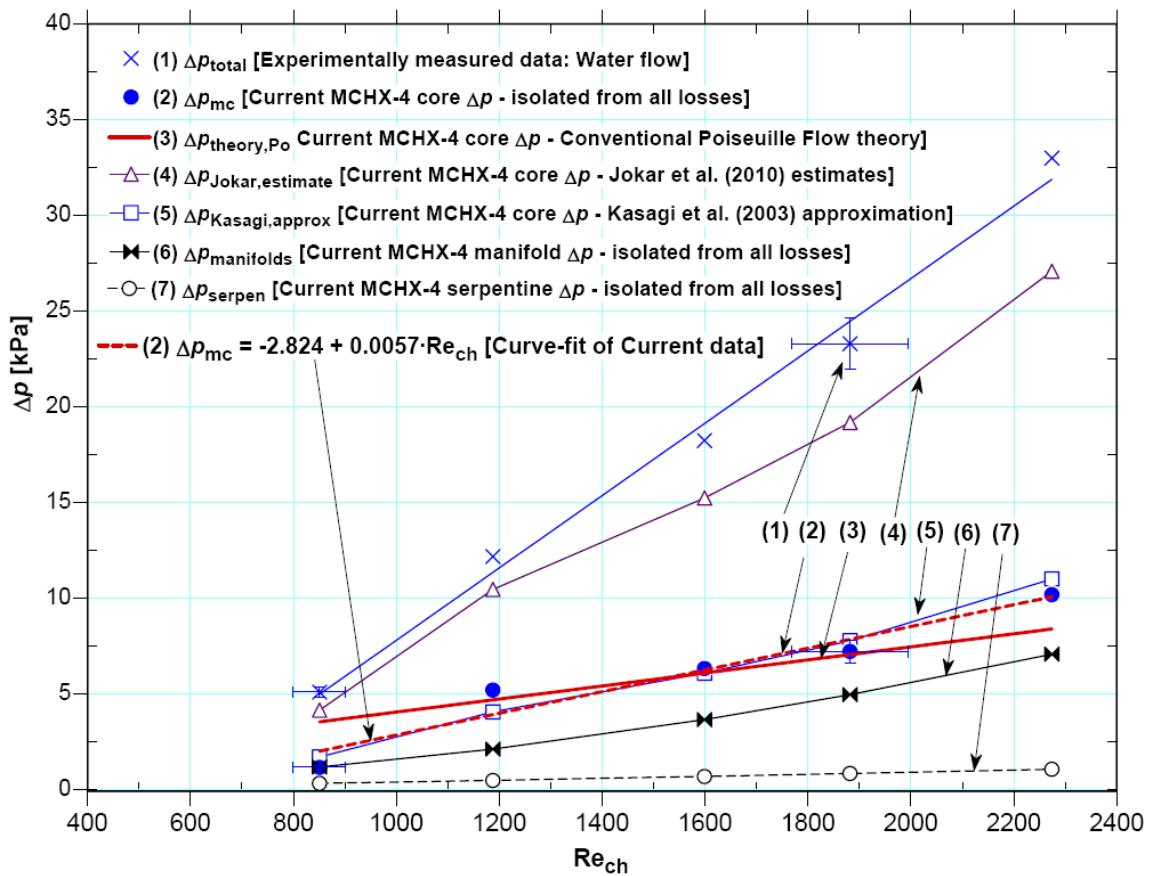


Figure 7.5. Variation of Δp with respect to channel side Re_{ch} for Water flow in MCHX-4.

The Δp_{total} nearly linearly increased with the increase of Re . All other pressure losses linearly increased with the increase of Re as expected. The theoretical pressure

drop, estimated from Poiseuille flow law for conventional pipe, is shown as in solid line (#3). If all the losses are properly taken into account, current core pressure drop could be compared with theoretical line, which is the case in here. The core pressure drop was isolated using the pressure balance model formulated above. The first data point is somewhat off the comparison, which might have happened in the process of data handling or due to some experimental error. There are some variations between the theoretical line and the other experimental data points. These variations can be explained by: the experimental uncertainty and the difference between an already fully developed flow (theoretical) and a calculated fully developed flow by deducting coupled losses.

The method used by Jokar et al. [200] could not predict the core pressure drop for current test specimen. This is because deducting only the manifolds' pressure losses from the total measured pressure drop is not sufficient to get the core pressure drop; other possible losses must be taken into proper account. Kasagi et al. [233] approximation did not compare theoretical Δp very well at the lowest and highest data points. It however estimated current core pressure drop closer, which is much better than Jokar et al. [200]. Within the experimental uncertainty it however compared theoretical Δp for the intermediate data points, as can be seen in Figure 7.5.

The slope of Kasagi et al. [233] and current core Δp line are steeper than the theoretical Δp line. This can be explained that the theoretical line is based only on fully developed laminar flow in conventional pipe that excludes any other losses. Whereas current case is a developing laminar flow that includes all the losses for fittings, bends,

manifolds, flow areas changes etc., which have been excluded from measured pressure drop by using a pressure balance model. This little difference is reasonable as can be seen further from a numerical comparison.

The pressure drops in the inlet and exit manifolds and in the serpentine bend are isolated using the same pressure model as formulated above in section 6.1. The core pressure drop in the straight part of the top and bottom slabs is the highest, which is due to flow friction. This study showed that the second highest areas of pressure losses are the inlet and exit manifold together. The lowest pressure loss occurred in the serpentine bend. The serpentine portion has less pressure drop than the manifolds and it helps mixing of fluid streams inside bend and also creates second flow developing effect at the entrance of the bottom slab. All these effects are beneficial for heat transfer in a heat exchanger.

Figure 7.6 compared the experimentally measured and the numerically simulated Δp_{total} results with respect to Re [232]. As usual the Δp_{total} increased as the Re increased. Both the experimental and numerical Δp_{total} compared very well within an average percentile difference of 6.2% respectively. The model isolated the total pressure drops into three segments (as seen in Figure 7.7). The results show that the highest pressure drop occur along the straight flow paths (top and bottom slabs), which is due to the flow friction and the lowest around the serpentine bend due to the flow reversal. The inlet and exit manifolds have the next highest pressure drops, which probably because of the complex manifold geometry and 90-degree flow turns. The numerical results are well inline with the findings of current study as can be seen in Figures 7.5, 7.6, and 7.7.

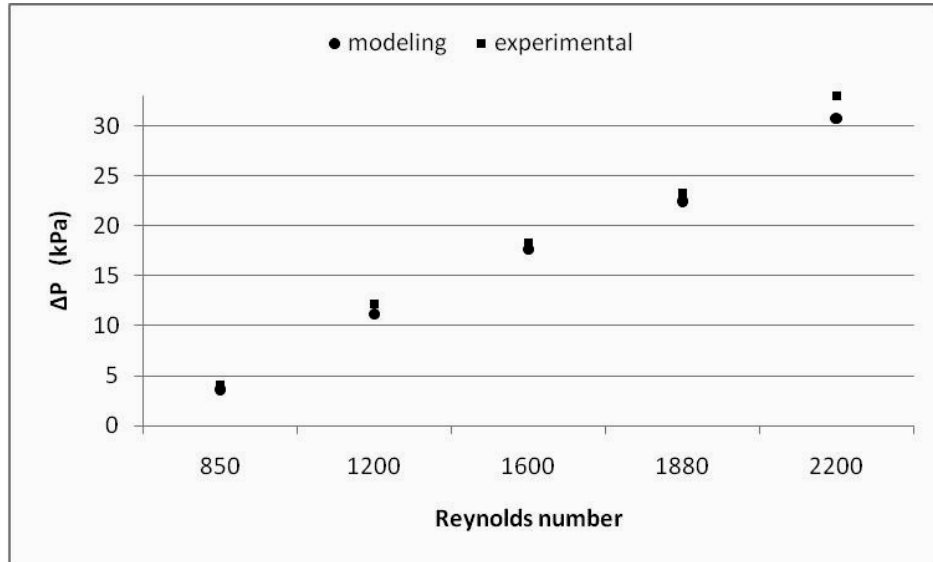


Figure 7.6. Variation of water flow Δp with Re_{ch} (Experimental & numerical comparisons) [232]

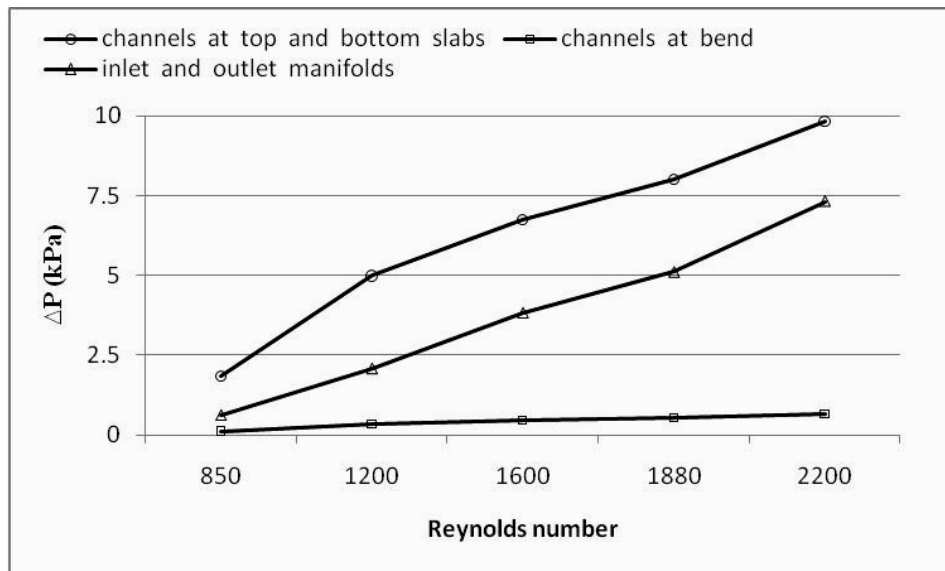


Figure 7.7. Variation of water flow Δp with Re_{ch} (Segment-wise Numerical results) [232]

7.3.2 Heat transfer characteristics

From the measured values of the fundamental parameters, the waterside and airside heat transfer rates, q_w and q_a were deduced using Equations 4.13a and 4.13b. The heat balance between two fluids was performed using Equation 4.14b. The percentile difference of heat transfer rates between two fluids were quite well within the ASME PTC-30 [216] recommended limit of 15%. The waterside inlet to exit temperature differences ΔT_w and the heat rates q_w are plotted against Re_{ch} in Figure 7.8.

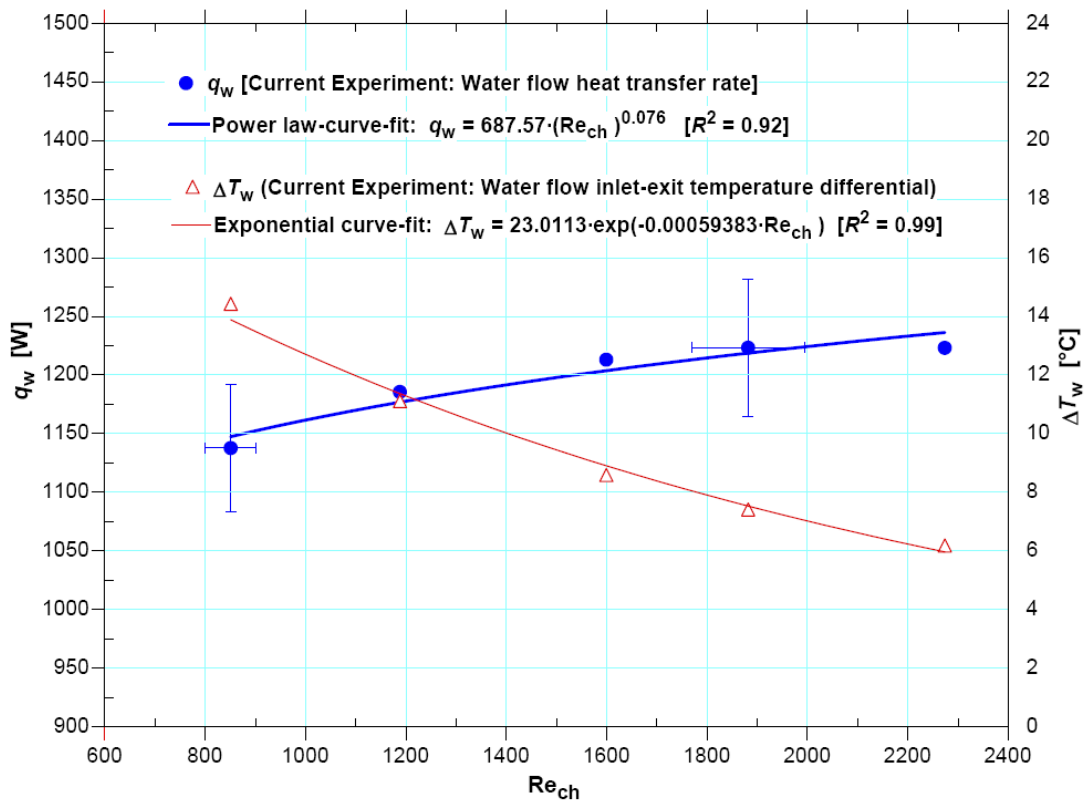


Figure 7.8. Variations of water flow q and ΔT with respect to channel side Re_{ch} .

Expectedly the ΔT_w decreased with the increase of Re. The airside and waterside inlet temperatures were maintained constant. As a result the exit temperature of water flow was driven by the heat transfer mechanism. At lower flow rate and hence at the lower Re the fluid residence time inside the channel is more than what is at higher Re. This dictates the fluid to lose more temperature at lower Re than at higher Re. Therefore the exit temperature is lower at lower Re and higher at higher Re causing the inlet-to-exit temperature difference to be higher at lower Re and lower at higher Re. The ΔT_w and Re relationship in current data can be described well by exponential variation with the goodness of curve-fit coefficient of $R^2 = 0.99$ (Figure 7.8). The measured and the numerically obtained water flow exit temperatures compared very well with the maximum and minimum deviations of only 2.7% and 0.52% [232]. The deviation is higher at lower Re and decreases as the Re increases, which can be explained that the experimental uncertainty in exit temperature measurement is higher at lower temperature driven by the lower Re.

As seen in Figure 7.8, the q_w on the other hand increased with the increase of Re and vice versa, which is also expected. It is known fact that the increase of Re generally increases the q . This can be explained that the decrease of ΔT_w with the increase of Re is adjusted by the increase of mass flow rate in a way that the q increases with the increase of Re. The variation of q_w with Re in current data could be defined by the power law curve-fit, which shows best curve-fit coefficient of $R^2 = 0.92$ than other curve-fits. All the q_w data in the investigated range were captured by this curve-fit line well within the

experimental uncertainty. Good agreement was observed in comparing current q_w data with the numerically obtained q_w results within 7% variation [232].

The measurement of surface temperature for a finned heat exchanger that represents the mean surface temperature is very difficult and not common task. In current study this task was performed by making the inlet, serpentine bend, and the exit portions of the test specimen as zones of no heat transfer (adiabatic) where the probes were placed to measure the surface temperature (described above with illustration). This measurement represented the mean surface temperature very well as seen in Figure 7.9 from the comparison of measured data with numerically obtained results [232]. The maximum deviation between measured data and numerical result was only 0.60%.

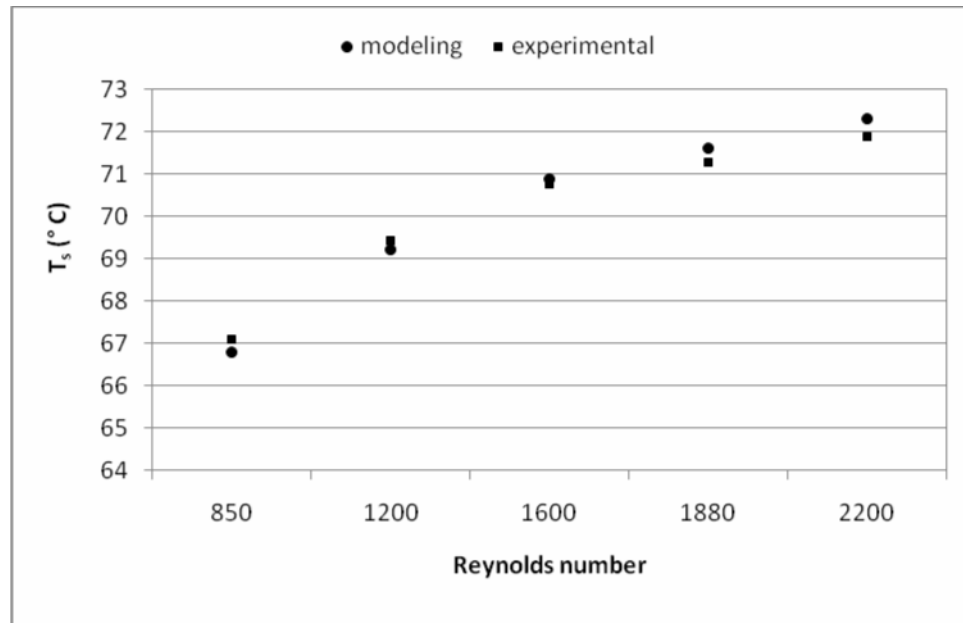


Figure 7.9. Variations of surface temperature with Re_{ch} (Measured data & Numerical results).

From the experimentally measured parameters, the waterside Nusselt number, Nu_w was deduced using Equations 5.11, 5.28, and 5.30. The Nu_w is plotted against Re_{ch} in Figure 7.10. The fully developed laminar Nu for conventional pipe flow, at both T and H boundary conditions, are also charted in Figure 7.10. The experimental Nu increased with the increase of Re showing dependency on Re .

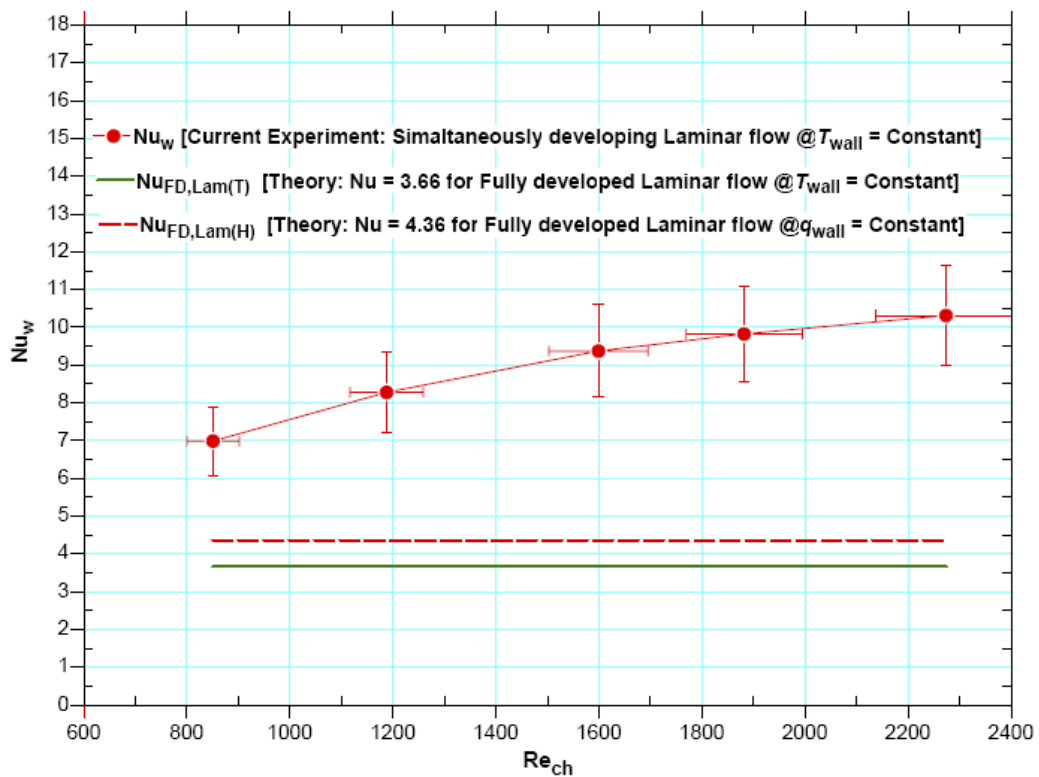


Figure 7.10. Variations of experimental Nu_w with respect to Re_{ch} for Water flow in MCHX-4.

The experimental Nu showed higher values than the fully developed Nu values. This is expected since of the flow steps were neither hydrodynamically nor thermally fully developed before entering the straight flow path of the channels. And the variation of Nu with Re in developing flow should be higher and proven to follow the trend of

Equation 2.12c. All the flow steps however became developed before exiting from the test slabs. It is known fact the Nu is higher in simultaneously developing flow than in hydrodynamically developed but thermally developing flow.

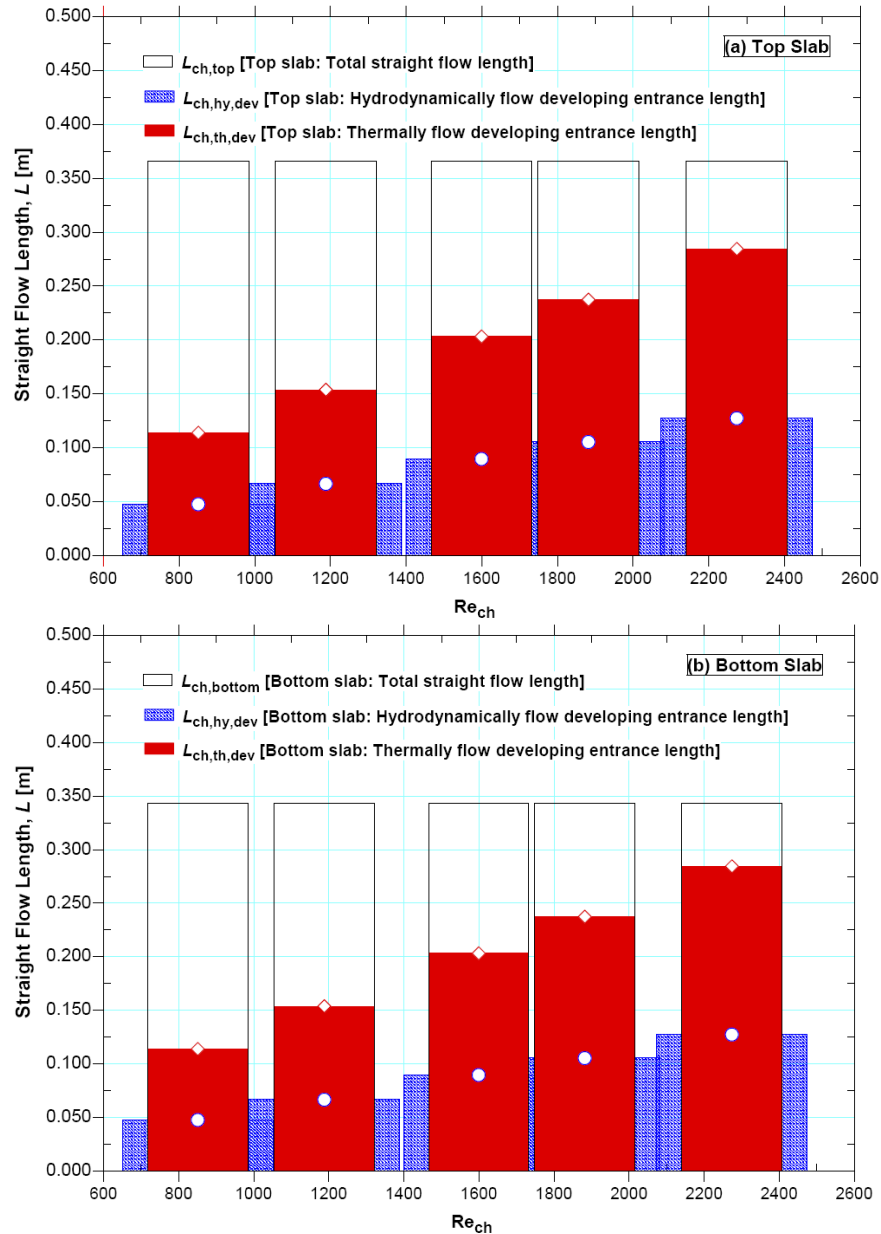


Figure 7.11. Variation of entrance lengths, L_{hy} & L_{th} with respect to Re_{ch} in current experiments. (a) Straight flow path of 1st pass (Top slab), and (b) Straight flow path of 2nd pass (Bottom slab)

The flow steps in current study could be described as simultaneously developing flow, as shown in Figure 7.11. Since the entrance length correlation for microchannel flow is not available, the lengths were estimated from conventional correlations for large diameter pipes using Equations 2.16a and 2.29a. As seen in Figure 7.11, the countable portions of the flows were in the developing zone that caused increased the heat transfer.

The heat transfer is affected by the thermal boundary conditions for flows that are not developed and therefore in addition on Re the Nu also depends on the Prandtl number Pr. The Nu as a function of both Re and Pr are plotted in Figure 7.12. The variation followed a power law relationship with a curve-fit goodness coefficient of $R^2 = 0.97$.

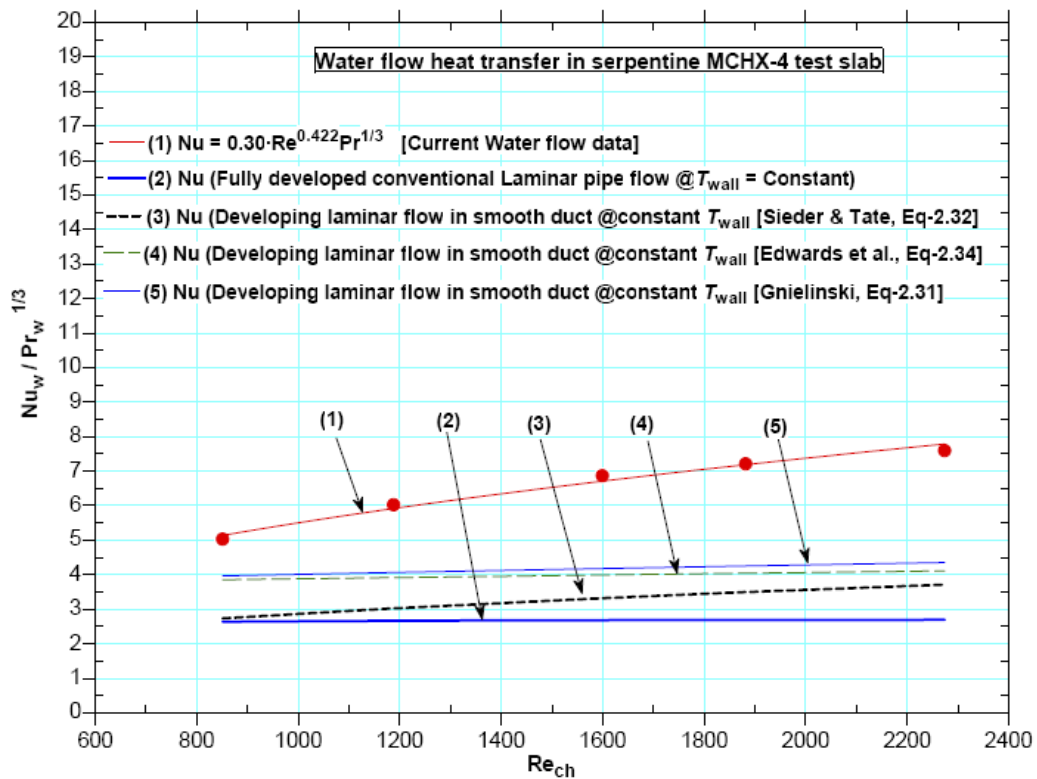


Figure 7.12. Comparison of $Nu_w = f(Re_{ch}, Pr_w)$; Experimental result & available correlations

Some commonly used heat transfer correlations for conventional developing laminar pipe flow are also compared in Figure 7.12. The experimental Nu was significantly higher and none of the correlations could compare current data. The correlations compared in Figure 7.12 were developed with the assumption that the flow is already hydrodynamically developed before entering the heat transfer section. The correlation proposed by Edwards et al. seen by number (4) in Figure 7.12 (Equation 2.34) is recommended to be valid also for simultaneously developing flow [11, 75].

The reasons for higher Nu in current study than conventional correlations could be that the compared correlations themselves since they were not for simultaneously developing flow. The reason could also be that the correlations were developed by taking only one flow developing effect into account for the stream-wise straight flow, which was caused by the flow inlet condition. Whereas two flow developing effects, one at the entrance of each test slab, exist in current study for the same chunk of fluid flow. First developing effect is caused by 90-degree flow turn and area change in the inlet manifold of the top slab and the second and new flow developing effect occurs at the entrance of the bottom slab, which is formed by the presence of serpentine bend.

The adiabatic serpentine segment can be viewed in Figures B2.4a and 2.4c. The presence of this serpentine U-bend at the exit of 1st slab (top slab) and at the entrance of 2nd slab (bottom slab) enhances heat transfer in the test section. Upon exchanging heat and hence losing the temperature, the fully developed fluid streams from the 1st pass (top slab) enter the serpentine bend. The near wall fluid elements lose more temperature

than the centerline fluid particles. For fully developed flow, the centerline fluid particles are the fast moving and the near wall elements are the least moving ones. Inside the serpentine bend the relatively hotter centerline fluid elements move outward to the outer wall of the bend due to centrifugal action, which results in secondary flow pattern. The secondary flow causes the relatively colder least moving fluid particles from the near wall to move toward the centerline and the inner wall of the bend. Therefore all the fluid particles get agitated and well mixed inside the serpentine.

Since no heat transfer occurs around this serpentine, the well mixed fluid particles further exchange heat in the 2nd pass (bottom slab) inside test section. The fluid mixing itself results in increased heat transfer. Due to the presence of U-serpentine new entrance region is formed at the beginning of the 2nd pass (bottom slab). This new entrance region causes the flow to be further simultaneously developing as it passes. The extra heat transfer enhancement acquired in current study could have been attributed to these two effects, which are absent in the compared correlations. The higher Nu in current study as compared to the conventional correlations is therefore reasonable and quite expected. A $Nu_w = f(Re_{ch}, Pr_w)$ correlation for simultaneously developing laminar water flow in circular channels is developed in current study as presented by Equation 7.5. The correlation developed for the investigated range $850 \leq Re \leq 2200$ is expected to be useful in the design of heat exchanger with geometric configuration similar to current study.

$$Nu_w = 0.30 \cdot Re_w^{0.422} Pr_w^{1/3}; \quad 850 \leq Re \leq 2200. \quad (7.5)$$

7.4 Conclusions on water flow

The necessity and importance for thermo-hydraulic studies of liquid flow in an applied geometry in the developing laminar flow regime is described in the literature review in Chapter 3 and in section 6.4.4. Experiments have been conducted on laminar developing hot water flow, in range of $850 \leq Re \leq 2250$, in parallel multi-port microchannel slabs having serpentine U-bend. The tests were aimed at understanding the pressure drop and heat transfer characteristics of the liquid flow in the test specimen and building the experimental database. The experimental data were compared with numerical simulation having the same geometry and operating conditions [232]. Very good agreements between them were found. The experimentally obtained data are provided in Table D3 in Appendix D.

For the investigated range, the experimental Δp linearly increased with the increase of Re , which compared very well with numerical results. The core pressure drop estimated from general formulation cannot predict current core pressure drop. Current core pressure drop isolated from measured pressure drop using a comprehensive pressure balance model, as described in section 6.1, compares the theoretical pressure drop line well. Kasagi et al. [233] one-third approximation of total pressure drop could roughly estimate the channel side pressure drop. The highest pressure drop occurred in the straight parts of the channel due to flow friction and the next highest occurred in the inlet and exit manifolds. At the serpentine U-bend the pressure drop was however the least,

which is beneficial for heat transfer. This is because the bend mixes the fluid stream and also creates a second flow developing or entrance effect at the inlet of the 2nd slab (2nd pass). This means that the existence of this type of serpentine bend with parallel multi-port flow channels in a heat exchanger will promote the heat transfer with less pressure drop tax; as compared to the heat transfer enhancement and pressure drop penalty attributed to the entrance effect caused by the inlet manifolds.

The waterside heat transfer rate increased with the increase of Re in a power law manner. The inlet to exit temperature differences decreased exponentially as the Re increased. As the Re increased the Nu also increased and the dependency could be well described by the power law relationship. Current test condition was simultaneously developing. The conventional correlations for developing laminar flow could not predict experimental Nu data. Current Nu was higher than the conventional fully developed or hydrodynamically developed but thermally developing Nu values. The near wall and far wall fluid elements from the 1st pass get well mixed in the serpentine bend before entering the 2nd pass. New temperature profile is created via the flow reversal. Since the serpentine is adiabatic, the mixed fluid exchanges heat only in the test section at the 2nd pass. The presence of serpentine bend creates a new entrance condition at the beginning of the 2nd pass, which causes another step increased heat transfer. Therefore the higher Nu in current study is expected and reasonable.

The existence of serpentine U-bend in multi-port flat slab enhances more heat transfer with less pressure drop penalty as compared to the entrance condition caused by

the inlet manifold when flow enters the channel inlet at beginning of the flow. From current data, a Nu versus Re and Pr correlation is developed. The acquired experimental data and the findings in this study will be useful in further research in this area and in the design of heat exchanger using multi-port microchannel slab.

CHAPTER – 8

HEAT TRANSFER AND PRESSURE DROP CHARACTERISTICS OF ETHYLENE GLYCOL-WATER MIXTURE FLOW IN 2-PASS MULTI-PORT SERPENTINE MICROCHANNEL SLAB HEAT EXCHANGER

8.0 HEAT TRANSFER AND PRESSURE DROP CHARACTERISTICS OF ETHYLENE GLYCOL-WATER MIXTURE FLOW IN 2-PASS MULTI-PORT SERPENTINE MICROCHANNEL SLAB HEAT EXCHANGER

Many practical heat exchangers use multi-port configurations as their core and ethylene glycol-water mixture as the heat transfer fluid, such as automotive and HVAC industry to name a few. Some works on large diameter pipes are available for hydrodynamically developed but thermally developing laminar flow using water as the fundamental working fluid. Such studies in narrow channels with continuous smooth serpentine bend are scarce. Narrow channel heat exchangers experience simultaneously developing laminar flow because of their short flow path (miniature device).

Study of ethylene glycol-water mixture flow in a simultaneously developing laminar regime in this type of applied geometry, to the best of candidate's knowledge, is not available in the open literature. Therefore experiments have been conducted on 50% ethylene glycol-water mixture flow in parallel multi-port serpentine microchannel test slab (MCHX-4) in 2-pass flow configurations with U-type serpentine bend. The experimental findings and pressure drop and heat transfer data are presented in this chapter. The findings and results from this experiment are documented through peer reviewed publication [234].

8.1 Methods of experiments and measurements

The details of the experimental facility instrumentation and calibration, and the test procedures in general are provided in Chapter 4. The rest details are described above in section 7.1 in water flow study. The status of the flow i.e. whether developed or developing before and after entering the heat transfer test section, was estimated from the conventional hydrodynamic entrance lengths relationship using Equations 2.16 and 2.25.

As shown in Figure 7.1, the hot liquid (here glycol-water mixture) flow entered the inlet at 'A' and took a 90-degree flow turn to the left from the inlet manifold. From the inlet manifold the stream equally distributed through all the 68 channels and flowed towards the entrance of the serpentine bend (end of 1st pass). The liquid flow is reversed by the serpentine bend. The streams then flowed back (2nd pass) to the exit manifold where they are combined together and exited at 'B'. The wind tunnel cold air on the other hand flowed inside the test chamber across the test specimen along positive Z-direction. The heat transfer took place between glycol-water mixture and the air within the effective heat transfer test section in the test chamber (see Figure B2.4a).

The heat transfer and pressure drop parameters were measured similar to the process as water flow (section 7.1). All the measurements were taken at steady state condition, which for current study, is explained in section 4.7. The data were monitored and recorded into a DAQ system.

8.2 Treatment and separation of pressure losses in the test slab

The ethylene glycol-water mixture flow in current study used the same test specimen (MCHX-4) as the water flow in Chapter 7. The temperature and pressure sensors and the measurement locations are also the same. Therefore the treatments of pressure drops and the separation of all the losses from the measured total pressure drop follow the same pressure balance model as described in section 7.2 in Chapter 7 and in section 6.1 in Chapter 6. The segment-wise pressure drops route is illustrated in Figure 7.2 and the calculation procedures are described via Equations 7.1 to 7.4.

8.3 Results and discussions on glycol-water mixture flow

In order to obtain the general pressure drop and heat transfer data and the nature of the test fluid, experiments have been conducted on 50% ethylene glycol and water solution in a serpentine microchannel slab (MCHX-4) having 68 individual channels of 1 mm diameter. The Reynolds number effects on pressure drop, heat transfer, test specimen NTU and effectiveness, overall thermal resistance, and on the Nusselt number are documented in peer-reviewed publication [234], which are presented in this section.

Hot glycol-water solution was pumped through the test slab Reynolds number range between 400 and 1800 and the cold wind tunnel air was blown over the test slab with a constant velocity of 16.7 ± 0.2 m/s. The hot glycol-water inlet temperature to the test specimen was maintained at $76.0 \pm 0.4^\circ\text{C}$ and the bulk temperature of the cold wind tunnel airflow was kept constant at $9.0 \pm 0.2^\circ\text{C}$. The glycol-water mixture flow in the test slab was in the simultaneously developing laminar flow regime.

The inlet temperature of liquid was maintained using heater controller (Figures 4.1 and 4.10). To employ the Wilson Plot Technique, it was required to keep the airside bulk flow temperature constant. It was realized by manipulating the cold water flow rate through the wind tunnel built-in internal heat exchanger (Figure B4.b) using the flow mixing network (Figure 4.6). The liquid side flow rates on the other were varied and maintained by means of variable speed gear pump (Figures 4.1 and 4.9) and a needle

valve (Figure 4.1 and B4.e). At each flow rate, several thousands of steady state samples were collected using DAQ system and their mean and standard deviations were recorded. A single data set in current study i.e. the TAMDS was acquired using Equation 4.12.

The glycol-water mixture flow inside the channels is the focus of current study. Assumptions were made that the liquid is an incompressible Newtonian fluid and its properties are independent of pressure but the functions of temperature. Since the hydraulic diameter of the distributing manifold was about 10 times larger than the diameter of a channel, the liquid was assumed to be equally distributed through all the channels in the test slab. This assumption was reasonable based on the explanations provided in section 7.3 via Figures 7.3 and 7.4 and also according to [235].

Dehghandokht, Mesbah, and co-workers (2011) numerically studied water and 50% glycol-water mixture flows in current test specimen with the same geometry and same experimental operating situations as the boundary conditions [235]. They compared the numerical results for water and glycol-water mixture with current experimental data set. The numerical model compared current data and the experimental findings well. The glycol-water mixture mass flow rate also was well distributed through all the channels in the test slab from the inlet manifold as can be seen in from Figure 8.1 [235]. This justifies the assumption of equal flow distributions in all the channels. The flow directions and the channel number designations for Figure 8.1 is given in Figure 7.4.

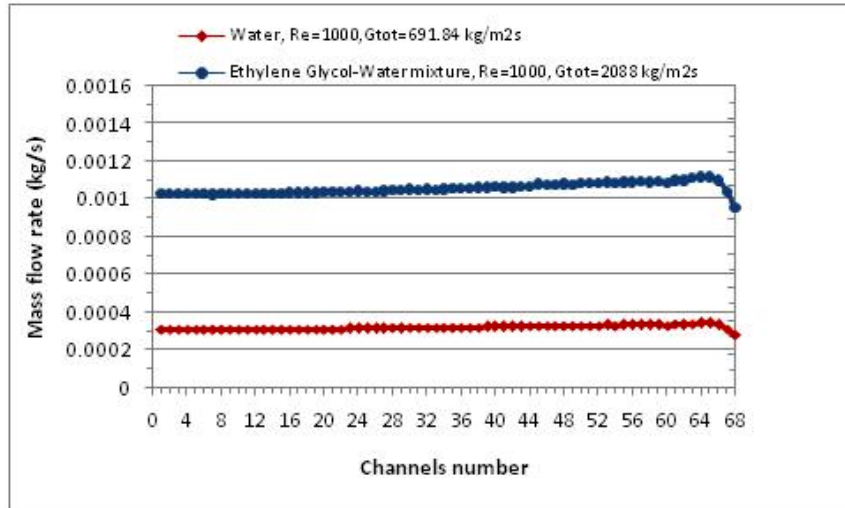


Figure 8.1. Flow distribution of water and glycol-water mixture through the channels in MCHX-4 test slab (numerical simulation [235]).

The flow distributions in Figure 8.1 followed the patterns of Figure 7.3. There is a little drop in flow through channel numbers from 68 to 66. This can be explained by the expansion and change of momentum in flow due to area change since the tube diameter before the inlet manifold is smaller than the diameter of the inlet manifold itself. At the entrance of the inlet manifold (around channels 68 to 66), due to increase in flow area the flow gets decelerated (Figure 7.4). In an expanded flow, the fluid streams around the corner edges also experience flow turn-around (reverse flow / circulation) and often the effect of secondary flow causing slightly less quantity of fluid flow in these areas. A little lower mass flow rate in channels 68 to 66 has happened because of the above reasons. The lower flow in these three channels however has insignificant effect on the average of total 68 channels. Therefore the consideration of mean single channel flow as the average of all 68 channels was reasonable.

The primary independent parameters i.e. the mass flow rate and inlet and exit temperatures and pressures of the liquid flow; and the velocity and inlet and exit temperatures and absolute pressure of the air flow were directly measured for 20 different operating conditions. The thermophysical properties were evaluated at the bulk flow temperatures. The glycol-water solution properties were derived from the ASHRAE Handbook of Fundamentals 2005 [212] and for the air they were evaluated from EES built-in property functions [218].

In view of Equation 2.1, the channel side (liquid flow) Reynolds number, Re_{ch} in a single channel of the test slab was calculated using Equations 4.15, 5.6 and 6.2. The forced convection heat transfer rates of liquid and the air flows were computed from Equations 5.11 and 4.13b. The derivation methods for other dependent parameters are provided next in respective section. The uncertainty analyses were carried out in light of the Editorials of ASME Journal of Heat Transfer and Journal of Fluids Engineering [25-26] as described in Section 5.6. The estimated mean uncertainties for some liquid side key parameters are given in Table 8.1.

Table 8.1. Mean experimental uncertainty in the study of glycol-water mixture flow

Parameters	Mean uncertainty
Measured pressure drop, $\Delta p_{total, g}$ [Pa]	$\pm 6.7 \%$
Measured total mass flow rate, \dot{m}_g , [kg/s]	$\pm 1.35 \%$
Reynolds number in a channel in test slab, Re_{ch}	$\pm 6.0 \%$
Nusselt number, Nu_g	$\pm 12.5 \%$

8.3.1 Total, core and segment-wise pressure drops

The pressure drops in the core of MCHX-4 (straight top and bottom slabs) were separated from the measured total pressure drop using Equations 6.2 to 6.16 and 7.1 to 7.4 according to the flow route shown in Figure 7.2. The pressure drop along the core of the test slabs was empirically isolated from Δp_{total} as per estimation and approximation used by Jokar et al. [200] and Kasagi et al. [233]. To determine the core pressure drop, Jokar et al. [200] deducted only the manifold pressure losses from the total measured pressure drop and Kasagi et al. [233] approximated the core pressure drop to be the one-third of the total measured pressure drop. The theoretical Δp for fully developed conventional laminar pipe flow for current test conditions was deduced from Equation 6.19. The core pressure drop varied from 25 to 80 kPa/m of the flow length.

The glycol-water side total measured pressure drops, Δp are plotted against Re_{ch} in Figure 8.2. The measured total Δp non-linearly increased with the increase of Re , which is reasonable since it includes the core and other pressure losses. The theoretical, experimental, estimated, and approximated core pressure drops as well as the separated segment-wise pressure drops for the inlet and exit manifolds and for the serpentine bend are also plotted in Figure 8.2. All the Δp increased with the increase of Re except for the manifold, which increased non-linearly. The non-linear variations may be due to the flow development effects since the Δp is always higher around the entrance regions.

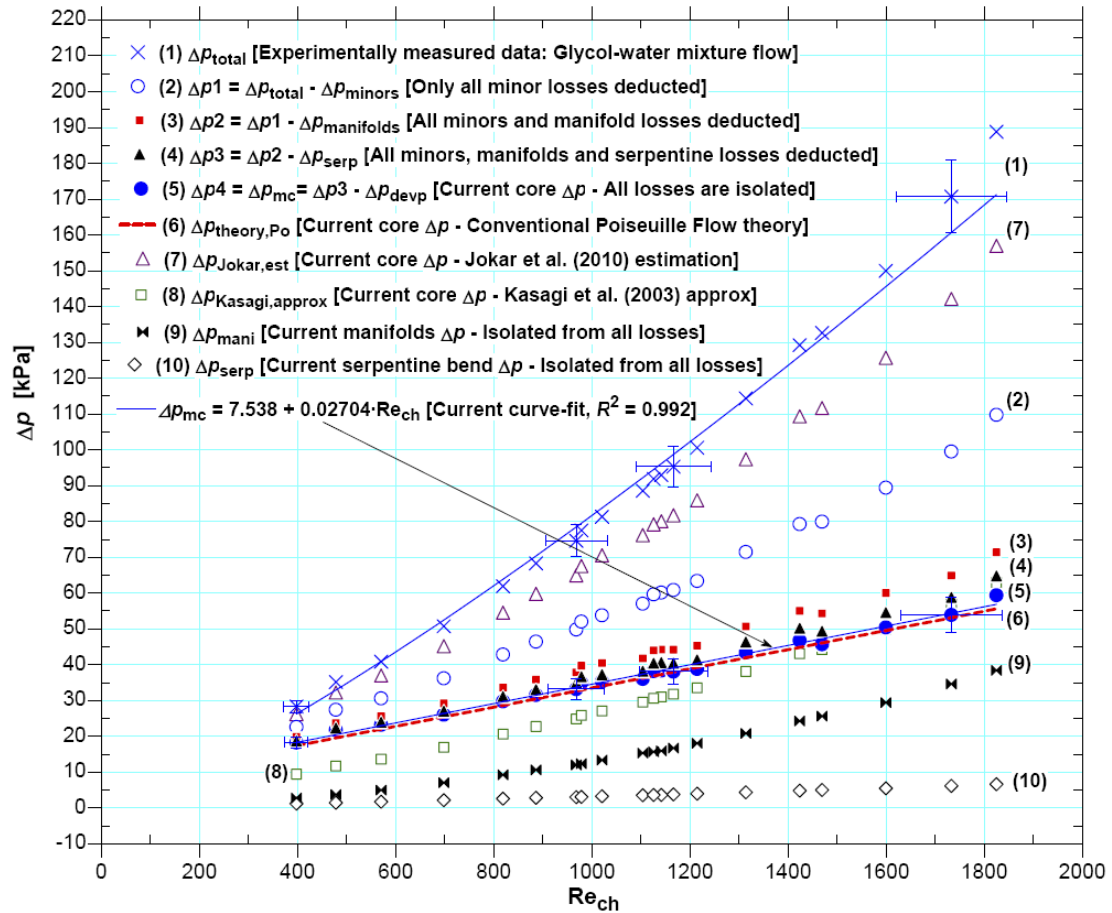


Figure 8.2. Variations of segment-wise glycol-water mixture flow Δp with respect to Re_{ch} .

Kasagi et al. [233] approximation showed closeness to the Poiseuille theoretical Δp as well as to the current core Δp better than Jokar et al. estimation; it however underestimated the Δp for the most part of the investigated range. Jokar et al. [200] estimation overestimated current core Δp . This may be because their channels had some bumps that affected the core Δp and their approximation possibly only valid in their test situations. The method used by Jokar et al. [200] could not predict the core Δp for current

test specimen. This is because deducting only the manifolds' pressure losses from the total measured pressure drop is not sufficient to get the core pressure drop. Other possible losses must be taken into proper account.

The step-by-step pressure isolation from that of the measured total pressure drop is shown in Figure 8.2. Data no. 2 is the Δp that excludes all the minor losses but includes the core, manifold, serpentine bend, and flow development losses. Data no. 3 excludes all the minor losses and inlet and exit manifold losses but includes the core, serpentine bend, and the flow development losses. Data no. 4 excludes all the minor losses, inlet and exit manifold losses, and serpentine bend losses. The core Δp still includes the flow development pressure defects. Data no. 5 is the final core Δp after isolating all the possible losses. Current core Δp compared very well with the theoretical Δp line when all the losses were properly treated and isolated from the measured total Δp . This signifies that improper pressure balance will lead to an error or differing result.

Other noticeable findings in current study are that the highest pressure drop occurred in the straight flow path (top and bottom slabs), next highest occurred in the manifolds, and the least loss was incurred by the serpentine bend. These findings are inline with the findings in water flow above. This shows that the pressure drop penalty at serpentine portion is less than the manifold side. The serpentine portion helps mixing of fluid streams inside bend and also initiates second flow developing effect at the entrance of the bottom slab, which are particularly beneficial for heat transfer in a heat exchanger.

8.3.2 Heat balance between glycol-water mixture and air

The glycol-water side and the airside heat transfer rates, q_g and q_a were calculated from Equations 5.11 and 4.13b. The air side heat rates are plotted in Figure 8.3 against glycol-water side heat rates in order to compare the deviations. The data followed a linear variation with some scatters within $\pm 2.6\%$. Ideally the heat rates should be the same i.e. $q_g \approx q_a$ since the heat released by one is taken away by the other. However, practically this is rarely the case because of the existence of errors in system response, experiments, heat leakage etc. To address this variation, the heat balance procedures described in sections 4.8 and 5.3 are followed.

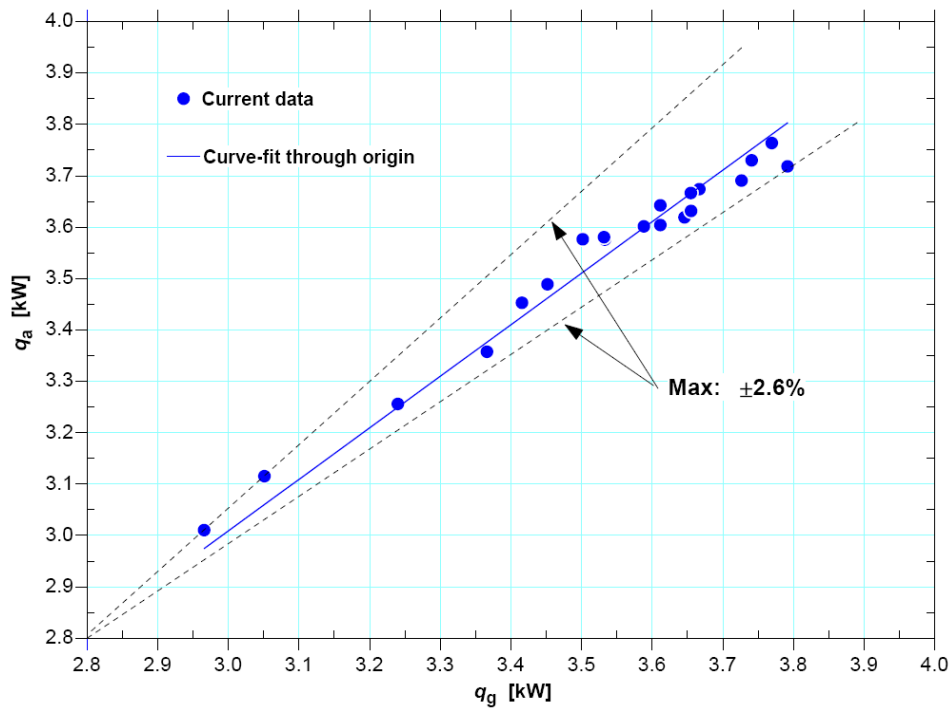


Figure 8.3. Deviations of airside heat transfer rate from that of glycol-water side

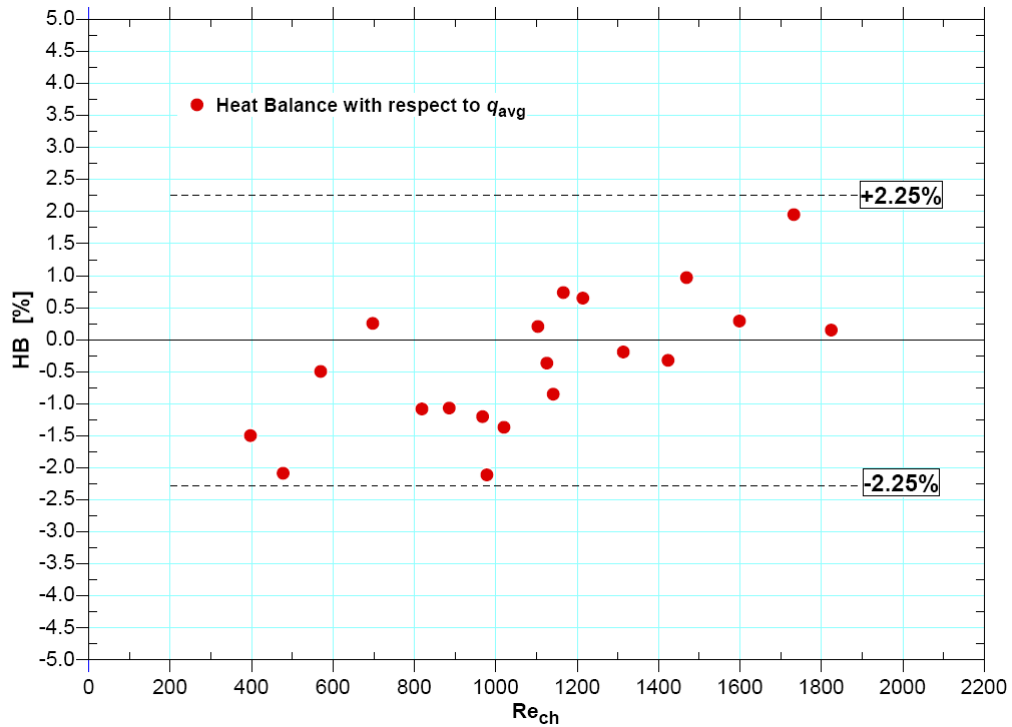


Figure 8.4. Heat balance between two fluids (glycol-water mixture & air) with respect to Re_{ch} .

According to ASME PTC-30-1991 [216], the percentage difference between the heat lost by the liquid and that gained by the air is defined as the heat balance (HB) in current study, which is expressed by Equation 4.14b. The HB results are presented in Figure 8.4 with respect to Re_{ch} . From q_{avg} the deviations of q_g were observed to be from -2.11% to +1.95% and that for q_a from -2.13% to +1.93% respectively. The differences were within only a maximum deviation of $\pm 2.25\%$. This very good HB not only shows the integrity of the developed test facility, it also demonstrates the reliability and accuracy of the acquired experimental data.

The ASME PTC 30-1991 recommends an acceptable limit of $\pm 15\%$ for which any of the heat rates i.e. q_g , q_{avg} , or q_a can be used for heat transfer calculations. Because of using ultra precise RTD for liquid side temperature measurements, as more reliable choice, the liquid side heat rate q_g was taken in subsequent calculations in this study.

8.3.3 Heat transfer rate and temperature variations

The overall log-mean temperature difference ΔT_{LMTD} is calculated from Equation 5.15. The surface temperatures are measured using 48 thermocouple probes whose locations can be viewed in Figure B8.4a. The mean T_s is consolidated using Equation 5.10b. The measurement of surface temperature for a finned heat exchanger is a difficult task. In current study a method is devised to perform this job, which is described in sections 5.2.3 and 7.2.2. This measurement approach could represent the mean surface temperature very well as has been shown in Figure 7.8 [232].

The liquid side inlet to exit temperature differential ΔT_g , the ΔT_{LMTD} , and the T_s are plotted with respect to Re in Figure 8.5. Expectedly the ΔT_g decreased with the increase of Re . The variation followed a power relationship with negative exponent. The airside bulk and glycol-water side inlet temperatures were maintained constant. As a result the exit temperature of glycol-water flow was dictated by the heat transfer mechanism. At the lower flow rate and hence at the lower Re the fluid residence time

inside the channel is more than the higher Re. This allows the fluid to lose more temperature at lower Re than at higher Re. Therefore the exit temperature becomes lower at lower Re and higher at higher Re thereby causing the inlet-to-exit temperature difference to be higher at lower Re and lower at higher Re. The ΔT_g dependency on Re could be described by exponential variation with a curve-fit coefficient of $R^2 = 0.995$.

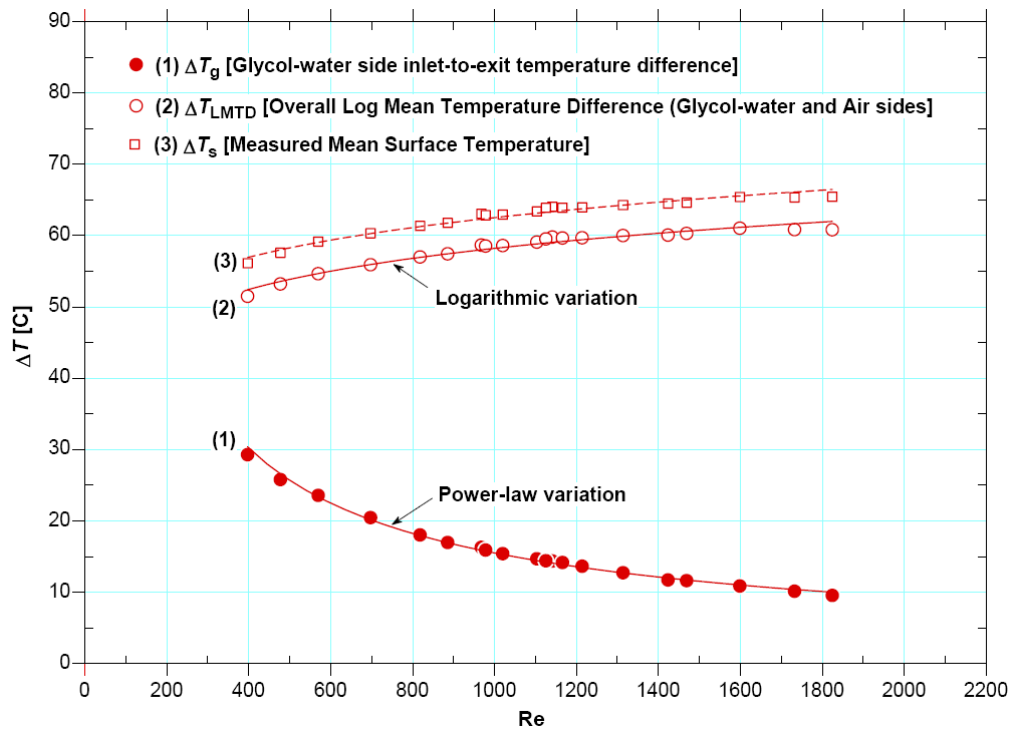


Figure 8.5. Variations of temperatures (ΔT_g , ΔT_{LMTD} and T_s) with respect to channel side Re.

As seen in Figure 8.5 the ΔT_{LMTD} and the T_s both increased with the increase of Re. This is also expected because the ΔT_g is higher at lower Re, which keeps the heat exchanger wall surface colder at lower Re. As Re increases the ΔT_g decreases meaning less temperature exchange and therefore the surface gradually becomes hotter at higher

Re. The dependency of T_s and ΔT_{LMTD} on Re in current data could be defined by power law and logarithmic variations.

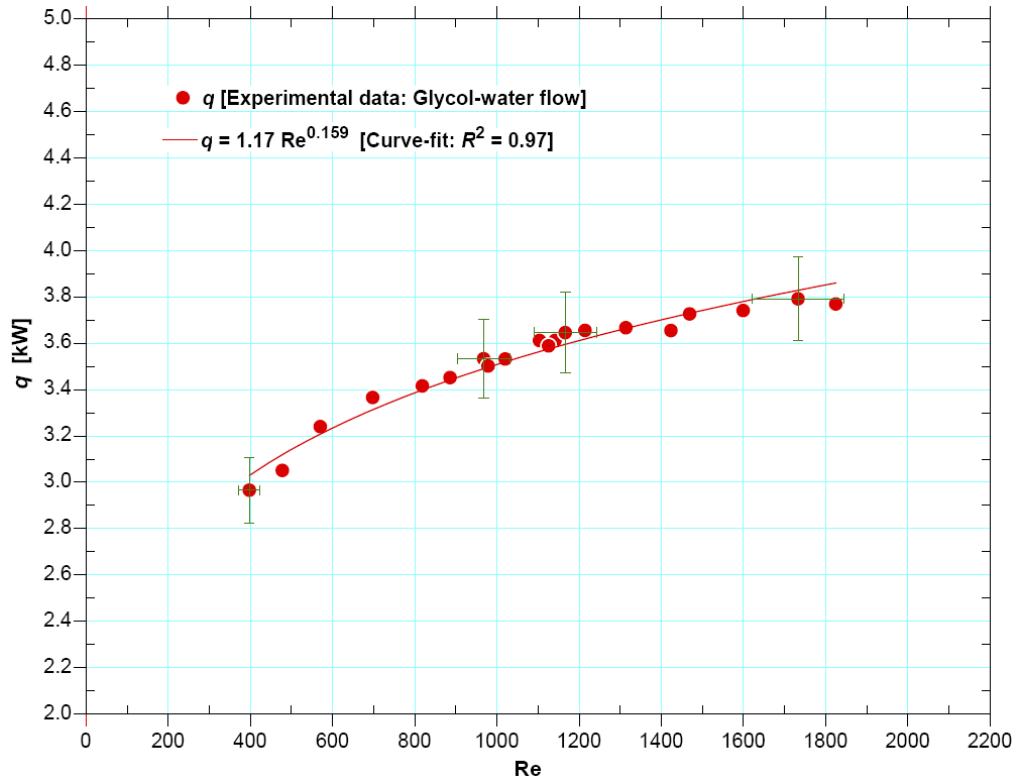


Figure 8.6. Variation of q_g with respect to channel side Re.

Determined from Equation 5.11, the heat transfer rate q_g is plotted against Re_{ch} in Figure 8.6. As expected the q_g increased with the increase of Re and vice versa. This can be explained that the decrease of ΔT_g with the increase of Re is compensated by the increase of glycol-water mass flow rate in a way that the q increases with the increase of Re. As compared to other curve-fits, the variation could be best described by a power-law relationship with an R^2 value of 0.97. Few scatters in data are seen at relatively higher Re,

which might have generated from little flow and temperature fluctuations during experiments. The deviations are however well within the experimental uncertainty. On an average about 4 kW of heat transfer could be achieved from the test slab with an LMTD of 61°C within current test conditions.

8.3.4 The NTU and Effectiveness of the test specimen

The effectiveness ε and NTU for the test specimen are determined using Equations 5.24 through 5.27 and are plotted with respect to channel side Re in Figure 8.7. Both ε and NTU monotonically decreased with the increase of Re. The ε decreased from 0.43 to 0.14 and the NTU from 0.57 to 0.16. For a given operating condition, especially the flow regime such as the Re, Figure 8.7 can provide values of both ε and NTU for a heat exchanger. This sort of presentation helps in designing and in operating a heat exchanger for a chosen flow regime based on a given condition.

In Figure 8.8 the heat transfer rate q_g and the isolated core pressure drop Δp_{mc} both are plotted against the ε . Both the q_g and Δp_{mc} both decreased when the ε increased. The q_g decreases linearly and Δp decreases in power-law manner. At higher effectiveness both the q_g and Δp_{mc} are lower and at the lower effectiveness they both are higher. This means that at lower flow rate and hence at lower Re the heat transfer rate is lower as well as the core pressure drop is also lower. This kind of parametric representation is common in heat exchanger subject area [187]. This plotting helps in designing a heat exchanger

and in optimizing an operating point for a particular chosen duty. The trends of current results in Figure 8.8 showed excellent qualitative agreement with Kang and Tseng [187].

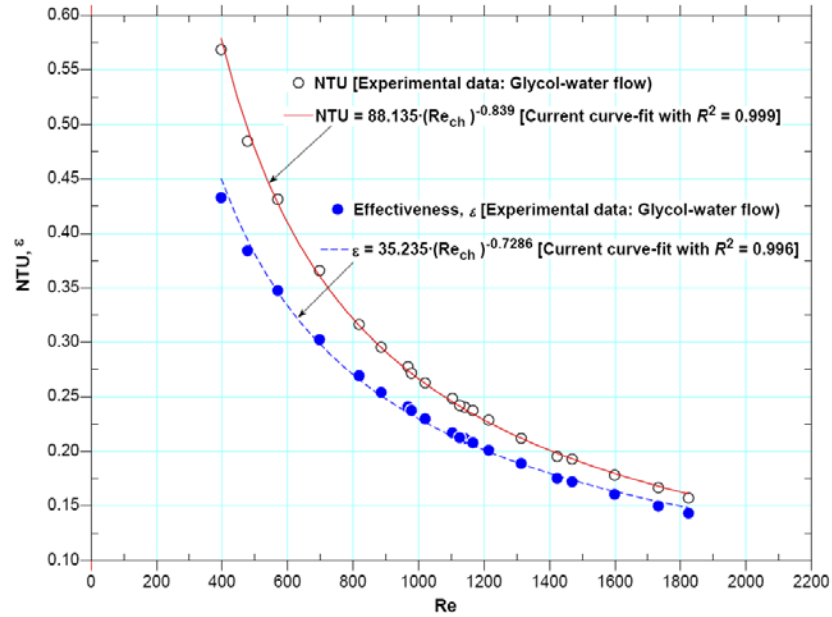


Figure 8.7. Variations of NTU and effectiveness with respect to channel side Re .

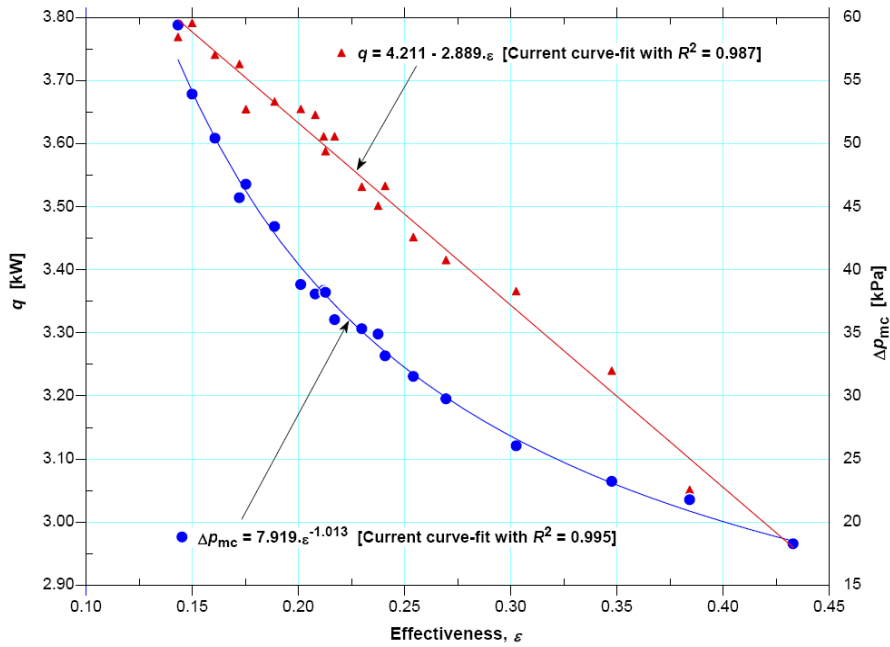


Figure 8.8. Variations of glycol-water side q_g and Δp with respect to test slab effectiveness.

8.3.5 Overall thermal resistance ($R_{th,ov} = 1/UA$)

The overall thermal resistance $R_{th,ov}$ based on experimentally measured parameters was calculated from Equations 5.17 and 5.18. The same $R_{th,ov}$ was also predicted for current test conditions using Khartabil and Christensen [224] improved scheme of modified Wilson Plot Technique. The modified Wilson Plot Technique was proposed by Briggs and Young [221]. The details of the original, modified and improved scheme of Wilson Plot Technique are described in section 5.5 and the applicable experimental procedures are provided, which were followed in current study.

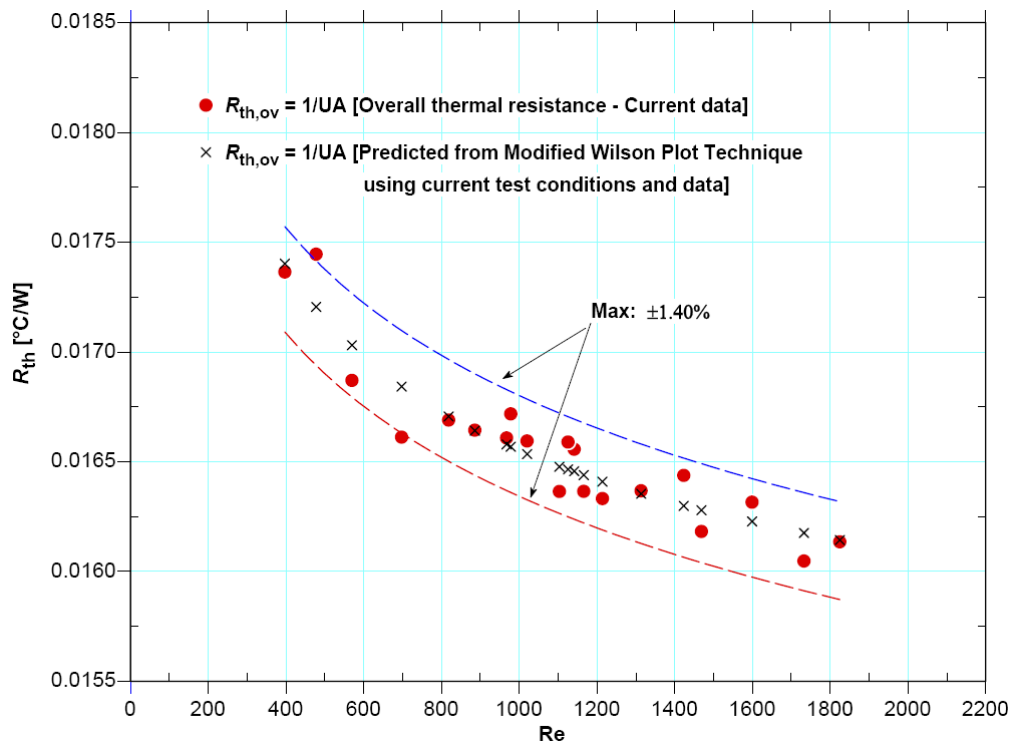


Figure 8.9. Variation of overall thermal resistance $R_{th,ov}$ with Re_{ch} (Current data & Wilson Plot)

The $R_{th,ov}$ for measured data and that predicted from Wilson Plot Technique are plotted against channel side Re in Figure 8.9 . Both the $R_{th,ov}$ asymptotically decreased with the increase of Re . The $R_{th,ov}$ predicted from Wilson Plot Technique was well bounded by the scatters in experimentally measured $R_{th,ov}$ data. The maximum deviation between the measured and the predicted results was no more than $\pm 1.50\%$. This closeness of results in $R_{th,ov}$ provides supports the better accuracy of experimentally measured data.

8.3.6 Nusselt number characteristics

The glycol-water flow experimental Nusselt numbers Nu_g were deduced in two ways; one from liquid side using Equations 5.11, 5.28 and 5.30 and the other via airside using Equations 5.18, 5.20, 5.22, 5.23, and 5.29. They are plotted against channel side Re in Figure 8.10. As expected the Nu increased with the increase of Re and the variations followed power-law relationships. At low Re some differences are observed in Nu data between. These variations can be explained that the airside heat transfer rate was used for airside thermal resistance and there is already a little difference ($\pm 2.25\%$) between airside and liquid side heat transfer rates as seen in the heat balance section (Figure 8.4). In addition to this, since more parameters are involved in airside thermal resistance calculation, little more experimental errors have contributed to these differences. At higher Re , the differences are however less.

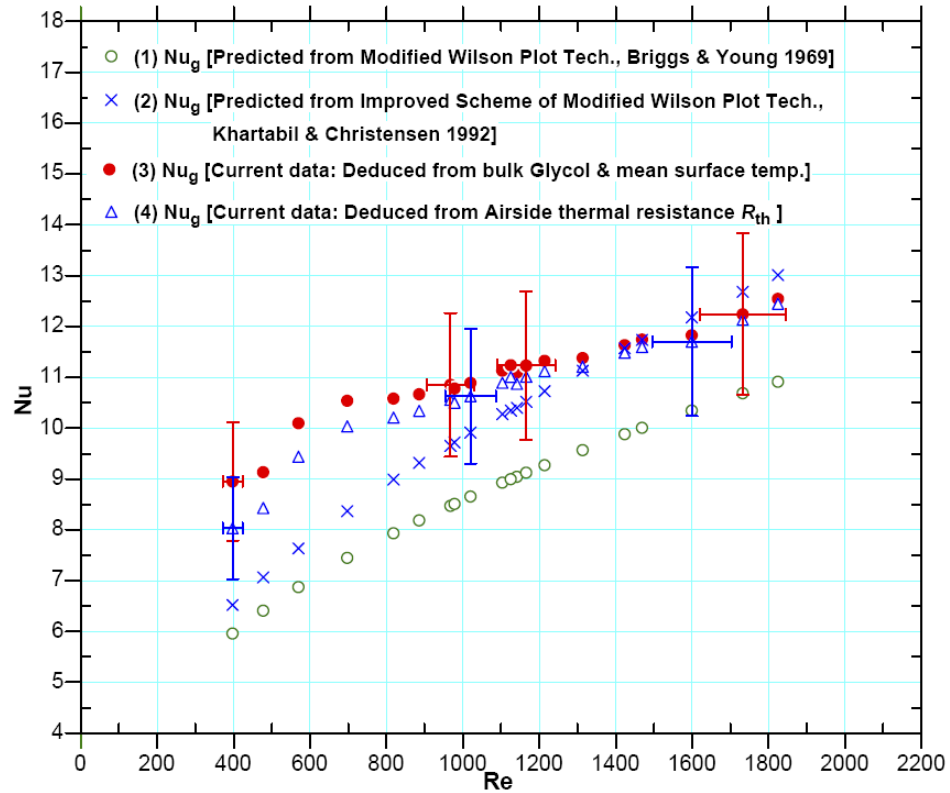


Figure 8.10. Variation of Nu_g with respect to channel side Re (Current data & Wilson Plot)

For current test conditions the Nu_g were also predicted from Briggs and Young [221] proposed modified Wilson Plot Technique and from Khartabil and Christensen [224] improved scheme using Equations 5.31 to 5.38. For the interest of comparison, they are also plotted against Re in Figure 8.10. Briggs and Young [221] prediction (Equations 5.40 to 5.42) underestimated the Nu , which are lower than both the experimental data and the prediction from Khartabil and Christensen [224] scheme (Equations 5.33 to 5.39). In Briggs and Young proposed modified Wilson Plot Technique, the non-linear equations were solved through two successive linear regression analyses.

Some of the Khartabil and Christensen experimental data sets could not produce expected result using Briggs and Young such regression model. Because of this variation in prediction, Khartabil and Christensen proposed an improved scheme to solve the non-linear equations using non-linear regression analyses, which eventually produced good results. Therefore their scheme is used in current study.

All the experimental Nu values are higher than the Briggs and Young prediction. They are higher than Khartabil and Christensen scheme only in the range $400 \leq Re \leq 1300$. Above this range the Nu values overlap with each other. There are some scatters in experimental Nu data more in the range $400 \leq Re_g \leq 1300$ and less thereafter. This can be explained that the T_s were more stable at higher Re than at lower Re. As seen from the error bars in Figure 8.10, the experimental Nu data can be bound by the values predicted from Khartabil and Christensen scheme. The Briggs and Young prediction could not compare current data even within the scope of experimental uncertainty.

The heat transfer is influenced by the thermal boundary conditions for flows which are not developed and therefore in addition on Re the Nu also depends on the Prandtl number Pr. To account for the effect of Pr, the Nu as a function of both Re and Pr i.e. $Nu = f(Re, Pr)$ are plotted in Figure 8.11. The variation followed a power law relationship similar to Equation 5.31. In Figure 8.11 experimental Nu result is compared with available conventional and microchannel flow correlations. None of the conventional or microchannel correlations could compare experimental Nu data. Current results are higher than fully developed conventional laminar flow at T ($Nu_T = 3.66$) and H

($Nu_H = 4.36$) boundary conditions and also higher than the conventional thermally developing laminar flow correlation with T-condition proposed by Gnielski [77]. This correlation was developed with the assumption that the flow is already hydrodynamically developed before entering the heat transfer section. One can expect higher Nu in simultaneously developing flow (current data) than a flow which is only thermally developing (Gnielinski correlation [77]).

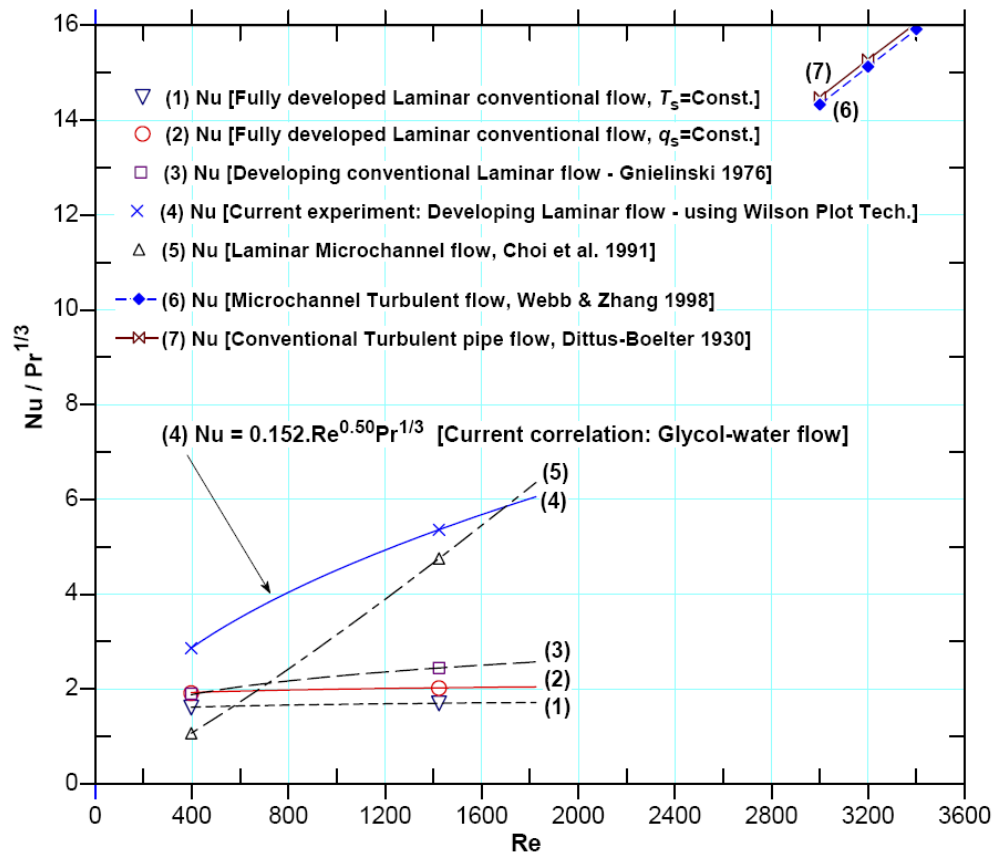


Figure 8.11. Variation of Nu_g with channel side Re and Pr (Comparisons of Current data with available correlations)

Choi et al. [88] proposed correlation for laminar microchannel flow underestimated the Nu for the entire Re range and crossed current Nu data for $Re > 1600$, which is not a comparable correlation. The Dittus and Boelter [57] correlation for conventional turbulent pipe flow and Webb and Zhang [125] correlation for turbulent flow in microchannel predicted much higher Nu than current data. This indicates that, although the laminar flow Nu is higher in current study, its trend do not follow the trend of turbulent flow heat transfer as found by Jokar et al. [200].

Several factors may be responsible for the higher Nu values in present study such as: the presence of smooth U-type serpentine bend, internal narrowness at the entrance and exit manifold connectivity due to manufacturing imperfections, inner channel shrinking due to bending around serpentine, flow developing nature in narrow channels could be different from the conventional formulation of $L_{th} = 0.056Re.Pr.D$ etc. However, the candidate believes that the presence of serpentine bend and twice the effect of flow developing are the major reasons.

The reason for predicting lower Nu by the compared correlations could also be that the compared correlations were developed by considering only one flow developing effect into account for the stream-wise straight flow path (caused by the flow inlet condition only). Whereas two flow developing effects, one at the entrance of each test slab, exist in current study for the same fluid flow. First developing effect is caused by 90-degree flow turn and area change in the inlet manifold of the top slab and the second

and new flow developing effect occurs at the entrance of the bottom slab formed with the presence of serpentine U-bend.

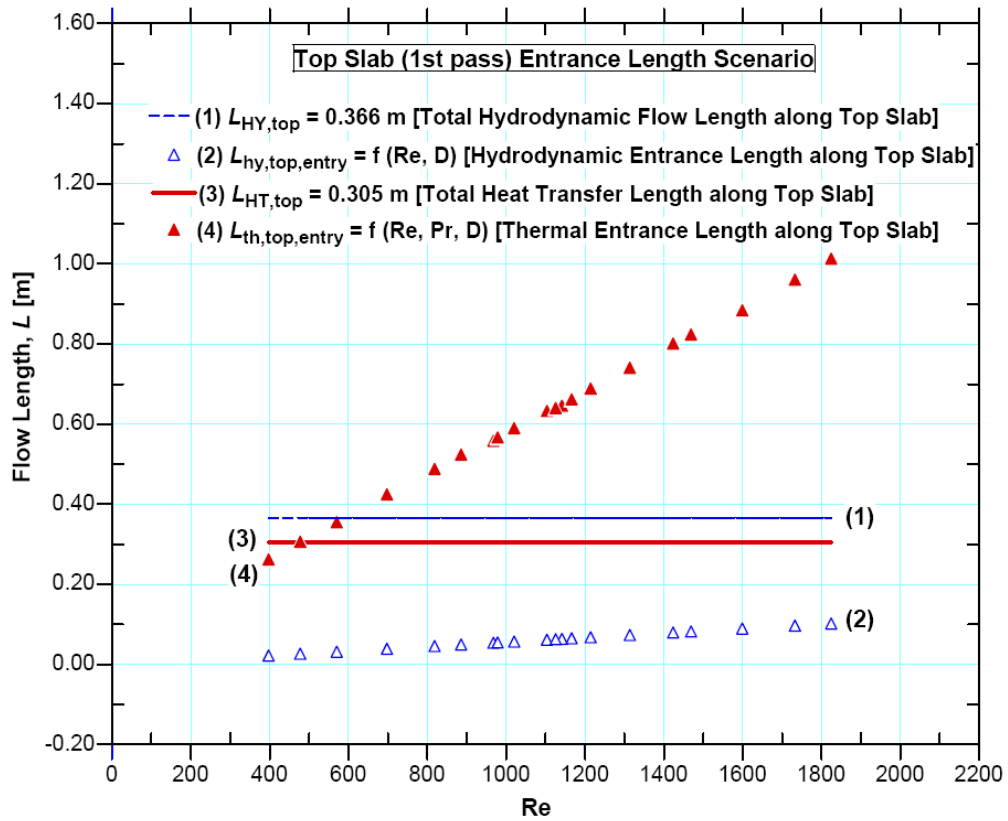


Figure 8.12. Range of current hydrodynamic and thermal entrance lengths with respect to Re

Since the entrance length correlation for microchannel flow is not available, these lengths were estimated from conventional correlations for large diameter pipes using Equations 2.16a and 2.29a. For illustration purpose, the hydrodynamic and thermal entrance lengths for the 1st pass (top slab) are plotted against Re in Figure 8.12. As seen, none of the flow is hydrodynamically developed before entering the heat transfer section

but all the flow gained developed status before exiting the section. None of the flow steps is thermally developed before entering the heat transfer section and except for the 1st flow step none of them gained developed status before exiting the heat transfer section and entering the serpentine bend portion. The flow is then reversed at the serpentine and a new entrance is formed at the entrance of the bottom slab (2nd-pass) as a result none of the flow steps had any chance to be thermally developed. Glycol-water mixture possesses higher viscosity than water. The thermal entrance length thus occupied the entire flow length causing higher heat transfer. Therefore the flow steps in current study could be well described by the simultaneously developing flow, as shown in Figure 8.12.

The adiabatic serpentine segment can be viewed in Figures B2.4a and 2.4c. The presence of this serpentine U-bend at the exit of 1st slab (top slab) and at the entrance of 2nd slab (bottom slab) enhances heat transfer in the test section. Upon exchanging heat and hence losing the temperature, the fully developed fluid streams from the 1st pass (top slab) enter the serpentine bend. The near wall fluid elements lose more temperature than the centerline fluid particles. For fully developed flow, the centerline fluid particles are the fast moving and the near wall elements are the least moving ones. Inside the serpentine bend the relatively hotter centerline fluid elements move outward to the outer wall of the bend due to centrifugal action, which results in secondary flow pattern. The secondary flow causes the relatively colder least moving fluid particles from the near wall to move toward the centerline and the inner wall of the bend. Therefore all the fluid particles get agitated and well mixed inside the serpentine.

Since no heat transfer occurs around this serpentine, the well mixed fluid particles further exchange heat in the 2nd pass (bottom slab) inside test section. The fluid mixing itself results in increased heat transfer. Due to the presence of U-serpentine new entrance region is formed at the beginning of the 2nd pass (bottom slab). This new entrance region causes the flow to be further simultaneously developing as it passes. The extra heat transfer enhancement acquired in current study could have been attributed to these two effects, which are absent in the compared correlations.

For the above reasons the higher Nu in current study as compared to the conventional correlations is reasonable and expected. A $Nu = f(Re, Pr)$ correlation for simultaneously developing laminar glycol-water mixture flow in parallel multi-port serpentine circular channels is developed in current study as presented by Equation 8.1. The correlation developed for the investigated range of $400 \leq Re \leq 1800$, which is anticipated to be very useful in the design of heat exchanger with geometric configuration similar to current study and in the research of narrow channel heat exchangers..

$$Nu = 0.152 \cdot Re^{0.50} Pr^{1/3}; \quad \text{for } 400 \leq Re \leq 1800. \quad (8.1)$$

8.4 Conclusions on glycol-water mixture flow

The multi-port finned or un-finned serpentine flat slabs as the core elements and the ethylene glycol-water mixture as the heat transfer fluid are frequently encountered in practical heat exchangers. Research on these applied geometries and on this fluid using narrow channel is rare in the open literature. The necessity and importance for thermo-hydraulic studies of liquid flow in an applied geometry in the developing laminar flow regime is described in the literature review in Chapter 3 and in section 6.4.4.

In present study, experiments have been conducted on simultaneously developing laminar flow of 50% ethylene glycol-water solution in a parallel multi-port finned serpentine bend microchannel channel slab in liquid-to-air crossflow orientation. The liquid attained the developing laminar flow in the Reynolds number range between 400 and 1800. The objectives of the study were to investigate the pressure drop and heat transfer characteristics of the test fluid inside channels, the performance of the test slab as a heat exchanger, and to acquire experimental database on the test fluid. The findings in this study are documented through peer-reviewed publication [234]. The experimentally obtained data are provided in Table D4 in Appendix D.

The total measured pressure drop non-linearly increased from 28 to about 190 kPa with the increase of Re . This non-linear variation is due to the presence of other major and minor losses in the flow route. The core pressure drop, isolated using general approach, cannot be predicted by the conventional Poiseuille flow theory for fully

developed flow. In order to separate the core pressure drop a comprehensive pressure balance model is formulated, which described in sections 6.1 and 7.2. Taking all the possible losses into account, the core pressure drop separated using the pressure balance model could be predicted well by the traditional Poiseuille flow theory. As expected the core pressure drop increased linearly with the increase of Re ranging from 18 to 60 kPa with the gradient from 25 to 80 kPa/m of the flow length. The core pressure drop roughly compared with Kasagi et al. [233] one third approximation.

The pressure drops in three major segments i.e. the manifolds (inlet and exit combined, serpentine bend, and the straight flow paths (top and bottom slabs combined) are separated from the measured total pressure drop. It is found that the highest pressure drop occurs in the straight flow path (top and bottom slabs), which is dominated by the flow frictional pressure drop. The second highest loss occurs in the manifolds due to complex geometric configuration, flow area change and flow turn. The serpentine bend incurs the least pressure drop. As an example at $Re = 1020$ the percentage share of the total pressure drop are 43.45% (core), 16.44% (manifolds), 4.02% (serpentine bend), and 33.83% (others). The smooth U-type bend in current study with serpentine radius to channel diameter ratio (R_{sp}/D_{ch}) > 3 and straight flow length to channel diameter ratio (L/D_{ch}) > 10 has least pressure drop but it has better heat transfer contribution as compared to the inlet contribution caused by the inlet manifold. Therefore use of this type of serpentine bends with multi-port parallel channels as heat exchanger core can enhance heat transfer performance of a heat exchanger significantly with least pressure drop tax.

About 4 kW of heat transfer could be achieved from the test slab with an LMTD of 61°C in the test conditions considered. With the increase of Re the q increased in a power-law manner and the effectiveness (ϵ) decreased linearly. The NTU and ϵ both decreased with Re. The core pressure drop nonlinearly decreased with the increase of ϵ , which signifies that the pressure drop is low at higher ϵ and high at lower ϵ . The higher q is achieved at lower ϵ but at the expense of higher pressure drop. These variations help optimize the design and operation of a heat exchanger. The NTU and ϵ values for current test slab were found to vary from 0.16 to 0.57 and from 0.14 to 0.43 respectively.

The Nu determined experimentally and predicted from modified Wilson Plot Technique both compared very well. Expectedly the Nu increased with Re in power law manner and the mean value was higher than the values of conventional laminar developing flow correlations. None of the flow entered the heat transfer section which is hydrodynamically developed. Moreover, owing to the higher viscosity of glycol-water mixture than water, the thermal boundary condition was such that all the flow steps were developing and the thermal entrance lengths occupied the entire flow length for all the Re investigated. Therefore the higher Nu has been attributed to the magnitude of thermal entrance length, the presence of serpentine and to the effects of second developing flow.

One can argue that the flow reversal around a serpentine bend enhances heat transfer but it also increases the pressure drop. In a heat exchanger the inlet manifold usually is responsible for the entrance related pressure drop and heat transfer rise for the

entrance flow disturbance. In sections 7.3.1 and 7.4.1 for both water and glycol-water mixture flows, it has been shown that the pressure drop in current smooth U-type serpentine bend is much lower than the manifolds but the heat transfer is noticeably higher. This finding in current study is expected to significantly help heat exchanger design, operation, and further research in this area.

For the studied geometry in the range $400 \leq Re \leq 1800$, a heat transfer correlation for simultaneously developing laminar flow of glycol-water solution is obtained in the form of $Nu = 0.152 \cdot Re^{0.50} Pr^{1/3}$, which will be useful in the design of heat exchanger and may serve as a roadmap in this promising area.

REFERENCES

REFERENCES

1. Zimparov V. Energy conservation through heat transfer enhancement techniques. *International Journal of Energy Research* 2002; 26:675-696.
2. Webb RL, Kim N-H. *Principles of Enhanced Heat Transfer*. 2nd ed., Taylor & Francis: New York, USA, 2005.
3. Webb RL. Advances in modeling enhanced heat transfer surfaces. *Proceeding of the 10th International Heat Transfer Conference*, 1994. Brighton, UK, Aug. 14-18.
4. Steinke ME, Kandlikar SG. Review of single-phase heat transfer enhancement techniques for application in microchannels, minichannels and microdevices. *Heat and Technology* 2004; 22:3-11.
5. Shah RK, Sekulic DP. *Fundamentals of Heat Exchanger Design*. John Wiley & Sons Inc. : New Jersey, USA, 2003.
6. Shah RK, Webb RL. *Compact and Enhanced Heat Exchangers*. *Heat Exchangers: Theory and Practice*; (Eds.) Taborek J, Hewitt GF, Afgan N. McGraw-Hill: New York, USA, 1983.
7. Shah RK. Compact heat exchanger technology and applications. *Heat Exchange Engineering, Volume 2: Compact Heat Exchangers: Techniques of Size Reduction* 1991; (eds.) Foumaeny EA, Heggs PJ. Ellis Horwood: London, 1991.
8. Wang C-C. Recent progress on the air-side performance of fin-and-tube heat exchangers. *International Journal of Heat Exchangers* 2000; 1:49-76.
9. Rugh JP, Pearson JT, Ramadhyani S. A study of a very compact heat exchanger used for passenger compartment heating in automobiles. *Compact Heat Exchangers for Power and Process Industries HTDS ASME* 1992; 201:15-24.

10. Luo L, Fan Y, Tondeur D. Heat exchanger: from micro- to multi-scale design optimization. *International Journal of Energy Research* 2007; 30:1266-1274.
11. Kakac S, Liu H. *Heat Exchangers: Selection, Rating, and Thermal Design*. CRC Press : Florida, USA, 2002.
12. Detlef W, Kurt WR, James B. Microchannel heat exchangers – emerging technologies. *ASHRAE Journal* 2003; Dec : 107-109.
13. Naterer GF. Guest editorial: Recent advances in micro and nano energy systems. *International Journal of Energy Research* 2007; 31:547.
14. Glockner PS, Naterer GF. Recent advances in nano-electromechanical and microfluidic power generation. *International Journal of Energy Research* 2007; 31:603-618.
15. Morse JD. Micro-fuel cell power sources. *International Journal of Energy Research* 2007; 31:576-602.
16. Naterer GF. Reducing energy availability losses with open parallel microchannels embedded in a micropatterned surface. *International Journal of Energy Research* 2005; 29:1215-1229.
17. Chen K. Second-law analysis and optimization of microchannel flows subjected to different thermal boundary conditions. *International Journal of Energy Research* 2004; 29:249–263.
18. Kandlikar SG, Garimella S, Li Di, Colin S, King MR. *Heat Transfer and Fluid Flow in Minichannels and Microchannels*. Elsevier Ltd.: Oxford, U.K., 2006.
19. Kandlikar SG. Microchannels and minichannels – History, terminology, classification and current research needs. *Proceedings of the 1st International Conference on Microchannels and Minichannels ICMM2003*; Paper # ICMM2003-1000: ASME Publications, NY, USA, April 24-25, 2003.

20. Kandlikar SG, Grande WJ. Evolution of microchannel flow passages – Thermohydraulic performance and fabrication technology. *Heat Transfer Engineering* 2003; 24(1):3-17.
21. Hasan MI, Rageb AA, Yaghoubi M, Homayoni H. Influence of channel geometry on the performance of a counter flow microchannel heat exchanger. *International Journal of Thermal Sciences* 2009; 48:1607-1618.
22. Harris C, Despa M, Kelly K. Design and fabrication of a cross flow micro heat exchanger. *Journal of Microelectromechanical Systems IEEE* 2000; 9(4):502-508.
23. Morini GL. Single-phase convective heat transfer in microchannels: a review of experimental results. *International Journal of Thermal Sciences* 2004; 43:631-651.
24. Wahib O, Bjorn P. Experimental investigation of single-phase convective heat transfer in circular microchannels. *Experimental Thermal and Fluid Science* 2004; 28:105-110.
25. Hetsroni G, Mosyak A, Pogrebnyak E, Yarín LP. Fluid flow in micro-channels. *International Journal of Heat and Mass Transfer* 2005; 48:1982-1998.
26. Qi SL, Zhang P, Wang RZ, Xu LX. Single-phase pressure drop and heat transfer characteristics of turbulent liquid nitrogen flow in micro-tubes. *International Journal of Heat and Mass Transfer* 2007; 50:1993-2001.
27. Mokrani O, Bourouga B, Castelain C, Peerhossaini H. Fluid flow and convective heat transfer in flat microchannels. *International Journal of Heat and Mass Transfer* 2009; 52:1337-1352.
28. Garimella SV, Singhal V. Single-phase flow and heat transport and pumping considerations in microchannel heat sinks. *Heat Transfer Engineering* 2004; 25(1):15-25.

29. Harris C, Kelly K, Wang T, McCandless A, Motakef S. Fabrication, modeling, and testing of micro-cross-flow heat exchangers. *IEEE Journal of Microelectromechanical Systems* 2002; 11(6):726-735.
30. Kim J, Groll E. Performance and reliability of microchannel heat exchangers in unitary equipment. *NewsLetter* 2003; 10(1): April 2003. Ray W. Herrick Labs, Purdue University.
31. Ravi A, Tad D, Laura S. Microchannel heat exchangers improve LNG economics. *HART (Velocys): Gas-to-Liquids News* 2004; March 2004:5-8.
32. Sparrow EM, Baliga BR, Patakar SV. Forced convection heat transfer from a shrouded fin-array with and without tip clearance. *Journal of Heat Transfer* 1978; 100:572-579.
33. Tuckerman DB, Pease RFW. High-performance heat sinking for VLSI. *IEEE Electron Device Letters* 1981; EDL-2(5):126-129.
34. Tuckerman DB. Heat transfer microstructures for integrated circuits. *Ph.D Thesis*. Stanford University, Stanford, CA, USA, 1984.
35. Munding DR, Beach R, Bennett W, Solarz R, Sperry V. Laser diode cooling for high average power applications. *LLNL* 1989; UCRL-100245.
36. Goodling JS. Microchannel heat exchangers – a review. *High Heat Flux Engineering II, Proceedings of the Society of Photo-Optical Instrumentation Engineers SPIE* 1993; 1997:66-82.
37. Steinke ME, Kandlikar SG. Single-phase liquid friction factors in microchannels. *International Journal of Thermal Sciences* 2006; 45:1073-1083.
38. Tang GH, Zhuo Li, He YL, Tao WQ. Experimental study of compressibility, roughness and rarefaction influences on microchannel flow. *International Journal of Heat and Mass Transfer* 2007; 50:2282.

39. Mala GM, Li D. Flow characteristics of water in microtubes. *International Journal of Heat and Fluid Flow* 1999; 20:142-148.
40. Peter MYC. An experimental study of single-phase and two-phase flows in microchannels. *PhD Dissertation*; University of Toronto, Ontario, Canada, 2003.
41. Mala GM, Li S, Dale JD. Heat Transfer and fluid flow in microchannels. *International Journal of Heat and Mass Transfer* 1997; 40(13):3079-3088.
42. Harpole GM, Eninger JE. Microchannel heat exchanger optimization. *Proceedings of the 7th IEEE Semi-Therm Symposium* 1991; CH2972-8/91: 59-63.
43. *Proceedings of the 1st, 2nd, 3rd International Conferences on Microchannels and Minichannels (ICMMCs)*, 2003, 2004, 2005; New York, New York, Toronto.
44. Microchannel Technology - More efficient, compact, and corrosion resistant technology for air-cooled chiller applications. *Carrier Corporation* 2006; New York, USA.
45. Heun MK, Dunn WE. Performance and optimization of microchannel condenser. *Airconditioning and Refrigeration Center (ACRC)*; ACRC Project 48 (TR-81) Report July 1995: University of Illinois at Urbana-Champaign, USA.
46. Kulkarni T, Bullard CW. Design tradeoffs in microchannel heat exchangers. *Airconditioning and Refrigeration Center (ACRC)*; ACRC Project 124 (TR-208) Report February 2003: University of Illinois at Urbana-Champaign, USA.
47. Zhao Y, Ohadi MM, Radermacher R. Microchannel heat exchangers with carbon dioxide. *Center for Environmental Energy Engineering (CEEE)*; Final Report (21CR-ARTI) September 2001: University of Maryland, USA.
48. Iyengar M, Singhal V, Garimella S. System-level analysis of microchannel cooling systems. *Design for energy efficiency and manufacturability, JSME Project Meeting October 2003, Cooling Technologies Research Center (CTRC)*, Purdue University, USA.

49. Pettersen J, Rieberer R, Leister A. Heat transfer and pressure drop characteristics of super-critical CO₂ in microchannel tubes under cooling. *Norwegian University of Science and Technology (NTNU)* 2000; IIF-IIR Commission B1, B2, E1, and E2 Publication:99-106, Purdue University, USA.
50. Bahrami M, Yovanovich MM, Culham, JR. A novel solution for pressure drop in singly connected microchannels of arbitrary cross-section. *International Journal of Heat and Mass Transfer* 2007; 50:2492-2502.
51. Kays WM, London AL. *Compact Heat Exchangers*. 3rd ed., McGraw-Hill : New York, USA, 1984.
52. Incropera FP, DeWitt DP. *Fundamentals of Heat and Mass Transfer*. 5th ed., John Wiley & Sons, Inc : New York, USA, 2002.
53. Cengel YA. *Heat Transfer - a practical approach*. McGraw-Hill : New York, USA, 2007.
54. Tso CP, Mahulikar SP. Experimental verification of the role of Brinkman number in microchannels using local parameters. *International Journal of Heat and Mass Transfer* 2000; 43:1837-1849.
55. Žukauskas A. Heat transfer from tubes in crossflow. *Advances in Heat Transfer*, 1972; 8:93-160. eds. Hartnett JP, Irvine TF Jr. Academic Press : New York, USA.
56. Žukauskas A, Ulinskas R. *Heat transfer in tube banks in cross flow*. Hemisphere Publishing Corporation : Washington DC, USA 1988.
57. Dittus FW, Boelter LMK. Heat transfer in automobile radiators of the tubular type. *University of California Publications in Engineering* 1930; 2:443-461.
58. Winterton RHS. Where did the Dittus and Boelter equation come from? *International Journal of Heat and Mass Transfer* 1998; 41:809-810.

59. Munson BR, Young DF, Okiishi TH. *Fundamentals of Fluid Mechanics*. 4th ed., John Wiley & Sons Inc. : New York, USA, 2002.
60. Idelchik IE. *Handbook of Hydraulic Resistance*. 3rd ed., Translated by Malyaskaya GR, eds. Martynenko OG, Shteinberg MO, CRC Press Inc. : Florida, USA, 1994.
61. Shah RK, Bhatti MS. *Laminar convective heat transfer in ducts*. In *Handbook of Single-Phase Convective Heat Transfer*, eds. Kakac S, Shah RK, Aung W. John Wiley & Sons Inc. : New York, USA, 1987.
62. Shah RK, London AL. *Laminar Forced Convection in Ducts*. Academic Press : New York, USA, 1978.
63. Kakac S, Shah RK, Aung W. *Handbook of Single-Phase Convective Heat Transfer*. John Wiley & Sons Inc. : New York, USA, 1987.
64. Kays WM, Crawford ME. *Convective Heat and Mass Transfer*. 3rd ed., McGraw-Hill: New York, USA, 1993.
65. Hornbeck RW. Laminar flow in entrance region of a pipe. *Applied Science Research* 1964; 13:224-232.
66. Chen RY. Flow in the entrance region at low Reynolds number. *Journal of Fluids Engineering*. 1973; 95: 153-158.
67. Olsson CO, Sunden B. Pressure drop characteristics of small-sized tubes. *Proceedings of the International Mechanical Engineering Congress & Exposition* 1994; Chicago, IL, USA, November 6-11.
68. Bhatti MS, Shah RK. *Turbulent and transition convective heat transfer in ducts*. In *Handbook of Single-Phase Convective Heat Transfer*, eds. Kakac S, Shah RK, Aung W. John Wiley & Sons Inc. : New York, USA, 1987.
69. Churchill SW. Frictional equation spans all fluid flow regimes. *Chemical Engineering* 1977; 84:91-92.

70. Petukov BS. *Heat transfer and friction in turbulent pipe flow with variable physical properties*. In *Advances in Heat Transfer* 1970; 6. eds. Irvine & Hartnett. Academic Press : New York, USA.
71. Michelsen ML, Villadsen J. The Graetz problem with axial heat conduction. *International Journal of Heat and Mass Transfer* 1974; 17:1391-1402.
72. Gnielinski V. *Forced Convection in Ducts*. In *Heat Exchanger Design Handbook*, 1983;2.5.1-2.5.3. Schlunder EU ed. Hemisphere:Washington DC, USA, 1983.
73. Sieder EN, Tate GE. Heat transfer and pressure drop of liquids in tubes. *Ind. Eng. Chem* 1936; 28: 1429-1436.
74. Whitaker S. Forced convection heat transfer correlations for flow in pipes, past flat plates, single cylinders, single spheres, and flow in packed beds and tubes. *AIChE Journal* 1972; 18: 361-371.
75. Edwards DK, Denny VE, Mills AF. *Transfer process*. 2nd ed., Hemisphere: Washington DC, USA, 1979.
76. Petukov BS, Popov VN. Theoretical calculation of heat exchange in turbulent flow in tubes of an incompressible fluid with variable physical properties. *High Temperature* 1963; 1(1):69-83.
77. Gnielinski V. New equations for heat and mass transfer in turbulent pipe and channel flow. *International Journal of Chemical Engineering* 1976; 16(2):359-368.
78. Churchill SW. Comprehensive correlating equations for heat, mass, and momentum transfer in fully developed flow in smooth tubes. *Ind. Eng. Chem. Fundam.* 1977; 16(1): 109-116.
79. Davies SJ, White CM An experimental study of the flow of water in pipes of rectangular section. *Proceedings of the Royal Society of London, Series A* 1928; 119(781):92-107.

80. Gambill, W. and Bundy, R. Heat transfer studies of turbulent water flow in the rectangular channels HFIR. *ORNL-3079 UC-80-Reactor Technology* 1961; Oak Ridge, TN, USA.
81. Wu PY, Little WA. Measurement of friction factors for the flow of gases in very fine channels used for microminiature Joule–Thompson refrigerators. *Cryogenics* 1983; 23(5):273-277.
82. Wu PY, Little WA. Measurement of the heat transfer characteristics of gas flow in fine channel heat exchangers used for microminiature refrigerators. *Cryogenics* 1984; 24(8):415-420.
83. Acosta R, Muller R, Tobias C. Transport processes in narrow (capillary) channels. *Journal of AIChE* 1985; 31:473-482.
84. Harley J, Bau HH, Zemel JN, Dominko V. Fluid flow in micron and submicron size channels. *Proceedings of the IEEE* 1989; MEMS:25-28.
85. Missaggia LJ, Walpole JN, Liao ZL, Phillips RJ. Microchannel heat sinks for two-dimensional high-power-density diode laser arrays. *IEEE Journal of Quantum Electronics* 1989; 25(9):1988-1992.
86. Nakagawa S, Shoji S, Esashi M. A micro chemical analyzing system integrated on silicon chip. *Proceedings of the IEEE* 1990; MEMS:89-94, Napa Valley CA, USA.
87. Pfahler J, Harley J, Bau HH. Liquid transport in micron and submicron channels. *Sensors and Actuators* 1990; A21-A22:431-434.
88. Choi SB, Barron RF, Warrington RO. Fluid flow and heat transfer in microtubes. *Micromechanical Sensors, Actuators, and Systems ASME* 1991; (Eds.) Choi et al. 1991, DSC-32:123-134.
89. Lin S, Kwok CCK, Li RY, Chen ZH, Chen ZY. Local frictional pressure drop during vaporization of R-12 through capillary tubes. *International Journal of Multiphase Flow* 1991; 17:95-102.

90. Pfahler J, Harley J, Bau HH, Zamel JN. Gas and liquid flow in small channels. *Micromechanical Sensors, Actuators and Systems ASME* 1991; (Eds.) Choi et al. 1991; DSC-32:49-60.
91. Riddle RA, Contolini RJ, Bernhardt AF. Design calculations for the microchannel heat sink. *Proceedings of the Technical Program – National Electronic Products Conference* 1991; 1:161-171.
92. Weisberg A, Bau HH, Zamel JN. Analysis of microchannels for integrated cooling. *International Journal of Heat and Mass Transfer* 1992; 35(10):2465-2474.
93. Peng XF, Wang BX. Forced convection and flow boiling heat transfer for liquid flowing through microchannels. *International Journal of Heat and Mass Transfer* 1993; 36:3421-3427.
94. Rahman MM, Gui FJ. Design, fabrication, and testing of microchannel heat sinks for aircraft avionics cooling. *Proceedings of the 28th Intersociety Energy Conversion Engineering Conference* 1993; 1:1-6.
95. Rahman MM, Gui FJ. Experimental measurements of fluid flow and heat transfer in microchannel cooling passages in a chip substrate. *Advances in Electronic Packaging, ASME* 1993; 199(4):685-692.
96. Urbanek W, Zemel JN, Bau HH. An investigation of the temperature dependence of Poiseuille numbers in microchannel flow. *Journal of Micromechanics and Microengineering* 1993; 3:206-208.
97. Arkilic EB, Breuer KS, Schmidt MA. Gaseous flow in microchannels. *Application of Microfabrication to Fluid Mechanics, ASME FED* 1994; 197:57-66.
98. Bowers MB, Mudawar I. High flux boiling in low flow rate low pressure drop minichannel and microchannel heat sinks. *International Journal of Heat and Mass Transfer* 1994; 37(2):321-332.

99. Peng XF, Peterson GP, Wang BX. Heat transfer characteristics of water flowing through microchannels. *Experimental Heat Transfer* 1994; 7(4):265-283.
100. Pong K, Ho C, Liu J, Tai YC. Non-linear pressure distribution in uniform microchannels. *Application of Microfabrication to Fluid Mechanics, ASME FED* 1994; 197:51-56.
101. Wang BX, Peng, XF. Experimental investigation on liquid forced convection heat transfer through microchannels. *International Journal of Heat and Mass Transfer* 1994; 37(1):73-82.
102. Wilding P, Pfahler J, Zemel JN, Bau HH, Kricka LJ. Manipulation and flow of biological fluids in straight channels micromachined in silicon. *Clinical Chemistry* 1994; 40(1):43-47.
103. Peng XF, Peterson GP, Wang BX. Frictional flow characteristics of water flowing through rectangular microchannels. *Experimental Heat Transfer* 1995; 7(4):249-264.
104. Gui FJ, Scaringe RP. Enhanced heat transfer in the entrance region of microchannels. *Proceedings of the 30th Intersociety Energy Conversion Engineering Conference* 1995; 2:289-294.
105. Harley J, Huang Y, Bau HH, Zemel JN. Gas flow in microchannels. *Journal of Fluid Mechanics* 1995; 284:257-274.
106. Jiang XN, Zhou ZY, Yao J, Li Y, Ye XY. Micro-fluid flow in microchannel. *Proceedings of the 8th International Conference on Solid-State Sensors and Actuators and Eurosensors IX* 1995; 317-320.
107. Liu J, Tai YC, Ho CM. MEMS for pressure distribution studies of gaseous flows in microchannels. *Proceedings of the 8th IEEE Annual International Workshop on MEMS* 1995; 209-215.

108. Peng XF, Peterson GP. The effect of thermofluid and geometrical parameters on convection of liquids through rect. microchannels. *International Journal of Heat and Mass Transfer* 1995; 38(4):755-758.
109. Peng XF, Wang BX, Peterson GP, Ma HB. Experimental investigation of heat transfer in flat plates rectangular microchannels. *International Journal of Heat and Mass Transfer* 1995; 38(1):127-137.
110. Yu D, Warrington RO, Barron RF, Ameel TA. An experimental and theoretical investigation of fluid flow and heat transfer in micro-tubes. *Proceedings of the ASME/JSME Thermal Engineering Joint Conference* 1995; 1:523-530, Maui, HI.
111. Cuta JM, McDonald CE, Shekarriz A. Forced convection heat transfer in parallel channel array microchannel heat exchanger. *Advances in Energy Efficiency, Heat/Mass Transfer Enhancement, ASME-PID* 1996; 33:17-23.
112. Nguyen NT, Bochnia D, Kiehnscherrf R, Dözel W. Investigation of forced convection in microfluid systems. *Sensors and Actuators* 1996; A55:49-55.
113. Peng XF, Peterson GP. Convective heat transfer and flow friction for water flow in microchannel structures. *International Journal of Heat and Mass Transfer* 1996; 39(12):2599-2608.
114. Peng XF, Peterson GP. Forced convection heat transfer of single-phase binary mixtures through microchannels. *Experimental Thermal Fluid Science* 1996; 12:98-104.
115. Ravigururajan TS, Cuta JM, McDonald CE, Dorst MK. Single-phase thermal performance characteristics of a parallel micro-channel heat exchanger. *Proceeding of the US National Heat Transfer Conference, ASME-HTD* 1996; 329:157-166.
116. Shih JC, Ho CM, Liu J, Tai YC. Monatomic and polyatomic gas flow through uniform microchannels. *Proceedings of the ASME* 1996; DSC-59:197-203.

117. Arkilic EB, Schmidt MA, Breuer KS. Gaseous slip flow in long microchannels. *Journal of Microelectromechanical Systems* 1997; 6(2):167-178.
118. Harms TM, Kazmierczak MJ, Gerner FM, Holke A., Henderson HT, Pilchowski J, Baker K. Experimental investigation of heat transfer and pressure drop through deep microchannels in a <110> silicon substrate. *Proceedings of the ASME HTD* 1997; 351(1):347-357.
119. Jiang XN, Zhou ZY, Huang XY, Liu CY. Laminar flow through microchannels used for microscale cooling systems. *Proceedings of the IEEE/CPMT Electronic Packaging Technology Conference* 1997; 119-122.
120. Richter M, Woias P, Weiss D. Microchannels for applications in liquid dosing and flow-rate measurement. *Sensors and Actuators A* 1997; A62:480-483.
121. Stanley RS, Barron RF, Ameel TA. Two-phase flow in microchannels. *Proceedings of the Micro-Electro-Mechanical Systems (MEMS) ASME* 1997; DSC-62:143-152.
122. Adams TM, Abdel-Khalik SI, Jeter SM, Qureshi ZH. An experimental investigation of single-phase forced convection in microchannels. *International Journal of Heat and Mass Transfer* 1998; 41(6-7):851-857.
123. Pfund DA, Shekarriz A, Popescu A, Welty JR. Pressure drops measurements in microchannels. *Proceedings of the MEMS, ASME* 1998; DSC-66:193-198.
124. Vidmar RJ, Barker RJ. Microchannel cooling for a high-energy particle transmission window, an RF transmission window, and VLSI heat dissipation. *IEEE Transactions, Plasma Science* 1998; 26(3):1031-1043.
125. Webb RL, Zhang M. Heat transfer and friction in small diameter channels. *Microscale Thermophysical Engineering* 1998; 2:189-202.

126. Adams TM, Ghiaasiaan SM, Abdel-Khalik SI. Enhancement of liquid forced convection heat transfer in microchannels due to the release of dissolved noncondensables. *International Journal of Heat and Mass Transfer* 1999; 42:3563-3573.
127. Adams TM, Dowling MF, Abdel-Khalik SI, Jeter SM. Applicability of traditional turbulent single-phase forced convection correlations to non-circular microchannels. *International Journal of Heat and Mass Transfer* 1999; 42:4411-4415.
128. Harms TM, Kazmierczak MJ, Gerner FM. Developing convective heat transfer in deep rectangular microchannels. *International Journal of Heat and Fluid Flow* 1999; 20:149-157.
129. Papautsky I, Gale BK, Mohanty S, Ameen TA, Frazier AB. Effects of rectangular microchannel aspect ratio on laminar friction constant. *Proceedings of the Society of Photo-Optical Instrumentation Engineers (SPIE)* 1999; 3877:147-158.
130. Papautsky I, Brazzle J, Ameen TA, Frazier AB. Laminar fluid behavior in microchannels using micropolar fluid theory. *Sensors and Actuators* 1999; 73(2):101-108.
131. Xu B, Ooi KT, Wong NT, Liu CY, Choi WK. Liquid flow in microchannels. *Proceedings of the 5th ASME/JSME Joint Thermal Engineering Conference* 1999; 150-158, San Diego, CA, USA.
132. Araki T, Soo KM, Hiroshi I, Kenjiro S. An experimental investigation of gaseous flow characteristics in microchannels. *Proceedings of the International Conference on Heat Transfer and Transport Phenomena in Microscale* 2000; 155-161. (Eds.) Celata et al., Begell House: NY, 2000.

133. Celata GP, Cumo M, Guglielmi M, Zummo G. Experimental investigation of hydraulic and single-phase heat transfer in 0.130 mm capillary tube. *Proceedings of the International Conference on Heat Transfer and Transport Phenomena in Microscale* 2000; 108-113. (Eds.) Celata et al., Begell House: NY, 2000.
134. Ding LS, Sun H, Sheng XL, Lee BD. Measurement of friction factors for R134a and R12 through microchannels. *Proceedings of the Symposium on Energy Engineering in the 21st Century* 2000; 2:650-657.
135. Judy J, Maynes D, Webb BW. Liquid flow pressure drop in microtubes. *Proceedings of the International Conference on Heat Transfer and Transport Phenomena in Microscale* 2000; 149-154. (Eds.) Celata et al., Begell House: NY, 2000.
136. Li ZX, Du DX, Guo ZY. Characteristics of frictional resistance for gas flow in microtubes. *Proceedings of the Symposium on Energy Engineering in 21st Century* 2000; 2:658-664.
137. Li ZX, Du DX, Guo ZY. Experimental study on flow characteristics of liquid in circular microtubes. *Proceedings of the International Conference on Heat Transfer and Transport Phenomena in Microscale* 2000; 162-167. (Eds.) Celata et al., Begell House: NY, 2000.
138. Pfund D, Rector D, Shekarriz A, Popescu A, Welty J. Pressure drop measurements in a microchannel. *AIChE Journal* 2000; 46(8):1496-1507.
139. Qu W, Mala M, Li D. Pressure-driven water flows in trapezoidal silicon microchannels. *International Journal of Heat and Mass Transfer* 2000; 43:353-364.
140. Qu W, Mala GM, Li D. Heat transfer for water flow in trapezoidal silicon microchannels. *International Journal of Heat and Mass Transfer* 2000; 43:3925-3936.

141. Rahman MM. Measurements of heat transfer in microchannel heat sinks. *International Communications in Heat and Mass Transfer* 2000; 27(4):495-506.
142. Sharp KV, Adrian RJ, Beebe DJ. Anomalous transition to turbulence in microtubes. *Proceedings of the International Mechanical Engineering Congress and Exposition* 2000; 150-158, 5th Microfluidic Symposium, Orlando, FL, USA.
143. Tso CP, Mahulikar SP. Experimental verification of the role of Brinkman number in microchannels using local parameters. *International Journal of Heat and Mass Transfer* 2000; 43:1837-1849.
144. Xu B, Ooi KT, Wong NT, Choi WK. Experimental investigation of flow friction for liquid flow in microchannels. *International Communications in Heat and Mass Transfer* 2000; 27(8):1165-1176.
145. Yang CY, Chien HT, Lu SR, Shyu RJ. Friction characteristics of water, R-134a and air in small tubes. *Proceedings of the International Conference on Heat Transfer and Transport Phenomena in Microscale* 2000; 168-174. (Eds.) Celata et al., Begell House: NY, 2000.
146. Debray F, Franc JP, Maitre T, Reynaud S. Mesure des coefficient de transfert thermique par convection forcée en mini-canaux. *Mécanique & Industries* 2001; 2(5):443-454.
147. Ghiaasiaan SM, Laker TS. Turbulent forced convection in microtubes. *International Journal of Heat and Mass Transfer* 2001; 44:2777-2782.
148. Jiang PX, Fan MH, Si GS, Ren ZP. Thermal-hydraulic performance of small scale micro-channel and porous-media heat-exchangers. *International Journal of Heat and Mass Transfer* 2001; 44:1039-1051.
149. Kandlikar SG, Joshi S, Tian S. Effect of channel roughness on heat transfer and fluid flow characteristics at low Reynolds numbers in small diameter tubes. *Proceedings of the 35th National Heat Transfer Conference* 2001; Paper #NHTC01-12134; 2:1609-1618.

150. Ren L, Qu W, Li D. Interfacial electrokinetic effects on liquid flow in microchannels. *International Journal of Heat and Mass Transfer* 2001; 44:3125-3134.
151. Chung PM-Y, Kawaji M, Kawahara A. Characteristics of single-phase flow in microchannels. *Joint US-European Fluids Engineering Division Conference, ASME-FED* 2002; 1(A-B):1219-1228.
152. Gao P, Le Person S, Favre-Marinet M. Hydrodynamics and heat transfer in a two dimensional microchannel. *Proceedings of the 12th International Heat Transfer Conference* 2002; 2:183-188.
153. Gao P, Le Person S, Favre MM. Scale effects on hydrodynamics and heat transfer in two-dimensional mini and microchannels. *International Journal of Thermal Sciences* 2002; 41:1017-1027.
154. Hegab HE, Bari A, Ameel T. Friction and convection studies of R-134A in microchannels within the transition and turbulent flow regimes. *Experimental Heat Transfer* 2002; 15:245-259.
155. Judy J, Maynes D, Webb BW. Characterization of frictional pressure drop for liquid flows through microchannels. *International Journal of Heat and Mass Transfer* 2002; 45:3477-3489.
156. Kandlikar SG. Fundamental issues related to flow boiling in minichannels and microchannels. *Experimental Thermal and Fluid Science* 2002; 26:389-407.
157. Kang S-W, Chen Y-T, Chang GS. The manufacture and test of (110) orientated silicon based micro heat exchanger. *Tamkang Journal of Science and Engineering* 2002; 5(3):129-136.
158. Maynes D, Webb AR. Velocity profile characterization in sub-millimeter tubes using molecular tagging velocimetry. *Experiments in Fluids* 2002; 32:3-15.

159. Qu W, Mudawar I. Experimental and numerical study of pressure drop and heat transfer in a single-phase micro-channel heat sink. *International Journal of Heat and Mass Transfer* 2002; 45:2549-2565.
160. Toh KC, Chen XY, Chai JC. Numerical computation of fluid flow and heat transfer in microchannels. *International Journal of Heat and Mass Transfer* 2002; 45:5133-5141.
161. Turner SE, Sun H, Faghri M, Gregory OJ. Gas flow through smooth and rough microchannels. *Proceedings of the 12th International Heat Transfer Conference* 2002; 1:501-506.
162. Guo ZY, Li ZX. Size effect on microscale single-phase flow and heat transfer. *International Journal of Heat and Mass Transfer* 2003; 46:149-159.
163. Bucci A, Celata GP, Cumo M, Serra E, Zummo G. Fluid flow and single-phase flow heat transfer of water in capillary tubes. *Proceedings of the 1st International Conference on Microchannels and Minichannels ICMM2003*; ASME Publications, NY, USA, April 24-25, 2003.
164. Jung JY, Kwak HY. Fluid flow and heat transfer in microchannels with rectangular cross section. *Proceedings of the 1st International Conference on Microchannels and Minichannels ICMM2003*; Paper # 1032: ASME Publications, April 24-25, NY, USA, 2003.
165. Kandlikar SG, Joshi S, Tian S. Effect of surface roughness on heat transfer and fluid flow characteristics at low Re in small diameter tubes. *Heat Transfer Engineering* 2003; 24:4-16.
166. Kim M-H, Lee SY, Mehendale SS, Webb RL. Microchannel heat exchanger design for evaporator and condenser applications. *Advances in Heat Transfer* 2003; (Eds.) Hartnett JP, Irvine TF, Cho YI, Greene GA. 37:297-429.

167. Lee P-S, Garimella SV. Experimental investigation of heat transfer in microchannels. *Proceedings of the ASME Summer Heat Transfer Conference 2003*; 391-397.
168. Li ZX, Du DX, Guo ZY. Experimental study on flow characteristics of liquid in circular microtubes. *Microscale Thermophysical Engineering* 2003; 7(3):253-265.
169. Tu X, Hrnjak P. Experimental investigation of single-phase flow pressure drop through rectangular microchannels. *Proceedings of the 1st International Conference on Microchannels and Minichannels ICMM2003*; Paper # 1028: ASME Publications, April 24-25, NY, USA, 2003.
170. Wu HY, Cheng P. Friction factors in smooth trapezoidal silicon microchannels with different aspect ratios. *International Journal of Heat and Mass Transfer* 2003; 46:2519–2525.
171. Wu HY, Cheng P. An experimental study of convective heat transfer in silicon microchannels with different surface conditions. *International Journal of Heat and Mass Transfer* 2003; 46:2547-2556.
172. Baviere R, Ayela F, Le Person S, Favre-Marinet M. An experimental study of water flow in smooth and rough rectangular microchannels. *Proceedings of 2nd the International Conference on Microchannels and Minichannels ICMM2004*; NY. Later it appeared in *Physics of Fluids*. 2005; 17.
173. Cui HH, Silber-Li ZH, Zhu SN. Flow characteristics of liquids in microtubes driven by high pressure. *Physics of Fluids* 2004; 16:1803-1810.
174. Hsieh S-S, Lin C-Y, Huang C-F, Tsai H-H. Liquid flow in a microchannel. *Journal of Micromechanics and Microengineering* 2004; 14(4):436-445.
175. Lelea D, Nishio S, Takano K. The experimental research on microtube heat transfer and fluid flow of distilled water. *International Journal of Heat and Mass Transfer* 2004; 47:2817–2830.

176. Sharp KV, Adrian RJ. Transition from laminar to turbulent flow in liquid filled microtubes. *Experiments in Fluids* 2004; 36:741-747.
177. Jokar A, Hosni MH, Eckels SJ. Correlations for heat transfer and pressure drop of glycol-water and air flows in minichannel heat exchangers. *ASHRAE Transactions: Research* 2005; 111(2):213-224.
178. Kohl MJ, Abdel-Khalik SI, Jeter SM, Sadowski DL. An experimental investigation of microchannel flow with internal pressure measurements. *International Journal of Heat and Mass Transfer* 2005; 48:1518-1533.
179. Lee P-H, Garimella SV, Liu D. Investigation of heat transfer in rectangular microchannels. *International Journal of Heat and Mass Transfer* 2005; 48:1688-1704.
180. Yang W-H, Zhang J-Z, Cheng H-E. The study of flow characteristics of curved microchannel. *Applied Thermal Engineering* 2005; 25:1894-1907.
181. Bavière R, Le Person S, Favre-Marinet M. Bias effects on heat transfer measurements in microchannel flows. *International Journal of Heat and Mass Transfer* 2006; 49:3325-3337.
182. Rands C, Webb BW, Maynes D. Characterization of transition to turbulence in microchannels. *International Journal of Heat and Mass Transfer* 2006; 49:2924-2930.
183. Caney N, Marty P, Bigot J. Friction losses and heat transfer of single-phase flow in a mini-channel. *Applied Thermal Engineering* 2007; 27:1715-1721.
184. Xiong R, Chung JN. Flow characteristics of water in straight and serpentine microchannels with miter bends. *Experimental Thermal and Fluid Science* 2007; 31:805-812.

185. Celata GP, Cumo M, McPhail SJ, Tesfagabir L, Zummo G. Experimental study on compressible flow in microtubes. *International Journal of Heat and Fluid Flow* 2007; 28:28-36.
186. Hrnjak P, Tu X. Single phase pressure drop in microchannels. *International Journal of Heat and Fluid Flow* 2007; 28:2-14.
187. Kang S-W, Tseng S-C. Analysis of effectiveness and pressure drop in micro cross-flow heat exchanger. *Applied Thermal Engineering* 2007; 27:877-885.
188. Liu J-T, Peng X-F, Wei-Mon Yan W-M. Numerical study of fluid flow and heat transfer in microchannel cooling passages. *International Journal of Heat and Mass Transfer* 2007; 50:1855-1864.
189. Wang L, Liu F. Forced convection in slightly curved microchannels. *International Journal of Heat and Mass Transfer* 2007; 50:881-896.
190. Park HS, Punch J. Friction factor and heat transfer in multiple microchannels with uniform flow distribution. *International Journal of Heat and Mass Transfer* 2008; 51:4535-4543.
191. Jiang J, Hao Y, Shi M. Fluid flow and heat transfer characteristics in rectangular microchannels, *Heat Transfer - Asian Research*, 2008; 37(4):197-207.
192. Naphon P, Khonseur O. Study on the convective heat transfer and pressure drop in the micro-channel heat sink. *International Communications in Heat and Mass Transfer* 2009; 36:39-44.
193. Phillips RJ. Forced convection liquid cooled microchannel heat sinks. *MSME Thesis*. Department of Mechanical Engineering, MIT, Cambridge, MA, USA, 1987.
194. Gruss J-A, Bouzon C, Thonon B. Extruded microchannel-structured heat exchangers. *Heat Transfer Engineering* 2005; 26(3):56-63.

195. Kasagi N, Suzuki Y, Shikazono S, Oku T. Optimal design and assessment of high performance micro bare-tube heat exchangers. *Proceedings of the 4th International Conference on Compact Heat Exchangers and Enhancement Technologies for the Process Industries* 2003 241-246. Crete, Oct. 3.
196. Kasagi N, Shikazono N, Suzuki Y, Oku T. Assessment of high-performance compact micro bare-tube heat exchangers for electronic equipment cooling. *Proceedings of the 1st International Symposium on Process Intensification & Miniaturization* 2003; University of Newcastle upon Tyne, Aug. 18-21.
197. Hantz D, Pra P, Bensafi A. Microchannel and finned coils: performance comparison in single phase and in condensation. *Proceedings of the International Congress of Refrigeration*; Washington DC, USA, 2003.
198. Yin JM, Bullard CW, Hrnjak PS. Single-phase pressure drop measurements in a microchannel heat exchanger. *Heat Transfer Engineering* 2002; 23(4):3-12.
199. Ferguson AD, Bahrami M, Culham JR. 2005. Review of experimental procedure for determining liquid flow in microchannels. *Proceedings of the 3rd International Conference on Microchannels and Minichannels ICMM2005*; Paper # ICMM2005-75126, Toronto, Ontario, Canada, June 13-15, 2005.
200. Jokar A, Eckels SJ, Hosni MH. Single-phase flow in meso-channel compact heat exchangers for air conditioning applications. *Heat Transfer Engineering* 2010; 31(1):3-16.
201. Mesbah G Khan, Fartaj A. A review on microchannel heat exchangers and potential applications. *International Journal of Energy Research* 2010; DOI: 10.1002/er.1720 Published online (www.interscience.wiley.com) in the Wiley InterScience.
202. Mr. Michael Greene, Product Applications Engineer, *Hydro Aluminum, Precision Tubing North America, USA*. Personal communication (2005-2008).

203. Haglund Stignor C. Laminar-flow liquid-to-air heat exchangers - energy-efficient display cabinet applications. *Ph.D Thesis*. Lund University, Lund, Sweden, 2009.
204. Ozdemir Ozkan E. Thermal performance comparison between microchannel and round tube heat exchangers. *M.S Thesis*. Oklahoma State University, Oklahoma, USA, 2009.
205. Haglund Stignor C, Sunden B, Fahlen P, Eriksson D. Optimal operation for cooling-coils for display cabinets in secondary loop refrigeration systems. *Proceedings of the 21st International Congress of Refrigeration 2003*. Paper # ICR0275. Washington DC, USA.
206. Lemczyk TF. Research topics in low Reynolds flow heat exchangers. *Dana Long Manufacturing*. Oakville, ON, Canada, 1995.
207. Stephan MY. Analytical and experimental study of fluid friction and heat transfer in low Reynolds number flow heat exchangers. *PhD Dissertation*. University of Waterloo, ON, Canada, 1999.
208. Steinke ME, Kandlikar SG, Magerlein J, Colgan E, Raisanen A. Development of an experimental facility for investigating single-phase liquid flow in microchannels. *Heat Transfer Engineering* 2006; 27(4):41-52.
209. Mesbah G Khan, Fartaj A, Ting DS-K. An experimental characterization of cross-flow cooling of air via an in-line elliptical tube array. *International Journal of Heat and Fluid Flow* 2004; 25(4):636-648.
210. Mesbah G Khan, Fartaj A, Ting DS-K. Study of cross-flow cooling and heating of air via an elliptical tube array. *ASHRAE Transactions* 2005; 111(Part-1):423-433. American Society of Heating, Refrigerating, and Air-conditioning Engineers, Inc. (Paper # TECH-00077-2004).
211. ASHRAE Standard 111-1988. *Practices for measurement, testing, adjusting and balancing of building heating, ventilation, air-conditioning and refrigeration systems*. Atlanta, GA, USA 1988.

212. ASHRAE. *Handbook of Fundamentals*. American Society of Heating, Refrigerating and Air-Conditioning Engineers. Atlanta, GA, USA, 2005.
213. Documentation and operating manuals on *Pitot static tube probe and methods, FKT series flow / pressure measurements with acquisition system, and User manual*. [<http://www.flowmeterdirectory.com>] FlowKinetics LLC, Texas, USA, 2008.
214. Haglund Stignor C, Sunden B, Fahlen P. An experimental study of liquid-phase heat transfer in multiport minichannel tubes. *Heat Transfer Engineering* 2009; 30(12):941-951.
215. Haglund Stignor C, Sunden B, Fahlen P. Liquid side heat transfer and pressure drop in finned-tube cooling-coils operated with secondary refrigerants. *International Journal of Refrigeration* 2007; 30:1278-1289.
216. ASME. *Air cooled heat exchangers*. An American National Standard, Performance Test Code (PTC) 30-1991. American Society of Mechanical Engineers (ASME): NY, USA, 1991.
217. Mesbah G Khan, Mosa MMA, Siddiqui FA, Fartaj A. Experimental comparative study on heat transfer performances of circular, elliptical, and microchannel heat exchangers. In: *Proceedings of the Canadian Society for Mechanical Engineering Forum, CSME FORUM 2010*; Victoria, British Columbia, Canada, June 7-9, 2010.
218. EES (Engineering Equation Solver), Academic Version.
219. Bowman RA, Mueller AC, Nagle WM. Mean temperature difference in design. *Transactions of the ASME* 1940; 62:283-294.
220. Wilson EE. A basis for rational design of heat transfer apparatus. *Transactions of the ASME* 1915; 27: 47-70.
221. Briggs DE, Young EH. Modified Wilson plot techniques for obtaining heat transfer correlations for shell and tube heat exchangers. *Chemical Engineering Progress Symposium Series (AIChE)* 1969; 65(92):35-45.

222. Khartabil HF, Christensen RN, Richards DE. A modified Wilson Plot Technique for determining heat transfer correlations. In: *Proceedings of the 2nd UK National Conference on Heat Transfer-II* 1988; pp. 1331-1357, UK 1988.
223. Shah RK. Assessment of modified Wilson Plot Techniques for obtaining heat exchanger design data. In: *Proceedings of the 9th International Heat Transfer Conference* 1990;5:51-56, Jerusalem, Israel, August 1990.
224. Khartabil HF, Christensen RN. An improved scheme for determining heat transfer correlations from heat exchanger regression models with three unknowns. *Experimental Thermal Fluid Science* 1992; 5:808-819.
225. Editorial. Journal of Heat Transfer: Policy on reporting uncertainties in experimental measurements and results. *Transactions of the ASME, Journal of Heat Transfer* 1993; 115:5-6.
226. Editorial. Journal of Fluids Engineering: Policy on reporting uncertainties in experimental measurements and results. *Transactions of the ASME, Journal of Fluids Engineering* 1991; 113: 313-314.
227. Coleman HW. Steele WG. *Experimentation and uncertainty analysis for engineers*. John Wiley & Sons Inc.: New York, USA, 1989.
228. Kline SJ, McClintock FA. Describing uncertainties in single-sample experiments. *Mechanical Engineering* 1953;75:3-8.
229. Kline SJ. The purposes of uncertainty analysis. *Journal of Fluids Engineering, Transaction of the ASME* 1985;107:153-160.
230. Abernethy RB, Benedict RP, Dowdell RB. ASME Measurement uncertainty. *Journal of Fluids Engineering, Transaction of the ASME* 1985;107:161-164.

231. Mesbah G Khan, Fartaj A. Experiments of ethylene glycol-water mixture in multi-port circular straight microchannel slab. In: *Proceedings of the Society of Automotive Engineers (SAE) World Congress 2010* (Paper #2010-01-0326), Detroit, MI, USA, April 13-15, 2010.
232. Dehghandokht M, Mesbah G Khan, Fartaj A, Sanaye S. The numerical study of fluid flow and heat transfer in a multi-port serpentine meso-channel heat exchanger. *Applied Thermal Engineering* 2011; DOI:10.1016/j.applthermaleng.2011.01.035.
233. Kasagi N, Shikazono N, Suzuki Y, Oku T. Assessment of high-performance compact micro bare-tube heat exchangers for electronic equipment cooling. In: *Proceedings of the 1st International Symposium on Process Intensification & Miniaturization* 2003; University of Newcastle upon Tyne, Aug. 18-21.
234. Mesbah G Khan, Fartaj A. Heat transfer experiments of ethylene glycol-water mixture in multi-port serpentine meso-channel heat exchanger slab (FEDSM-ICNMM2010-31131). In: *Proceedings of the 3rd Joint US-European Fluids Engineering Summer Meeting (FEDSM) and 8th International Conference on Nanochannels, Microchannels, and Minichannels (ICNMM)*, August 1-5, 2010, Montreal, Quebec, Canada 2010.
235. Dehghandokht M, Mesbah G Khan, Fartaj A, Sanaye S. Flow and heat transfer characteristics of water and ethylene glycol-water in a multi-port serpentine meso-channel heat exchanger. *International Journal of Thermal Sciences* 2011; DOI: 10.1016/j.ijthermalsci.2011.03.004.
236. Moshfeghian M. Fluid flow and heat transfer in U-bend. *PhD Dissertation*; The Oklahoma State University, Oklahoma, USA, 1978.
237. User's Manual and DAQ Systems Specifications 2006-2009, National Instruments.

APPENDIX – A

TABULAR REPRESENTATION OF KEY OBSERVATIONS IN PREVIOUS LITERATURE SURVEY

Appendix - A

Table A. Summary of literature survey of some papers appeared during 1928-2009 dealing with the heat transfer and/or fluid flow in small diameter tubes, microchannels, microtubes, MCHS, and MCHX [24-27, 33, 37-39, 41, 79-192]

Ref.	Author (s)	Year	Test module	x-sec	Ch	D_h [μm]	Test fluids	Study method	Re test range	Re_{cr} /Trans	f	Po = fRe	Nu	Major focus / area of author(s) study
[79]	Davies & White	1928	Pipe	R	306-334	H ₂ O	H ₂ O	Experiment	60-4600	140-1440	NR	ND	NA	Flow of H ₂ O in rectangular pipe
[80]	Gambill & Bundy	1961	Channels	R	1000 - 1450	H ₂ O	H ₂ O	Experiment	9000-270000	NA	\approx	NA /NT	\uparrow	HT study of turbulent H ₂ O flow in ch
[33]	Tuckerman & Pease	1981	MCHS / Si	R	85.8-95.3	H ₂ O	H ₂ O	Experiment	730	NR	\approx	\approx	\uparrow	HT and FF in MCHS
[81]	Wu & Little	1983	MC/Glass/Si	R	48-92	N ₂ , H ₂ , Ar	N ₂ , H ₂ , Ar	Experiment	100-15000	350- 900	\uparrow	\uparrow	NA	f for laminar & turb. gas flows in MCs
[82]	Wu & Little	1984	MC/Glass/Si	Trp	134-164	N ₂ Gas	N ₂ Gas	Experiment	400-20000	1000-3000	NA	NT	\uparrow	HT in fine ch HX used in refrigeration
[83]	Acosta et al.	1985	MCs	R	0.2-0.5mm gap	H ₂ O, He	H ₂ O, He	Experiment	1300-22000	ND	\uparrow	\approx	\approx	Transport process in narrow passage
[84]	Harley & Bau	1989	MC/ KOH Si	Trp,R	45, 67	Isopropanol	Isopropanol	Experiment	2-250	NA	\uparrow	\uparrow	NA	Influence of liquid velocity & property
[85]	Missaggia et al.	1989	MCs	R	160	H ₂ O	H ₂ O	Experiment	2350	NC	\uparrow	\uparrow	ND	f & HT in MCHS in electronic cooling

Appendix – A: Table A. (Cont'd ...)

Ref.	Author (s)	Year	Test module	x-sec	Ch D_h [μm]	Test fluids	Study method	Re _{cr} /Trans	f	Po = f Re	Nu	Major focus / area of author(s) study
[86]	Nakagawa et al.	1990	MC / Si	R	9.75-9.94	DI H2O	Experiment	ND	\approx	ND	ND	MEMS analysis on Si chips
[87]	Pfahler et al.	1990	MC/ KOH Si	R	1.6-76	N-Propanol	Experiment	0.0008-300	$\uparrow f(\text{Re})$	$\uparrow f(\text{Re})$	NA	Liq transport in micron, submicron ch
[88]	Choi et al.	1991	MT/ Silica	C	3-81	N2 Gas	Experiment	20-20000	\downarrow	\downarrow	\uparrow	f and HT of N2 in Microtube, corrl
[89]	Lin et al.	1991	MT / Cu	C	660-1170	R-12/2-ph	Experiment	4640-37600	\uparrow	NA	NA	Local f , Δp during vaporiz in capillary
[90]	Pfahler et al.	1991	MC/ KOH Si	Trp	0.96-39.7	Si-oil, N2, He	Experiment	0.005-1000	\downarrow	\downarrow	NA	Gas and liquid f in small channels
[91]	Riddle et al.	1991	MCHS	R	86-96	H2O	Experiment	96-982	$\downarrow \approx \uparrow$	$\downarrow \approx \uparrow$	ND	Design and calculation of MCHS
[92]	Weisberg & Bau	1992	MCHS, 9ch	R	86-104	NC	Numerical	NC	NT	ND	NR	Optimization of thermal performance
[93]	Peng & Wang	1993	MC, SS	R	646	H2O	Experiment	NC	NA	NC	Diff.	Forced conv & FB HT of H2O in MC
[94]	Rahman & Gui	1993	MCHS / Si	Trp	338-388	H2O	Experiment	900-3000	\uparrow	\uparrow	\uparrow	Design of MCHS for avionics cooling
[95]	Rahman & Gui	1993	MCHS / Si	Trp	176-325	H2O	Experiment	275-3234	\approx	\uparrow	\uparrow	FF and HT in MC cooling passages

Appendix – A: Table A. (Cont'd ...)

Ref. Author (s)	Year	Test module	x-sec	Ch D_h [μm]	Test fluids	Study method	Re test range	Re_{cr} /Trans	f	Po = f/Re	Nu	Major focus / area of author(s) study
[96] Urbanek et al.	1993	MC/ KOH Si	Trp	5-25	1-3 Propanol	Experiment	NR	ND	$\uparrow f(T\uparrow)$	$\uparrow f(T\uparrow)$	NA	Temp dependent Po in MC flow
[97] Arkilic et al.	1994	MCs	R	2.6	He Gas	Experiment	<0.5	NA	\downarrow	\downarrow	NA	Slip and no-slip flow in MC
[98] Bowers & Mudawar	1994	MCHS	C	510-2450	R-113, 2-ph	Experiment	-	-	-	-	-	Boiling Δp of 2-ph in MCHS, corrl
[99] Peng et al.	1994	MCs/SS	R	133-367	H2O	Experiment	50-4000	200-700	\uparrow	NR	\downarrow	HT of H2O flow through MC, corrl
[100] Pong et al.	1994	MCs	R	1.94-2.33	N2, He 1-ph	Experiment	NC	NC / NA	\downarrow	\downarrow	NA	Δp of gas flow in MCs
[101] Wang & Peng	1994	MCs / SS	R	311-747	H2O/Methanol	Experiment	50-4000	300-800	NA	NR	\downarrow	1-ph conv of H2O in MCs, corrl
[102] Wilding et al.	1994	MC/ KOH Si	Trp	27-63	H2O, Blood	Experiment	10-100	NA	\uparrow	\uparrow	NA	f of H2O, blood and bio fluids in MCs
[103] Peng et al.	1994	MCs / SS	R	133-367	H2O	Experiment	50-4000	200-700	\uparrow	$\uparrow f(Re\uparrow)$	NA	f of H2O flow in MCs, corrl
[104] Gui & Scaringe	1995	MCs	Trp	338-388	H2O	Experiment	834-9955	1400	\uparrow	\uparrow	\uparrow	HT of H2O in MC entrance region
[105] Harley et al.	1995	MC/ KOH Si	Trp	1-67	N2, Ar, He	Exp/Theoretical	5-1200	NA	\downarrow	\downarrow	NA	Compressibility & rarefaction on Po

Appendix – A: Table A. (Cont'd ...)

Ref.	Author (s)	Year	Test module	x-sec	Ch D_h [μm]	Test fluids	Study method	Re _{cr} /Trans	f	Po = f Re	Nu	Major focus / area of author(s) study
[106]	Jiang et al.	1995	MC/ Glass	C	8-42	H2O	Experiment	0.3-1.2	NA	\approx	NA	f of H2O through MCs and nozzles
[107]	Liu et al.	1995	MCs / Si	R	2-33	N2, He gas	Experiment	< 0.01	NA	\downarrow	NA	MEMS for p distm of N2, He in MCs
[108]	Peng & Peterson	1995	MC/metallic	R	311-747	H2O/Methanol	Experiment	200~2800	300-1000	NA	NR	Diff. Fluid property, ch shape effect on Nu
[109]	Peng et al.	1995	Grooves/SS	R	310-646	Methanol	Experiment	700-2000	NR	NA	NT	Diff. HT characteristics of methanol in MCs
[110]	Yu et al.	1995	MT /Silica	C	19.6-102	N2 & H2O	Exp/Theoretical	250-20000	1700-6000	\downarrow	\downarrow	f and HT of N2 & H2O in Microtube
[111]	Cuta et al.	1996	MCHX	R	425	R-124	Experiment	101-578	NA	\approx	NT	Forced convective Nu in MCHX
[112]	Nguyen et al.	1996	MC/ KOH Si	Trip	690	H2O	Experiment	100-4500	1285	NA	NR	Forced convection in MFD
[113]	Peng & Peterson	1996	MCs /SS	R	133-367	H2O	Experiment	50-4000	200-700	\uparrow	$\downarrow\uparrow$	Conv. HT and f of H2O in MCs, corrl
[114]	Peng & Peterson	1996	MCHX /Cu	R	133-367	H2O/Methanol	Experiment	6-3500	70-400	NT	NT	Diff. Conv. HT of H2O, binary fluid in MC
[115]	Ravigururajan et al.	1996	MCHX	R	425	R-124	Experiment	Turbulent/NC	NC	NA	NR	\uparrow Conv HT inside rectangular MCHX

Appendix – A: Table A. (Cont'd ...)

Ref.	Author (s)	Year	Test module	x-sec	Ch D_h [μm]	Test fluids	Study method	Re _{cr} /Trans	f	Po = f Re	Nu	Major focus / area of author(s) study	
[116]	Shih et al.	1996	MCs	R	2.33	N ₂ , He gas	Experiment	< 0.1	NA	↓	NA	Gas flow in MC	
[117]	Arkilic et al.	1997	MC/ KOH Si	R	2.59	He gas	Exp/Analytical	0.001-0.01	NA	↓	NA	Slip flow in MC	
[118]	Harms et al.	1997	1/multi-ch MC	R	404-1923	DI H ₂ O	Experiment	173-12900	1500	≈	↑	Po and HT in 1-ph forced convection	
[119]	Jiang et al.	1997	MCs/Glass	C	8-42	H ₂ O	Experiment	0.01-4	NA	≈	NA	Laminar Δp & f in MC cooling system	
[41]	Mala et al.	1997	MC	R	Arbitrary	Liq.	Numerical	10-500	N/A	↑	↑	EDL effects on HT and FF in MCs	
[120]	Richter et al.	1997	MC/ KOH Si	Tri	23-147	H ₂ O	Experiment	NR	ND	≈	NA	FF & viscosity nature of H ₂ O in MCs	
[121]	Stanley et al.	1997	MCs/Al.	R	56-256	H ₂ O & 2-ph	Experiment	50-10000	1500	≈	≈	Liquid and 2-ph flow in MCs	
[122]	Adams et al.	1998	MCs / Al	C	760-1090	H ₂ O	Experiment	2600-23000	NA	NR	↑	Turb forced conv HT of H ₂ O in MCs	
[123]	Pfund et al.	1998	MCs / Si	R	200-900	H ₂ O	Experiment	40-2300	1450	≈	≈	Δp measurement in MCs	
[124]	Vidmar et al.	1998	Capillary/SS	C	131	H ₂ O, C ₇ H ₁₆	Experiment	7800- 38000	NA	NC	NR	≈	MC heat dissipatn, electronic cooling

Appendix – A: Table A. (Cont'd ...)

Ref.	Author (s)	Year	Test module	x-sec	Ch D_h [μm]	Test fluids	Study method	Re _{cr} /Trans	f	Po = f Re	Nu	Major focus / area of author(s) study
[125]	Webb & Zhang	1998	10ch/MC/Al	R	960 - 2130	R-134a	Experiment	6000-25000	NA	\approx	\approx	HT and f in small diameter channels
[126]	Adams et al.	1999	MCs / Cu	C	760	H2O	Experiment	5000-23000	NA	NA	\uparrow	Influence dissolve gas on HT in MCs
[127]	Adams et al.	1999	MC/Cu	Non-C	1130	H2O	Experiment	3900-21400	NA	NA	\approx	Applicability of turb correl to MC
[128]	Harms et al.	1999	68ch MC/Si	R	1000x251	DI H2O	Experiment	173-12900	1500	\approx	$\downarrow \approx \uparrow$	Forced conv HT- f in single & multi-ch
[39]	Mala and Li	1999	MT /Si, SS	C	50-254	DI H2O	Experiment	80-2500	300-900	\uparrow	NA	f of H2O in Microtubes
[129]	Papautsky et al.	1999	MiPip/metal	R	44-48	H2O	Experiment	0.001-10	NA	\uparrow	NA	Effect of MC axis ratio on laminar f .
[130]	Papautsky et al.	1999	MiPip/metal	R	28-58	H2O	Exp/Numerical	1-20	NA	\uparrow	NA	Laminar FF behavior in MCs
[131]	Xu et al.	1999	MCs	R	50-300	H2O	Experiment	NC	NC	\downarrow	NA	f for H2O flow in MCs
[132]	Araki et al.	2000	MC/ KOH Si	Trp	3-10	N2, He gas	Experiment	0.006-4.2	NA	\downarrow	NA	f of N2 and He in trapezoidal MCs
[133]	Celata et al.	2000	Capillary/SS	C	130	R-114	Experiment	100-8000	1881-2479	$\approx \uparrow$	$\downarrow \approx \uparrow$	f and HT in capillary tube for R114

Appendix – A: Table A. (Cont'd ...)

Ref.	Author (s)	Year	Test module	x-sec	Ch D_h [μm]	Test fluids	Study method	Re test range	Re_{cr} /Trans	f	Po = fRe	Nu	Major focus / area of author(s) study
[134]	Ding et al.	2000	MCs / SS	R, Tri	400-600	R-134a, R-12	Experiment	NC	1400-1800	\uparrow	$\uparrow f(Re\uparrow)$	NA	Δp and f of R-134a & R-12 in MCs
[135]	Judy et al.	2000	MTs / Si	C	20-150	H ₂ O, Hexane	Experiment	20-2000	NC	\downarrow	\downarrow	NA	Δp and f loss of liq in Microtubes
[136]	Li et al.	2000	MTs/Glass	C	80-180	N ₂ gas	Experiment	NC	≈ 2300	\uparrow	\uparrow	NA	f character of N ₂ in Microtubes
[137]	Li et al.	2000	MT / Gls, Si, SS	C	80-206	H ₂ O	Experiment	350-2300	1700-2000	$\approx \uparrow$	$\approx \uparrow$	NA	f of H ₂ O in MTs of diff. materials
[138]	Pfund et al.	2000	MCs / PolyC	R	128-1050	H ₂ O	Experiment	60-3450	1700	\uparrow	\uparrow	NA	f of H ₂ O in MCs of high axis ratio
[139]	Qu et al.	2000	MCs / Si	Trp	51-169	DIUF H ₂ O	Experiment	94-1491	1000	\uparrow	$\uparrow f(Re\uparrow)$	NA	f of H ₂ O in trapezoidal Si MCs
[140]	Qu et al.	2000	MCs / Si	Trp	62-169	DIUF H ₂ O	Exp/Numerical	100-1500	NC	NA	ND	\downarrow	HT of H ₂ O in trapezoidal si MCs
[141]	Rahman	2000	MCHS / Si	R	176 – 491	H ₂ O	Experiment	275-3234	NR	\uparrow	\uparrow	\uparrow	HT and f of H ₂ O in Si MCHS
[142]	Sharp et al.	2000	MTs / SS	C	75-242	H ₂ O	Experiment	50-2500	$\approx 2,300$	\approx	\approx	NA	Deviation from tran to turb. in MCs
[143]	Tso & Mahulikar	2000	MCs / Al	C	717-741	H ₂ O	Experiment	12-47	NA	NA	NR	\downarrow	Role of Br in viscous dissipatn in MCs

Appendix – A: Table A. (Cont'd ...)

Ref.	Author (s)	Year	Test module	x-sec	Ch D_h [μm]	Test fluids	Study method	Re test range	Re_{cr} /Trans	f	Po = fRe	Nu	Major focus / area of author(s) study
[144]	Xu et al.	2000	MCs / Al	R	30-344	H2O	Experiment	20-4000	1500	\approx	\approx	NA	f for Liquid flow in MCs
[145]	Yang et al.	2000	MCs / Cu	C	173-4010	H2O, R134a	Experiment	100-18000	1200-3800	\approx	\approx	NA	f of R134a & H2O in small tubes
[145]	Yang et al.	2000	MCs / Cu	C	173-4010	Air	Experiment	200-40000	1200-3800	\downarrow	\downarrow	NA	f of air in small tubes
[146]	Debray et al.	2001	MiniChs	R	590-2220	H2O	Experiment	70-53000	\approx	\approx	\approx	$\downarrow \approx \uparrow$	f of H2O in Minichannels
[147]	Ghiaasiaan & Laker	2001	MTs	C	760-1090	H2O	Review/model	5000-23000	NA	NA	NA	\uparrow	Turb conv in MC, particles effects
[148]	Jiang et al.	2001	MCHXs /Cu	R	300	H2O	Exp/Analytical	60-3000	600	\uparrow	\uparrow Corrl	\uparrow	HT and f performance of two MCHXs
[149]	Kandlikar et al.	2001	MC /SS	C	620-1067	H2O	Experiment	500-3000	\approx	\approx	\approx	\downarrow	Ch roughness on HT and f in MCs
[150]	Ren et al.	2001	MCs / Si	R	28 – 80	H2O, KCl	Exp/Analytical	1-60	NA	\uparrow	\uparrow	NA	Electrokinetic effect of liq in MC
[151]	Chung et al.	2002	Glass capillary	C	100	DI H2O	Experiment	~ 3237	NR	\approx	\approx	NA	Δp and f characters of H2O in MC
[151]	Chung et al.	2002	Glass capillary	C	100	N2 gas	Experiment	~ 662	NA	\uparrow	$\uparrow f(Re \uparrow)$	NA	Δp and f characters of N2 gas in MC

Appendix – A: Table A. (Cont'd ...)

Ref.	Author (s)	Year	Test module	x-sec	Ch D_h [μm]	Test fluids	Study method	Re _{cr} /Trans	f	Po = f Re	Nu	Major focus / area of author(s) study
[152]	Gao et al.	2002	MCs / Si	R	199-1923	H2O	Experiment	20-7400	\approx	\approx	Diff.	Forced conv. HT and f in MCs
[153]	Gao et al.	2002	MCs / Si	R	199-1923	H2O	Experiment	100-8000	\approx	\approx	$\approx \downarrow$	MC size effects on f & HT for H2O
[154]	Hegab et al.	2002	MCs / Al.	R	112 – 210	R-134a	Experiment	1280-13000	\downarrow	\downarrow	\downarrow	f and HT of R134a in MCs
[155]	Judy et al.	2002	MCs / Si, SS	C, S	15-150	H2O/Methanol	Experiment	8 – 2300	NF	\approx	NA	Frictional Δp of liq. flows in MCs
[156]	Kandlikar	2002	Mini/MCs	Various	Various	Various	Review	Various	Various	$\approx 1^{\text{st}}$	$\approx 1^{\text{st}}$	HT and Δp behavior at FB in MC
[157]	Kang et al.	2002	MCHX / Si	R	66.67	DI H2O	Experiment	80-820	NA	NR	$\downarrow \approx \uparrow$	Design and testing of a Si MCHX
[158]	Maynes & Webb	2002	MT / Silica	C	705	H2O	Experiment	600-5000	\approx	\approx	NA	Δp & velocity in sub-millimeter tube
[159]	Qu & Mudawar	2002	21-ch HS / Cu	R	349	DI H2O	Exp/Numerical	139-1672	NF	\approx	\approx	$\Delta p, f$ and HT of H2O flow in MCHS
[160]	Toh et al.	2002	200-ch HS	R	86-104	H2O	Numerical	0-600	NA	$\downarrow \approx$	$\approx \downarrow f(T, Re)$	FF and HT in MC for exp data of [25]
[161]	Turner et al.	2002	MCs/Si	R	4.7-95.8	N2, He, Air	Experiment	NC	NR	\approx	ND	f for compressible gas flows in MCs

Appendix – A: Table A. (Cont'd ...)

Ref.	Author (s)	Year	Test module	x-sec	Ch D_h [μm]	Test fluids	Study method	Re _{cr} /Trans	f	Po = f Re	Nu	Diff	Size effects on HT & f at micro-scale
[162]	Guo & Li	2003	Various	Various	Various	Various	Review	Various	< 2300	Diff	NR	NR	Size effects on HT & f at micro-scale
[163]	Bucci et al.	2003	Capillary/SS	C	290-520	H2O	Experiment	Up to 5300	2800-3200	\approx	\approx	\approx	1-ph f and HT of H2O flow in MCs
[164]	Jung & Kwak	2003	MCs /Si	R	100-133	H2O, FC-72	Experiment	55-330	NA	$\downarrow \approx \uparrow$	\uparrow	\uparrow	FF and HT in rectangular MCs
[165]	Kandlikar et al.	2003	MCs /SS	C	620-1067	H2O	Experiment	500-3000	\approx	\uparrow	\approx	\approx	Ch roughness effect on HT, f in MCs
[166]	Kim et al.	2003	MCs / Si	C	5-100	N2, Ar, He	Experiment	3-30	NA	\downarrow	NR	NR	f for gas flows in MCs
[167]	Lee & Garimella	2003	MCs / Si	R	318-903	H2O	Experiment	558-3636	NC	NR	NR	\approx	HT of H2O flow in MCs
[168]	Li et al.	2003	MT/Glass,SS	C	80 – 206	DI H2O	Experiment	350-2500	1700	$\uparrow \approx$	$\uparrow \approx$	NA	FF of H2O in Microtubes
[169]	Tu & Hrnjak	2003	MCs / Si	R	69-305	R-134a	Experiment	112-3500	NC	\approx	\approx	NA	1-ph flow Δp of R-134a in MCs
[170]	Wu & Cheng	2003	MCs / Si	Trp	26-291	DI H2O	Experiment	0-3200	1500-2000	$\uparrow \approx$	$\uparrow \approx$	NA	Laminar f of H2O in Si MCs
[171]	Wu & Cheng	2003	MCs / Si	Trp	26-291	DI H2O	Experiment	0-1400	NA	\uparrow	$\uparrow f(\text{Re}\uparrow)$	\approx	Conv HT in MC, diff surface condition

Appendix – A: Table A. (Cont'd ...)

Ref.	Author (s)	Year	Test module	x-sec	Ch D_h [μm]	Test fluids	Study method	Re _{cr} /Trans	f	Po = f Re	Nu	Major focus / area of author(s) study
[172]	Baviere et al.	2004	MCs/Si	R	9-40	H2O	Experiment	0.1-300	NA	\approx	NA	f of H2O in MCs
[173]	Cui et al.	2004	MTs /Glass	C	3-10	DI H2O	Experiment	0.6-24	NA	\approx	NA	Flow character of hi p H2O in MCs
[173]	Cui et al.	2004	MTs /Glass	C	3-10	Isopro, CC14	Experiment	0.1-14	NA	\uparrow	NA	Flow character of hi p liq in MCs
[174]	Hsieh et al.	2004	MCs/Si	R	146	DI H2O	Experiment	0-1000	240	\uparrow	NA	H2O flow friction in rectangular MC
[175]	Lelea et al.	2004	MTs /SS	C	100-500	DIS H2O	Exp/Numerical	50 – 800	NF	\approx	\approx	HT and FF of H2O in SS Microtube
[24]	Owhaib & Palm	2004	MCs /SS	C	800-1700	R-134a	Experiment	1000-17000	NT	NA	NR	Conv HT of R134a in MCs
[176]	Sharp & Adrian	2004	MTs / Silica	C	50-247	H2O, Propanol	Experiment	20-2900	1800-2000	\approx	NA	Liq. trans-to-turb. in Microtubes
[177]	Jokar / Amir et al.	2005	MCHE/ Al	R	2600-4100	R134a, Glycol	Experiment	\sim 800	NR	\uparrow	NR	HT & FF of R134a, Glycol in MCHE
[25]	Hestroni et al.	2005	Various	Various	1.01-4010	Gas & Liq	Exp/Review	0.001-4000	1800-2200	\approx	NA	Liq /Gas MC flow literature compared
[178]	Kohl et al.	2005	MC/ KOH Si	R	25-100	H2O, Air	Experiment	4.9- 2068	NF	\approx	NA	f of H2O, Air in MC by internal p measure

Appendix – A: Table A. (Cont'd ...)

Ref.	Author (s)	Year	Test module	x-sec	Ch D_h [μm]	Test fluids	Study method	Re _{cr} /Trans	f	Po = f Re	Nu	Major focus / area of author(s) study
[179]	Lee et al.	2005	10-ch MC/Cu	R	318-903	DI H2O	Exp/Numerical	300-3500	1500-2000	NA	NT	$\uparrow \approx$ HT in rectangular MCs using H2O
[180]	Yang et al.	2005	MCs /Cu	C	167-182	H2O	Exp/Numerical	40-2000	1000-1600	\uparrow	NA	H2O f characters in curved MCs
[181]	Baviere et al.	2006	MC /Brass, SS	R	285-583	DI H2O	Exp/Numerical	200-8000	3400-4500	\approx	\downarrow	Bias effect on HT measure in MCs
[182]	Rands et al.	2006	MTs / Si	C	16.6-32.2	DDI H2O	Experiment	300-3400	2100-2500	\approx	NA	Frictional Δp for H2O flow in MC
[37]	Steinke & Kandlikar	2006	28-ch MC/ Si	Trp	8-990	H2O, Others	Review /Exp	0.002-5000	NC	\approx	NA	1-ph liq flow f in MCs
[183]	Caney et al.	2007	MC / Al	S	1000	NC / Liq.	Experiment	310-7780	\approx	\approx	\approx	f and HT in 1-ph flow in Minichannel
[184]	Xiong & Chung	2007	MCs /Si srt	R	209-549	DI H2O	Experiment	47-2268	1500-1700	\approx	NA	FF of H2O in straight/serpentine MCs
[184]	Xiong & Chung	2007	MCs /Si serp	R	209-549	DI H2O	Experiment	47-2268	100-200	\uparrow	NA	FF of H2O in straight/serpentine MCs
[185]	Celata et al.	2007	MTs /Si	C	30-254	He Gas	Experiment	0.8-500	NA	\approx	NA	Compressible gas flow in Microtube
[186]	Hrnjak & Tu	2007	MCs / PVC	R	70-305	R134 liq, vap	Experiment	112-9180	1570-2290	$\approx \uparrow$	\approx	Δp of R134a liquid and vapor in MCs

Appendix – A: Table A. (Cont'd ...)

Ref.	Author (s)	Year	Test module	x-sec	Ch D_h [μm]	Test fluids	Study method	Re test range	Re_{cr} /Trans	f	Po = f Re	Nu	Major focus / area of author(s) study
[187]	Kang & Tseng	2007	MCHX / Si	R	66.67	H2O	Numerical	NR	NR	NR	NR	ND	ε - Δp model Micro crossflow HX
[188]	Liu et al.	2007	1-ch MC	C	100	H2O	Numerical	10-200	NA	\approx	\approx	\uparrow	Numerical study of FF and HT in MC
[26]	Qi et al.	2007	MTs / Cu	C	531-1931	Liq. N2	Experiment	10000-90000	NA	\uparrow	NA	\uparrow	Δp and HT of liq N2 in Microtubes
[38]	Tang et al.	2007	MTs / SS	C	119-300	N2, He gas	Exp/compare	14-5200	900-1800	\uparrow	\uparrow	NA	Compressibility-roughness-rarefaction, MC
[38]	Tang et al.	2007	MTs / Si	S	10-201	N2, He gas	Exp/compare	3-6200	\approx	\approx	\approx	NA	Compressibility-roughness-rarefaction, MC
[189]	Wang & Liu	2007	Arbitrary	S	Arbitrary	Arbitrary	Numerical	130-541	NA	\uparrow	\uparrow	\uparrow	Ch curvature effect on HT in MC
[190]	Park & Punch	2008	MCs / Si	R	106-307	DI H2O	Experiment	69-800	NA	\approx	\approx	\uparrow	f and HT of H2O in multi-port MCs
[191]	Jiang et al.	2008	13-ch MC	R	504	DI H2O	Experiment	300-6000	1100	\downarrow	\downarrow	$\downarrow \approx \uparrow$	FF and HT in rectangular MC
[27]	Mokrani et al.	2009	MC / SS	R	100-1000	H2O	Experiment	100-5000	2000-3000	\approx	\approx	\approx	FF and HT in flat rectangular MC
[192]	Naphon & Khonseur	2009	MCHS / Acrl	R	333-500	Air	Experiment	200-1000	N/A	IC	NR	\uparrow	Air conv HT and Δp in rectangular MCHS

Appendix – A: Table A. (Cont'd ...)

Elaboration of terminology / short forms used in Table – A

Acrl	= Acrylic	f(x)	= Function of x	NA	= Not available / applicable	SS	= Stainless steel (NOT Chemical formal)
Al	= Aluminum	FB	= Flow boiling	NC	= No comments / Not clear	Trans	= Transition
C	= Circular	FF	= Fluid flow	ND	= No data	Tri	= Triangular
ch	= Channel	H2O	= Water	NF	= Not found / observed	Trp	= Trapezoidal
Conv	= Convective / convection	HT	= Heat transfer	NM	= Not measured	Turb	= Turbulent
Corrl	= Correlation proposed	IC	= Inconclusive	Non-C	= Non-circular	vap	= Vapor
Cu	= Copper	Isopro	= Isopropanol	NR	= Not reported	x-sec	= Cross-section
D_h	= Hydraulic diameter	Lam	= Laminar	NT	= Not tested	Δp	= Pressure drop
DDI	= Distilled deionized	Liq.	= Liquid	ph	= Phase	' \approx '	= Similar to classical / traditional theory or value
DI	= Deionized	MC	= Microchannel	PloyC	= Polycarbonate	\uparrow	= Higher than classical / conventional value
Diff	= Different than classical nature	MCHE	= Minichannel heat exchanger	R	= Rectangular	\downarrow	= Lower than classical / conventional value
	or inconclusive or chaotic	MCHS	= Microchannel heat sink	Ref	= Reference	$\downarrow \approx \uparrow$	= In the same experiment, lower or higher than
DIS	= Distilled	MCHX	= Microchannel heat exchanger	S	= Square		or similar to classical prediction i.e. chaotic
DIUF	= Deionized Ultra-filtered	MiniChs	= Minichannels	Serp	= Serpentine		
EDL	= Electric double layer	MiPip	= Micropipette	Si	= Silicon		
Exp	= Experiment	MT	= Microtube	Srt	= Straight		
f	= Friction factor	MTs	= Microtubes				

APPENDIX – B

DETAILS OF THE DEVELOPED TEST FACILITY, TEST SPECIMENS, TEST CHAMBERS, INSTRUMENTS ETC.

APPENDIX – B1

DETAILS OF THE DEVELOPED EXPERIMENTAL TEST FACILITY

Appendix – B1. Details of the developed experimental test facility

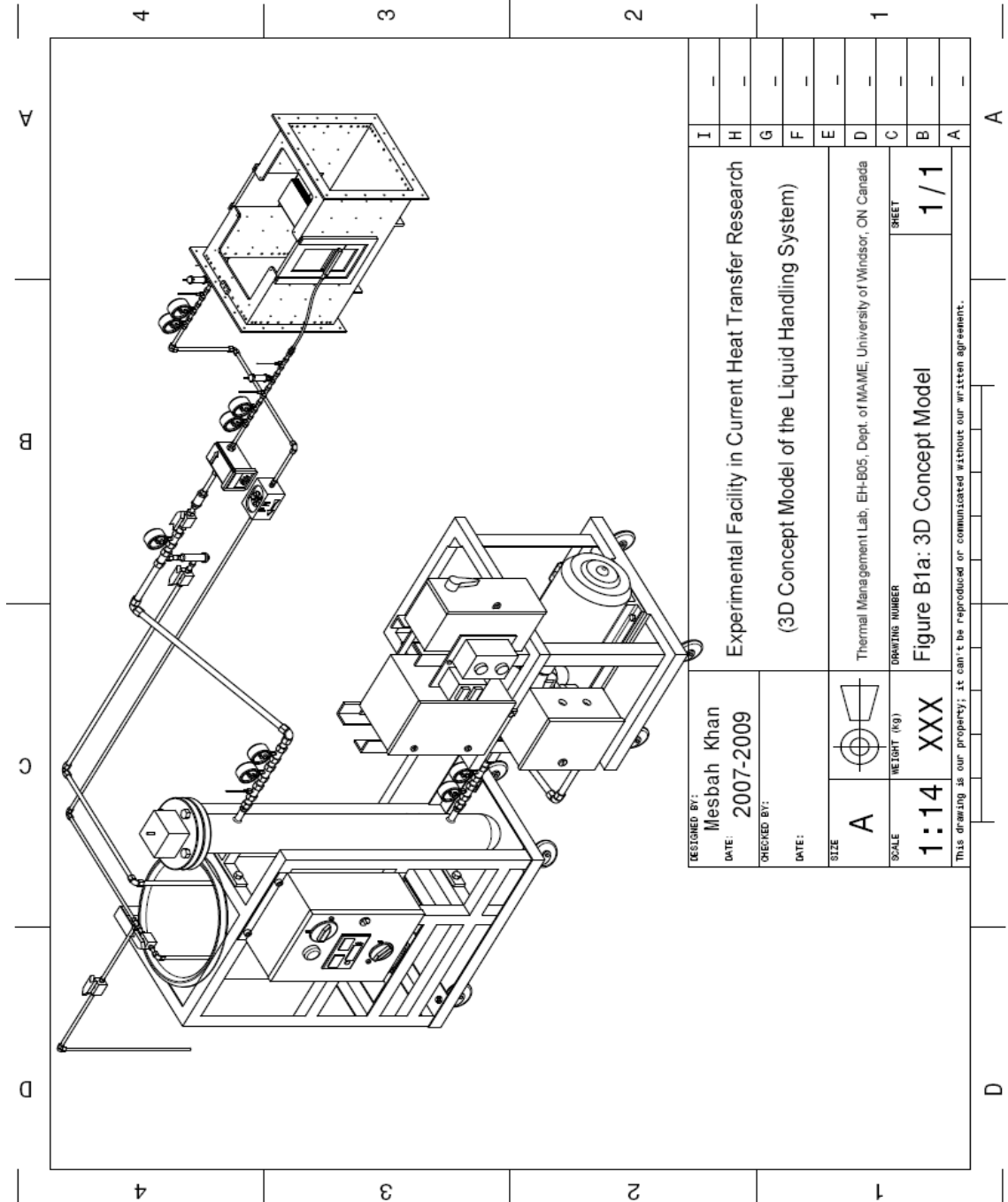


Figure B1a. 3D Models of the developed thermo-fluid experimental facility in current research.

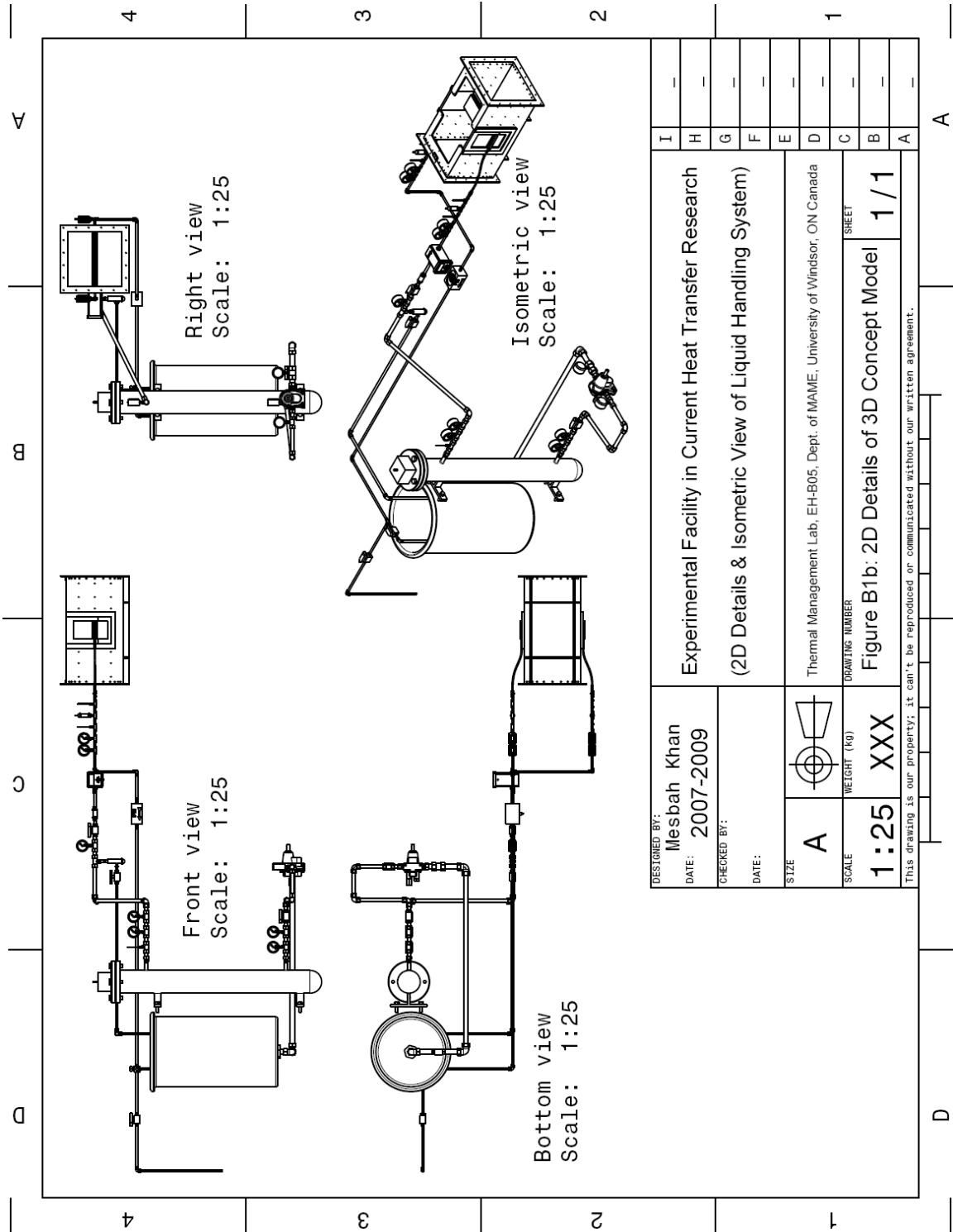


Figure B1b. 2D Details of the developed thermo-fluid experimental facility in current research.

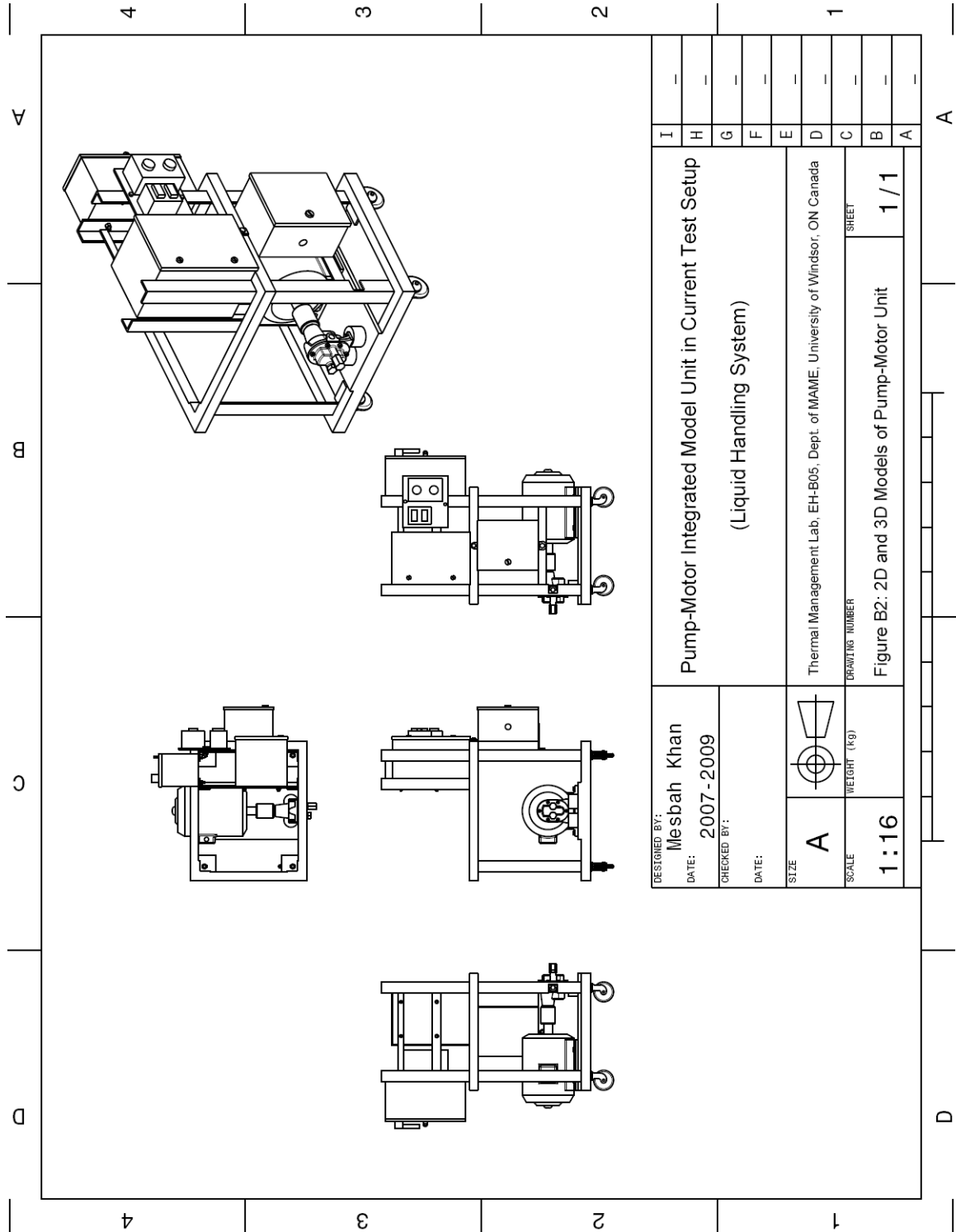
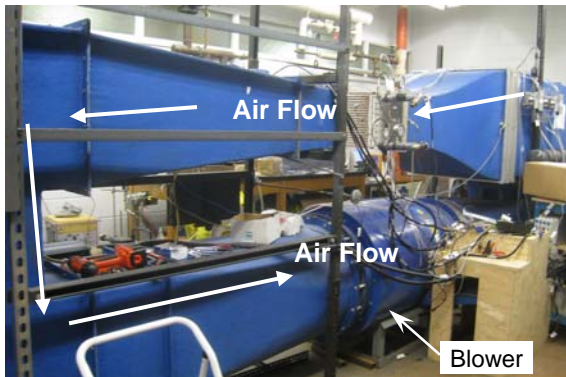
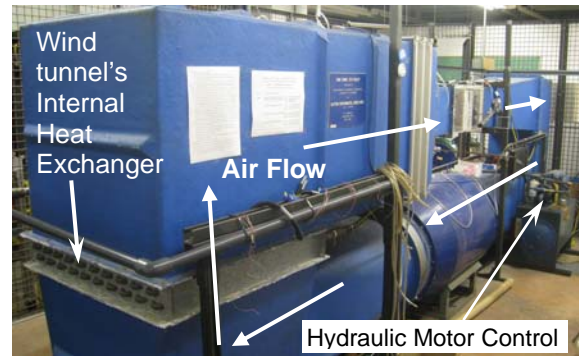


Figure B2. Detail 2D layout of Pump-Motor unit for the experimental facility in current research.



a. Wind tunnel front (no liquid handling system)



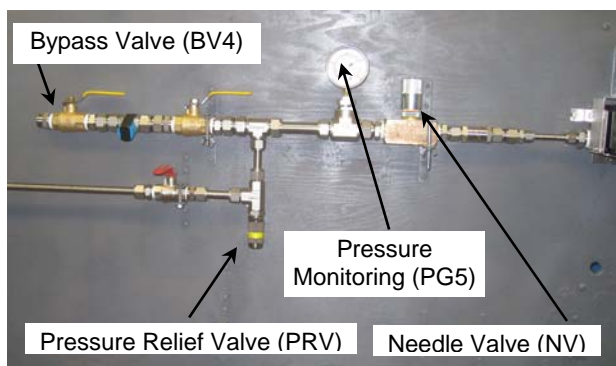
b. Wind tunnel back (no liquid handling system)



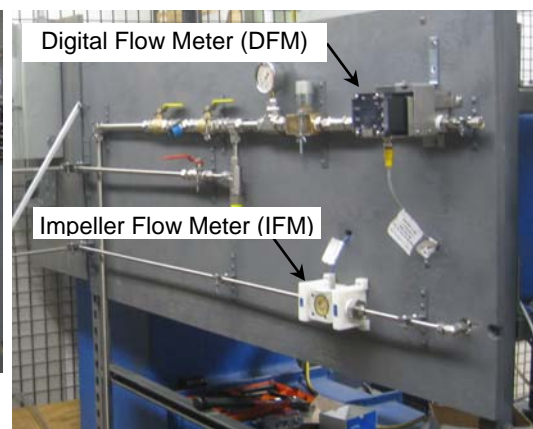
c. Liquid handling system panel construction-1



d. Liquid handling system panel construction-2



e. Liquid handling system panel construction-3

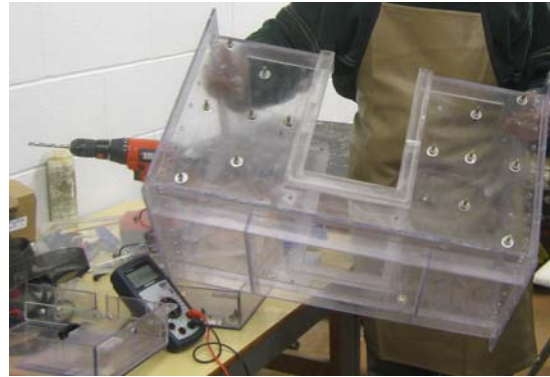


f. Liquid system panel construction-4

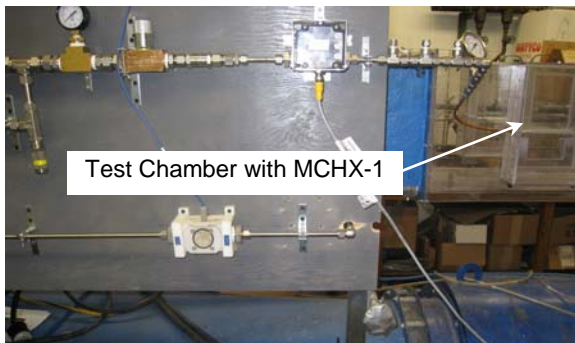
Figure B4. Photographs in construction phase as test facility development progresses



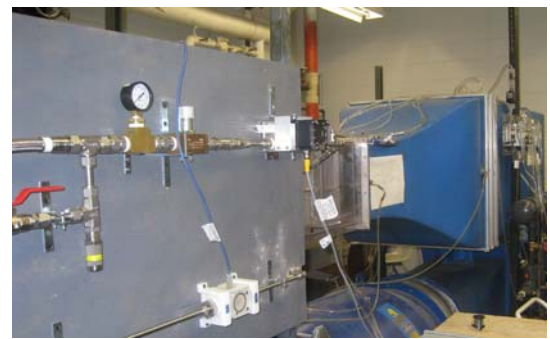
g. Test Chamber Finishing and Assembling-1



h. Test Chamber Finishing and Assembling-2



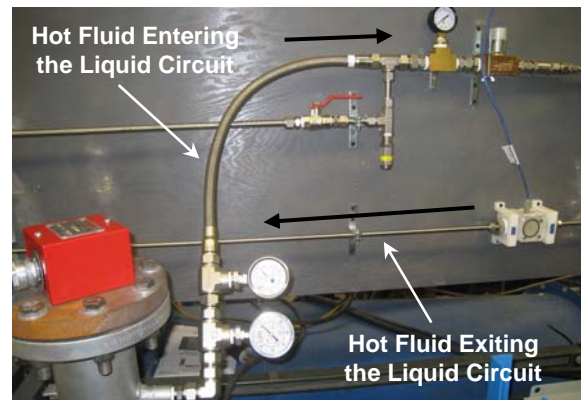
i. Liquid handling system panel construction-5



j. Liquid handling system panel construction-6

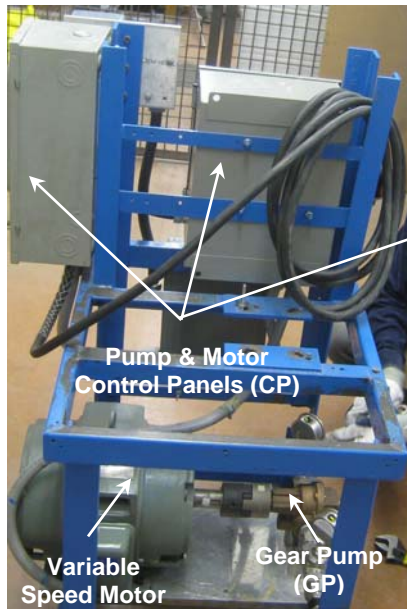


k. Tank-Heater Cart Unit Assembly & Fitting

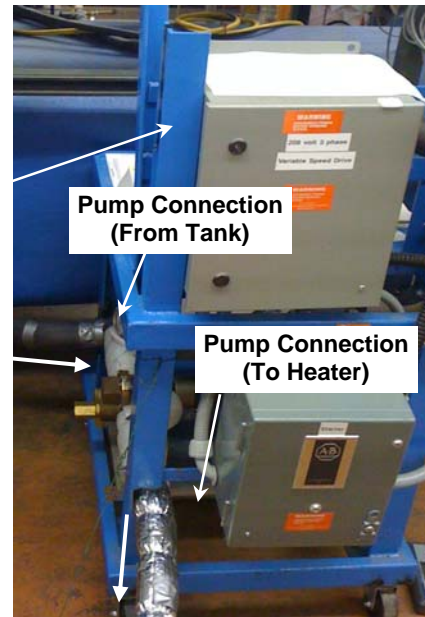


l. Tank-Heater Cart Unit Trial Connection with the Liquid Handling System

Figure B4. Photographs in construction phase as test facility development progresses (cont'd)



m. Pump-Motor Cart Unit Assembly & Fitting



n. Pump-Motor Cart Unit Trial Connection



o. Airside Pressure Transducers Testing



p. Airside Pressure Transducers Wiring

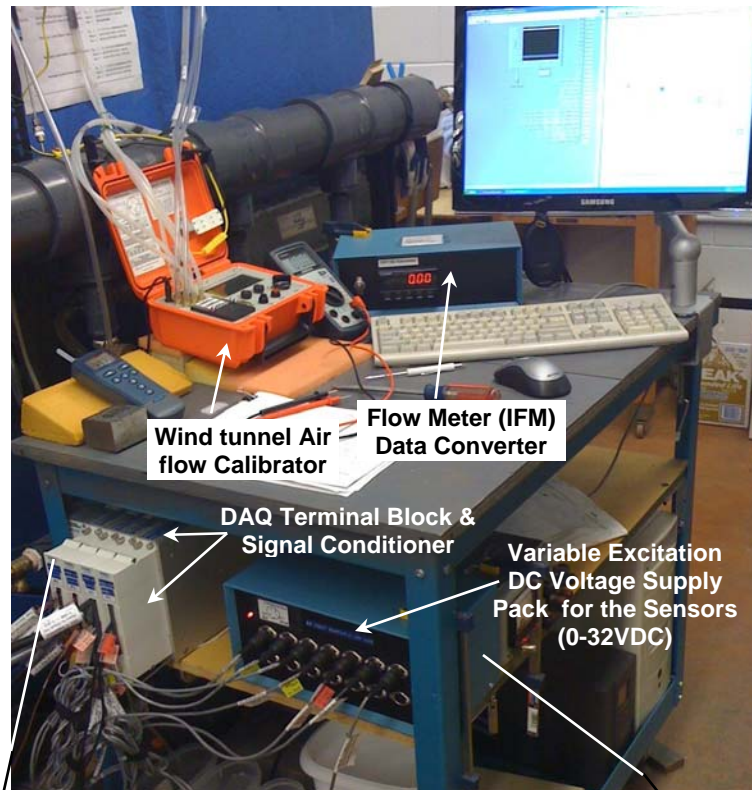


q. Airside Pressure Transducers Panel Making



r. Airside Pressure Transducers Panel Mounting

Figure B4. Photographs in construction phase as test facility development progresses (cont'd)



s. Data Acquisition (DAQ) System Assembly Cart

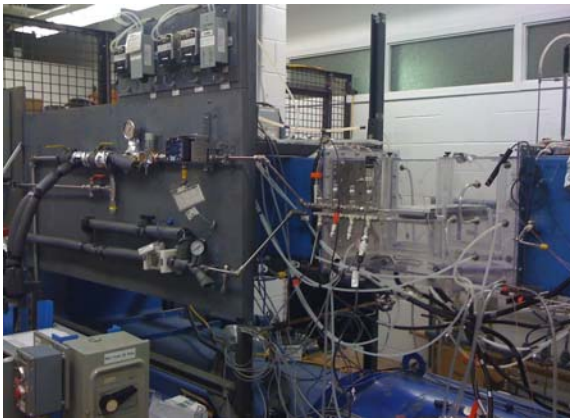


t. DAQ TB (Measurement Signal Receptor)



u. DC Excitation Voltage Supply Unit for Measurement Sensors & Instruments

Figure B4. Photographs in construction phase as test facility development progresses (cont'd)



v. Instrumentation and System Insulation-1



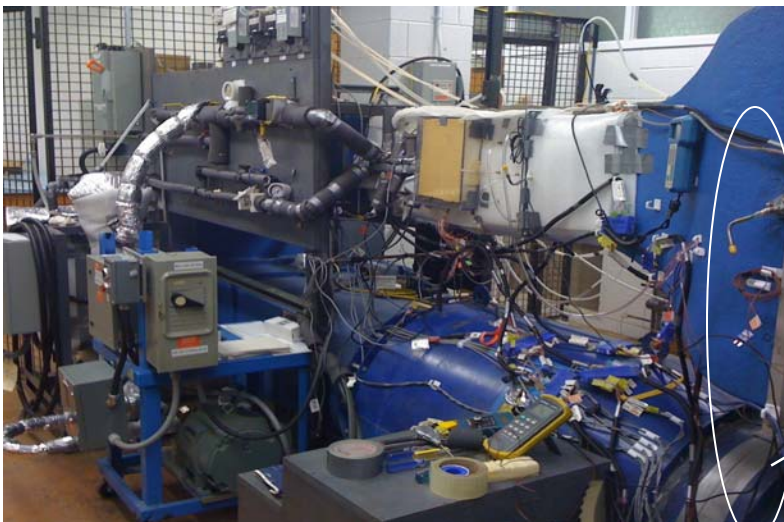
w. Instrumentation and System Insulation-2



x. Instrumentation and System Insulation-3



y. Instrumentation and System Insulation-4



z. Fully instrumented and insulated Complete Test Facility



DAQ System

Figure B4. Photographs in construction phase as test facility development progresses (cont'd)

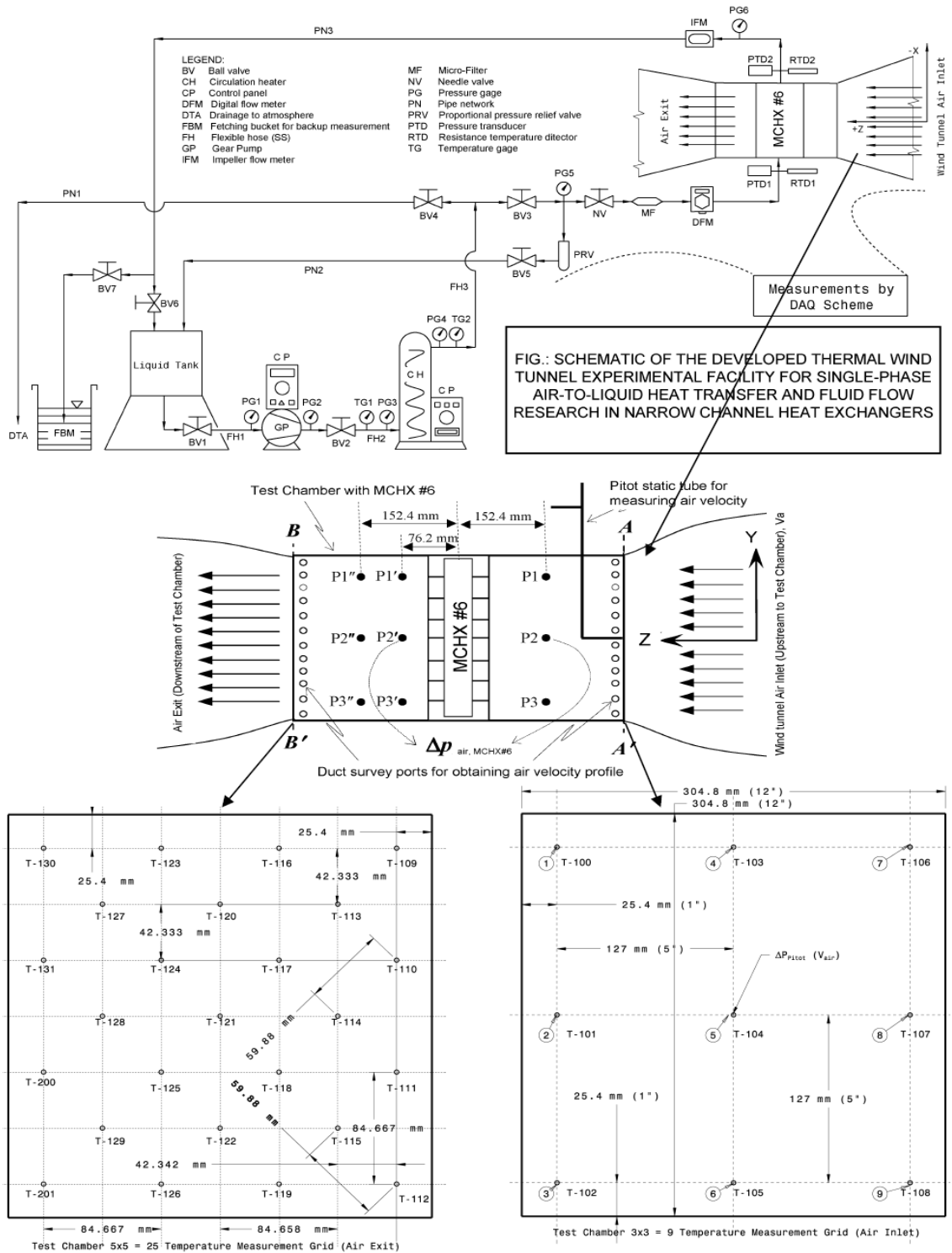


Figure B5. Experimental Facility with wind tunnel test section and thermal measurement grids

APPENDIX – B2

DETAILS OF THE DESIGN AND FABRICATED MCHX TEST SPECIMENS

Appendix – B2. Details of the design and fabricated MCHX test specimens

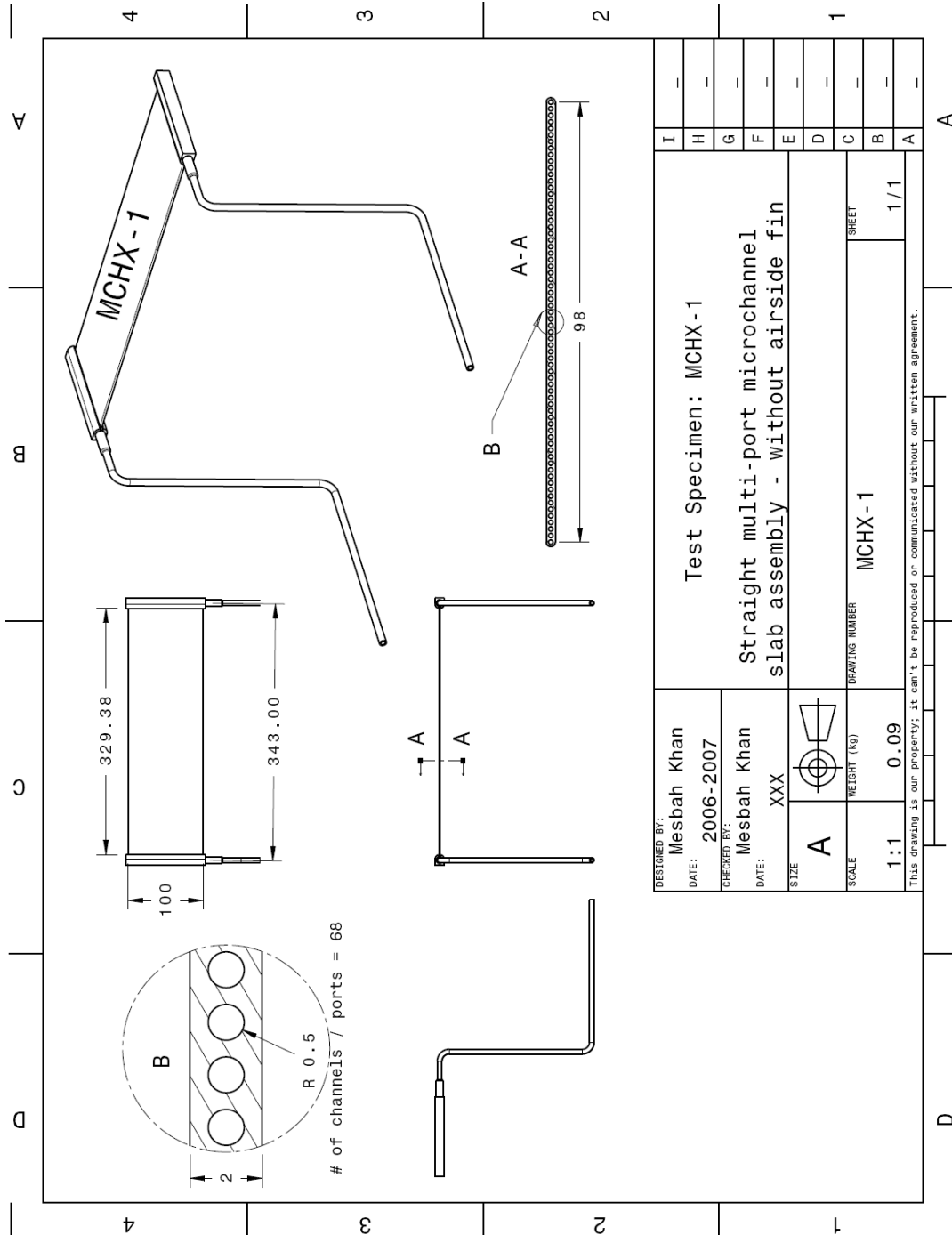


Figure B2.1a. Multi-port microchannel test specimen design (3D/2D) for current study – MCHX-1

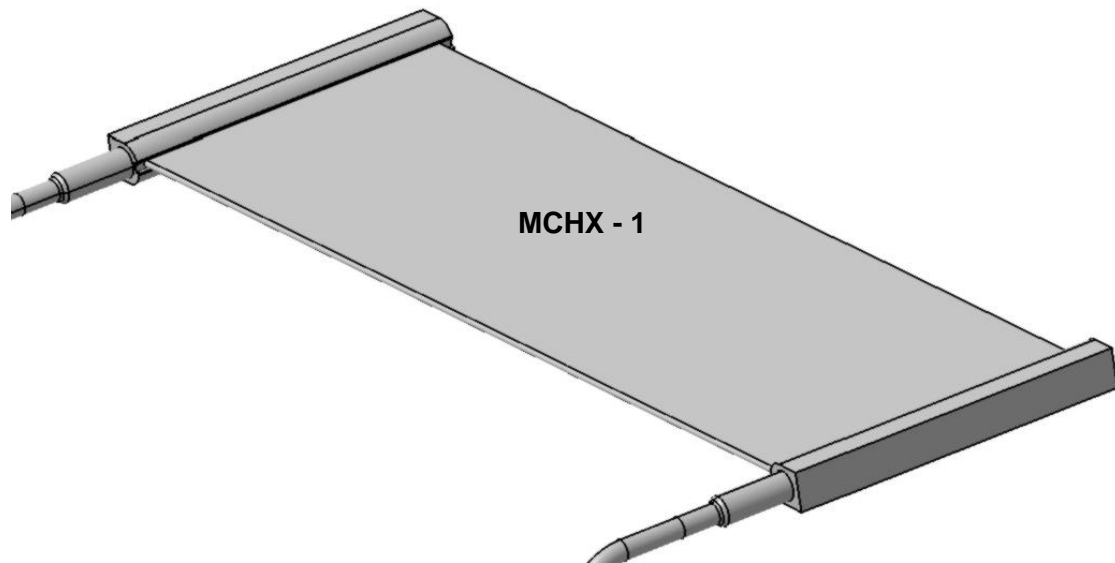


Figure B2.1b. Solid Model of current fabricated multi-port microchannel test specimen – MCHX-1

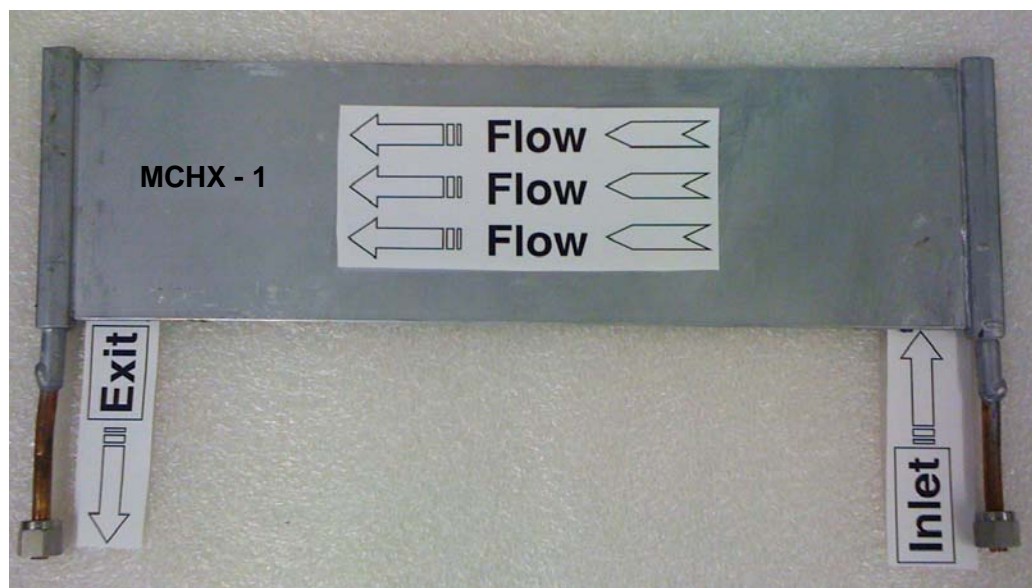


Figure B2.1c. Photograph of current fabricated multi-port microchannel test specimen – MCHX-1

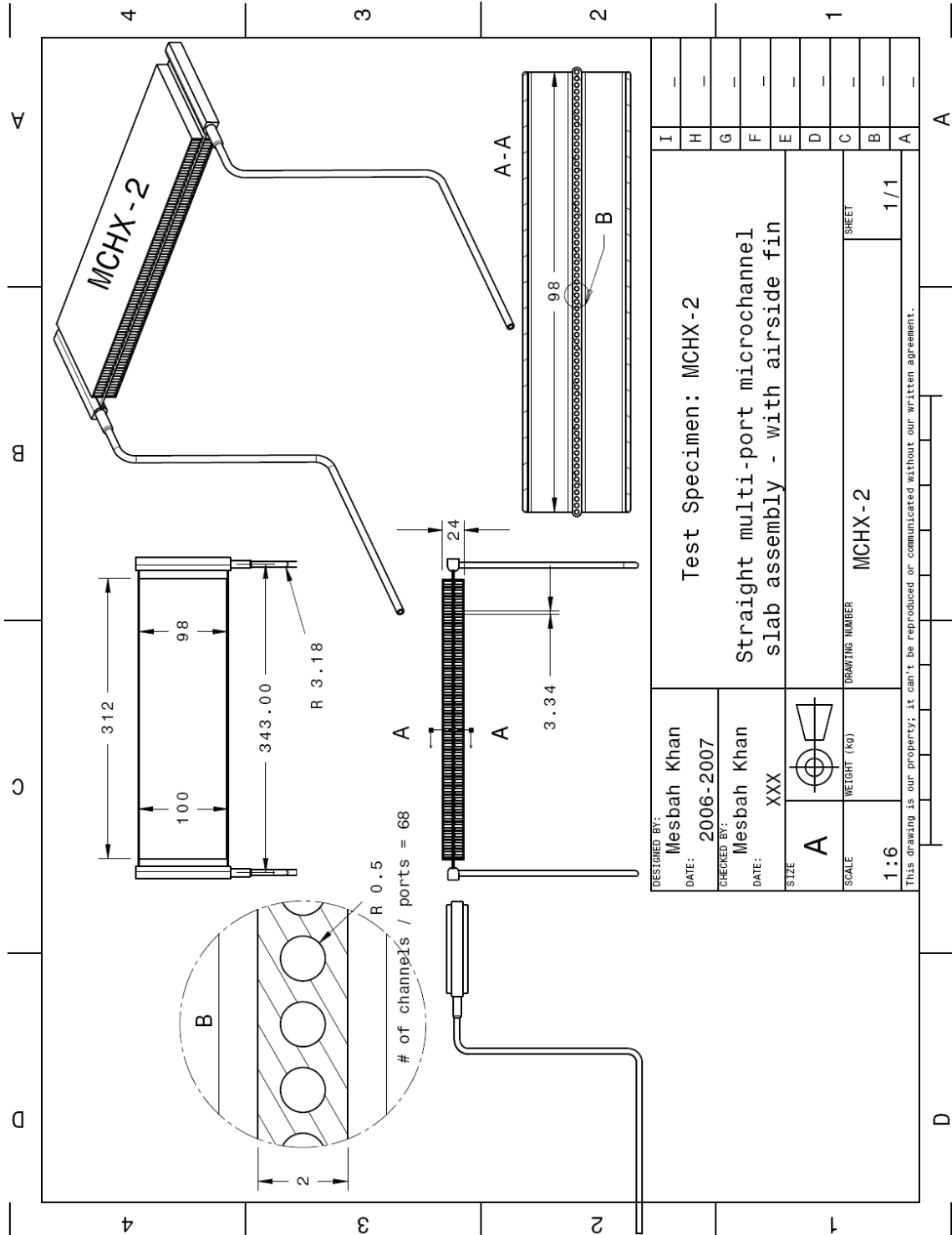


Figure B2.2a. Multi-port microchannel test specimen design (3D /2D) for current study – MCHX-2

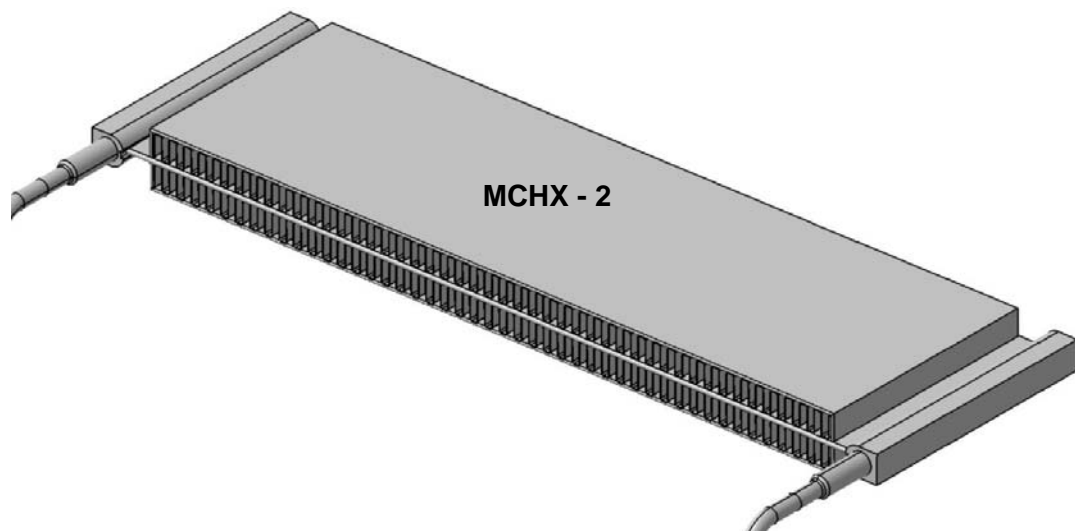


Figure B2.2b. Solid Model of current fabricated multi-port microchannel test specimen – MCHX-2

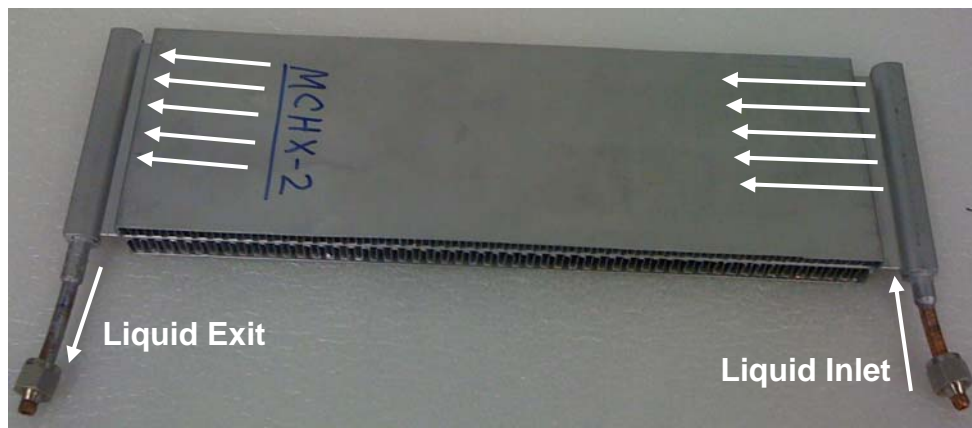


Figure B2.2c. Photograph of current fabricated multi-port microchannel test specimen – MCHX-2

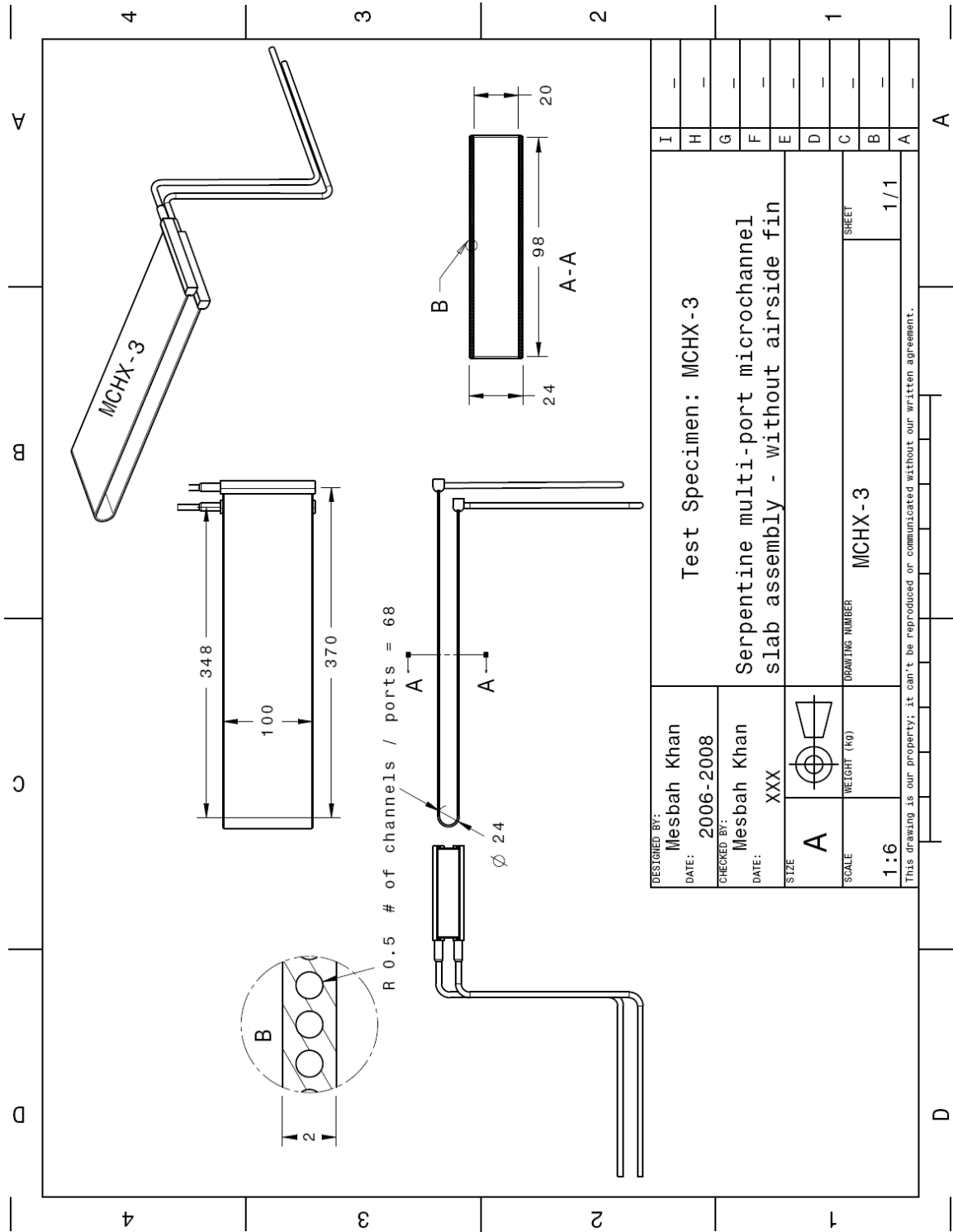


Figure B2.3a. Multi-port microchannel test specimen design (3D / 2D) for future study – MCHX-3

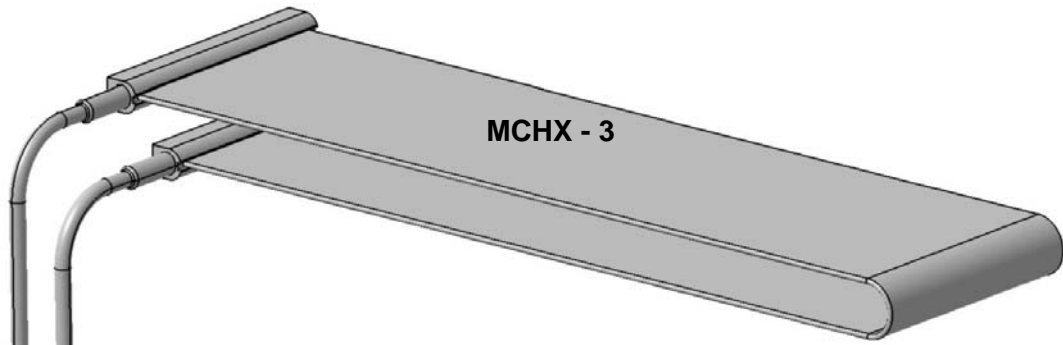


Figure B2.3. Solid Model of fabricated multi-port microchannel test specimen – MCHX-3
(proposed for future study)

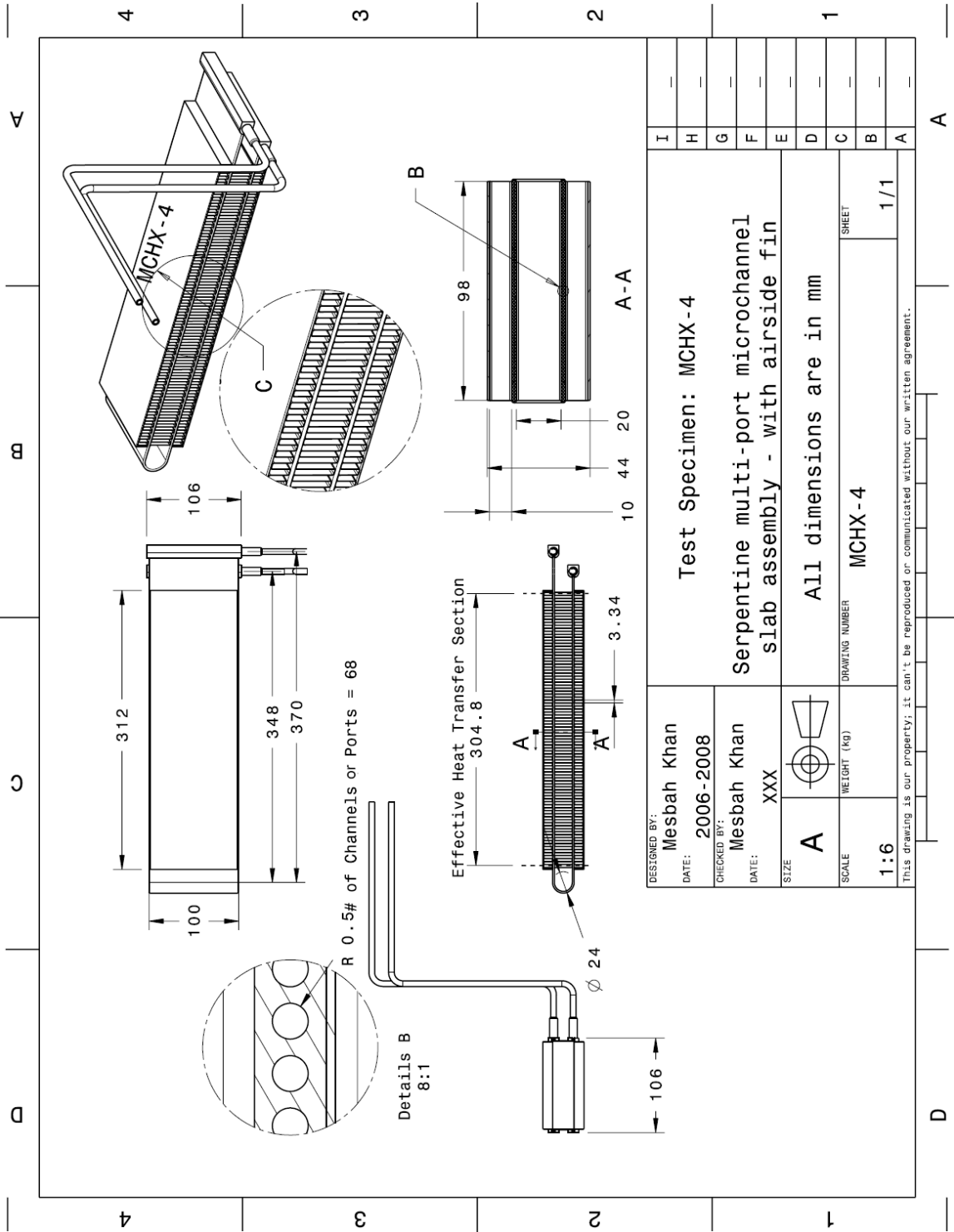


Figure B2.4a. Multi-port microchannel test specimen design (3D/2D) for current study – MCHX-4

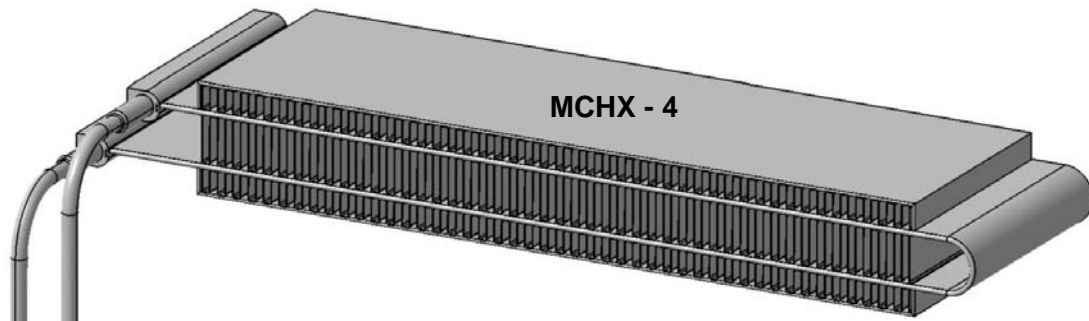


Figure B2.4b. Solid Model of current fabricated multi-port microchannel test specimen – MCHX-4

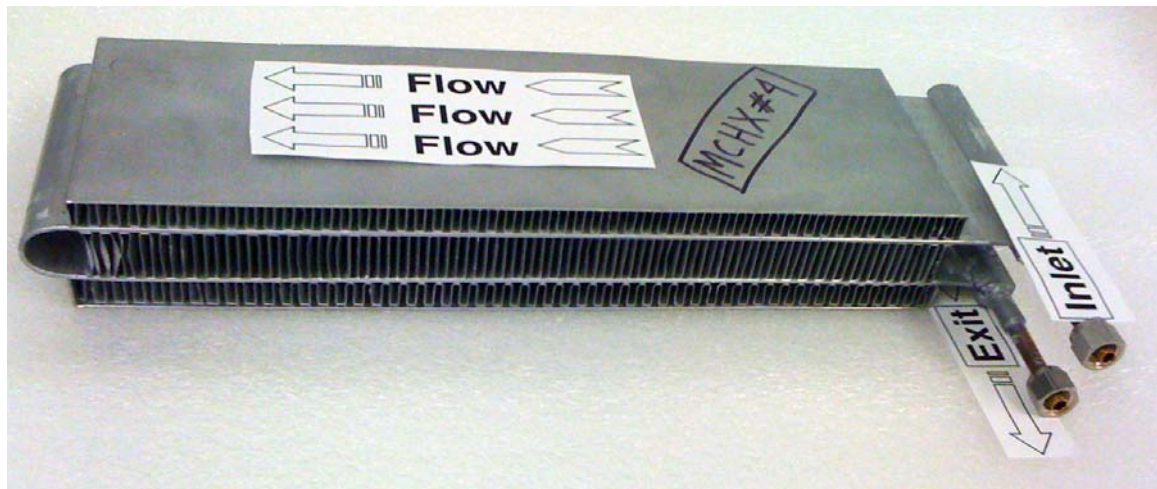


Figure B2.4c. Photograph of current fabricated multi-port microchannel test specimen – MCHX-4

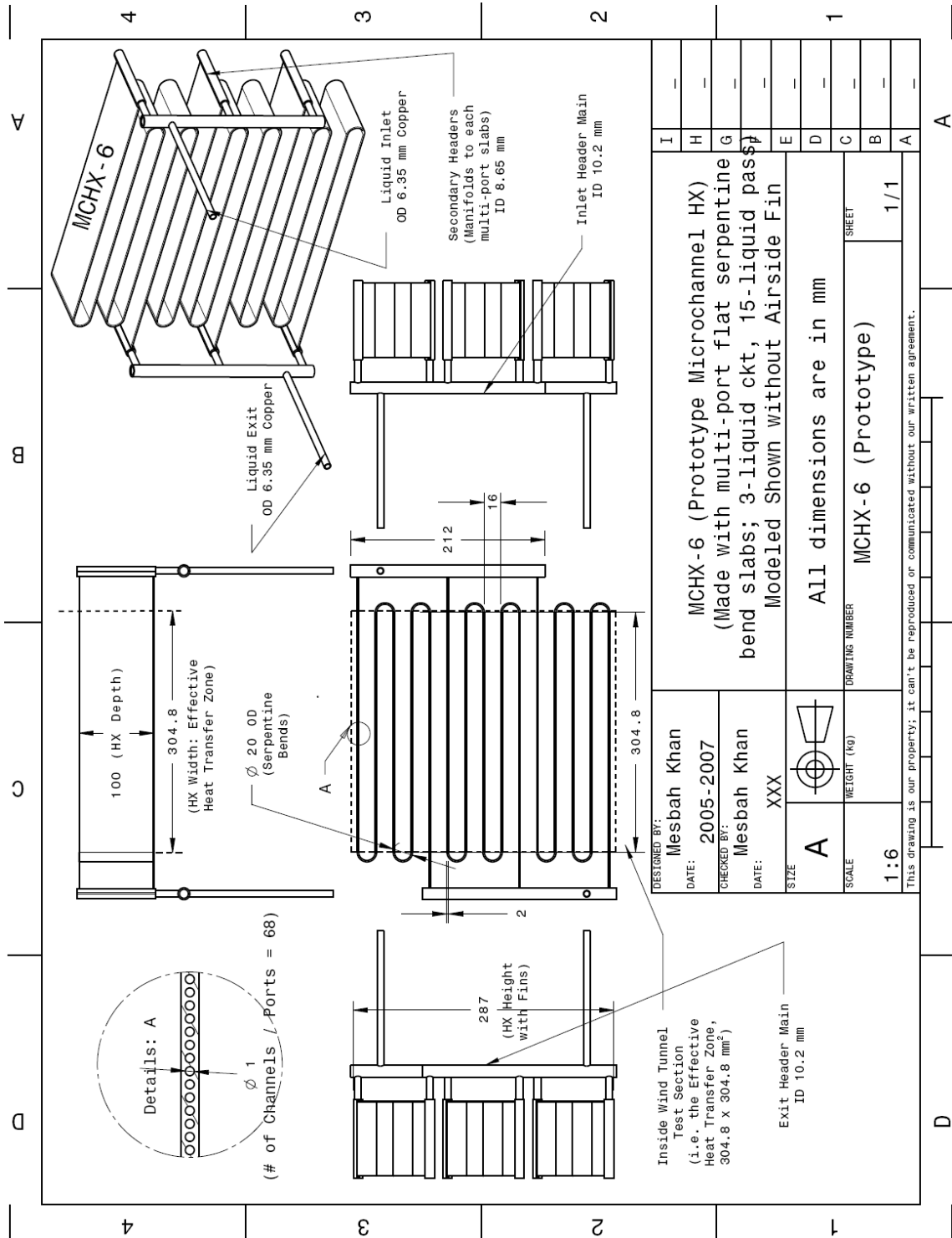


Figure B2.6a. Multi-port microchannel prototype design (3D/2D) for current study – MCHX-6

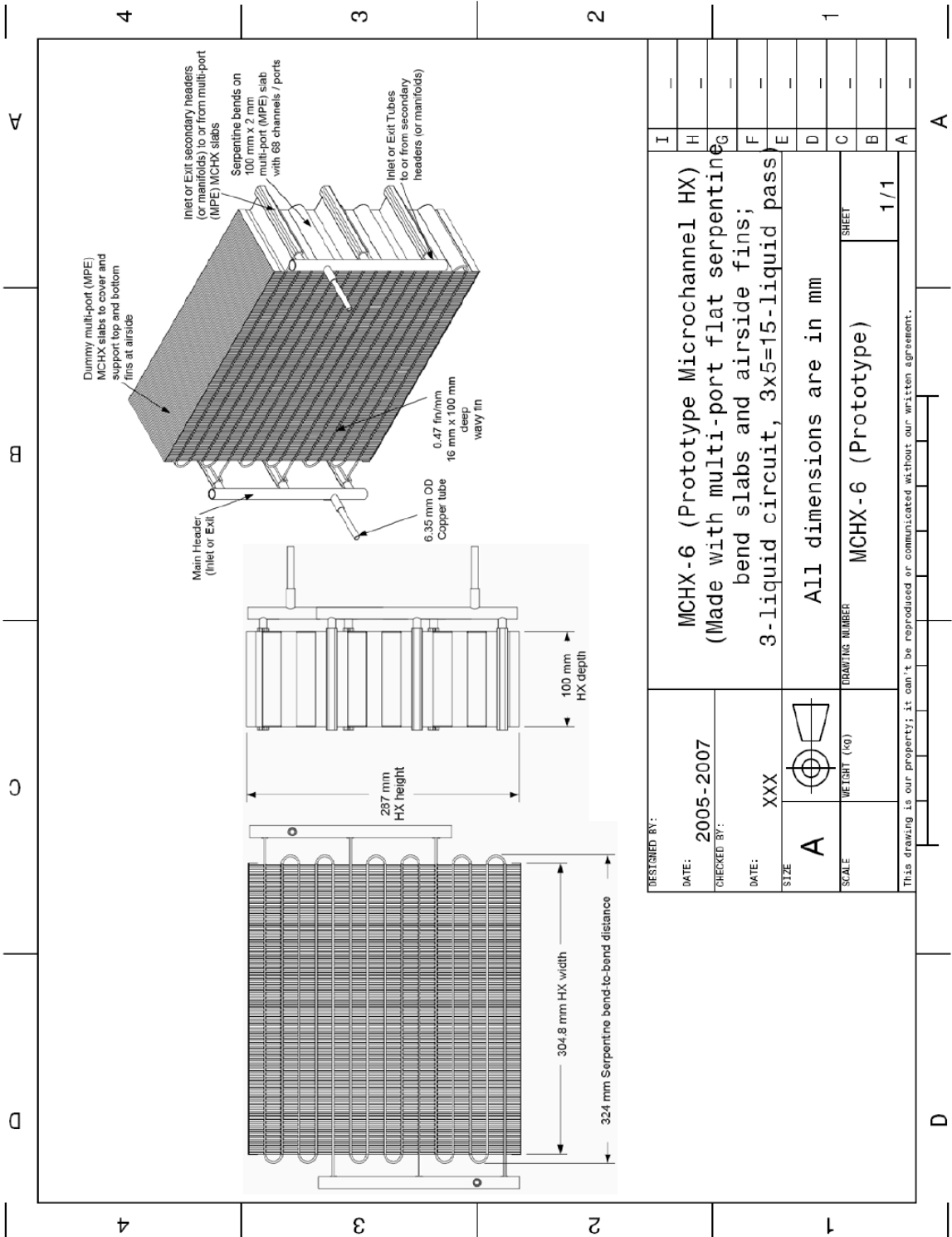


Figure B2.6b. Multi-port microchannel prototype design for current study – MCHX-6 (with Fins)

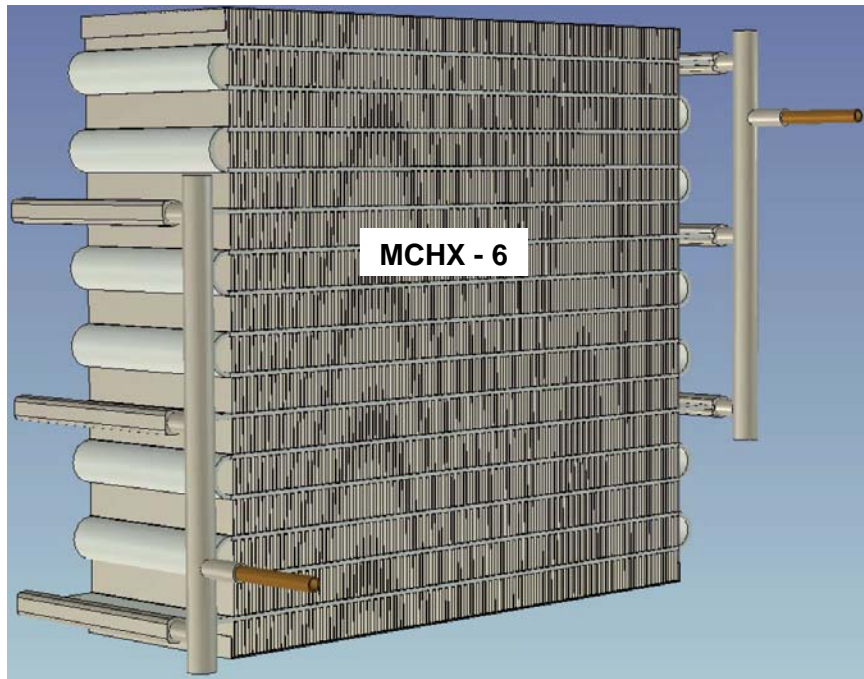


Figure B2.6c. Solid model of fabricated microchannel prototype design in current study– MCHX-6



Figure B2.6d. Photograph of fabricated microchannel prototype design in current study– MCHX-6

APPENDIX – B3

DETAILS OF THE DESIGNED & FABRICATED TEST CHAMBERS FOR MCHX

Appendix – B3 Details of the designed & fabricated test chambers for MCHX

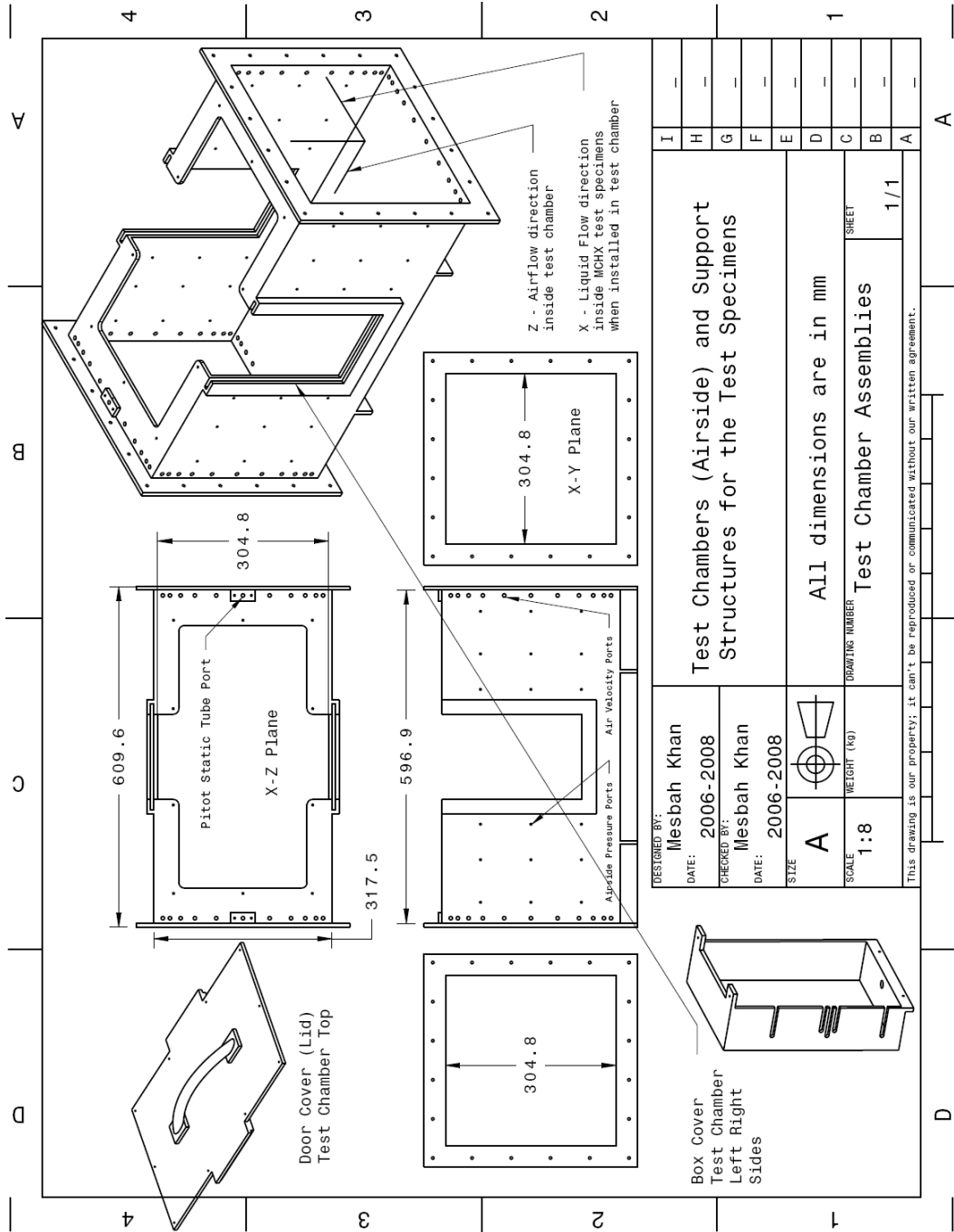


Figure B3. Design of support test chamber for MCHX test specimens for current study (General)

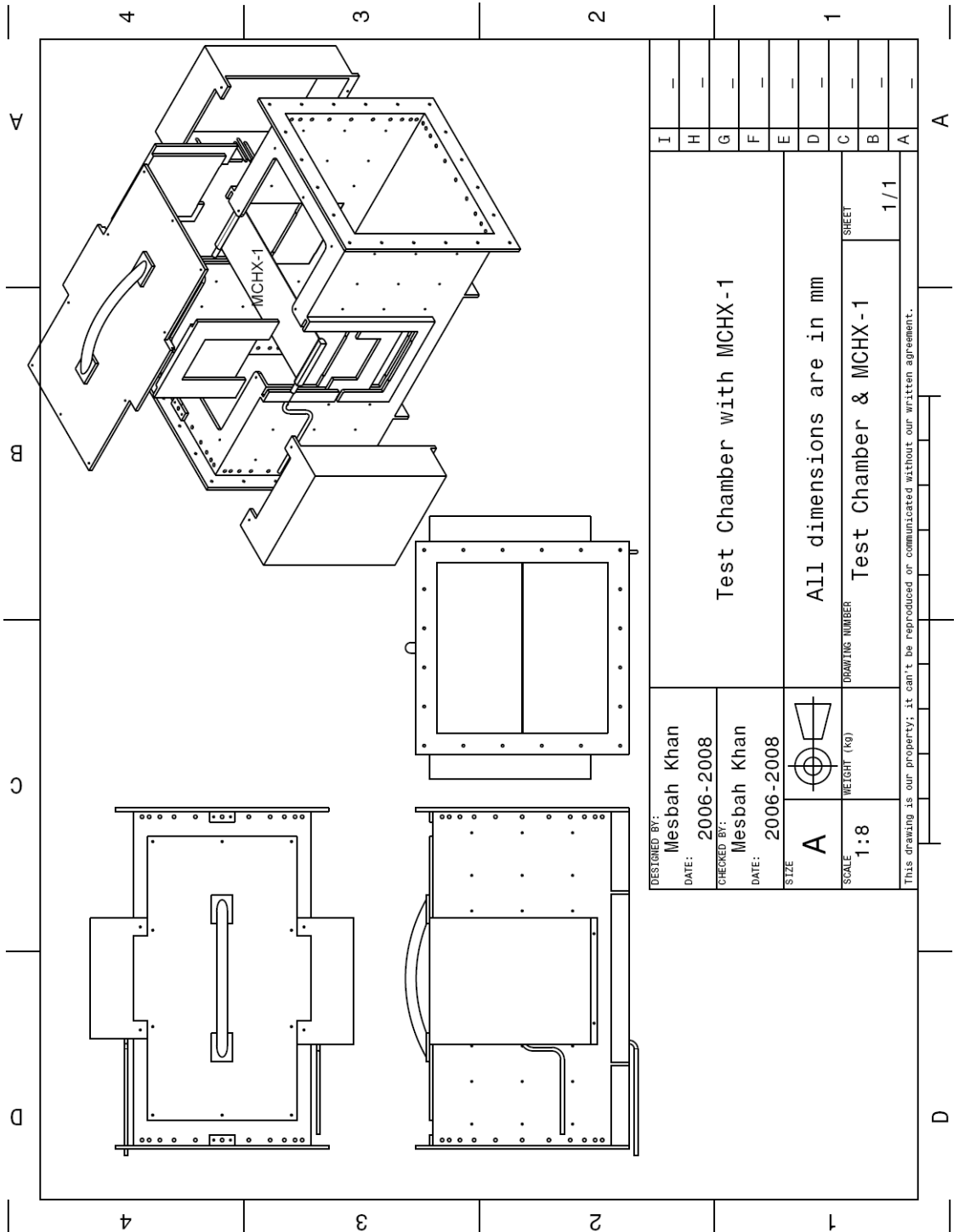


Figure B3.1 Design of test chamber support structures for test specimens MCHX-1

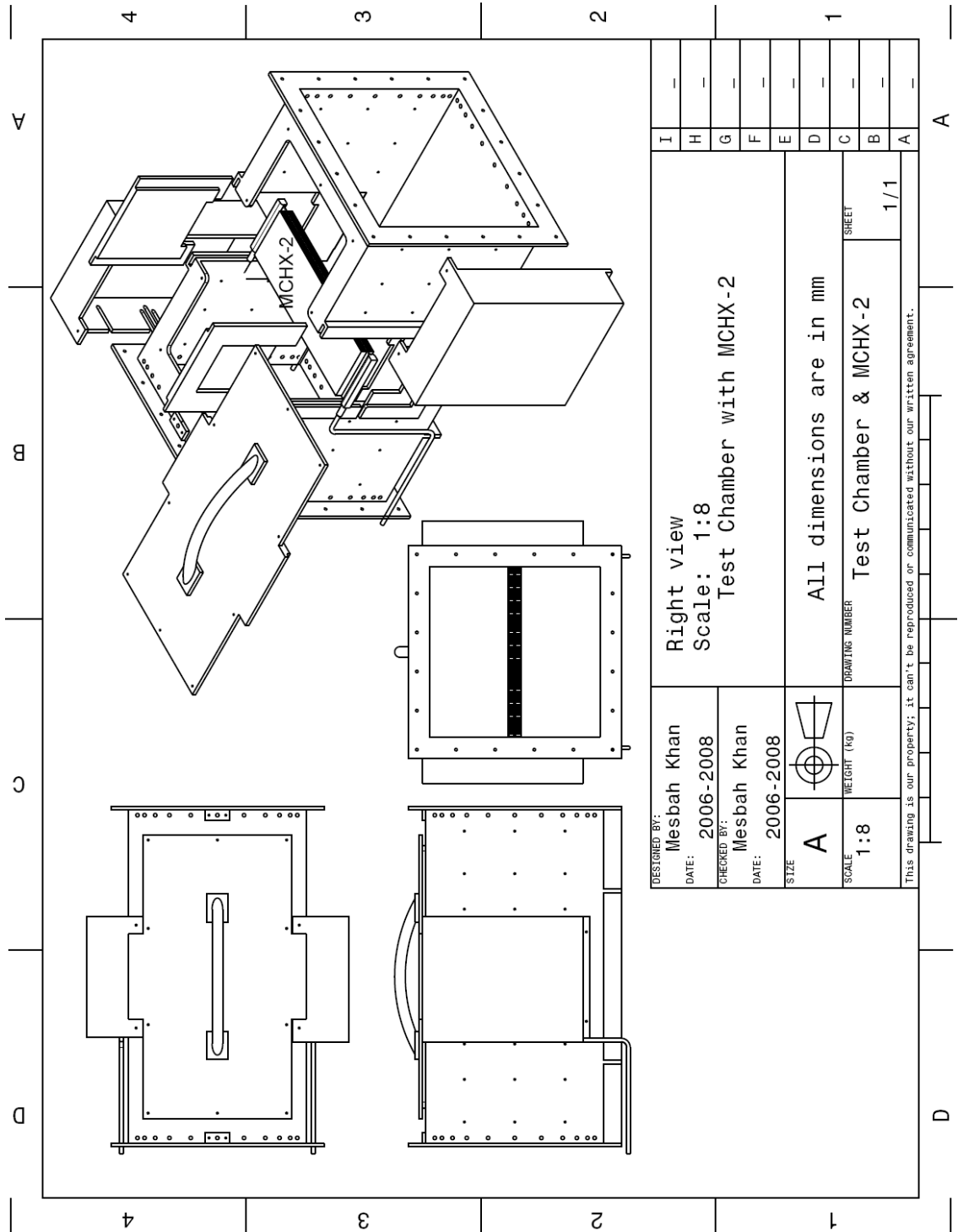


Figure B3.2. Design of test chamber support structures for test specimens MCHX-2

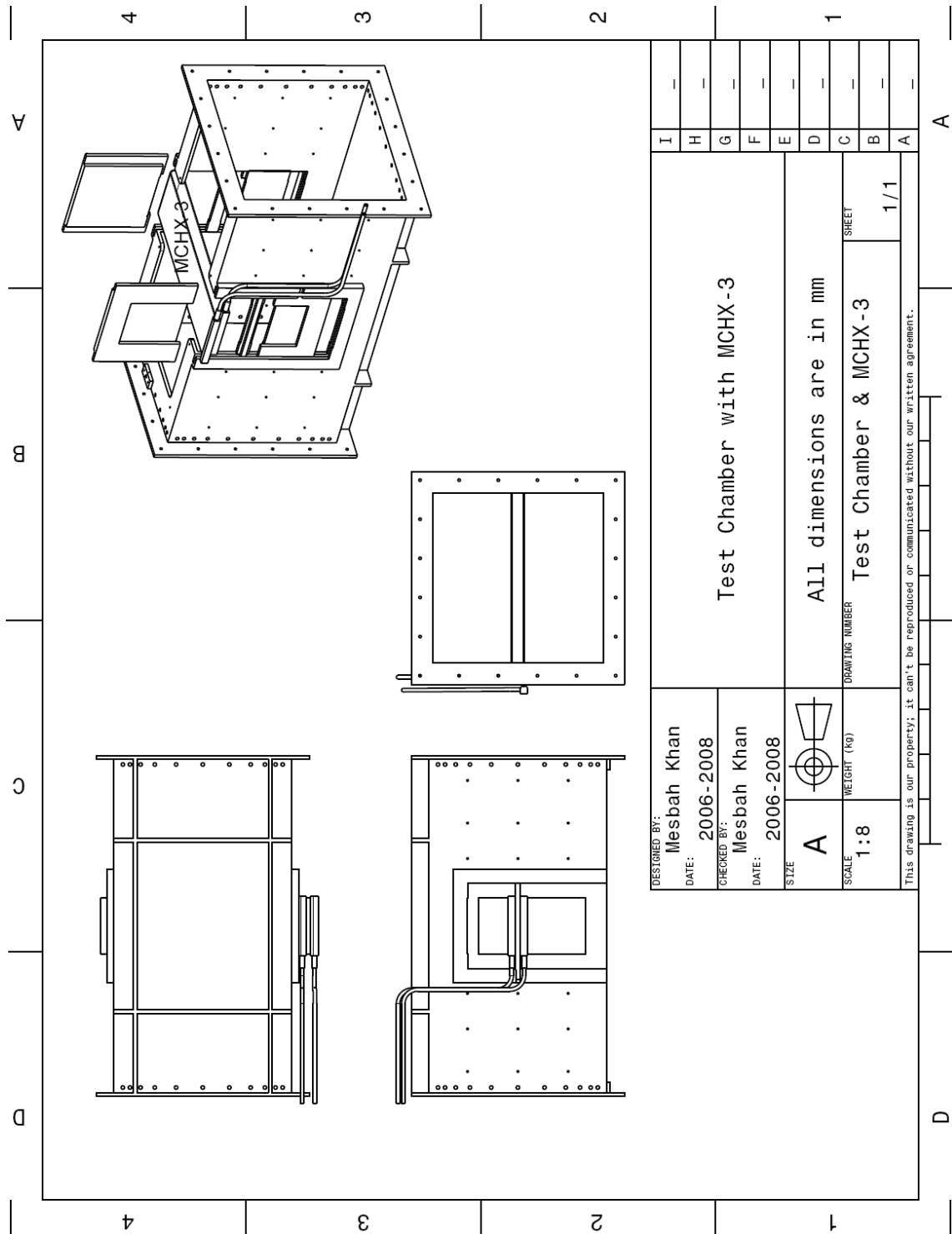


Figure B3.3. Design of test chamber support structures for test specimens MCHX-3

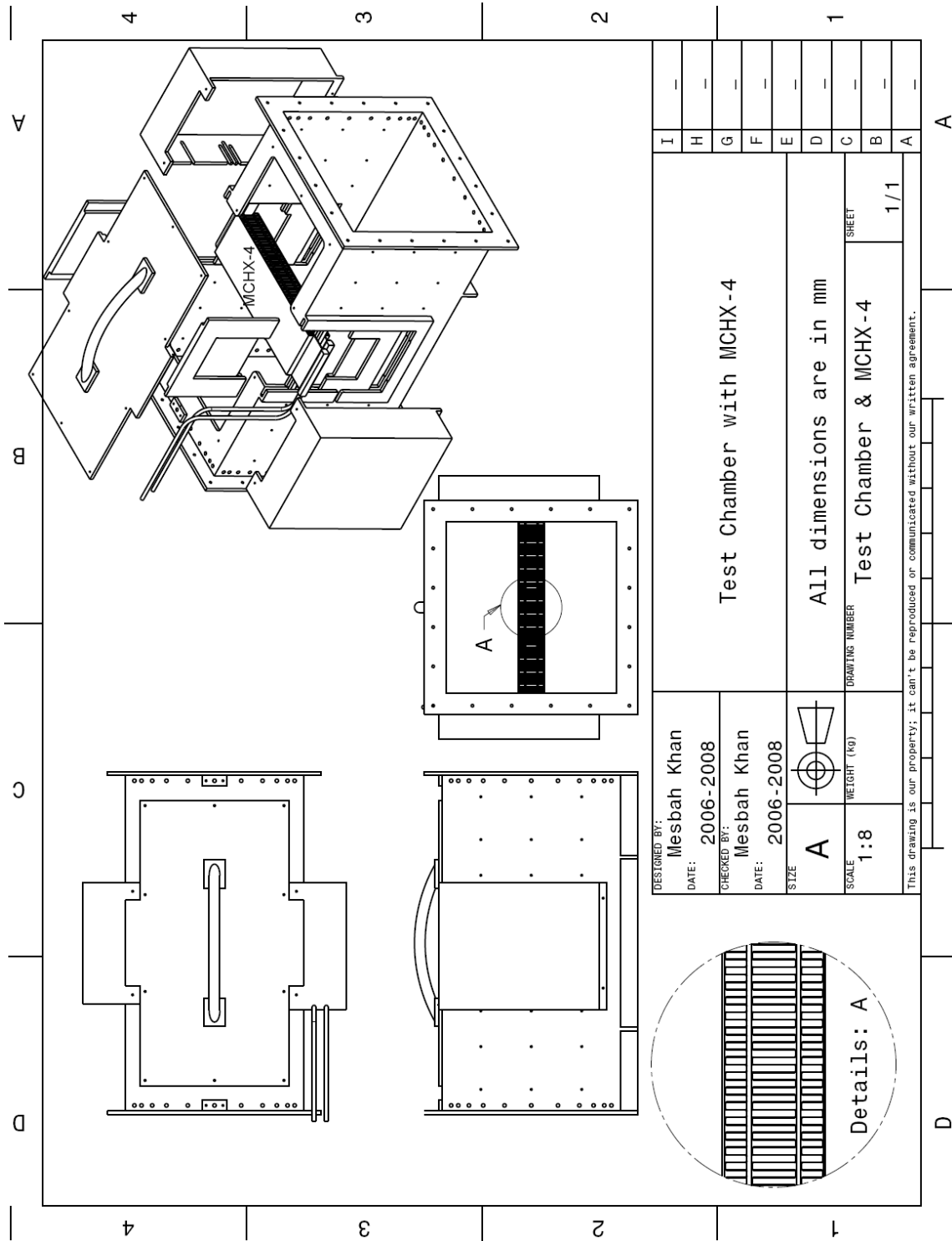


Figure B3.4. Design of test chamber support structures for test specimens MCHX-4

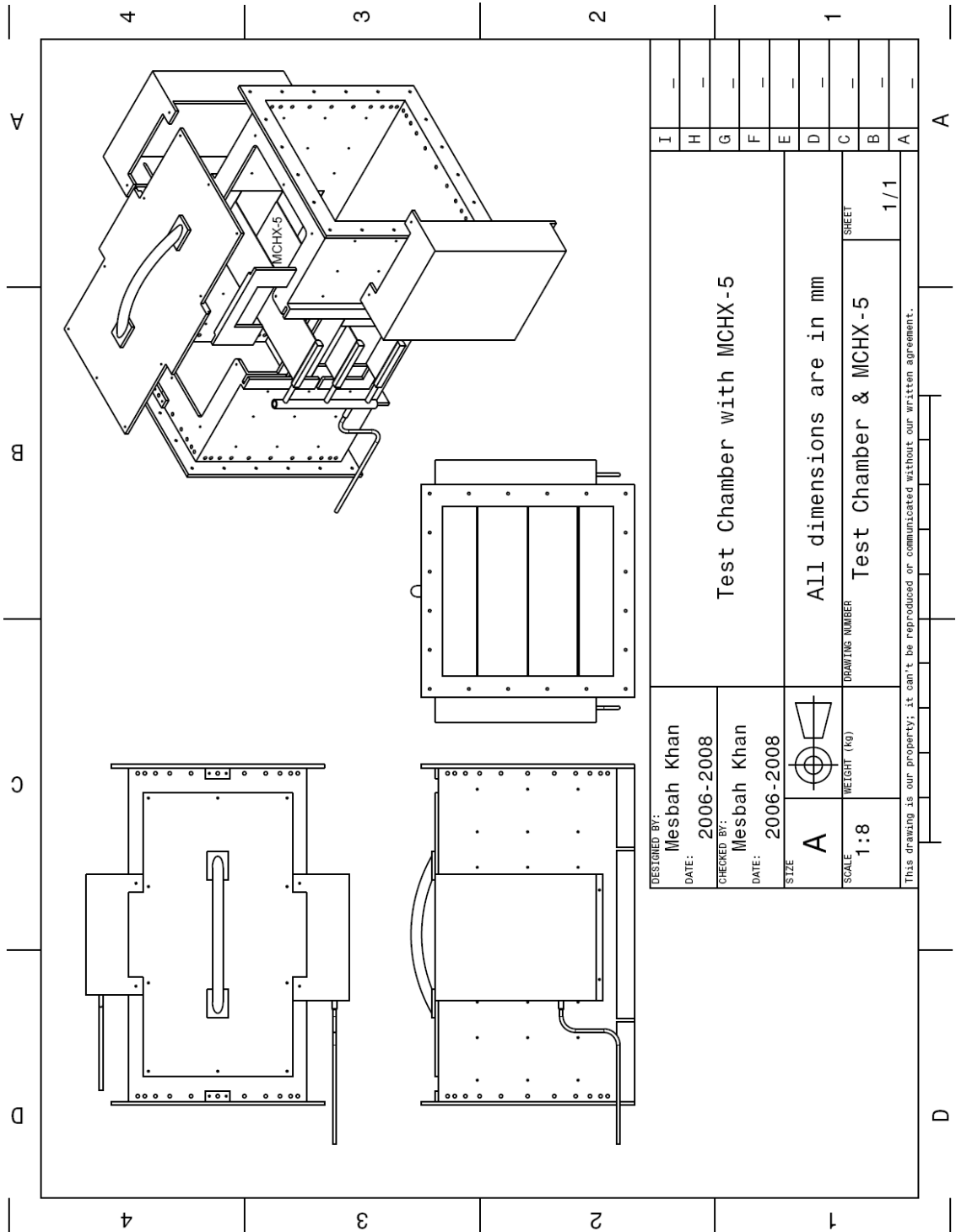


Figure B3.5. Design of test chamber support structures for test specimens MCHX-5

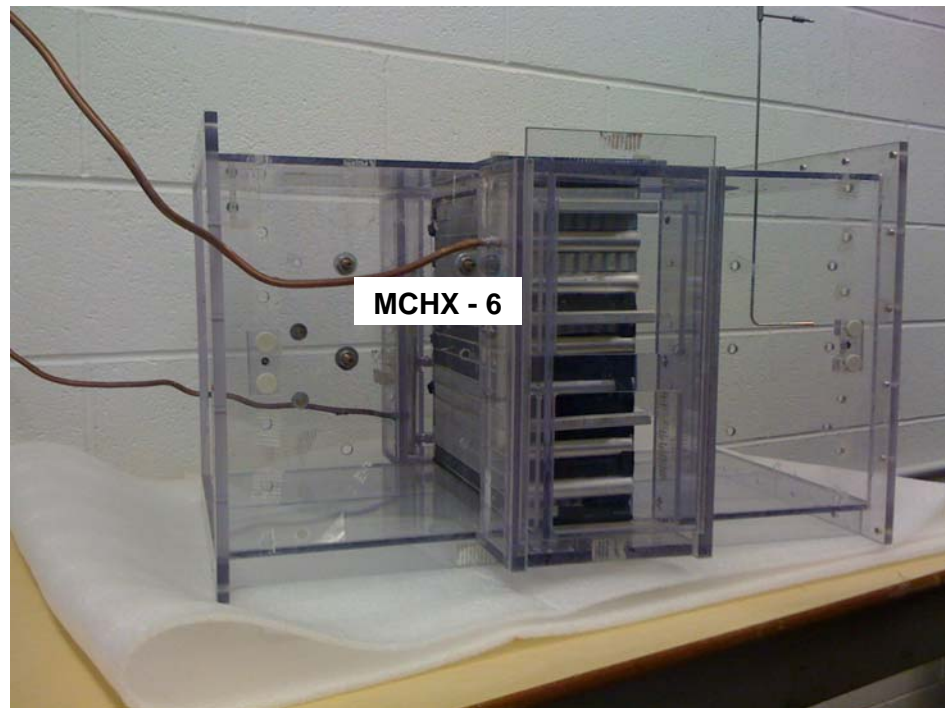


Figure B3.6a. Design of test chamber support structures for test specimens MCHX-6.

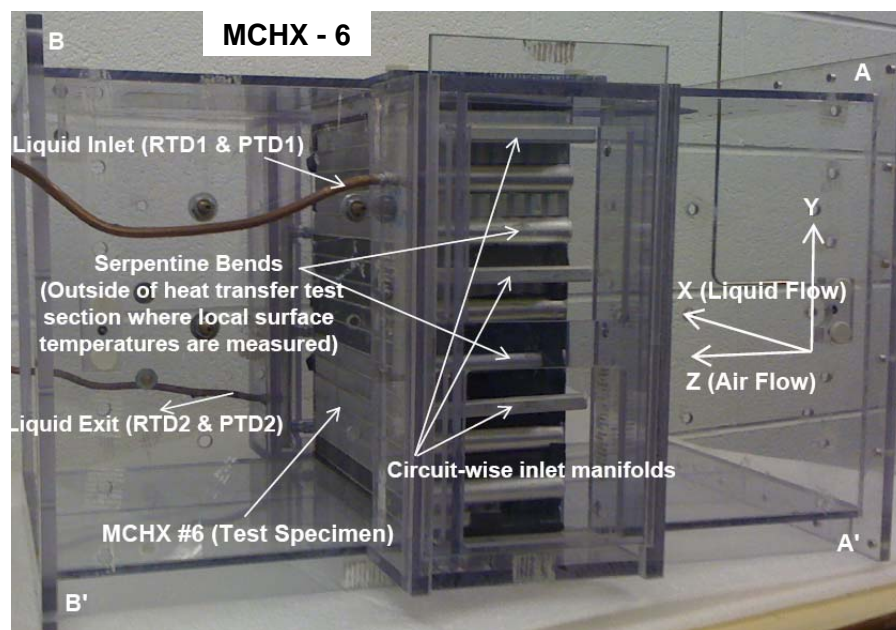


Figure B3.6b. Design of test chamber support structures for test specimens MCHX-6.

APPENDIX – B4

DETAILS OF THE DESIGNED AND CONSTRUCTED WATER FLOW MIXING AND SUPPLY NETWORK FOR WIND TUNNEL INTERNAL HEAT EXCHANGER

Appendix – B4. Details of the designed and constructed water flow mixing and supply network for wind tunnel internal heat exchanger

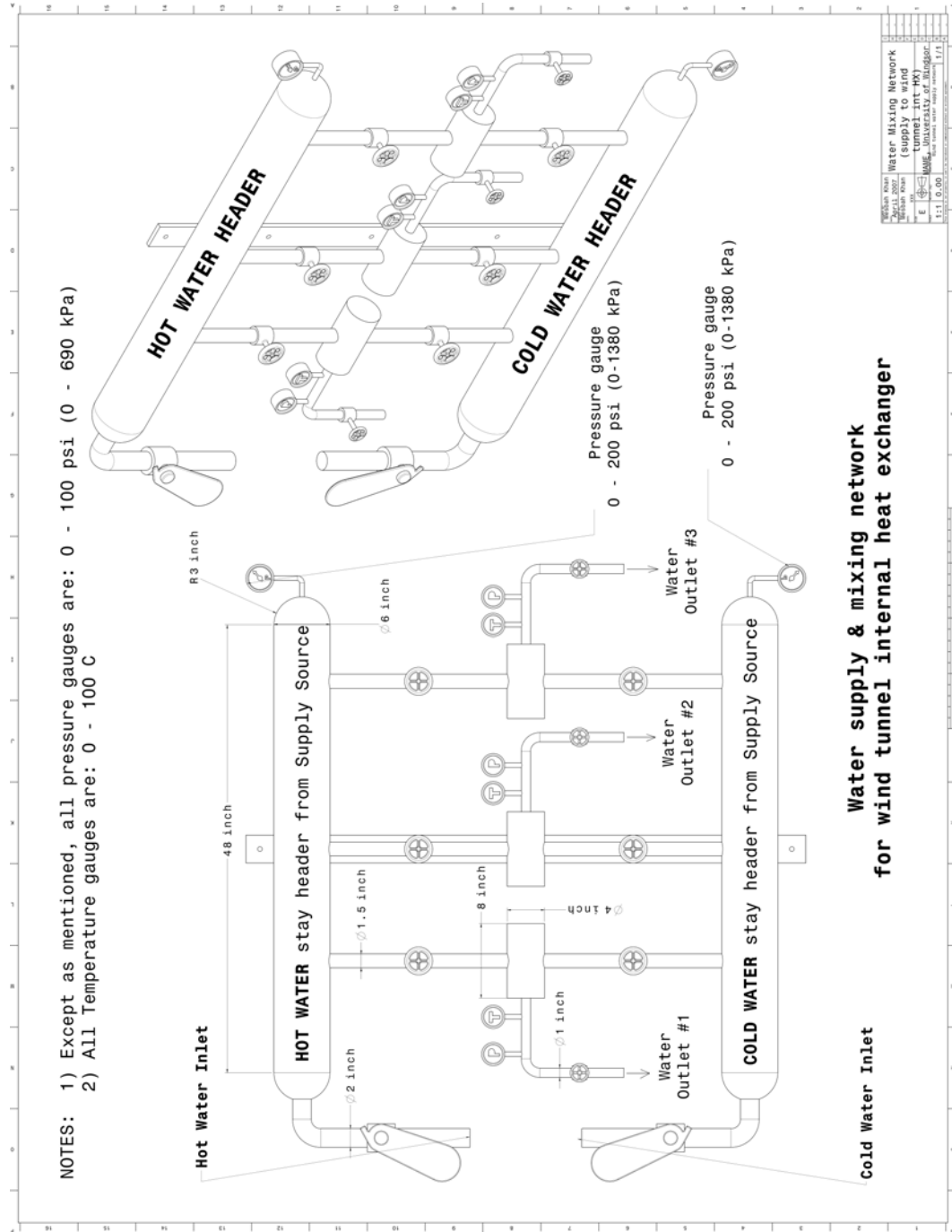


Figure B4. Design of water flow mixing network for wind tunnel internal heat exchanger (3D/2D)

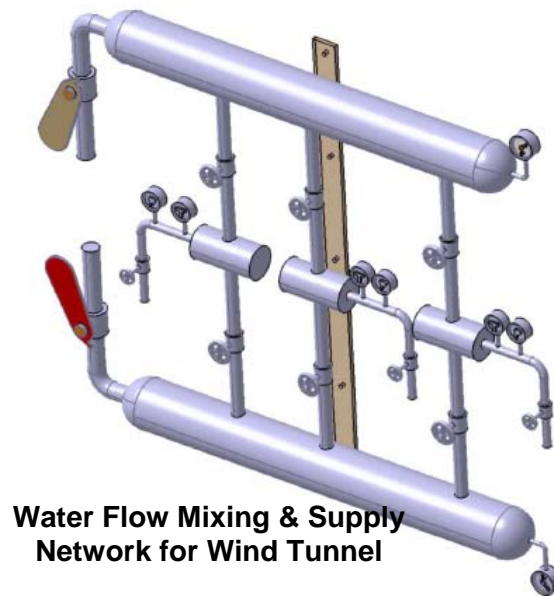


Figure B4.1. Solid model of water flow mixing network for wind tunnel internal heat exchanger

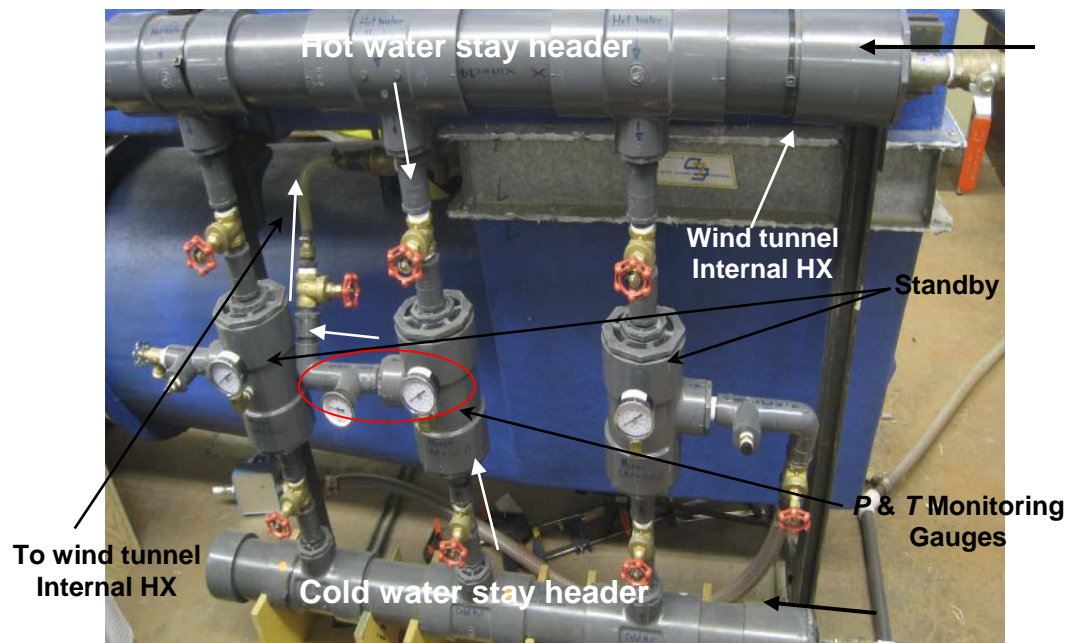


Figure B4.2. Photograph of constructed and installed water flow mixing and supply network for wind tunnel internal heat exchanger

APPENDIX – B5

DETAILS OF FLOW METER (DFM) CALIBRATION CERTIFICATE AND CURVE

Appendix – B5. Details of flow meter (DFM) calibration certificate and curve

Proteus Industries Inc. - 4000 Series Calibration Certificate
 Certificate ID/File Name: 00143490.xls
 Customer Name: WINDSOR PURCHASING
 Calibration Type: New Calibration
 SO #: 078023
 Body Type: 4001
 Body Material: SS-316 Stainless Steel
 Flow Range: 16
 Output Type: 0-5VDC
 Serial Number: 00143490
 Display Software Revision displayed initial power-on: REV.C
 Software Revision per MasterControl Software Vault: REV.C

Temperature Probe: Meial Body/Heal Response Range (0-100%)
 Pressure Probe: Meial Body/Heal Response Range (0-100%)
 Temperature Baths filled with water and water(ethy)lene-glycol

Temperature
 Required Maximum Temperature: 70C (89.8 to 70.2C) (158F (157.6 to 158.4F))
 Required Minimum Temperature: 20C (19.8 to 20.2C) (68F (67.9 to 68.4F))
 Required Maximum Temperature: 20C (19.8 to 20.2C) (68F (67.9 to 68.4F))
 Required Minimum Temperature: 0C (-0.2C to 0.2C) (32F (31.6 to 32.4F))
 Display Readings: 69.6
 Measured Temperature Trip Point (within 10% of reading) C: 55.0 Passes
 Trip Point (within 10% of reading) F: 328.2 K (131 F)

Calibrate Pass/Fail? Pass

Pressure
 Required Maximum Pressure: 100 (99.5 to 100.5) PSI (241.25 (237.3 to 244.7) kPa)
 Required Mid-point Pressure: 50 (49.5 to 50.5) PSI (241.25 (237.3 to 244.7) kPa)
 Required Minimum Pressure: 0 (-0.5 to +0.5) PSI (241.25 (237.3 to 244.7) kPa)
 Display Readings: 99.2
 Pressure Trip Point (within 10% of reading) PSI: 50 Passes
 Trip Point (within 10% of reading) kPa: 344.64 kPa

Calibrate Pass/Fail? Pass

Flow Rate
 Required Maximum Flow Rate: 16 (15.92 to 16.08) GPM (60.57 (60.26 to 60.87) LPM)
 Required Mid-Flow Rate: 7.2 (7.16 to 7.24) GPM (27.25 (27.12 to 27.39) LPM)
 Required Minimum Flow Rate: 1.60 (1.59 to 1.61) GPM (6.06 (6.03 to 6.09) LPM)
 Display Readings: 16.1
 Pressure Reference Gauge: WKA-342.11; Ue = 0.67PSI of reading
 Trip Point (25% of full range) GPM: 4
 Passes: 15.14 LPM

Calibrate Pass/Fail? Pass

Plumbing Standard Pipe Used

Calibrated by: SBZ/CAL
Date of Cal: 13-Mar-2007
Approved by: AVG/CAL
Next Cal Due: 12-Mar-08

Flow Rate Calibrator Used: Flow Stand 1 - Liquid flow base & Fluke 45 DMM (Uc = 1.28% of reading, for water, 18C to 25C)
Flow Stand Calibration Due Date: DAILY
Fluke 45 DMM Cal Due Date: 13-Mar-07

Calibration Passes/Final Value Trip Points Passes

Procedures used: 4000 Temperature, Pressure, Flow Rate Calibration
 Equipment operated at room ambient temperature, unless otherwise noted
 Expanded Measurement Uncertainty (U0) by expansion coefficient k = 2

This Calibration Certificate should not be reproduced except in full, without written approval of Proteus Industries Inc.
 Document: 640003, Revision: Revision Date: 19 December 2006

Page 1 of 1

Figure B5.1. Digital flow meter (DFM-1) calibration data and certificate

Proteus Industries Inc. - 4000 Series Calibration Certificate with Viscosity Conversion for 50/50 Ethylene-Glycol/Water

Certificate ID/File Name: 00168771.xls

Calibration Type: SO #: 082615

Customer Name: WINDSOR Serial Number: 00168771

Body Type: 4004 1 Display

Temperature Probe: Pressure Probe:

Display Software Revision displayed initial power-on: REV.C

Software Revision per MasterControl Software Vault: REV.C

Default Trip Point: 55C Rising

Measured Temperature Trip Point (within 10% of reading): 55C

Temperature Baths filled with water and water/ethylene-glycol

Liquid Temp Baths Hart 6102, 7102 (#1) & 7102 (#2)

Equipment ID# 69655 Calibration Date: DAILY

Equipment ID# N9858 Calibration Date: 28-Feb-09

Temperature Reference Hart 5612-1502; Uc = 0.05C of reading

Fluke 45 DMM; Uc = 0.000VDC of reading

Default Trip Point: 50 PSI Rising

Measured Pressure Trip Point (within 10% of reading): 50 PSI

Pressure Reference Gauge: WIKA 342.11; Uc = 0.67PSI of reading

Fluke 45 DMM; Uc = 0.000VDC of reading

Default Trip Point (25% of full range):

Flow Rate Trip Point (within 10% of reading) GPM: 0.35

Passes

Trip Point Calibrations: Passes

Readings	Required Maximum Output	Required Minimum Output	Pass/Fail?
69.7	3.50	0.00	Pass
19.7	3.55 VDC	1.00	Pass
0.1	1.05 VDC	0.05 VDC	Pass

Readings +/-1.5% full scale

Readings	Required Maximum Output	Required Minimum Output	Pass/Fail?
99.7	5.00	0.00	Pass
49.7	5.15 VDC	2.50	Pass
0	2.65 VDC	0.15 VDC	Pass

Readings +/-3% full scale

Readings	Required Maximum Output	Required Minimum Output	Pass/Fail?
1.40	5.10	0.39	Pass
0.63	2.12	0.14	Pass
0.14	2.4 VDC	0.65 VDC	Pass

Readings +/-3% full scale

Standard Pipe Used

Calibrated by: SBZ Flow Rate Calibrator Used:

Date of Cal: 10-Mar-2009 Flow Stand 1 - Liquid Flow Rate & Fluke 45 DMM (Uc = 1.28% of reading, for water 18C to 25C)

Approved by: AVG Calibration Passes

Next Cal Due: 10-Mar-10 Fluke 45 DMM ID# AA1178

Fluke 45 DMM Cal Due Date: DAILY

28-Feb-09

Procedures used: 4000 Temperature, Pressure, Flow Rate Calibration

Equipment operated at room ambient temperature, unless otherwise noted.

Expanded Measurement Uncertainty (Uc) by expansion coefficient k = 2

Figure B5.2. Digital flow meter (DFM-2) calibration data and certificate

Proteus Industries Inc. - 4000 Series Calibration Certificate with Viscosity Conversion for 50/50 Ethylene-Glycol/Water

Customer Name: WINDSOR

SO #: 082615

Serial Number: 00168771

Certificate ID/File name: 00168771.xls

	GPM	GPM	GPM
Flow Rate (Room Ambient Water)	1.40	0.63	0.14
Projected 50/50 Glycol/Water (15C) 4.39cSt	1.51	0.67	0.13
Projected 50/50 Glycol/Water 4.0 cSt	1.50	0.65	0.12
Projected 50/50 Glycol/Water (25C) 3.21 cSt	1.47	0.65	0.12
Projected 50/50 Glycol/Water 2.3 cSt	1.45	0.64	0.13
Projected 50/50 Glycol/Water (40C) 2.12cSt	1.44	0.64	0.13
Projected 50/50 Glycol/Water (60C) 1.36 cSt	1.42	0.64	0.13

VDC: 5.10 2.12 0.39

Projections based upon viscosity data collected by 3rd Party Laboratory on like units.

Viscosities for 40C & 60C data from standard automotive antifreeze table

Viscosities for 15C & 25C based upon linear projections between 10C/20C & 20C/30C

Figure B5.2. Digital flow meter (DFM-2) calibration data and certificate (cont'd...)

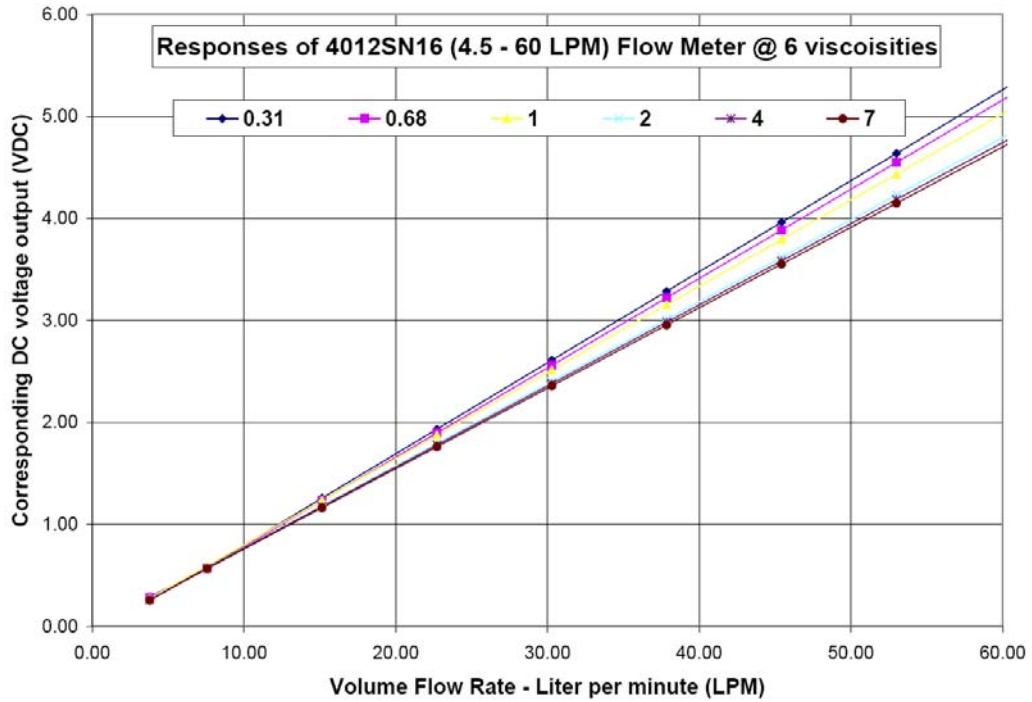


Figure B5.3a. Digital flow meter (DFM-1) calibration curves at six different viscosities.

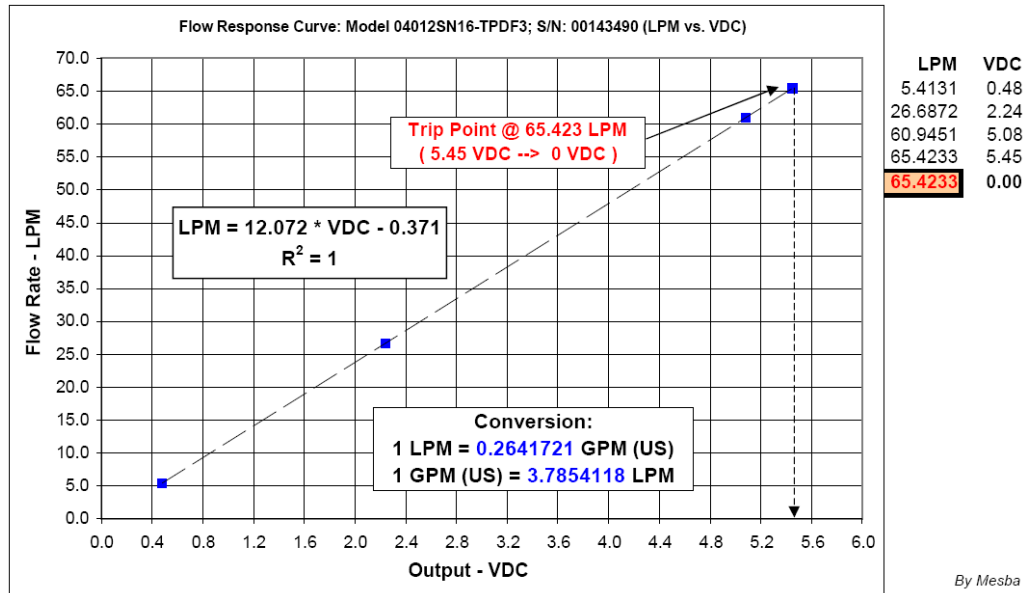


Figure B5.3b. Digital flow meter (DFM-1) response, trip point & calibration curve – LPM vs. VDC.

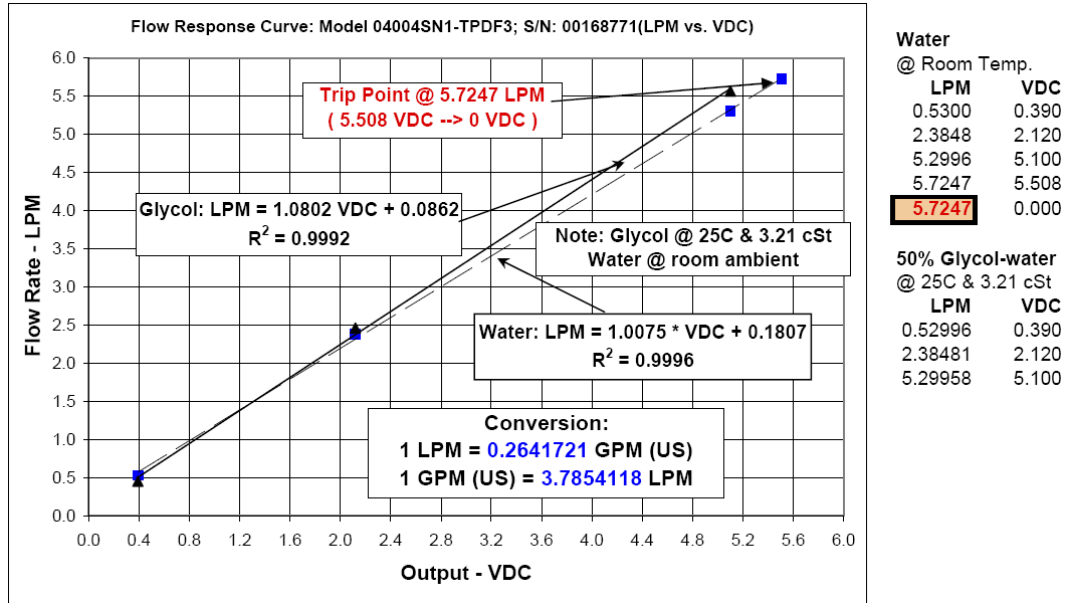


Figure B5.4a Digital flow meter (DFM-2) response & calibration curve - LPM vs VDC (Glycol/Water)

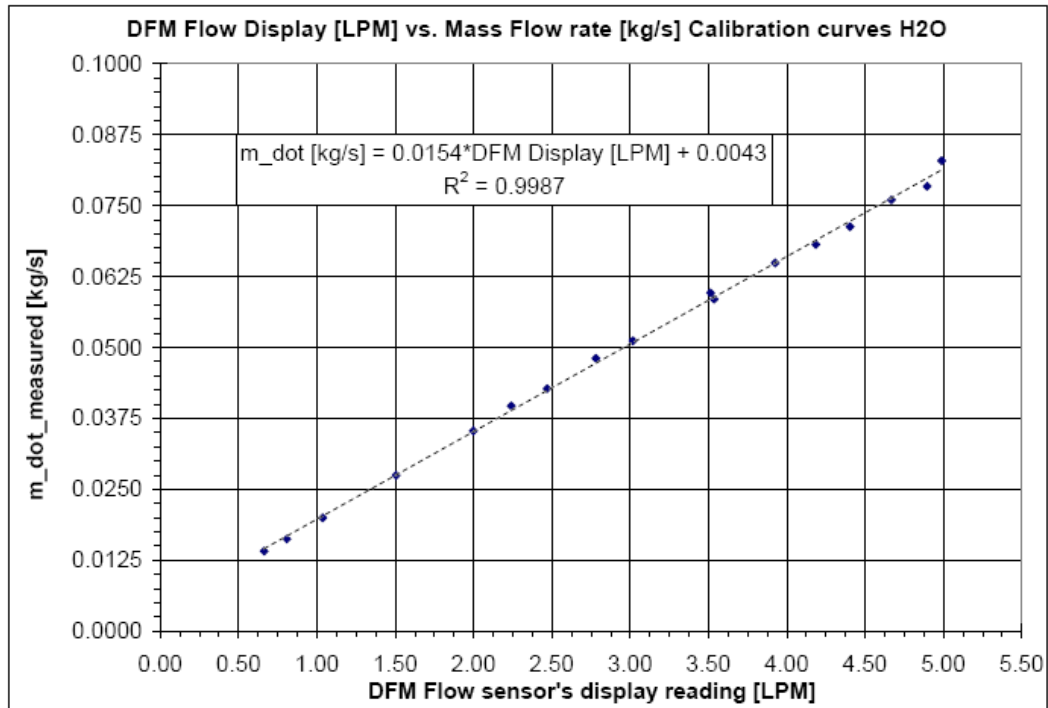


Figure B5.4b. Digital flow meter (DFM-2) calibration curve – Display LPM vs kg/s (Water)

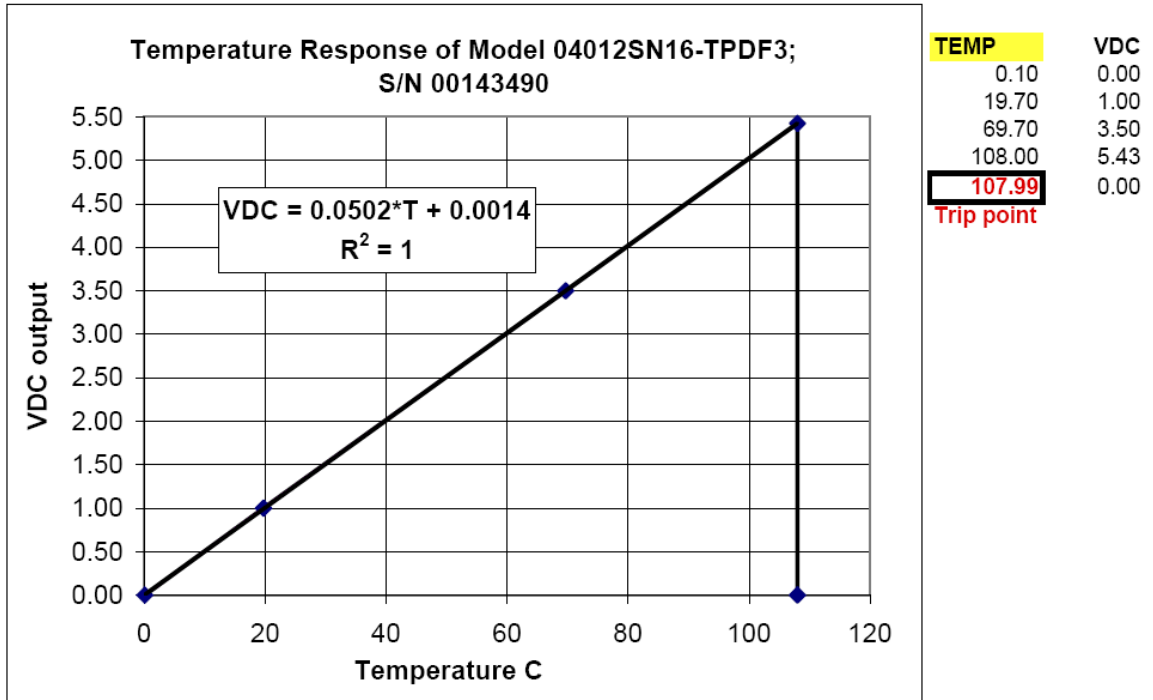


Figure B5.5. Digital flow meter (DFM-1) temperature response & trip point – T vs. VDC.

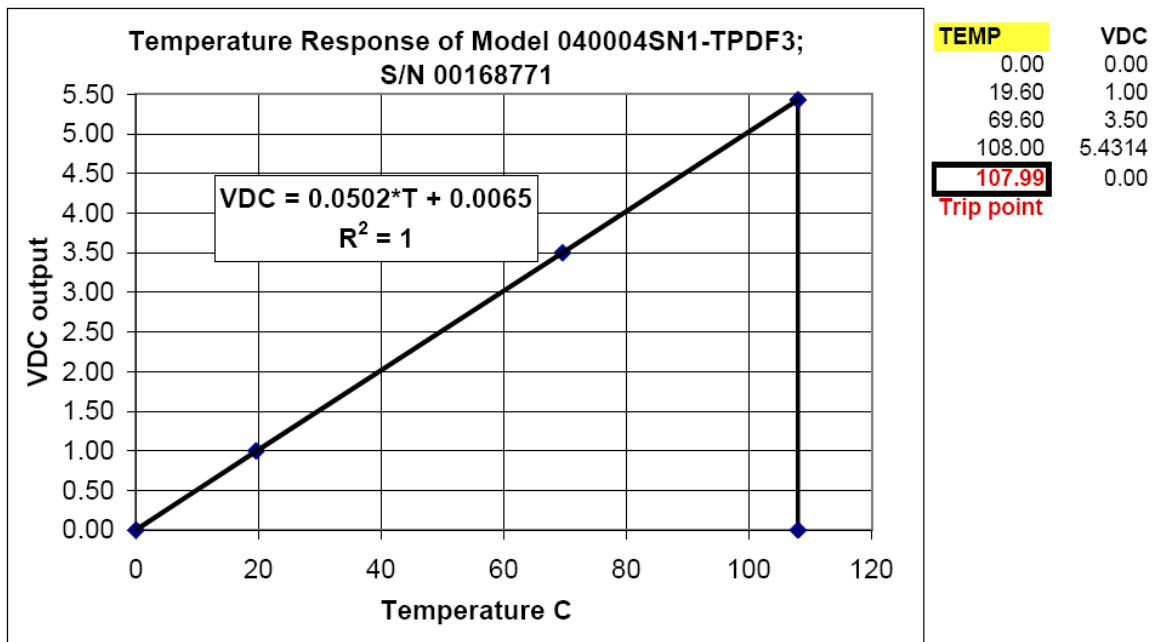


Figure B5.6. Digital flow meter (DFM-2) temperature response & trip point – T vs. VDC.

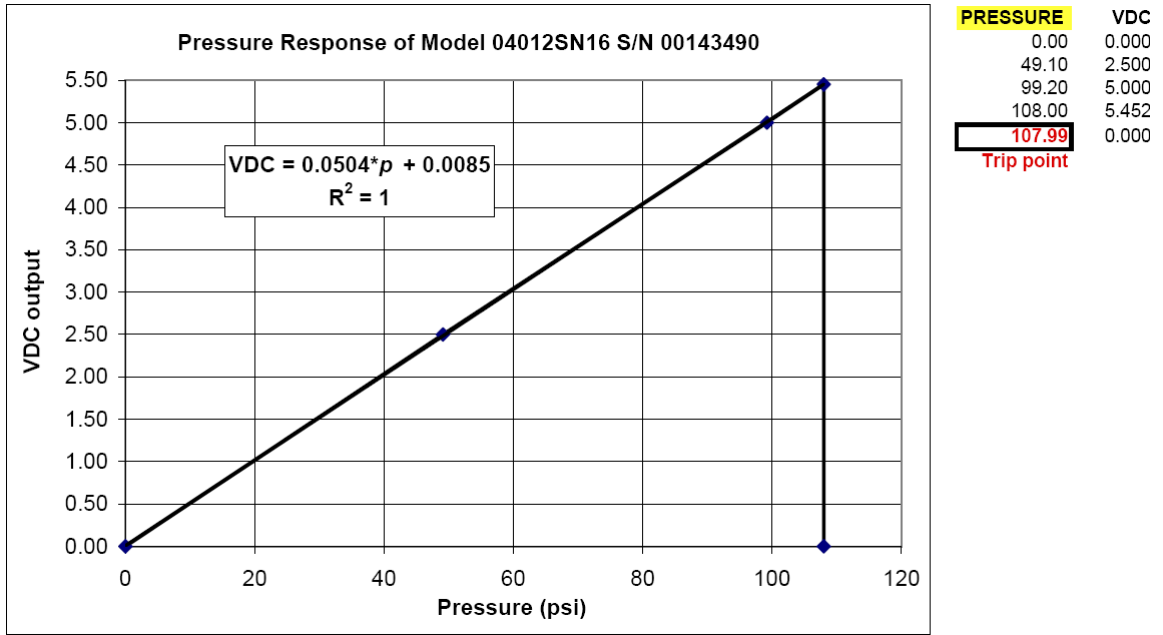


Figure B5.7. Digital flow meter (DFM-1) pressure response & trip point – p vs. VDC.

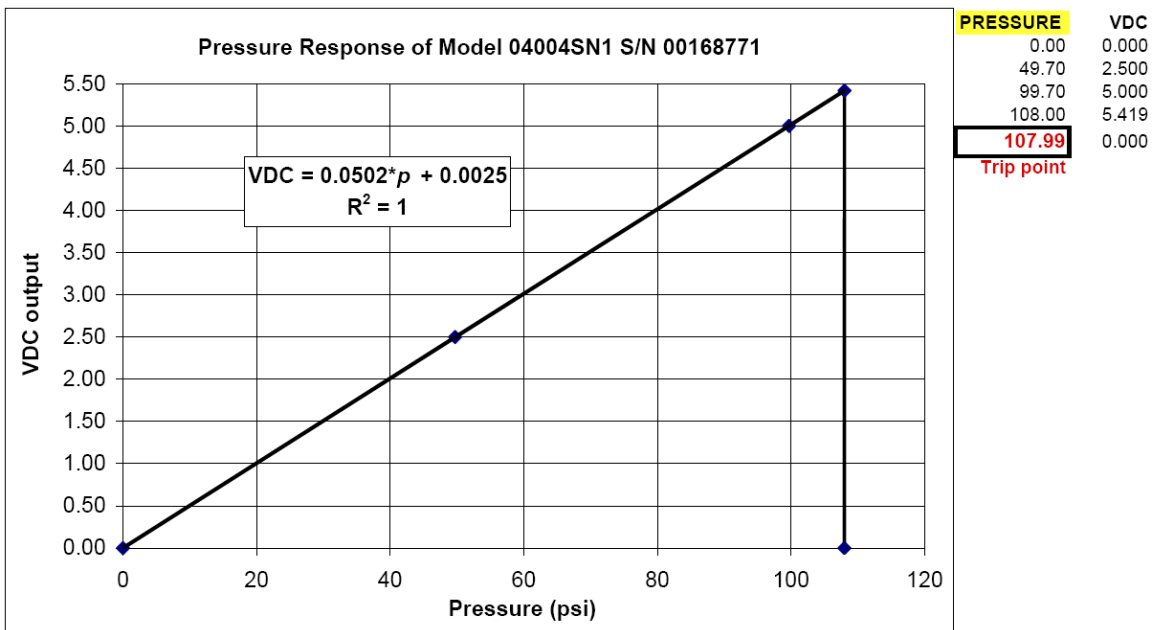


Figure B5.8. Digital flow meter (DFM-2) pressure response & trip point – p vs. VDC.

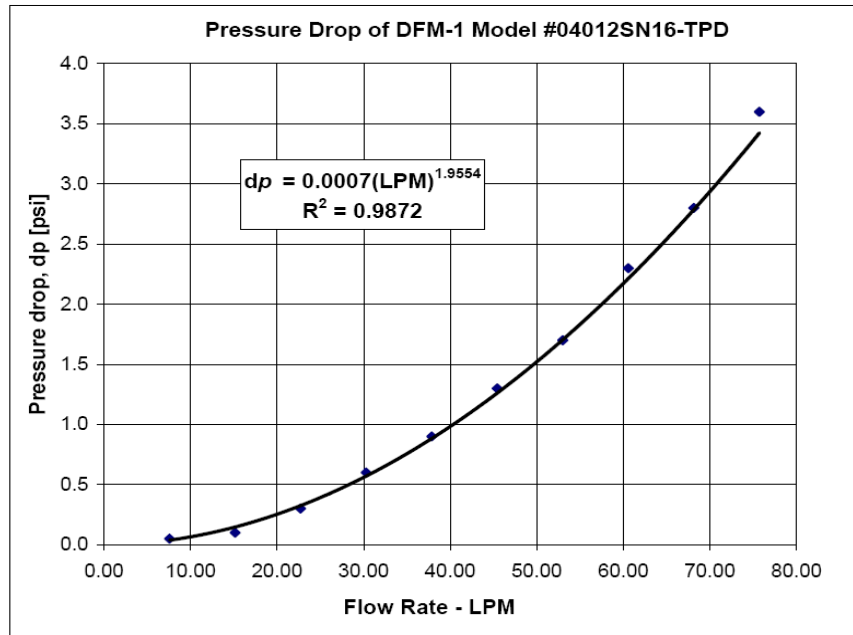


Figure B5.9. Digital flow meter (DFM-1) pressure drop curve – dp vs. LPM.

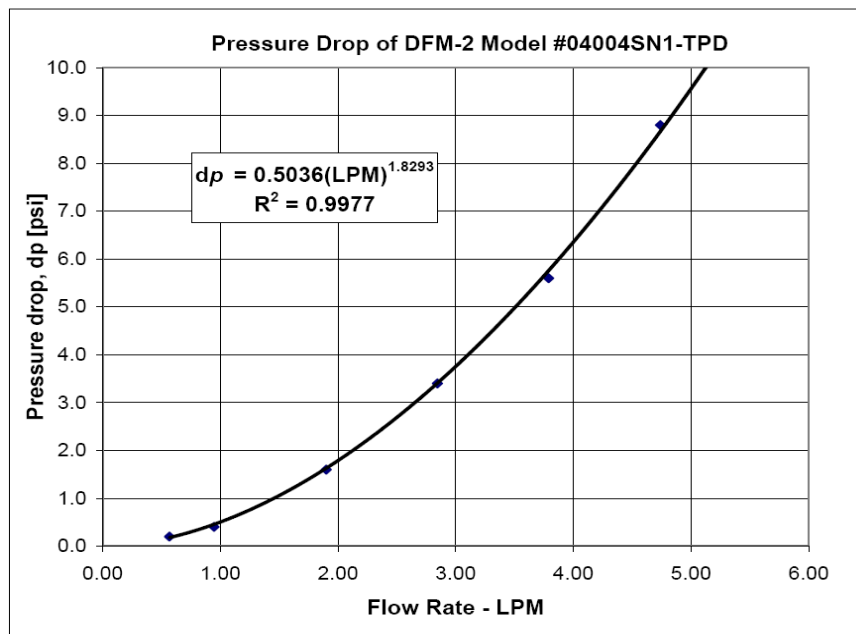


Figure B5.10. Digital flow meter (DFM-2) pressure drop curve – dp vs. LPM.

APPENDIX – B6

DETAILS OF LIQUID SIDE PRESSURE TRANSDUCER (PTD) CALIBRATION

Appendix – B6 Details of liquid side pressure transducer (PTD) calibration

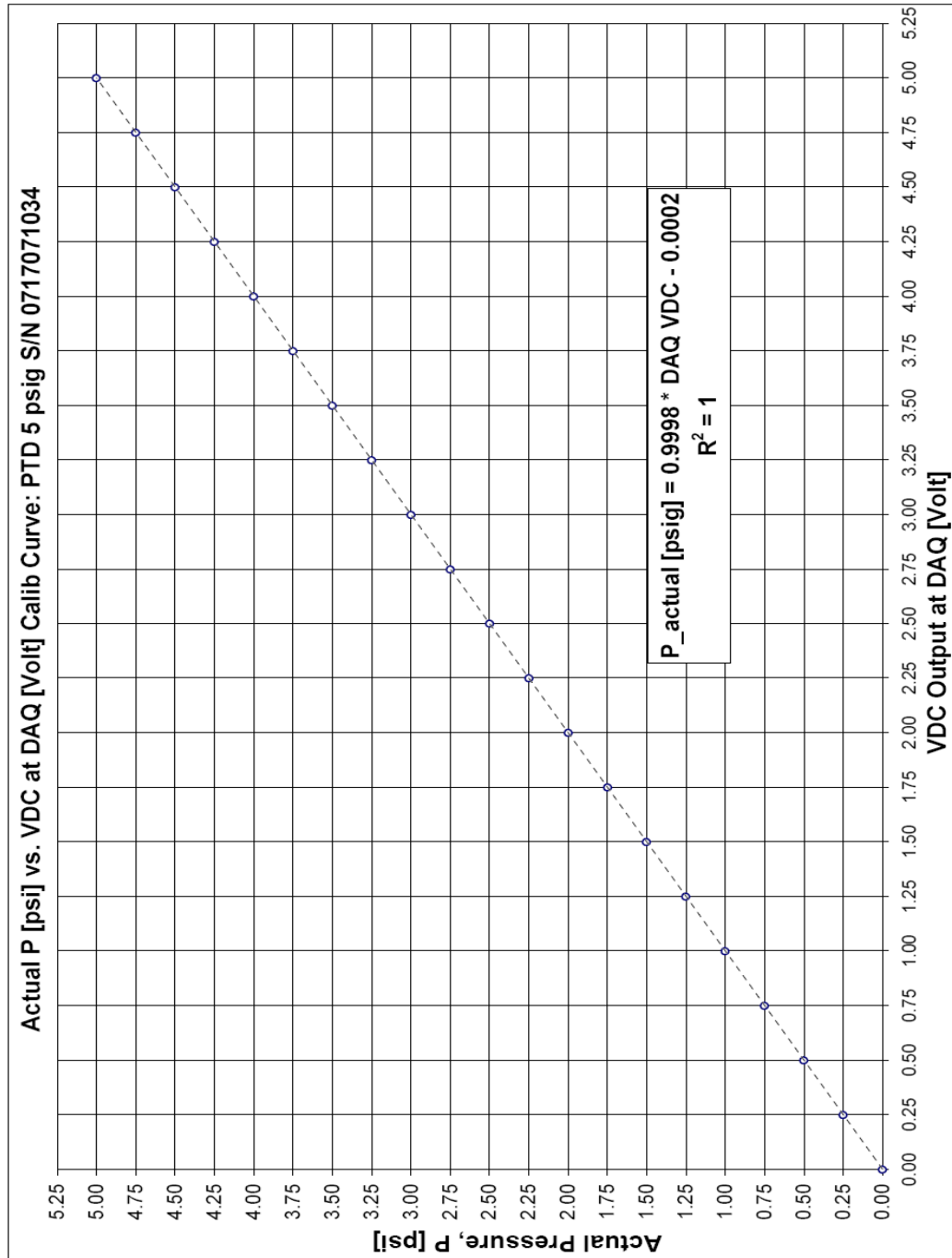


Figure B6.1. Liquid side pressure transducer calibration curve (PTD S/N. - 0717071034).

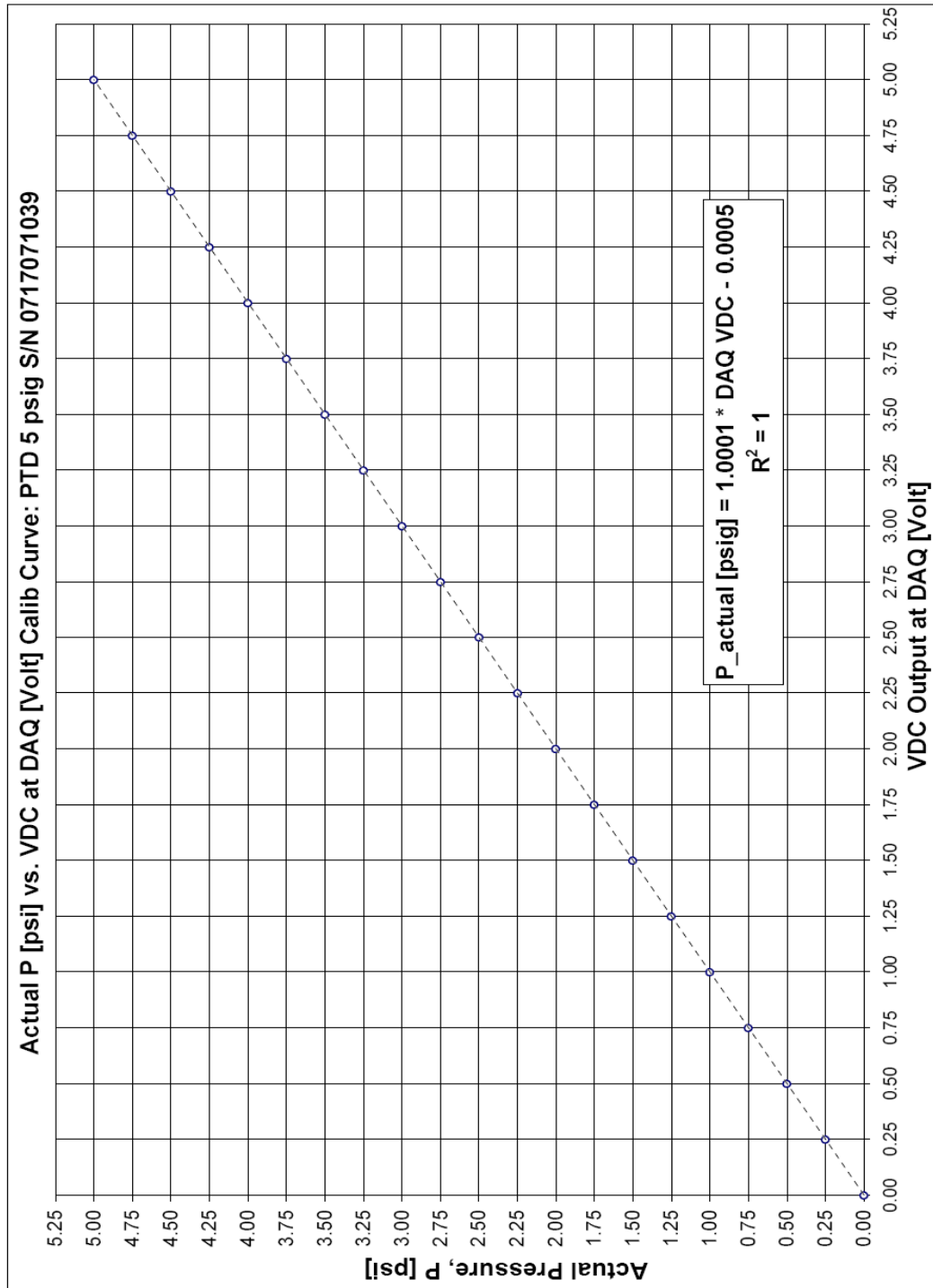


Figure B6.2. Liquid side pressure transducer calibration curve (PTD S/N. - 0717071039).

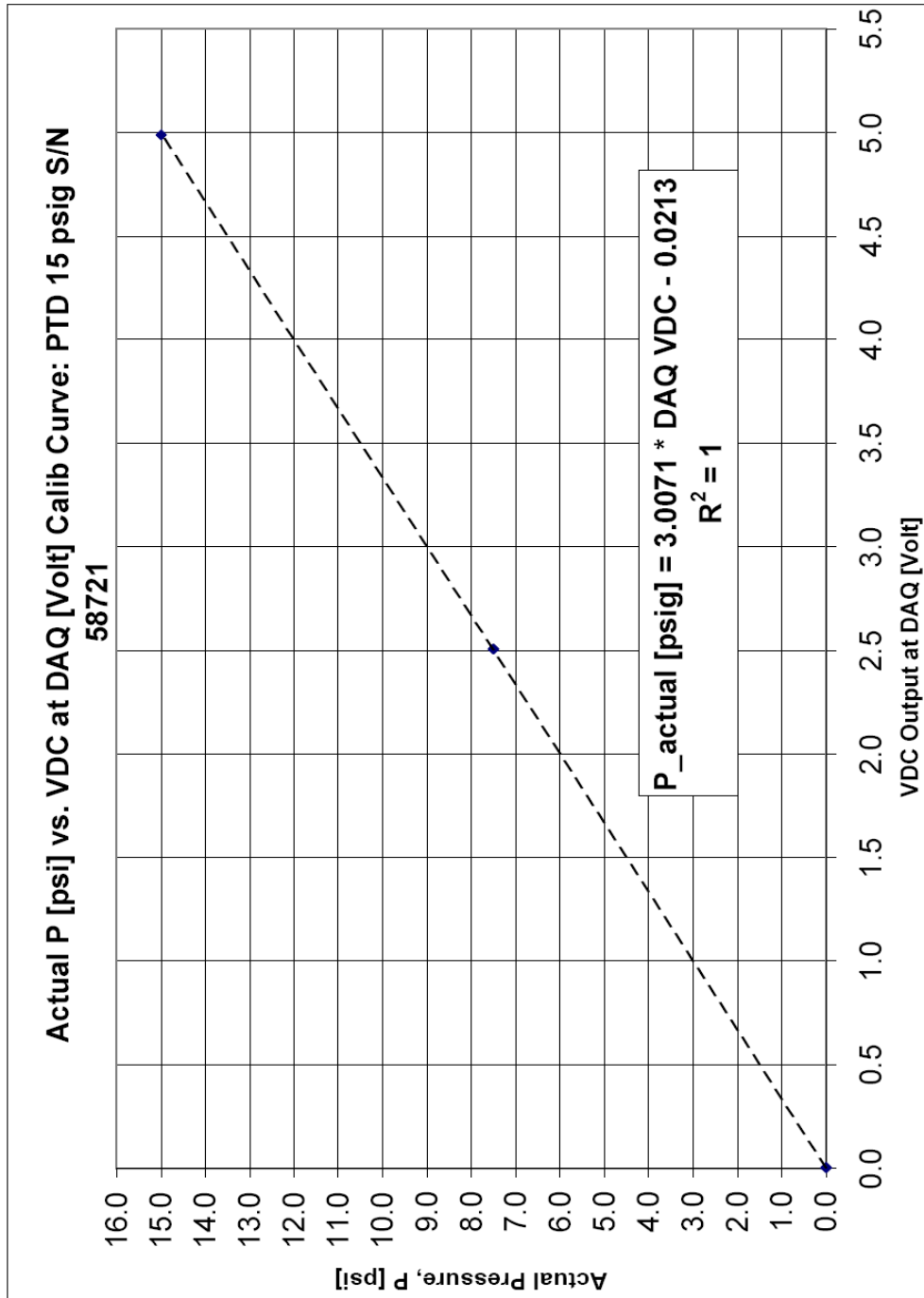


Figure B6.3. Liquid side pressure transducer calibration curve (PTD S/N. - 58721).

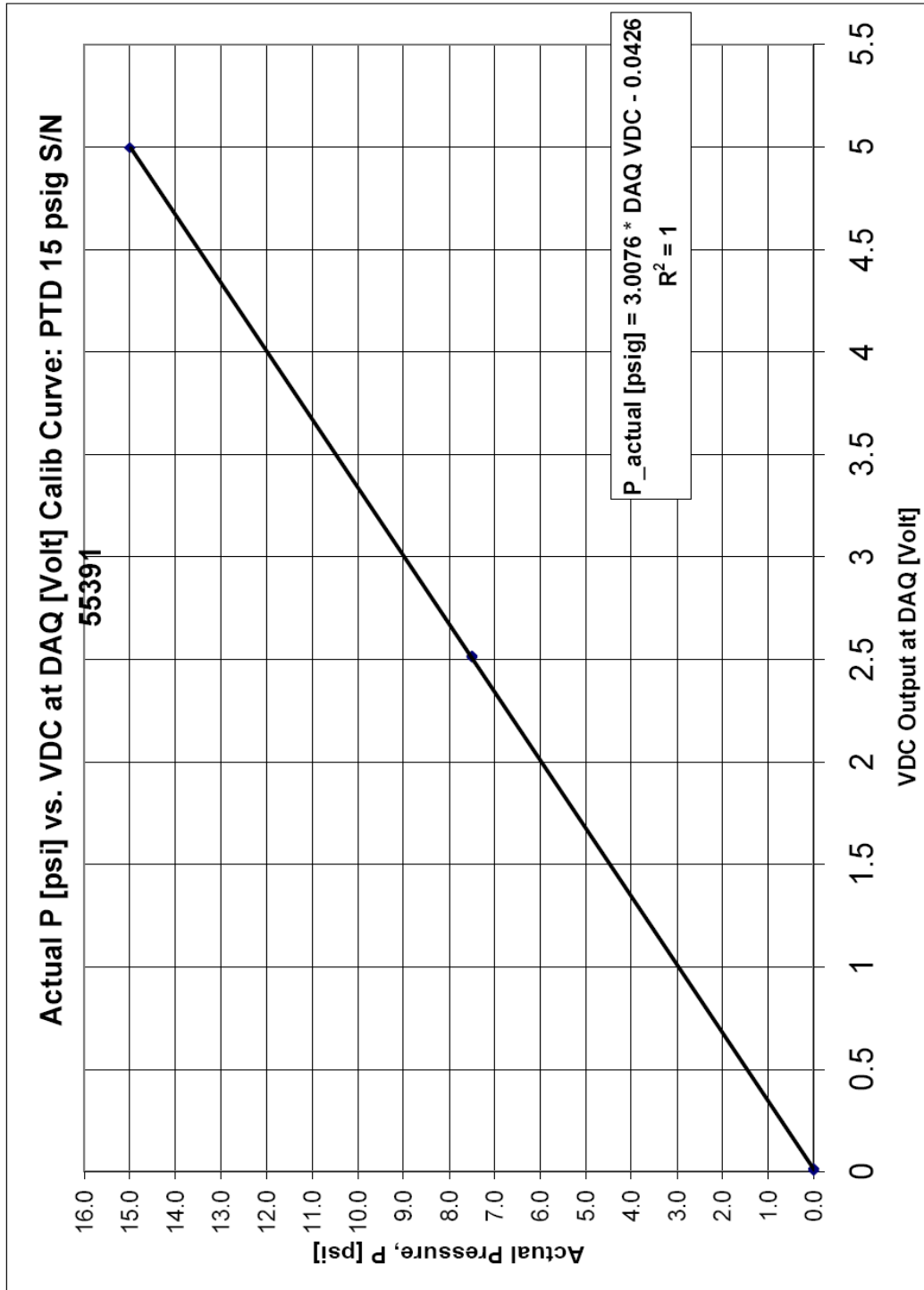


Figure B6.4. Liquid side pressure transducer calibration curve (PTD S/N. - 55391).

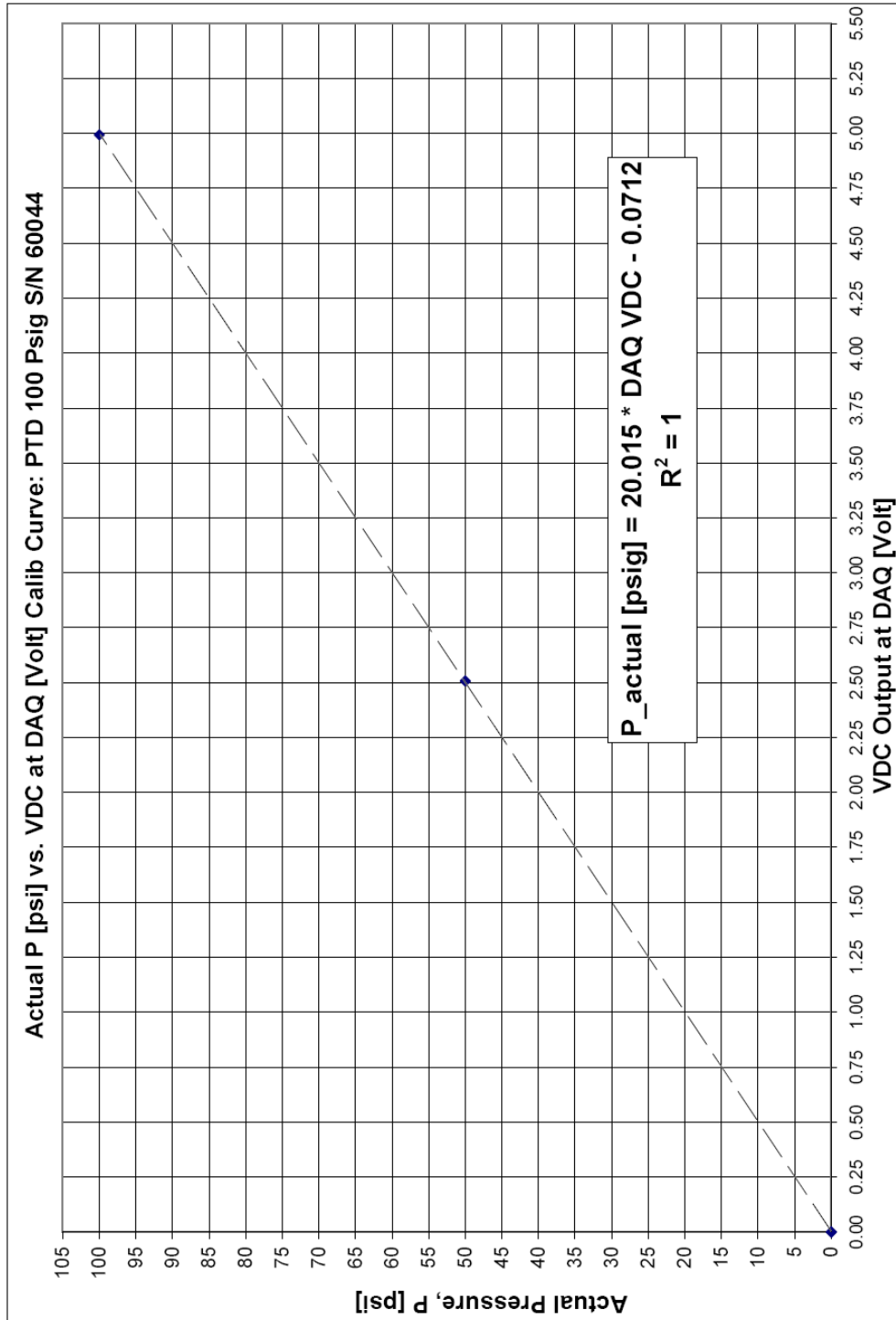


Figure B6.5. Liquid side pressure transducer calibration curve (PTD S/N. - 60044).

OMEGADYNE INC. CERTIFICATE OF CALIBRATION

Model Number: PX419-001G5V

Serial Number: 401690

Date: 10/1/2008

Capacity: 1.00 PSIG

Excitation: 24.00 Vdc

Technician: KAPOME

Pressure Connection: 1/4-18 NPT Male

WIRING CODE

Electrical Connection: PIN 1 = + EXCITATION
 PIN 2 = - EXCITATION
 PIN 3 = + OUTPUT
 PIN 4 = N/C

CALIBRATION WORKSHEET

Pressure PSIG	OUTPUT Vdc
0.00	0.005
0.50	2.508
1.00	5.013
0.50	2.509
0.00	0.006

NIST Traceable Number(s): C-1954, C-2491

Omegadyne Inc. certifies that the above instrumentation has been calibrated and tested to meet or to exceed the published specifications. This calibration was performed using instrumentation and standards that are traceable to the National Institute of Standards and Technology. This document also ensures that all testing performed complies with MIL-STD 45662-A, ISO 10012-1, and ANSI/NCSL Z540-1-1994 requirements. After Final Calibration our products are stored in an environmentally controlled stock room and are considered in bonded storage. Depending on environmental conditions and severity of use, factory calibration is recommended every one to three years after the initial service installation date.

Bruce Lott

Accepted and Certified By

10/1/2008

Date

Figure B6.6. Liquid side pressure transducer calibration curve (PTD S/N. - 401690).

OMEGADYNE INC. CERTIFICATE OF CALIBRATION

Model Number: PX419-10WG5V

Serial Number: 410326

Date: 9/19/2008

Capacity: 10.00 in H₂O

Excitation: 24.00 Vdc

Technician: KAPOME

Pressure Connection:

1/4-18 NPT Male

WIRING CODE

Electrical Connection: PIN 1 = + EXCITATION

PIN 2 = - EXCITATION

PIN 3 = + OUTPUT

PIN 4 = N/C

CALIBRATION WORKSHEET

Pressure in H ₂ O	OUTPUT Vdc
0.00	0.001
5.00	2.504
10.00	5.007
5.00	2.504
0.00	0.001

NIST Traceable Number(s): C-1954, C-2491

Omegadyne Inc. certifies that the above instrumentation has been calibrated and tested to meet or to exceed the published specifications. This calibration was performed using instrumentation and standards that are traceable to the National Institute of Standards and Technology. This document also ensures that all testing performed complies with MIL-STD 45662-A, ISO 10012-1, and ANSI/NCSL Z540-1-1994 requirements. After Final Calibration our products are stored in an environmentally controlled stock room and are considered in bonded storage. Depending on environmental conditions and severity of use, factory calibration is recommended every one to three years after the initial service installation date.

Bruce Lott

Accepted and Certified By

9/19/2008

Date

Figure B6.7. Liquid side pressure transducer calibration curve (PTD S/N. - 410326).

APPENDIX – B7

DETAILS OF AIRSIDE DIFFERENTIAL PRESSURE TRANSDUCERS (PTDD) AND WIND TUNNEL AIR VELOCITY CALIBRATIONS

Appendix – B7. Details of airside differential pressure transducers (PTDD) and wind tunnel air velocity calibrations

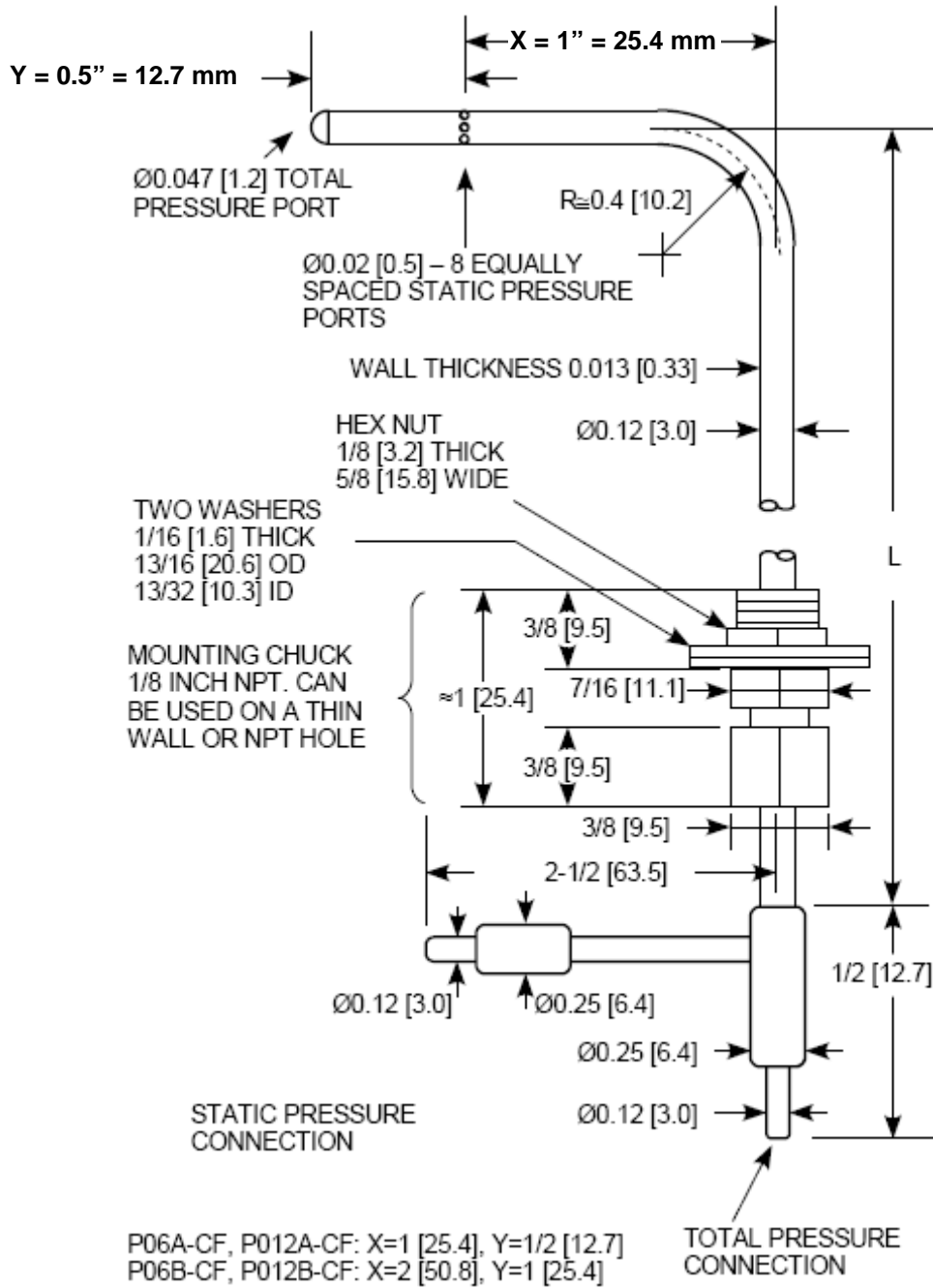


Figure B7.1a. Dimensions of the Pitot static probe used in current study [with permission, 213].

Table B7.1. Wind tunnel air velocity [m/s] measurement: FKT calibrator vs converted DAQ-PTDD

Air Velocity Directly measured by FKT calibrator [Va m/s]	Air Velocity Indirectly measured by DAQ via Pitot probe & PTDD [Volt]	Air Velocity DAQ VDC into Pressure PTDD conversion [Pa]	Air Velocity DAQ [Pa] into Velocity [m/s] Using Eqn. (4.9)	Y	X	Y-X	(Y-X) ²	
5.00	0.5973	14.88	4.98	5.00	4.98	0.0206	0.00042	
8.10	1.5782	39.31	8.09	8.10	8.09	0.0057	0.00003	
10.20	2.5067	62.44	10.20	10.20	10.20	-0.0010	0.00000	
13.05	4.0265	100.29	12.93	13.05	12.93	0.1212	0.01469	
15.20	5.6111	139.76	15.26	15.20	15.26	-0.0623	0.00388	
17.90	7.5911	189.08	17.75	17.90	17.75	0.1480	0.02192	
20.10	9.6542	240.47	20.02	20.10	20.02	0.0805	0.00649	
4.95	0.6121	15.25	5.04	4.95	5.04	-0.0910	0.00827	
9.90	2.3924	59.59	9.97	9.90	9.97	-0.0657	0.00432	
14.90	5.4193	134.98	15.00	14.90	15.00	-0.0992	0.00983	
17.75	7.7496	193.03	17.94	17.75	17.94	-0.1863	0.03471	
20.40	9.9470	247.76	20.32	20.40	20.32	0.0793	0.00628	
5.20	0.6877	17.13	5.34	5.20	5.34	-0.1433	0.02052	
10.00	2.4256	60.42	10.03	10.00	10.03	-0.0347	0.00121	
15.20	5.6285	140.19	15.29	15.20	15.29	-0.0859	0.00738	
17.10	7.1360	177.74	17.21	17.10	17.21	-0.1116	0.01245	
19.05	8.8659	220.83	19.18	19.05	19.18	-0.1347	0.01814	
19.00	8.7652	218.32	19.08	19.00	19.08	-0.0755	0.00570	
20.25	9.8189	244.57	20.19	20.25	20.19	0.0605	0.00366	
Std. Deviation ->							0.0950	
MSE ->							0.00947	

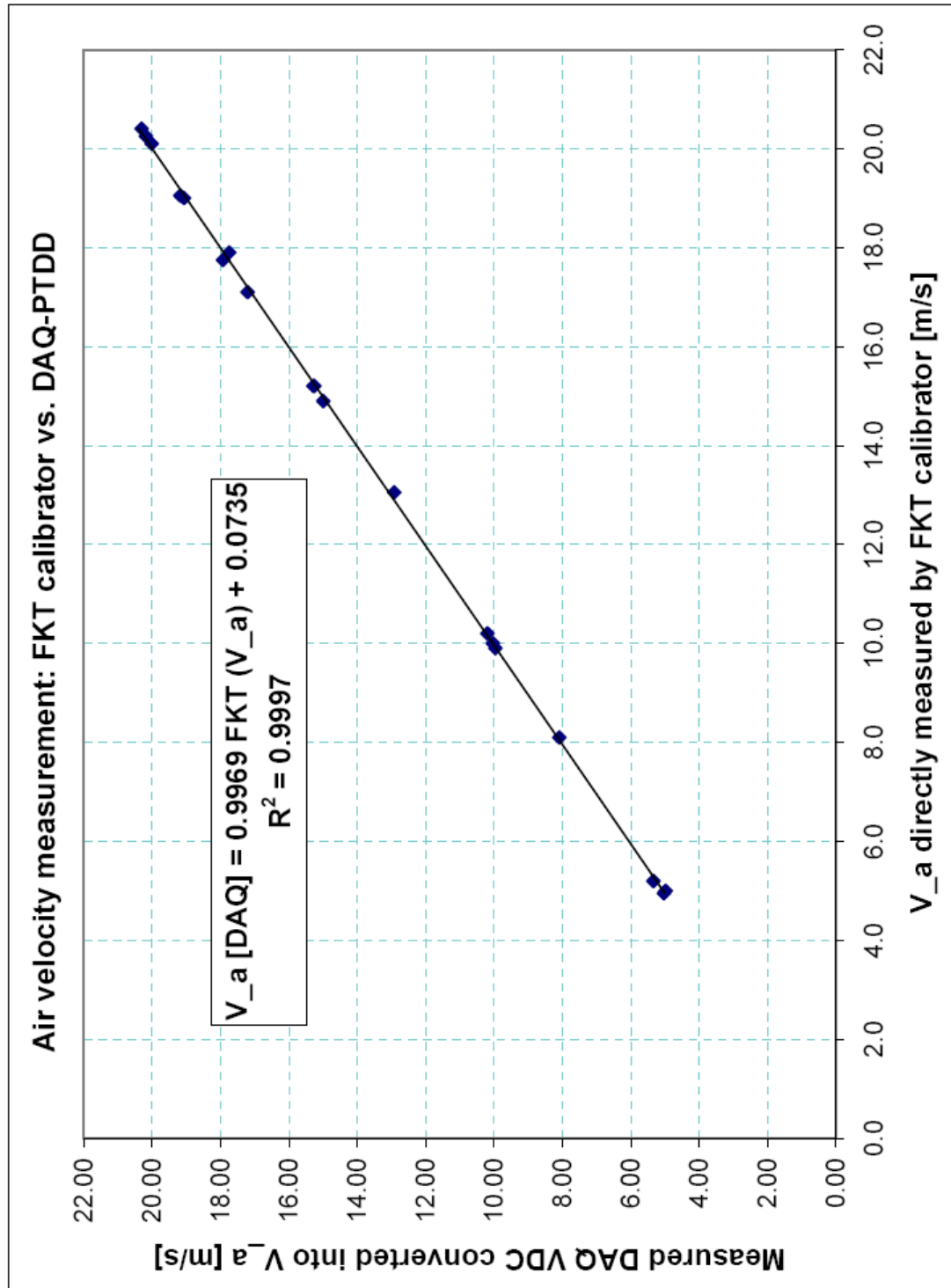


Figure B7.2. Wind tunnel air velocity measurements [m/s]: FKT calibrator vs. DAQ-PTDD.

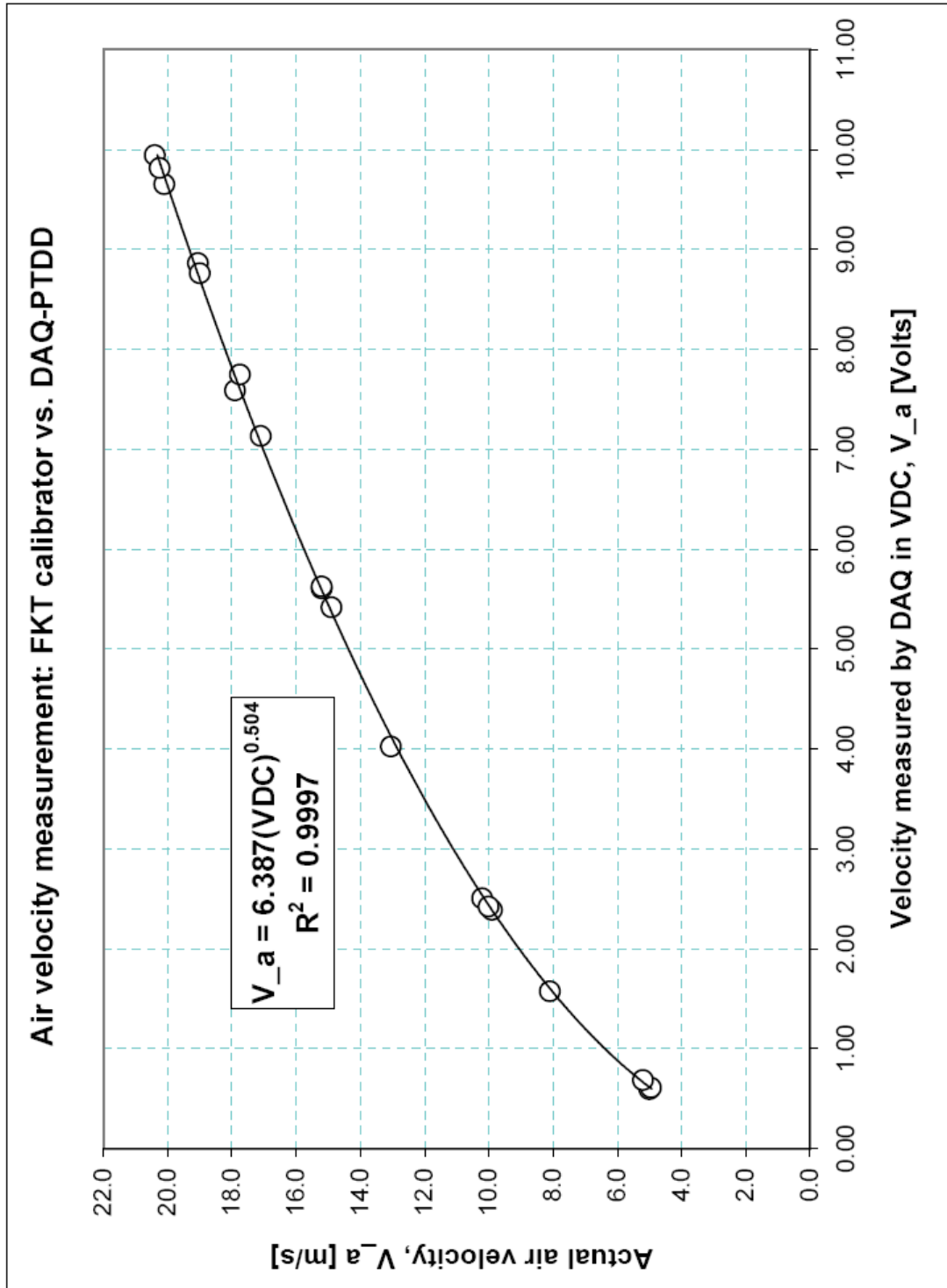


Figure B7.3. Wind tunnel air velocity calibration curve: FKT calibrator [m/s] vs. DAQ-PTDD [Volt].

LIBRATION REPORT

Accuracy Class: .5 %
 Pressure Range: 0.00 / 3.00 "WC
 Output Type: 1 - 5 VDC
 Serial Number: 80509378
 Date: 05-13-2008

Pressure "WC (Ref 4C)	Output VDC/ma	Error % FSO	Error % BSL
0.000	1.004	0.11	0.19
0.750	2.003	0.06	0.15
1.500	2.998	-0.04	0.03
2.250	3.990	-0.26	-0.19
3.000	4.991	-0.23	-0.16
2.250	3.994	-0.14	-0.07
1.500	3.000	0.01	0.09
0.750	2.004	0.09	0.17
0.000	1.004	0.10	0.18

Excitation Voltage: 24VDC
 System Number: I

We certify that our calibration system complies with ISO 10012-1, ANSI/NCSL Z540-1 and that all standards used for calibration are traceable to the National Institute of Standards and Technology. Pressure Standards: #215451, & #737/202491-60. Electrical Standards: DC Volts 251625, AC Volts 245061, Res 811/251319, Freq VLF WWVB, Resistor - AC 100072, DC 100071, R 100073 and FWVVBULSREC.

$$\% \text{ FSO Error} = \frac{V_{out} - \left[V_{FS} \times \frac{\text{PRESSURE} - \text{PRESSURE}_{0\%}}{\text{PRESSURE}_{FS}} + V_{out}_{0\%} \right]}{V_{FS}} \times 100$$

$$V_{FS} = V_{out_{100\%}} - V_{out_{0\%}} \text{ (Theoretical Max and Min)}$$

Reference ANSI/ISA-S51.1 & ANSI/ISA-S37.1 *

3515
 Calibrator

Figure B7.4. Vendor supplied calibration report for airside diff. pressure transducer (PTDD).

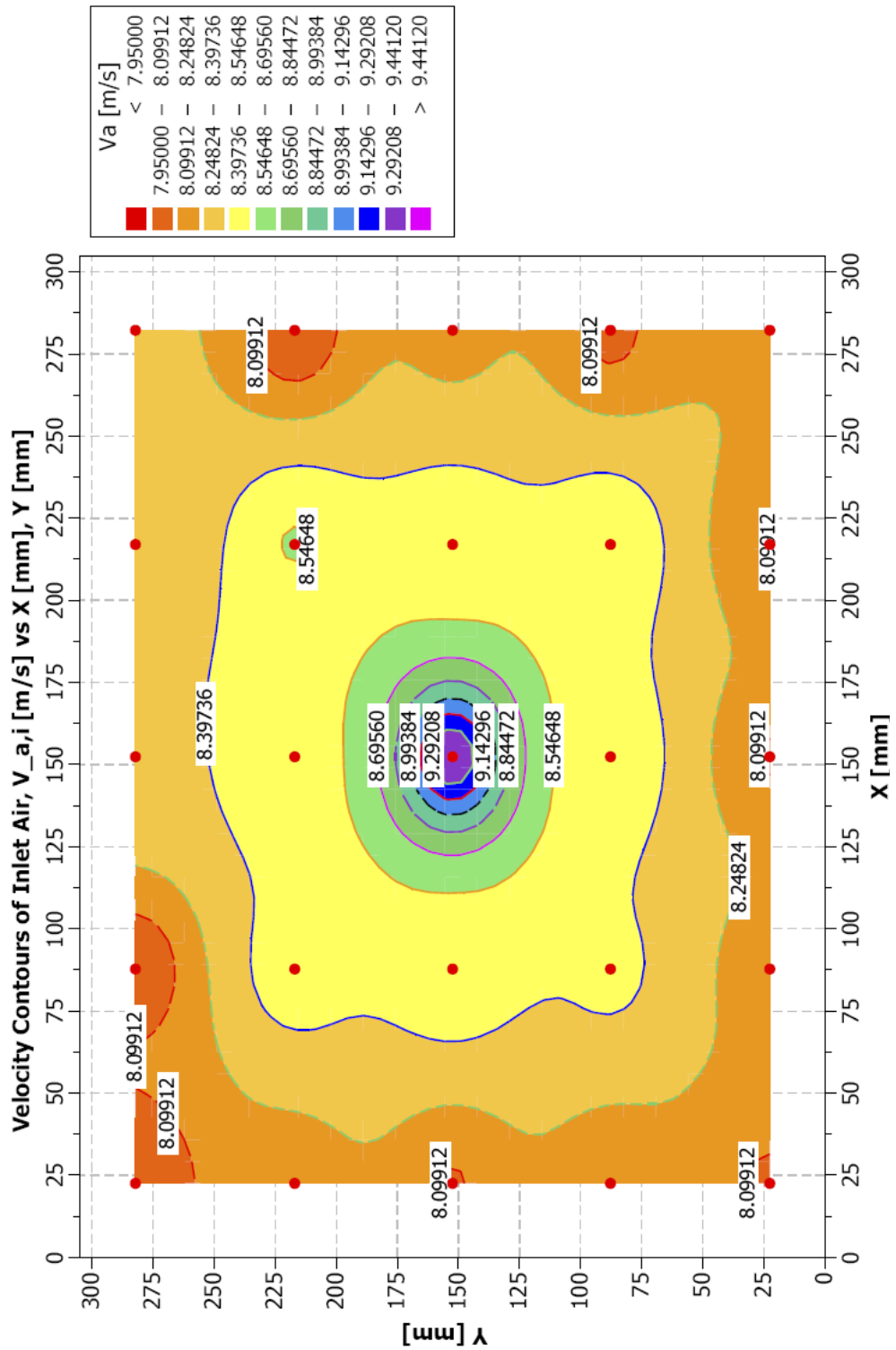


Figure B7.5a. Air velocity contours at the inlet plane using *Log-Tchebycheff* 5-point distribution.

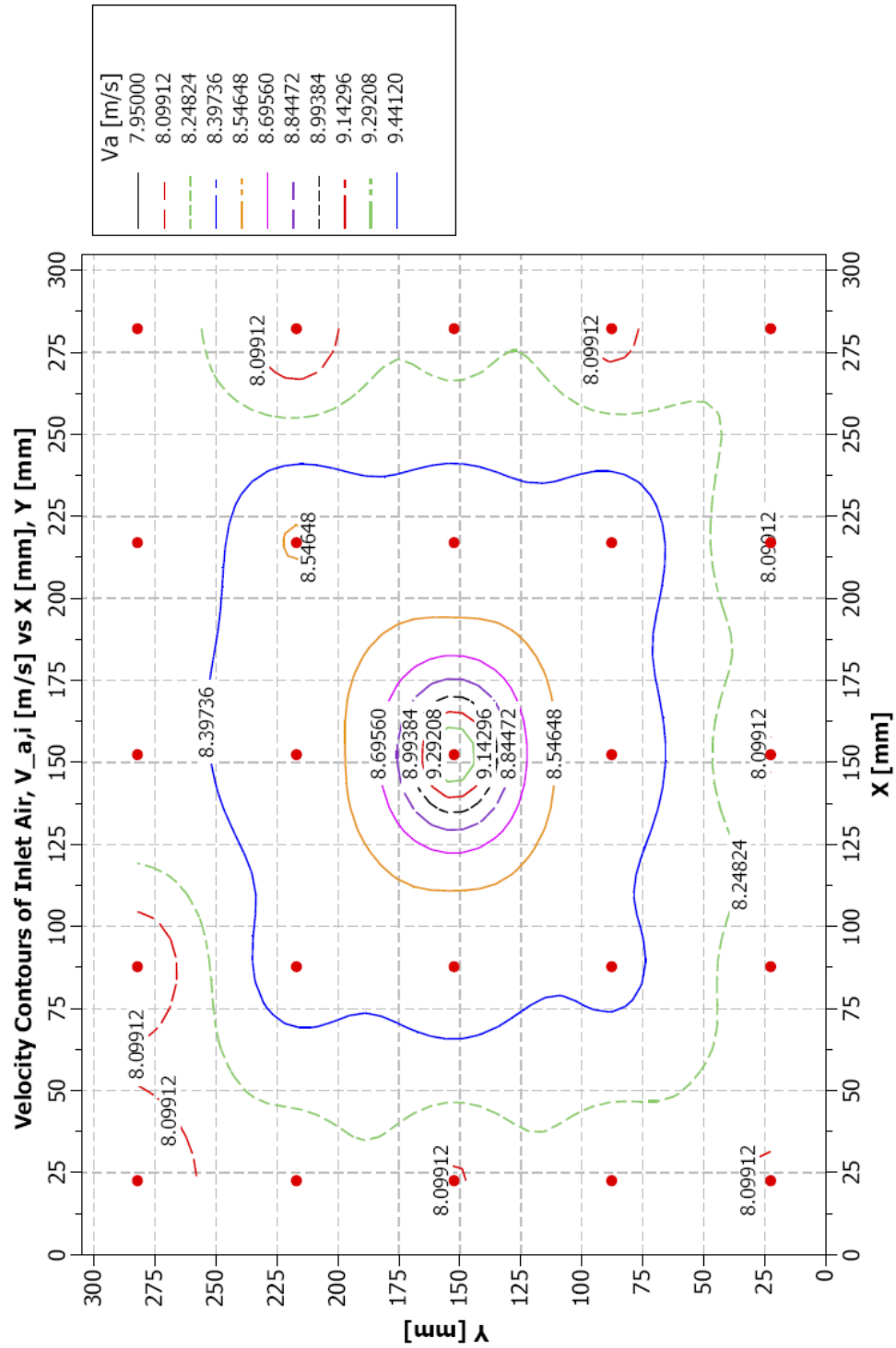


Figure B7.5b. Air velocity contours at the inlet plane using *Log-Tchebycheff* 5-point distribution.

APPENDIX – B8

TEMPERATURE DISTRIBUTION AND PROFILES AT WIND TUNNEL THERMAL GRIDS AND ON TEST SPECIMEN SURFACE

Appendix – B8. Temperature distribution and profiles at wind tunnel thermal grids and on test specimen surface

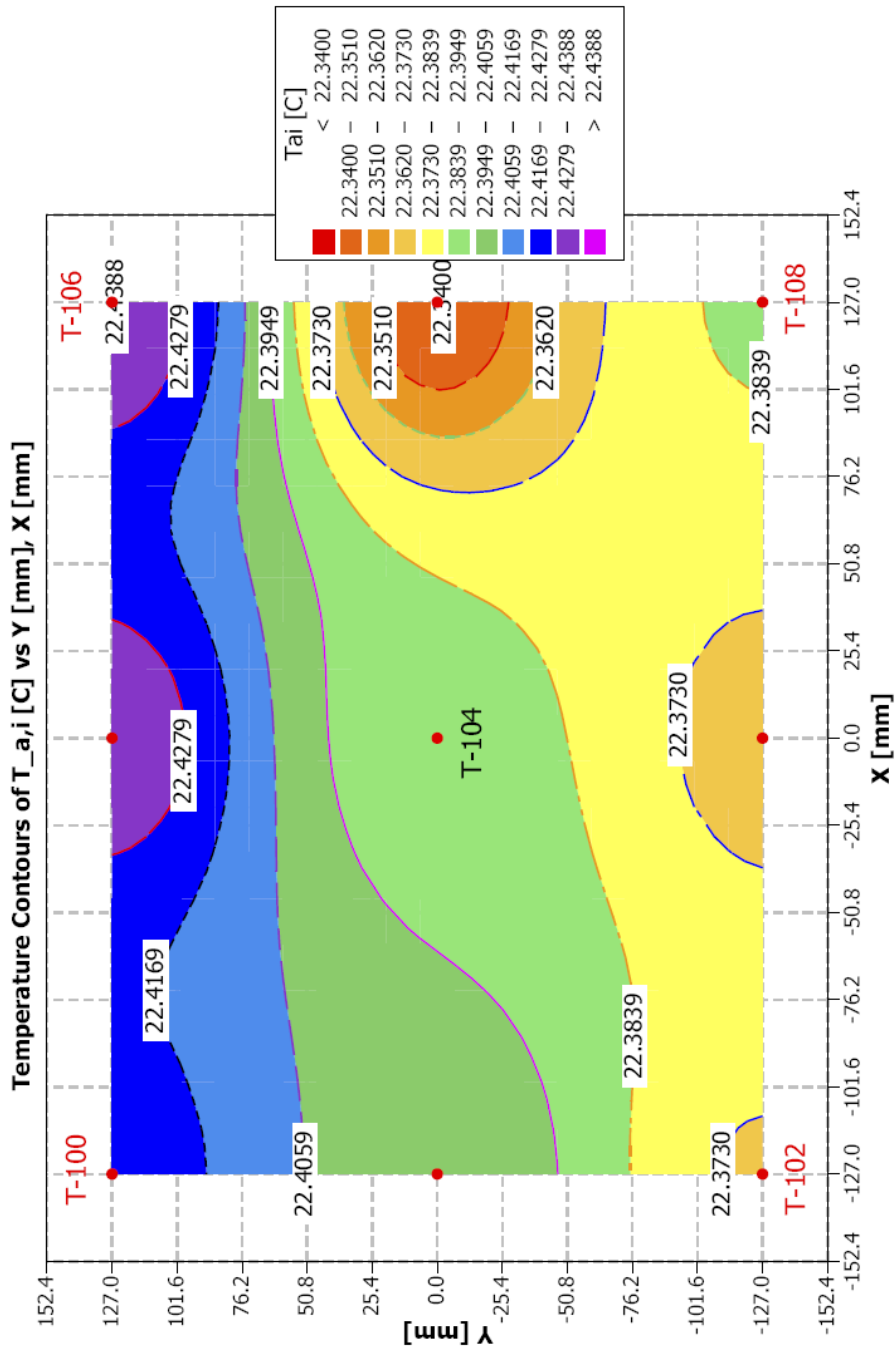


Figure B8.1a. Airside temperature contours at inlet thermal grid at A-A' (Figures 4.7a & 4.8a).

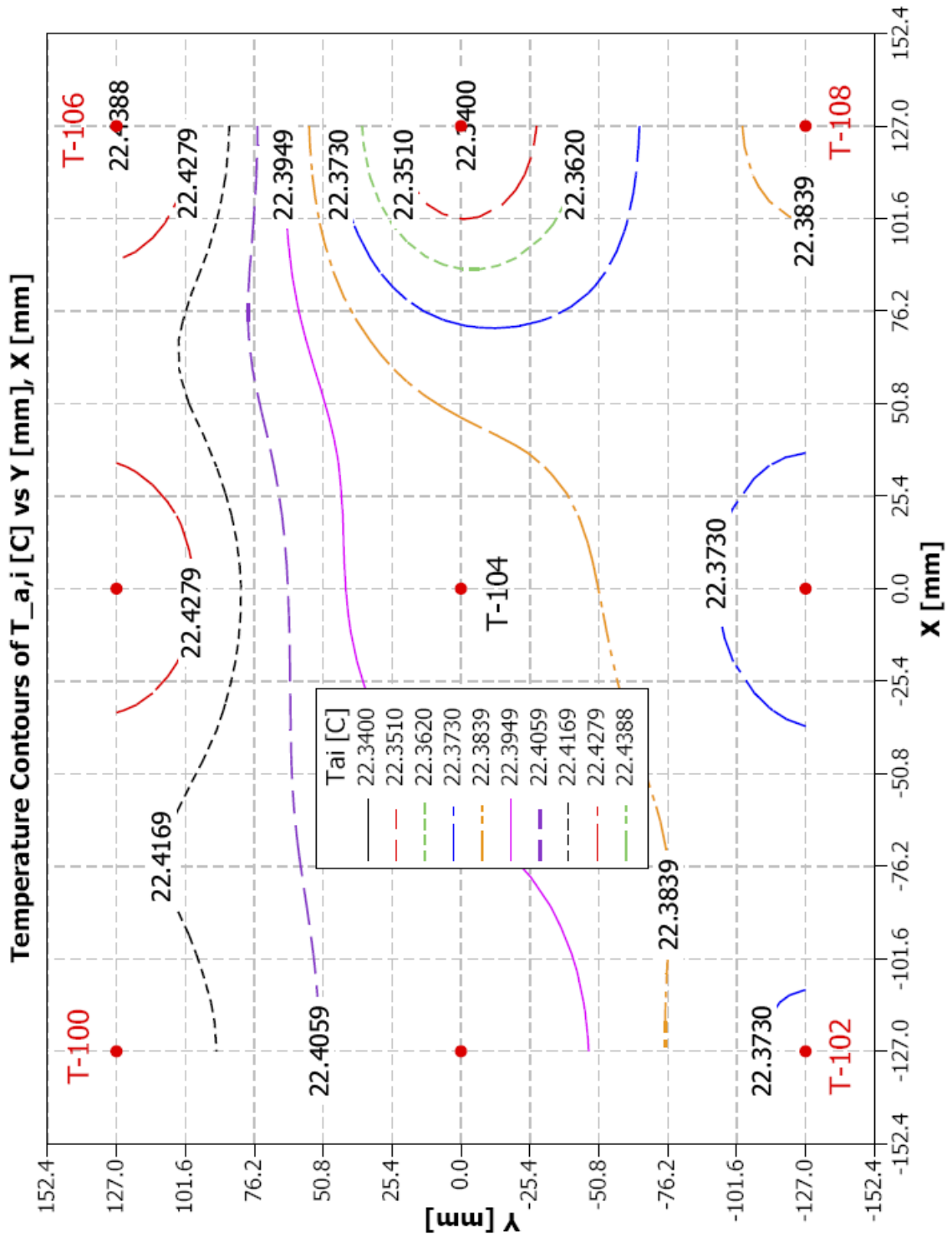


Figure B8.1b. Airside temperature contours at inlet thermal grid at A-A' (Figures 4.7a & 4.8a).

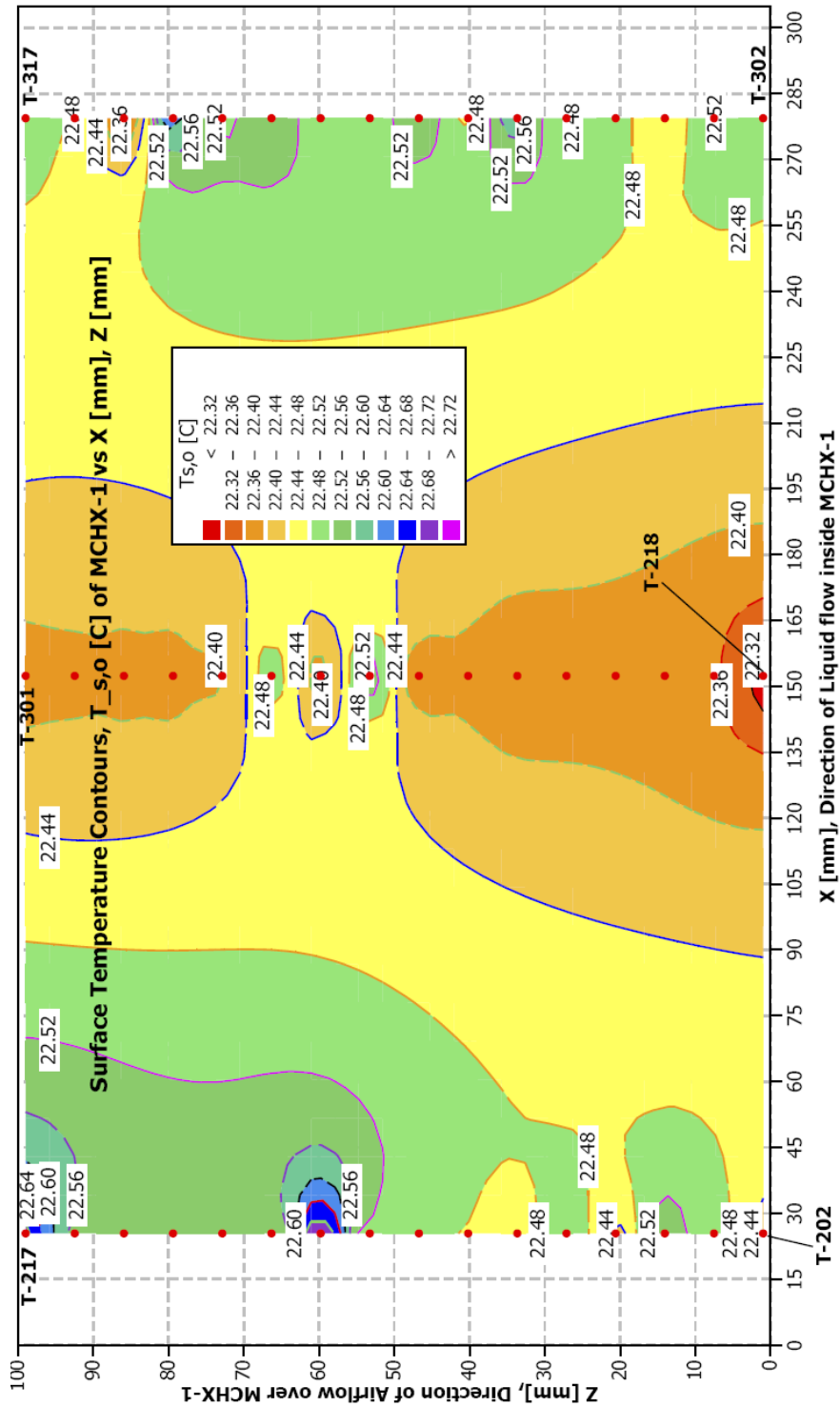


Figure B8.3b. Surface temperature contours at surface thermal grid of MCHX #1.

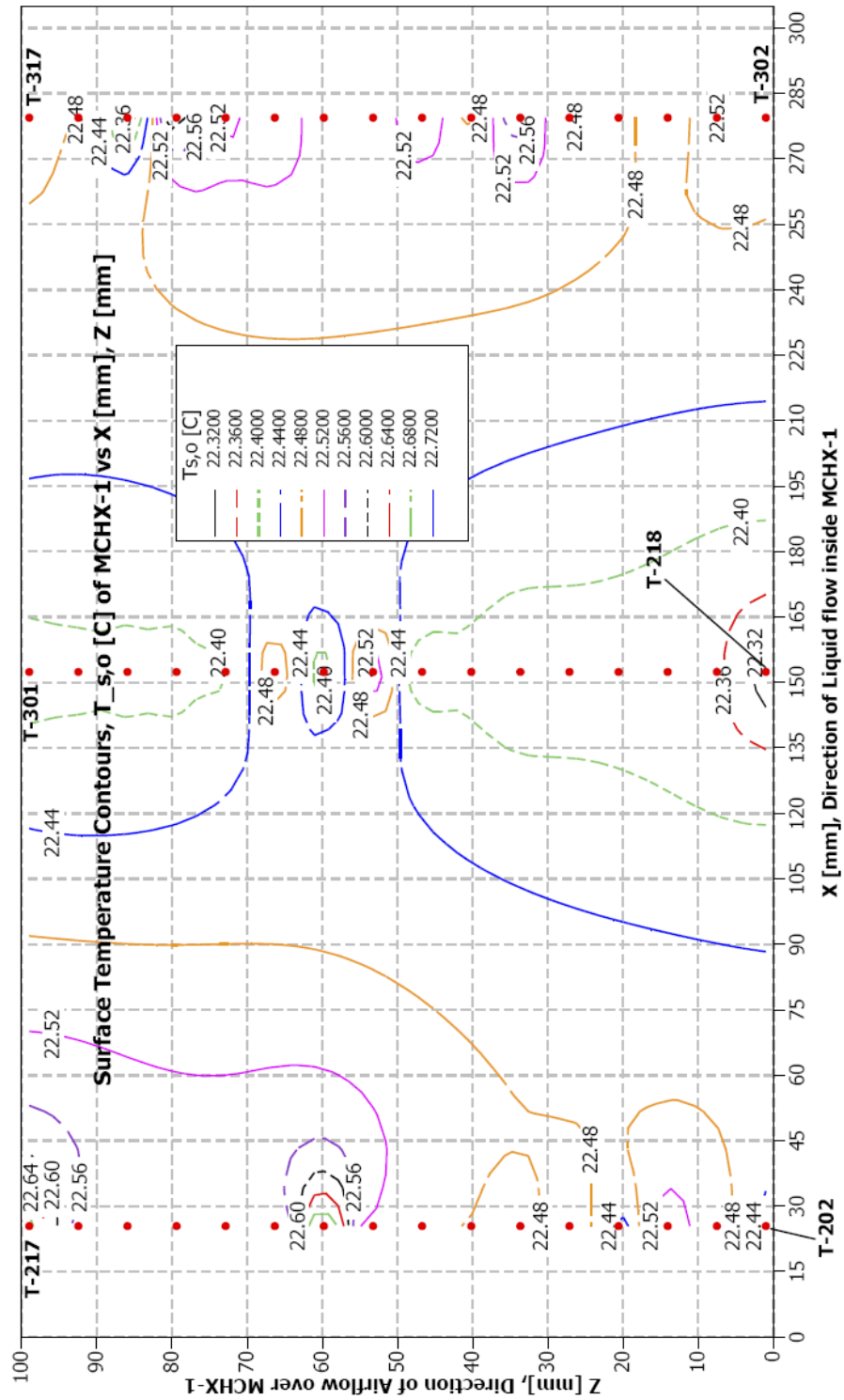


Figure B8.3c. Surface temperature contours at surface thermal grid of MCHX #1.

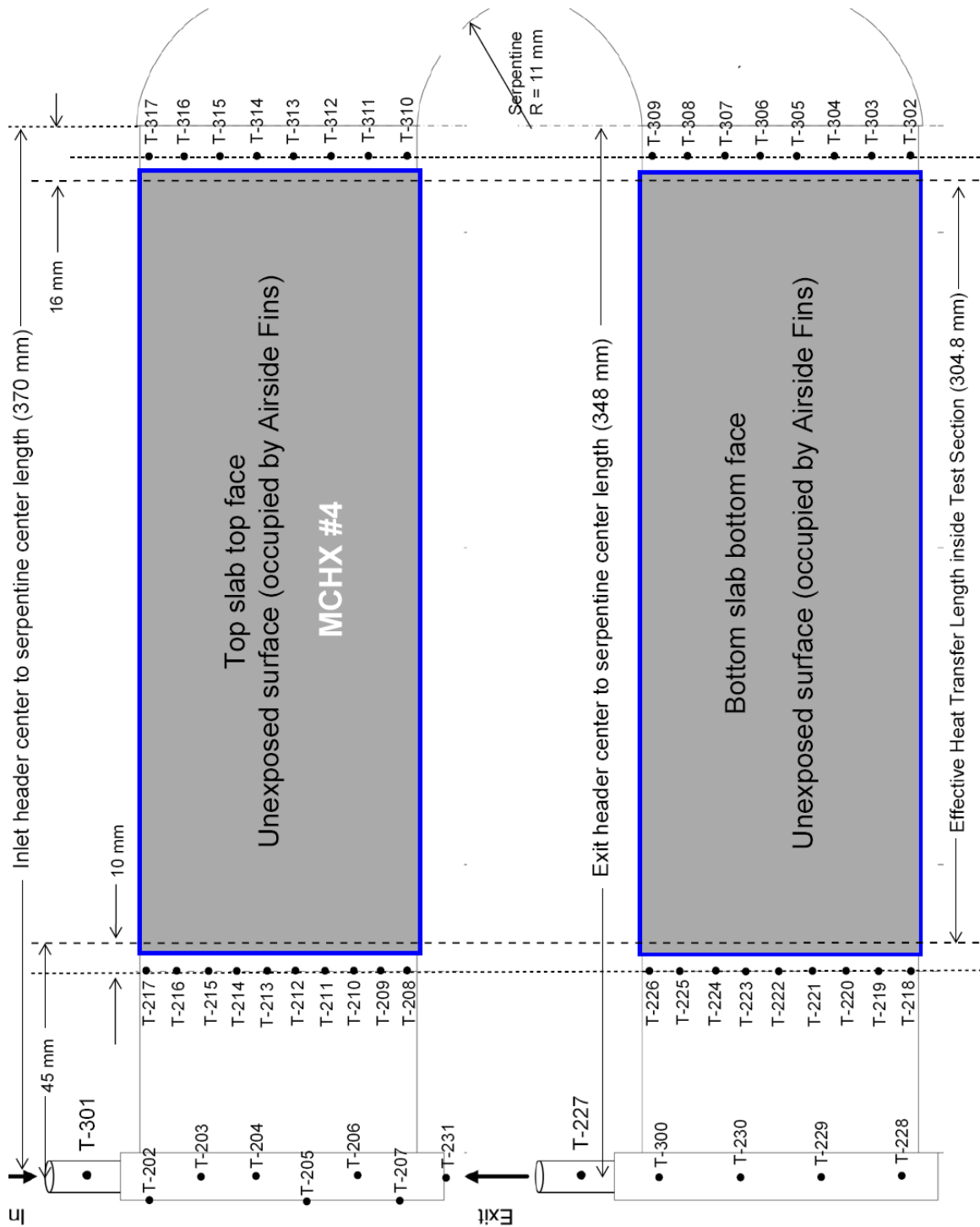


Figure B8.4a. Test specimen surface thermocouple locations with identifying numbers – MCHX #4.

APPENDIX – C

FLOW CHART AND TABLE FOR SOLVING THE NON-LINEAR REGRESSION EQUATIONS OF WILSON PLOT TECHNIQUE TO FIND HEAT TRANSFER COEFFICIENT

APPENDIX C: FLOW CHART AND TABLE FOR SOLVING THE NON-LINEAR REGRESSION EQUATIONS OF WILSON PLOT TECHNIQUE TO FIND HEAT TRANSFER COEFFICIENT

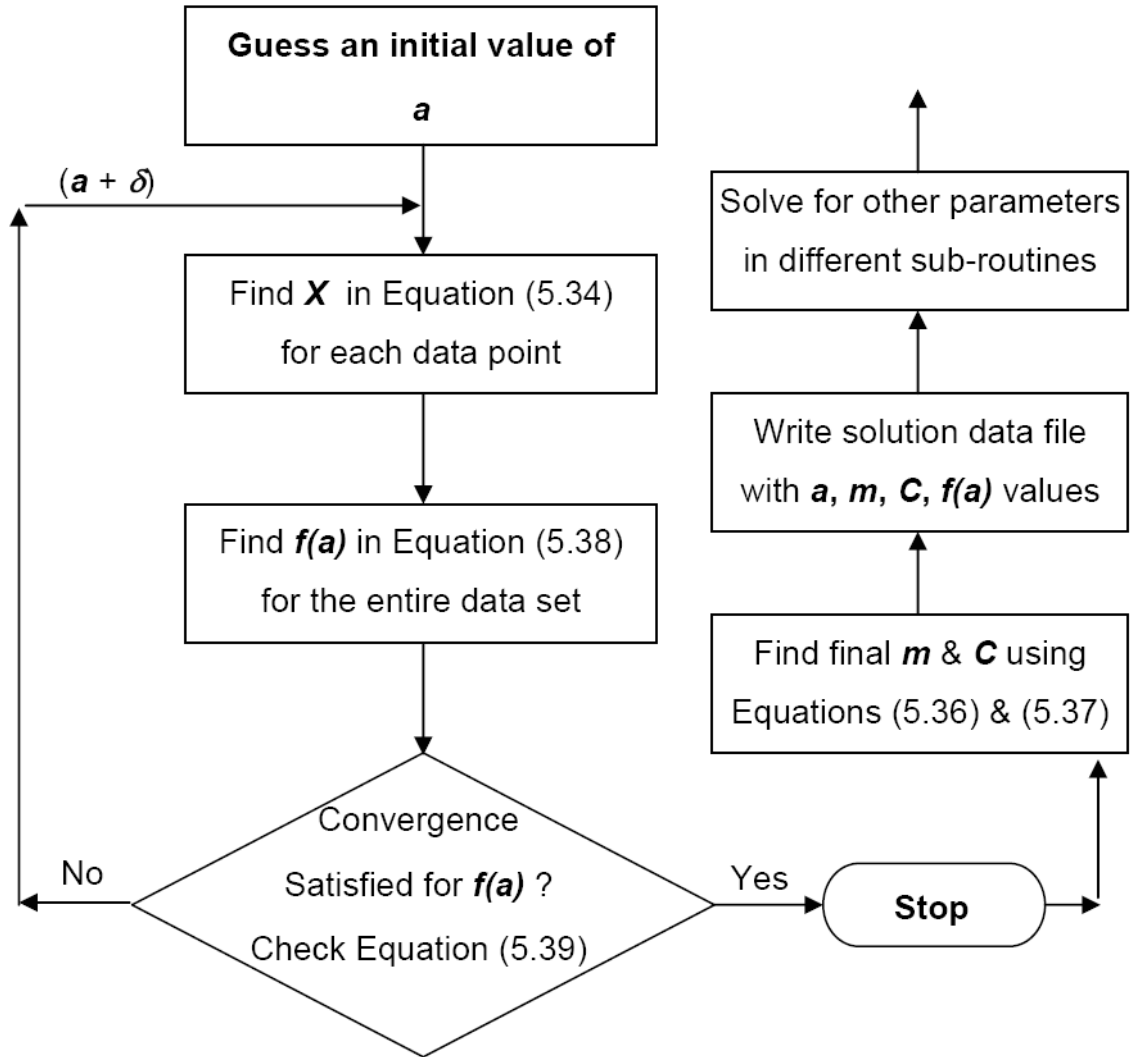


Figure C1. Developed flow chart to iteratively solve the equations of Wilson Plot Technique using non-linear regression analysis

Table C1. Developed data table to iteratively solve equations of Wilson Plot Technique using non-linear regression analysis

(Parameters associated to solving non-linear equations of Wilson Plot Technique)

Tests	Re_{liq}	W	$X = \frac{1}{Re^a W}$	$Y = R_{ov} = 1/UA$	$m = 1/C_1$	C	$\ln(Re_{liq})$	$f(a)$
1	Measure experimentally	Deduce from known and measured parameters	Deduce by assuming an initial value of "a" with small increment	Deduce from experimental data	For N data points, find from	For N data points, find from	Deduce from experimental data	Deduce from Eqn. (5.38) and
2	Measure	Deduce	Deduce	Deduce	iteration	iteration	Deduce	Check
3	Measure	Deduce	Deduce	Deduce	using Eqn. (5.36)	using Eqn. (5.37)	Deduce	for zero
4	Measure	Deduce	Deduce	Deduce			Deduce	or the
5	Measure	Deduce	Deduce	Deduce			Deduce	minimum
NOTE: Do it for several values of 'a'. If $f(a)$ in Eqn. (5.38) is not the minimum, repeat the process.								

APPENDIX – D

TABLES OF EXPERIMENTALLY OBTAINED DATA FOR WATER AND 50%-50% ETHYLENE GLYCOL-WATER MIXTURE FLOWS IN MCHX TEST SPECIMENS

APPENDIX D: TABLES OF EXPERIMENTALLY OBTAINED DATA FOR WATER AND 50%-50% ETHYLENE GLYCOL-WATER MIXTURE FLOWS IN MCHX TEST SPECIMENS

Table D1. Data for Water flow in multi-port straight microchannel slab (MCHX-1)

Total Mass Flow Rate, \dot{m}_w [kg/s]	Inlet Temperature, $T_{w,i}$ [C]	Exit Temperature, $T_{w,o}$ [C]	Total Inlet Pressure, $p_{w,i}$ [Pa]	Total Exit Pressure, $p_{w,o}$ [Pa]	MCHX-1 side $\Delta p_{ch,w}$ [Pa]	MCHX-1 side $Re_{ch,w}$	MCHX-1 side $f_{ch,w}$
0.024907	21.43	21.50	18636.54	100.87	10269.98	482.21	0.117730
0.025950	21.46	21.53	20022.38	449.26	10645.48	502.76	0.112302
0.026882	21.48	21.55	21394.44	790.14	11064.62	521.06	0.108687
0.027769	21.50	21.57	22842.34	1150.74	11551.28	538.52	0.106274
0.028746	21.53	21.61	24262.66	1506.51	11935.57	557.92	0.102381
0.029699	21.57	21.64	25717.45	1874.00	12338.04	576.91	0.099059
0.030631	21.64	21.70	27199.83	1989.14	13018.39	595.93	0.098241
0.030742	21.60	21.66	27213.62	2249.07	12687.46	597.52	0.094961
0.031629	21.66	21.72	28702.89	2372.49	13379.45	615.65	0.094594
0.032628	21.68	21.75	30268.00	2755.84	13781.13	635.46	0.091476
0.033604	21.71	21.77	31826.21	3146.77	14164.94	654.86	0.088556
0.034579	21.74	21.80	33432.69	3548.04	14566.33	674.36	0.085919
0.034713	21.76	21.82	35025.38	3556.32	16040.30	677.28	0.094152
0.035711	21.80	21.86	36721.49	3953.46	16493.68	697.42	0.091400
0.036687	21.83	21.89	38396.92	4356.80	16917.97	716.99	0.088752
0.037618	21.89	21.95	39996.50	4759.45	17288.30	736.24	0.086183
0.038461	21.91	21.97	41678.82	5167.62	17796.94	753.10	0.084831
0.039503	21.94	22.00	43416.30	5605.44	18129.16	774.06	0.081820
0.040435	21.96	22.02	45215.84	6053.60	18596.13	792.70	0.080048
0.041167	21.99	22.05	47049.84	6476.25	19300.57	807.62	0.080157
0.042320	22.03	22.09	49001.06	6936.13	19654.63	831.04	0.077139
0.043451	22.06	22.12	50917.80	7398.08	19966.27	853.86	0.074236
0.044449	22.11	22.17	52758.70	7853.13	20322.70	874.50	0.072131
0.045514	22.14	22.20	54744.39	8315.08	20723.87	896.09	0.070080
0.045957	22.18	22.24	56633.56	8783.92	21671.47	905.67	0.071949
0.046955	22.21	22.27	58633.04	9280.35	22091.55	926.00	0.070195
0.047798	22.25	22.31	60646.31	9756.09	22699.56	943.51	0.069584
0.048595	22.30	22.37	62307.95	10183.56	23040.98	960.51	0.068280
0.049505	22.32	22.39	64362.58	10693.77	23549.06	978.95	0.067205
0.050436	22.36	22.42	66424.12	11197.09	24029.15	998.19	0.066019

Table D1. Data for Water flow in multi-port straight microchannel slab (MCHX-1) ... cont'd

Total Mass Flow Rate, \dot{m}_w [kg/s]	Inlet Temperature, $T_{w,i}$ [C]	Exit Temperature, $T_{w,o}$ [C]	Total Inlet Pressure, $p_{w,i}$ [Pa]	Total Exit Pressure, $p_{w,o}$ [Pa]	MCHX-1 side $\Delta p_{ch,w}$ [Pa]	MCHX-1 side $Re_{ch,w}$	MCHX-1 side $f_{ch,w}$
0.051368	22.39	22.46	68527.02	11700.41	24532.60	1017.47	0.064938
0.052299	22.42	22.49	70671.29	12217.51	25045.33	1036.65	0.063914
0.053031	22.45	22.52	72326.03	12617.41	25412.62	1051.90	0.063038
0.053962	22.49	22.55	74463.41	13155.20	25866.41	1071.26	0.061922
0.054849	22.53	22.60	76531.84	13651.62	26331.67	1090.02	0.060974
0.055802	22.57	22.64	78738.16	14175.63	26805.56	1110.01	0.059923
0.056778	22.61	22.68	81013.43	14768.58	27231.99	1130.48	0.058751
0.057709	22.65	22.73	83219.75	15299.47	27691.17	1150.24	0.057787
0.058707	22.69	22.76	85563.97	15864.84	28146.00	1171.09	0.056708
0.059660	22.73	22.80	87977.14	16464.69	28675.89	1191.23	0.055907
0.060569	22.77	22.84	90114.51	16974.90	29062.34	1210.52	0.054927
0.061500	22.81	22.88	92320.84	17533.37	29421.74	1230.28	0.053886
0.064426	22.98	23.05	100870.34	19239.83	32106.69	1293.88	0.053570
0.065378	23.08	23.16	103007.72	19763.83	32335.56	1316.31	0.052330
0.067272	22.57	22.66	109109.58	21184.15	33978.66	1337.85	0.051704
0.072026	22.17	22.25	123485.15	24262.66	37929.45	1419.43	0.050498
0.073024	22.17	22.25	126105.16	24862.50	38328.11	1439.10	0.049597
0.073999	22.25	22.33	128863.06	25531.30	38825.62	1461.08	0.048889
0.074819	22.29	22.37	131138.34	26082.88	39191.81	1478.68	0.048239
0.075727	22.37	22.46	133758.34	26710.30	39671.55	1499.63	0.047633
0.076658	22.45	22.53	136378.35	27337.72	40095.80	1520.75	0.046943
0.077544	22.51	22.60	138998.36	27951.36	40591.37	1540.69	0.046413
0.078452	22.61	22.70	141549.42	28571.89	40963.70	1562.41	0.045722
0.079404	22.70	22.79	144307.33	29240.68	41398.69	1584.73	0.045069
0.081019	22.90	23.00	148995.76	30392.10	42097.54	1624.77	0.043955
0.081639	22.97	23.06	150926.30	30847.16	42468.57	1639.70	0.043654
0.082525	23.03	23.12	153615.25	31495.26	42911.88	1659.82	0.043137
0.082700	23.15	23.24	154028.94	31612.47	42909.15	1668.02	0.042939
0.083162	23.35	23.44	155132.10	31881.37	42931.95	1685.18	0.042455
0.083404	23.46	23.55	155752.63	31502.16	43506.31	1694.41	0.042794
0.083757	23.53	23.63	157407.37	32246.79	43778.00	1704.56	0.042692
0.085505	23.77	23.86	162992.13	33556.80	44838.70	1749.63	0.041909
0.085503	23.84	23.92	162923.18	33032.80	45307.92	1752.23	0.042377
0.086433	23.91	24.00	165681.08	34191.11	45164.31	1774.36	0.041271
0.086431	23.99	24.08	165543.19	33618.85	45616.22	1777.61	0.041712

Table D1. Data for Water flow in multi-port straight microchannel slab (MCHX-1) ... **cont'd**

Total Mass Flow Rate, \dot{m}_w [kg/s]	Inlet Temperature, $T_{w,i}$ [C]	Exit Temperature, $T_{w,o}$ [C]	Total Inlet Pressure, $\rho_{w,i}$ [Pa]	Total Exit Pressure, $\rho_{w,o}$ [Pa]	MCHX-1 side $\Delta p_{ch,w}$ [Pa]	MCHX-1 side $Re_{ch,w}$	MCHX-1 side $f_{ch,w}$
0.087338	24.08	24.17	168232.14	34232.48	45978.00	1800.00	0.041138
0.087338	24.08	24.17	168232.14	34232.48	45978.00	1800.00	0.041138
0.087957	24.18	24.27	170093.73	34742.70	46158.68	1816.94	0.040692
0.088355	24.25	24.34	171403.73	35197.75	46258.55	1828.09	0.040395
0.088730	24.32	24.41	172369.00	35383.91	46322.84	1838.82	0.040090
0.090540	23.71	23.81	177126.38	35811.38	46988.90	1850.32	0.038992
0.091252	23.59	23.69	179401.66	36321.60	47314.43	1859.69	0.038629
0.092280	23.29	23.40	177402.17	31447.00	48070.98	1867.76	0.038364
0.094660	23.95	24.05	190502.22	38900.24	48999.30	1945.28	0.037072
0.094654	24.18	24.28	190364.32	38831.29	48989.22	1955.51	0.037066
0.095730	24.65	24.75	193466.97	39500.08	49294.92	1999.17	0.036416
0.097023	24.37	24.47	198293.30	40672.19	50183.84	2013.22	0.036070
0.026291	76.21	74.68	14279.17	309.02	5541.26	1310.23	0.054280
0.026252	76.44	74.89	14243.43	354.36	5480.43	1312.03	0.053673
0.039980	76.73	75.68	32578.41	5216.96	8687.08	2012.19	0.035911
0.041573	76.32	75.34	36653.59	7107.93	9425.40	2082.21	0.036054
0.042256	76.49	75.55	37812.04	7144.16	9917.13	2121.73	0.036766
0.044089	76.13	75.15	41202.44	8030.42	10668.98	2202.85	0.036311
0.044658	76.36	75.41	42239.01	8082.08	11100.82	2238.45	0.036857
0.045218	76.57	75.70	43282.59	8183.33	11493.58	2273.70	0.037244
0.045825	76.31	75.44	44374.88	8351.66	11806.22	2296.59	0.037256
0.046475	76.03	75.15	45579.89	8527.70	12172.87	2320.63	0.037361
0.047090	76.04	75.17	46710.16	8599.37	12600.55	2351.62	0.037692
0.047760	76.03	75.16	47911.14	8824.07	12880.83	2384.95	0.037440
0.048889	75.75	74.91	50191.65	9569.29	13219.57	2432.86	0.036623
0.050005	76.18	75.39	52426.99	10132.62	13695.42	2503.12	0.036230
0.051018	76.29	75.53	54292.25	10119.22	14461.97	2557.96	0.036790
0.052308	74.76	73.97	56749.88	10969.24	14591.68	2570.31	0.035238
0.051583	76.27	75.53	55504.51	10699.12	14463.34	2585.91	0.035933
0.053116	75.50	74.76	57941.72	10786.60	15057.23	2636.15	0.035250
0.054027	76.17	75.46	60329.07	11619.37	15567.31	2705.44	0.035208
0.055751	75.94	75.24	64034.11	12244.54	16597.56	2783.61	0.035263
0.058056	75.98	75.33	69062.70	13450.19	17593.44	2901.16	0.034406
0.060189	75.59	74.91	74099.56	14721.25	18641.69	2991.90	0.033890
0.062118	75.72	75.07	78945.44	14748.39	20936.14	3093.76	0.035880

Table D1. Data for Water flow in multi-port straight microchannel slab (MCHX-1) ... **cont'd**

Total Mass Flow Rate, \dot{m}_w [kg/s]	Inlet Temperature, $T_{w,i}$ [C]	Exit Temperature, $T_{w,o}$ [C]	Total Inlet Pressure, $p_{w,i}$ [Pa]	Total Exit Pressure, $p_{w,o}$ [Pa]	MCHX-1 side $\Delta p_{ch,w}$ [Pa]	MCHX-1 side $Re_{ch,w}$	MCHX-1 side $f_{ch,w}$
0.064132	75.40	74.74	84464.76	14636.21	23842.12	3180.66	0.038529
0.066621	75.36	74.74	90986.17	16072.01	25460.45	3302.97	0.038102
0.066484	76.04	75.49	92591.03	16005.81	27344.27	3327.05	0.041283
0.068307	75.13	74.55	97583.23	17126.23	28578.72	3377.43	0.040873
0.068464	75.54	74.98	97666.54	15459.28	30114.16	3403.76	0.042994
0.070548	75.14	74.61	103130.79	16668.25	31286.53	3489.80	0.042020
0.072365	75.42	74.94	108391.47	17803.61	32674.53	3594.12	0.041680
0.074365	75.33	74.86	113425.23	18896.91	33515.64	3689.11	0.040409
0.075950	75.57	75.13	117664.11	19837.27	34313.02	3780.35	0.039605

Table D2. Data for 50% Ethylene glycol-water mixture flow in multi-port straight microchannel slab (MCHX-2)

Total mass flow rate, \dot{m}_g [kg/s]	Inlet temperature, $T_{g,i}$ [C]	Exit temperature, $T_{g,o}$ [C]	Total Inlet Pressure, $p_{g,i}$ [Pa]	Total Exit Pressure, $p_{g,o}$ [Pa]	MCHX-2 side $\Delta p_{ch,g}$ [Pa]	MCHX-2 side $Re_{ch,g}$ [-]	MCHX-2 side $f_{ch,g}$ [-]
0.022527	64.42	64.17	14550.70	905.76	6671.93	346.27	0.157600
0.022527	65.06	65.19	14514.50	1135.22	6412.11	353.14	0.151300
0.022527	66.47	66.59	14327.10	1396.53	5973.82	364.81	0.140600
0.022527	67.87	68.03	14790.16	1809.12	6033.98	376.90	0.142000
0.024092	66.46	65.76	15751.84	3.45	7823.33	386.38	0.161600
0.022527	69.26	69.49	15437.71	2457.50	6043.32	389.32	0.142100
0.024092	67.42	67.19	15908.56	111.90	7881.43	397.23	0.162700
0.024092	67.39	67.37	16115.33	301.51	7898.66	397.86	0.163000
0.024092	67.55	67.52	15976.47	194.43	7868.75	399.31	0.162400
0.031138	63.41	63.38	29845.97	6874.63	9915.84	468.61	0.122000
0.031138	63.82	63.82	29791.43	6851.19	9889.40	473.40	0.121600
0.031138	64.40	64.45	29617.75	6743.70	9831.28	480.22	0.120800
0.031138	64.99	65.06	28850.43	6191.77	9623.68	487.00	0.118200
0.032581	66.37	65.78	33543.56	8321.49	11005.45	522.17	0.123500
0.032581	67.44	67.35	34054.60	9321.23	10534.01	538.30	0.118000
0.032581	67.53	67.55	34020.61	9280.48	10543.57	540.01	0.118100
0.034464	66.17	65.76	42232.68	13760.56	12619.38	550.93	0.126700
0.034464	67.07	67.18	42389.88	13874.81	12679.23	565.86	0.127200
0.034464	67.08	67.30	42394.85	13960.92	12597.91	566.65	0.126400
0.038000	65.94	66.38	48444.58	19606.90	9683.62	610.16	0.078700
0.040836	63.75	63.89	54615.67	19740.18	12803.72	620.84	0.090720
0.038000	67.05	67.55	48558.21	19709.36	9714.03	626.38	0.078920
0.040836	64.32	64.45	54189.57	18949.49	13179.43	629.06	0.093450
0.043549	61.75	61.74	68398.16	27404.33	15943.94	630.20	0.099780
0.043549	62.04	62.07	68005.84	27430.25	15531.97	634.87	0.097090
0.038000	68.11	68.67	48808.14	19872.35	9818.46	642.16	0.079760
0.043549	62.54	62.59	68926.36	28408.76	15485.35	642.77	0.096760
0.043549	63.17	63.25	68562.53	28193.91	15351.84	652.60	0.095870
0.040836	66.60	66.80	55514.19	21058.87	12440.29	663.91	0.087920
0.043549	63.90	64.02	68254.54	27940.26	15314.25	664.24	0.095590
0.043942	66.48	67.03	69870.19	32130.34	12361.36	715.40	0.074980
0.043942	66.80	66.85	71060.57	32661.65	13020.05	716.39	0.079140
0.043942	67.27	67.79	70669.64	33174.07	12133.63	728.19	0.073500
0.051074	63.69	64.07	88026.99	38320.18	15637.93	777.56	0.070110
0.051074	64.75	65.21	88192.60	38451.25	15703.37	797.86	0.070380

Table D2. Data for 50% Ethylene glycol-water mixture flow in multi-port straight microchannel slab (MCHX-2) ... **cont'd**

Total mass flow rate, \dot{m}_g [kg/s]	Inlet temperature, $T_{g,i}$ [C]	Exit temperature, $T_{g,o}$ [C]	Total Inlet Pressure, $p_{g,i}$ [Pa]	Total Exit Pressure, $p_{g,o}$ [Pa]	MCHX-2 side $\Delta p_{ch,g}$ [Pa]	MCHX-2 side $Re_{ch,g}$ [-]	MCHX-2 side $f_{ch,g}$ [-]
0.051074	65.71	66.23	88112.55	38393.26	15709.88	816.46	0.070380
0.051725	65.73	65.71	92540.23	40919.30	16755.92	822.09	0.073330
0.051725	66.13	66.53	92477.49	40771.82	16858.64	833.77	0.073780
0.051725	66.29	66.66	92632.55	40800.43	16988.57	836.65	0.074360
0.063771	64.38	64.91	138017.86	64902.58	20697.68	988.54	0.059010
0.063771	64.97	65.50	138168.16	64945.47	20829.16	1002.07	0.059390
0.066617	63.98	64.51	148036.98	68676.29	22279.80	1022.83	0.058180
0.070409	62.30	62.46	173479.95	84787.97	25028.15	1034.57	0.058590
0.067492	63.96	64.47	154947.67	73808.41	22588.70	1035.50	0.057430
0.066617	64.55	65.13	148080.00	68821.70	22204.75	1037.29	0.057960
0.067492	64.36	64.94	155078.25	74247.74	22301.58	1046.21	0.056640
0.070409	62.87	63.07	173720.99	84941.93	25145.45	1049.14	0.058860
0.069113	63.76	64.23	171089.54	86659.82	23100.48	1055.19	0.055930
0.069113	64.25	64.71	168306.40	82460.57	24542.26	1067.11	0.059620
0.070409	63.85	64.14	173245.19	84532.79	25126.15	1074.98	0.058780
0.078305	63.54	63.92	204517.61	98856.72	27451.41	1187.97	0.051550
0.078305	64.71	65.15	203377.98	97383.04	27856.82	1221.83	0.052330
0.080726	63.80	64.25	241231.59	128217.16	30043.82	1233.29	0.053170
0.079003	65.53	65.92	214339.82	104262.22	30617.75	1255.95	0.056740
0.080726	64.71	65.24	241734.42	128831.69	29988.41	1260.75	0.053040
0.079003	66.00	66.65	213349.52	103751.59	30172.20	1273.25	0.055850
0.080726	65.56	66.19	229602.26	112932.10	33807.15	1287.49	0.060200
0.087453	63.69	64.14	261112.08	130988.51	33151.86	1332.37	0.049810
0.087453	64.64	65.19	260991.63	130943.21	33148.02	1364.00	0.049780
0.087453	65.43	66.06	261354.84	131089.31	33416.06	1390.88	0.050180
0.089569	65.28	65.84	270681.80	133262.96	35937.46	1418.27	0.051540
0.089569	65.41	65.81	270844.24	133465.39	35903.66	1419.95	0.051490
0.103125	61.04	61.32	359048.14	183562.64	41534.21	1472.52	0.044620
0.103125	61.14	61.37	354192.09	176523.09	43716.24	1474.99	0.047140
0.103125	61.15	61.44	359087.58	182848.83	42293.84	1476.69	0.045490
0.103125	63.27	63.41	353707.53	176408.30	43542.26	1550.19	0.046880
0.108356	62.19	62.63	389072.89	194710.71	46964.81	1593.27	0.045750
0.103125	64.54	64.93	353821.09	176432.15	43761.30	1601.62	0.047100
0.108356	63.28	63.84	389517.40	194967.75	47267.90	1637.25	0.046040

Table D3. Heat transfer and pressure drop data for Water flow in multi-port serpentine microchannel slab (MCHX-4)

Test Runs	Waterside Total Mass Flow Rate, \dot{m}_w [kg/s]	Waterside Inlet Temperature, $T_{w,i}$ [C]	Waterside Exit Temperature, $T_{w,o}$ [C]	Waterside Total Inlet Pressure, $p_{w,i}$ [Pa]	Waterside Total Exit Pressure, $p_{w,o}$ [Pa]	Waterside Total Pressure Drop Δp [Pa]	MCHX-4 Surface Temperature, T_s [C]
1.	0.01883668	75.37	60.94	105316.37	101317.40	3998.98	66.50
2.	0.02548844	75.97	64.86	114630.80	102458.62	12172.18	68.96
3.	0.03372392	75.99	67.40	128667.95	110430.53	18237.42	70.38
4.	0.03942096	75.89	68.48	140263.65	116967.51	23296.14	70.92
5.	0.04725660	75.87	69.69	162093.87	129103.14	32990.73	71.58

Table D3. Heat transfer and pressure drop data for Water flow in multi-port serpentine microchannel slab (MCHX-4) ... **cont'd**

Test Runs	Channel side Water Flow $Re_{ch,w}$	Waterside Heat Transfer Rate, q_w [W]	Waterside Heat Transfer Coefficient, h_w [W/m ² .C]	Waterside Nusselt Number, Nu_w	Airside Total Mass Flow Rate, \dot{m}_a [kg/s]	Airside Inlet Temperature, $T_{a,i}$ [C]	Airside Exit Temperature, $T_{a,o}$ [C]
1.	850.93	1137.73	4528.89	6.99	0.506203	14.03	16.23
2.	1187.88	1185.68	5378.61	8.28	0.507468	14.00	16.31
3.	1599.22	1213.16	6100.18	9.37	0.506641	13.95	16.32
4.	1881.73	1223.38	6393.02	9.82	0.507569	13.82	16.22
5.	2273.78	1223.21	6722.27	10.32	0.507312	13.86	16.31

Table D4. Heat transfer and pressure drop data for 50% Ethylene glycol-water mixture flow in multi-port serpentine microchannel slab (MCHX-4)

Test Runs	Glycol-side Total Mass Flow Rate, \dot{m}_g [kg/s]	Glycol-side Inlet Temp. $T_{g,i}$ [C]	Glycol-side Exit Temp. $T_{g,o}$ [C]	Glycol-side Total Inlet Pressure, $p_{g,i}$ [kPa]	Glycol-side Total Exit Pressure, $p_{g,o}$ [kPa]	Glycol-side Total Pressure Drop, Δp [kPa]	MCHX-4 side core Pressure Drop (in straight top & bottom slabs), Δp [kPa]	MCHX-4 side Pressure Drop in inlet & exit manifolds, Δp [kPa]	MCHX-4 side Pressure Drop in serpentine U-bend, Δp [kPa]
1.	0.029429	76.18	46.89	140226.77	111879.77	28.3500	18.2875	2.7742	1.1915
2.	0.039810	76.15	52.57	160409.04	119523.61	40.8900	23.2335	4.9835	1.7274
3.	0.047605	75.74	55.28	182959.91	132191.76	50.7700	26.0578	7.0552	2.1675
4.	0.054718	75.61	57.57	206653.27	144727.72	61.9300	29.7824	9.2517	2.5831
5.	0.058719	75.52	58.54	228102.13	159799.70	68.3000	31.5604	10.6149	2.8265
6.	0.062555	76.46	60.17	245623.35	171050.62	74.5700	33.1855	12.0046	3.0310
7.	0.063495	76.07	60.16	246603.23	169094.34	77.5100	34.9164	12.3601	3.1004
8.	0.066113	75.89	60.48	259184.34	177842.21	81.3400	35.3404	13.3736	3.2712
9.	0.070882	75.98	61.29	274404.42	185818.14	88.5900	36.0632	15.3196	3.5740
10.	0.072357	76.48	62.10	284699.62	191731.79	92.9700	38.3749	15.9450	3.6452
11.	0.074137	76.23	62.06	287625.21	192328.13	95.3000	38.0974	16.7206	3.7734
12.	0.077154	76.00	62.35	302278.90	201689.79	100.5900	38.8519	18.0755	3.9809
13.	0.082967	75.84	63.11	337350.91	222970.37	114.3800	43.4478	20.8296	4.3744
14.	0.092263	75.56	63.93	381024.68	248345.43	132.6800	45.7356	25.6335	5.0315
15.	0.099010	75.96	65.09	422630.60	272670.18	149.9600	50.4469	29.4236	5.4863
16.	0.107597	75.43	65.29	465443.12	294698.00	170.7500	53.9475	34.6233	6.1493
17.	0.113464	75.06	65.50	514898.21	326092.24	188.8100	59.4260	38.4148	6.6116
18.	0.089733	75.43	63.70	365982.35	236747.00	129.2400	46.7981	24.2781	4.8571
19.	0.071711	76.25	61.83	282698.89	190793.33	91.9100	38.2268	15.6692	3.6123
20.	0.034314	75.92	50.12	150448.58	115295.68	35.1500	21.7750	3.7358	1.4386

Table D4. Heat transfer and pressure drop data for 50% Ethylene glycol-water mixture flow in multi-port serpentine microchannel slab (MCHX-4) ... **cont'd**

Test Runs	MCHX-4 Surface Temp. T_s [C]	Channel side Glycol Flow Reynolds number $Re_{ch,g}$	Glycol-side Heat Transfer Rate, q_g [kW]	Glycol-side Experimental Heat Transfer Coefficient, h_g [W/m ² .C]	Glycol-side Experimental Nusselt Number, Nu_g	Glycol-side Wilson Plot predicted Nusselt Number, Nu_g	Airside Total Mass Flow Rate, \dot{m}_a [kg/s]	Airside Inlet Temp. $T_{a,i}$ [C]	Airside Exit Temp. $T_{a,o}$ [C]
1.	56.13	397.28	2.9659	3622.07	8.950	6.520	1.9298	8.02	9.57
2.	59.14	569.92	3.2400	4097.07	10.100	7.640	1.9257	8.13	9.81
3.	60.32	697.63	3.3662	4281.21	10.540	8.370	1.9172	8.20	9.94
4.	61.35	818.43	3.4158	4302.85	10.580	8.990	1.9166	8.30	10.09
5.	61.78	885.73	3.4519	4340.05	10.670	9.320	1.9151	8.34	10.15
6.	63.04	967.69	3.5332	4421.24	10.860	9.650	1.9101	8.41	10.27
7.	62.85	978.29	3.5018	4390.31	10.780	9.720	1.9105	8.36	10.22
8.	62.93	1020.10	3.5319	4436.43	10.890	9.910	1.9024	8.38	10.25
9.	63.38	1103.49	3.6117	4536.61	11.130	10.270	1.9048	8.36	10.24
10.	64.02	1141.31	3.6117	4523.78	11.100	10.400	1.8948	8.32	10.23
11.	63.89	1166.01	3.6459	4579.63	11.230	10.520	1.8925	8.32	10.22
12.	63.95	1214.12	3.6552	4617.63	11.330	10.730	1.8891	8.33	10.24
13.	64.26	1313.61	3.6669	4641.32	11.380	11.130	1.8913	8.33	10.26
14.	64.61	1468.92	3.7266	4790.35	11.740	11.740	1.8901	8.34	10.28
15.	65.41	1598.92	3.7410	4827.69	11.830	12.180	1.8909	8.40	10.36
16.	65.35	1732.49	3.7917	4995.70	12.240	12.680	1.8849	8.44	10.40
17.	65.42	1824.57	3.7695	5119.66	12.550	13.010	1.8887	8.39	10.37
18.	64.48	1423.39	3.6548	4744.25	11.630	11.570	1.8875	8.39	10.32
19.	63.87	1125.51	3.5884	4581.49	11.240	10.350	1.8833	8.34	10.24
20.	57.58	477.53	3.0512	3702.28	9.140	7.070	1.8875	8.06	9.70

APPENDIX – E

UNCERTAINTY ANALYSIS

APPENDIX E: UNCERTAINTY ANALYSES

The errors in experiments may originate from various sources and can influence the measured primary variables. The errors then propagate into the dependent parameters and into the end results according to the parametric relationships involved in the analysis. The error sources can be divided into two *bias* (B) and the *precision* (P) components. In treating and identifying the error limits assumptions, considerations, logics and judgments are applied depending on the experimental situation. The overall uncertainty issue is addressed in light of the ASME Journal of Heat Transfer Editorial (1993) and ASME Journal of Fluids Engineering Editorial (1991) [225-226]. Other resources are also consulted [227-230]. Brief descriptions and procedures are provided in section 5.6 above. Details of the uncertainty calculations are presented below.

E1. Addressing the uncertainty issues

The independent or primary variables are the parameters that are directly measured in current study using various instruments. The independent variables in this study include the basic geometric dimensions of the test specimens such as the channel diameter, flow length, slab height and width, fin height, width, and thickness, etc. that are tabulated in Table 4.1. The other independent variables include the liquid side and air side measured parameters as listed in section 5.0. The dependent or secondary variables are not directly measured but they are the functions of the primary measured parameters

and the thermophysical properties of the fluids. The dependent variables in current study are briefly listed below by their symbols and the notations are provided in nomenclature.

1. Geometric dimensions: A, A_c, A_s, P, D_h , and the fin dimensions (Figure 5.3),
2. Thermophysical properties of fluids: ρ, c_p, μ, k, Pr , etc.,
3. Heat transfer and fluid flow parameters:
 - a. Liquid side: $T_b, \Delta T, \dot{m}, Re, \Delta p, q, h, Nu, C, R_{th}, L_{hy}, L_{th}$ etc.
 - b. Air side: $T_b, \Delta T, V, \dot{m}, Re, q, h, Nu, C, R_{th}$ etc.
 - c. Test specimens: $T_s, LMTD, NTU, \varepsilon, C^*, UA, R_{th, ov}$ etc.

Bias Limit (B):

The instruments' resolution as applicable (± 0.5 times of the instrument scale resolution) is considered as the 0th order uncertainty. The other instrumental errors, consolidated by RSS of all errors (Equation 5.40), are taken as the 1st order uncertainty. The bias limit for instruments as the design stage uncertainty is calculated from root sum square (RSS) as follows.

$$B_1 = U_d = \sqrt{u_0^2 + I_{RSS}^2} = \sqrt{u_0^2 + u_I^2} . \quad (E1a)$$

Other possible sources of errors are also considered as the bias, for example in case of thermocouple, the wire length (B_1), probe (B_2), location (B_3), etc. and the overall bias is estimated as follows.

$$B = \sqrt{U_d^2 + B_1^2 + B_2^2 + B_2^2 + \dots + B_N^2} . \quad (\text{E1b})$$

Precision Error (P):

From the known and judged sources of information the precision error is calculated using RSS of all errors as follows,

$$P = \sqrt{P_1^2 + P_2^2 + P_3^2 + \dots + P_N^2} . \quad (\text{E2})$$

where P_1, P_2, \dots are the repeatability, special, temporal, and other error components in multiple samples such as the standard deviation, probe-to-probe variations etc.

E1.1 Uncertainty in independent (primary) parameters

Single sample measurement ($N = 1$):

The absolute and relative uncertainty of an independent parameter say an arbitrary variable of 'X', which is directly measured as a single point sample, is calculated from the root sum square (RSS) of bias and precision errors (Equation E1.1) as follows:

$$U_x = \pm \sqrt{B^2 + P^2} \quad (\text{absolute}) \quad (\text{E1.1a})$$

and

$$\frac{U_x}{X} = \pm \sqrt{\frac{B^2 + P^2}{X^2}} , \quad (\text{relative}). \quad (\text{E1.1b})$$

Multiple samples measurement ($N > 1$):

In this case the bias limit is considered the same as Equation E1b. The precision however is dependent on the experimental samples and the standard deviation, which for an arbitrary independent variable 'X' is expressed at 95% confidence limit as follows.

$$P_{\bar{X}} = (t_{N-1, 95\%})(S_{\bar{X}}) = (t_{N-1, 95\%})\left(\frac{S_X}{\sqrt{N}}\right) \text{ for number of samples, } N < 20 \quad (\text{E1.2a})$$

and

$$P_{\bar{X}} = (t_{N, 95\%})(S_{\bar{X}}) = (t_{N, 95\%})\left(\frac{S_X}{\sqrt{N}}\right) \text{ for number of samples, } N \geq 20 \quad (\text{E1.2b})$$

where \bar{X} and t are the sample mean and student t -distribution and $S_{\bar{X}}$ is the standard deviation of sample mean. The S_X is the standard deviation defined by Equations E1.3. For all the experiments the average sample size was $N \geq 1000$ and thus $t = 1.962$ was set.

$$S_X = \sqrt{\frac{1}{N-1} \sum_{i=1}^N (X_i - \bar{X})^2} \text{ for number of samples, } N < 20 \quad (\text{E1.3a})$$

and

$$S_X = \sqrt{\frac{1}{N} \sum_{i=1}^N (X_i - \bar{X})^2} \text{ for number of samples, } N \geq 20 \quad (\text{E1.3b})$$

Taking the precision error calculated from Equations E1.2 and E1.3, the uncertainty of multiple samples of an independent parameter is determined using Equation E1.1.

E1.2 Uncertainty in dependent (secondary) parameters

Now let us consider an arbitrary dependent variable ‘A’ that depends on other primary parameters such as $A_1, A_2, A_3 \dots$ etc. according to the following functional relationship.

$$A = f(A_1, A_2, A_3, \dots, A_n) . \tag{E1.4}$$

The absolute uncertainty of the dependent variable ‘A’ is calculated from the root sum square (RSS) of the partial derivatives is expressed by,

$$U_A = \sqrt{\left(\frac{\partial A}{\partial A_1} U_{A_1}\right)^2 + \left(\frac{\partial A}{\partial A_2} U_{A_2}\right)^2 + \left(\frac{\partial A}{\partial A_3} U_{A_3}\right)^2 + \dots + \left(\frac{\partial A}{\partial A_n} U_{A_n}\right)^2} , \text{ and} \tag{E1.5a}$$

the relative uncertainty from Equations E1.5a and E1.4 is given as follows.

$$\frac{U_A}{A} = \sqrt{\frac{\left(\frac{\partial A}{\partial A_1} U_{A_1}\right)^2 + \left(\frac{\partial A}{\partial A_2} U_{A_2}\right)^2 + \left(\frac{\partial A}{\partial A_3} U_{A_3}\right)^2 + \dots + \left(\frac{\partial A}{\partial A_n} U_{A_n}\right)^2}{[A = f(A_1, A_2, A_3, \dots, A_n)]^2}} . \tag{E1.5b}$$

The partial derivatives $\frac{\partial A}{\partial A_1}, \frac{\partial A}{\partial A_2}, \frac{\partial A}{\partial A_3}, \dots$ are derived from the functional relationship given in Equation E1.4. The uncertainties in independent parameters $U_{A_1}, U_{A_2}, U_{A_3}, \dots$ are obtained from Equations E1.1, E1.2, and E1.3. Usually the absolute uncertainty is represented by $A \pm U_A$. For clarity the sign is however ignored throughout the write up.

E1.3 Uncertainty in thermophysical property evaluations

The uncertainty for respective thermophysical property may be 0.25 to 0.5 times the absolute value [225-227]. If taken from any table, sometimes they are considered as bias error limit even though they may have some precision error. For a given operating condition, the temperatures are measured several times to give different population and from where the mean, maximum, and minimum values are obtained. In current study the thermophysical properties are considered as the dependent variables since they are evaluated mostly at bulk temperatures, which are functions of independent parameters at two different locations. Therefore their uncertainties are calculated as follows.

$$U_A = \frac{1}{2} \left| \left(A@T_{b, \max} - A@T_{b, \min} \right) \right|, \quad (\text{E1.6})$$

where T_b is the bulk temperature as defined by Equation 5.1. The dependent variable ‘A’ is any property of fluid i.e. $A = \rho, c_p, \mu, k,$ or Pr.

E2 Uncertainties in instruments, DAQ system, and sensors

These uncertainties include the errors in digital caliper used for geometric dimension measurements, DAQ system engaged for data recording, and sensors employed for measurements such as the thermocouple, RTD, pressure transducer, flow meter, Pitot Static probe etc. The treatments of their uncertainties are described below.

E2.1 Digital caliper and geometric measurements

A Mitutoyo (Mitutoyo Corporation, Japan, Model CD CS 500-196), digital caliper is used to measure various geometric dimensions of the test samples. The caliper has a resolution (0^{th} order bias limit) of $B_{\text{res}} = B_0 = 0.0125 \text{ mm} = 0.0000125 \text{ m}$ and an accuracy of $B_{\text{accu}} = B_1 = 0.025 \text{ mm} = 0.000025 \text{ m}$. The total 0^{th} order bias error, which is fixed for other dimensional measurements in this series, is estimated as,

$$B_{\text{caliper}} = B_{\text{geometry}} = \sqrt{B_1^2 + B_0^2} = 2.795 \times 10^{-2} \text{ mm} = 2.795 \times 10^{-5} \text{ m} \quad (\text{E2.1})$$

The total uncertainty in any independent geometric parameter 'X' is calculated as from Equations E1.2 and E2.1 as follows.

$$U_X = \sqrt{B_{\text{caliper}}^2 + P_X^2} \quad (\text{E2.2})$$

Independent and dependent parameters in geometric measurements

The independent geometric parameters such as the L , D , H , W , t etc. associated with each test specimen, wind tunnel test section and the inlet and exit pipe connections were several times measured for $N \geq 20$ and their mean values were obtained. Since the population was more than 20, their precisions at 95% confidence limits were determined using Equations E1.2b and E1.3b. The total uncertainties were then calculated from Equation E2.2. The exception is the microchannel diameter, which could not be measured but as mentioned in section 4.1 its uncertainty information was obtained from the manufacturer to be $U_D \approx \pm 1.5\% \approx \pm 0.000015$ m [202].

The uncertainties in the dependent parameters such as the A_c , A_s , D_h , etc. were determined using Equations E1.4 and E1.5. As an example, the uncertainty calculation of the surface area of a single channel is explained below.

$$A_s = \pi DL, \quad \dots \text{ partial derivation with respect to } D \text{ and } L \text{ gives,}$$

$$\frac{\partial A_s}{\partial D} = \pi L \text{ and } \frac{\partial A_s}{\partial L} = \pi D; \text{ using Equations E7a and E7b one deduces}$$

$$U_{A_s} = \sqrt{\left(\frac{\partial A_s}{\partial D} U_D\right)^2 + \left(\frac{\partial A_s}{\partial L} U_L\right)^2} = \sqrt{(\pi L U_D)^2 + (\pi D U_L)^2} \quad \text{and} \quad (E2.3)$$

$$\text{in relative form, } \frac{U_{A_s}}{A_s} = \sqrt{\left(\frac{U_D}{D}\right)^2 + \left(\frac{U_L}{L}\right)^2}$$

Putting the values of $A_s = 0.0009574 \text{ m}^2$, $U_D \approx \pm 0.000015 \text{ m}$ and $U_L \approx \pm 0.000106 \text{ m}$ in Equation E2.3, the absolute and relative uncertainties in surface area are estimated to be $U_{A_s} = \pm 0.00001437 \text{ m}^2 = \pm 1.5004\%$. Other parameters are similarly calculated.

E2.2 Data Acquisition (DAQ) System

The DAQ system and its components, shown in Figures 4.1b and 4.20, were obtained from National Instruments and configured in house. It has a PCI acquisition card, multiplex mode signal cable, SCXI signal conditioner, and SCXI terminal block. All these components, whatever little they may be, contribute to measurement errors, which are treated and consolidated below. The accuracy specifications for these components were collected from the manufacturer, which are given in Table E1 below. It is noted that except for the PCI Card the combined accuracy of all other SCXI modules (cable, signal conditioner, and terminal block) were supplied by the manufacturer.

Table E1. Accuracy specifications of DAQ components (Notes: m = milli, μ = micro, V = volt)

Error sources	DAQ Card (16-bit PCI-6052E)		All SCXI modules combined		Remarks / others
	0– 5 VDC input	0–10VDC input	0– 5 VDC input	0–10VDC input	
Resolution (B_0)	28.6 μ V	57.3 μ V	-	-	See Eqn. E2.3
Accuracy (B_0)	0.0353% of rdg; Max =2.119 mV	0.0071% of rdg; Max =1.232 mV	0.035% of rdg; or Max = 1.75 mV	0.025% of rdg; Max = 1.5 mV	See Eqns. E2.4 & E2.14
Off-set (B_{11})	241.0 μ V	476.0 μ V	290.0 μ V	500.0 μ V	
Quantization & Noise (B_{11})	21.7 μ V 245.0 mV	43.5 μ V 491.0 mV	25.0 μ V 300.0 mV	50.0 μ V 600.0 mV	Samples $N \geq 100$ Sample, $N = 1$
Temperature drift (B_{13})	0.0006% rdg/ $^{\circ}$ C Max = 0.75 mV	0.0001% rdg/ $^{\circ}$ C Max = 0.25 mV	50.0 μ V / $^{\circ}$ C; Max = 1.25 mV	20.0 μ V / $^{\circ}$ C; Max = 0.70 mV	15-35 $^{\circ}$ C Ambient operation $\approx 25^{\circ}$ C
Sensitivity (B_{14})	2.50 μ V	2.50 μ V	-	-	
Non-linearity (B_{15})	$\frac{1}{2} B_0 = 14.3 \mu$ V	$\frac{1}{2} B_0 = 28.65 \mu$ V	0.005% of rdg; Max = 0.25 mV	0.005% of rdg; Max = 0.50 mV	
Digitization width, precision (P_0)	76.3 μ V	152.6 μ V	-	-	See Eqn. E2.6

Uncertainty in Data Acquisition Card:

The *resolution* of the 16-bit card (1 in 65,536) as the 0th order bias limit is calculated as follows.

$$B_0 = \frac{Input_{max} - Input_{min}}{Gain * 2^{16}}, \text{ where } \begin{cases} Gain = 2 & \text{for 0 - 5 VDC input range} \\ Gain = 1 & \text{for 0 - 10 VDC input range} \end{cases} \quad (E2.4a)$$

The *relative accuracy* as the instrumental error is calculated as,

$$B_{10} = \begin{cases} 354 * 10^{-6} * V_{DAQ}, & \text{for 0 - 5 VDC input range} \\ 71 * 10^{-6} * V_{DAQ}, & \text{for 0 - 10 VDC input range} \end{cases} \quad (E2.4b)$$

or the *maximum absolute accuracy* at full scale (FS) could be given by,

$$B_{10} = \begin{cases} 2119 * 10^{-6} \text{ Volt}, & \text{for 0 - 5 VDC input range} \\ 1232 * 10^{-6} \text{ Volt}, & \text{for 0 - 10 VDC input range} \end{cases} \quad (E2.4c)$$

Either of Equations E2.4b or E2.4c can be considered but not both. Equation E2.4a is the actual accuracy with the output of DAQ system by any given sensor. Equation E2.4b maximum estimate of accuracy regardless of any sensor's output via DAQ.

The *temperature drift* given in Table E1 is based on the ambient temperature during operation of the DAQ system in the range $15 \leq T_{amb} \leq 35^\circ\text{C}$. All the experiments and the DAQ was operated within the ambient temperature range of 20 to 25°C. The reasonable maximum B_{13} value from Table E1 at $T_{amb} = 25^\circ\text{C}$ is taken in all error

calculations. If the system had to operate in an ambient temperature beyond this range i.e. $T_{amb} < 15^\circ\text{C}$ or $T_{amb} > 35^\circ\text{C}$, the following expressions would have to be considered.

$$B_{13} = \left(\underbrace{\text{Reading} * 0.0006\% / ^\circ\text{C}}_{\text{for ambient}} + \underbrace{\text{Reading} * 0.001\% / ^\circ\text{C}}_{\text{for offset}} \right) * \Delta T, \quad (E2.5)$$

where $\begin{cases} \Delta T = T_{amb} - 35, & \text{for } T_{amb} > 35^\circ\text{C} \\ \Delta T = 15 - T_{amb}, & \text{for } T_{amb} < 15^\circ\text{C} \end{cases}$

The digitization code for the DAQ card is considered as the *precision error*, which is calculated as follows.

$$P_0 = \frac{\text{Input}_{\max} - \text{Input}_{\min}}{\text{Gain} * 2^{16}}, \text{ where } \begin{cases} \text{Gain} = 2 & \text{for } 0 - 5 \text{ VDC input range} \\ \text{Gain} = 1 & \text{for } 0 - 10 \text{ VDC input range} \end{cases} \quad (E2.6)$$

The total bias and the precision for the DAQ card is estimated from Table E1 and Equations E2.3 to E2.6 using the RSS of all the bias elements as follows.

$$B_{\text{DAQ-Card}} = \sqrt{\underbrace{B_0^2}_{\text{Resolution}} + \underbrace{B_{10}^2}_{\text{Accuracy}} + \underbrace{B_{11}^2}_{\text{Off-set}} + \underbrace{B_{12}^2}_{\text{Noise}} + \underbrace{B_{13}^2}_{\text{Temp. drift}} + \underbrace{B_{14}^2}_{\text{Sensitivity}} + \underbrace{B_{14}^2}_{\text{Non-linearity}}} \quad (E2.7)$$

and

$$P_{\text{DAQ-Card}} = \sqrt{\underbrace{P_0^2}_{\text{Digitization code width}}} \quad (E2.8)$$

From Equations E2.7 and E2.8 the uncertainty in DAQ Card is calculated as,

$$U_{\text{DAQ-Card}} = \sqrt{\underbrace{B_{\text{DAQ-Card}}^2}_{\text{Bias}} + \underbrace{P_{\text{DAQ-Card}}^2}_{\text{Precision}}} \quad (E2.9)$$

0 – 5 VDC Range:

As applicable by adopting the relative and absolute values for bias and precision limits from Table E1 into Equation E2.9, we can re-write the following expressions for voltage input range of 0 – 5 Volt DC as,

$$\begin{aligned}
 U_{\text{DAQ-Card}} &= \sqrt{(10^{-6} \text{ Volt})^2 * [(28.6)^2 + (353 * V_{\text{DAQ}})^2 + (241)^2 + (21.7)^2 \\
 &\quad + (150 * V_{\text{DAQ}})^2 + (2.5)^2 + (143.3)^2 + (76.3)^2]} \quad . \quad (\text{E2.10}) \\
 &= \left[\sqrt{85732.68 + 147109 * (V_{\text{DAQ}})^2} \right] * 10^{-6} \text{ Volt}
 \end{aligned}$$

where V_{DAQ} is the DC voltage output of the DAQ system from a given sensor. The maximum absolute uncertainty or the uncertainty at full-scale reading (FSR) is calculated from Equation E2.10 by introducing $V_{\text{DAQ}} = 5 \text{ VDC}$ as follows.

$$U_{\text{DAQ-Card}} = 1939.96 * 10^{-6} \text{ Volt} = 1.94 \text{ mV} . \quad (\text{E2.11})$$

To eliminate the calculation complexity, the absolute uncertainty in DAQ card can be calculated using Equation E2.11 with an upper limit of error. Otherwise it can be calculated using actual sensor supplied and DAQ measured voltage from Equation E2.10.

0 – 10 VDC Range:

Similarly by adopting the relative and absolute values for bias and precision limits from Table E1 into Equation E2.9, we can re-write the following expressions for voltage input range of 0 – 10 Volt DC as,

$$\begin{aligned}
 U_{\text{DAQ-Card}} &= \sqrt{(10^{-6} \text{ Volt})^2 * [(57.3)^2 + (71 * V_{\text{DAQ}})^2 + (476)^2 + (43.5)^2 \\
 &\quad + (25 * V_{\text{DAQ}})^2 + (2.5)^2 + (28.65)^2 + (152.6)^2]} \quad . \quad (\text{E2.12}) \\
 &= \left[\sqrt{255865.37 + 5666 * (V_{\text{DAQ}})^2} \right] * 10^{-6} \text{ Volt}
 \end{aligned}$$

And by introducing $V_{\text{DAQ}} = 10$ VDC in Equation E2.12 the maximum absolute or the FSR uncertainty is calculated as follows.

$$U_{\text{DAQ-Card}} = 906.9 * 10^{-6} \text{ Volt} = 0.91 \text{ mV} . \quad (\text{E2.13})$$

To eliminate the calculation complexity, the absolute uncertainty in DAQ card can be calculated using Equation E2.13 with an upper limit of error. Otherwise it can be calculated using actual sensor supplied and DAQ measured voltage from Equation E2.12.

Uncertainty in Data Acquisition SCXI modules together:

The combined *relative* and the combined *maximum absolute accuracies* at FSR of all the SCXI modules are given by Equation E2.14.

$$B_{10} = \begin{cases} 350 * 10^{-6} * V_{\text{DAQ}}, & \text{for } 0 - 5 \text{ VDC input range} \\ 250 * 10^{-6} * V_{\text{DAQ}}, & \text{for } 0 - 10 \text{ VDC input range} \end{cases} \quad (\text{E2.14a})$$

and

$$B_{10} = \begin{cases} 1750 * 10^{-6} \text{ Volt}, & \text{for } 0 - 5 \text{ VDC input range} \\ 1500 * 10^{-6} \text{ Volt}, & \text{for } 0 - 10 \text{ VDC input range} \end{cases} \quad (\text{E2.14b})$$

The expressions for *temperature drift* follow Equation E2.5 except for the different values in Table E1. No precision limit for digitization code-width is available

for the SCXI modules. The total bias is calculated from Table E1 using the RSS of all the bias elements for the combined SCXI components as follows.

$$B_{\text{DAQ-SCXI}} = \sqrt{\underbrace{B_{10}^2}_{\text{Accuracy}} + \underbrace{B_{11}^2}_{\text{Off-set}} + \underbrace{B_{12}^2}_{\text{Noise}} + \underbrace{B_{13}^2}_{\text{Temp. drift}} + \underbrace{B_{14}^2}_{\text{Non-linearity}}} \quad (\text{E2.15})$$

And the total uncertainty in SCXI components is given by Equation E2.16,

$$U_{\text{DAQ-SCXI}} = \sqrt{\underbrace{B_{\text{DAQ-SCXI}}^2}_{\text{Bias}} + \underbrace{P_{\text{DAQ-SCXI}}^2}_{\text{Precision}} = 0} = B_{\text{DAQ-SCXI}} \cdot \quad (\text{E2.16})$$

The consolidated uncertainties in SCXI for 0 – 5 VDC and 0 – 10 VDC ranges follow the Equations E2.10 to E2.13 with different values, which are given below.

SCXI in 0 – 5 VDC Range:

$$\begin{aligned} U_{\text{DAQ-SCXI}} &= \sqrt{(10^{-6} \text{ Volt})^2 * [(350 * V_{\text{DAQ}})^2 + (290)^2 \\ &\quad + (25)^2 + (1.25)^2 + (250 * V_{\text{DAQ}})^2]} \quad (\text{E2.17}) \\ &= \left[\sqrt{84726.56 + 185000 * (V_{\text{DAQ}})^2} \right] * 10^{-6} \text{ Volt} \end{aligned}$$

and

$$U_{\text{DAQ-SCXI}} = 2170.2 * 10^{-6} \text{ Volt} = 2.17 \text{ mV} \cdot \quad (\text{E2.18})$$

SCXI in 0 – 10 VDC Range:

$$\begin{aligned} U_{\text{DAQ-SCXI}} &= \sqrt{(10^{-6} \text{ Volt})^2 * [(250 * V_{\text{DAQ}})^2 + (500)^2 \\ &\quad + (50)^2 + (0.5)^2 + (500 * V_{\text{DAQ}})^2]} \quad (\text{E2.19}) \\ &= \left[\sqrt{252500.25 + 312500 * (V_{\text{DAQ}})^2} \right] * 10^{-6} \text{ Volt} \end{aligned}$$

and

$$U_{\text{DAQ-SCXI}} = 5612.71 * 10^{-6} \text{ Volt} = 5.61 \text{ mV} . \quad (\text{E2.20})$$

Total uncertainty in the DAQ system:

Using the RSS method the total uncertainty in the DAQ system is estimated from Equations E2.9 and E2.16 as follows and details are given in Equations E2.22 to E2.25.

$$U_{\text{DAQ}} = \sqrt{U_{\text{DAQ-Card}}^2 + U_{\text{DAQ-SCXI}}^2} . \quad (\text{E2.21})$$

0 – 5 VDC Range:

Based on actual DAQ voltage output for a given sensor,

$$U_{\text{DAQ}} = \left[\sqrt{170459.24 + 332109 * (V_{\text{DAQ}})^2} \right] * 10^{-6} \text{ Volt} , \text{ here V is in Volt} \quad (\text{E2.22})$$

and at the FSR ($V_{\text{DAQ}} = 5 \text{ VDC}$) i.e. the maximum absolute uncertainty,

$$U_{\text{DAQ}} = 2910.87 * 10^{-6} \text{ Volt} = 2.91 \text{ mV} , \quad (\text{E2.23})$$

0 – 10 VDC Range:

Based on actual DAQ voltage output for a given sensor,

$$U_{\text{DAQ}} = \left[\sqrt{508365.62 + 318166 * (V_{\text{DAQ}})^2} \right] * 10^{-6} \text{ Volt} , \quad (\text{E2.24})$$

and at the FSR ($V_{\text{DAQ}} = 10 \text{ VDC}$) i.e. the maximum absolute uncertainty,

$$U_{\text{DAQ}} = 5685.5 * 10^{-6} \text{ Volt} = 5.69 \text{ mV} , \quad (\text{E2.25})$$

E2.3 Temperature sensors – RTDs and Thermocouples

Resistance Temperature Detectors (RTDs)

The specifications, connection details, and the calibration process of the RTDs used to measure the inlet and exit liquid flow temperatures are provided in Sections 4.4 and 4.5 and Table 4.2. The ultra-precise 1/10 DIN RTDs have total absolute instrumental accuracy of $B_{\text{RTD}} = 0.012^\circ\text{C}$ (Equation E1b). Since the sample size for all experimental runs were $N \geq 1000$, the student t was set to 1.962 in precision error calculation. The uncertainty in RTD was estimated using Equations E1, E1.1, E1.2b and E1.3b as follows.

$$U_{\text{RTD}} = \sqrt{B_{\text{RTD}}^2 + P_{\text{RTD}}^2} = \sqrt{(0.012)^2 + \left(1.962 * \frac{S_X}{\sqrt{N}}\right)^2} \quad [^\circ\text{C}]. \quad (\text{E2.26})$$

The total uncertainty in temperature that was measured using RTD and DAQ together is,

$$U_{\text{T,RTD}} = \sqrt{U_{\text{RTD}}^2 + U_{\text{DAQ}}^2} = \sqrt{(0.012)^2 + \left(1.962 * \frac{S_X}{\sqrt{N}}\right)^2 + U_{\text{DAQ}}^2} \quad [^\circ\text{C}]. \quad (\text{E2.27})$$

The uncertainty in DAQ due to RTD is obtained through the RTD sensitivity (K_{RTD}) linked with the DAQ response using RTD-Voltage output relationship as follows.

$$V_{\text{RTD}} = I_{\text{EX}} R_{\text{T}}. \quad (\text{E2.28})$$

where I_{EX} is the RTD excitation current (100 mili-Amp = 0.1 Amp in current study) and R_{T} is the resistance and temperature relationship of RTD material.

The R_T is generally obtained from widely used approximated curve-fit equation proposed by Calendar-Van Dusen as follows [237].

$$R_T = R_0 \left[1 + AT + BT^2 + C(T - 100)^3 \right] \text{ ohm, where } \begin{cases} A = 3.9083 * 10^{-3} \\ B = -5.775 * 10^{-7} \\ C = 0 \text{ for } T > 0 \end{cases}, \quad (\text{E2.29})$$

By combining Equations E2.28 and E2.29 together and getting partial derivatives of V with respect to T , the RTD sensitivity K_{RTD} can be obtained.

$$V_{\text{RTD}} = R_0 I_{\text{EX}} + R_0 I_{\text{EX}} AT + R_0 I_{\text{EX}} BT^2, \quad (\text{E2.30})$$

and

$$K_{\text{RTD}} = \frac{\partial V_{\text{RTD}}}{\partial T} = R_0 I_{\text{EX}} A + 2R_0 I_{\text{EX}} BT = R_0 I_{\text{EX}} (A + 2BT) \text{ Volt}/^\circ\text{C}, \quad (\text{E2.31})$$

Dividing Equations E2.22 or E2.24, as applicable, by Equation E2.31, the uncertainty in DAQ in terms of temperature can be deduced to use in Equation E2.27. With 4-wire connectivity the RTDs were directly online calibrated in DAQ system using dry-block precision calibrator and the cold junction compensation of the DAQ was activated to built-in. These helped greatly reduce the other errors associated with resolution, wire, connection, DAQ system, DAQ response with RTD sensitivity etc. It has been observed that the magnitude of U_{DAQ} in Equation E2.27 is negligible as compared to the magnitude of U_{RTD} . Thus to minimize the complexity in calculations the Equations E2.28 to E2.31 were ignored and the Equation E2.27 was used in all calculations by dropping the term U_{DAQ} without much sacrifice in error estimation.

Thermocouples (TCs)

Type-T thermocouple is used in current study with an accuracy of 0.5°C at a resolution of 0.1°C . The instrumental error was estimated as follows (Equation E1b).

$$B_{\text{TC}} = \sqrt{(0.1)^2 + (0.5)^2} = 0.509^\circ\text{C} . \quad (\text{E2.32})$$

Since the sample size for all experimental runs were $N \geq 1000$, the student t was set to 1.962 in precision error calculation. The uncertainty in TC was estimated using Equations E1, E1.1, E1.2b and E1.3b as follows.

$$U_{\text{TC}} = \sqrt{B_{\text{TC}}^2 + P_{\text{TC}}^2} = \sqrt{(0.509)^2 + \left(1.962 * \frac{S_x}{\sqrt{N}}\right)^2} \quad [^\circ\text{C}]. \quad (\text{E2.33})$$

The total uncertainty in temperature that was measured using TCs and DAQ together is,

$$U_{\text{T,TC}} = \sqrt{U_{\text{TC}}^2 + U_{\text{DAQ}}^2} = \sqrt{(0.509)^2 + \left(1.962 * \frac{S_x}{\sqrt{N}}\right)^2} + U_{\text{DAQ}} \quad [^\circ\text{C}]. \quad (\text{E2.34})$$

where the $U_{\text{DAQ-TC}}$ can be deduced similar to Equation E2.31.

The TCs were directly online calibrated in DAQ system using dry-block precision calibrator and the DAQ cold junction compensation was set to built-in, which helped greatly reduce the other errors. Thus except for the accuracy the errors associated with wire lengths, connections, TC spherical tips, DAQ system, TC sensitivity, linearity, repeatability, etc. are considered to be already compensated in the calibration. It is also seen that the U_{DAQ} in Equation E2.34 is negligible as compared to U_{TC} magnitude. Therefore to avoid tedious calculation the term U_{DAQ} was dropped from Equation E2.34 without any significant tax in error estimation.

E2.4 Pressure transducers (PTD) – Liquid side

As mentioned before to capture best narrow range accuracy several PTD sets were used depending on the range of liquid flow rate. Manufacturer supplied RSS accuracies including all errors are given in Table 4.2 as $B_{PTD} = 0.25\%$ & 0.08% of FS V_{DAQ} reading. The sample size in all experiments were $N \geq 1000$ i.e. $t = 1.962$ for precision error calculation. The uncertainty in PTD was estimated using Equations E1 and E1.1 to E1.3.

$$U_{PTD[V]} = \sqrt{B_{PTD}^2 + P_{PTD}^2} = \sqrt{(0.0025V_{DAQ})^2 + \left(1.962 * \frac{S_X}{\sqrt{N}}\right)^2} \quad [V]. \quad (E2.35)$$

The Equations E2.22 and E2.23 for U_{DAQ} are applicable here since the PTDs were set to 0-5 Volt DC nominal output to the DAQ system. The total uncertainty in volt unit in pressure that was measured using PTDs and DAQ together is,

$$\begin{aligned} U_{p[V]} &= \sqrt{U_{PTD}^2 + U_{DAQ}^2} = \sqrt{(0.0025V_{DAQ})^2 + \left(1.962 * \frac{S_X}{\sqrt{N}}\right)^2 + U_{DAQ}^2}, \\ &= \sqrt{\left(4.12867 * 10^{-4}\right)^2 + \left(25.65562 * 10^{-4} * V_{DAQ}\right)^2 + \left(1.962 * \frac{S_X}{\sqrt{N}}\right)^2} \quad [V] \end{aligned} \quad (E2.36a)$$

and at full scale reading of 5 Volt DC i.e. the maximum uncertainty in pressure,

$$U_{p[V],max} = \sqrt{\left(132.40677 * 10^{-4}\right)^2 + \left(1.962 * \frac{S_X}{\sqrt{N}}\right)^2} \quad [V] \quad (E2.36b)$$

Equation E2.36 gives the uncertainty in PTD in voltage unit that need to be converted first into psi and then into Pa unit. This is usually done using the voltage vs psi calibration data supplied by the manufacturer and curve produced and verified by the candidate during experiment. There are a number of linear calibration curves produced (as presented by Equation 4.7 in Table 4.6 in Section 4.5.2) all of which follow the form,

$$p_{[\text{psi}]} = mV_{\text{DAQ}} - C, \text{ where } m = \text{slope and } C = \text{constant vertical distance.} \quad (\text{E2.37})$$

The uncertainty in p in psi unit is obtained from the slope of the calibration curve, which is the sensitivity of the PTD. This is achieved by partial derivation of Equation E2.37.

$$\begin{aligned} \frac{\partial p_{[\text{psi}]}}{\partial V_{\text{DAQ}}} &= m, \text{ [psi/Volt]} \\ U_{p_{[\text{psi}]}} &= \sqrt{\left(\frac{\partial p_{\text{psi}}}{\partial V_{\text{DAQ}}} * U_{p[\text{v}]}\right)^2} = \sqrt{(m * U_{p[\text{v}]})^2} = m * U_{p[\text{v}]} \text{ [psi]} \end{aligned} \quad (\text{E2.38})$$

The uncertainty in p in Pascal unit (Pa) is obtained from the relationship of unit conversion between the psi and Pa as follows,

$$\begin{aligned} p_{[\text{Pa}]} &= 6894.76 p_{[\text{psi}]} \text{ [Pa]}, \text{ and } \frac{\partial p_{[\text{Pa}]}}{\partial p_{[\text{psi}]}} = 6894.76 \text{ [Pa/psi]} \\ U_{p_{[\text{Pa}]}} &= \sqrt{\left(\frac{\partial p_{[\text{Pa}]}}{\partial p_{[\text{psi}]}} * U_{p_{[\text{psi}]}}\right)^2} = \sqrt{(6894.76 * U_{p_{[\text{psi}]}})^2} = 6894.76 * U_{p_{[\text{psi}]}} \text{ [Pa]} \end{aligned} \quad (\text{E2.39})$$

According to the range of PTD used in the experimental runs, the uncertainties in respective pressure measurements are estimated using Equations E2.35 to E2.39 and 4.7.

E2.5 Mass flow rate measurements – Liquid side

Digital volume flow meter (DFM)

The liquid side mass flow rates were calculated from the volume flow rates measured using the DFM. The DFM is shown in Figure 4.11a and the manufacturer supplied total absolute accuracy specifications and the calibration data are given in Tables 4.2 and 4.4. The maximum error in DFM is $B_{DFM} = 2.5\%$ of FSO V_{DAQ} reading. The uncertainty in DFM was deduced using Equations E1, E1.1, E1.2b and E1.3b.

$$U_{DFM[V]} = \sqrt{B_{DFM}^2 + P_{DFM}^2} = \sqrt{(0.025V_{DAQ})^2 + \left(1.962 * \frac{S_X}{\sqrt{N}}\right)^2} \quad [V]. \quad (E2.40)$$

The Equations E2.22 and E2.23 for U_{DAQ} are applicable here since the DFM was set to 0-5 Volt DC nominal output to the DAQ system. The total uncertainty in volt unit in volume flow rate that was measured using in combination of DFM and DAQ is,

$$\begin{aligned} U_{\dot{V}[V]} &= \sqrt{U_{DFM}^2 + U_{DAQ}^2} = \sqrt{(0.025V_{DAQ})^2 + \left(1.962 * \frac{S_X}{\sqrt{N}}\right)^2 + U_{DAQ}^2}, \\ &= \sqrt{(4.12867 * 10^{-4})^2 + (250.07 * 10^{-4} * V_{DAQ})^2 + \left(1.962 * \frac{S_X}{\sqrt{N}}\right)^2} \quad [V] \end{aligned} \quad (E2.41a)$$

or at full scale reading of 5 Volt DC i.e. the maximum uncertainty in volume flow rate,

$$U_{\dot{V}[V],max} = \sqrt{(1254.46 * 10^{-4})^2 + \left(1.962 * \frac{S_X}{\sqrt{N}}\right)^2} \quad [V] \quad (E2.41b)$$

Equation E2.41 gives the uncertainty in DFM volume flow rate in voltage unit that is converted into LPM and then m^3/s unit. This is usually done using the voltage vs LPM calibration data supplied by the manufacturer and curve produced and verified by during experiments. There are two curves, one for water flow and the other for glycol-water mixture flow as illustrated in Figure 4.13c. Both curves have following linear form,

$$\dot{V}_{[\text{LPM}]} = mV_{\text{DAQ}} + C, \text{ where } m = \text{slope, and } C = \text{constant vertical distance.} \quad (\text{E2.42})$$

The uncertainty in \dot{V} in LPM unit is obtained from the slope of the calibration curve, which is also the sensitivity of the DFM and derived from Equation E2.42 as follows.

$$\begin{aligned} \frac{\partial \dot{V}_{[\text{LPM}]}}{\partial V_{\text{DAQ}}} &= m, \text{ [LPM/Volt]} \\ U_{\dot{V}_{[\text{LPM}]}} &= \sqrt{\left(\frac{\partial \dot{V}_{[\text{LPM}]}}{\partial V_{\text{DAQ}}} * U_{\dot{V}_{[\text{V}]}} \right)^2} = \sqrt{(m * U_{\dot{V}_{[\text{V}]}})^2} = m * U_{\dot{V}_{[\text{V}]}} \text{ [LPM]} \end{aligned} \quad (\text{E2.43})$$

The uncertainty in \dot{V} in m^3/s is obtained from the relationship of unit conversion relationship between LPM and m^3/s as follows,

$$\begin{aligned} \dot{V}_{[\text{m}^3/\text{s}]} &= \frac{\dot{V}_{[\text{LPM}]}}{60000} \text{ [m}^3/\text{s}], \quad \text{and} \quad \frac{\partial \dot{V}_{[\text{m}^3/\text{s}]}}{\partial \dot{V}_{[\text{LPM}]}} = 1.667 * 10^{-5} \text{ [m}^3/\text{s}/\text{LPM}] \\ U_{\dot{V}_{[\text{m}^3/\text{s}]}} &= \sqrt{\left(\frac{\partial \dot{V}_{[\text{m}^3/\text{s}]}}{\partial \dot{V}_{[\text{LPM}]}} * U_{\dot{V}_{[\text{LPM}]}} \right)^2} = 1.667 * 10^{-5} * U_{\dot{V}_{[\text{LPM}]}} \text{ [m}^3/\text{s}] \end{aligned} \quad (\text{E2.44})$$

The uncertainty in liquid side total mass flow rate measurement using DFM was obtained by partial derivation of Equation 5.6a as follows,

$$\dot{m} = \rho \dot{V}_{[m^3/s]} \text{ [kg/s]}, \text{ getting partial derivatives, } \frac{\partial \dot{m}}{\partial \rho} = \dot{V}_{[m^3/s]} \text{ and } \frac{\partial \dot{m}}{\partial \dot{V}_{[m^3/s]}} = \rho;$$

$$U_{\dot{m}\text{-DFM}} = \sqrt{\left(\frac{\partial \dot{m}}{\partial \rho} * U_{\rho}\right)^2 + \left(\frac{\partial \dot{m}}{\partial \dot{V}_{[m^3/s]}} * U_{\dot{V}_{[m^3/s]}}\right)^2} = \sqrt{\left(\dot{V}_{[m^3/s]} * U_{\rho}\right)^2 + \left(\rho * U_{\dot{V}_{[m^3/s]}}\right)^2} \text{ [kg/s]} \quad \text{(E2.45a)}$$

In relative term the absolute uncertainty in Equation E2.45a takes the following form,

$$\frac{U_{\dot{m}\text{-DFM}}}{\dot{m}} * 100 = \left(\sqrt{\left(\frac{U_{\rho}}{\rho}\right)^2 + \left(\frac{U_{\dot{V}_{[m^3/s]}}}{\dot{V}_{[m^3/s]}}\right)^2} \right) * 100 \text{ [\%]}. \quad \text{(E2.45b)}$$

Manual mass flow rate measurements- bucket-weigh-stop watch method

All the experimental runs for water flow were carried out using the DFM backed by manual measurement using bucket-weigh-stop watch method. In some of the glycol flow experiments the manual measurements were taken into consideration. A digital stop-watch and a digital weighing scale were used in this measurement.

Errors in stop-watch: The stopwatch has an accuracy of $B_{\text{accuracy}} = B_I = 0.5$ sec, instrumental 0th order bias limit (half of the resolution) of $B_{\text{resolution}} = B_0 = 0.125$ sec and a digital error of $B_{\text{digit}} = 0.05$ sec. A digital device may have some digital error, which is

usually taken as one half times the least digit and is considered as the bias error. In light of Equation E1b, the total bias error associated with the stopwatch was estimated as,

$$B_{\text{stopwatch}} = \sqrt{B_1^2 + B_0^2 + B_{\text{digit}}^2} = \sqrt{0.5^2 + 0.125^2 + 0.05^2} = 0.518 \text{ sec.} \quad (\text{E2.46})$$

The human errors such as the digit readability (taken as one half times the least scale division of the stopwatch i.e. 0.05 sec) and handling the on-off switch in exact time of liquid mass collection (assumed maximum 0.5 sec) were considered as the precision errors. These gave a total stopwatch precision error as follows,

$$P_{\text{stopwatch}} = \sqrt{P_{\text{readability}}^2 + P_{\text{handling}}^2} = \sqrt{(0.05)^2 + (0.5)^2} = 0.502 \text{ sec} \quad (\text{E2.47})$$

The uncertainty in stopwatch was estimated to be,

$$U_t = \sqrt{B_{\text{stopwatch}}^2 + P_{\text{stopwatch}}^2} = \sqrt{(0.518)^2 + (0.502)^2} = 0.723 \text{ sec.} \quad (\text{E2.48})$$

Errors in weighing scale: A Pelouze 70 kg Model-4010 digital weighing scale was used, which has a full-scale accuracy of $B_{\text{accuracy}} = B_1 = 0.0453$ kg. The resolution or the instrumental 0th order bias limit of the scale was taken to be half of the accuracy i.e. $B_{\text{resolution}} = B_0 = 0.02265$ kg. The total bias error for the scale was as,

$$B_{\text{weighing-scale}} = \sqrt{B_1^2 + B_0^2} = \sqrt{(0.0453)^2 + (0.02265)^2} = 0.05065 \text{ kg.} \quad (\text{E2.49a})$$

The human errors associated with bucket handling and a little fluctuation of flow were treated as the precision errors. These errors were assumed to be half of the scale accuracy i.e. $P_{\text{bucket}} = 0.0227$ kg and $P_{\text{fluctuation}} = 0.0227$ kg and introduced as,

$$P_{\text{weighing-scale}} = \sqrt{P_{11}^2 + P_{12}^2} = \sqrt{(0.0227)^2 + (0.0227)^2} = 0.0321 \text{ kg} . \quad (\text{E2.49b})$$

The uncertainty in weighing scale was estimated as follows,

$$U_m = \sqrt{B_{\text{weighing-scale}}^2 + P_{\text{weighing-scale}}^2} = \sqrt{(0.05065)^2 + (0.0321)^2} = 0.059 \text{ kg} . \quad (\text{E2.50})$$

The uncertainty in liquid side total mass flow rate measurement using bucket-weigh-stopwatch method was obtained by partial derivation of Equation 5.6b as follows,

$$\begin{aligned} \dot{m} &= \frac{m}{t} \text{ [kg/s]}, \text{ getting partial derivatives, } \frac{\partial \dot{m}}{\partial m} = t^{-1} \text{ and } \frac{\partial \dot{m}}{\partial t} = mt^{-2}; \\ U_{\text{in-bucket}} &= \sqrt{\left(\frac{\partial \dot{m}}{\partial m} * U_m\right)^2 + \left(\frac{\partial \dot{m}}{\partial t} * U_t\right)^2} = \sqrt{\left(\frac{U_m}{t}\right)^2 + \left(\frac{m * U_t}{t^2}\right)^2} \text{ [kg/s]} . \quad (\text{E2.51a}) \\ &= \sqrt{\left(\frac{0.059 \text{ kg}}{t}\right)^2 + \left(\frac{m * (0.723 \text{ sec})}{t^2}\right)^2} \text{ [kg/s]} \end{aligned}$$

In relative term the absolute uncertainty in Equation E2.51a takes the following form,

$$\begin{aligned} \frac{U_{\text{in-bucket}}}{\dot{m}} * 100 &= \left(\sqrt{\left(\frac{U_m}{m}\right)^2 + \left(\frac{U_t}{t}\right)^2} \right) * 100 \text{ [%]} \\ &= \left(\sqrt{\left(\frac{0.059 \text{ kg}}{m}\right)^2 + \left(\frac{(0.723 \text{ sec})}{t}\right)^2} \right) * 100 \text{ [%]} \end{aligned} . \quad (\text{E2.51b})$$

E2.6 Velocity and mass flow measurements – Air side

The air flow velocity was measured at the center of the test section inlet. The measurements were performed in combination with a differential pressure transducer (PTDD), a Pitot Static Tube, and the DAQ system. This velocity was used to calculate the mass flow rate across the test specimen in the wind tunnel test section. The manufacturer supplied total RSS accuracy of the PTDD is $\pm 1\%$ of FS (Table 4.2). The Pitot probe and PTDD are shown in Figures 4.16c and 4.19a and their error analyses are presented below.

Errors in PTDD: The PTDD was set to 0–10 VDC output of the DAQ. From Equations E1 and E2, the total maximum uncertainty in PTDD is as follows.

$$U_{PTDD} = \sqrt{B_{PTDD}^2 + P_{PTDD}^2} = \sqrt{(1*10/100)^2 + (0)^2} = 0.1 \text{ Volt} = 100 \text{ mV}. \quad (\text{E2.52})$$

Errors in Pitot Static Probe: The stem of the Pitot-static tube has to be installed as perpendicularly to the incoming air flow as possible. This means to make the total pressure port at the tip perfectly parallel to the air flow. In practical situations some misalignment may exist although a $\pm 15^\circ$ variation is acceptable. To be more concerned in uncertainty an installation bias error of $\pm 0.5\%$ of the full scale reading is introduced [227] to account for this error. In light of Equations E1 and E2, the maximum total uncertainty in Pitot static probe was estimated to be,

$$U_{Pitot} = \sqrt{B_{Pitot}^2 + P_{Pitot}^2} = \sqrt{(0.5*10/100)^2 + (0)^2} = 0.05 \text{ Volt} = 50 \text{ mV}. \quad (\text{E2.53})$$

Errors in DAQ System: The actual and maximum uncertainties in DAQ system are calculated by Equations E2.24 and E2.25 for the PTDD output of 0 – 10 VDC.

Errors in measurement: The error in measurements of Pitot static probe reading (the dynamic pressure difference) at DAQ system in voltage unit is considered as the precision error. This precision error is calculated using Equations E1.2 and E1.3 for sample size of $N \geq 1000$.

The total actual and maximum uncertainties in Δp_{pitot} reading in voltage unit are estimated from the RSS of Equations E1.2b, E2.24, E2.25, E2.52, and E2.53 as follows.

$$\begin{aligned}
 U_{\Delta p_{\text{pitot}}}[\text{V}] &= U_{V_{\text{DAQ}}}[\text{V}] = \sqrt{U_{\text{PTDD}}^2 + U_{\text{Pitot}}^2 + U_{\text{DAQ}}^2 + U_{\text{Measurement}}^2} \\
 &= \sqrt{12.5 * 10^{-3} + 3.18166 * 10^{-7} * (V_{\text{DAQ}})^2 + \left(1.962 * \frac{S_X}{\sqrt{N}}\right)^2} [\text{V}], \text{ (Actual)} \quad (\text{E2.54})
 \end{aligned}$$

and

$$\begin{aligned}
 U_{\Delta p_{\text{pitot}}}[\text{V}] &= U_{V_{\text{DAQ}}}[\text{V}] = \sqrt{U_{\text{PTDD}}^2 + U_{\text{Pitot}}^2 + U_{\text{DAQ}}^2 + U_{\text{Measurement}}^2} \\
 &= \sqrt{12.532 * 10^{-3} + \left(1.962 * \frac{S_X}{\sqrt{N}}\right)^2} [\text{V}], \text{ (Maximum)} \quad (\text{E2.55})
 \end{aligned}$$

where the V_{DAQ} (mean of N samples) and S_X (standard deviation of N samples) are in voltage units. Any of the Equations E2.54 or E2.55 can be used in uncertainty calculation without much difference since the errors are mainly dictated by the error in PTDD.

Errors in conversion of velocity (voltage unit to m/s): The error is deduced from the sensitivity of the PTDD-Pitot-DAQ combination as follows using the calibration equation presented in Figure 4.16e.

$$V_{[m/s]} = 6.387 * V_{DAQ[V]}^{0.504} \text{ [m/s]}, \text{ from partial derivatives, } \frac{\partial V_{[m/s]}}{\partial V_{DAQ[V]}} = 3.21905 * V_{DAQ[V]}^{-0.496} .$$

$$U_{V[m/s]} = \sqrt{\left(\frac{\partial V_{[m/s]}}{\partial V_{DAQ[V]}} * U_{V_{DAQ}[V]} \right)^2} = \sqrt{\left(\frac{\partial V_{[m/s]}}{\partial V_{DAQ[V]}} * U_{\Delta p_{Pitot}[V]} \right)^2} \quad , \quad (E2.56)$$

$$= (3.21905 * V_{DAQ[V]}^{-0.496}) * U_{\Delta p_{Pitot}[V]} \text{ [m/s]}$$

where $U_{\Delta p_{Pitot}[V]}$ is taken from Equations E2.54 or E2.55.

Uncertainty in air side mass flow rate calculation

The mass flow rate of air flow through the wind tunnel test section was deduced from the continuity principles as discussed in section 4.3.1 and given by Equation 4.3. The absolute uncertainty in air flow mass flow rate is calculated as follows.

$$\dot{m}_a = \rho_a A_c V_a \text{ [kg/s]}; \text{ getting partial derivatives with respect to } \rho_a, A_c, \text{ and } V_a :$$

$$\frac{\partial \dot{m}_a}{\partial \rho_a} = A_c V_a, \quad \frac{\partial \dot{m}_a}{\partial A_c} = \rho_a V_a, \quad \text{and} \quad \frac{\partial \dot{m}_a}{\partial V_a} = \rho_a A_c; \text{ from where the uncertainty is,}$$

$$U_{\dot{m}_a} = \sqrt{\left(\frac{\partial \dot{m}_a}{\partial \rho_a} * U_{\rho_a} \right)^2 + \left(\frac{\partial \dot{m}_a}{\partial A_c} * U_{A_c} \right)^2 + \left(\frac{\partial \dot{m}_a}{\partial V_a} * U_{V_a} \right)^2} \quad , \quad (E2.57a)$$

$$= \sqrt{(A_c V_a U_{\rho_a})^2 + (\rho_a V_a U_{A_c})^2 + (\rho_a A_c U_{V_a})^2}$$

and the relative uncertainty is deduced by Equation E2.57b below.

$$\frac{U_{\dot{m}_a}}{\dot{m}_a} * 100 = \left[\sqrt{\left(\frac{U_{\rho_a}}{\rho_a} \right)^2 + \left(\frac{U_{A_c}}{A_c} \right)^2 + \left(\frac{U_{V_a}}{V_a} \right)^2} \right] * 100 \text{ [%]}. \quad (E2.57b)$$

The A_c in Equation E2.57 is the 304.8 mm x 304.8 mm square inlet cross-sectional area of the wind tunnel test section, which is inheritably set by the manufacturer. Therefore no dimensional measurement of the area is taken and the uncertainty in area is set to $U_{A_c} \approx 0$. The V_a , ρ_a , and \dot{m}_a are the mean values of density, velocity, and mass flow rate of air for any particular experimental run. The uncertainties in density (U_{ρ_a}) and velocity (U_{V_a}) are calculated from Equations E1.6 and E2.56. Using these values the absolute and relative uncertainty in mass flow rate of air is deduced from Equation E2.57a and E2.57b.

E3. Uncertainty in basic dependent parameters

The uncertainties in the basic dependent parameters, that are a part of the pressure drop and heat transfer results in this study, are first analyzed below.

E3.1 Bulk flow temperatures – Liquid and Air

By partial derivation of *liquid side bulk temperature* (defined by Equation 5.1a), the following can be deduced,

$$T_{b,liq} = \frac{T_{liq,i} + T_{liq,o}}{2}; \quad \frac{\partial T_{b,liq}}{\partial T_{liq,i}} = \frac{1}{2} \quad \& \quad \frac{\partial T_{b,liq}}{\partial T_{liq,o}} = \frac{1}{2}; \quad \text{the absolute uncertainty is,}$$

$$U_{T_{b,liq}} = \sqrt{\left(\frac{\partial T_{b,liq}}{\partial T_{liq,i}} * U_{T_{liq,i}}\right)^2 + \left(\frac{\partial T_{b,liq}}{\partial T_{liq,o}} * U_{T_{liq,o}}\right)^2} = \frac{1}{2} \sqrt{U_{T_{liq,i}}^2 + U_{T_{liq,o}}^2}, \quad (E3.1)$$

and the relative uncertainty is, $\frac{U_{T_{b,liq}}}{T_{b,liq}} * 100 = \frac{\sqrt{U_{T_{liq,i}}^2 + U_{T_{liq,o}}^2}}{T_{liq,i} + T_{liq,o}} * 100$ [%]

where the $U_{T_{liq,i}}$ and $U_{T_{liq,o}}$ are obtained from Equation E2.27.

Similarly by partial derivation of air side bulk temperature (defined by Equation 5.1b) one determines the following,

$$\begin{aligned} \text{The absolute uncertainty, } U_{T_{b,a}} &= \frac{1}{2} \sqrt{U_{T_{a,i}}^2 + U_{T_{a,o}}^2}, \text{ and} \\ \text{The relative uncertainty, } \frac{U_{T_{b,a}}}{T_{b,a}} * 100 &= \frac{\sqrt{U_{T_{a,i}}^2 + U_{T_{a,o}}^2}}{T_{a,i} + T_{a,o}} * 100 \quad [\%] \end{aligned} \quad (E3.2)$$

where the $U_{T_{a,i}}$ and $U_{T_{a,o}}$ are determined as follows.

$$U_{T_{a,i}} = \frac{1}{N} \sqrt{\sum_{i=1}^N U_{T_i}^2} \text{ for } N = 9 \text{ and } U_{T_{a,o}} = \frac{1}{N} \sqrt{\sum_{i=1}^N U_{T_i}^2} \text{ for } N = 25. \quad (E3.3)$$

The term U_{T_i} is obtained from Equation E2.34 above.

E3.2 Inlet-exit temperature differentials – Liquid and Air

By partial derivation of liquid side inlet and exit temperature differential (defined by Equation 5.3), the following are obtained,

$$\begin{aligned} \Delta T_{liq} &= T_{liq,i} - T_{liq,o}; \quad \frac{\partial \Delta T_{liq}}{\partial T_{liq,i}} = 1 \ \& \ \frac{\partial \Delta T_{liq}}{\partial T_{liq,o}} = -1; \text{ the absolute uncertainty is,} \\ U_{\Delta T_{liq}} &= \sqrt{\left(\frac{\partial \Delta T_{liq}}{\partial T_{liq,i}} * U_{T_{liq,i}} \right)^2 + \left(\frac{\partial \Delta T_{liq}}{\partial T_{liq,o}} * U_{T_{liq,o}} \right)^2} = \sqrt{U_{T_{liq,i}}^2 + U_{T_{liq,o}}^2}, \end{aligned} \quad (E3.4)$$

$$\text{and the relative uncertainty is, } \frac{U_{\Delta T_{liq}}}{\Delta T_{liq}} * 100 = \frac{\sqrt{U_{T_{liq,i}}^2 + U_{T_{liq,o}}^2}}{\Delta T_{liq}} * 100 \quad [\%]$$

where the $U_{T_{liq,i}}$ and $U_{T_{liq,o}}$ are obtained from Equation E2.27.

Similarly for air side inlet and exit temperature differential one determines,

$$\begin{aligned} \text{The absolute uncertainty, } U_{\Delta T_a} &= \sqrt{U_{T_{a,i}}^2 + U_{T_{a,o}}^2}, \text{ and the} \\ \text{relative uncertainty, } \frac{U_{\Delta T_a}}{\Delta T_a} * 100 &= \frac{\sqrt{U_{T_{a,i}}^2 + U_{T_{a,o}}^2}}{\Delta T_a} * 100 \text{ [\%]} \end{aligned} \quad (E3.5)$$

where the $U_{T_{a,i}}$ and $U_{T_{a,o}}$ are determined from Equation E3.3.

E3.3 Microchannel cross-sectional area – Single channel

The internal diameter of a channel in the multi-port slab test specimens could not be measured for uncertainty analysis. Manufacturer's supplied mean diameter $D = 1$ mm and the maximum uncertainty of $U_D = 1.5\%$ of diameter (as described in section 4.1) were taken for the uncertainty estimation.

$$\begin{aligned} A &= \frac{\pi D^2}{4}; \Rightarrow \frac{\partial A}{\partial D} = \frac{\pi D}{2}; \text{ the absolute uncertainty is,} \\ U_A &= \sqrt{\left(\frac{\partial A}{\partial D} * U_D\right)^2} = \frac{\pi D U_D}{2} = 0.02356 \text{ mm}^2 = 2.3562 * 10^{-5} \text{ m}^2 \text{ and} \\ \text{the relative uncertainty, } \frac{U_A}{A} * 100 &= \frac{2U_D}{D} * 100 = 3.0 \text{ [\%]} \end{aligned} \quad (E3.6)$$

E3.4 Heat transfer surface area – Liquid side

The liquid side single channel surface area calculation is given by Equation E2.3.

E3.5 Surface temperature – Test specimen wall

As mentioned before, 48 thermocouples were used to measure the surface temperatures of the test slab at different locations along the flows. The uncertainty in this surface temperature measurements were estimated as follows.

$$U_{T_s} = \frac{1}{N} \sqrt{\sum_{i=1}^N U_{T_i}^2} \text{ for } N = 48. \quad (\text{E3.7})$$

The U_{T_i} for each of 48 thermocouple probes is obtained from Equation E2.34 above.

E3.6 Log-mean temperature difference (LMTD) – Overall

The overall LMTD used in current study is defined by Equation 5.15. From the partial derivatives the uncertainty is calculated as follows.

$$\Delta T_{\text{LMTD}} = \frac{\Delta T_1 - \Delta T_2}{\ln\left(\frac{\Delta T_1}{\Delta T_2}\right)};$$

$$\frac{\partial \Delta T_{\text{LMTD}}}{\partial \Delta T_1} = \frac{\ln\left(\frac{\Delta T_1}{\Delta T_2}\right) - \left(1 - \frac{\Delta T_2}{\Delta T_1}\right)}{\left[\ln\left(\frac{\Delta T_1}{\Delta T_2}\right)\right]^2} \text{ and } \frac{\partial \Delta T_{\text{LMTD}}}{\partial \Delta T_2} = \frac{-\ln\left(\frac{\Delta T_1}{\Delta T_2}\right) + \left(\frac{\Delta T_1}{\Delta T_2} - 1\right)}{\left[\ln\left(\frac{\Delta T_1}{\Delta T_2}\right)\right]^2}; \quad (\text{E3.8})$$

$$\text{The absolute uncertainty, } U_{\Delta T_{\text{LMTD}}} = \sqrt{\left(\frac{\partial \Delta T_{\text{LMTD}}}{\partial \Delta T_1} * U_{\Delta T_1}\right)^2 + \left(\frac{\partial \Delta T_{\text{LMTD}}}{\partial \Delta T_2} * U_{\Delta T_2}\right)^2}$$

The $U_{\Delta T_1}$ and $U_{\Delta T_2}$ are calculated via Equations E3.9 and E3.10 below,

$$\Delta T_1 = T_{\text{liq},i} - T_{\text{a},o}; \Rightarrow \frac{\partial \Delta T_1}{\partial T_{\text{liq},i}} = 1 \ \& \ \frac{\partial \Delta T_1}{\partial T_{\text{a},o}} = -1;$$

$$U_{\Delta T_1} = \sqrt{\left(\frac{\partial \Delta T_1}{\partial T_{\text{liq},i}} * U_{T_{\text{liq},i}} \right)^2 + \left(\frac{\partial \Delta T_1}{\partial T_{\text{a},o}} * U_{T_{\text{a},o}} \right)^2} = \sqrt{U_{T_{\text{liq},i}}^2 + U_{T_{\text{a},o}}^2}, \text{ and similarly} \quad (\text{E3.9})$$

$$U_{\Delta T_2} = \sqrt{\left(\frac{\partial \Delta T_2}{\partial T_{\text{liq},o}} * U_{T_{\text{liq},o}} \right)^2 + \left(\frac{\partial \Delta T_2}{\partial T_{\text{a},i}} * U_{T_{\text{a},i}} \right)^2} = \sqrt{U_{T_{\text{liq},o}}^2 + U_{T_{\text{a},i}}^2}, \quad (\text{E3.10})$$

where the $U_{T_{\text{liq},i}}$, $U_{T_{\text{liq},o}}$, $U_{T_{\text{a},i}}$, and $U_{T_{\text{a},o}}$ are obtained from Equations E2.27 and E3.3.

E3.7 Mass velocity or mass flux – Liquid side

The liquid side mass velocity for a single channel in the test slab is defined by Equation 6.3 from where by partial derivatives the uncertainty is calculated as follows.

$$G = \frac{\dot{m}}{A}; \Rightarrow \frac{\partial G}{\partial \dot{m}} = \frac{1}{A} \text{ and } \frac{\partial G}{\partial A} = -\frac{\dot{m}}{A^2}; \text{ the absolute uncertainty,}$$

$$U_G = \sqrt{\left(\frac{\partial G}{\partial \dot{m}} * U_{\dot{m}} \right)^2 + \left(\frac{\partial G}{\partial A} * U_A \right)^2} = \sqrt{\left(\frac{U_{\dot{m}}}{A} \right)^2 + \left(-\frac{\dot{m} U_A}{A^2} \right)^2}, \text{ and } \quad (\text{E3.11})$$

$$\text{the relative uncertainty, } \frac{U_G}{G} * 100 = \sqrt{\left(\frac{U_{\dot{m}}}{\dot{m}} \right)^2 + \left(\frac{U_A}{A} \right)^2} * 100 \text{ [\%]}$$

where the $U_{\dot{m}}$ is calculated from Equations E2.45 or 2.51 as applicable and U_A is obtained from Equation E3.6.

E3.8 Reynolds number – Liquid side

The Reynolds number for single channel is given by Equations 4.15 and 6.17.

$$\text{Re} = \frac{4\dot{m}}{\pi\mu D} = \frac{GD}{\mu} \Rightarrow \frac{\partial \text{Re}}{\partial G} = \frac{D}{\mu}, \quad \frac{\partial \text{Re}}{\partial D} = \frac{G}{\mu}, \quad \text{and} \quad \frac{\partial \text{Re}}{\partial \mu} = -\frac{GD}{\mu^2};$$

$$\text{Absolute uncertainty, } U_{\text{Re}} = \sqrt{\left(\frac{D}{\mu}U_G\right)^2 + \left(\frac{G}{\mu}U_D\right)^2 + \left(-\frac{GD}{\mu^2}U_\mu\right)^2}; \quad , \quad (\text{E3.12})$$

$$\text{Relative uncertainty, } \frac{U_{\text{Re}}}{\text{Re}} * 100 = \sqrt{\left(\frac{U_G}{G}\right)^2 + \left(\frac{U_D}{D}\right)^2 + \left(\frac{U_\mu}{\mu}\right)^2} * 100 \quad [\%]$$

The $U_D = 0.015$ mm (supplied) and U_G and U_μ are taken from Equations E3.11 and E1.6.

E4. Uncertainty in fluid flow parameters – Liquid side

The uncertainties in liquid side fluid flow parameters are presented below.

E4.1 Pressure drops – Total measured & core theoretical

The uncertainty in liquid side total pressure drop is calculated from the total pressures measured at the inlet and exit of the test slab as follows.

$$\Delta p_{\text{total}} = p_i - p_o \Rightarrow \frac{\partial \Delta p_{\text{total}}}{\partial p_i} = 1 \quad \text{and} \quad \frac{\partial \Delta p_{\text{total}}}{\partial p_o} = -1; \quad \text{now the}$$

$$\text{Absolute uncertainty, } U_{\Delta p_{\text{total}}} = \sqrt{\left(\frac{\partial \Delta p_{\text{total}}}{\partial p_i} U_{p_i}\right)^2 + \left(\frac{\partial \Delta p_{\text{total}}}{\partial p_o} U_{p_o}\right)^2} = \sqrt{U_{p_i}^2 + U_{p_o}^2}, \quad (\text{E4.1})$$

$$\text{and the relative uncertainty, } \frac{U_{\Delta p_{\text{total}}}}{\Delta p_{\text{total}}} * 100 = \frac{\sqrt{U_{p_i}^2 + U_{p_o}^2}}{\Delta p_{\text{total}}} * 100 \quad [\%]$$

where the $U_{p,i}$ and $U_{p,o}$ are obtained from Equation E2.39 for respective transducer.

The uncertainty in liquid side theoretical core pressure drop is calculated from the Poiseuille conventional fully developed laminar pipe flow relation from Equation 6.19.

$$\begin{aligned}\Delta p_{th, Po} &= \frac{128\mu GL}{\rho D^2} \Rightarrow \frac{\partial \Delta p_{th, Po}}{\partial \mu} = \frac{128GL}{\rho D^2}, \quad \frac{\partial \Delta p_{th, Po}}{\partial G} = \frac{128\mu L}{\rho D^2}, \\ \frac{\partial \Delta p_{th, Po}}{\partial L} &= \frac{128\mu G}{\rho D^2}, \quad \frac{\partial \Delta p_{th, Po}}{\partial \rho} = \frac{-128\mu GL}{\rho^2 D^2} \text{ and } \frac{\partial \Delta p_{th, Po}}{\partial D} = \frac{-256\mu GL}{\rho D^3}; \\ U_{\Delta p_{th, Po}} &= \frac{128}{\rho D^2} \sqrt{\left(GLU_{\mu} \right)^2 + \left(\mu LU_G \right)^2 + \left(\mu GU_L \right)^2 + \left(\mu GL \frac{U_{\rho}}{\rho} \right)^2 + \left(2\mu GL \frac{U_D}{D} \right)^2}, \quad (E4.2) \\ \frac{U_{\Delta p_{th, Po}}}{\Delta p_{th, Po}} * 100 &= \sqrt{\left(\frac{U_{\mu}}{\mu} \right)^2 + \left(\frac{U_G}{G} \right)^2 + \left(\frac{U_L}{L} \right)^2 + \left(\frac{U_{\rho}}{\rho} \right)^2 + \left(2 \frac{U_D}{D} \right)^2} * 100 \quad [\%]\end{aligned}$$

where $U_D = 0.015$ mm (supplied). The U_{μ} and U_{ρ} are obtained from Equation E1.6 and U_G and U_L are derived from Equations E3.11 and E2.3.

E4.2 Friction factor – Liquid side

The experimental uncertainty in liquid side friction factor at the channel core of the MCHX test slab is calculated from simplified form of Equation 6.18 as follows.

$$\begin{aligned}f &= \frac{D}{L} \left[\frac{2\rho\Delta p}{G^2} - K_{\infty} \right] \Rightarrow \frac{\partial f}{\partial \rho} = \frac{2D\Delta p}{G^2}, \quad \frac{\partial f}{\partial D} = \frac{1}{L} \left[\frac{2\rho\Delta p}{G^2} - K_{\infty} \right], \\ \frac{\partial f}{\partial L} &= \frac{D}{L^2} \left[K_{\infty} - \frac{2\rho\Delta p}{G^2} \right], \quad \frac{\partial f}{\partial G} = -\frac{4\rho D\Delta p}{LG^3} \text{ and } \frac{\partial f}{\partial \Delta p} = \frac{2\rho D}{LG^2}; \\ U_f &= \frac{1}{L^2 G^2} \sqrt{\left[(2\rho L\Delta p - K_{\infty} G) U_D \right]^2 + \left(2DL\Delta p U_{\rho} \right)^2 + \left(2\rho DL U_{\Delta p} \right)^2 \\ &\quad + \left[D \left(K_{\infty} G^2 - 2\rho\Delta p \right) U_L \right]^2 + \left(\frac{4\rho DL\Delta p}{G} U_G \right)^2}\end{aligned} \quad (E4.3)$$

where $U_D = 0.015$ mm. The U_{ρ} , $U_{\Delta p}$, U_L and U_G are obtained from Equations E1.6, E4.1 or E4.2, E2.3 and E3.11 respectively.

E4.3 Poiseuille number – Liquid side

The liquid side Poiseuille number is defined by Equation 2.10 from where by partial derivatives the uncertainty is calculated as follows.

$$Po = f Re \Rightarrow \frac{\partial Po}{\partial f} = Re, \quad \frac{\partial Po}{\partial Re} = f;$$

$$\text{The absolute uncertainty, } U_f = \sqrt{(ReU_f)^2 + (fU_{Re})^2}, \text{ and} \quad (E4.4)$$

$$\text{The relative uncertainty, } \frac{U_{Po}}{Po} * 100 = \sqrt{\left(\frac{U_f}{f}\right)^2 + \left(\frac{U_{Re}}{Re}\right)^2} * 100 \text{ [\%]}$$

where the U_f and U_{Re} are taken from Equations E4.3 and E3.12..

E5. Uncertainty in heat transfer results

The uncertainties in heat transfer results are presented below.

E5.1 Heat transfer rates – Liquid and Air sides

The liquid side heat transfer rate is given in Equations 4.13a and 5.11 from where by partial derivatives the uncertainty is calculated as follows.

$$q_{liq} = (\dot{m}c_p\Delta T)_{liq}, \text{ from partial derivatives ...}$$

$$\left(\frac{\partial q}{\partial \dot{m}}\right)_{liq} = (c_p\Delta T)_{liq}, \quad \left(\frac{\partial q}{\partial c_p}\right)_{liq} = (\dot{m}\Delta T)_{liq} \text{ and } \left(\frac{\partial q}{\partial \Delta T}\right)_{liq} = (\dot{m}c_p)_{liq};$$

$$\text{Absolute uncertainty, } U_{q_{liq}} = \sqrt{(c_p\Delta T U_{\dot{m}})_{liq}^2 + (\dot{m}\Delta T U_{c_p})_{liq}^2 + (\dot{m}c_p U_{\Delta T})_{liq}^2}, \quad (E5.1)$$

$$\text{Relative uncertainty, } \frac{U_{q_{liq}}}{q_{liq}} * 100 = \sqrt{\left(\frac{U_{\dot{m}}}{\dot{m}}\right)_{liq}^2 + \left(\frac{U_{c_p}}{c_p}\right)_{liq}^2 + \left(\frac{U_{\Delta T}}{\Delta T}\right)_{liq}^2} * 100 \text{ [\%]}$$

where the U_{Cp} , $U_{\dot{m}}$ and $U_{\Delta T}$ are obtained using Equations E1.6, E2.45/E2.51 and E3.4.

The air side heat transfer rate is defined by Equation 4.13b. Similar to liquid side, the uncertainty in airside heat transfer rate is calculated as follows.

$$\begin{aligned} \text{Absolute uncertainty, } U_{q_a} &= \sqrt{\left(c_p \Delta T U_{\dot{m}}\right)_a^2 + \left(\dot{m} \Delta T U_{c_p}\right)_a^2 + \left(\dot{m} c_p U_{\Delta T}\right)_a^2}, \\ \text{Relative uncertainty, } \frac{U_{q_a}}{q_a} * 100 &= \sqrt{\left(\frac{U_{\dot{m}}}{\dot{m}}\right)_a^2 + \left(\frac{U_{c_p}}{c_p}\right)_a^2 + \left(\frac{U_{\Delta T}}{\Delta T}\right)_a^2} * 100 \quad [\%], \end{aligned} \quad (\text{E5.2})$$

where the U_{C_p} , $U_{\dot{m}}$ and $U_{\Delta T}$ are obtained using Equations E1.6, E2.57a and E3.5.

E5.2 Heat transfer coefficient – Liquid side

The liquid side heat transfer coefficient is deduced from Newton's law of cooling as defined by Equation 5.12a. From there the uncertainty is calculated as follows.

$$\begin{aligned} h_{\text{liq}} &= \left(\frac{q}{A_s \Delta T_{b,s}}\right)_{\text{liq}} \Rightarrow \left(\frac{\partial h}{\partial q}\right)_{\text{liq}} = \left(\frac{1}{A_s \Delta T_{b,s}}\right)_{\text{liq}}, \quad \left(\frac{\partial h}{\partial A_s}\right)_{\text{liq}} = \left(-\frac{q}{A_s^2 \Delta T_{b,s}}\right)_{\text{liq}} \\ \text{and } \left(\frac{\partial h}{\partial \Delta T_{b,s}}\right)_{\text{liq}} &= \left(-\frac{q}{A_s (\Delta T_{b,s})^2}\right)_{\text{liq}}; \text{ now the uncertainties are:} \\ \text{Absolute, } U_{h_{\text{liq}}} &= \sqrt{\left(\frac{1}{A_s \Delta T_{b,s}} U_q\right)_{\text{liq}}^2 + \left(\frac{q}{A_s^2 \Delta T_{b,s}} U_{A_s}\right)_{\text{liq}}^2 + \left(\frac{q}{A_s (\Delta T_{b,s})^2} U_{\Delta T_{b,s}}\right)_{\text{liq}}^2}, \quad (\text{E5.3}) \\ \text{Relative, } \frac{U_{h_{\text{liq}}}}{h_{\text{liq}}} * 100 &= \sqrt{\left(\frac{U_q}{q}\right)_{\text{liq}}^2 + \left(\frac{U_{A_s}}{A_s}\right)_{\text{liq}}^2 + \left(\frac{U_{\Delta T_{b,s}}}{\Delta T_{b,s}}\right)_{\text{liq}}^2} * 100 \quad [\%] \end{aligned}$$

The U_q and U_{A_s} are obtained from Equations E5.1 and E2.3 and the $U_{\Delta T_{b,s}}$ is given below.

$$\Delta T_{b,s} = T_{b,\text{liq}} - T_s; \quad \frac{\partial \Delta T_{b,s}}{\partial T_{b,\text{liq}}} = 1 \text{ and } \frac{\partial \Delta T_{b,s}}{\partial T_s} = -1; \quad U_{\Delta T_{b,s}} = \sqrt{U_{T_{b,\text{liq}}}^2 + U_{T_s}^2}. \quad (\text{E5.4})$$

where the $U_{T_{b,\text{liq}}}$ and U_{T_s} are calculated using Equations E3.1 and E3.7.

E5.3 Nusselt number – Liquid side

The liquid side Nusselt number is defined by Equation 5.30. The uncertainty is calculated by Equation E5.5. The U_h and U_k are obtained from Equations E5.3 and E1.6.

$$\text{Nu}_{\text{liq}} = \left(\frac{hD}{k} \right)_{\text{liq}} \Rightarrow \frac{\partial \text{Nu}}{\partial h} = \frac{D}{k}, \quad \frac{\partial \text{Nu}}{\partial D} = \frac{h}{k}, \quad \text{and} \quad \frac{\partial \text{Nu}}{\partial k} = -\frac{hD}{k^2};$$

$$\text{Absolute uncertainty, } U_{\text{Nu}} = \sqrt{\left(\frac{D}{k} U_h \right)^2 + \left(\frac{h}{k} U_D \right)^2 + \left(\frac{hD}{k^2} U_k \right)^2}, \quad \text{and} \quad , \quad (\text{E5.5})$$

$$\text{Relative uncertainty, } \frac{U_{\text{Nu}}}{\text{Nu}} * 100 = \sqrt{\left(\frac{U_h}{h} \right)^2 + \left(\frac{U_D}{D} \right)^2 + \left(\frac{U_k}{k} \right)^2} * 100 \quad [\%]$$

E5.4 Thermal resistances – Overall and Liquid side

The overall thermal resistance is defined by Equation 5.18. The uncertainty is calculated by Equation E5.6 as follows.

$$R_{\text{ov}} = \frac{1}{UA} = \frac{F \Delta T_{\text{LMTD}}}{q_{\text{liq}}} \Rightarrow \frac{\partial R_{\text{ov}}}{\partial \Delta T_{\text{LMTD}}} = \frac{F}{q} \quad \text{and} \quad \frac{\partial R_{\text{ov}}}{\partial q} = -\frac{F \Delta T_{\text{LMTD}}}{q^2};$$

$$\text{Absolute uncertainty, } U_{R_{\text{ov}}} = F \sqrt{\left(\frac{U_{\Delta T_{\text{LMTD}}}}{q} \right)^2 + \left(-\frac{F \Delta T_{\text{LMTD}}}{q^2} U_q \right)^2}, \quad \text{and} \quad , \quad (\text{E5.6})$$

$$\text{Relative uncertainty, } \frac{U_{R_{\text{ov}}}}{R_{\text{ov}}} * 100 = \sqrt{\left(\frac{U_{\Delta T_{\text{LMTD}}}}{\Delta T_{\text{LMTD}}} \right)^2 + \left(\frac{U_q}{q} \right)^2} 100 \quad [\%]$$

where the $U_{\Delta T_{\text{LMTD}}}$ is determined from Equations E3.8 and E3.9 and the U_q is calculated using Equation E5.1. The value of F is usually 0.99 to 1 in current test conditions.

The thermal resistance for liquid side is given by Equation 5.19. The uncertainty is calculated in Equation E5.7 as follows.

$$R_{th,liq} = \frac{1}{h_{liq} A_{liq}} = \frac{\Delta T_{b,s}}{q_{liq}} \Rightarrow \frac{\partial R_{th}}{\partial \Delta T_{b,s}} = \frac{1}{q} \text{ and } \frac{\partial R_{th}}{\partial q} = -\frac{\Delta T_{b,s}}{q^2};$$

$$\text{Absolute uncertainty, } U_{R_{th}} = \sqrt{\left(\frac{U_{\Delta T_{b,s}}}{q}\right)^2 + \left(-\frac{\Delta T_{b,s}}{q^2} U_q\right)^2}, \text{ and } , \quad (E5.7)$$

$$\text{Relative uncertainty, } \frac{U_{R_{th}}}{R_{th}} * 100 = \sqrt{\left(\frac{U_{\Delta T_{b,s}}}{\Delta T_{b,s}}\right)^2 + \left(\frac{U_q}{q}\right)^2} * 100 \text{ [\%]}$$

where the U_q and $U_{\Delta T_{b,s}}$ are determined from Equations E5.1 and E5.4.

E5.5 Test specimen Effectiveness

The effectiveness of the heat exchangers i.e. the test specimens MCHX4 and MCHX6 is given by Equation 5.24 from which the uncertainty is calculated as follows.

$$\varepsilon = \frac{q_{liq}}{q_{max}}, \Rightarrow \frac{\partial \varepsilon}{\partial q} = \frac{1}{q_{max}} \text{ and } \frac{\partial \varepsilon}{\partial q_{max}} = -\frac{q}{q_{max}^2};$$

$$\text{Absolute uncertainty, } U_{\varepsilon} = \sqrt{\left(\frac{U_q}{q_{max}}\right)^2 + \left(-\frac{q}{q_{max}^2} U_{q_{max}}\right)^2}, \text{ and } , \quad (E5.8)$$

$$\text{Relative uncertainty, } \frac{U_{\varepsilon}}{\varepsilon} * 100 = \sqrt{\left(\frac{U_q}{q}\right)^2 + \left(\frac{U_{q_{max}}}{q_{max}}\right)^2} * 100 \text{ [\%]}$$

where the U_q is obtained from Equation E5.1 and the $U_{q_{max}}$ is derived below.

The q_{\max} is described by Equations 5.25 and 5.26. The uncertainty is derived as follows.

$$q_{\max} = C_{\min} \Delta T_i, \quad \Rightarrow \frac{\partial q_{\max}}{\partial C_{\min}} = \Delta T_i \quad \text{and} \quad \frac{\partial q_{\max}}{\partial \Delta T_i} = C_{\min};$$

$$\text{Absolute uncertainty, } U_{q_{\max}} = \sqrt{(\Delta T_i U_{C_{\min}})^2 + (C_{\min} U_{\Delta T_i})^2}, \quad \text{and} \quad , \quad (\text{E5.9})$$

$$\text{Relative uncertainty, } \frac{U_{q_{\max}}}{q_{\max}} * 100 = \sqrt{\left(\frac{U_{C_{\min}}}{C_{\min}}\right)^2 + \left(\frac{U_{\Delta T_i}}{\Delta T_i}\right)^2} * 100 \quad [\%]$$

where the $U_{\Delta T_i}$ and $U_{C_{\min}}$ are calculated below.

$$\Delta T_i = T_{\text{liq},i} - T_{\text{a},i} \quad \Rightarrow \quad \frac{\partial \Delta T_i}{\partial T_{\text{liq},i}} = 1 \quad \& \quad \frac{\partial \Delta T_i}{\partial T_{\text{a},i}} = -1 \quad \Rightarrow \quad \Delta T_i = \sqrt{(U_{T_{\text{liq},i}})^2 + (U_{T_{\text{a},i}})^2}, \quad , \quad (\text{E5.10})$$

where the $U_{T_{\text{liq},i}}$ and $U_{T_{\text{a},i}}$ are obtained from Equations E2.27 and E3.3.

The C_{\min} is defined by Equation 5.26, which can be either for liquid side or for air side depending on the minimum magnitude. The uncertainty in general (without any subscript for liquid or air) is calculated as follows.

$$C = \dot{m} c_p \quad \Rightarrow \quad \frac{\partial C}{\partial \dot{m}} = c_p \quad \text{and} \quad \frac{\partial C}{\partial c_p} = \dot{m} \quad \Rightarrow \quad U_C = \sqrt{(c_p U_{\dot{m}})^2 + (\dot{m} U_{c_p})^2},$$

$$U_{C_{\min}} = \min \left[\left(\sqrt{(c_p U_{\dot{m}})^2 + (\dot{m} U_{c_p})^2} \right)_{\text{liq}}, \left(\sqrt{(c_p U_{\dot{m}})^2 + (\dot{m} U_{c_p})^2} \right)_{\text{a}} \right]. \quad (\text{E5.11})$$

The U_{c_p} and $U_{\dot{m}}$ are calculated using Equation E1.6 and either of Equations E2.45 or E2.51 (as applicable) when $(\dot{m}c_p)_{\text{liq}} < (\dot{m}c_p)_{\text{a}}$. If air side is the minimum i.e. $(\dot{m}c_p)_{\text{a}} < (\dot{m}c_p)_{\text{liq}}$, the U_{c_p} and $U_{\dot{m}}$ are calculated using Equations E1.6 and E2.57.

E5.6 Test specimen NTU

The NTU for the heat exchanger test specimens is defined by Equation 5.27. The uncertainty is calculated as follows.

$$NTU = \frac{UA}{C_{\min}} = \frac{1}{R_{\text{ov}} C_{\min}}; \Rightarrow \frac{\partial(NTU)}{\partial R_{\text{ov}}} = \frac{-1}{R_{\text{ov}}^2 C_{\min}} \ \& \ \frac{\partial(NTU)}{\partial C_{\min}} = \frac{-1}{R_{\text{ov}} C_{\min}^2};$$

$$\text{Absolute uncertainty, } U_{NTU} = \sqrt{\left(\frac{U_{R_{\text{ov}}}}{R_{\text{ov}}^2 C_{\min}}\right)^2 + \left(\frac{U_{C_{\min}}}{R_{\text{ov}} C_{\min}^2}\right)^2}, \text{ and} \quad , \quad (\text{E5.12})$$

$$\text{Relative uncertainty, } \frac{U_{NTU}}{NTU} * 100 = \sqrt{\left(\frac{U_{R_{\text{ov}}}}{R_{\text{ov}}}\right)^2 + \left(\frac{U_{C_{\min}}}{C_{\min}}\right)^2} * 100 \text{ [\%]}$$

where the $U_{R_{\text{ov}}}$ and $U_{C_{\min}}$ are obtained from Equations E5.6 and E5.11.

APPENDIX – F

LIST OF CONTRIBUTIONS

LIST OF CONTRIBUTIONS

1. Literature review in microchannel heat transfer and fluid flow subject areas reveals varied and inconsistent reported results. There exists controversy on the applicability of macro scale theory in microchannel flow. Current experimental investigations suggest that the friction factors for developing laminar flows of water and ethylene glycol-water mixture in 1 mm channel could be predicted by macro scale theory. However the heat transfer of simultaneously developing laminar flows of these fluids cannot be estimated by macro scale correlations because they are higher in 1 mm channel and need new correlations, which have been developed in current research.
2. Heat transfer and fluid flow in narrow channel parallel multi-port heat exchanger core having continuous smooth serpentine bend has rarely been studied, which has been investigated in current work.
3. In the open literature, there is a continuous urge for experimental data on narrow channel flow, especially on microchannel heat exchanger. Current study generates experimental database on heat transfer and pressure drop of water and ethylene glycol-water mixture flows in various microchannel slabs and heat exchanger, which will significantly contribute to further research, development and design of miniature heat transfer and fluid flow devices.

4. The heat transfer correlations for hydrodynamically developed but thermally developing laminar flow in conventional pipe are widely available that account for a single flow developing effect. The heat transfer correlation is not yet available in the open literature for a conventional pipe flow which has twice hydrodynamically and thermally developing effects. Current research experimentally investigated the heat transfer characteristics of water as well as glycol-water mixture flows in microchannel in double flow developing situations.
5. The heat transfer in simultaneously developing laminar flow of water in parallel multi-port serpentine microchannel slab is found higher than the conventional heat transfer correlations. A new $Nu = f(Re, Pr)$ correlation is developed in current study that includes double flow development effects in a same flow path.
6. 50% ethylene glycol-water mixture is a commercially important heat transfer fluid used in many heat exchangers. The research on simultaneously developing laminar flow of this fluid is rare in the open literature and not available for 1 mm parallel multi-port serpentine channels. The heat transfer in simultaneously developing laminar flow of glycol-water mixture in parallel multi-port serpentine microchannel slab is observed to be higher than the traditional heat transfer correlations. A new $Nu = f(Re, Pr)$ correlation is developed in current study that takes the effect of double flow development in a same flow stream.
7. The Wilson Plot Technique is a very useful tool for determining the heat transfer coefficient in a heat exchanger where the surface temperature information is not available. This technique is rarely used in conventional heat exchanger analysis

because of difficulty to maintain its stringent experimental operating conditions. Many literatures suggest that the modified version of this technique could predict more accurate results in narrow channel heat exchanger over other methods. To employ the modified Wilson Plot Technique for serpentine microchannel heat exchanger, a problem statement and solution methodology is developed and applied in current study in determining the heat transfer coefficient. This formulation will help one determine heat transfer coefficient in microchannel heat exchanger of current style provided the required experimental operating conditions are maintained.

8. Estimation of heat transfer coefficient requires the data on surface temperature. Measuring the surface temperature is very difficult job in a finned surface heat exchanger. An approach is devised in current study to measure the mean surface temperature of a finned heat exchanger. The measured surface temperatures are verified and validated with numerical simulation within less than 1% variation. The heat transfer coefficients determined from the measured surface temperature compared very good with the Wilson Plot Technique prediction. Now one can use the devised approach to measure the surface temperature of a finned heat exchanger and determine the heat transfer coefficient.
9. Current study described and used a comprehensive pressure balance model to account for the pressure losses in a multi-port parallel serpentine microchannel heat exchanger. This model can be used to accurately separate the pressure drops in each component of a heat exchanger. Present research finds the pressure drop

in the core (straight part) is the highest, in the manifolds is the second highest and in the serpentine is the least. This information would be very useful in the research and design of a microchannel heat exchanger.

10. This study finds that the presence of adiabatic smooth U-type serpentine bend enhances heat transfer significantly with the least penalty of pressure drop as compared to the initial entrance geometry. Therefore the use of such adiabatic serpentine bend in heat exchanger core will greatly increase the heat transfer with minimal pressure drop. This finding will greatly contribute to the research and design of a microchannel heat exchanger.

11. The heat transfer characteristics (Nu, thermal resistance, temperature drops, Re) and the performances (temperature differentials, effectiveness, NTU, pressure drop) of a prototype multi-port microchannel heat exchanger, having parallel channels with adiabatic serpentine bends, are experimentally investigated in this study. The information from the investigation and the acquired experimental data will help in designing a microchannel and in optimizing the appropriate operating conditions for such heat exchanger for given duty. The study provides an indication that there could be a certain numbers of serpentine bends above which the effect of increased heat transfer diminishes. Further experimental and numerical study can help to identify this. However the information from this work will help in designing; redesigning, optimizing and identifying the trade-off between the cost and performance of a heat exchanger for a given heat duty.

VITA AUCTORIS

VITA AUCTORIS

NAME	Md. Mesbah-ul Ghani Khan
PLACE OF BIRTH	Dhawakola, Bogra, Bangladesh
YEAR OF BIRTH	1963
EDUCATION	<p>1973. Completed elementary school (Gr. V) at Dhawakola Govt. Primary School, Bogra, Bangladesh and promoted to Grade VI.</p> <p>1978. Completed 10-year schooling at Gokul T. U. High School, Bogra, Bangladesh and passed the first compulsory public exam SSC (Secondary School Certificate) in Science.</p> <p>1980. Completed 2-year college schooling at Govt. A. H. College, Bogra, Bangladesh and passed the second compulsory public exam HSC (Higher Secondary Certificate) in Science.</p> <p>1986. Received the Degree of Bachelor of Science (B.Sc.) in Mechanical Engineering from Engineering College, Rajshahi, University of Rajshahi, Bangladesh (renamed as Rajshahi University of Engineering and Technology – RUET).</p> <p>2000. Received the Degree of Master of Science (M.Sc.) in Renewable Energy from the University of Oldenburg, Germany.</p> <p>2004. Received the Degree of Master of Applied Science (MASc.) in Mechanical Engineering from the University of Windsor, Ontario, Canada.</p>
EXPERIENCE	<p>1986-2001. Served as Mechanical and senior Mechanical Engineers in two Energy Utility Operators in Bangladesh.</p>
CURRENT	<p>2010-Till. Serving as Heat Transfer Product Development Engineer (HVAC & Chiller), TRANE-Ingersoll Rand, WI, USA.</p> <p>2004-2011. A candidate for the degree of Doctor of Philosophy (Ph.D) in Mechanical Engineering at the University of Windsor, Ontario, Canada. Expecting to graduate in Summer 2011 (May).</p>